



DEGRADATION OF POLYMER-COATED METALS

G.S. Frankel, R.G. Buchheit, H.C. Allen

The Ohio State University

October 2013

Final Report

DISTRIBUTION STATEMENT A. Approved for public release; distribution is unlimited.

© 2013 The Ohio State University

This material is based on research sponsored by the US Air Force Academy under agreement number W9132T-09-2-0021. The U.S. Government is authorized to reproduce and distribute reprints for Governmental purposes notwithstanding any copyright notation thereon. The views and conclusions contained herein are those of the authors and should not be interpreted as necessarily representing the official polices and endorsements, either expressed or implied of the US Air Force Academy or the US Government.

**Office of the Under Secretary of Defense
Acquisition, Technology and Logistics
DoD Corrosion Policy and Oversight
3000 Defense Pentagon
Washington, DC 20301**

Approved for public release; distribution unlimited.

Report Documentation Page			<i>Form Approved OMB No. 0704-0188</i>	
<p>Public reporting burden for the collection of information is estimated to average 1 hour per response, including the time for reviewing instructions, searching existing data sources, gathering and maintaining the data needed, and completing and reviewing the collection of information. Send comments regarding this burden estimate or any other aspect of this collection of information, including suggestions for reducing this burden, to Washington Headquarters Services, Directorate for Information Operations and Reports, 1215 Jefferson Davis Highway, Suite 1204, Arlington VA 22202-4302. Respondents should be aware that notwithstanding any other provision of law, no person shall be subject to a penalty for failing to comply with a collection of information if it does not display a currently valid OMB control number.</p>				
1. REPORT DATE OCT 2013	2. REPORT TYPE N/A	3. DATES COVERED -		
4. TITLE AND SUBTITLE Degradation of Polymer-Coated Materials			5a. CONTRACT NUMBER	
			5b. GRANT NUMBER	
			5c. PROGRAM ELEMENT NUMBER	
6. AUTHOR(S)			5d. PROJECT NUMBER	
			5e. TASK NUMBER	
			5f. WORK UNIT NUMBER	
7. PERFORMING ORGANIZATION NAME(S) AND ADDRESS(ES) The Ohio State University 1960 Kenny Road Columbus, Ohio 43210-1016			8. PERFORMING ORGANIZATION REPORT NUMBER	
9. SPONSORING/MONITORING AGENCY NAME(S) AND ADDRESS(ES)			10. SPONSOR/MONITOR'S ACRONYM(S) CERL, ERDC	
			11. SPONSOR/MONITOR'S REPORT NUMBER(S)	
12. DISTRIBUTION/AVAILABILITY STATEMENT Approved for public release, distribution unlimited				
13. SUPPLEMENTARY NOTES				
14. ABSTRACT This report contains details summaries of investigations related to corrosion and degradation of coated metals, with applications to Army and other DoD service problems. There are projects on the connection of performance in accelerated test conditions to field exposures with a focus on parameters such as ozone and UV that have not received much attention. Many projects describe new, innovative, and sensitive approaches for assessing the degradation of coated metals including direct optical interrogation, AFM scratching, scanning Kelvin Probe, Raman spectroscopy, different IR spectroscopies, and combinations of these techniques. Also included is a study of the degradation of uncoated copper and the influence of parameters such as chloride deposition rate. These topics have also been captured in peer reviewed papers and thesis dissertations, so is being disseminated widely.				
15. SUBJECT TERMS				
16. SECURITY CLASSIFICATION OF:			17. LIMITATION OF ABSTRACT SAR	18. NUMBER OF PAGES 298
a. REPORT unclassified	b. ABSTRACT unclassified	c. THIS PAGE unclassified	19a. NAME OF RESPONSIBLE PERSON	

Abstract

This report contains the findings of investigations into polymer degradation and corrosion. There were seven tasks on different subjects. Following is a short summary of each task.

Task 1. An approach referred to as “Direct Optical Interrogation” (DOI) has been developed as an extension of the thin film pitting approach developed and used by Frankel and others to study and quantify corrosion damage accumulation under corrosion resistant organic coatings. Al and Al-Cu alloy metallizations about 800 nm thick were deposited on glass substrates and then coated with various coatings and coating systems. Samples were introduced to aggressive environments and the progression of corrosion of the metallization under the coating was monitored in situ using low power videography through the transparent backside of the sample. DOI showed that corrosion under coatings was episodic, i.e. marked by periods of intense corrosion propagation and long periods of passivation. Concurrent DOI and electrochemical impedance spectroscopy (EIS) measurements show that EIS results must be interpreted with caution. EIS measurements made when gas bubbles were trapped under coatings or when corrosion sites were temporarily passivated yielded spectra that indicated high corrosion resistance when, in fact, corrosion damage had occurred. Under free corrosion conditions, under coating corrosion occurred at the very margins of stability. Availability of cathodic current appeared to limit corrosion site growth. Systematic exploration of the effects of a chromate and chromate-free conversion coatings, chromate and chromate-free primer coatings and the presence or absence of a polyurethane topcoat confirmed the extraordinary corrosion protection by chromates. A commercial praseodymium-pigmented primer coating was not particularly effective in retarding undercoating corrosion site growth unless paired with a chromate conversion coating. The presence of a topcoat in a conversion coating-primer coating-top coat system dramatically reduced undercoating corrosion and masked many deficiencies of a conversion coating or primer. DOI was used to compare undercoating corrosion that developed due to exposure in ASTM B117, ASTM G85-A5 and outdoor environments. Results showed that similar corrosion morphologies developed in ASTM B117 and static immersion exposures. ASTM G85-A5 exposure produced different corrosion morphologies. Calculation of corrosion growth rates indicated that, initially, the ASTM G85 environment was mild compared with the ASTM B117 and static immersion exposures. However, with time, as the local environments evolved, the ASTM G85 exposure produced a massive number of corrosion sites resulting in severe deterioration. Overall, the evidence was consistent with the idea that both hydrogen reduction and oxygen reduction support local corrosion site growth. In practical embodiments of corrosion protection, every effort should be made to restrict oxygen reduction to slow corrosion growth rates.

Task 2. This project established links between lab and field testing of coated steel samples with the goal of improving prediction of coating failure and painted component lifetime. Carbon steel samples were coated with different polymers, but most of the work was performed with PVB and Eponol coatings. Coating failure can result from changes in properties of the bulk coating polymer or of the coating/substrate interface. Bulk coating properties were assessed using infrared spectroscopy and interface properties with a Scanning Kelvin Probe (SKP). The SKP is a tool that measures the rate of cathodic delamination, and it has previously only been used on model systems. This is the first use of SKP as an assessment tool for the effects of prior degradation during exposure to corrosive conditions. The exposures included several outdoor sites in Hawaii and across the continental US, in ASTM standard cabinet tests, and in a specially constructed chamber that allowed control of certain atmospheric parameters. Both bulk polymer and interface degradation were observed. SKP was found to provide a sensitive assessment of the interface degradation, which allows for a shortening of the exposure time required for evaluation of a coating system. Field exposed samples exhibited both blisters and filiform corrosion (FFC). As a result, a more detailed analysis of FFC was performed, including experiments used to reproduce FFC in the lab. Raman spectroscopy was used to investigate the details of the iron oxide formed as a function of the form of corrosion and exposure conditions. It was possible to use the various measures to rank the corrosivity of the different field sites and to assess the important exposure parameters by investigating weather databases. The roles of exposure conditions, like UV and ozone, were investigated in the special chamber and in the standard cabinets. Finally, the degradation of some commercial coating systems was investigated.

Task 3. Attenuated total reflection Fourier transform infrared (ATR-FTIR) spectroscopy has been used to detect changes at the interfaces between poly(vinyl butyral-co-vinyl alcohol-co-vinyl acetate) (PVB) and ZnSe upon exposure to ozone, humidity and UV-B light. Also, the response of PVB/Al interfaces to water has been studied and compared with the same for Eponol (epoxy resin, diglycidyl ether of bisphenol A)/Al interfaces. In the presence of ozone, humidity and UV-B radiation, an increase in carbonyl group intensity was observed at the PVB/ZnSe interface indicating structural degradation of the polymer near the interface. However, such changes were not observed when PVB-coated ZnSe samples were exposed to moisture and UV-B light in the absence of ozone showing that ozone is responsible for the observed structural deterioration. Water uptake kinetics for the degraded PVB monitored using ATR-FTIR indicated a degradation of the physical structural organization of the polymer film. Exposure of PVB-coated Al thin film to deionized (DI) water showed water incorporation at the interface. There were evidences for polymer swelling, delamination, and corrosion of the Al film under the polymer layer. In contrast, delamination/swelling of the polymer was not observed at the Eponol/Al interface, although water was

still found to be incorporated at the interface. Al-O species were also observed to form beneath the polymer layer. A decrease of the C-H intensities was detected at the PVB/Al interface during the water uptake of the polymer, whereas an increase of the C-H intensities was observed for the Eponol polymer under these conditions. This is assigned to rearrangement of the macromolecular polymer chains upon interaction with water.

Task 4. The effects of environmental exposure on polymer coating degradation were studied by atomic force microscopy (AFM) scratching. Adhesion was assessed by the coating removal rate during controlled-force contact mode scratching in the AFM. Low carbon steel coupons were coated by an ultra high molecular weight epoxy resin and exposed to environments with high relative humidity and exposure to ultraviolet light. AFM scratching was performed both in air and in water to assess the effect of water on adhesion degradation. The average coating removal rate increased when samples were first degraded by environmental exposure and by scratching in water. AFM scratching is shown to be a quantitative method for the assessment of adhesion and adhesion degradation for coatings less than about 4 μm in thickness.

Task 5. The effects of UV, ozone and NaCl on the atmospheric corrosion of Cu have been studied by two types of laboratory exposures of Cu. The first type was exposure of Cu with NaCl deposited before exposure. Initial stage of Cu corrosion was studied via this type of laboratory exposure. The other was exposure of Cu with constant deposition of NaCl during exposure. Kinetics of Cu corrosion under constant deposition of NaCl was studied via the second type of lab exposure. The corrosion products were analyzed by x-ray diffraction and quantified by coulometric reduction. Surface morphology after exposure was studied by scanning electron microscopy. The protection effect of naturally-formed copper oxide was shown by comparing the corrosion behaviors of Cu and Ag with UV and ozone but in the absence of NaCl. UV illumination had a significant accelerating effect on Cu corrosion regardless of presence of ozone. With ozone and NaCl, the accelerating effect of UV was more evident at low RH (60%) than at high RH (90%). Loading of NaCl is critical for formation of $\text{Cu}_2(\text{OH})_3\text{Cl}$, a common corrosion product of Cu in marine environment. Oxidation of Cu_2O to $\text{Cu}_2(\text{OH})_3\text{Cl}$ in the presence of NaCl by oxygen and ozone is a possible pathway for formation of $\text{Cu}_2(\text{OH})_3\text{Cl}$. A laboratory environment chamber with a constant deposition rate of NaCl was built. With this chamber, the corrosion behavior of Cu during constant NaCl deposition was investigated with different CO_2 concentrations and ultraviolet (UV) illumination. An Na_2CO_3 solution was found to be more suitable than KCl solutions for quantification of Cu corrosion products. Cuprite was always the dominant corrosion product during exposure of Cu in various environments. UV illumination accelerated formation of cuprite significantly but had very little effect on formation of cupric corrosion product. CO_2 in the environment was

important in determination of cupric corrosion products. With 350 ppm CO₂, paratacamite was the dominant product, while tenorite was dominant with <1 ppm CO₂. This explains why tenorite is not a common cupric corrosion product in the field. Pitting corrosion was always the dominant form of corrosion at the beginning of the exposure period but uniform corrosion dominated at later times. The new environment chamber enables the determination of Cu corrosion kinetics in the lab, especially the formation of paratacamite, which provides insight into Cu atmospheric corrosion in the field.

Task 6. A probe head for Raman spectroscopy was installed in the sample chamber of a height-regulated Kelvin Probe (KP) in order to focus a laser beam on polymer coated steel samples directly beneath the KP needle and to detect light scattered at the sample surface. This allowed a simultaneous analysis of the polymer/metal interface structure based on Raman spectra and on Volta potential studies performed by the Kelvin Probe during sample exposure in humid and dry air. The interface sensitivity of the assembled setup was demonstrated with the detected sulfate signatures in Raman spectra recorded from Na₂SO₄ particles precipitated at the buried polymer/steel interface. The observed spectral changes were compared to KP data of potential shifts induced by structural rearrangement processes during drying and humidification of the interfacial region. To track the lifting and descent of the polymer layer, the distance between Kelvin Probe needle and polymer surface was monitored in parallel to the KP potential. These data reveal that spectral alterations, potential shifts and distance changes occurred with varying sequence, but were clearly interrelated. The combined KP-Raman spectroscopy approach consequently provides spectroelectrochemical information that is not available from each technique separately and that will be helpful for more detailed interface studies in the future.

Task 7. A laser beam focused beneath a Kelvin probe needle allows for evaluation of laser-induced Volta potential shifts that can be used to identify (ir)reversible structural rearrangements at the sample surface. This work investigates the impact of laser irradiation on different substrate materials and the influence of laser power and wavelength to explore possible additional areas of analytical applications. Complete and instantaneous potential recovery was achieved with a 785 nm beam, whereas inverse and less meaningful potential shifts result for highly reflective Si-wafers. Moreover, similarities to photovoltage transients recorded on solar cell devices are discussed.

Table of Contents

<u>Section</u>	<u>Page</u>
Abstract	ii
Forward	vii
Preface	viii
Task 1 Direct optical interrogation of underfilm corrosion	1
Task 2 Atmospheric Corrosion of Coated Steel; Relationship between Laboratory and Field Testing	100
Task 3 Detection of Degradation at Polymer/Substrate Interfaces by Attenuated Total Reflection Fourier Transform Infrared Spectroscopy	177
Task 4 Assessment of Coating Adhesion Degradation by AFM Scratching	209
Task 5 Atmospheric Corrosion of Cu	218
Task 6 A Simultaneous In Situ Kelvin Probe and Raman Spectroscopy Analysis of Electrode Potentials and Molecular Structures at Polymer Covered Salt Layers on Steel	262
Task 7 Laser Effects on Volta Potential Transients Recorded by a Kelvin Probe	284

Forward

This report provides a detailed summary of the work performed by researchers at The Ohio State University under contract to the US Army Construction Engineering Research Laboratory. The CERL project began in 2009 and finished in 2013. The principle investigators are Gerald Frankel, Rudolph Buchheit, and Heather Allen. The work comprises seven different tasks that are reported separately below.

This project is the second in a series of four-year programs organized through the Office of Corrosion Policy and Oversight in the Office of the Secretary of Defense as part of the University (Technical) Corrosion Collaboration. The focus of much of the work performed in this project is in the area of coatings, primarily coating breakdown and failure. Corrosion protective coatings are tested by exposure to aggressive environments, either controlled in laboratory exposure cabinets such as the ASTM B117 salt spray environment, or on the seashore where natural salt spray and UV radiation are abundant. The challenge is in relating the behavior in these extremely aggressive environments to other field exposures, where components and structures would spend their service life. Even predicting the performance of a corrosion protective coating on the seashore based on the behavior in a salt spray cabinet is not straight forward. There is a real need for a better understanding of the influence of stressing factors on coating performance and for more sensitive testing methods that would allow performance assessments in shorter time periods. These are the topics of several of the tasks described herein.

Preface

The authors of this report gratefully acknowledge the financial support for this work from the Office of the Secretary of Defense and the guidance provided by the Office of Corrosion Policy and Oversight, in particular the director, Dan Dunmire, as well as Rich Hays, Dave Robertson, Dave Oaks and Chris Scurlock. Interactions with Bill Abbott of Battelle are also greatly appreciated. Some samples were provided by the group of Craig Matzdorf at NAVAIR. Outdoor exposures were performed with the help of Lloyd Hihara and his group at the University of Hawaii and Prof. Barkley Sive at the University of New Hampshire. Finally, funding in support of the work done by Dr. Ralf Posner, as post-doctoral researcher was partially provided by the Feodor-Lynen Program of the Alexander von Humboldt Foundation.

This work could not have been possible without the ongoing collaborations with the other members of the Technical Corrosion Collaboration program, in particular those from the University of Virginia, the University of Hawaii, and the University of Southern Mississippi. The OSU students benefited enormously from inputs provided during the review meetings and interactions throughout the year.

The authors of this report are immensely indebted to the dedicated and hard-working graduate students and post docs who did the work reported here. This list of collaborators includes:

Severine Cambier, graduate student
Jinwook Seong, graduate student
Meng Tong Lopez-Garrity, graduate student
Dr. Huang Lin, graduate student
Dr. Christine Lemon, graduate student
Arijit Ghosh, graduate student
Dr. Ralf Posner, post-doc
Dominique Verreault, post doc
Roxanna Sierra, post-doc

Task 1: Direct optical interrogation of underfilm corrosion

1.1 Summary

An approach referred to as “Direct Optical Interrogation” (DOI) has been developed as an extension of the thin film pitting approach developed and used by Frankel and others to study and quantify corrosion damage accumulation under corrosion resistant organic coatings. Al and Al-Cu alloy metallizations about 800 nm thick were deposited on glass substrates and then coated with various coatings and coating systems. Samples were introduced to aggressive environments and the progression of corrosion of the metallization under the coating was monitored *in situ* using low power videography through the transparent backside of the sample. DOI showed that corrosion under coatings was episodic, i.e. marked by periods of intense corrosion propagation and long periods of passivation. Concurrent DOI and electrochemical impedance spectroscopy (EIS) measurements show that EIS results must be interpreted with caution. EIS measurements made when gas bubbles were trapped under coatings or when corrosion sites were temporarily passivated yielded spectra that indicated high corrosion resistance when, in fact, corrosion damage had occurred. Under free corrosion conditions, under coating corrosion occurred at the very margins of stability. Availability of cathodic current appeared to limit corrosion site growth. Systematic exploration of the effects of a chromate and chromate-free conversion coatings, chromate and chromate-free primer coatings and the presence or absence of a polyurethane topcoat confirmed the extraordinary corrosion protection by chromates. A commercial praseodymium-pigmented primer coating was not particularly effective in retarding undercoating corrosion site growth unless paired with a chromate conversion coating. The presence of a topcoat in a conversion coating-primer coating-top coat system dramatically reduced undercoating corrosion and masked many deficiencies of a conversion coating or primer. DOI was used to compare undercoating corrosion that developed due to exposure in ASTM B117, ASTM G85-A5 and outdoor environments. Results showed that similar corrosion morphologies developed in ASTM B117 and static immersion exposures. ASTM G85-A5 exposure produced different corrosion morphologies. Calculation of corrosion growth rates indicated that, initially, the ASTM G85 environment was mild compared with the ASTM B117 and static immersion exposures. However, with time, as the local environments evolved, the ASTM G85 exposure produced a massive number of corrosion sites resulting in severe deterioration. Overall, the evidence was consistent with the idea that both hydrogen reduction and oxygen reduction support local corrosion site growth. In practical embodiments of corrosion protection, every effort should be made to restrict oxygen reduction to slow corrosion growth rates.

1.2 Metallurgical Effects on Corrosion of Thin Metallic Films Under Organic Coatings

1.2.1 List of Figures and Tables

Figure 1.2.1 Instrumental configuration with the side view of the sample.

Figure 1.2.2 Equivalent circuit models for the EIS fittings, (a) Simplified Randles circuit, (b) defective coating model.

Figure 1.2.3 Sequence of images taken of the evolution of aluminum thin film coated with a neat epoxy resin exposed to 0.3M HCl solution

Figure 1.2.4 (a) Total resistance, R , and (b) capacitance, C , of an Al thin film metallization with neat epoxy coatings over top. This sample was exposed to 0.3M HCl.

Figure 1.2.5 Sequence of images taken of the evolution of aluminum thin film under a neat epoxy resin during exposure to a 0.5M NaCl solution.

Figure 1.2.6 OCP results of the pure Al sample coated with neat epoxy exposure to aerated 0.5M NaCl solution.

Figure 1.2.7 Bode plot and phase angle plot of pure Al thin film under neat epoxy coating immersed in 0.5M aerated NaCl solution.

Figure 1.2.8 Bode magnitude and phase angle plots of pure Al thin film under neat epoxy coating immersed in 0.5M aerated NaCl solution. (b) Nyquist plots from the same experiments.

Figure 1.2.9 (a) Linear extrapolation of Coating capacitance C_c at 0 hour exposure. (b) Water uptake for sample pure Al thin film under epoxy coating.

Figure 1.2.10 XRD results of “As sputtered” Al-Cu thin films (a) and “Aged” Al-Cu thin films (b).

Figure 1.2.11 Cross-section of Al-Cu thin film in the aged condition.

Figure 1.2.12 (a) Bode magnitude and phase angle plots of Al-Cu thin film under neat epoxy coating immersed in 0.5M aerated NaCl solution. (b) Nyquist plots from the same experiments.

Figure 1.2.13 (a) Coating capacitance C_c and defect capacitance C_d as function of time; (b) Coating resistance R_{po} and the total resistance R_{tot} at 0.01Hz as function of time.

Figure 1.2.14 Corrosion morphologies developed under neat epoxy applied to “as-deposited” (left) and aged Al-Cu thin films (right) at different exposure times.

Figure 1.2.15 SEM and EDS results of “As-deposited” Al-Cu thin film. (a) site 1; (b) site 2; (3) site 3; (d) high magnification of circled area in (a); (e) high magnification of site 2.

Figure 1.2.16 SEM and EDS results of “Aged” Al-Cu thin film. (a) Whole corroded area; (b) high magnification of circled area in (a); (c) high magnification of circled area in (b).

Figure 1.2.17 Single site perimeter (a) and pit bottom area (b) as a function of time by the image analysis. The closed symbols indicate the original data; the regular lines are the linear fitting results.

Figure 1.2.18 (a) Variation of the perimeter as a function of time for the first corrosion site in the pure Al thin film, (b) plot of the site bottom area as a function of time for the first site (c) anodic current densities as a function of time for the first corrosion site. The dotted lines are the original data, the solid lines are fitting data.

Figure 1.2.19 (a) plot of the variation of the perimeter length as a function of time for site 3 in the as-deposited thin film, b) a plot of the site bottom area as a function of time for site #3 in the as-deposited thin film, c) anodic current densities as a function of time for sites #2 and 3 in the as-deposited thin film. The dotted lines are the original data, the solid lines are fitting data.

Figure 1.2.20 (a) plot of the variation of the perimeter as a function of time for single corrosion site in the aged thin film, b) a plot of the site bottom area as a function of time; c) anodic current densities as a function of time for single corrosion site in Al-Cu thin films. The dotted lines are the original data, the solid lines are fitting data.

1.2.2 Introduction and Background

Organic coatings are an important method for protecting metals and alloys against corrosive environments[1]. It is reported that 90% of metals used in engineering applications are covered with coatings[2]. However, due to the permeable nature of many organic coatings, water and oxygen can penetrate through and reach the metal interface [3-6]. Therefore, the possibility of eventual undercoating corrosion is a concern [7, 8].

It is useful to develop a method that can detect and visualize corrosion under organic coatings[9], since most of the understanding of undercoating corrosion is derived from indirect characterization methods such as electrochemical measurements[10], sensing coating systems and coatings adhesion testing. Visual assessment of corrosion on coated substrates is usually performed after-the-fact on an ex-situ basis and is not an approach for monitoring corrosion during coating service. Therefore, a method to directly visualize corrosion occurring under a coating system brings the possibility of characterizing and understanding the corrosion processes in new and important ways; particularly if those methods can be carried out in real time and in situ.

Some forms of corrosion, such as pitting, have been visualized directly from microscopic measurements[11]. Edeleanu examined the pit propagation in thin aluminum foils that were glued to glass foils. In this way, pit propagation along the aluminum foil could be observed in-situ from the backside by a microscope[12]. Later, Baumgärtner applied the same technique to study the pit growth in pure aluminum[13] and pitting in Al-Cu and Al-Zn solid solutions was investigated by Knörnschild[14]. Crystallographic tunnels were observed to rapidly propagate with sidewalls in (100) planes. The average rate of single tunnel event over its lifetime was equivalent to 10 A/cm^2 , but the momentary rates could reach 100 A/cm^2 . Later studies by Newman et al. used 304 stainless steel foils sandwiched between two optical glass sheets to study corrosion under potentiostatic conditions in 1 M NaCl solution[15]. Corrosion site growth was recorded by a video camera in real time. Pit morphology, especially pit depth and pit width were monitored and estimates of pit growth kinetics were made.

Thin film pitting corrosion provides a unique opportunity to study corrosion in situ [16]. As is the case with the earlier thin foil corrosion experiments, the small thickness dimension of thin film metallizations results in corrosion that rapidly penetrates the metallization and reaches the substrate. Corrosion then grows outward in two dimensions. Frankel was one of the first to study so-called “thin film pitting” corrosion[17]. In his study, pure Al thin films with thicknesses of 150 nm were deposited on glass slides using physical vapor deposition. Thin films then were polarized at different potentials in 0.1 M NaCl solutions and pit growth was estimated visually, Frankel found that both current densities and pit morphologies were dependent on the applied potential[17]. At high potentials, pits were round and smooth and corrosion was controlled by mass transport control, while at low potentials, pits were irregularly shaped convoluted and pit growth occurred under ohmic control. In addition, hydrogen bubbles were observed at the pit periphery, where metal thin films were actively dissolving.

Measurement of pit growth under open circuit potential (OCP) conditions is very difficult to study because pit growth rates are much slower. Generally speaking, OCP pit morphology is more variable because it is constrained by the rate of the supporting cathodic process[18]. Studies were focused on the influence of Cl^- and oxidizing agent such as Fe^{3+} concentrations on the morphology of pits growth in pure aluminum thin films by Balazs[18]. Results showed that pit morphologies were circular dense in high Fe^{3+} concentrations, which Fe^{3+} reduction provided an additional cathodic reaction to support pit growth. Increasing Cl^- concentration would generate a smoother corrosion front, but this corrosion front extended out into the thin films in the form of branches. Other factors reported to affect the pit geometry include acidity and total ion concentration in solution[19].

Pitting corrosion in thin film metallization alloys has received a fair amount of attention. Studies have been made on Al binary alloys[20], stainless steels [21] and NiFe alloys[22]. Newman et al. found that the pitting resistance of stainless steels thin films was higher than bulk materials. In addition, the same trends of current density with applied potentials were found for NiFe thin films as in Al thin films. However, the limiting current densities at high potentials were found to decrease with increasing metallization thickness, which indicated that mass transport and ohmic potential drop were dominant as the metallization thickness increased.

It is well known that an addition of Cu rich precipitates in Al matrix will enhance the mechanical strength of 2xxx and 7xxx series alloys, which are commonly used in aerospace applications. Al-Cu alloy thin films are often used in microelectronic devices due to the fact that Cu can prevent electromigration damage. However, the present of Cu precipitates will increase the susceptibility pitting corrosion in thin films. It has been reported that Cu precipitates can affect the thin film oxide layer thickness and integrity[23]. Moreover, The formation of constituent θ phase (Al_2Cu) also acts as cathodic reduction site, which increases corrosion rates[24]. Studies on the microstructure of Al-Cu thin films have been studied by Frear et al. by using magnetron-sputtered Al-2wt% Cu[25]. Results showed that θ phase was evenly distributed throughout the film both at aluminum grain boundaries and within aluminum grains in the as-deposited condition. However, thin films annealed below the solvus temperature resulted in the θ phase becoming coarse at grain boundaries and diminished within the grains. In a separate study, the morphology of sputtered Al-0.5wt.% Cu thin films was compared with of pure Al thin films with 50nm in thickness under free corrosion conditions. Results showed that the morphology of pits developed in Al-Cu thin films was fractal-like and the precipitates caused more convolution in shape[26]. However, no further work on Al-Cu thin films has been reported.

The Direct Optical Interrogation (DOI) technique is based on thin film pitting corrosion approach. Coatings are applied on top of thin films and undercoating corrosion is in-situ monitored by a microscope from the backside of the sample, which is deposited on a transparent glass slide.

The objective of this research is to develop a technique to supplement traditional investigation approaches for characterizing corrosion underneath of coatings by extending the thin film pitting approach to coated metallizations. Studies reported in this chapter focus on the effects of the metallurgical aspects of thin films under organic coatings on corrosion formation, morphology and growth kinetics. Metallic thin films consisted of pure aluminum, Al-4.9 wt.% Cu in both the as-deposited and artificially aged conditions. Undercoating corrosion damage of three different metallic thin film substrates were monitored in situ using the DOI method.

Corrosion morphology and corrosion growth kinetics of three metallic thin films under the neat epoxy coatings were studied.

1.2.3 Experimental

Al thin films approximately 800 nm thick were deposited on transparent 75 x 25 x 1 mm glass slides of size using a 99.99% pure aluminum source in a vacuum electron beam evaporator. The average deposition rate was 10 Å/s at an evaporation pressure of about 3×10^{-6} Torr.

The Al-Cu thin films 800nm in thickness were deposited on the same transparent glass slide by physical vapor deposition using an Al-4wt%Cu target. The deposition rate was 1.8 Å/s at 5.5×10^{-7} Torr. The compositions of Al-Cu thin films were confirmed to be Al-4.9wt%Cu by using inductively coupled plasma-optical emission spectroscopy (ICP-OES).

Two types of Al-Cu thin films were used. “As-deposited” samples were tested as fabricated without any further heat treatment and were essentially solid solution alloys. The “artificially aged” samples were heat-treated in air at 190 °C for 24 hours to induce precipitation of θ ”, θ' and θ phase (Al₂Cu).

Al-Cu thin films were degreased for several seconds in a solution comprising 1.0 L deionized of (DI) water containing 48.0g Na₂CO₃ and 32.4g Na₂SiO₃ at 65°C. After using DI water to rinse the thin films, they were deoxidized for 3 minutes in a solution comprising 1.0 L of DI water, 30.0g Sanchem 1000TM and 72.0 mL HNO₃ at 55°C. Samples rinsed with DI water and air dried at ambient temperature. Pure Al thin films were rapidly attacked by these solutions, and contact times were limited to 1-2 seconds.

Organic coatings were applied using a spin coater. Coatings were applied using a rotation rate of 250 RPM for 5 minutes. A neat epoxy primer PD381-94 (Aerospace blank coating-no inhibitor) from Akzo Nobel was used. In order to simulate a coating with defects, an artificial defect through the coating around 0.1 mm in diameter was made in the middle of the sample by manual scratching with a sharp stylus.

A schematic of the DOI fixture is shown in Figure 1.2.1. A polymethylmethacrylate cell with an o-ring and an exposed area of about 1 cm² was placed on top of the sample. A backing plate of PlexiglassTM attached to the bottom of the cell was used to hold the sample. In the middle of the plate a hole was made in order to allow capture of images of the sample using a microscope. A transmitted light source located above the sample was used for illumination. A QImagingTM Go-3 color CMOS camera attached to an Olympus SZ61 stereomicroscope was located underneath the electrochemical cell and the sample. As corrosion progressed, the thin sputtered film was perforated and transmitted light passed through the sample to the camera. The progression of corrosion was recorded by TemplateTM video recording software. Selected images of pit shape and size were collected using KMPlayerTM and movies were made by VideoMatchTM frame grabbing. Analysis of the collected images was conducted using ImageJTM.

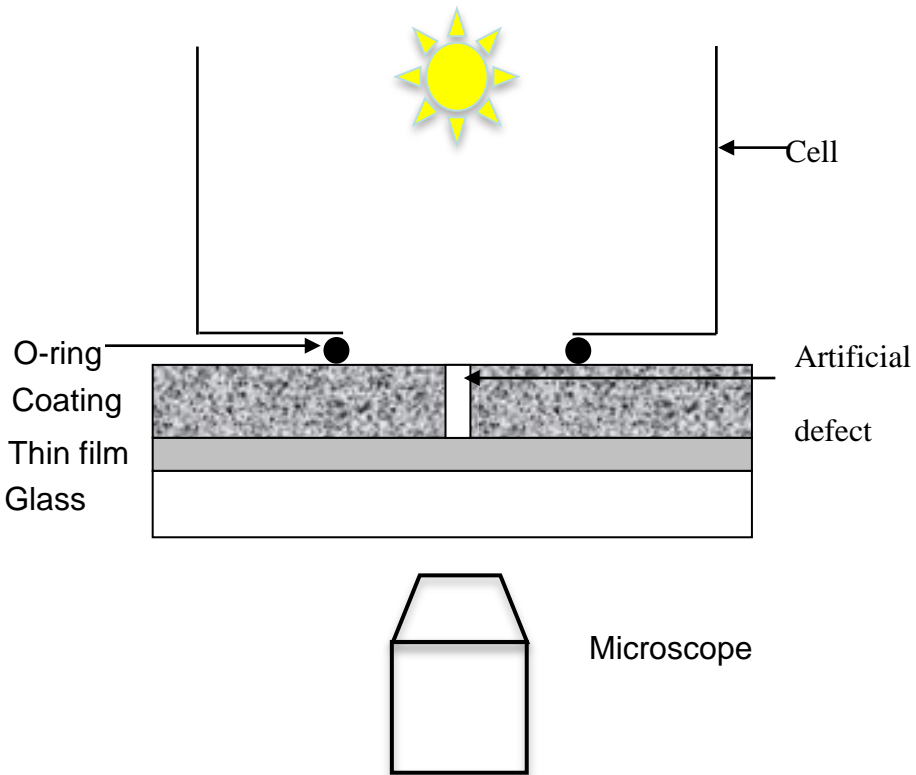


Figure 1.2.1 Instrumental configuration with the side view of the sample.

Electrochemical impedance spectroscopy (EIS) was carried out using a Gamry Reference 600 potentiostat. Periodically measured EIS spectra were used to relate the extent and nature of corrosion to imaging experiments. A standard three-electrode setup was used consisting of a saturated calomel reference electrode and a platinum mesh counter electrode. Experiments were carried out in naturally aerated 0.5 M NaCl solutions. In these experiments, the open circuit potential was monitored for 20 minutes before conducting EIS measurement. The measurements themselves were performed at a frequency range of 10^5 to 10^{-2} Hz using a 10mV sinusoidal voltage perturbation applied with respect to OCP.

The EIS spectra were analyzed using Echem Analyst from Gamry Instruments Inc. The impedance spectra for coated samples in 0.3M HCl solution was fit to a simplified Randles model as shown in Figure 1.2.2 (a). R_s is the solution resistance. R and C are the total sample resistance and capacitance, respectively. In the case of sample exposed to 0.5M NaCl solutions, the coating acted as a barrier yielding a strongly capacitive response (C_c) as shown in Figure 1.2.2 (b). Due to the presence of pores within the coating that act as ionic pathways, the resistance of the pores must also be taken into account and the resistance is represented by the parameter R_{po} . R_d is the defect resistance when corrosion occurs at the interface and C_d is the corresponding capacitance. The constant phase element (CPE) is used instead of pure capacitance in the circuit because the capacitor does not exhibit an ideal capacitance response but rather behaves like a “leaky” capacitor in the practical situation. The real capacitance can be extracted from the following equation[27]:

$$C = Y^{\frac{1}{n}} R^{\frac{1-n}{n}}$$

Equation 1.2.1

In this equation, C is the true capacitance, Y and n are CPE constant and exponent respectively, R is the resistance.

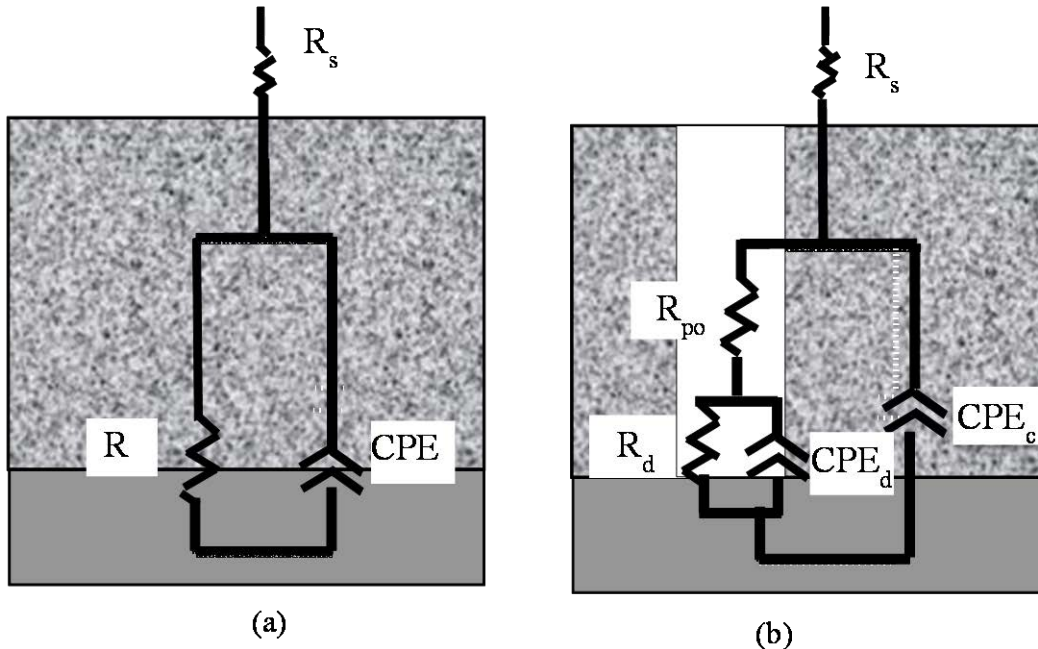


Figure 1.2.2 Equivalent circuit models for the EIS fittings, (a) Simplified Randles circuit, (b) defective coating model.

Low angle X-ray diffraction (XRD) was carried out using Bruker D8 Discover High-Resolution Triple Axis X-Ray Diffractometer with Cu K_{α1} radiation at 40 kV and 40mA. The incident angle was set to 1° and the detector scanned from 10° to 90° with scan speed at 0.1 sec/step and increment at 0.05. Data processing was conducted by Leptos™ and Topaz™.

Cross-section samples of Al-Cu aged thin films were cut by focus ion beam (FIB) milling and characterization was performed by transmission electron microscopy (TEM). Scanning electron microscope (SEM) and energy dispersive spectrometer (EDS) was conducted after sample exposure.

1.2.4 Results

In this study, all experiments were repeated at least in triplicate. There was variability among experiments due to the complexity of the measurement and the nature of the corrosion process. However, when replicate responses are not shown, the results used to illustrate observations were judged to be representative.

The first task of the study was to determine if the DOI approach was capable resolving the undercoating corrosion. Thus, several preliminary investigations were performed. Experiments were conducted on the pure Al thin films coated with neat epoxy and exposed to 0.3

M HCl solution. The evolution of undercoating corrosion morphology is shown in Movie 1.2.1. The evolution of corrosion followed a general sequence of events. First, the corrosion activated and quickly penetrated the thin film. Corrosion sites often formed away from the artificial defect as shown Figure 1.2.2 (a). These sites tended to passivate temporarily resulting in episodic growth. The second stage of corrosion involved uniform corrosion of the thin film sample. This manifested as a gradual brightening of images as the Al thin film dissolved uniformly in Figure 1.2.3 (b).

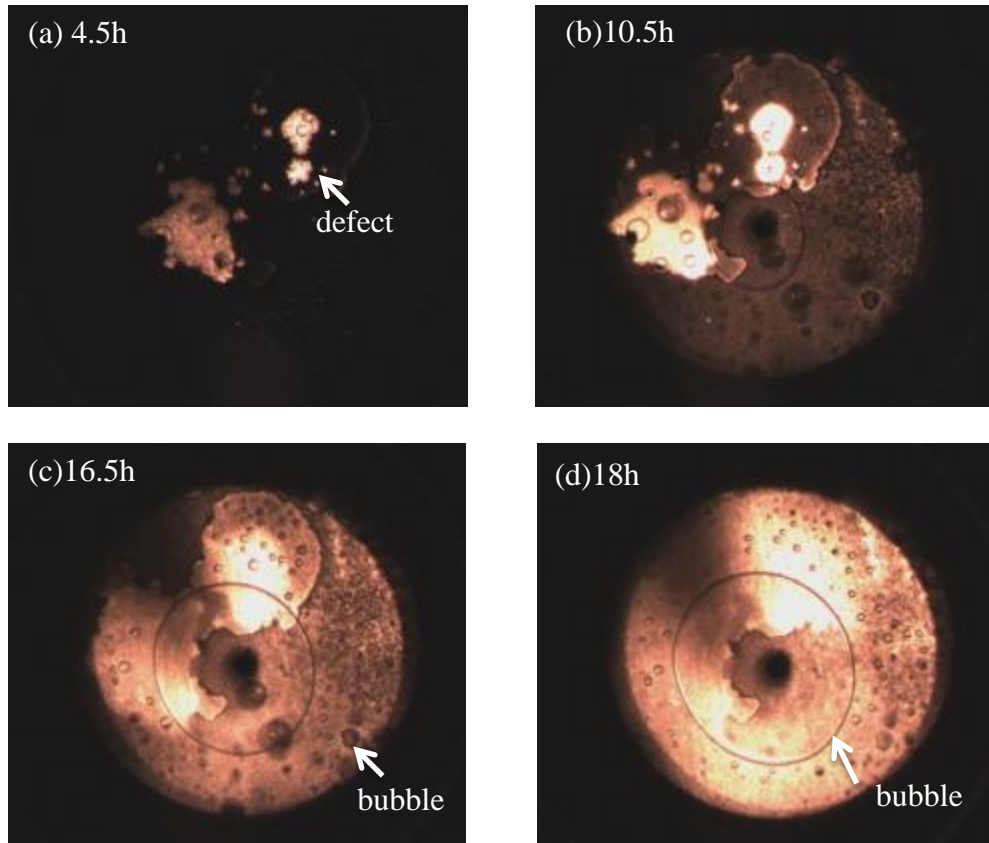
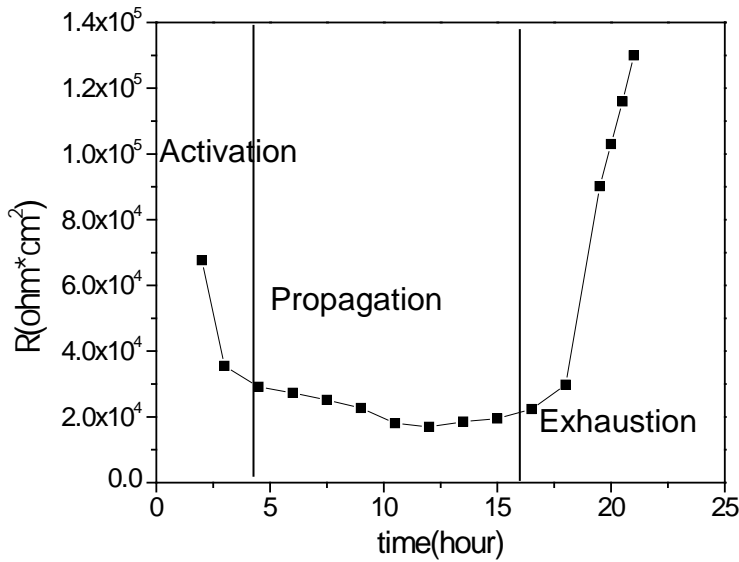


Figure 1.2.3 Sequence of images taken of the evolution of aluminum thin film coated with a neat epoxy resin exposed to 0.3M HCl solution.

Hydrogen gas bubbles were commonly observed throughout the corrosion process (Figure 1.2.3). When uniform corrosion started to occur, many small bubbles nucleated across the surface of the coated sample. Because these bubbles were out of focus, they appear to be attached to the top of the polymer coating and in the bulk electrolyte (Figure 1.2.3 (c)). These bubbles are distinct from larger hydrogen bubbles in corroded regions under the coating. An undercoating bubble from hydrogen gas coalesces under the coating and does not usually escape through the small defect in the organic coating. Such bubbles are in the plane of focus and clearly seen under the organic coating (Figure 1.2.3 (d)). The final stage of corrosion in these experiments involves complete dissolution of the thin Al film and a decrease in of hydrogen gas generation as the thin film becomes completely dissolved as shown in Figure 1.2.3(d).

(a)



(b)

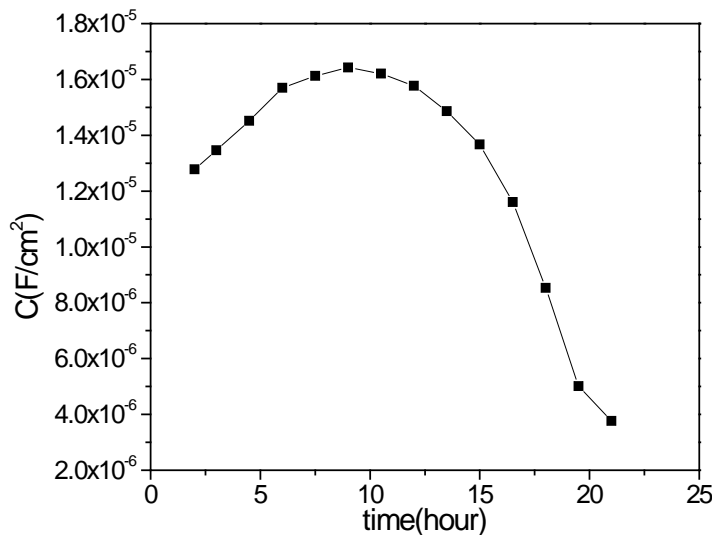


Figure 1.2.4 (a) Total resistance, R , and (b) capacitance, C , of an Al thin film metallization with neat epoxy coatings over top. This sample was exposed to 0.3M HCl.

EIS spectra collected during these exposure experiments exhibit only one broad time constant. Due to the intentional defect present in the samples from the outset of the exposure, the HCl solution immediately contacts the Al thin film and the measured impedance is dominated by the defect impedance. Measured spectra were fitted with a simplified Randles circuit model as shown in Figure 1.2.2 (a) from which the total resistance (R) and sample capacitance (C) were estimated. The variation in polarization resistance and capacitance as function of exposure time are shown in Figure 1.2.4. There are three distinct regimes in both data sets that can be

discriminated based in part by variations in the fitted R and C parameters and partly by visual observations from DOI. At early times, corrosion was activating and increasing. R is observed to fall and the sample capacitance increased. DOI shows multiple corrosion sites nucleating and growing. This regime is termed “activation”. At intermediate times, R is steady at a low value and capacitance is steady at relatively high values. This response is consistent with propagation of corrosion. Because the corrosion process is occurring under free corrosion conditions, the corrosion rate in this regime may be limited by factors that control cathodic reaction kinetics. At the end of the exposure period, DOI shows that corrosion sites have consumed large amounts of the metallization with general thinning attacking the remainder. In this regime, R is observed to increase and C decreases in a manner that is consistent with “exhaustion” of the corrosion process due to complete consumption of the Al metallization.

Movie 1.2.2 shows the nucleation and growth of corrosion sites in an Al thin film covered by a neat epoxy resin during exposure to aerated 0.5 M NaCl solution. The images were collected every 2 hours. The first site started to grow after the sample was exposed to the solution for 16 hours. The images show that morphology of the site was round and smooth and it appeared to have nucleated at random locations across the sample and was not necessarily associated with the intentional defect introduced before the exposure (Figure 1.2.5(a)). This site grew in short episodes separated by long periods of passivity. As time elapsed, more corrosion sites nucleated at different locations across the sample surface. All these sites connected with one another until the aluminum layer was completely dissolved (Figure 1.2.5(d, e)). As was the case in 0.3 M HCl exposures, gas bubble formation and trapping under the coating was observed (Figure 1.2.5(f)).

Corrosion site growth was recorded every 2 minutes as shown in Movie 1.2.3. The growth of a single site was episodic. In this experiment, the first site nucleated when the sample was exposed to the solution for 16 hours and grew for a short period of time (30 minutes) followed by the site passivation for 7 hours. The second stage of the same corrosion site growth started after the sample was exposed to solution for 24 hours with growth period of 26 minutes. After the site repassivated for 5.5 hours, a second corrosion site started to grow with a short growth time followed by growth of a third site. Moreover, the first site was still passive (i.e. the corrosion site size did not change) during growth periods for the second and third sites (Figure 1.2.5(b, c)). This suggests that there is a limitation on the cumulative dissolution rate, or the ability to generate and sustain a critical local environment chemistry that is imposed by the cathodic reaction.

Electrochemical impedance spectroscopy (EIS) was carried out during exposure and imaging experiments to relate the extent and nature of corrosion to periodically measured EIS spectra. In these experiments, the open circuit potential (OCP) was monitored for 20 minutes before conducting the EIS measurement. Figure 1.2.6 shows the OCP results changing with exposure time. The OCP initially moved to higher values due to the incubation time of solution penetrated through the pores of coating and reached the substrates, which resulting in increasing cathodic area to support the oxygen reduction reaction. The first site started to grow indicated by the sudden drop in OCP to about -1.1V vs. SCE, which agreed with the movie captured by the microscope. The OCP then increased due to repassivation of the first site followed by the dramatic fluctuations of OCP resulting from the subsequent nucleation and growth of corrosion sites at different locations. It is known that the fluctuation of potential on the metal surface associated with the changing corrosion rate and changing corrosion morphology[18]. In this case,

time-lapse microscopy suggests that time-dependent potential changes are due to episodic growth multiple corrosion sites.

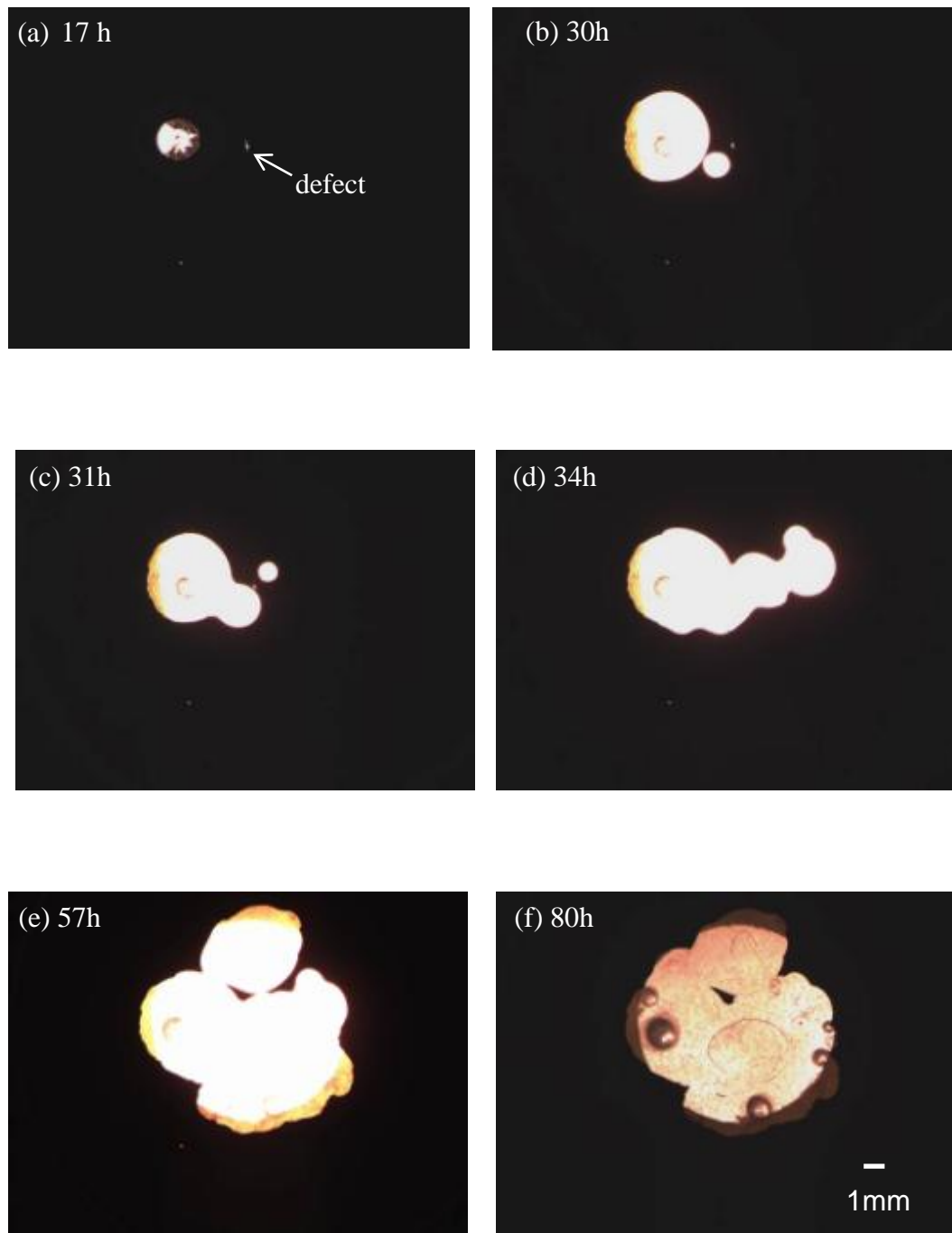


Figure 1.2.5 Sequence of images taken of the evolution of aluminum thin film under a neat epoxy resin during exposure to a 0.5M NaCl solution.

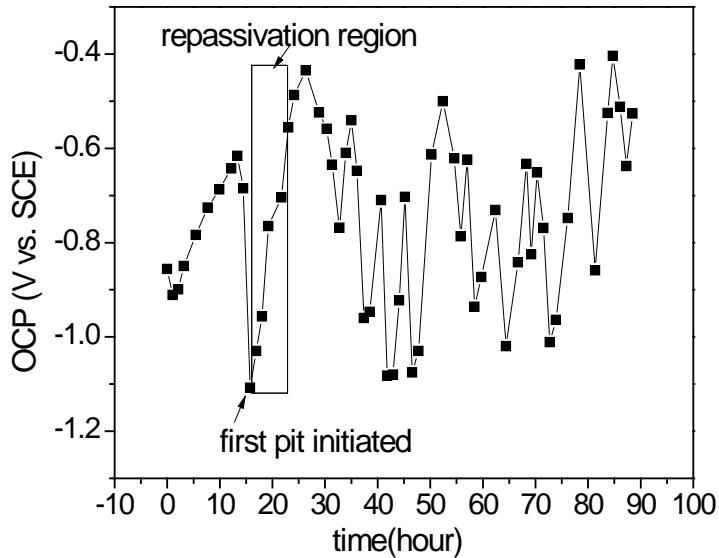


Figure 1.2.6 OCP results of the pure Al sample coated with neat epoxy exposure to aerated 0.5M NaCl solution.

The EIS spectra of an Al metallization coated with a neat epoxy resin exposed to aerated 0.5 M NaCl solution are shown in Figure 1.2.7. The Bode plots indicate a defective coating and progressive corrosion is indicated. Up to 16 hours of exposure, the decrease in impedance in the high frequency regime (> 10 Hz) indicates water uptake. Movie 1.2.2 shows that the thin film was intact up to 16 hours of immersion. The sudden drop at in the impedance magnitude at 16 hours of exposure indicated that undercoating corrosion initiated.

Regular trends in coating resistances and capacitances can be affected by bubbles that block exposed surface areas or by corrosion product that plug coating defects, resulting in an increase in total resistance after corrosion has initiated as shown in Figure 1.2.8 (a). The low frequency regime, which represents corrosion at interface, only shows capacitive behavior after 16 hours. Moreover, the Bode plot curves shift to larger magnitudes after 16 hours. The Nyquist plot of the sample is shown in Figure 1.2.8 (b) shows the irregular trend of the low frequency regime, which the defect resistance increased and decreased with longer exposure.

The coating capacitance C_c is sensitive to water uptake. Brasher and Kingsbury proposed an empirical relation that is widely used to estimate the water uptake from the coating capacitance [10, 28-31]:

$$\emptyset_v = \frac{\log(\frac{C_t}{C_0})}{\log \epsilon_{H_2O}} \quad \text{Equation 1.2.2}$$

In this equation, \emptyset_v is the water volume fraction, C_t is the capacitance at time t , C_0 is the capacitance at time $t = 0$ when the coating is “dry”[29]. In this expression, the permittivity of

pure water, ϵ_{H_2O} is usually taken to be 80 [32]. Equation 1.2.2 is based on the assumption that the capacitance is dictated by relative permittivity of the coating as it takes up water[28].

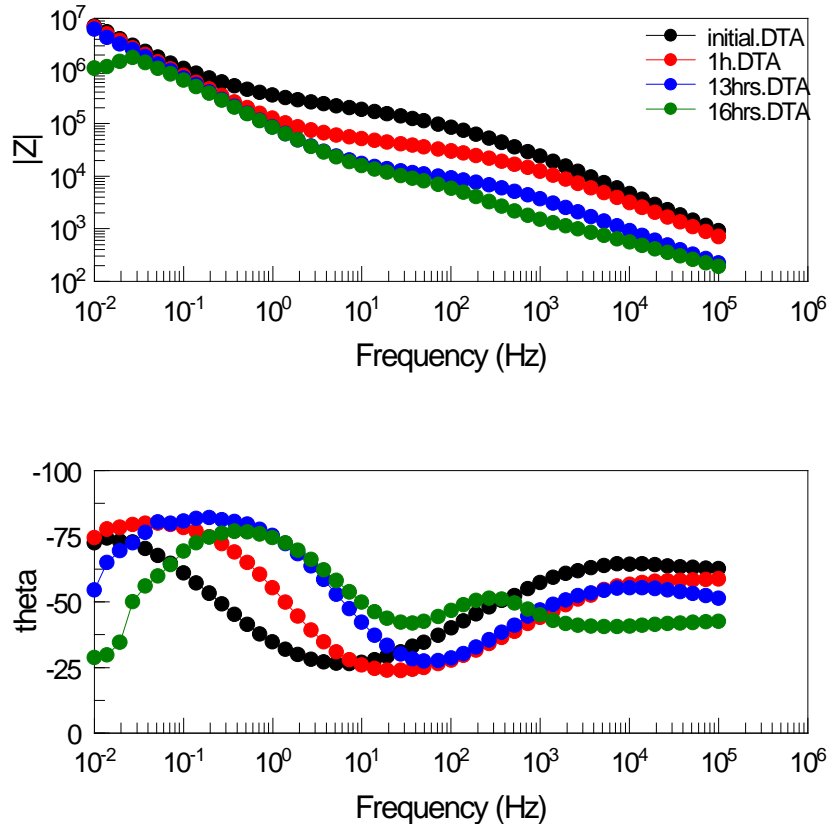


Figure 1.2.7 Bode plot and phase angle plot of pure Al thin film under neat epoxy coating immersed in 0.5M aerated NaCl solution.

The coating capacitance determined as a function of time is shown in Figure 1.2.9 (a). It should be noted that coating capacitance linearly increased until 11 hours of exposure and leveled off at the later stage. Water uptake was calculated according to Equation 1.2.2 and is shown in Figure 1.2.9 (b). In this figure, water content increased up to 25% in a short time and reached a plateau afterwards.

Corrosion evolution for as-deposited Al-Cu thin films and artificially aged Al-Cu thin films were studied and compared. Low angle x-ray diffraction (XRD) in Figure 1.2.10 shows as-deposited thin films are Al-Cu solid solutions and only aluminum diffraction peaks were detected. Al-Cu metallizations aged at 190 °C for 24 hours show Al₂Cu diffraction peaks in addition to aluminum peaks indicating a dispersion of Al₂Cu (θ phase and its precursors θ'' and θ').

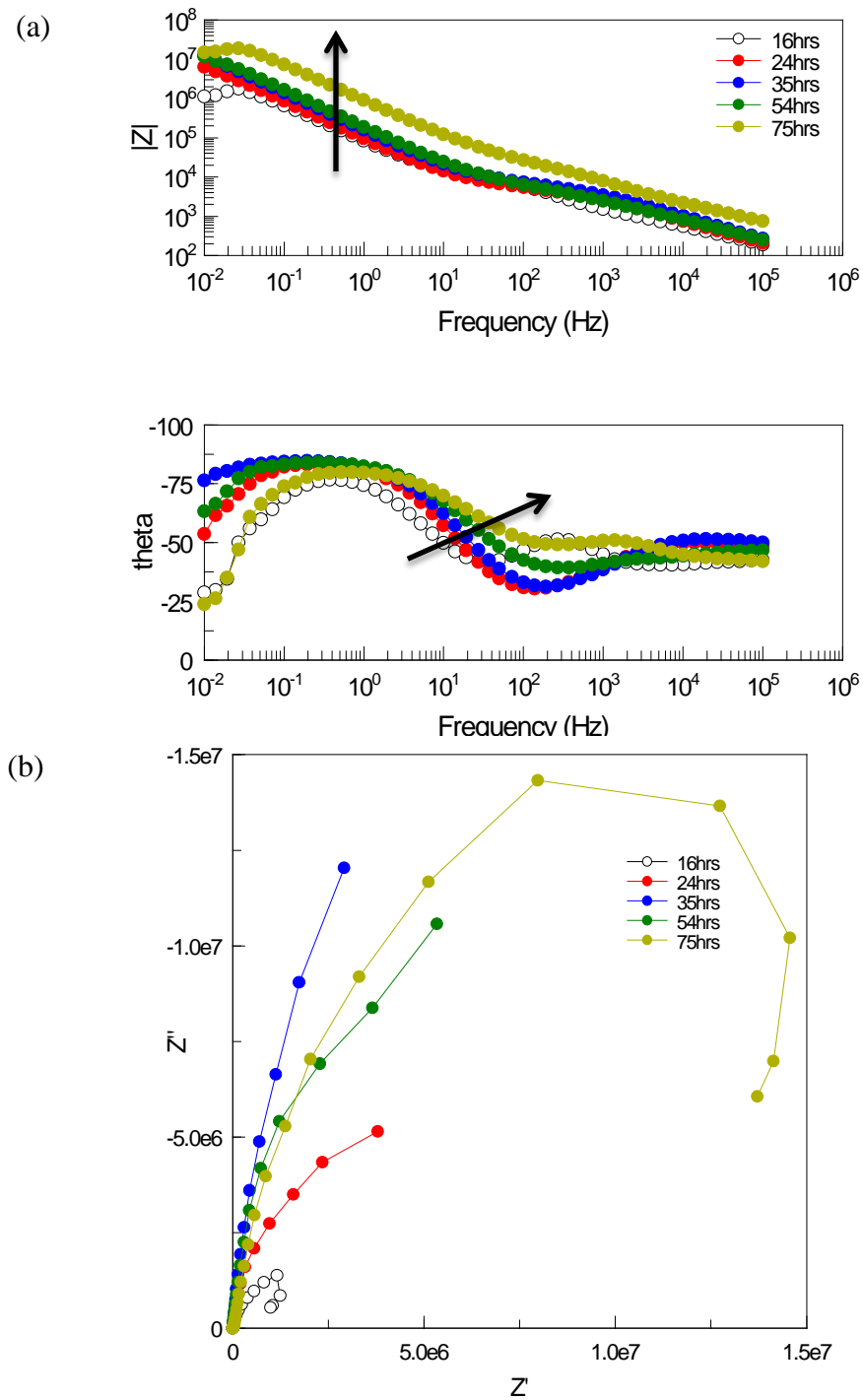
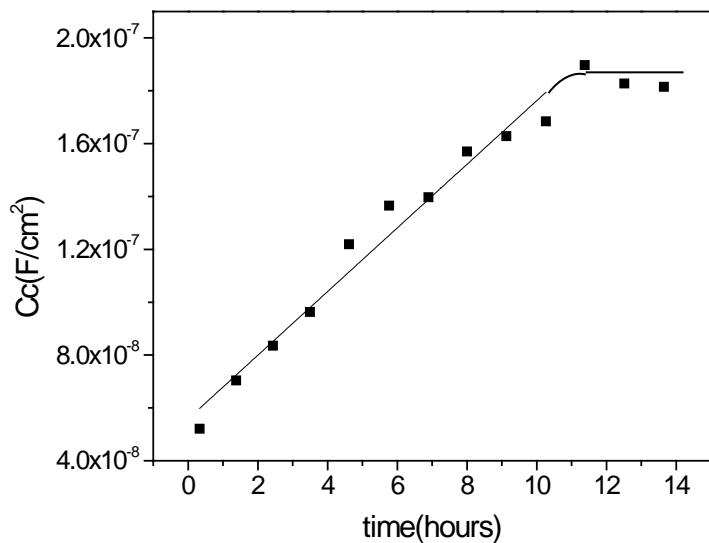


Figure 1.2.8 Bode magnitude and phase angle plots of pure Al thin film under neat epoxy coating immersed in 0.5M aerated NaCl solution. (b) Nyquist plots from the same experiments.

(a)



(b)

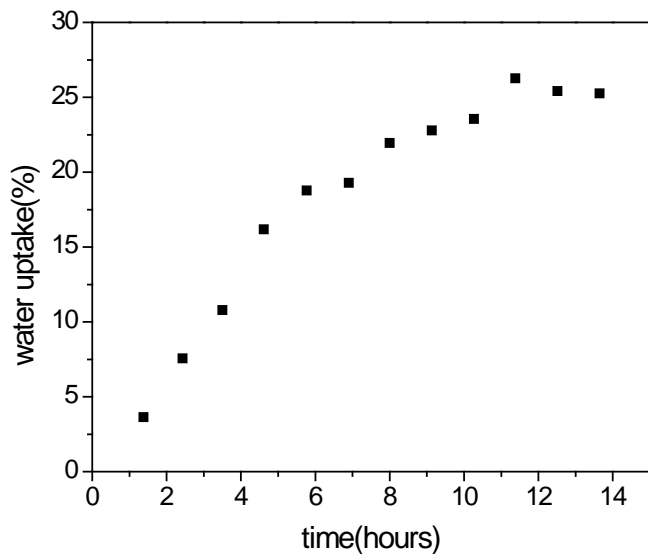


Figure 1.2.9 (a) Linear extrapolation of Coating capacitance C_c at 0 hour exposure. (b) Water uptake for sample pure Al thin film under epoxy coating.

The microstructure of aged Al-Cu metallizations is shown in the cross-section TEM micrograph in Figure 1.2.11. The Al-Cu aged films consisted of columnar grains small white, plate shape precipitates distributed at the grain boundaries with a length around 150 nm. A large amount of spherically shaped particles that were aggregated at the substrate interface were also observed. Both two types of precipitates were rich in Cu as shown in Figure 1.2.11.

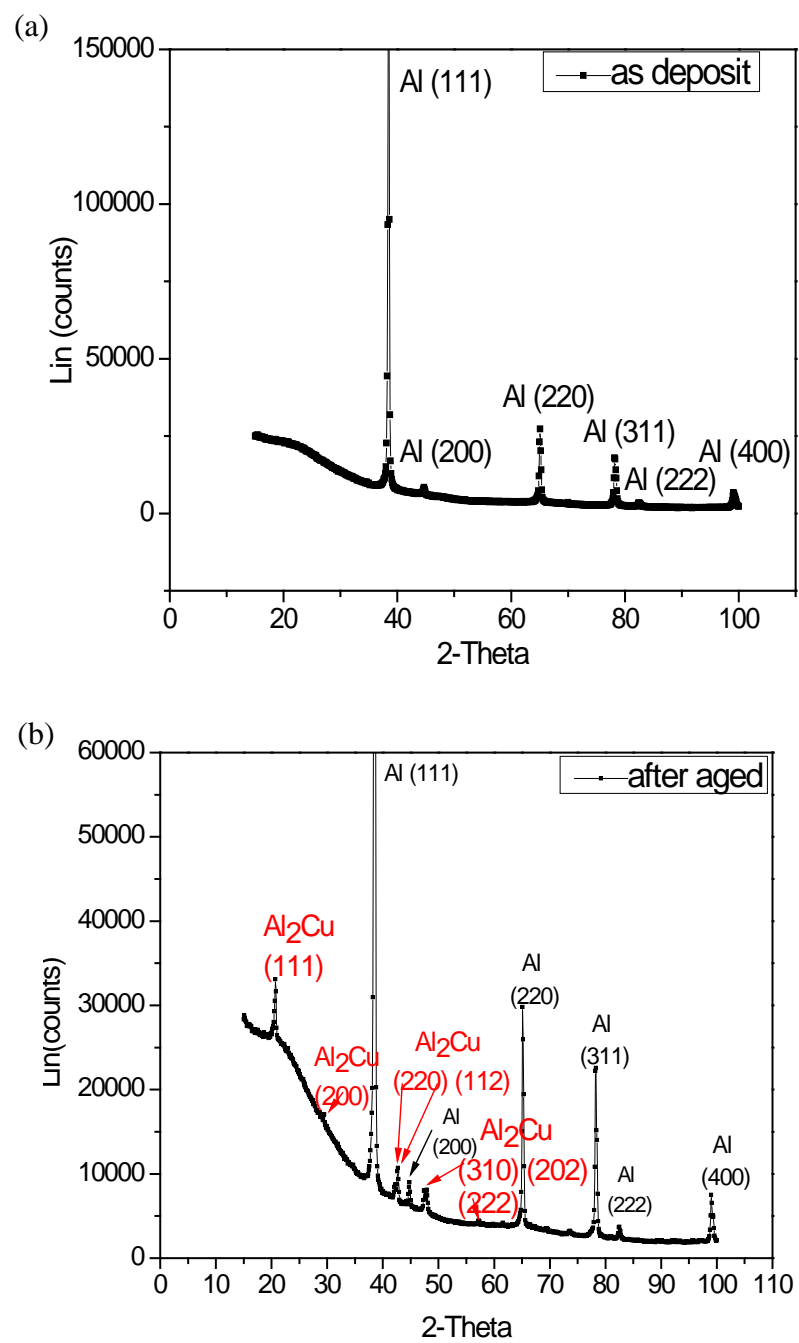


Figure 1.2.10 XRD results of “As sputtered” Al-Cu thin films (a) and “Aged” Al-Cu thin films (b).

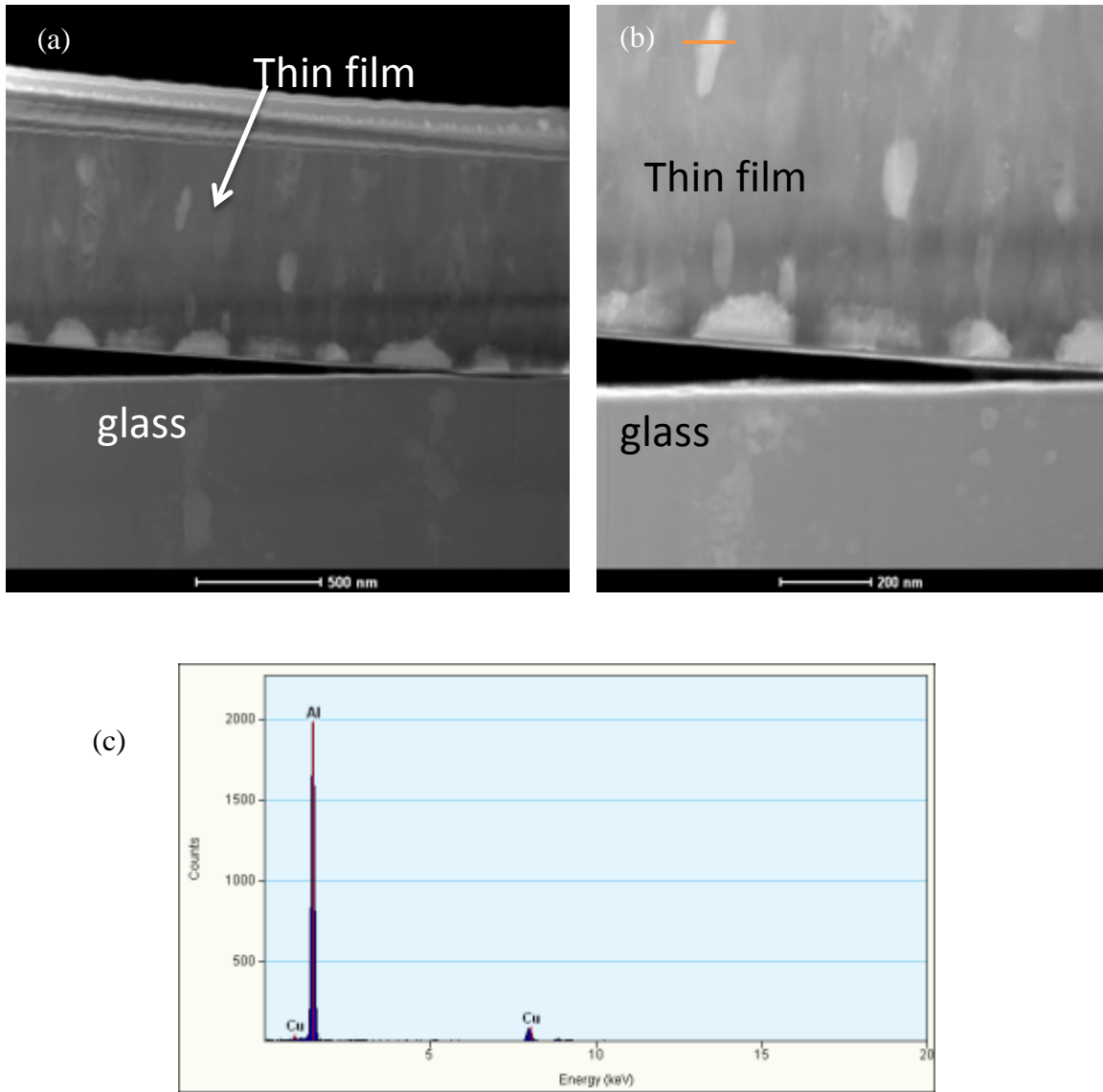


Figure 1.2.11 Cross-section of Al-Cu thin film in the aged condition.

Movie 1.2.4 shows as-deposited Al-Cu thin film coated with a neat epoxy resin exposed to aerated 0.5M NaCl solutions. The experiment was terminated before one of the corrosion sites undercut the mask. In the example shown in Movie 1.2.4, the first site nucleated at the intentionally introduced defect. Unlike the round shaped sites formed during corrosion of pure Al thin films under epoxy coating, corrosion in Al-Cu thin films occurred rapidly along an irregular front. An irregularly shaped site was formed within 7 days of immersion. With the first corrosion site passivated, two new small sites with round shapes nucleated subsequently. However, one of the sites rapidly passivated after short episode of growth, the other continued to grow in certain directions and formed an irregularly shape site. Overall, each corrosion site grew slower and growth was more sporadic. Site stability appeared to be reduced resulting in multiple site

attempts and multiple small corrosion sites. A third corrosion site initiated and grew in a smooth round shape initially suggesting mass transport controlled growth. At longer times, this pit grew irregularly suggesting growth under ohmic control[33].

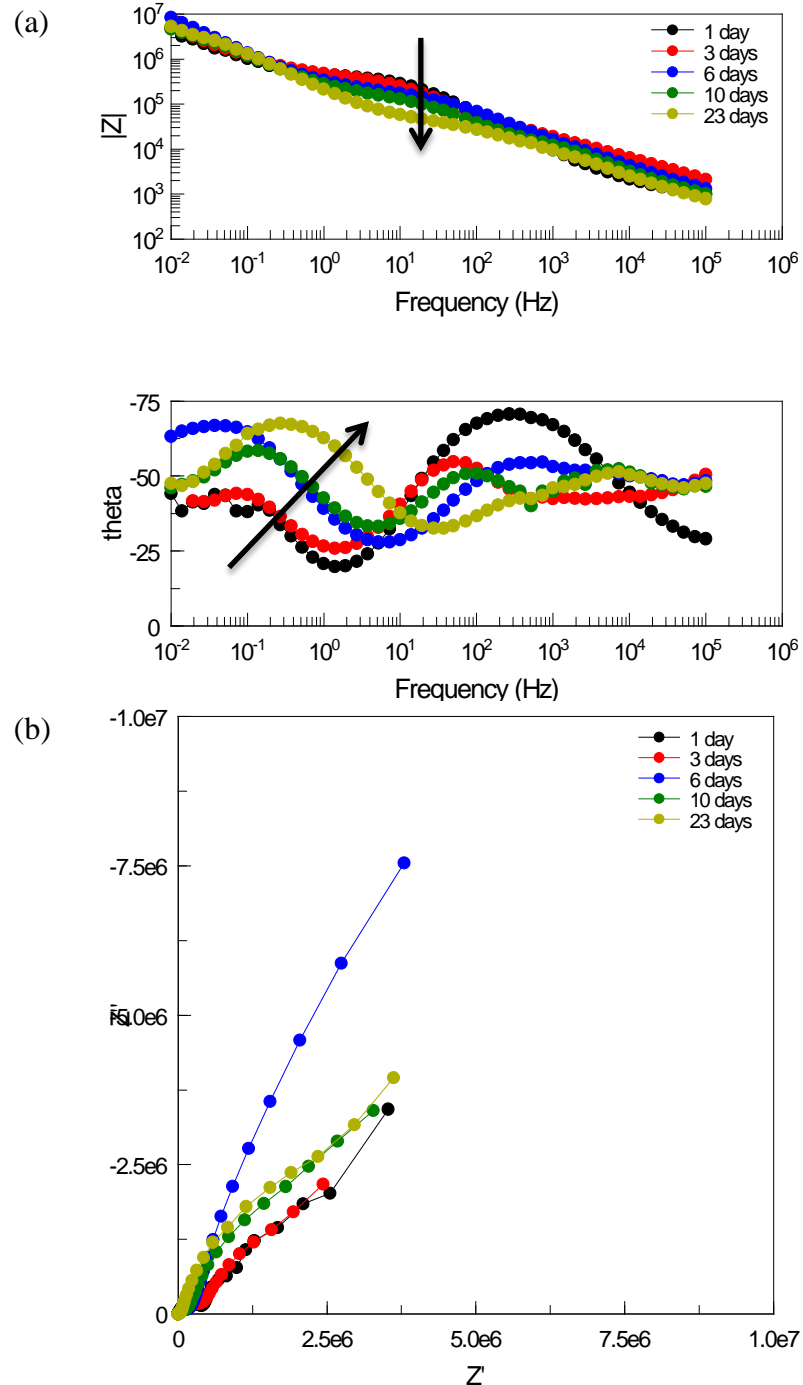


Figure 1.2.12 (a) Bode magnitude and phase angle plots of Al-Cu thin film under neat epoxy coating immersed in 0.5M aerated NaCl solution. (b) Nyquist plots from the same experiments.

The growth of a single site over the span of a day was recorded by collecting one frame every 20 minutes as shown in Movie 1.2.5. From the movie, two types of corrosion propagation

were observed. The first was extension of the corrosion site from perimeter by growth of short, thin channels into the undissolved metal layer. The growing segment changed directions randomly. Segments that were observed to stop were never observed to grow again. When a growing perimeter segment stopped, a new segment activated and grew. The second propagation mode was growth along the entire perimeter. The perimeter moved along at the same speed into the undissolved metal film region.

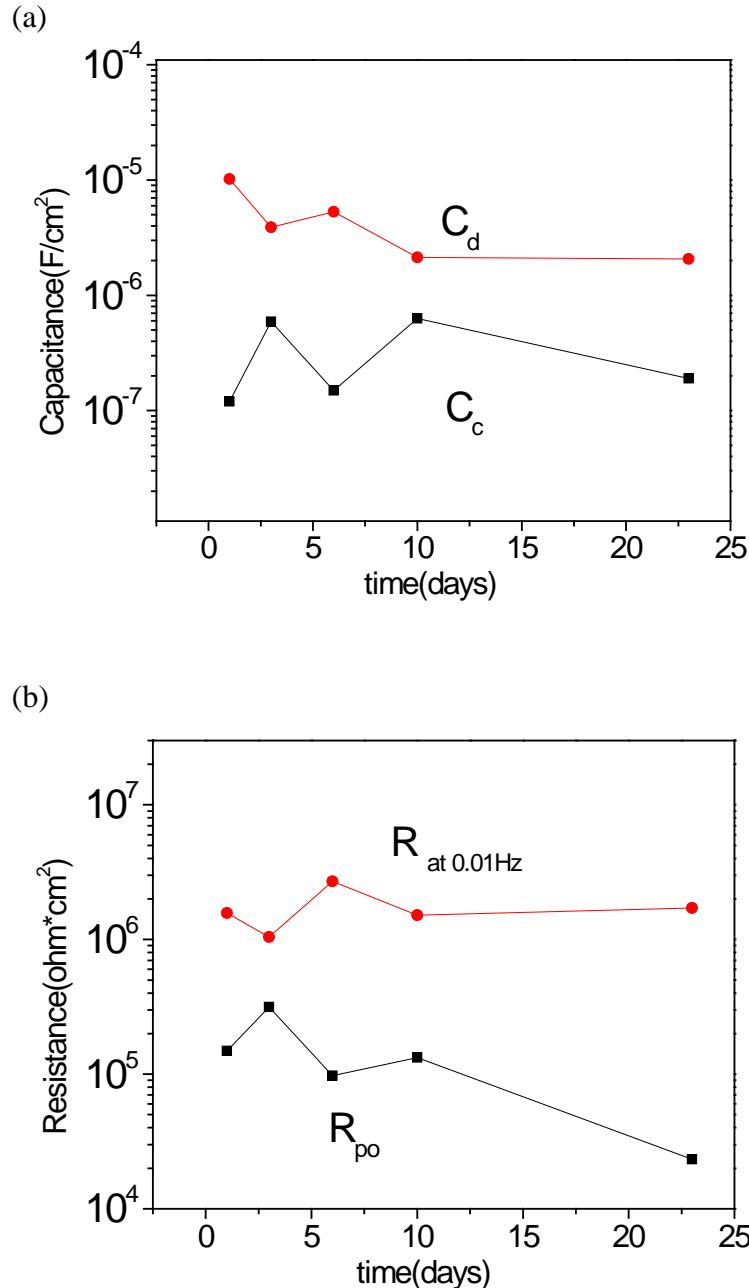


Figure 1.2.13 (a) Coating capacitance C_c and defect capacitance C_d as function of time; (b) Coating resistance R_{po} and the total resistance R_{tot} at 0.01Hz as function of time.

Bode and Nyquist plots of EIS data collected during free corrosion exposure of a neat epoxy coated Al-Cu metallization in aerated 0.5 M NaCl solution are shown in Figure 1.2.12. From the Bode plots (Figure 1.2.12 (a)), a defective coating response characterizes the data for the most part. An exception is the persistent capacitive behavior at the lowest measured frequencies. At these frequencies, a resistive response is often found when corrosion is occurring under a coating—as was the case in these experiments. Because periods of active corrosion were sporadic, it is possible that the EIS spectra were collected at periods where sites were not growing quickly or were not growing at all. The coating capacitance (C_c), pore resistance (R_{po}), defect capacitance (C_d) and defect resistance (R_d) were extrapolated from fitting EIS spectra with Echem AnalystTM. Due to the capacitive behavior of EIS response at the very low frequency, the defect resistance could not be obtained from fitting results. Thus, total impedance at 0.01 Hz was used to represent the defect resistance. The results are shown in Figure 1.2.13. It should be noted that the coating capacitance increased only slightly and the resistance decreased. However, the defect capacitance and total impedance did not show a regular trend as function of time. Therefore, the EIS response could not detect the undercoating corrosion accurately if the site growth was intermittent in nature.

Movie 1.2.6 shows a representative example of an aged Al-Cu thin film coated with neat epoxy. Images were captured at 20 minutes time intervals. A single corrosion site nucleated at the intentional defect made in the sample and grew as a cluster in one direction following a winding path outward from the defect, similar to the corrosion growth behavior of as-deposited Al-Cu thin films. Once the corrosion front stopped growing either by touching the other corrosion fronts or touching the tail of the site itself, another site initiated and started to propagate. Only one site was observed to propagate at a time and segments from different regions of the perimeter propagated alternately. The evolution of single site growth over longer periods of exposure was recorded in movie 1.2.7. In this movie, the site grew outward radially from its perimeter and the corrosion front proceeded in random directions. A comparison of corrosion morphologies that developed in as-deposited and aged thin films is shown in Figure 1.2.14.

Under neat epoxy resins, Al-Cu thin films produced different corrosion morphologies and different growth kinetics depending on metallurgical conditions (as-deposited vs. aged) and corrosion site age. Early in the growth process, corrosion site growth was consistent from one site to the next in aged and as-deposited samples (Figure 1.2.14 (a), (b)). At longer times, multiples sites nucleated in the as-deposited thin films, while few or only a single site nucleated in the aged sample (Figure 1.2.14 (c), (d)). Another observation worth noting was that in the aged sample, the corrosion site propagated and circled around the defect resulting in the formation of undissolved islands (Figure 1.2.14 (d), (f)). Once these islands detached from the bulk surrounding thin film, they were not exposed to further dissolution until new sites propagated inside of the islands and after the circled area was consumed, the corrosion path extended out in a new direction (Figure 1.2.14 (f)). The corrosion front became smooth at the repassivation region and a ring was formed at the corrosion front wall.

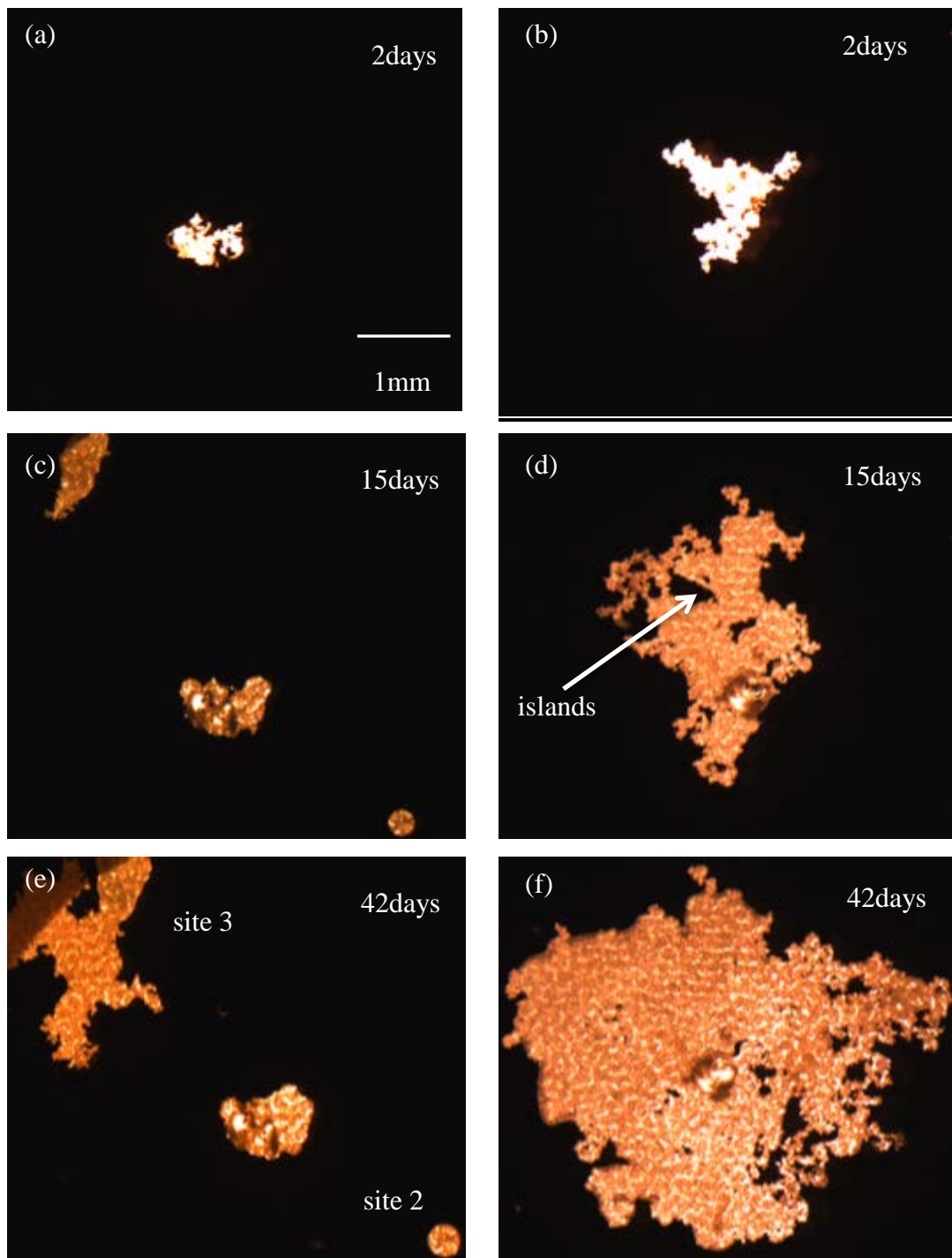
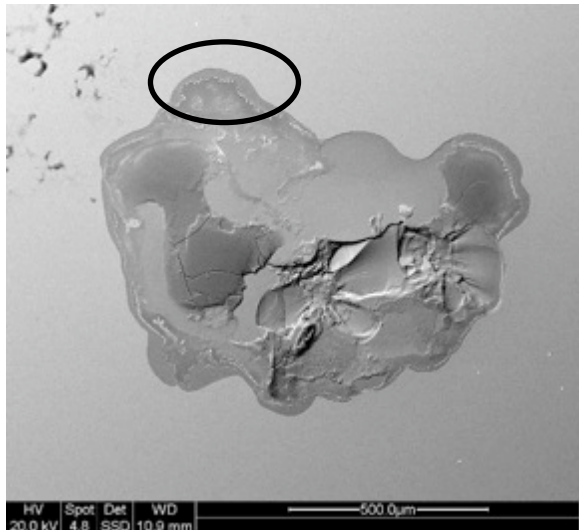


Figure 1.2.14 Corrosion morphologies developed under neat epoxy applied to “as-deposited” (left) and aged Al-Cu thin films (right) at different exposure times.

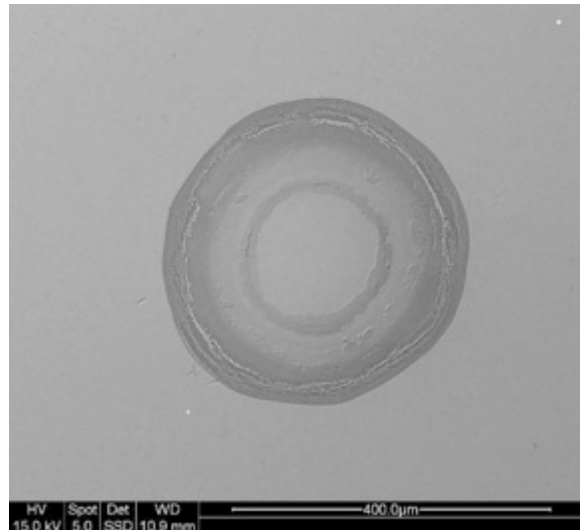
After corrosion experiments, the neat epoxy coating was removed using a PR-3500 Aircraft Epoxy paint remover. Scanning electron microscopy (SEM) was carried out to analyze the corroded area under the coating (Figure 1.2.15 and Figure 1.2.16). In the as-deposited metallization sample in Figure 1.2.15, all three corrosion sites were covered with a layer of

corrosion product inside of corroded area. These sites contained concentric rings of corrosion product at the corrosion front wall. Figure 1.2.15 (d) shows a higher magnification SEM micrograph from the circled surface region of Figure 1.2.15 (a). White dendrites precipitated inside of the site separated from the undissolved Al-Cu thin film by corrosion products. Similar results were shown in Figure 1.2.15 (e) for the second round shape site nucleated at 7 days of exposure.

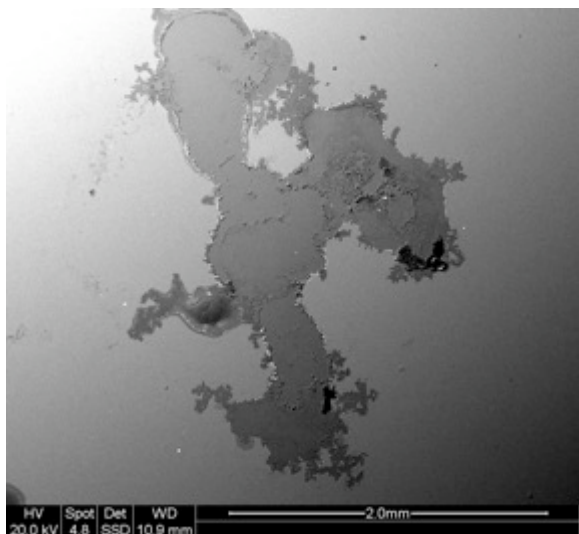
(a)



(b)



(c)



(d)

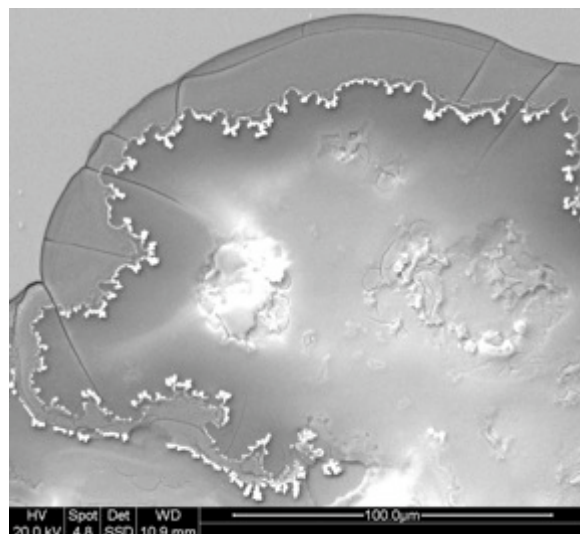
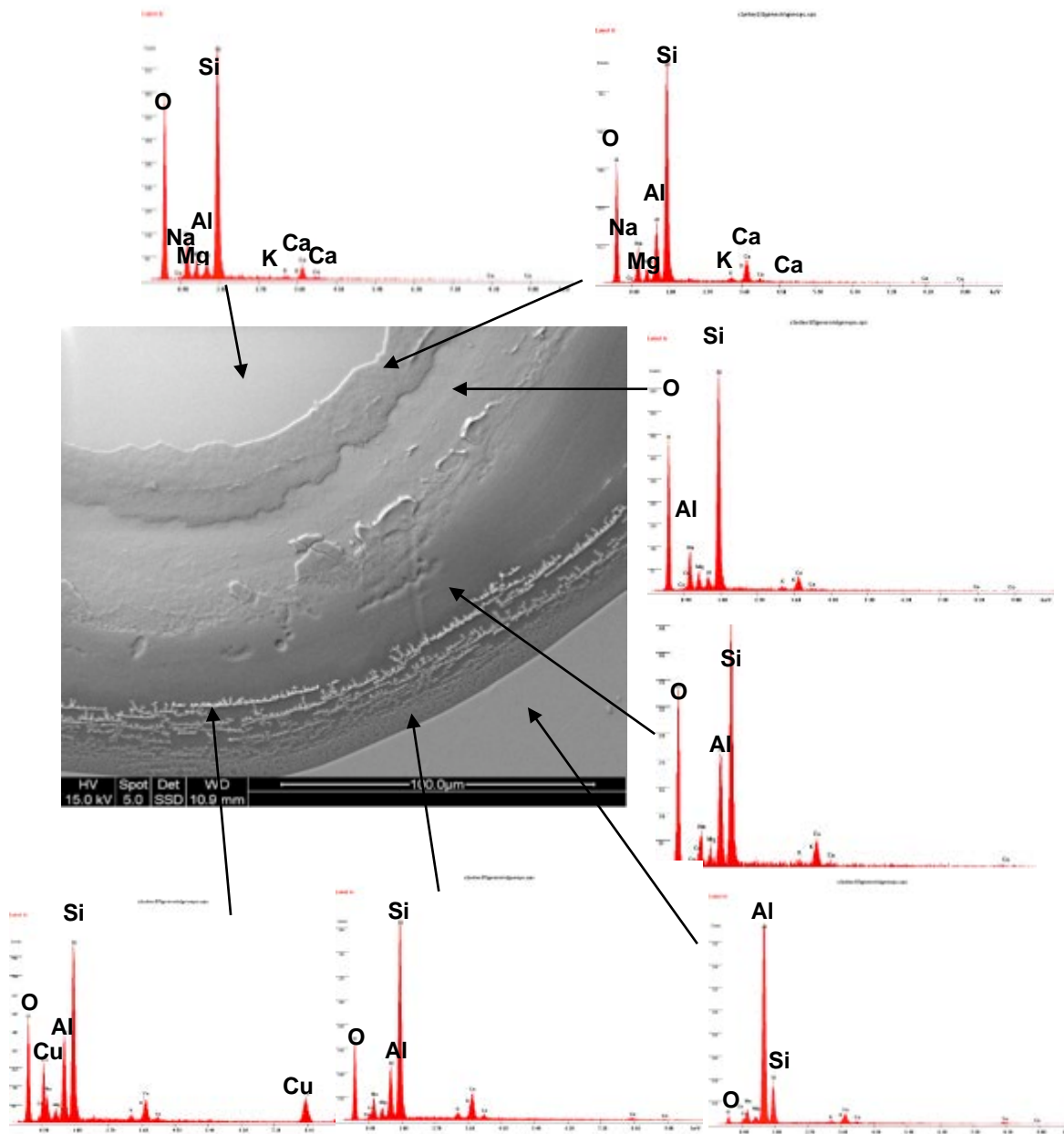


Figure 1.2.15 SEM and EDS results of “As-deposited” Al-Cu thin film. (a) site 1; (b) site 2; (3) site 3; (d) high magnification of circled area in (a); (e) high magnification of site 2. Continued.

(e) Figure 1.2.15 Continued



The chemical composition of the surface layer was analyzed using EDS. The site contained two rings (indicated by darker grey color) separated by the light grey gap. EDS results shown that inner rings contained corrosion product with higher concentration of Al compared with the surrounding light grey area, where the corrosion products were removed when the coating was removed. The other element such as Ca, Na, K, Mg et al. were from the glass slide substrates doped with these elements. The outer rings closest to the corrosion front wall contained corrosion product same as the inner ring. Moreover, white precipitates were Cu-rich dendrites that had formed by dissolution and replating[24] in the area close to the wall. These

dendrites were continuous concentric ring with several layers, which represented corrosion front at different times during evolution of the site. These may have played a role in passivating the corrosion front wall surface, thereby interrupting corrosion site growth and preventing the formation of large corrosion sites. A porous layer of corrosion products was formed between the wall and the Cu-rich ring.

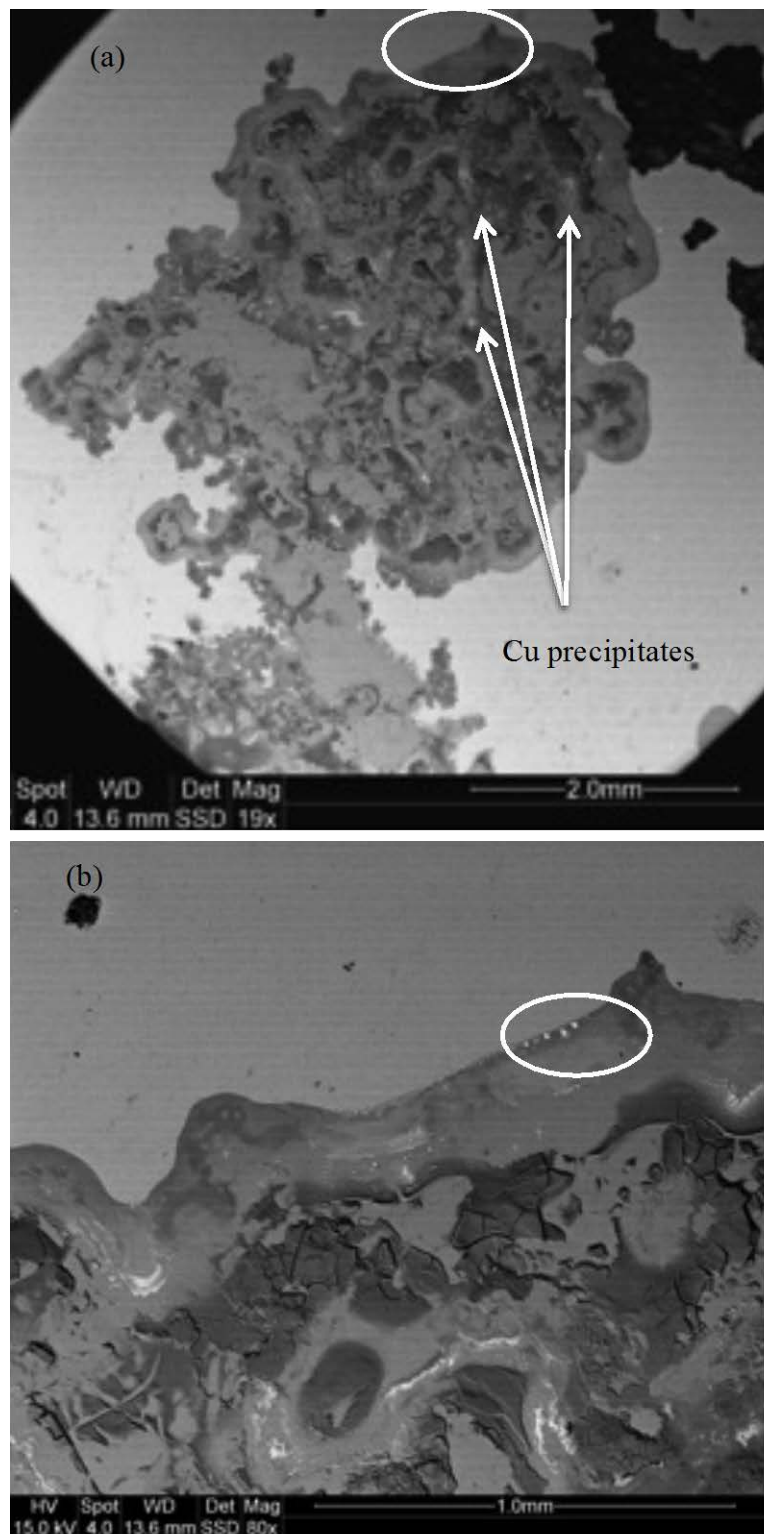


Figure 1.2.16 SEM and EDS results of “Aged” Al-Cu thin film. (a) Whole corroded area; (b) high magnification of circled area in (a); (c) high magnification of circled area in (b).

Continued

Figure 1.2.16 Continued.

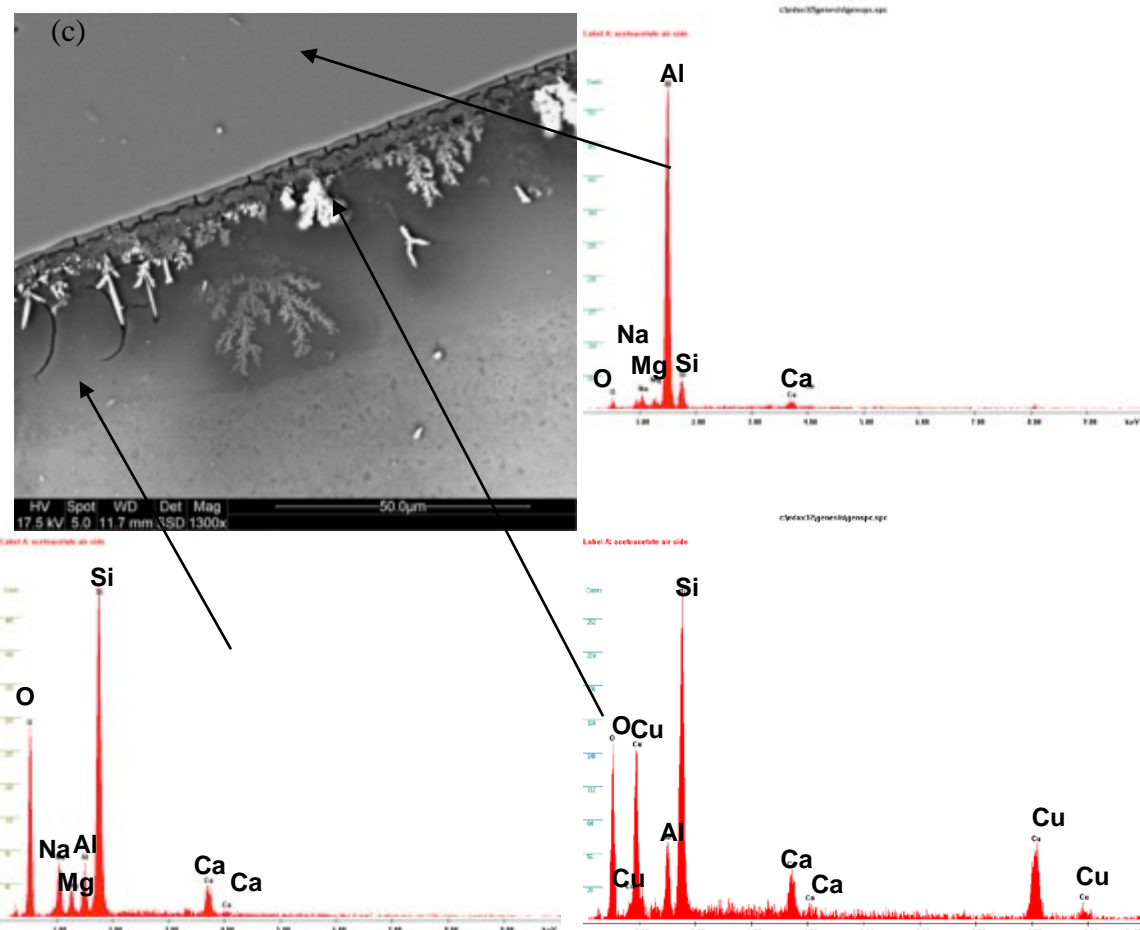


Figure 1.2.16 shows the SEM and EDS results of corrosion in an aged thin film metallization. Corrosion product covered the entire corrosion area. Cu-rich dendrites appear as white spots in Figure 1.2.16 (a) were also observed inside of the site. Similar to the as-deposited metallization, Cu precipitated at the wall Figure 1.2.16 (b) and (c)). Two types of Cu precipitates were formed. One was the dendrite with the size around 10-15 um and the other was needle shape with smaller size. This morphology suggests Cu dissolution and replating as is the case in the as-deposited sample, but in a different corrosion morphology perhaps due to a lesser degree of Cu dendrite layer continuity along the corroding wall.

1.2.5 Discussion

Several conditions were investigated of metallic thin film corrosion under epoxy coatings at the open circuit potential. The thin film nature of the samples makes the corrosion attack under

the coating visible. Therefore, the DOI approach provides a unique opportunity to study the undercoating corrosion damage accumulation both qualitatively and quantitatively.

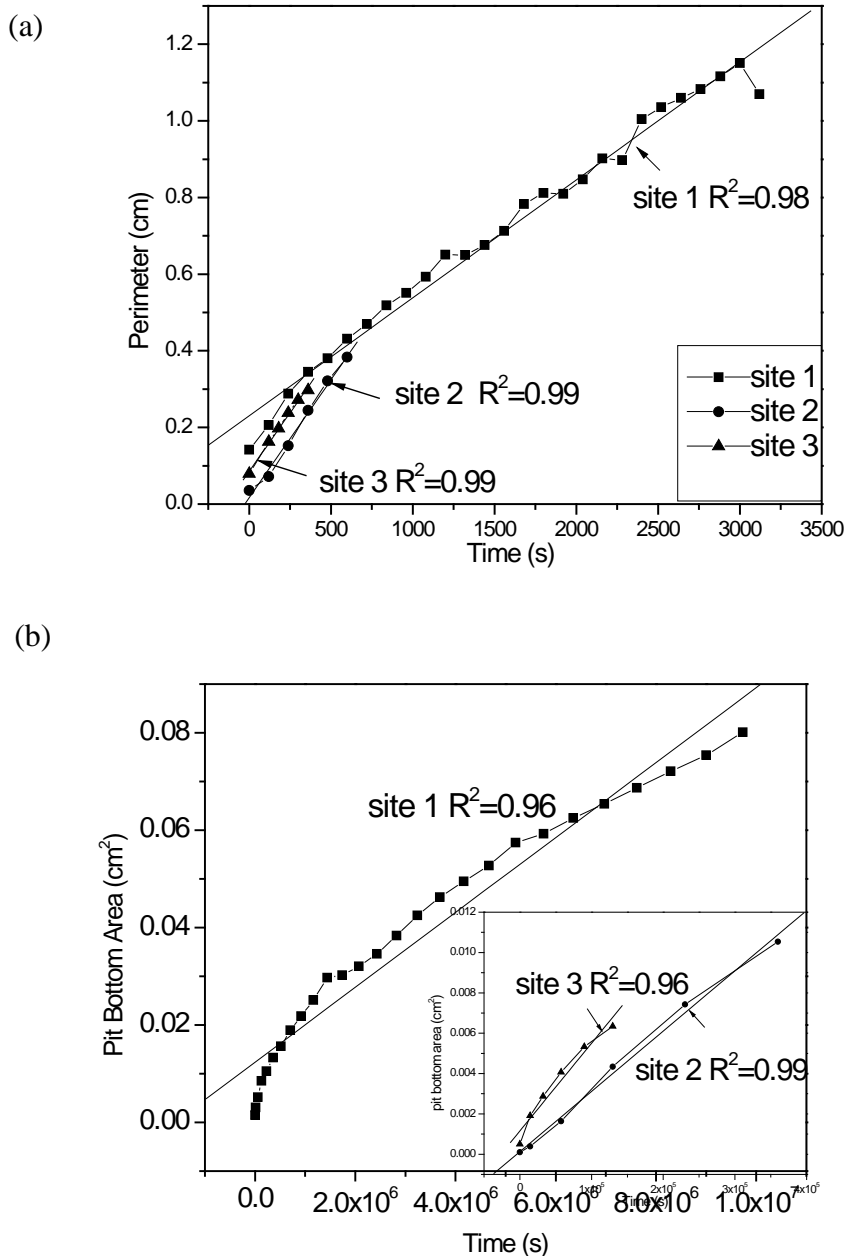


Figure 1.2.17 Single site perimeter (a) and pit bottom area (b) as a function of time by the image analysis. The closed symbols indicate the original data; the regular lines are the linear fitting results.

Due to the thinness of the metallizations, the corrosion damage of thin films spread out laterally under the organic coatings. In terms of classification, this corrosion is more similar to crevice corrosion than it is to pitting. Corrosion occurs at the margins of the corrosion site, which can be far away from the opening in the coating that connects to the bulk environment. The

distinction between crevice corrosion and pitting is important to consideration of the evolution of local environments and kinetic control of the corrosion process.

In the case of pure aluminum under epoxy coating, corrosion morphologies were observed to be smooth and in some cases nearly round. Corrosion sites each grew intermittently, at different rates and in complex shapes complicated the determination of site perimeter, area and current density. Corrosion sites also coalesced. However, at short exposure times, before coalescence, quantitative analysis of site growth kinetics was possible.

For example, in an epoxy-coated pure Al thin film metallization exposed to 0.5 M NaCl solution, 3 sites nucleated and grew (Figure 1.2.5 (a-c)). Corrosion site growth kinetics were assessed based on the study of bare thin film pitting corrosion model put forth by Frankel[17], the variation in site perimeter and area for the three sites is shown in Figure 1.2.17 prior to site coalescence.

After an initial induction period, the corrosion site perimeter and bottom area were observed to vary linearly with time and time squared, respectively. The site perimeter, P was linearly dependent on time, t , according to[17]:

$$P = C_1 \times t \quad \text{Equation 1.2. 3}$$

where C_1 (cm/s) is a constant whose value is estimated from the slope of the data shown in Figure 1.2.17 (a). The site bottom area, A_b was linearly dependent on the square of time, according to:

$$A_b = C_2 \times t^2 \quad \text{Equation 1.2. 4}$$

where C_2 (cm²/s²) is a constant whose value is estimated from the slope of the data shown in Figure 1.2.17 (b). From Faraday's Law, and the constant terms in equations 1.2.3 and 1.2.4, the anodic current density, i_a (A/cm²), can be estimated as[17]:

$$i_a = \frac{2n\rho F C_2}{MC_1} \quad \text{Equation 1.2. 5}$$

where ρ is the density of Al (g/cm³), n is equivalents of change per mole of Al reacted (eq/mol), M is molar mass of Al (g/mol) and F is Faraday's constant (C(eq).

Using this approach, the anodic current densities of the three sites were estimated to be 1.45 A/cm², 2.81 A/cm² and 4.12 A/cm², respectively. For comparison, in 100 nm bare Al thin film, pits growing under anodic polarized potentials exhibited anodic current densities ranging from 18-30 A/cm²[17]. It is reported that the anodic current densities were decreasing with increasing the thin film thickness[22]. Therefore, these values were in good agreement with other results[17, 34]. Not surprisingly, corrosion sites grow much slower under OCP conditions in the presence of an organic coating.

In the case of bare thin film pitting corrosion under potentiostatic control, the diffusion path and ohmic potential drop are constant and the pit current density is invariant with time[22]. This is not the case in these experiments. Both diffusion and ohmic potential drop were playing an important role in controlling the corrosion process and both were expected to change with time.

As a result, it was necessary to fit pit perimeter and pit bottom area data using nonlinear regression [22] as shown in Equation 1.2.6 and 1.2.7, and the resulting the current densities were time-dependent (Equation 1.2.8).

$$P = a_1 t + a_2 t^2 \quad \text{Equation 1.2.6}$$

$$A_b = b_1 t^2 + b_2 t^3 \quad \text{Equation 1.2.7}$$

$$i_a(t) = \frac{\rho n F}{M} \frac{\partial A_b(t)}{\partial t} \frac{1}{P(t)} \quad \text{Equation 1.2.8}$$

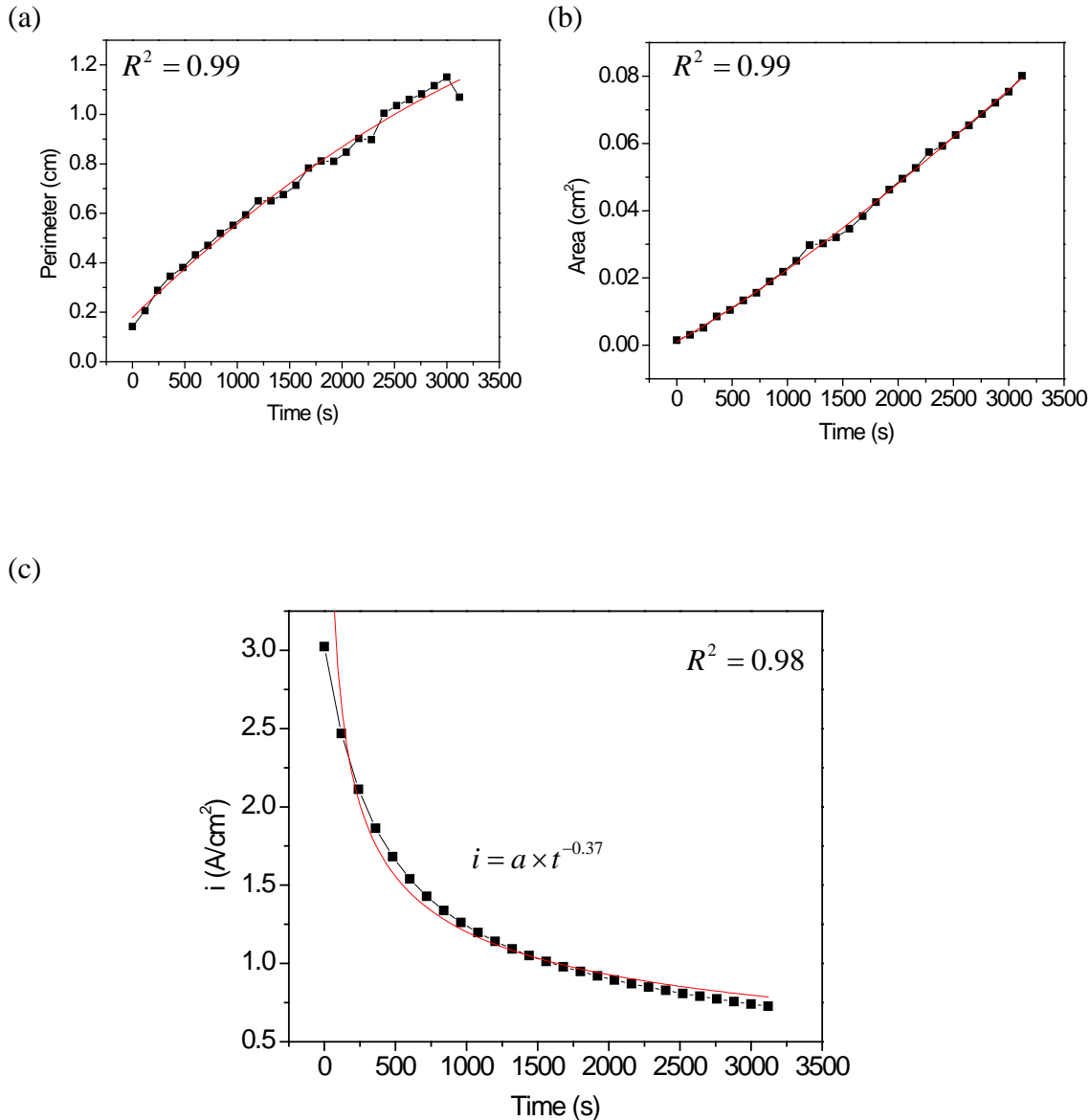


Figure 1.2.18 (a) Variation of the perimeter as a function of time for the first corrosion site in the pure Al thin film, (b) plot of the site bottom area as a function of time for the first site (c) anodic current densities as a function of time for the first corrosion site. The dotted lines are the original data, the solid lines are fitting data.

Where a_1 , a_2 , b_1 and b_2 are constants. Figure 1.2. 18 (a-b) shows the current density calculations for a neat epoxy pure Al thin film metallization. The closed symbols indicate the original data and the red curves were the fitting results for perimeter and bottom area, respectively. The fitting equations were substituted into Equation 1.2.8 and the anodic current density was calculated as shown in Figure 1.2. 18 (c). The analysis results show that the anodic current density itself decays with time. Growth kinetics obeyed power growth laws:

$$i = Kt^b \quad \text{Equation 1.2. 9}$$

where K and b were determined by fitting [34], and depend on alloy and environment[16, 35, 36] [37]. In this particular instance, site growth kinetics varied as:

$$i = K_1 t^{-0.37} \quad \text{Equation 1.2.10}$$

Corrosion sites growing in neat epoxy coated as-deposited Al-Cu thin film metallizations under free corrosion conditions are shown in Figure 1.2.14 (e). Pit growth kinetic calculations were carried out for “site 2” and “site 3”. Figure 1.2.19 (a) and (b) show the perimeter and area calculations of the site indicated as “site 3” in the as-deposited Al-Cu thin film in Figure 1.2.14 (e). The red curves indicate the polynomial fit. The anodic current density of “site 2” and “site 3” are shown in Figure 1.2.19(c). By fitting the anodic current density of “site 2” as a function of time, the equation is shown as follows:

$$i = K_2 t^{-0.74} \quad \text{Equation 1.2.11}$$

In the same way, analysis of site 3 lead to a power dependence of -0.98. The power dependence of the kinetics from a corrosion site in an aged thin film sample was -0.88.

The steady-state current density estimates from these expressions yield values that range from $4\text{mA}/\text{cm}^2$ down to $0.2\text{mA}/\text{cm}^2$. The current density of aged thin films is slightly higher than that of as-deposited condition. It should be noted that Cu additions to aluminum in solid solution decreased corrosion site growth. However, once the θ phase formed in aged Al-Cu thin films, stability of corrosion sites increased.

Electrochemical impedance spectroscopy (EIS) was carried out during exposure and imaging experiments to relate the extent and nature of undercoating corrosion to periodically measured EIS spectra. Results showed that metallic thin films in 0.5M NaCl solution exhibited defective coating response. The characterization of coating water uptake can be successfully obtained by extracting the coating capacitance C_C from EIS spectra. However, as for the undercoating characterization, a capacitance behavior was often revealed at the lowest measured frequencies regardless of observation of corrosion by DOI method. Images analysis showed that corrosion site growth was intermittent with long time in repassivation stages in between. If the periodic collecting EIS spectra fell in the repassivation regime, only capacitance behavior was observed at the very low frequency. Therefore, EIS measurement can only detect the corrosion during it occurring, but not necessarily the existence of corrosion itself.

At longer undercoating corrosion propagation stage in both 0.3M HCl and 0.5M NaCl solutions, the total resistance and capacitance varied irregularly with time, respectively. Different from bulk materials, which contained supplemental metal dissolution, corrosion attack in thin film corrosion was limited by the metallization thickness. The substrates exposure area was “exhausted” with corrosion propagation for longest times. Moreover, bubble formation was observed during corrosion propagation, which may have lead to an increase in the measured

resistance that was not anticipated. Therefore, the bubbles under real coatings may affect corrosion and EIS measurements.

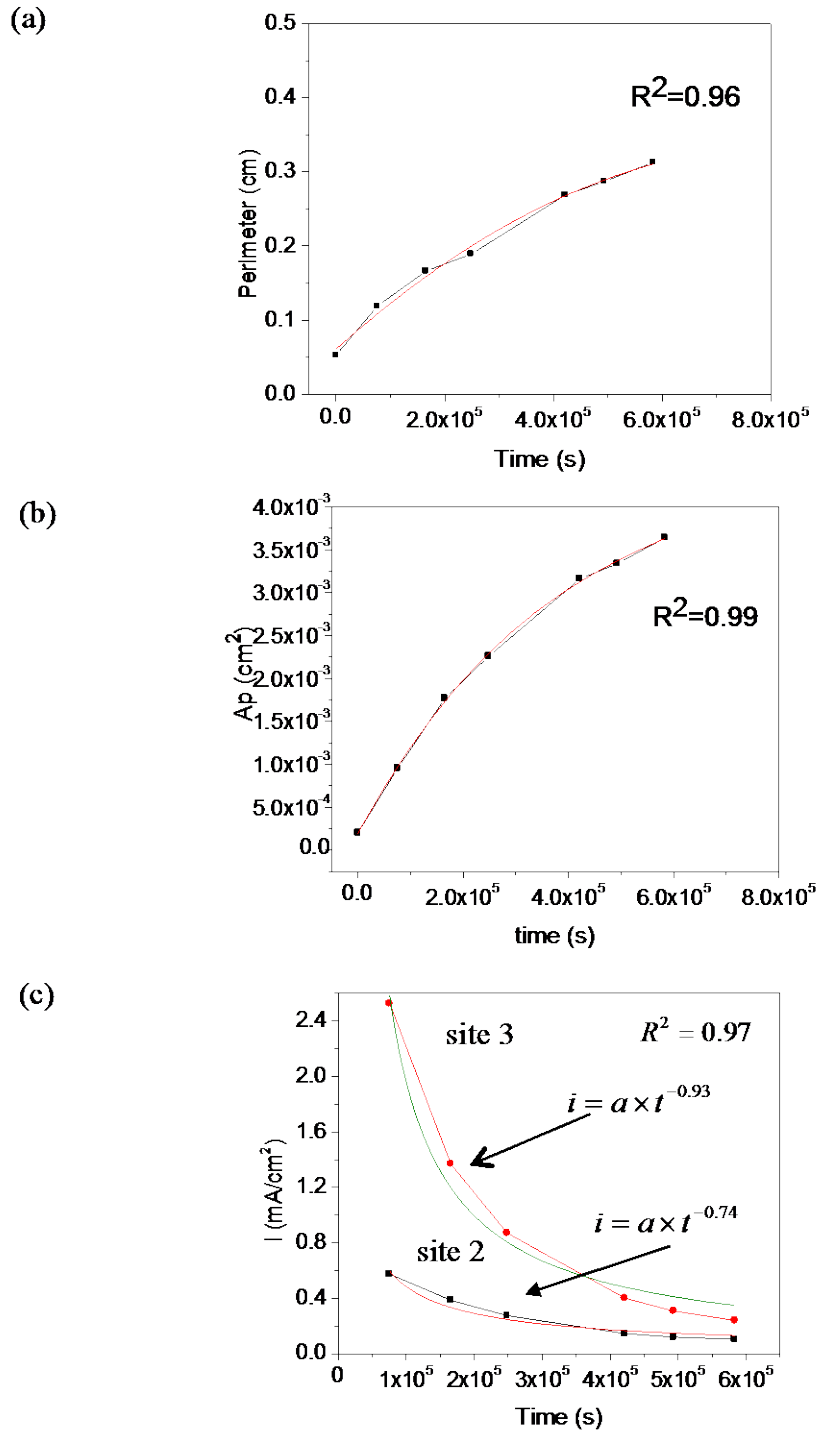


Figure 1.2.19 (a) plot of the variation of the perimeter length as a function of time for site 3 in the as-deposited thin film, b) a plot of the site bottom area as a function of time for site #3 in the as-deposited thin film, c) anodic current densities as a function of time for sites #2 and 3 in the as-deposited thin film. The dotted lines are the original data, the solid lines are fitting data.

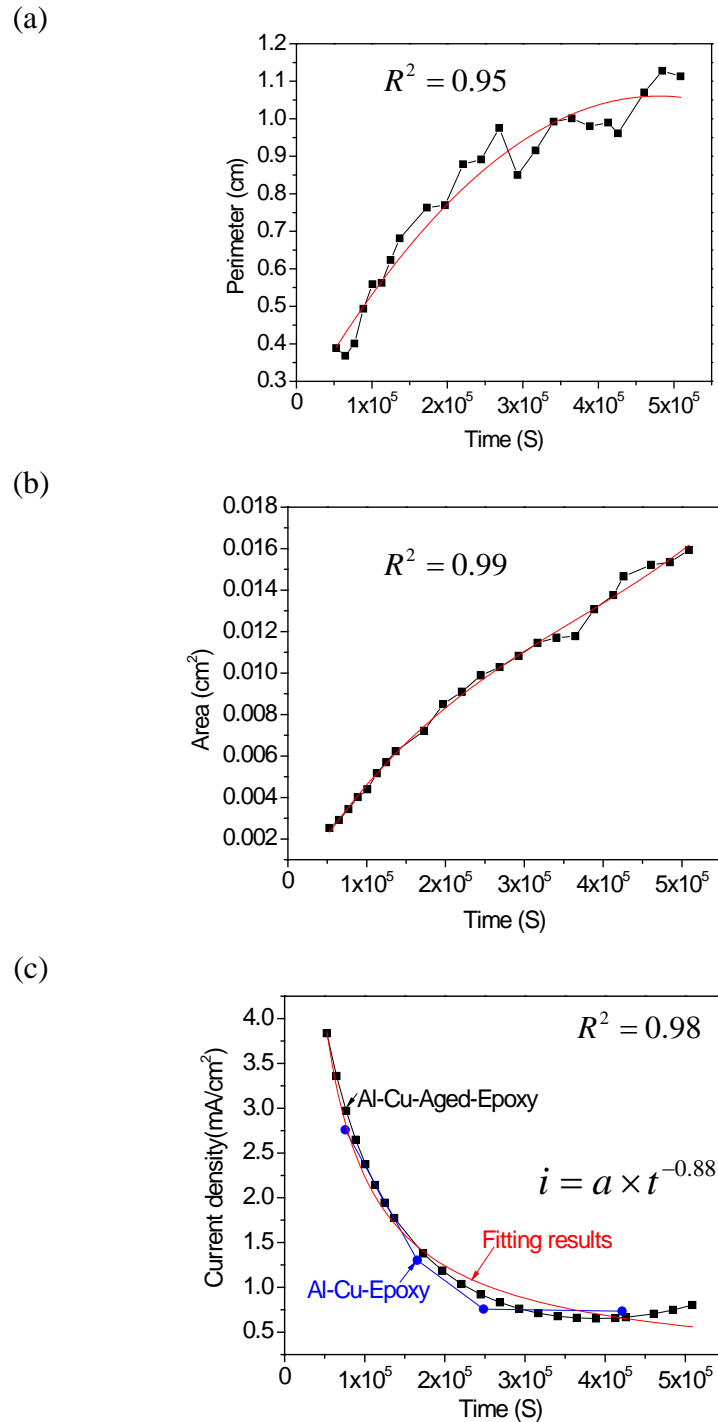


Figure 1.2.20 (a) plot of the variation of the perimeter as a function of time for single corrosion site in the aged thin film, b) a plot of the site bottom area as a function of time; c) anodic current densities as a function of time for single corrosion site in Al-Cu thin films. The dotted lines are the original data, the solid lines are fitting data.

1.2.6 Conclusions

1. The Direct Optical Interrogation (DOI) technique was developed to assess undercoating corrosion. Demonstration experiments were carried out using epoxy coatings on metallic thin films, which were deposited on transparent inert glass slides. Thin film corrosion accumulation underneath the coating systems was monitored in-situ using an inverted optical microscope.
2. Metallurgical effects were studied by using 3 different metallic substrates including pure Al thin films, Al-4.9wt% Cu thin films in the “as-deposited” condition and “artificially aged” conditions.
3. Single or multiple corrosion sites nucleated randomly across the exposure area. For pure Al thin films, these sites were round and smooth. For the Al-Cu thin films as-deposited and artificially aged condition, the corrosion occurred rapidly along an irregular front formed an island shape.
4. EIS was carried out concurrently to characterize under coating corrosion. Results showed that EIS was able to sense the water uptake of the coatings and nucleation of corrosion under coatings. However, EIS spectra showed irregular trends after corrosion sites started to propagate due to intermittent passivation and blocking due to bubble formation.
5. Ex-situ characterization was also conducted on the corroded samples under the coatings. Coatings were removed after the experiments for scanning electron microscopy (SEM) and energy dispersive spectroscopy (EDS) analysis. Results showed that for Al-Cu thin films, Cu-rich dendrites were formed on the corrosion front wall during the corrosion process.
6. Quantitative estimates of the undercoating corrosion damage accumulation rates were made. Corrosion rate (current density) was calculated using Faraday’s law by collecting the corrosion site perimeter and bottom area. Results showed that the current densities decayed with time according to power growth laws. However, different empirical constants were obtained depending on different metallic thin films.
7. Cu additions to aluminum in solid solution decreased the stability of single corrosion site growth. Multiple sites nucleated at the random locations suggested that Cu in solid solution did not inhibit the nucleation of metastable corrosion sites. Nonetheless, the lower current density in as deposited thin films suggested that Cu in solid solutions reduced corrosion site growth rates. Once the θ phase formed in aged Al-Cu thin films, corrosion site stability appeared to be increased.

1.2.7 References

1. Rammelt, U. and G. Reinhard, *Application of Electrochemical Impedance Spectroscopy (Eis) for Characterizing the Corrosion-Protective Performance of Organic Coatings on Metals*. Progress in Organic Coatings, 1992. **21**(2-3): p. 205-226.
2. Amirudin, A., *Application of Electrochemical Impedance Spectroscopy to Study the Degradation of Poly-coated Metals*. Progress in Organic Coatings, 1995. **26**: p. 1-28.
3. Oudar, P.M.a.J., (Ed.)*Corrosion Mechanism in Theory and Practice*1995: Marcel Dekker, Inc.

4. MiskovicStankovic, V.B., D.M. Drazic, and Z. KacarevicPopovic, *The sorption characteristics of epoxy coatings electrodeposited on steel during exposure to different corrosive agents*. Corrosion Science, 1996. **38**(9): p. 1513-1523.
5. Deflorian, F. and S. Rossi, *An EIS study of ion diffusion through organic coatings*. Electrochimica Acta, 2006. **51**(8-9): p. 1736-1744.
6. Sangaj, N.S. and V.C. Malshe, *Permeability of polymers in protective organic coatings*. Progress in Organic Coatings, 2004. **50**(1): p. 28-39.
7. Stratmann, M., R. Feser, and A. Leng, *Corrosion Protection by Organic Films*. Electrochimica Acta, 1994. **39**(8-9): p. 1207-1214.
8. Grundmeier, G. and M. Stratmann, *Adhesion and De-adhesion mechanisms at polymer/metal interfaces: Mechanistic understanding based on in situ studies of buried interfaces*. Annual Review of Materials Research, 2005. **35**: p. 571-615.
9. Leidheiser, H., *Corrosion of Painted Metals - a Review*. Corrosion, 1982. **38**(7): p. 374-383.
10. Bonora, P.L., F. Deflorian, and L. Fedrizzi, *Electrochemical Impedance Spectroscopy as a tool for investigating underpaint corrosion*. Electrochimica Acta, 1996. **41**(7-8): p. 1073-1082.
11. Baumgärtner M., K.H., *Microtunnelling During Localized Attack of Passive Aluminum - the Case of Salt Films vs Oxide-Films*. Corr. Sci., 1989. **29**: p. 363-378.
12. Edeleanu, C., *THE PROPAGATION OF CORROSION PITS IN METALS*. Journal of the Institute of Metals, 1960. **89**(3): p. 90-94.
13. Baumgärtner M., K.H., *Aluminum Pitting in Chloride Solutions - Morphology and Pit Growth-Kinetics*. Corr. Sci., 1990. **31**: p. 231-236.
14. Knörnschild G., K.H., *Localized corrosion of homogeneous binary Al-Zn and Al-Cu alloys*. The Electrochemical Society Fall Meeting, Toronto, Oct.11-16, 1992. **92-2**: p. 178.
15. Ernst, P. and R.C. Newman, *Pit growth studies in stainless steel foils. I. Introduction and pit growth kinetics*. Corrosion Science, 2002. **44**(5): p. 927-941.
16. Frankel, G.S., *Pitting corrosion of metals. A review of the critical factors (vol 145, pg 2186, 1998)*. Journal of the Electrochemical Society, 1998. **145**(8): p. 2970-2970.
17. Frankel, G.S., *The Growth of 2-D Pits in Thin-Film Aluminum*. Corrosion Science, 1990. **30**(12): p. 1203-1218.
18. Balazs, L. and J.F. Gouyet, *2-DIMENSIONAL PITTING CORROSION OF ALUMINUM THIN-LAYERS*. Physica A, 1995. **217**(3-4): p. 319-338.
19. Balazs, L., et al., *CORROSION PATTERN FORMATION IN ALUMINIUM THIN LAYERS*. Fractals-Complex Geometry Patterns and Scaling in Nature and Society, 1993. **1**(3): p. 416-424.
20. Frankel, G.S., et al., *PITTING CORROSION OF ELECTROPLATED PERMALLOY-FILMS*. Corrosion Science, 1993. **35**(1-4): p. 63-71.
21. Ryan, M.P., et al., *Corrosion pits in thin films of stainless steel*. Journal of the Electrochemical Society, 1999. **146**(1): p. 91-97.
22. Frankel, G.S., et al., *Pit Growth in NiFe Thin-Films*. Journal of the Electrochemical Society, 1992. **139**(8): p. 2196-2201.
23. Hernandez, S.E., et al., *The Effect of Thickness on the Corrosion Susceptibility of Al Thin-Film Metallizations*. Journal of the Electrochemical Society, 1995. **142**(4): p. 1215-1220.

24. Buchheit, R.G., et al., *Local dissolution phenomena associated with S phase (Al₂CuMg) particles in aluminum alloy 2024-T3*. Journal of the Electrochemical Society, 1997. **144**(8): p. 2621-2628.
25. Frear, D.R., et al., *The Evolution of Microstructure in Al-2 Pct Cu Thin-Films - Precipitation, Dissolution, and Reprecipitation*. Metallurgical Transactions a-Physical Metallurgy and Materials Science, 1990. **21**(9): p. 2449-2458.
26. Proost, J., et al., *Morphology of corrosion pits in aluminum thin film metallizations*. Journal of Solid State Electrochemistry, 1998. **2**(3): p. 150-155.
27. Deflorian, F., et al., *Organic coating capacitance measurement by EIS: ideal and actual trends*. Electrochimica Acta, 1999. **44**(24): p. 4243-4249.
28. Castela, A.S. and A.M. Simoes, *An impedance model for the estimation of water absorption in organic coatings. Part I: A linear dielectric mixture equation*. Corrosion Science, 2003. **45**(8): p. 1631-1646.
29. Bellucci, F. and L. Nicodemo, *Water Transport in Organic Coatings*. Corrosion, 1993. **49**(3): p. 235-247.
30. Popov, B.N., M.A. Alwohaibi, and R.E. White, *Using Electrochemical Impedance Spectroscopy as a Tool for Organic Coating Solute Saturation Monitoring*. Journal of the Electrochemical Society, 1993. **140**(4): p. 947-951.
31. Grundmeier, G., W. Schmidt, and M. Stratmann, *Corrosion protection by organic coatings: electrochemical mechanism and novel methods of investigation*. Electrochimica Acta, 2000. **45**(15-16): p. 2515-2533.
32. Hunkeler, F. and H. Bohni, *Mechanism of Pit Growth on Aluminum under Open Circuit Conditions*. Corrosion, 1984. **40**(10): p. 534-540.
33. Szklarska-Smialowska, Z., *Pitting corrosion of aluminum*. Corrosion Science, 1999. **41**(9): p. 1743-1767.
34. Alkire, R.C. and K.P. Wong, *The Corrosion of Single Pits on Stainless-Steel in Acidic Chloride Solution*. Corrosion Science, 1988. **28**(4): p. 411-&.
35. Cavanaugh, M.K., R.G. Buchheit, and N. Birbilis, *Evaluation of a simple microstructural-electrochemical model for corrosion damage accumulation in microstructurally complex aluminum alloys*. Engineering Fracture Mechanics, 2009. **76**(5): p. 641-650.

1.3 The Effect of Organic Coating Systems on Undercoating Thin Film Corrosion Formation, Morphology and Growth Kinetics

1.3.1 List of Figures and Tables

Figure 1.3.1 Instrumental configuration of the DOI setup.

Figure 1.3.2 (a) sample surface roughness. (b) Step height of the Deft primer on Al-Cu aged thin films. (c) Cross section of sample surface roughness in the longitude direction as shown in (a).

Figure 1.3.3 SEM Cross-section of the coating products: (a) Deft primer; (b) Boegel/Deft primer; (c) CCC/Deft primer; (d) Boegel/Deft primer/Topcoat.

Figure 1.3.4 Images of the evolution of corrosion on chromate conversion coated aged Al-Cu thin film exposed to 0.5M NaCl solution.

Figure 1.3.5 Image of Al-Cu aged sample coated with Deft primer after 6 days of exposure to aerated 0.5M NaCl solution under high incident light intensity.

Figure 1.3.6 SEM and EDS results of Al-Cu aged thin films under Deft primer. (a) Corrosion area under the primer. (b) Corrosion front at a repassivation region. (c) Corrosion front at active growth region. (d-e) White precipitates.

Figure 1.3.7 Photographs of sample under Boegel and Deft coating after exposure. (a) Front view; (b) Back view.

Figure 1.3.8 Images of the evolution of aged Al-Cu thin film with a Boegel conversion coating (left) or CCC (right) coated with Deft primer exposed to 0.5M NaCl solution.

Figure 1.3.9 SEM and EDS results of Al-Cu aged thin films coated with a CCC/Deft coating combination. (a) Corrosion area under the primer. (b) Corrosion front at a repassivation region. (c) Corrosion front of site 1. (d) Corrosion front of site 2. (e) EDS result of site 1. (f) EDS result of site 2. (g) EDS result of site 3.

Figure 1.3.10 Images of as deposited Al-Cu thin film under (a) Deft primer; (b)Boegel /Deft; (c) CCC/Deft; (d) Boegel/Deft/Topcoat; (e) CCC/Deft/Topcoat exposed to 0.5M NaCl solution.

Figure 1.3.11 Photograph of Al-Cu aged thin film coated with a SrCrO₄-pigmented epoxy exposed to 0.5M NaCl solution.

Figure 1.3.12 Average current density calculations of Al-Cu-aged thin films with Deft primer only as function of time. Three experiments were conducted under identical conditions.

Figure 1.3.13 Average current densities of (a) Al-Cu-aged thin films, (b) Al-Cu as deposited thin films under various coating systems.

Figure 1.3.14 (a) Al-Cu-aged thin film under Deft primer exposure for 7 days. The evolution of images captured by microscope every 300 minutes. (b) Vectors emanated from a point and intersected the perimeter at different directions, (c) Vectors were selected perpendicular to the corrosion front.

Figure 1.3.15 (a) Estimated local current densities along vectors shown in Figure 1.3.14 (b); (b) Estimated local current densities along vectors shown in Figure 1.3.14 (c).

Figure 1.3.16 Local current densities as function of time for various coating systems. Solid lines represent the average values of local current densities.

Figure 1.3.17 Single round shape corrosion site nucleated in the Al-Cu thin film at “as-deposited” condition coated with Boegel conversion coating and Deft primer. Site radius as function of growth time. Scatter plot was the original data and the red solid line was the fitting curves.

1.3.2 Introduction and Background

Detection and monitoring of corrosion underneath organic coatings is useful for diagnosing coating performance during service. Techniques that promise non-destructive and in-

situ features are necessary to develop for corrosion measurement, detection and monitoring[1]. In order to study the corrosion underneath organic coatings, it is necessary to take into account the properties of organic coating systems. Typically, coating systems consist of multiple layers with thicknesses ranging from nanometers to millimeters[2, 3]. These layers usually comprise a conversion coating, a primer and a topcoat, each having a different role in protecting the metal substrate against corrosion [4, 5]. Conversion coatings are formed by reaction of the metal surface in an aqueous solution, not only providing a barrier against corrosion but also increasing adhesion for the application of the primer[6]. The primer, which is usually an organic coating, contains the pigments that provide corrosion inhibition, significantly increasing the protection provided by the coating system[7]. The topcoat often acts as a direct barrier separating the metal from a corrosive environment [4].

Well known conversion coatings are phosphate layers on steel and chromate conversion coatings (CCC) on aluminum and its alloys[6]. The latter is used widely due to its excellent corrosion protection compared with other conversion coatings[8, 9]. Alodine 1200S is an example of a CCC that is used commonly in aircraft applications[10, 11]. CCCs are generally amorphous, nonporous inorganic coatings with the thicknesses ranging from 0.01um to 0.3um[12]. CCCs form spontaneously by the chemical and electrochemical reaction of substrates with aqueous solutions containing hexavalent chromium ions and acids (mainly HF with a pH of about 1.7). Up to 20% of the unreacted hexavalent chromate (Alodine 1200S) is adsorbed in the CCC as the coating is formed[6]. This fraction of chromate is leachable from the coating for some time after deposition and can be released and transported to coating defects where it acts to stifle electrochemical activity in a manner referred to as “self healing”, which is the signature property of CCCs.

Among the various types of coating systems, organic coatings are commonly utilized because they can effectively protect metal substrates against corrosion at low cost[2, 7]. Organic coatings can offer protection by forming a physical barrier that can retard the transport of aggressive agents (e.g. oxygen and water) to the metal surface. However, all coatings are permeable to water, oxygen and other ions that initiate the corrosion processes to some extent[2, 13]. In fact, most coatings contain some amount of water throughout most of the coating’s service life[6]. Therefore, barrier protection provided by the organic coatings is limited.

Studies have been conducted focusing on chemical inhibition provided by organic coatings. Actively inhibiting pigments are often added to primers, and primers containing SrCrO_4 -pigments are widely used for high strength Al alloys used in aerospace applications[14]. SrCrO_4 is a sparingly soluble pigment that dissolves yielding chromate and strontium ions[8]. The solubility of SrCrO_4 is such that chromate is released in quantities sufficient for inhibition, but not so high that wet adhesion is degraded or that the inhibitor reservoir is exhausted quickly[15]. It is known that chromates are good oxygen reduction reaction inhibitors[8]. They also passivate reactive intermetallic phases that exist in Al alloys[12]. Unfortunately, Cr^{6+} is toxic and a cancer-causing agent, whose use is severely restricted by international environmental regulations[16, 17]. As a result, significant efforts have been made to develop alternative chromium-free conversion and primer coatings[18].

Organic coatings containing environmentally friendly pigments such as rare earth compounds have been found to be potential candidates to replace chromate primers[19-23]. Among the common rare earths: Ce, La and Pr, Ce has been found to be the most effective by

many measures. Rare earth metal inhibitors provide cathodic inhibition by precipitation on the intermetallic particles, which reduces the oxygen reduction reaction rates and the rate of the corrosion cell process [23, 24]. The rare earth metal praseodymium (Pr) is also a corrosion inhibitor, but it is rarer, and less effective than Ce. Nonetheless, Pr-pigmented coatings have been developed and are qualified for military use. Pr compounds can be sparingly soluble as required for primer coating pigments and the ions released inhibit oxygen reduction thereby slowing the corrosion cell process[25]. Additionally, it has been shown that Pr ions are released from Pr-based coatings when they are exposed to a corrosive environment[26].

Practical tests and methods for monitoring the corrosion of organic coated metals has been the subject of considerable scientific investigation. Monitoring the process of corrosion underneath organic coatings can enable one to predict the lifetime of organic coatings [7]. Electrochemical impedance spectroscopy (EIS) is a well-established method that can provide quantitative coating failure mechanisms as well as information such as coating degradation, adhesion, and corrosion rate[18, 27-31]. EIS measurements can be made in simulated service conditions[32, 33], they can be performed *in situ*, allowing for the assessment of the coating quality and the monitoring of corrosion processes as a function of time[34, 35]. However, EIS is only an indirect method of assessing undercoating corrosion damage accumulation. Results of these measurements need to be interpreted properly and carefully to obtain meaningful results. In this regard, a method to directly observe undercoating corrosion damage accumulation may provide considerable advantages.

For these reasons, the objective of this work is to investigate an approach that can directly monitor the damage underneath organic coating systems *in situ*. After demonstrating the utility of this fabrication approach for idealized coating systems in Section 1.2, Direct Optical Interrogation (DOI) methods were extended to more realistic coating systems based on incumbent and emergent coating technologies. The effects of local environments in organic coating systems on thin film corrosion formation, morphology, and growth kinetics were assessed by DOI.

1.3.3 Experimental

The Al-Cu thin film metallizations 800nm in thickness were deposited on transparent glass slides by physical vapor deposition using an Al-4wt%Cu target. The deposition rate was 1.8Å/s at 5.5×10^{-7} Torr. The compositions of Al-Cu thin films were confirmed to be Al-4.9wt%Cu by using inductively coupled plasma-optical emission spectroscopy (ICP-OES).

Two types of Al-Cu thin films were used. “As-deposited” samples were tested as fabricated without any further heat treatment and were essentially solid solution alloys. The “artificially aged” samples were heat-treated in air at 190°C for 24 hours to induce precipitation θ'' , θ' and θ phase (Al₂Cu).

Al-Cu thin films were degreased for several seconds in a solution comprising 1.0 L deionized (DI) water containing 48.0g Na₂CO₃ and 32.4g Na₂SiO₃ at 65°C. After using DI water to rinse the thin films, they were deoxidized for 3 minutes in a solution comprising 1.0 L of DI water, 30.0g Sanchem 1000TM and 72.0 mL HNO₃ at 55°C. Samples were rinsed with DI water and air dried at ambient temperature.

After demonstrating the utility of this fabrication approach for idealized coating systems in Chapter 3, methods were extended to the preparation of new and more realistic coating systems.

Each coating systems consisted of a conversion coating and a primer. Some samples were then finished with a topcoat; others were not. The first conversion coating was a Boegel (AC131CB), which is a high performance non-chromate conversion coating. It is used to enhance the adhesion of the organic primer to metal substrates and is not intended to confer much corrosion resistance by itself[36, 37]. Formation of a mixed Zr/Si oxide coating results from a sol-gel reaction induced by an aqueous solution with 3 to 30% solids. Al-Cu thin films were immersed in the Boegel solution for 5 minutes and were then allowed to drain and air dry at ambient temperature for 24 hours before application of a primer coat. The resulting Boegel conversion coating was transparent. The second conversion coating used was a chromate conversion coating (CCC) (Alodine 1200S from Henkel Inc.). CCCs form a protective coating on the metal surface with iridescent golden color. The pH of the solution was measured to be 1.58. Al-Cu films were immersed into Alodine 1200S for 45 seconds and then rinsed with DI water at ambient temperature. Conversion coated samples were air dried at room temperature for 24 hours prior to application of a primer.

Several primer coatings were evaluated. The first is a chromium-free primer Deft 02GN084 (MIL-PRF-23377J 2), which is a 2-part epoxy primer pigmented with a blend of PrO/Pr(OH)_3 , CaSO_4 , and TiO_2 . The second was a home-made primer comprising a neat epoxy PD381-94 (Aerospace blank coating-no inhibitor) from Akzo Nobel and 5wt% SrCrO_4 pigment. All primers were mixed under ambient laboratory conditions and were applied by drawdown bar. The panels were air-dried at ambient temperature for 24 hours before being cured in the oven at 150°F for 48 hours.

A polyurethane Eclipse® high solids polyurethane aircraft topcoat was used on top of primers in certain experiments. This is a chemically cured, low VOC topcoat designed to provide premium gloss. The panels which were coved with a topcoat were also applied by drawdown bar.

Figure 1.3.1 illustrates the experimental setup used for direct optical imaging in these experiments. In this setup, electrical tape was applied to the sample as a mask on top of any coating. The exposure area was 0.32 cm^2 . A polyvinyl chloride (PVC) tube with a diameter larger than the exposure area was glued on top of the tape. All the experiments were terminated before the corrosion sites undercut the mask. A transmitted light source located above the sample was used for illumination. A QImaging™ Go-3 color CMOS camera attached to an Olympus SZ61 stereomicroscope was located underneath the sample. As corrosion progressed, the thin sputtered film was perforated and transmitted light passed through the sample to the camera. The progression of corrosion was recorded by Q-capture Pro™ recording software. Images of corrosion sites shape and size were collected at different time intervals. Analysis of the collected images was conducted using ImageJ™ and Photoshop. The movies were made by VideoMatch™ frame grabbing.

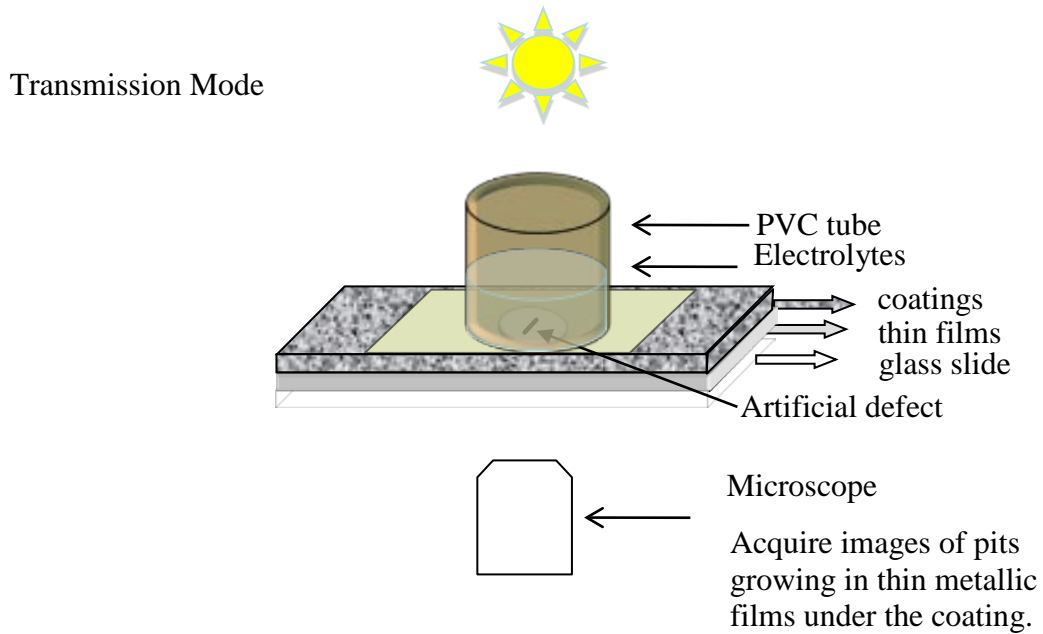


Figure 1.3.1 Instrumental configuration of the DOI setup.

1.3.4 Results

Each combination of metallic thin film substrate epoxy coating system was repeated at least in triplicate. Exact reproducibility is not attainable due to the complexity of each measurement. However, the results shown here were judged to be the most representative of the sample condition examined.

Coating thickness was determined by optical profilometry (Veeco Contour GT-K1 OP analysis). The edges of the samples were covered with scotch tape before applying the coatings. The scotch tape was removed immediately after applying the coating when the coatings were still wet. After curing the coatings, optical profilometry was carried out to measure the step height, which was taken as the coating thickness. The step heights were scanned from the center of the sample to the edge of the sample at 5 to 6 different areas in order to estimate average thickness. A typical scan is illustrated in Figure 1.3.2. The sample was Al-Cu-aged thin films covered with Deft primer. The Deft primer had a smooth surface (Figure 1.3.2(a) and (c)) and the thickness of the coatings was around $11.8\mu\text{m}$ from Figure 1.3.2(b). The SrCrO_4 primer coating thicknesses were around $10\mu\text{m}$ and polyurethane topcoats were around $15\mu\text{m}$ thick.

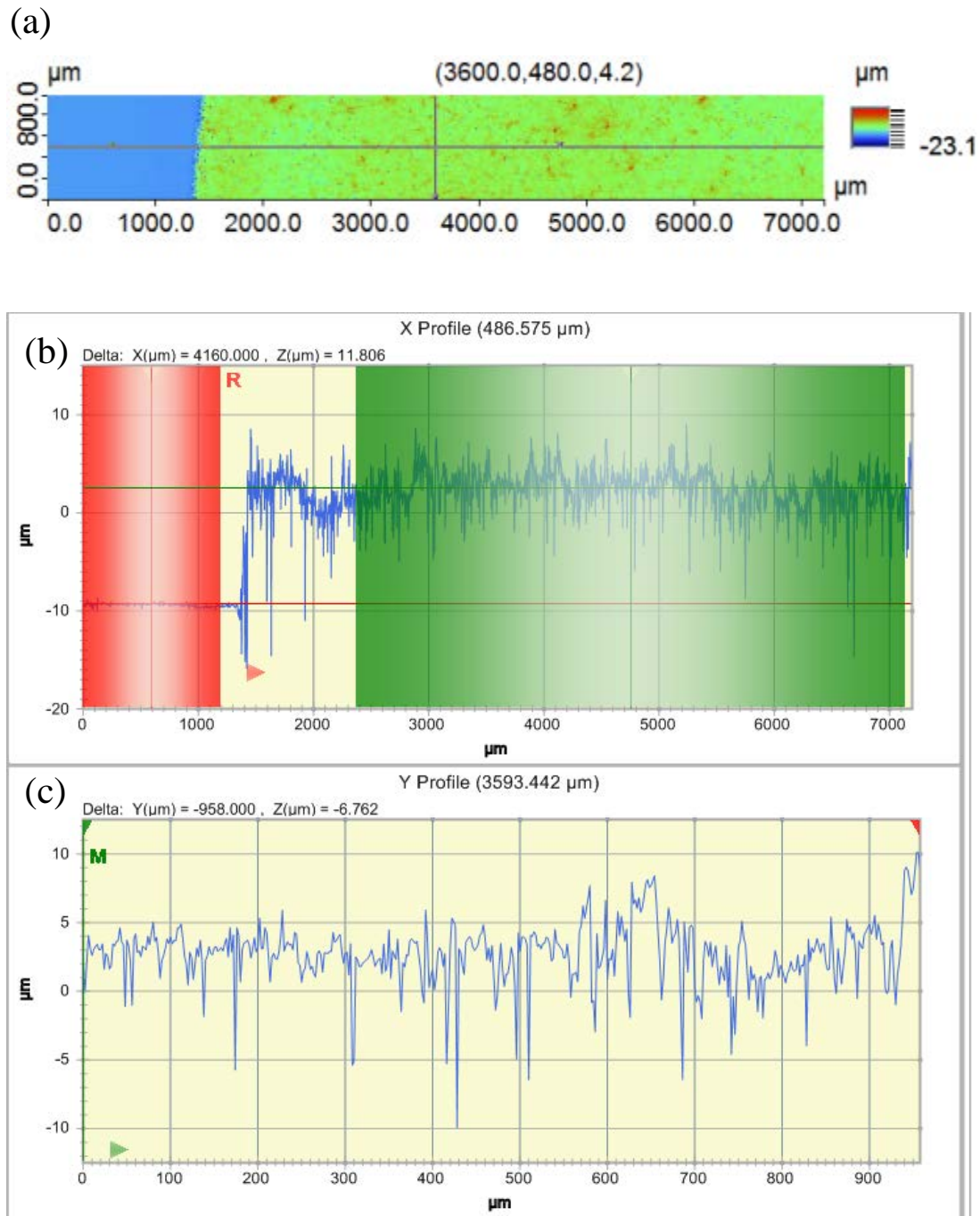


Figure 1.3.2 (a) sample surface roughness. (b) Step height of the Deft primer on Al-Cu aged thin films. (c) Cross section of sample surface roughness in the longitude direction as shown in (a).

Al-Cu thin films with different coating systems were mounted in epoxy and cross-sectioned. These sections were polished lightly with SiC abrasive paper from 600 to 1200 grit using successively finer papers. Samples were characterized by scanning electron microscopy (SEM). Resulting micrographs are shown in Figure 1.3.3. In these images the substrate is at the top of the micrograph and the coating components are towards the bottom. These images confirm

the primer and topcoat thickness estimates derived from profilometry measurements. Pigment particles inside of the Deft primer can be observed as white particles. The top coating was around 15 to 20 μm in thickness from Figure 1.3.3(d). It was difficult to distinguish both Boegel and chromate conversion coatings in the SEM micrographs because these coatings were thin and did not present a distinguishing contrast (Figure 1.3.3 (b-c)). The region of light contrast between the glass substrates and primer appeared to be Al-Cu metallic thin films.

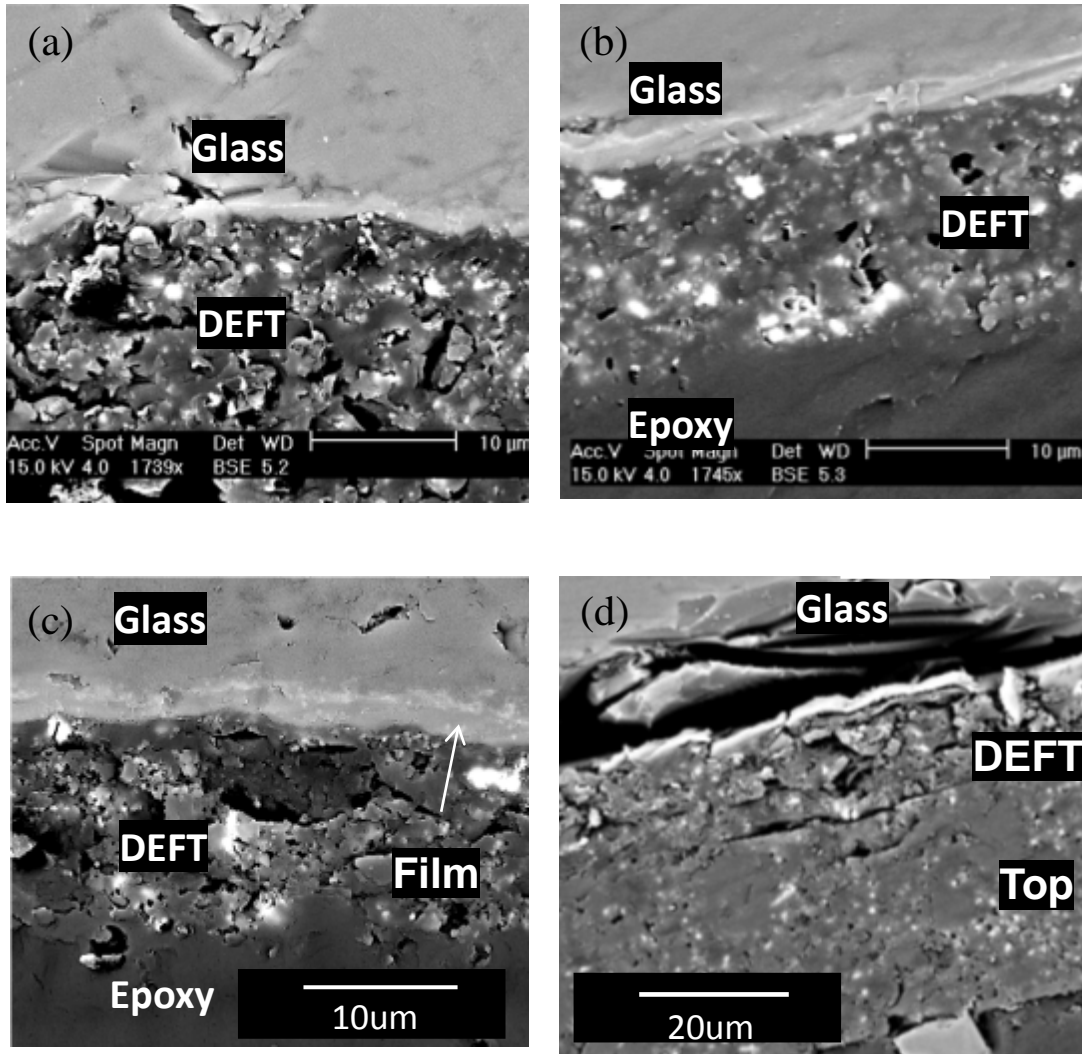


Figure 1.3.3 SEM Cross-section of the coating products: (a) Deft primer; (b) Boegel/Deft primer; (c) CCC/Deft primer; (d) Boegel/Deft primer/Topcoat.

Chromate conversion coatings provide corrosion protection to aluminum as stand alone coatings. Boegel coatings are adhesion promoters that are not intended to protect against corrosion in a stand-alone configuration. As a result, DOI imaging experiments were conducted on chromate conversion coated samples only to assess their impact on substrate corrosion behavior.

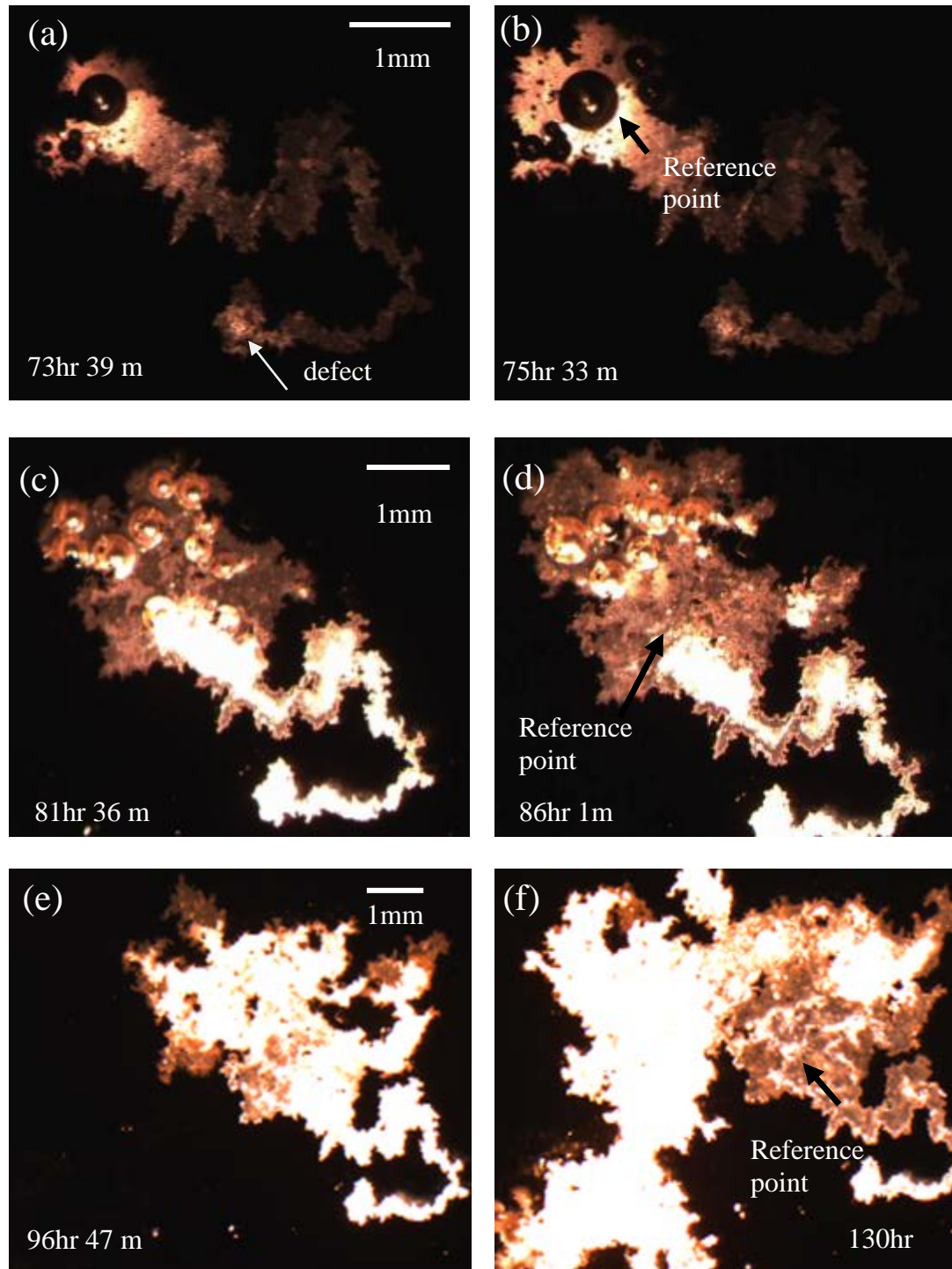


Figure 1.3.4 Images of the evolution of corrosion on chromate conversion coated aged Al-Cu thin film exposed to 0.5M NaCl solution.

Corrosion of conversion coated Al-Cu aged thin films was carried out during exposure to 0.5M NaCl solution. The evolution of undercoating corrosion morphology at 2 minutes intervals is shown in Movie 1.3.1. In this movie, the sample was imaged at a magnification of 53.5 \times

during an exposure period of 73 hours. In this experiment, corrosion initiated at an artificial defect in the coating, which was made by mechanically scratching before the experiment. Corrosion proceeded outward from the defect as shown in Figure 1.3.4(a). The initial stage of the growth involved filiform-like propagation of a corrosion site resulting in 0.5mm wide corrosion track. However, after 73 hours of exposure, the mode changed and corrosion began to spread radially from the tip of the site. The active front grew and then segments repassivated before several new localized sites began to propagate. A striking feature of the movie is significant hydrogen bubble formation occurring at the active margins of film corrosion site. Small bubbles moved away from active region and accumulated to form a big bubble behind the growing margins. As the corrosion front moved forward during dissolution, the bubbles were left behind in the interior of the corroded area attached to the glass substrate.

With longer exposure time, corrosion front moved out of the view of the microscope and lower magnifications (33 \times and 14 \times) were used in order to capture further images. Figure 1.3.4(c-f) shows the sample was exposed to solution for longer exposure time. In order to track the same spot in different magnifications, a reference point was indicated in Figure 1.3.4(b, d, f). Hydrogen bubbles continued formed at the corrosion front wall that were absorbed into larger bubbles behind the corroding margin. Due to the increase of incident light intensity, the black bubbles became bright.

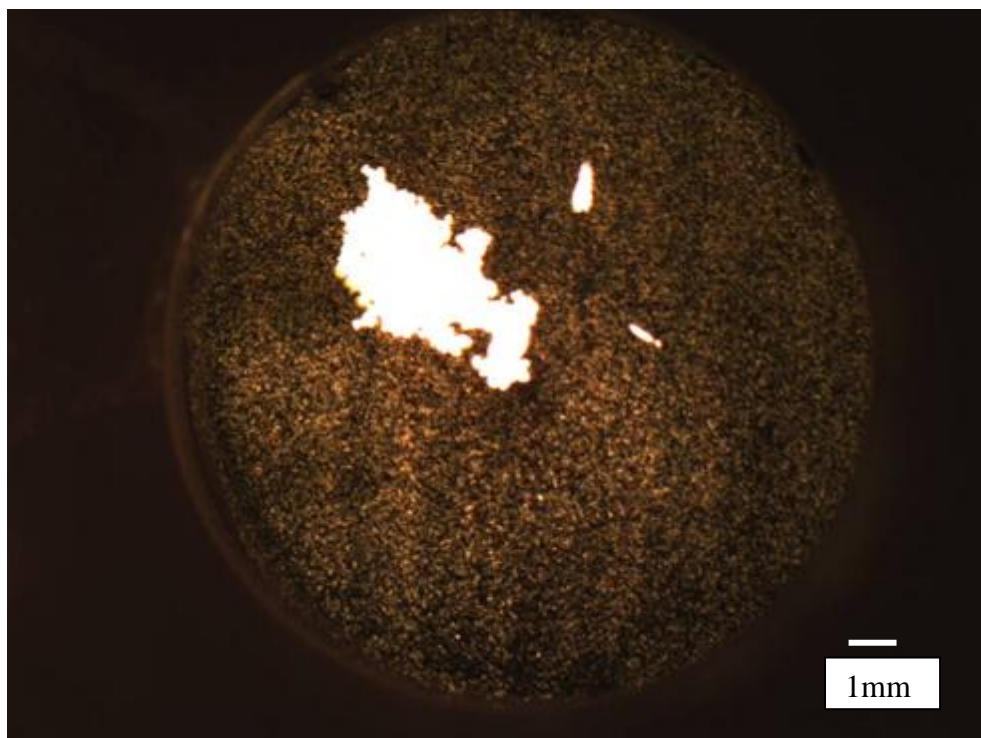


Figure 1.3.5 Image of Al-Cu aged sample coated with Deft primer after 6 days of exposure to aerated 0.5M NaCl solution under high incident light intensity.

The primer effects were investigated on artificially aged Al-Cu thin films coated with a Deft primer during exposure to aerated 0.5M NaCl solutions. In these experiments, corrosion site

morphologies and growth kinetics were observed and analyzed by the DOI method. These experiments were terminated before the corrosion front undercut the edge of the exposure region. Movie 1.3.2 shows the pictures captured every 10 minutes after the samples were exposed to the solution for 80 hours. A single corrosion site nucleated from a defect site and corrosion occurred rapidly along an irregular front and grew outward away from the defect. With one side of the corrosion site repassivated, the corrosion propagated primarily and preferentially in one direction. Eventually, the corrosion front at the repassivated region slowly became smooth with an obvious corrosion product ring trailing the corrosion front. The most striking difference between these experiments and the conversion coating-only experiments is that no hydrogen bubbles were observed in these experiments, which suggested that corrosion rate was slower than those samples under CCC. An image captured with higher incident light intensity is shown in Figure 1.3.5. A large number of discrete sites nucleated across the whole surface. This is consistent with a high-permeability, low-protection coating that allows ingress and interaction of electrolyte and dissolved oxygen with the substrate. Primer coatings are not intended to provide strong barrier protection as stand-alone coatings, and the widespread nucleation of corrosion sites was an indication of that characteristic of primers.

After exposure, the primer was chemically stripped from the substrate. Care was taken not to use mechanical action that would damage the underlying substrate, corrosion site or corrosion product. SEM images of the corrosion under the primer are shown in Figure 1.3.6. These images reveal bright corrosion product deposits along the edges of corrosion front at repassivation region. Some of the deposits are quite large; up to 50 μm in some cases (Figure 1.3.6(a)). EDS results show that these deposits were rich in Pr. Other deposits consist of collection of individual granules that are clustered tightly together, often in a band along the corrosion site perimeter. Higher resolution images of the precipitates are shown in Figure 1.3.6 (b-e). EDS of bands of granules along the corrosion front walls show that Cu and Pr enrichment. In order to eliminate the possibility that Pr was from the residual primer since both regions chosen were rich in Pr, a random region on the thin film was selected as shown in Figure 1.3.6 (d). EDS result shows that this region only rich in Al and the rest of the elements such as Si, Na, Ca, Mg were from glass substrate indicating that the primer was completely removed and that where Pr was detected, it was mostly incorporated as part of the corrosion product. This suggests dissolution of Pr pigment from the primer coating, release into the electrolyte in the coating and deposition in and around corrosion sites. The presence of corrosion suggests that the Pr released was not sufficient to inhibit undercoating corrosion in these experimental conditions.

The Cu observed in the corrosion product is present as discrete granules (Figure 1.3.6 (b, c, e)). These appear to be pure Cu crystallites or dendrites that have plated out from the electrolyte in the thin film corroded area. The fact that Cu appears as discrete crystallites rather than a continuous layer along a corroding margin suggests that Cu is released from the alloy during corrosion, perhaps by a non-faradaic pathway[38]. Cu ions in solution then plate out at local sites under the reducing conditions along the recently passivated corrosion margins leading to the morphologies observed. Video imaging showed the region in Figure 1.3.6 (b) was repassivated for only a short time prior to the conclusion of the experiment. Cu dendrites were not continuous along the corrosion front wall. Along segments of the corrosion site that were active up until the end of the experiment, Cu adopted a different morphology (Figure 1.3.6 (c)).

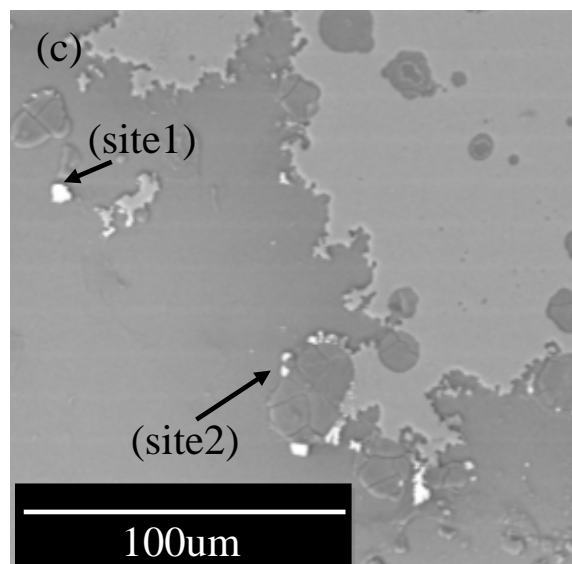
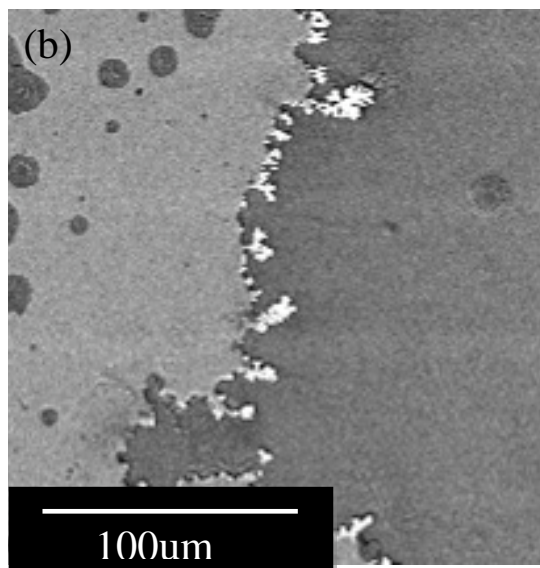
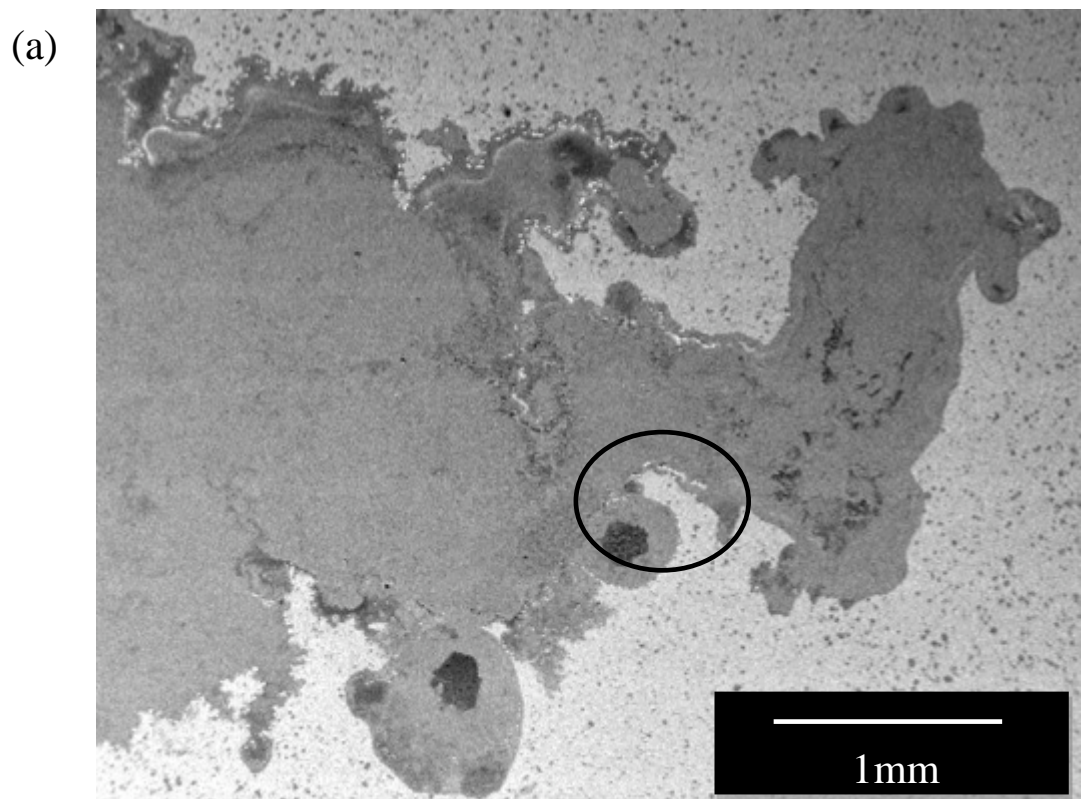
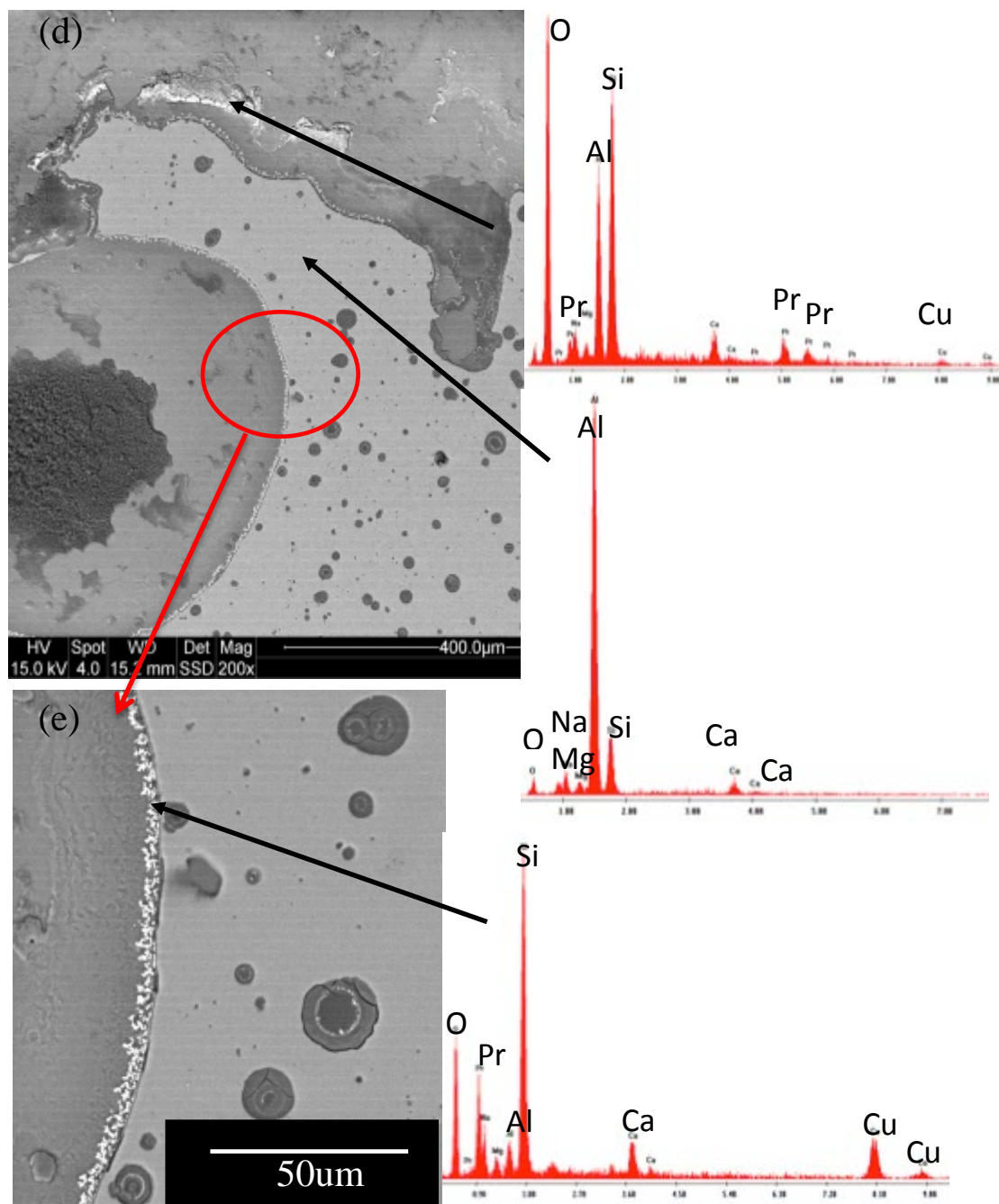


Figure 1.3.6 SEM and EDS results of Al-Cu aged thin films under Deft primer.

(a) Corrosion area under the primer. (b) Corrosion front at a repassivation region.

(c) Corrosion front at active growth region. (d-e) White precipitates. Continued.

Figure 1.3.6 Continued.



In most of the region, Cu precipitates were not detected along the wall instead Cu was found inside of the site such as “site 1”, which is a large, isolated Cu dendrite and “site 2” which is a Cu dendrite attached to a small island of the undissolved alloy thin film. Once these regions changed from active to repassivated, the Cu would precipitate along the wall similar as exhibited in Figure 1.3.6 (e). In addition, round shaped corrosion sites of various sizes were found. The largest of these was around 25um. In Figure 1.3.6(e), a white ring, which was rich in Cu, was separated from the wall by aluminum corrosion products.

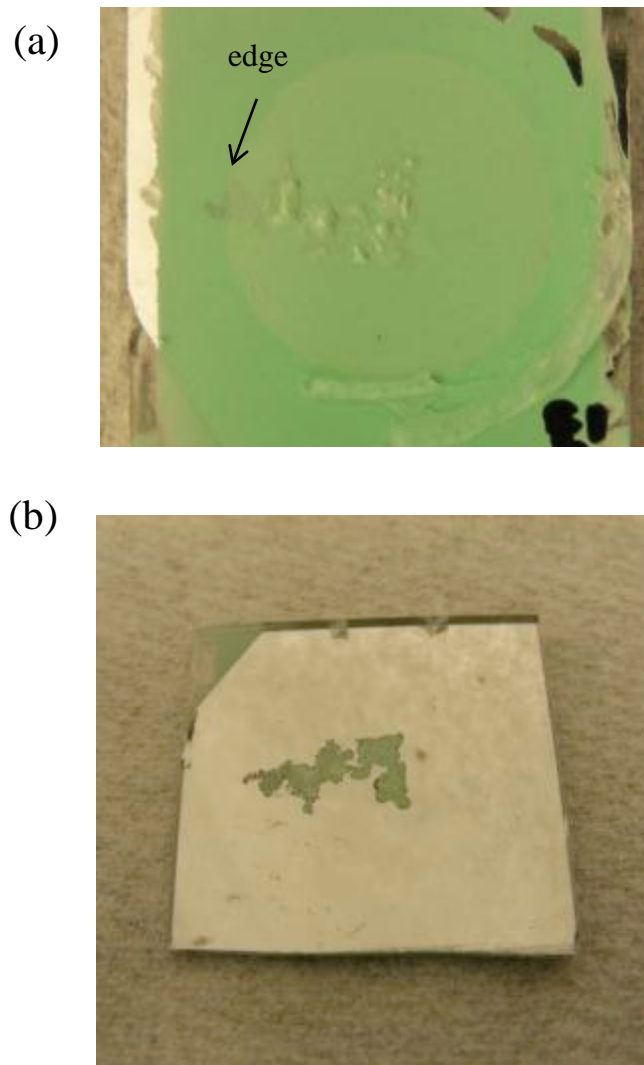


Figure 1.3.7 Photographs of sample under Boegel and Deft coating after exposure.
(a) Front view; (b) Back view.

It was found that Deft primer on its own did not provide strong corrosion inhibition. Coating systems combinations were studied using Al-Cu aged thin films pretreated with conversion coating (Boegel or CCC) and the Deft primer. Under the same primer, Al-Cu aged thin films produce different corrosion morphologies and different growth kinetics depending on

the conversion coating. A photograph of the sample with Boegel and Deft primer after exposure is shown Figure 1.3.7. From the front view of the photo, blisters were observed where the corrosion occurred underneath of the coating systems. The blisters extended out to the edge of exposure area, where a circle was separated by two different colors. The corrosion damage was also observed from the backside of the sample through the transparent glass slide. Movie 1.3.3 and Movie 1.3.4 show the early stages of corrosion growth under Boegel/Deft and CCC/Deft conversion coating/primer combinations, respectively. Images of the growing sites were recorded every 10 minutes. Similar growth modes were observed in other sites that propagated with a filamentary morphology. However, the filaments were thinner than was observed when a Boegel conversion coating was used. Comparisons were also made on corrosion site growth at further exposure time as shown in Movie 1.3.5 and Movie 1.3.6 with 10 minutes time intervals for the coating combinations of Boegel/primer and CCC/primer, respectively. In the case of thin films under Boegel/Deft, corrosion radiated outward from the tip of activated segments of the corrosion site similar to the case of thin films under Deft primer-only. Bubbles were observed both at the active corrosion region and repassivation region (Figure 1.3.8(e)). In the case of thin film under CCC/Deft, filiform corrosion behavior still continued with no bubbles observed during the experiment. Another interesting feature is that applying a layer of conversion coating either Boegel or CCC, suppresses widespread nucleation of corrosion sites. This is consistent with the fact that conversion coatings limited the oxygen reduction occurring on the surface across the exposure area.

Microstructural characterization of under coating damage was performed by SEM after exposure. The primer was not easily removed by a PR 3500, aircraft epoxy paint remover from the Boegel conversion coated samples, but was removed from CCC-treated surfaces. Therefore, SEM results only could be obtained from the CCC sample as shown in Figure 1.3.9. It should be noted that Pr rich deposits were observed both at the repassivation corrosion front and inside of the corroded region (Figure 1.3.9(a), (b) and (f)). High magnification of SEM results showed that at the corrosion front, there exhibited another form of precipitate other than Pr clusters (Figure 1.3.9(c) and (e)), which was rich in Cr. However, the amount of this type of deposit was small compared with the one rich in Pr. A random location as indicated as “site 3” was selected on the thin film surface. EDS revealed that Cr was still present on the thin film surface.

Conversion coated, primed and polyurethane topcoated Al-Cu aged metallizations approximated the material system used in aerospace applications. The benefit of a polyurethane topcoat was clearly evident as corrosion occurred much slower under these coating systems compared with the samples without topcoat. Movie 1.3.7 and 1.3.8 show samples containing a Boegel conversion coating and Deft primer and topcoat, and a CCC, Deft primer and topcoat respectively. Corrosion was slow, and images were collected no more frequently than once per day. Though slower, the nature of corrosion propagation was similar to the samples without topcoats. Corrosion occurred in episodes and periods of repassivation and growth lasted for several days.

Coating elements were applied in various combinations to as-deposited Al-Cu thin films. The same coating systems combinations were studied as described in section 1.3.2.3. The as-deposited Al-Cu metallizations are solid solutions and Cu-rich precipitates that localize corrosion and support oxygen reduction are absent.

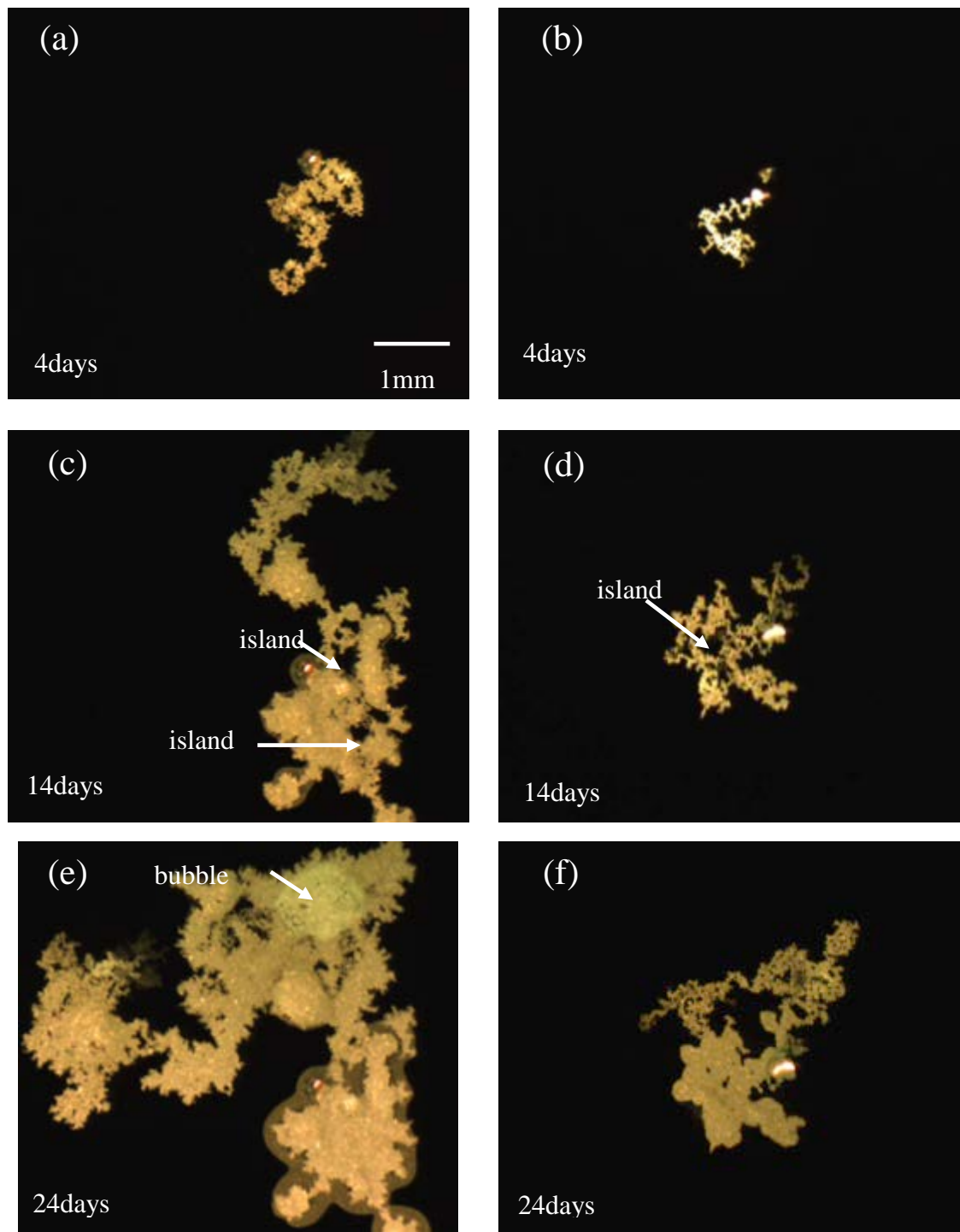


Figure 1.3.8 Images of the evolution of aged Al-Cu thin film with a Boegel conversion coating (left) or CCC (right) coated with Deft primer exposed to 0.5M NaCl solution.

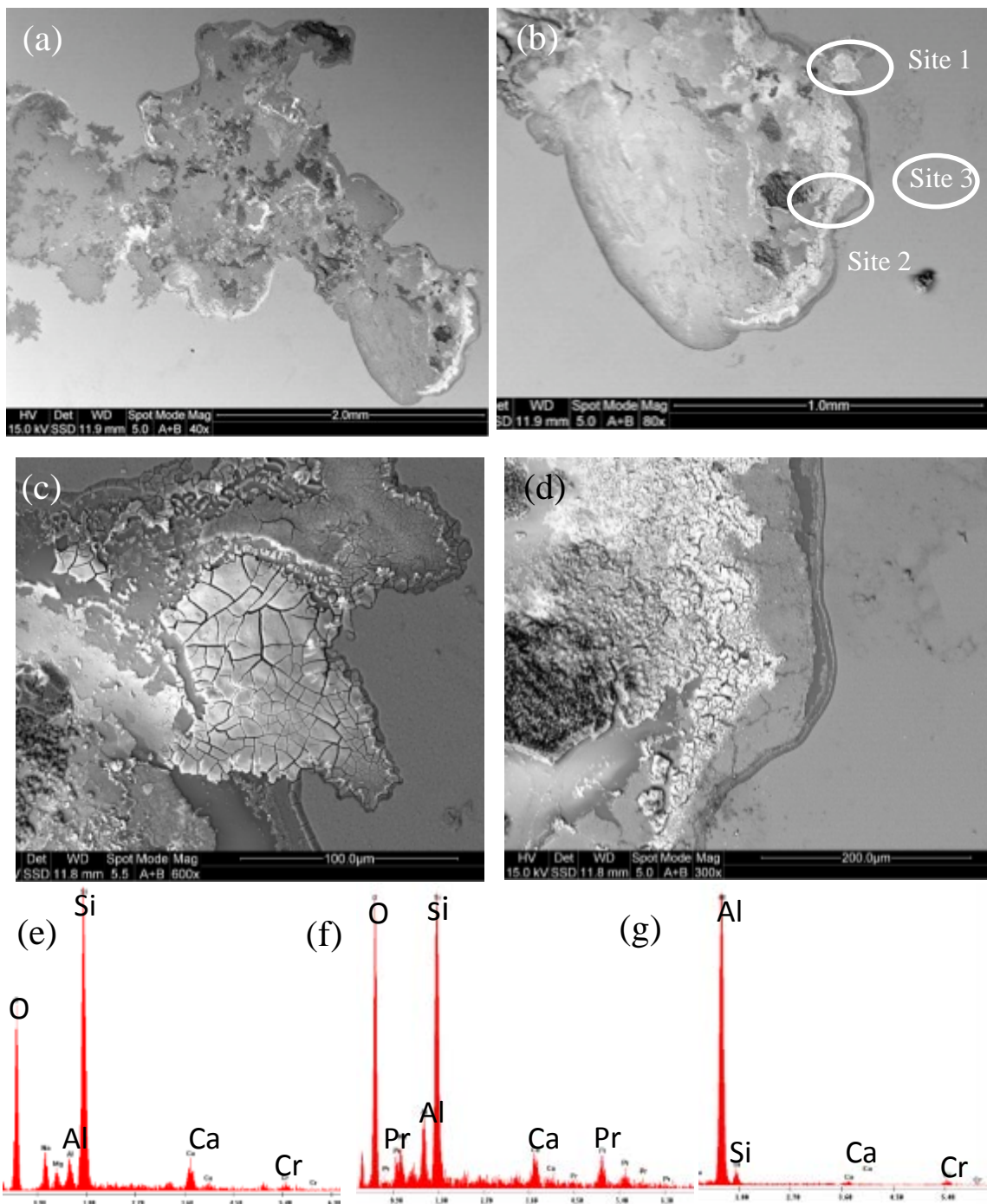


Figure 1.3.9 SEM and EDS results of Al-Cu aged thin films coated with a CCC/Deft coating combination. (a) Corrosion area under the primer. (b) Corrosion front at a repassivation region. (c) Corrosion front of site 1. (d) Corrosion front of site 2. (e) EDS result of site 1. (f) EDS result of site 2. (g) EDS result of site 3.

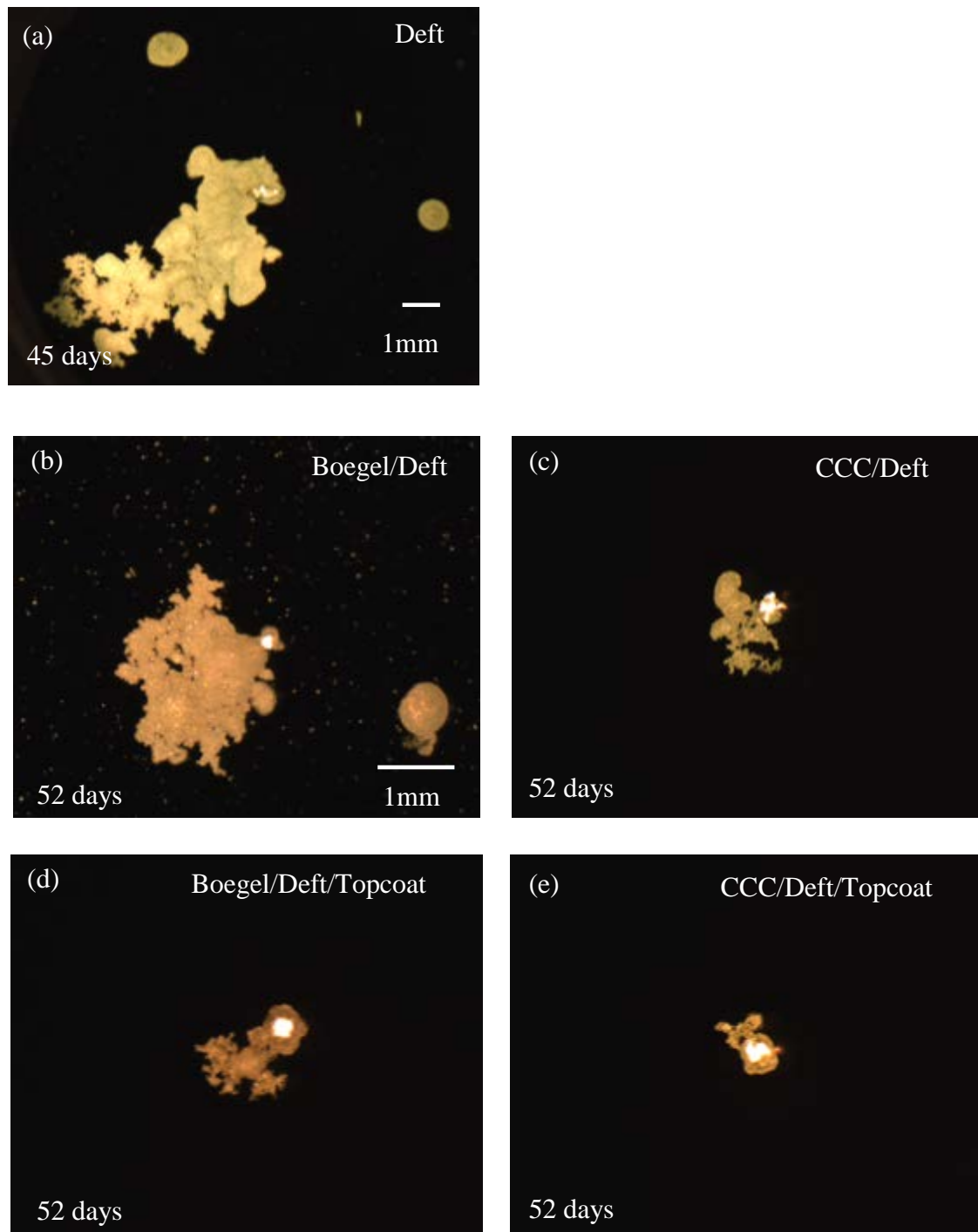


Figure 1.3.10 Images of as deposited Al-Cu thin film under (a) Deft primer; (b)Boegel/Deft; (c) CCC/Deft; (d) Boegel/Deft/Topcoat; (e) CCC/Deft/Topcoat exposed to 0.5M NaCl solution.

Localized corrosion nucleation was widespread in both the samples with Deft primer-only and Boegel/Deft combinations as shown in Figure 1.3.10(a-b). Due to the lower light intensity, these sites could not be observed in Figure 1.3.10(a). Movie 1.3.9 shows the propagation of small sites on the right side in Figure 1.3.10(b) with 10-minute intervals. The

Movie shows that as corrosion sites grow large one portion of the site is active at a time suggesting that the cathodic reaction was limited and only can support a certain amount of oxidation at any time. After a burst of growth, the round shape site became irregular like a consequence of a decrease in growth rate. In the end for both situations, the round shape site became irregular and grew steadily.

The CCC and extra layer of topcoat acted as physical and chemical barrier and were observed to reduce the initiation of corrosion sites Figure 1.3.10(c-e).

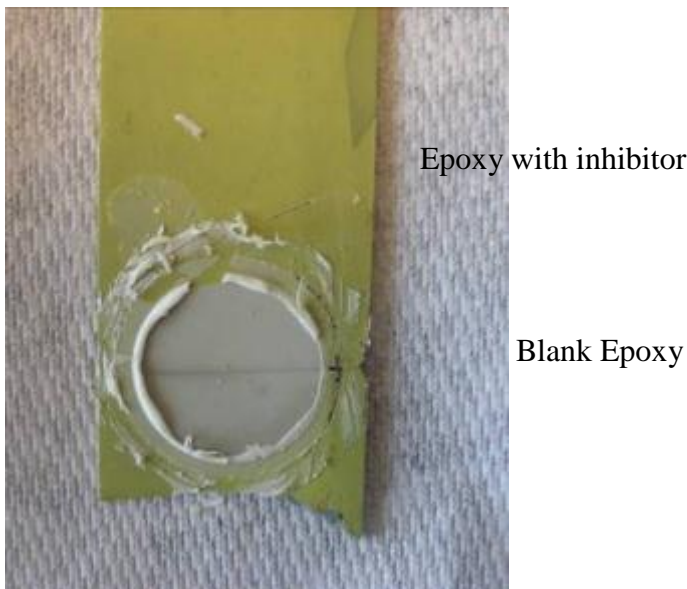


Figure 1.3.11 Photograph of Al-Cu aged thin film coated with a SrCrO₄-pigmented epoxy exposed to 0.5M NaCl solution.

A home-made primer comprising a neat epoxy PD381-94 (Aerospace no SrCrO₄ inhibitor) from Akzo Nobel and 5wt% SrCrO₄ pigment was applied as reference for detecting corrosion inhibition provided by coating systems. Results showed that there was no indication of corrosion initiation or growth in as-deposited or aged Al-Cu thin films under SrCrO₄ pigmented epoxy coatings even after 2 months. Chromate inhibitor release was indicated by blanching of the coating in the exposed area after exposure in aerated 0.5M NaCl (Figure 1.3.11). This suggested that the SrCrO₄ pigments dissolve into solution releasing chromate inhibitors that reinforce the passivity of the Al-Cu thin films alloy substrates.

1.3.5 Discussion

The DOI method, which takes advantages of using thin films as substrates, was utilized to investigate corrosion damage accumulation in Al-Cu thin films with various coating systems under free corrosion conditions in aerated NaCl solutions. The corrosion damage of thin films spread out laterally under the organic coatings and as corrosion sites grow they form deep lateral crevices under the coating.

The true anodic current density can be determined regardless of the cathodic reduction reaction rate within the corrosion site using the DOI method, which is a direct extension of the thin film pitting methods demonstrated by Frankel[39]. In the case of bare thin films polarized at different potentials, pit currents and pit current densities were constant at each applied potential if pit perimeter and pit bottom area varied linearly with time and time squared, respectively[40]. Because these experiments were made under free corrosion conditions in the presence of coatings, such regular changes did not occur and sites perimeters and bottom areas were fit using a nonlinear regression methods [40].

In most experiments, corrosion occurred at a single. These sites were irregularly shaped indicating that there were different local growth rates and different local current densities acting along the perimeter. In fact, observations show that large segments of the site perimeter were passivated for extended periods of time. To assess the corrosion growth kinetics in view of average variations of current density along the corrosion site perimeter, Frankel's model of calculating pit current density was utilized to calculate an “average anodic current density” to characterize corrosion growth as a function of time[41].

Even though the corrosion site morphology was irregularly shaped, the perimeter and bottom area could be accurately rendered. The time dependent site perimeter (P) and area (A_b) were determined through the course of the experiment and fitted according to Equation 1.3.1 and 1.3.2, respectively. The anodic current density as a function of time was determined by Equation 1.3.3, yielding the so-called “average anodic current density”:

$$P = a_1 t + a_2 t^2 \quad \text{Equation 1.3. 1}$$

$$A_b = b_1 t^2 + b_2 t^3 \quad \text{Equation 1.3. 2}$$

$$i_a(t) = \frac{\rho n F}{M} \frac{\partial A_p(t)}{\partial t} \frac{1}{P(t)} \quad \text{Equation 1.3. 3}$$

Where a_1 , a_2 , b_1 and b_2 are constants, ρ is the density of Al (g/cm³), n is equivalents of change per mole of Al reacted (eq/mol), M is molar mass of Al (g/mol) and F is Faraday's constant (C(eq)).

Figure 1.3.12 shows the average anodic current densities of aged Al-Cu thin films coated with a one-layer Deft primer coatings. To generate input for the average anodic current density calculation, 3 replicates were conducted for each unique coating system environment combination. An average calculation of these 3 replicates is also shown in Figure 1.3.12. It could be seen that this average current density as function of time was close to experiment 1. Therefore, experiment 1 was selected to represent the case of thin films under Deft primer-only.

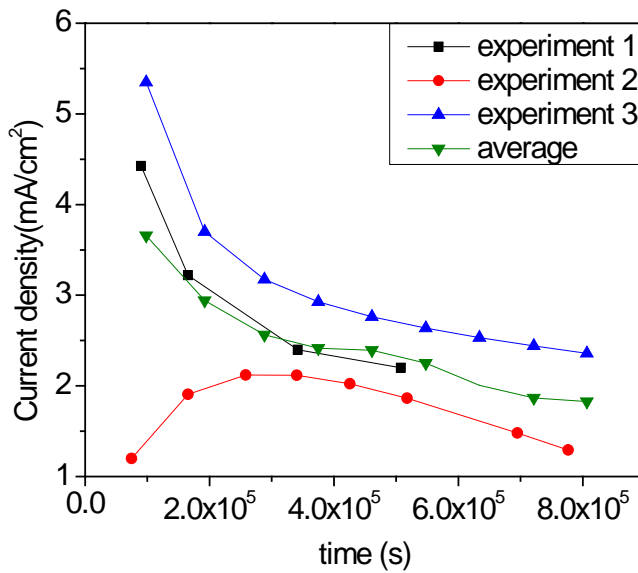


Figure 1.3.12 Average current density calculations of Al-Cu-aged thin films with Deft primer only as function of time. Three experiments were conducted under identical conditions.

In other coating systems, similar results were found and the average anodic current density with coating systems of various configurations applied is shown in Figure 1.3.13 for the Al-Cu thin films in the aged and as-deposited conditions. Overall, the average current densities were 3 times larger in aged thin films than in as-deposited thin films, which is attributed to the precipitation of θ phase (Al_2Cu) and its precursors that remove Cu from solid solution and thereby decrease the corrosion resistance of the α -Al solid solution phase[42]. In the case of Al-Cu aged thin films as shown in Figure 1.3.13 (a), the anodic current density was the highest when only single-layer Deft primer was present reflecting the permeable nature of this primer product. When the primer was applied on top of a conversion coating, average anodic current densities decreased notably with lower current densities observed for CCCs as compared to Boegel.

The presence of a polyurethane topcoat in the coating system has a dramatic effect on undercoating corrosion in these experiments. For both alloy substrate types, average anodic current densities are very low throughout the experiment without the initial “run-in” transient observed in the other data sets. This is probably due to the strongly increased barrier properties of the coating system that restrict oxygen reduction and decreased permeability that limits the interaction of electrolyte at the metal interface. Notably, when a topcoat was present, other differences in the make up of the coating system such as conversion coating type did not significantly affect the corrosion growth kinetics.

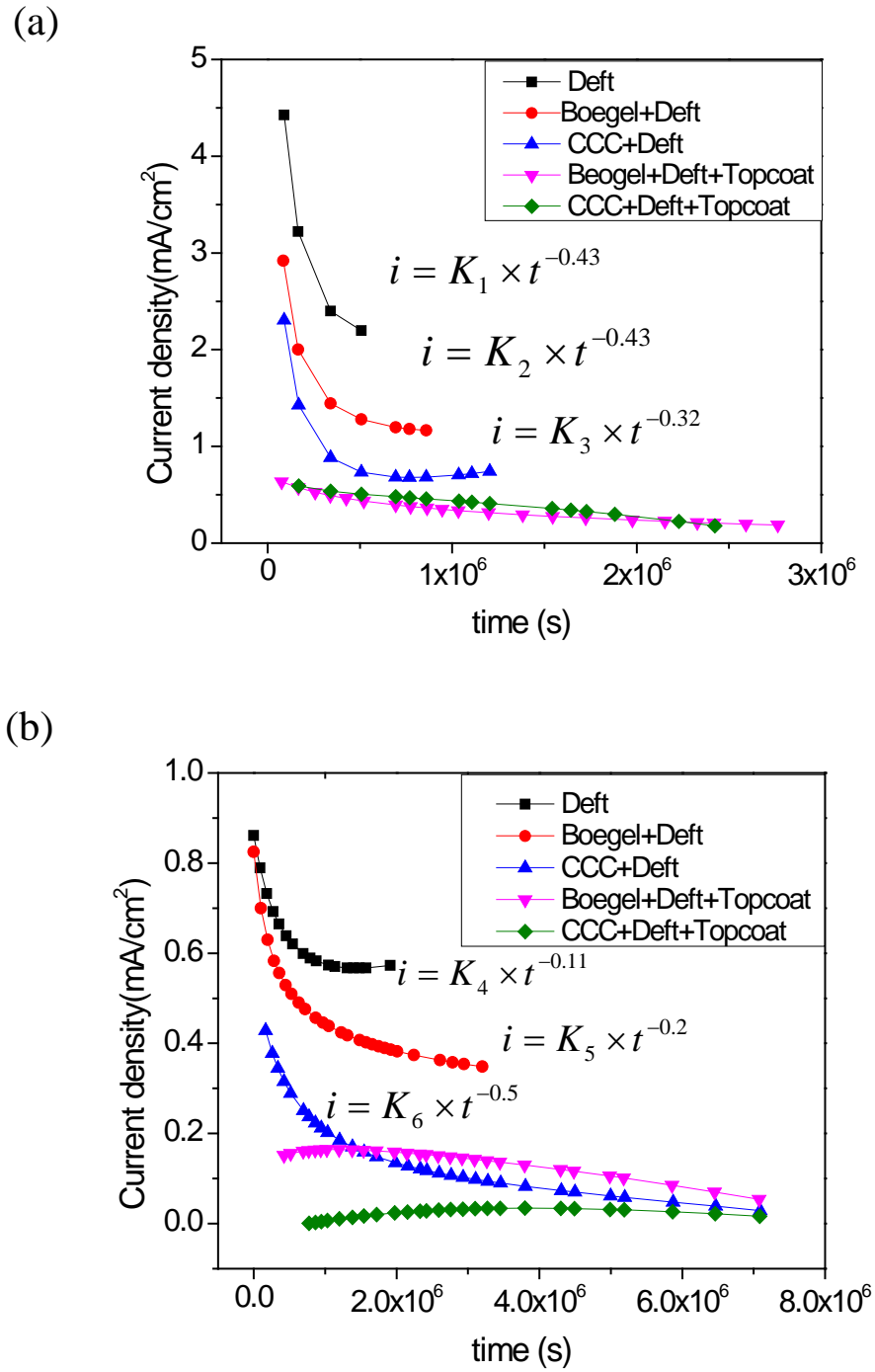
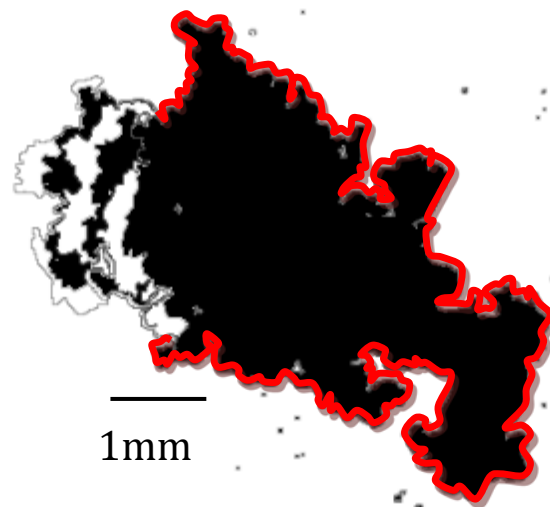
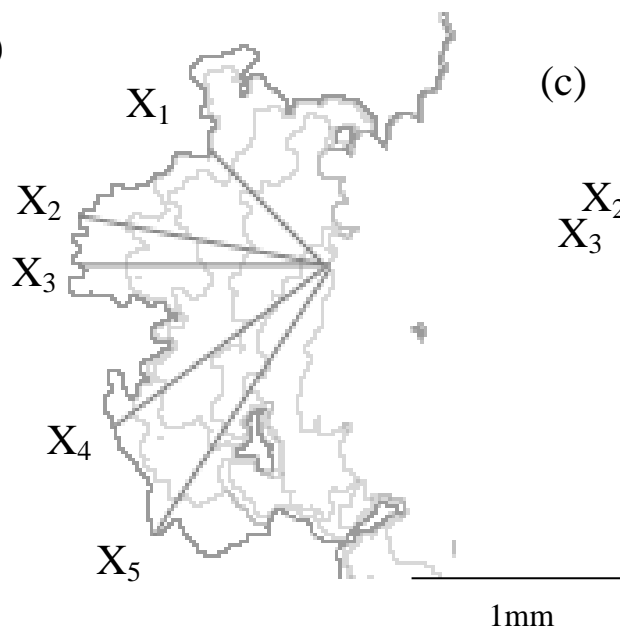


Figure 1.3.13 Average current densities of (a) Al-Cu-aged thin films.
 (b) Al-Cu as deposited thin films under various coating systems.

(a)



(b)



(c)

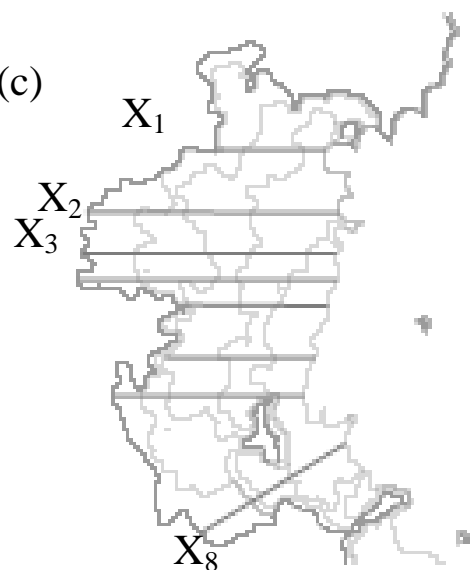


Figure 1.3.14 (a) Al-Cu-aged thin film under Deft primer exposure for 7 days. The evolution of images captured by microscope every 300 minutes. (b) Vectors emanated from a point and intersected the perimeter at different directions, (c) Vectors were selected perpendicular to the corrosion front.

In general, the average anodic current densities decayed with time and were fit to a power law:

$$i = Kt^b \quad \text{Equation 1.3.4}$$

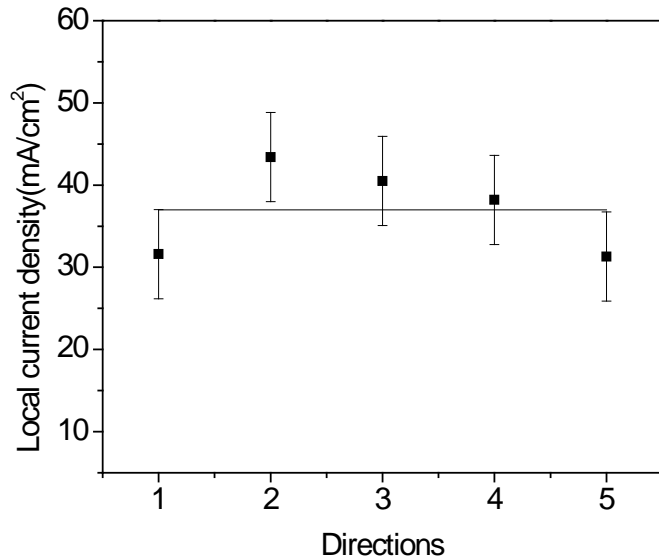
For aged Al-Cu substrates, the fitting results revealed that time exponent b ranged from -0.32 to -0.43. For as-deposited Al-Cu thin films, currents were lower and the decay in average anodic current density tended to be slower with the exception of the CCC-Deft primer sample, which passivated rapidly

Direct observations from virtually all experiments showed that corrosion sites growing under coatings at free corrosion conditions grew slowly and non-uniformly. In most cases, much of the corrosion site perimeter was in a passive state. Locally active regions were observed to propagate and image analysis-based on methods for estimating the current densities from these regions were developed and used to estimate local growth kinetics. Figure 1.3.14(a) is an example of a corrosion site growing only along a portion of its perimeter. In this example the previously corroded bottom region is black and the passive perimeter that does not move is highlighted in red. The active perimeter position changes with time and is marked at various locations using alternating white and black banding. Even along this front, variations in local growth rates exist and any estimate of kinetics is still and average across the active area. Nonetheless, calculations were conducted to determine how these growth rates compared with rates measured in other coating systems. In Figure 1.3.14(a), the outlines of the images, which show the evolution of corrosion site morphology captured by the microscope every 300 minutes, were overlapped using PhotoshopTM software. Several vectors were overlaid on the corrosion growth region so that they emanated from a point and intersected the perimeter at different directions as shown in Figure 1.3.14 (b). Other vectors were also selected perpendicular to the corrosion front as shown in Figure 1.3.14 (c). These particular vector array selections were analyzed to determine the sensitivity of local anodic current density to vector direction. The corrosion rate along a particular vector was calculated as the change in perimeter intersection point divided by exposure time (dx/dt). In order to calculate the current density, Faraday's Law was applied:

$$i = \frac{\rho n F}{M} v \quad \text{Equation 1.3.5}$$

Where ρ is the density of Al (g/cm^3), n is equivalents of change per mole of Al reacted (eq/mol), M is molar mass of Al (g/mol), F is Faraday's constant (C/eq) and v is the velocity of the perimeter along the vector (cm/s). Perimeter velocities were essentially constant allowing single-valued characterization of the rate. Using this method, the local current densities were determined as shown in Figure 1.3.15. Results shows that local current densities were 10 times higher than that of average current densities calculated for the whole corrosion site. Figure 1.3.15 (a) also shows that the highest current density is associated with vector 2 as might have been guessed from inspection of the vector placement on the growth region. However, a comparison of all 5 estimates shows that there is less than a factor of two variation in the mean current density along the vectors selected. Comparisons were also made on different vector arrays based on the corrosion propagation directions as shown in Figure 1.3.15 (c). It should be noted that the mean current density calculations fell in the same range as Figure 1.3.15 (b). Therefore, a reasonable, but arbitrary selection of a vector on a corrosion field is likely to yield a fair estimate of the local current density.

(a)



(b)

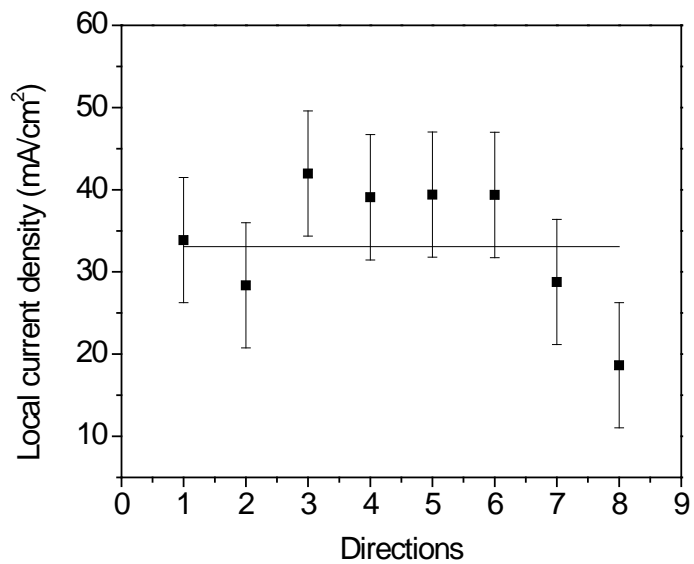


Figure 1.3.15 (a) Estimated local current densities along vectors shown in Figure 1.3.14 (b);
(b) Estimated local current densities along vectors shown in Figure 1.3.14 (c).

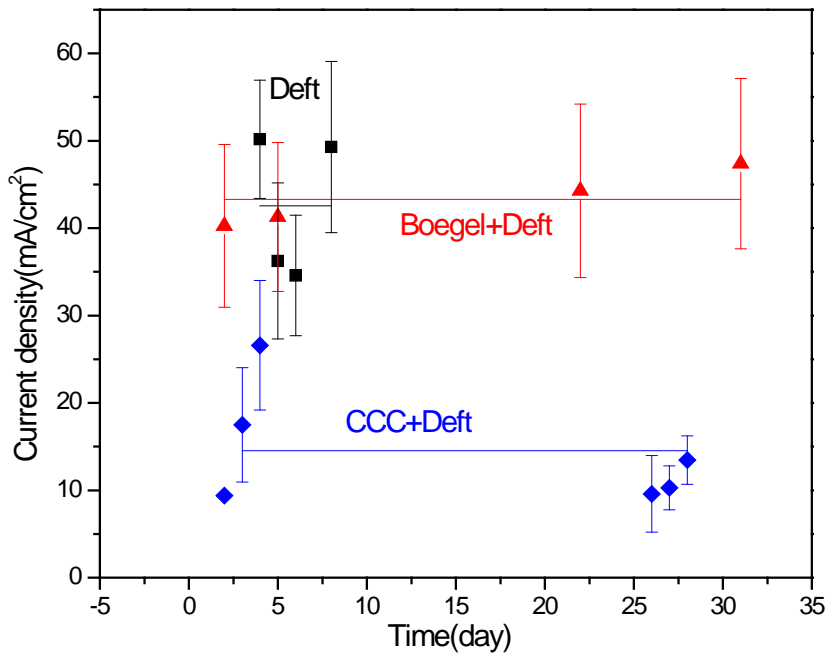


Figure 1.3.16 Local current densities as function of time for various coating systems. Solid lines represent the average values of local current densities.

Local corrosion growth kinetics among different coating systems was also examined. A plot showing a comparison is given in Figure 1.3.16. This plot compares Deft primer only, a Boegel plus Deft primer combination and a CCC plus Deft primer combination. These coating systems were applied to aged Al-Cu thin film. Average local current densities were in the range of 30 to 60 mA/cm² for the Deft primer-only sample and were among the highest current densities measured. The introduction of a Boegel conversion coating did nothing to decrease local current densities. However, the presence of a CCC dramatically decreased local current densities suggesting a strong inhibiting effect associated with this coating component.

In Movie 1.3.9, a single round corrosion site was observed during a short burst of growth before it became to an irregularly shaped. This sample was an as-deposited Al-Cu thin film coated with Boegel conversion coating and Deft primer. The corrosion rate was estimated from the increase corrosion site radius, $\partial r / \partial t$, over a time interval of 100 minutes. The average site radius was based on at least 3 measurements. The radius as function of time was shown in Figure 1.3.17. By fitting the data, it was found out that the corrosion site propagation velocity was constant. In order to determine the current density, Equation 1.3.5 was applied. The current density for this site was calculated to be 16mA/cm². It can be seen that the current density of as-deposited thin films was smaller than the aged thin films under the same coating systems due to the corrosion inhibition effect of Cu in solid solution.

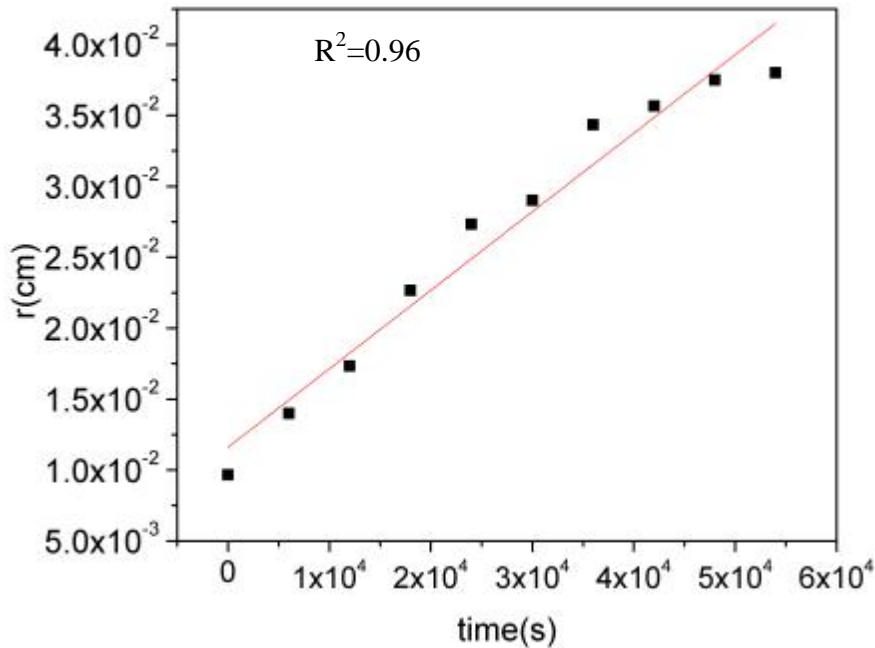


Figure 1.3.17 Single round shape corrosion site nucleated in the Al-Cu thin film at “as-deposited” condition coated with Boegel conversion coating and Deft primer. Site radius as function of growth time. Scatter plot was the original data and the red solid line was the fitting curves.

In this study, the effects of Boegel and chromate conversion coatings on undercoating corrosion were characterized and compared. Direct comparisons were possible from experiments where the conversion coatings were used as pretreatments for a subsequently applied Deft primer. As a negative control, corrosion imaging experiments were carried out on samples where the Deft primer was applied directly to the alloy thin film substrate without any conversion coating.

Deft coatings are permeable and do not provide significant active corrosion protection. As a result, in the absence of an underlying conversion coating, Al-Cu alloy thin films experience widespread nucleation of corrosion sites across the surface (Figure 1.3.5). Additionally, the highest average current densities were measured from samples with Deft primer only.

Application of a Boegel conversion coating in combination with the Deft primer to as-deposited Al-Cu substrates did not do much to improve corrosion resistance compared to the negative control sample. Many corrosion sites nucleated, though the total number of sites was somewhat reduced. On Al-Cu samples that were artificially aged, corrosion initiation rate was reduced and different corrosion morphologies were observed. Overall, it is suspected that the Boegel-Deft combination promotes some corrosion resistance by limiting the cathodic reaction sites and increasing primer coating adhesion.

Deft primers used in conjunction with CCC pretreatments showed significant resistance to corrosion. Widespread corrosion sites nucleation was totally suppressed in both aged and as-deposited thin film substrates. This is consistent with the general understanding that chromates are superior corrosion inhibitors when deployed within coating systems[12].

As discussed in 1.3.4.3.1, Deft primers applied directly on substrates did not provide substantial protection. It has been reported that rare earth compounds are not as effective as chromates[26]. Species such as PrO_x in the Pr-based epoxy-polyamide primers only exhibited corrosion protection when it was applied on top of a CCC treated substrate[43]. Pr was detected by EDS in corrosion product in samples analyzed after exposure. This indicates that Pr is released from the coating. However, it appears that it is not as effective in accomplishing corrosion protection as chromate.

The CCC-Deft primer pair, was much more effective in reducing the extent of corrosion. This is consistent with reports that having chromate in any part of a coating system will significantly improve the corrosion resistance of the overall system[12]. Little or no Cr was detected inside of corroded region in post-exposure characterization indicating that the concentration of chromate needed to accomplish protection is very low.

Application of a topcoat to a coatings system had a profound effect on undercoating corrosion damage in these experiments. Effects on both on corrosion morphology and growth kinetics were observed. Corrosion growth kinetics was slow and corrosion sites were only marginally stable. The presence of a topcoat dominated contributions to corrosion resistance from other components of the coating system, which appeared to be due to a significant increase in overall barrier properties limiting the interaction of the environment with the substrate and reducing the region that supported cathodic reaction on the metal surface.

1.3.6 Conclusions

1. The effects of the organic coating systems on thin film corrosion formation, morphology and growth kinetics were studied using two types of conversion coatings (Boegel and CCC), two primers (Deft primer and chromate pigmented primer) and in the presence or absence of a polyurethane topcoat on Al-4.9wt% Cu thin films at “as- deposited” and “artificially aged” condition.
2. Under free corrosion conditions, stable single corrosion sites grew with a filamentary morphology. They rarely grew uniformly or continuously—part of corrosion site was active while other was passive. Large numbers of discrete corrosion sites nucleated in the case of thin films coated with Deft primer alone. This is due to the high pigment loading in the Deft primer, which provides availability of oxygen and ingress of the electrolyte and the weaker inhibiting character of the primer.
3. Ex-situ characterization conducted on corroded areas showed that the Deft coating does release Pr. SEM and EDS results showed that Pr was found inside of the corroded area on samples prepared with Deft primers. Due to the large extent of corrosion, it does not appear that Pr was an effective inhibitor under these experimental conditions. In contrast, corrosion was completely suppressed by chromated primers and strongly suppressed with CCCs formed part of

the coating system. Cr was not readily detected in corrosion sites indicating that it does not act at corroded region or is present at amounts below detection limits.

4. Quantitative measurements of undercoating corrosion damage accumulation were made. Average corrosion rates (current density in mA/cm²) were calculated using Faraday's law by collecting corrosion site perimeter and bottom area. Results showed that the estimates of average current density can be used to rank different coating systems.

5. Local corrosion growth rates were derived from the corrosion site growth velocity and were found to be 10 times higher than that of average current densities. The local current densities eliminated the contribution of repassivation region, which was present in cases of thin films under coating systems.

6. Corrosion inhibition was greater when a Deft primer was used in combination with a CCC than with a Boegel conversion coating. As for the primer, corrosion nucleation and growth is strongly suppressed under a model chromate primers (epoxy with SrCrO₄ pigment) and less so under a Deft primer. The presence of a polyurethane top coating did not delay the onset of corrosion. However, it reduced the corrosion rate of single corrosion site growth.

1.3.7 References

1. Agarwala, V.S. and Siraj Ahmad, *Corrosion Detection and Monitoring - A Review*. CORROSION 2000, March 26 - 31, 2000 , Orlando, Fl, 2000.
2. Sangaj, N.S. and V.C. Malshe, *Permeability of polymers in protective organic coatings*. Progress in Organic Coatings, 2004. **50**(1): p. 28-39.
3. Wanner, M., et al., *Characterization of interphase adhesion in multi-layer coating systems*. Progress in Organic Coatings, 2010. **69**(3): p. 260-266.
4. Carbonini, P., et al., *Electrochemical characterisation of multilayer organic coatings*. Progress in Organic Coatings, 1996. **29**(1-4): p. 13-20.
5. Allahar, K.N., et al., *Water transport in multilayer organic coatings*. Journal of the Electrochemical Society, 2008. **155**(8): p. F201-F208.
6. Oudar, P.M.a.J., (Ed.)*Corrosion Mechanism in Theory and Practice*. 1995: Marcel Dekker, Inc.
7. Leidheiser, H., *Corrosion of Painted Metals - a Review*. Corrosion, 1982. **38**(7): p. 374-383.
8. Kendig, M.W. and R.G. Buchheit, *Corrosion inhibition of aluminum and aluminum alloys by soluble chromates, chromate coatings, and chromate-free coatings*. Corrosion, 2003. **59**(5): p. 379-400.
9. Ilevbare, G.O., et al., *Inhibition of pitting corrosion on aluminum alloy 2024-T3: Effect of soluble chromate additions vs chromate conversion coating*. Corrosion, 2000. **56**(3): p. 227-242.
10. Bierwagen, G., *The physical chemistry of organic coatings revisited - viewing coatings as a materials scientist*. Journal of Coatings Technology and Research, 2008. **5**(2): p. 133-155.
11. Cohen, S.M., *REVIEW - REPLACEMENTS FOR CHROMIUM PRETREATMENTS ON ALUMINUM*. Corrosion, 1995. **51**(1): p. 71-78.

12. Buchheit, R.G. and A.E. Hughes, *Chromate and Chromate-Free Conversion Coatings*, in *ASM Handbook Volume 13A, Corrosion: Fundamentals, Testing, and Protection (ASM International)*. 2003. p. 720-735.
13. Vanwesting, E.P.M., G.M. Ferrari, and J.H.W. Dewit, *The Determination of Coating Performance with Impedance Measurements .2. Water-Uptake of Coatings*. Corrosion Science, 1994. **36**(6): p. 957-977.
14. Bierwagen, G., et al., *EIS studies of coated metals in accelerated exposure*. Progress in Organic Coatings, 2003. **46**(2): p. 148-157.
15. McMurray, H.N., G. Williams, and S. O'Driscoll, *Chromate inhibition of filiform corrosion on organic coated AA2024-T3 studied using the scanning Kelvin probe*. Journal of the Electrochemical Society, 2004. **151**(7): p. B406-B414.
16. Forsyth, M., et al., *Inhibition of corrosion on AA2024-T3 by new environmentally friendly rare earth organophosphate compounds*. Corrosion, 2008. **64**(3): p. 191-197.
17. Amirudin, A. and D. Thierry, *Application of Electrochemical Impedance Spectroscopy to Study Efficiency of Anticorrosive Pigments in Epoxy-Polyamide Resin*. British Corrosion Journal, 1995. **30**(2): p. 128-134.
18. Deflorian, F. and I. Felhosi, *Electrochemical impedance study of environmentally friendly pigments in organic coatings*. Corrosion, 2003. **59**(2): p. 112-120.
19. Hinton, B.R.W., D.R. Arnott, and N.E. Ryan, *THE INHIBITION OF ALUMINUM-ALLOY CORROSION BY CEROUS CATIONS*. Metals Forum, 1984. **7**(4): p. 211-217.
20. Arnott, D.R., B.R.W. Hinton, and N.E. Ryan, *CATIONIC FILM-FORMING INHIBITORS FOR THE CORROSION PROTECTION OF AA 7075 ALUMINUM-ALLOY IN CHLORIDE SOLUTIONS*. Materials Performance, 1987. **26**(8): p. 42-47.
21. Arnott, D.R., B.R.W. Hinton, and N.E. Ryan, *CATIONIC-FILM-FORMING INHIBITORS FOR THE PROTECTION OF THE AA-7075 ALUMINUM-ALLOY AGAINST CORROSION IN AQUEOUS CHLORIDE SOLUTION*. Corrosion, 1989. **45**(1): p. 12-18.
22. Arnott, D.R., et al., *AUGER AND XPS STUDIES OF CERIUM CORROSION INHIBITION ON 7075-ALUMINIUM ALLOY*. Applications of Surface Science, 1985. **22-3**(MAY): p. 236-251.
23. Muster, T.H., et al., *An investigation of rare earth chloride mixtures: combinatorial optimisation for AA2024-t3 corrosion inhibition*. Surface and Interface Analysis, 2010. **42**(4): p. 170-174.
24. Proost, J., et al., *Morphology of corrosion pits in aluminum thin film metallizations*. Journal of Solid State Electrochemistry, 1998. **2**(3): p. 150-155.
25. Markley, T.A., et al., *Influence of praseodymium - Synergistic corrosion inhibition in mixed rare-earth diphenyl phosphate systems*. Electrochemical and Solid State Letters, 2007. **10**(12): p. C72-C75.
26. Treu, B.L., et al., *Effect of Phase on the Electrochemical and Morphological Properties of Praseodymium-based Coatings*. High Resolution Characterization of Corrosion Processes 2, 2011. **33**(35): p. 53-66.
27. Amirudin, A., *Application of Electrochemical Impedance Spectroscopy to Study the Degradation of Poly-coated Metals*. Progress in Organic Coatings, 1995. **26**: p. 1-28.
28. Skale, S., V. Dolecek, and M. Slemnik, *Electrochemical impedance studies of corrosion protected surfaces covered by epoxy polyamide coating systems*. Progress in Organic Coatings, 2008. **62**(4): p. 387-392.

29. Oliveira, C.G. and M.G.S. Ferreira, *Ranking high-quality paint systems using EIS. Part 1: intact coatings*. Corrosion Science, 2003. **45**(1): p. 123-138.
30. Sekine, I., *Recent evaluation of corrosion protective paint films by electrochemical methods*. Progress in Organic Coatings, 1997. **31**(1-2): p. 73-80.
31. Rammelt, U. and G. Reinhard, *Application of Electrochemical Impedance Spectroscopy (Eis) for Characterizing the Corrosion-Protective Performance of Organic Coatings on Metals*. Progress in Organic Coatings, 1992. **21**(2-3): p. 205-226.
32. Armstrong, R.D. and J.D. Wright, *Impedance Studies of Poly Ethylmethacrylate Coatings Formed Upon Tin-Free Steel*. Corrosion Science, 1992. **33**(10): p. 1529-&.
33. Loveday, D., P. Peterson, and B. Rodgers, *Evaluation of organic coatings with electrochemical impedance spectroscopy - Part 2: Application of EIS to coatings*. Jct Coatingstech, 2004. **1**(10): p. 88-93.
34. Titz, J., et al., *Characterization of Organic Coatings on Metal Substrates by Electrochemical Impedance Spectroscopy*. Corrosion, 1990. **46**(3): p. 221-229.
35. Grandle, J.A. and S.R. Taylor, *Electrochemical Impedance Spectroscopy of Coated Aluminum Beverage Containers .1. Determination of an Optimal Parameter for Large-Sample Evaluation*. Corrosion, 1994. **50**(10): p. 792-803.
36. Liu, J., et al., *Effect of surface morphology on crack growth at a sol-gel reinforced epoxy/aluminum interface*. Journal of Adhesion, 2006. **82**(5): p. 487-516.
37. Liu, J., et al., *Effect of Processing Conditions on Adhesion Performance of a Sol-Gel Reinforced Epoxy/Aluminum Interface*. Journal of Adhesion Science and Technology, 2008. **22**(10-11): p. 1159-1180.
38. Buchheit, R.G., et al., *Local dissolution phenomena associated with S phase (Al₂CuMg) particles in aluminum alloy 2024-T3*. Journal of the Electrochemical Society, 1997. **144**(8): p. 2621-2628.
39. Ryan, M.P., et al., *Corrosion pits in thin films of stainless steel*. Journal of the Electrochemical Society, 1999. **146**(1): p. 91-97.
40. Frankel, G.S., et al., *Pit Growth in NiFe Thin-Films*. Journal of the Electrochemical Society, 1992. **139**(8): p. 2196-2201.
41. Kim, Y. and R.G. Buchheit, *A characterization of the inhibiting effect of Cu on metastable pitting in dilute Al-Cu solid solution alloys*. Electrochimica Acta, 2007. **52**(7): p. 2437-2446.
42. Stoffer, J.O.R., MO, US), Yu, Pu (Rolla, MO, US), Morris, Eric L. (Irvine, CA, US), O'keefe, Thomas J. (Rolla, MO, US), Hayes, Scott A. (Rolla, MO, US), *Compounds for corrosion resistant primer coatings and protection of metal substrates* U. S. Patent App. 2004/0249023, 2004.

1.4 Using the DOI Method to Characterize Corrosion Damage Accumulation Due to Cabinet Exposure Testing

1.4.1 List of Figures and Tables

Figure 1.4.1 Demonstration of droplet cell setup for EIS measurements[25].

Figure 1.4.2 Images of a corrosion site in Al-Cu aged thin film with Deft primer exposed to salt spray chamber for 5 and 6 days.

Figure 1.4.3 (a-c) Images of a growing corrosion site in Al-Cu aged thin film with Deft primer exposed to salt spray chamber for 13 days at 4 hours time intervals; (d) Image of the same site in Al-Cu aged thin film with Deft primer exposed to salt spray chamber for 14 days under high incident light intensity.

Figure 1.4.4 SEM and EDS results of Al-Cu aged thin films under Deft primer exposed to salt spray chamber: (a) Corrosion area in site 1 in Figure 1.4.3 (a). (b) High magnification of white clusters in (a) at the corrosion front of repassivation region. (c) High magnification of white clusters in the circled area in (b). (d) EDS results of white clusters in (c).

Figure 1.4.5 SEM and EDS results of Al-Cu aged thin films under Deft primer exposed to salt spray chamber: (a) Corrosion area in site 2 in Figure 1.4.3 (a). (b) High magnification of white clusters in circled area in (a) at the corrosion front.

Figure 1.4.6 SEM and EDS results of Al-Cu aged thin films under Deft primer exposed to salt spray chamber: (a) Corrosion area in site 3 in Figure 1.4.3 (a). (b) High magnification of white particles in (a) at the corrosion front. (c) High magnification of white particles in circled area in (b). (d) EDS results of white particles in (c).

Figure 1.4.7 (a-c) Images of a growing corrosion site in Al-Cu aged thin film with Boegel conversion coating and Deft primer exposed to salt spray chamber for 13 days at 4 hours time intervals; (d) Image of corrosion site in Al-Cu aged thin film with Boegel conversion coating and Deft primer exposed to salt spray chamber for 14 days.

Figure 1.4.8 SEM and EDS results of Al-Cu aged thin films under CCC and Deft primer exposed to salt spray exposure: (a) Corrosion area under coating systems. (b) Corrosion area under the coating systems with white clusters in site 1 in (a). (c) EDS results of white clusters in (a). (d) Corrosion area under the coating systems with white film in site 2 in (a). (e) EDS results of white film in (d).

Figure 1.4.9 Images of single corrosion site in Al-Cu aged thin film under different coating systems exposed to salt spray chamber for 16 days.

Figure 1.4.10 Images of corrosion sites in Al-Cu thin film at “As deposited” condition under different coating systems exposed to salt spray chamber for 32 days.

Figure 1.4.11 Images of single corrosion site in Al-Cu aged thin film under SrCrO_4 primer exposed to salt spray chamber for 231 days.

Figure 1.4.12 Coating and interface properties of Al-Cu aged thin films under different coating systems extracted from EIS spectra: Coating capacitance (C_c); Coating resistance (R_{po}); defect capacitance (C_d) and total resistance R_d at 0.01Hz as function of time.

Figure 1.4.13 Images of corrosion sites in Al-Cu aged thin film under conversion coatings and primer exposed to ASTM G85 for different time.

Figure 1.4.14 Images of Corrosion sites in Al-Cu aged thin film under conversion coatings, primer and topcoat exposed to ASTM G85 for different time.

Figure 1.4.15 Images of corrosion sites in Al-Cu thin film at “As deposited” condition under different coating systems exposed to ASTM G85 for different exposure times.

Figure 1.4.16 Average current densities of (a) Al-Cu-aged thin films;(b) Al-Cu as deposited thin films under variety coating systems exposed to salt spray tests.

Figure 1.4.17 Outline of images for single corrosion site in Al-Cu aged thin film under Deft primer exposed to salt spray chamber at 19, 44, 94, 119, 160 hours. Lines with numbers showing the propagation directions along which corrosion rates were estimated.

Figure 1.4.18 Corrosion site velocity as function of directions (as indicated in Figure 1.4.18, line 1-4) for the single corrosion site in Al-Cu aged thin film under Deft primer exposed to salt spray chamber.

Figure 1.4.19 Local current densities as function of time for Al-Cu-aged thin films under variety coating systems exposed to salt spray tests.

Figure 1.4.20 Comparision of average current densities (left) and local current densities (right) of Al-Cu aged samples under different coating systems exposed to 3 different environments.

Table 1.4.1 Charge density calculations of various coating systems exposure to different environments for a period of 5 days.

1.4.2 Introduction and Background

Paints and coatings are an effective and inexpensive means to protect metals and alloys from corrosion[1, 2]. Coatings are never perfect and corrosion can nucleate and grow underneath them without detection. To maximize corrosion protection by paints and coatings, there is always a need to match coating type to substrate. For these reasons and others, there is a need to assess corrosion damage accumulation on coated metals[3]. Practical methods of corrosion assessment should reflect service conditions, should be discriminating and should not disturb the natural corrosion processes resulting in degradation[3, 4].

Organic coatings are usually used for outdoor applications. Therefore, exposure test methods are widely used for coating performance assessments. Among all the possible exposure tests for organic coatings, field exposures are often the most relevant and direct to assess organic coating corrosion protection [5, 6]. The length of the exposure time used in the assessment depends on the performance of the coating, but it is often the case that simulated service testing is too long for development of new coatings or study the fundamental properties of coatings and their mode of protection[7]. Therefore, there is a desire to shorten the test length. Accelerated exposure test addresses this need. It is established and standardized. These tests use aggressive condensing moisture environments enclosed in laboratory chambers. Among these tests, salt spray exposures are the most common protocol for testing the corrosion resistance of organic coatings[1]. Salt spray testing, codified in ASTM B117[8], is an environment of continuous spray of 5wt% NaCl at a moderately elevated temperature of 35°C. Scribed and unscribed samples are tested. Evaluation of the coating performance is often made by using visual signs of corrosion such as blisters in coating surface[9]. In this method, only visual inspections are used since they do not disturb the sample allowing continued assessment of coating performance. Although this accelerated test is standardized, it is criticized because exposure conditions are unrealistic and correlations between the test results and field performance is weak[3].

Recently, more sophisticated and realistic exposure protocols have been proposed to assess corrosion protection that are reproducible, accurate and discriminating. These tests are integrated with UV radiation, pollution, humidity, thermal cycling to accelerate corrosion, retain

similarity to outdoor exposures and avoid altering damage accumulation mechanisms[10]. In particular, cyclic test chamber protocols have improved to reproduce and accelerate natural corrosion process protected by organic coatings without changing the corrosion mechanism as occurs in practice[11]. Cyclic tests such as ASTM G85, the so called “Prohesion test”[12] are found to correlate better with natural corrosion than salt spray testing[13]. A typical ASTM G85 test includes a salt fog step exposure test for one hour at 25°C with dilute solution containing 0.05wt% NaCl and 0.35wt% $(\text{NH}_4)_2\text{SO}_4$ at pH 5.0-5.4 followed by one hour dry condition at 35°C [12, 14]. It has been shown that different forms of corrosion occurred during ASTM B117 salt spray and ASTM G85 exposure. Blistering tends to be accentuated by salt spray, and filiform corrosion is accentuated by ASTM G85 exposure conditions[13].

The effect of exposure environment on corrosion is based on visual examinations and evaluations. It is typical for results to be compared against visual rating scales such as ASTM D610 and ASTM 714[15]. Due to the subjective determination in evaluating the behavior of coatings[16], there is a need to develop a technique that can precisely quantify a coating’s protective properties and lifetime. Methods for detecting undercoating corrosion and corrosion occurring on small length scales and in advance of visible external signs of corrosion are desired[3].

Many corrosion sensing and detection methods have been paired with cabinet exposures to explore prospects for early and quantitative corrosion detection[17]. Electrochemical methods including electrochemical impedance spectroscopy (EIS) have been used extensively[2, 16]. EIS measurements are essentially nondestructive [18, 19], and can be performed in situ, allowing for the assessment of the coating quality and the monitoring of corrosion processes as a function of time[20, 21]. EIS is also sensitive to the very earliest stages of corrosion damage in coated metal systems. However, EIS is only an indirect method, and the data extracted from these measurements needs to be interpreted properly to obtain meaningful results.

Direct visualization techniques are appealing but challenging to develop for studying the basic corrosion reactions at the metal-polymer interfaces[2, 22, 23].

Nonetheless, a DOI method has developed as an extension of the thin film pitting corrosion studies by Frankel[24], which provides an opportunity to monitor the corrosion process underneath of organic coatings directly. After demonstrating the utility of DOI method on thin film corrosion for idealized and realistic coating systems under static immersion conditions (Chapters 3 and 4), the approach is now extended and integrated with more realistic exposure regimens, such as ASTM B117, ASTM G85-A5 and outdoor exposure.

1.4.3 Experimental

The Al-Cu thin films 800 nm in thickness were deposited on the transparent glass slides by physical vapor deposition using an Al-4wt%Cu target. The compositions of Al-Cu thin films were confirmed to be Al-4.9wt%Cu by using inductively coupled plasma-optical emission spectroscopy (ICP-OES). Two types of Al-Cu thin films were used. “As-deposited” samples were tested as fabricated without any further heat treatment. The “artificially aged” samples were heat-treated in air at 190°C for 24 hours to induce precipitation of θ'' , θ' and θ phase (Al_2Cu).

Deposited Al-Cu thin films were degreased for several seconds in a solution comprising 1.0 L deionized of (DI) water containing 48.0g Na₂CO₃ and 32.4g Na₂SiO₃ at 65°C. After using DI water to rinse the thin films, they were deoxidized for 3 minutes in a solution comprising 1.0 L of DI water, 30.0g Sanchem 1000TM and 72.0 mL HNO₃ at 55°C. Samples rinsed with DI water and air dried at ambient temperature.

The coating systems used in this study were identical to those described and used in Section 1.3. More realistic coating systems included a conversion coating and a primer finishing with or without a topcoat. The first conversion coating used was Boegel (AC131CB), which is a high performance non-chromate conversion coating. Al-Cu thin films were immersed in Boegel solution for 5 minutes, samples were removed and excess solution was allowed to drain off. The samples were then air dried at ambient temperature for 24 hours before applying the primer. The second conversion coating was a chromate conversion coating (CCC) (Alodine 1200S from Henkel Inc.). Thin film metallization samples were immersed into Alodine 1200S solution with pH around 1.58 for 45 seconds and then rinsed with DI water at ambient temperature. After air-drying at room temperature for 24 hours, a primer coating was applied to the samples.

Two primer coatings were evaluated. The first was a chromium-free primer product from Deft; 02GN084 (MIL-PRF-23377J 2), which is a 2-part epoxy primer pigmented with a blend of PrO/Pr(OH)₃, CaSO₄, and TiO₂. The second was a home-made primer comprising a neat epoxy PD381-94 (Aerospace blank coating-no inhibitor) from Akzo Nobel and 5wt% SrCrO₄ pigment. All primers were mixed at ambient laboratory temperature and applied using a drawdown bar. The panels were air-dried for 24 hours before being cured in the oven at 150°F for 48 hours.

A polyurethane Eclipse® high solids polyurethane aircraft topcoat was used on top of primers in certain experiments. The topcoats were also applied by drawdown bar following the same procedure as the primers.

Coated samples were subjected to different exposure conditions after an artificial defect was made in the center of each sample by manual scratching with a sharp stylus. Electrical tape was applied to the sample as a mask on top of any coatings as well as on the edge of the samples to avoid crevice corrosion. All the experiments were terminated before the corrosion sites undercut the mask.

Samples were subject to environmental exposure per ASTM B117, which specifies an environment formed using a continuous spray of 5wt% NaCl in a moderately elevated temperature of 35°C.

Tests were carried out under conditions of dilute electrolyte with fog/dry cycles. A mixture of 0.05 wt% NaCl and 0.35 wt% ammonium sulfate ((NH₄)₂SO₄) solution was used, which is much more dilute than traditional salt fog test (5 wt% NaCl). The testing cycles are 1 hour fog at 25°C and 1 hour dry-off at 35°C.

Samples were exposed with 45° of inclination in the south direction in a site on The Ohio State University Campus, Columbus, Ohio, which is an urban environment. The period was from October of 2012 to May of 2013. During the exposure period, all meteorological data were recorded and saved (temperature, humidity, etc.)

Samples were extracted from the chambers at regular intervals and examined for signs of corrosion under the microscope. A transmitted light source located above the sample was used for illumination. A QImagingTM Go-3 color CMOS camera attached to an Olympus SZ61

stereomicroscope was located underneath the sample. As corrosion progressed, the thin sputtered film was perforated and transmitted light passed through the sample to the camera. The progression of corrosion was recorded by Q-capture ProTM recording software. Analysis of the collected images was conducted using ImageJTM, PhotoshopTM. The movies were made by VideoMatchTM frame grabbing.

Each sample was subjected to an EIS measurement after extraction from the salt spray chamber and image collection. Samples were rinsed in distilled water before exposure to 5wt% NaCl solution. A droplet cell set up was used as illustrated in Figure 1.4.1[25]. A platinum mesh counter electrode was set between two pieces of filter paper that were wet with a 5wt% NaCl solution. A saturated calomel reference electrode was used to compress the filter paper/electrode stack on the specimen surface to keep it in position during the measurement. The exposure area was 0.32 cm².

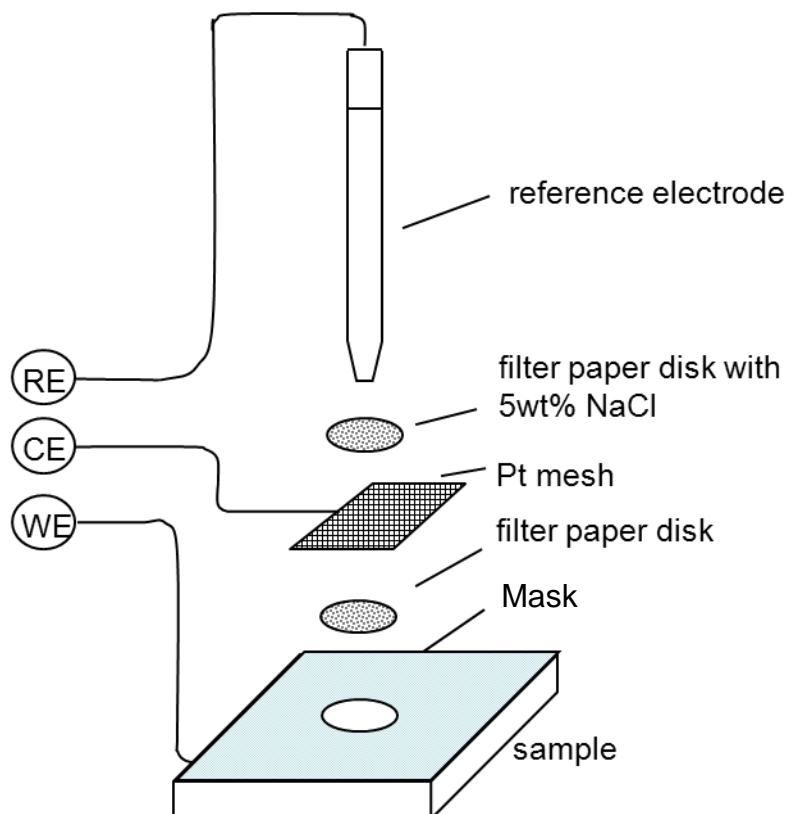


Figure 1.4.1 Demonstration of droplet cell setup for EIS measurements[25].

Electrochemical impedance spectroscopy (EIS) was carried out using a Gamry Reference 600 potentiostat (Gamry Instruments Inc.) to obtain the EIS spectra. In these experiments, the open circuit potential was monitored for 20 minutes before conducting the EIS measurement. The measurements themselves were performed at a frequency range of 10⁵ to 10² Hz using a 10 mV sinusoidal voltage perturbation applied with respect to OCP, with a sample acquisition rate of 7 points per decade.

1.4.4 Results

Each combination of metallic thin film substrate and epoxy coating were repeated at least in triplicate in the following experiments. Exact reproducibility was not attained due to the complexity of each measurement. However, the results shown were judged to be typical results among the results collected.

ASTM B117 Salt Spray Exposure Samples with various coating systems were exposed to salt spray according to ASTM B117 (5wt% NaCl at 35°C). In these experiments, samples were extracted from the salt spray chamber at regular intervals (usually one day) and the extent and morphology of corrosion was recorded by DOI. EIS measurements were conducted immediately after image collection. These samples were reintroduced to the salt spray chamber after EIS measurements. Experiments were terminated before the corrosion front undercut the edge of the exposure region, or before a second corrosion site was initiated on the edge of the exposure region.

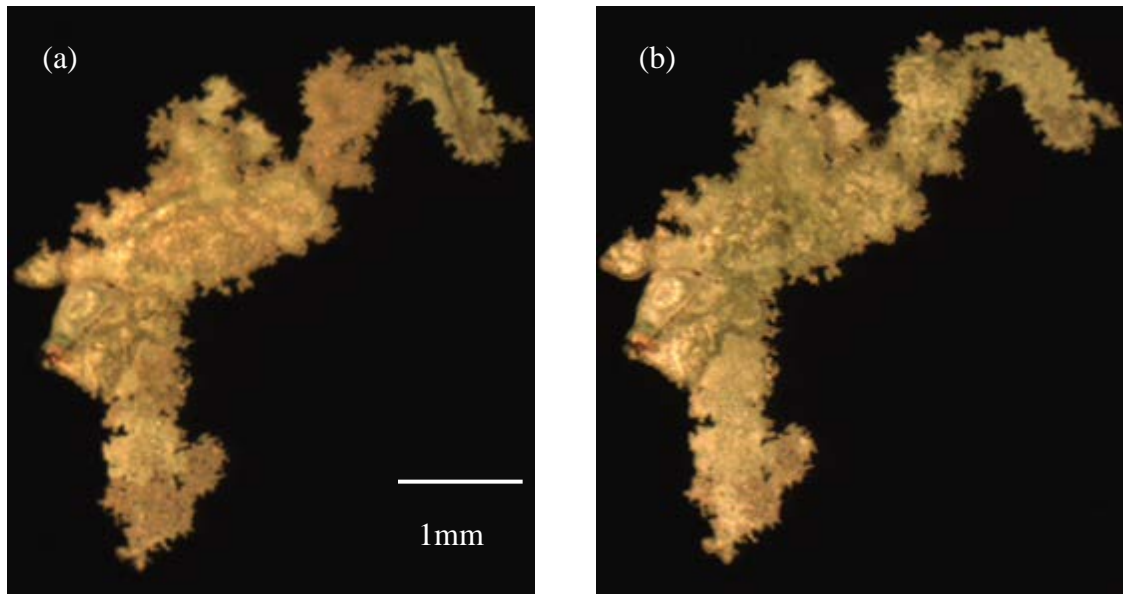


Figure 1.4.2 Images of a corrosion site in Al-Cu aged thin film with Deft primer exposed to salt spray chamber for 5 and 6 days.

Al-Cu Aged Thin Films under Deft Primers The primer effects were investigated on artificially aged Al-Cu thin films coated with a Deft primer (02GN084) and exposed to salt spray chamber for 16 days. Movie 1.4.1 shows the pictures captured every day on a sample exposed to the salt spray chamber. In this movie, the sample was displayed at a magnification of 33 \times during the initial phase of corrosion growth. With longer exposure time, the corrosion front moved out of the view of the microscope. Therefore, a lower magnification (14 \times) was used to capture subsequent images. A single corrosion site nucleated from a defect site and corrosion occurred rapidly along an irregular front and grew outward away from the defect as a broad channel. With further exposure, corrosion propagation not only occurred at the head of the channel, it also started from the side. After filamentary corrosion circled the defect, the corrosion front propagated primarily and preferentially in one direction. It should be noted that corrosion growth

was not continuous since no change in corrosion site size was detected between 5 and 6 days of exposure. A corrosion product ring precipitated out in this site decorating the corrosion front as shown in Figure 1.4.2. Eventually, the corrosion front passivated and slowly became smooth due to a second site that initiated at the corner.

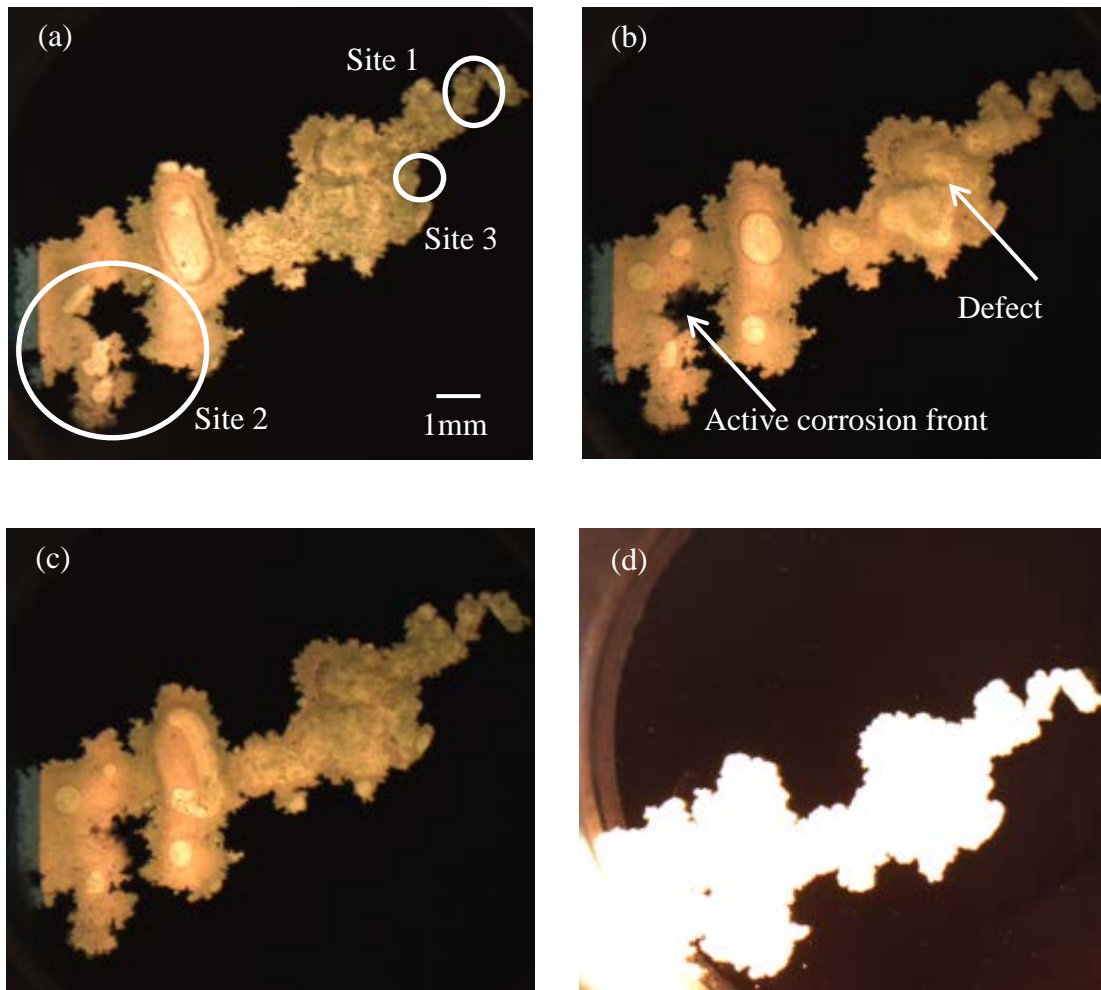


Figure 1.4.3 (a-c) Images of a growing corrosion site in Al-Cu aged thin film with Deft primer exposed to salt spray chamber for 13 days at 4 hours time intervals; (d) Image of the same site in Al-Cu aged thin film with Deft primer exposed to salt spray chamber for 14 days under high incident light intensity.

In ASTM B117 exposure experiments, bubbles were observed to form in side of corroded area. A sequence images made at 4 hour time intervals are shown in Figure 1.4.3(a-c). Bubbles were both observed at the active corrosion front and inside of previously corroded region away from the active front, but under the coating, which remained over the corroded area. It appeared that bubbles were formed at the corrosion front and coalesced; eventually escaping through the break in the coating associated with the artificial defect.

Figure 1.4.3(d) shows corrosion damage imaged using greater incident light intensity. The image shows a single large corrosion site with no smaller sites in other regions of the

sample. This is an apparently unremarkable image except when compared with thin film corrosion under a Deft primer subject to static immersion in an aqueous solution. In that case large numbers of discrete corrosion sites nucleated across the entire surface. The origins of the substantial difference in corrosion morphology have not been determined, but this is an important example illustrating the strong dependence of corrosion damage accumulation on environmental exposure conditions.

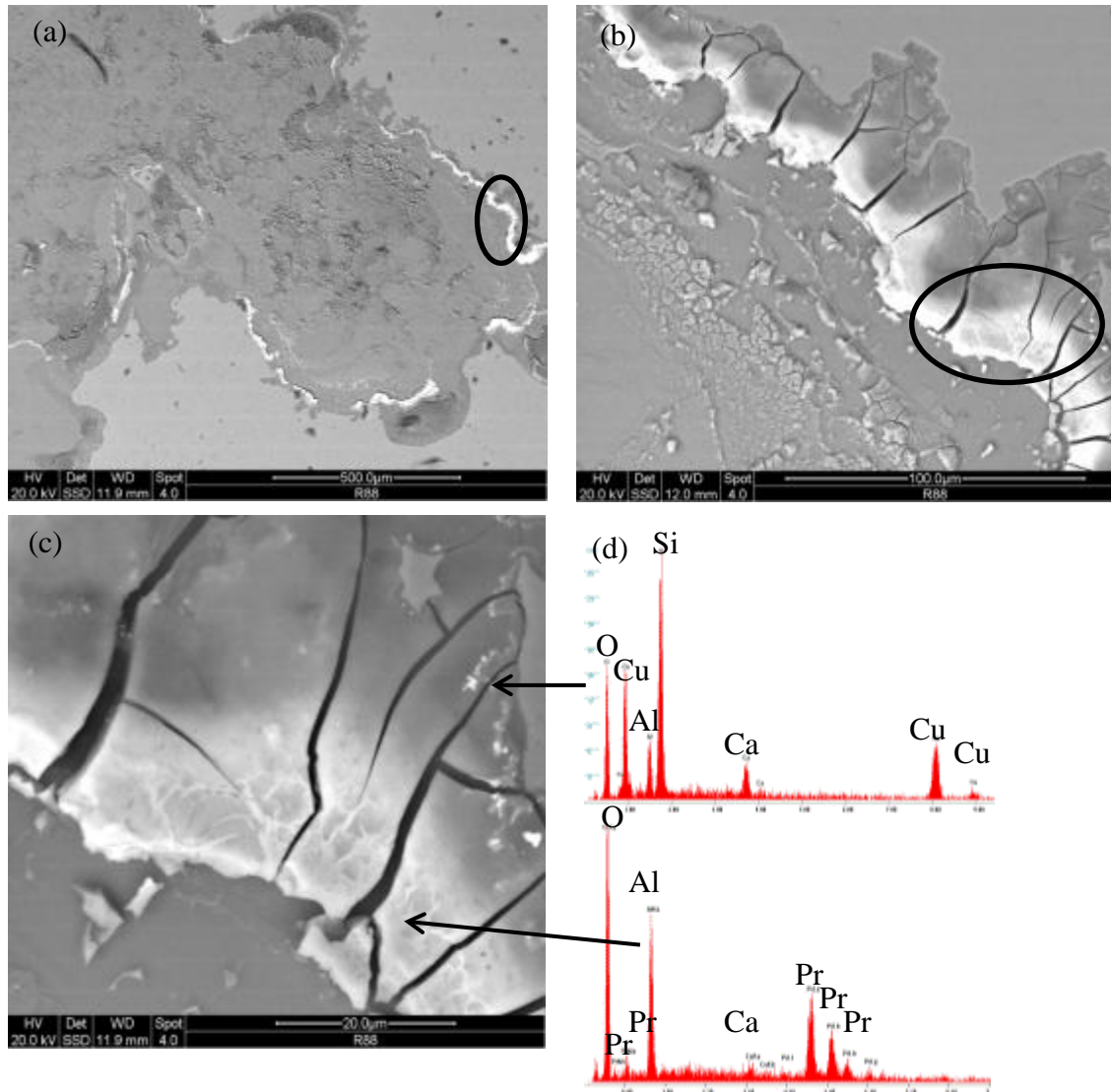


Figure 1.4.4 SEM and EDS results of Al-Cu aged thin films under Deft primer exposed to salt spray chamber:

- (a) Corrosion area in site 1 in Figure 1.4.3 (a).
- (b) High magnification of white clusters in (a) at the corrosion front of repassivation region.
- (c) High magnification of white clusters in the circled area in (b).
- (d) EDS results of white clusters in (c).

Post-exposure characterization was undertaken by removing the primer coating using the PR-3500 Aircraft Epoxy paint remover. Scanning electron microscopy (SEM) was carried out to

analyze the corroded area under the coating as shown in Figure 1.4.4, Figure 1.4.5 and Figure 1.4.6. The micrographs show corrosion product formed close to the corrosion front wall at a passivated region in Figure 1.4.4(a). Higher magnification images of the dehydrated and cracked product are shown in Figure 1.4.4 (b-c). EDS results show that this product was rich in Pr (Figure 1.4.4 (d)). Moreover, Cu dendrites, which form by plating of Cu ions in solution, form close to the corrosion margin (Figure 1.4.4 (d-e)). Dendrites were often clustered along a front that appeared to be a previous position of the corrosion margin. The fact that the corrosion margin migrated away from the Cu deposit indicates that replated Cu layers are not perfectly protective.

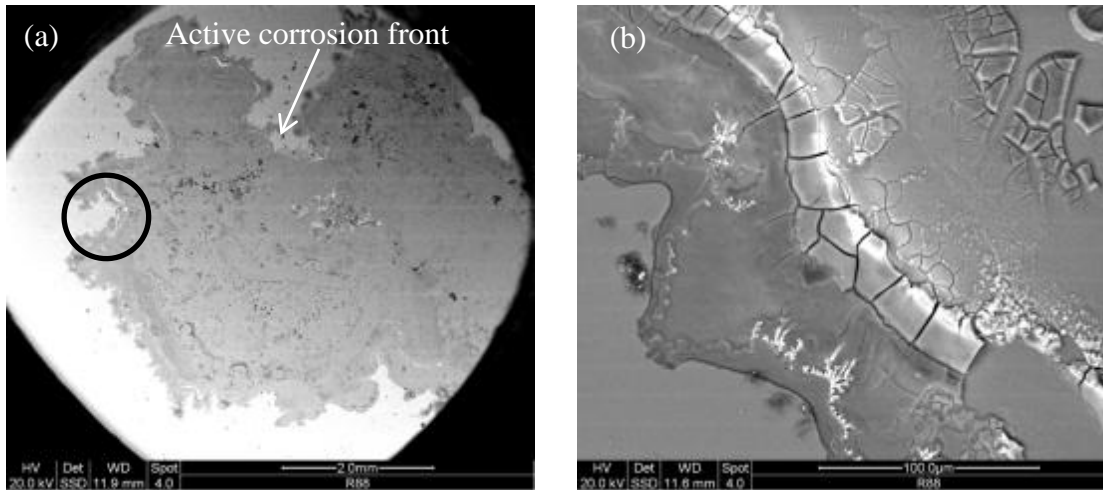


Figure 1.4.5 SEM and EDS results of Al-Cu aged thin films under Deft primer exposed to salt spray chamber:

(a) Corrosion area in site 2 in Figure 1.4.3 (a).

Figure 1.4.5 (a) shows a region along the corrosion site perimeter that had been repassivated for only a short time before the conclusion of the experiment. Both Pr-rich corrosion product and isolated Cu dendrites are observed. However, a different form of Cu was observed at the region where the corrosion front wall was smooth and passivated when the test was terminated as shown in Figure 1.4.6. Cu precipitates were detected as discrete particles right at the wall while Pr-rich corrosion product was found lining the entire margin. This suggests that Pr is precipitated along the wall, perhaps by local pH changes, while Cu plates out at specific sites by a nucleation and growth process.

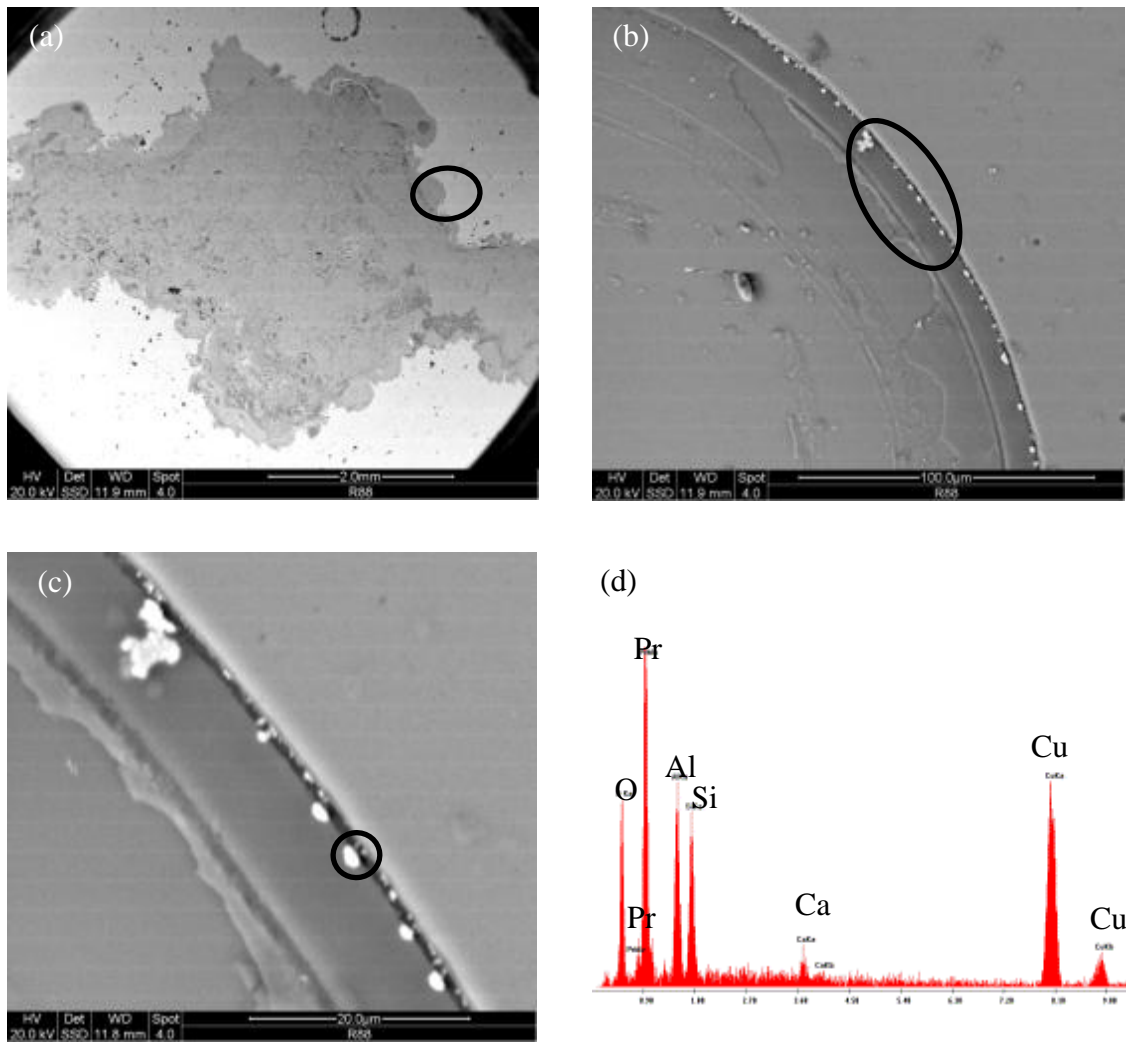


Figure 1.4.6 SEM and EDS results of Al-Cu aged thin films under Deft primer exposed to salt spray chamber:

- (a) Corrosion area in site 3 in Figure 1.4.3 (a).
- (b) High magnification of white particles in (a) at the corrosion front.
- (c) High magnification of white particles in circled area in (b).
- (d) EDS results of white particles in (c).

Corrosion Behavior of Conversion Coated and Primed Aged Al-Cu Thin Films The corrosion protection provided by conversion coatings and primer combinations was studied on aged Al-Cu thin films. The evolution of corrosion damage for Boegel/Deft and CCC/Deft conversion coating/primer combinations are shown in Movie 1.4.2 and Movie 1.4.3, respectively. Images of growing corrosion sites were captured every day during salt spray exposure. Movie 1.4.2 shows a corrosion site with a filamentary morphology. The corrosion front changed directions around the defect as it progressed. Images with short time intervals (4 hours) were shown in Figure 1.4.7. New sites extended out from the branch and grew for a short time before repassivating. Another site re-initiated from the defect and started to propagate until

touching the first site. The morphology and behavior of the corrosion site is in consistent with filiform corrosion.

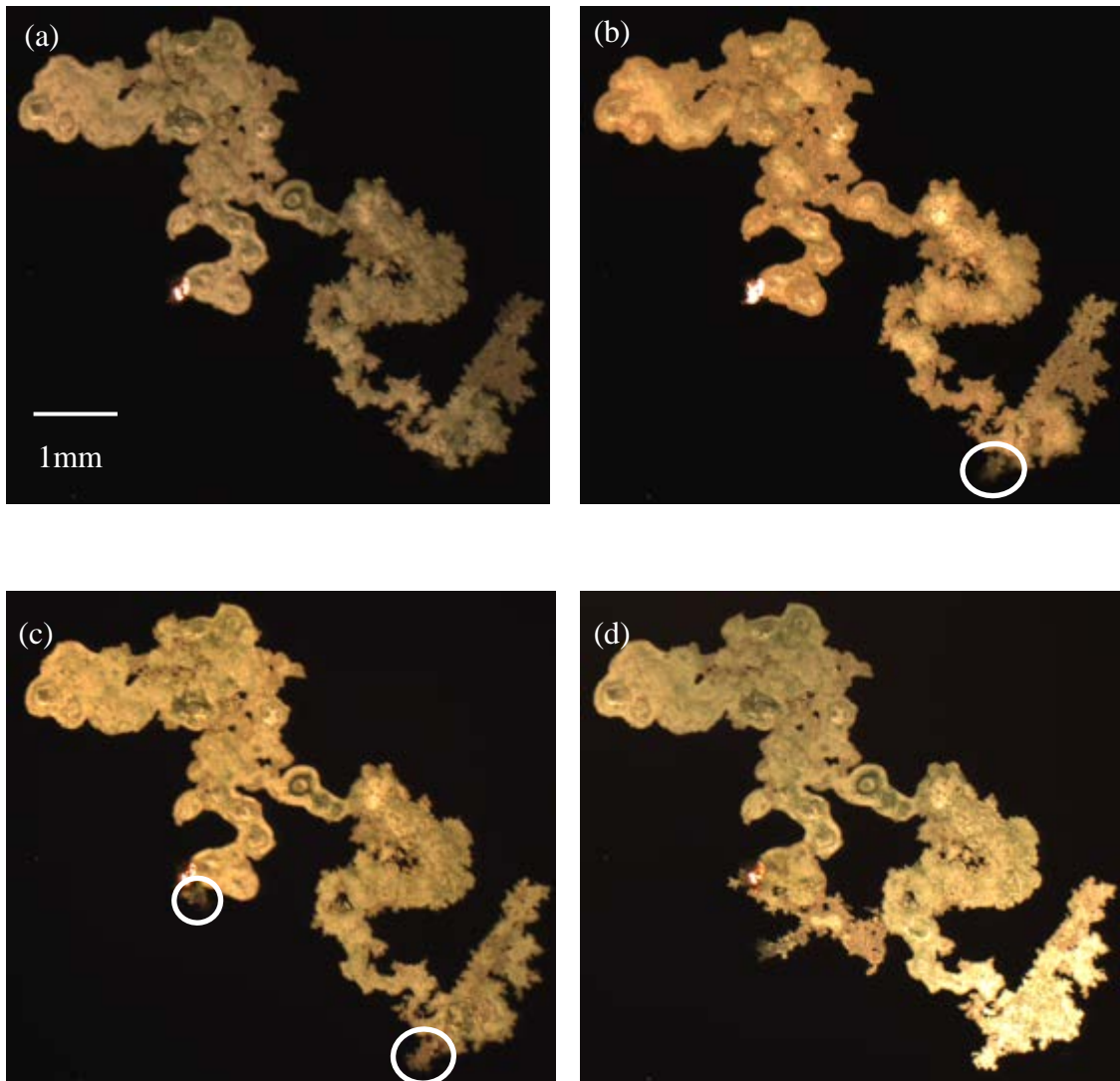


Figure 1.4.7 (a-c) Images of a growing corrosion site in Al-Cu aged thin film with Boegel conversion coating and Deft primer exposed to salt spray chamber for 13 days at 4 hours time intervals; (d) Image of corrosion site in Al-Cu aged thin film with Boegel conversion coating and Deft primer exposed to salt spray chamber for 14 days.

Similar corrosion growth characteristics were observed for samples with a CCC/Deft primer combination as shown in Movie 1.4.3. With the CCC, corrosion filaments were thinner than with Boegel. Furthermore, the corrosion front was more irregular than with Boegel, which created undissolved islands formed inside of the corroded area. The overall corrosion rates were lower when conversion coatings were present compared to experiments where they were not and hydrogen gas evolution was not observed.

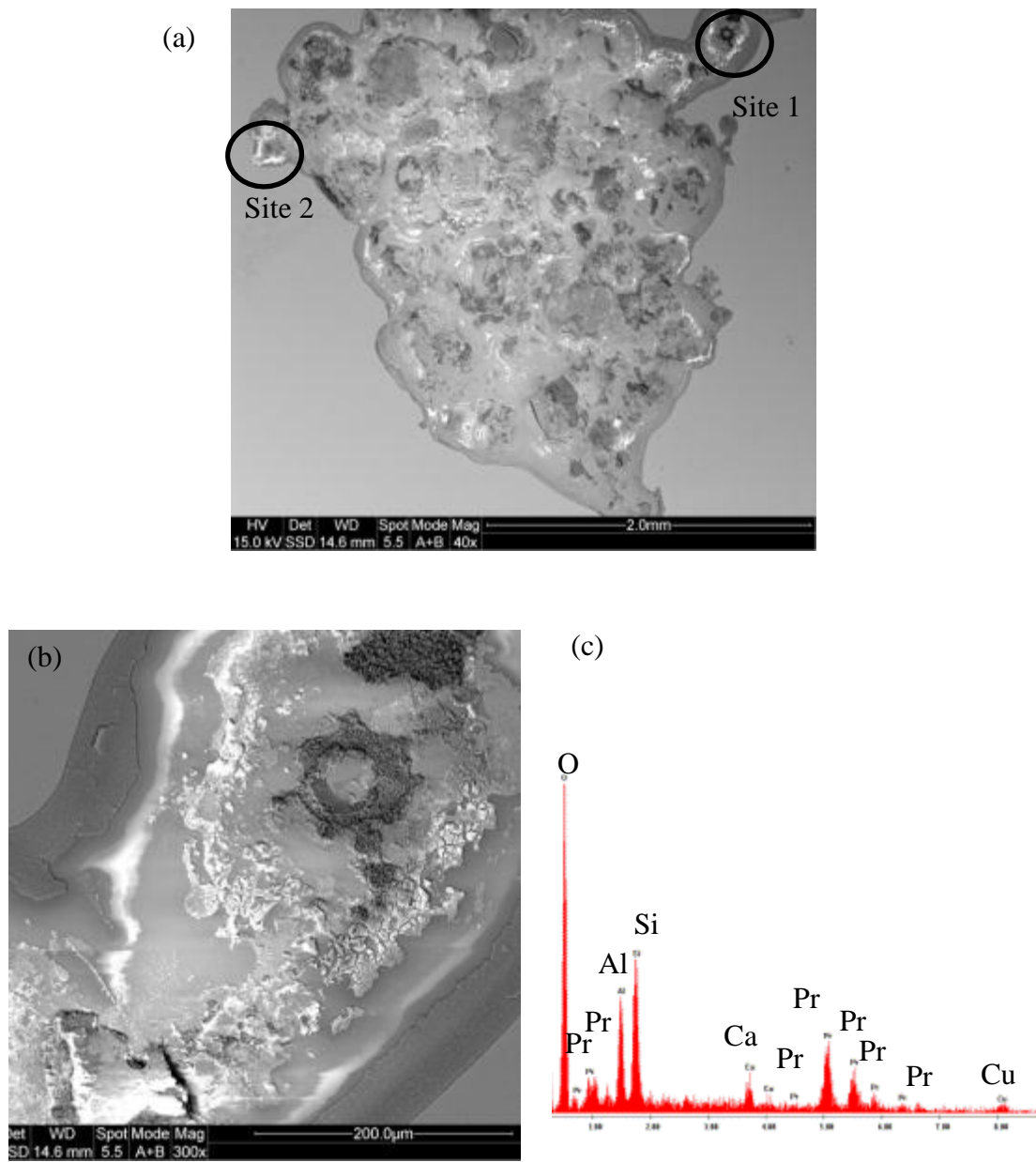
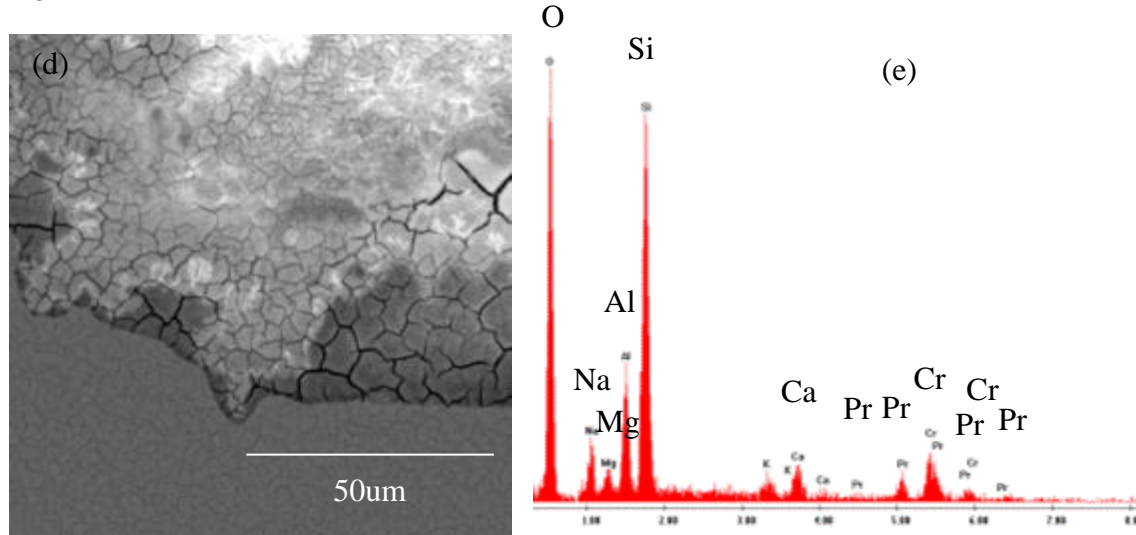


Figure 1.4.8 SEM and EDS results of Al-Cu aged thin films under CCC and Deft primer exposed to salt spray exposure: (a) Corrosion area under coating systems. (b) Corrosion area under the coating systems with white clusters in site 1 in (a). (c) EDS results of white clusters in (a); (d) Corrosion area under the coating systems with white film in site 2 in (a); (e) EDS results of white film in (d).

Continued.

Figure 1.4.8 Continued.



Under coating corrosion damage was characterized by SEM after exposure. The primer was not easily removed by a PR 3500, aircraft epoxy paint remover from the Boegel conversion coated samples, but was removed from CCC-treated surfaces. Therefore, SEM results only could be obtained from the CCC sample as shown in Figure 1.4.8. It should be noted that Pr-rich corrosion product was observed at the corrosion front and inside the corroded area (Figure 1.4.8(a-c)). Higher magnification of SEM results showed that at the corrosion front, a Cr-rich corrosion product was also formed (Figure 1.4.8(d) and (e)). However, the amount of this type of precipitates was small compared with the ones rich in Pr.

The Effect of a Topcoat on Conversion, Primed Aged Al-Cu Thin Films The effects of a topcoat on corrosion inhibition were studied by using Al-Cu aged thin films adding an extra layer of polyurethane aircraft topcoat on top of conversion coating and Deft primer. Results are shown in Movie 1.4.4 (combinations of Boegel conversion coating, Deft primer and topcoat) and Movie 1.4.5 (combinations of CCC, Deft primer and topcoat), respectively. It should be noted that the corrosion propagation for these coating systems was similar to the samples without topcoat. However, the corrosion filaments were thinner and the corrosion fronts were more irregular as shown in Figure 1.4.9. Additionally, the corrosion propagation rate was much slower and no hydrogen bubbles were observed during the corrosion process.

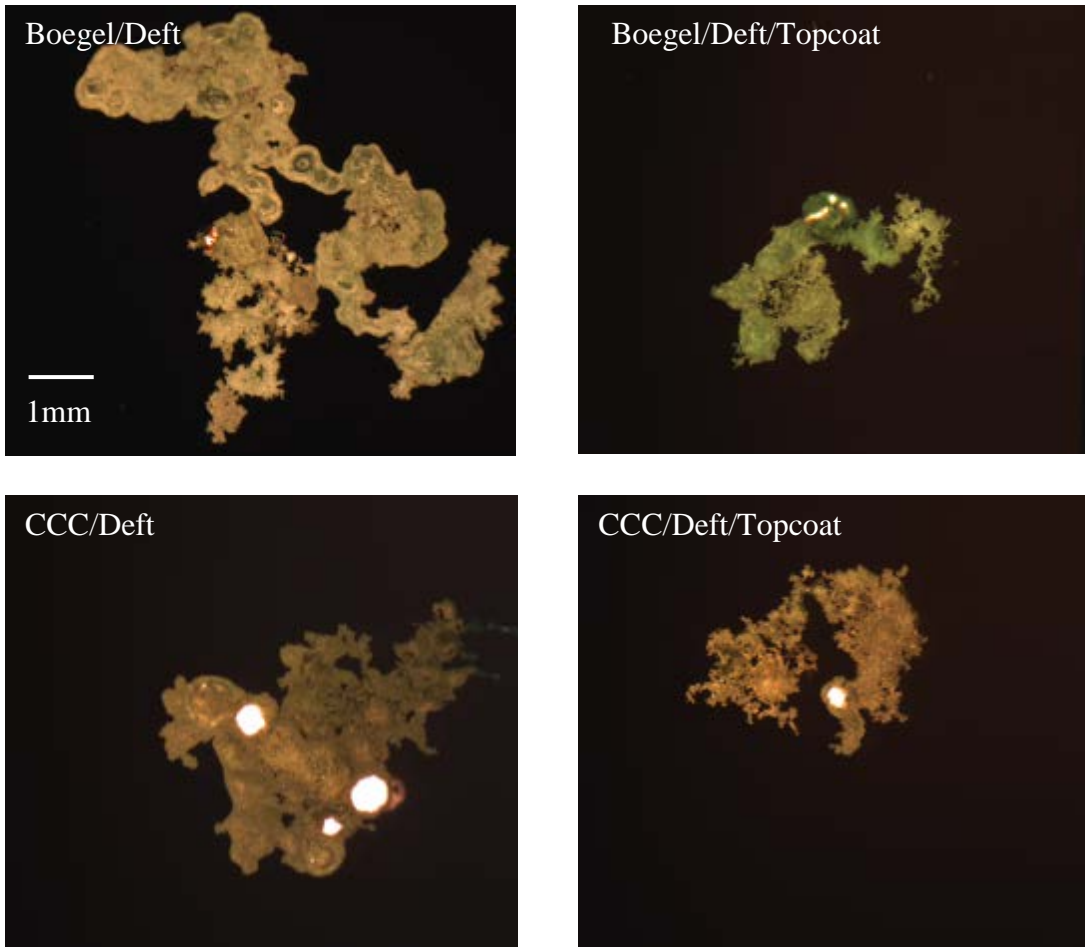


Figure 1.4.9 Images of single corrosion site in Al-Cu aged thin film under different coating systems exposed to salt spray chamber for 16 days.

Al-Cu Thin Films under Various Coating Combinations The metallurgical condition of the thin film substrate affected the corrosion morphology and growth kinetics. In this section, the substrates were changed to Al-Cu thin films in “as deposited” condition. The same coating systems combinations were studied as described in 1.4.1.3. Results were generally presented as shown in Figure 1.4.10. Unlike single and irregular stable corrosion site propagations in the case of aged thin films, as deposited thin films with the same coating systems, such as one layer of Deft primer and combinations of Boegel conversion coating and Deft primer, produced multiple metastable corrosion sites across the exposure area. These sites were round shape and nucleated after the single and irregular corrosion sites stopped growing at the defect sites (Figure 1.4.10(a-b)). In addition, these sites alternately propagated suggesting that cathodic reduction reaction only can support one site growth at a given time. After a burst of growth as round shape, sites became irregular likely a consequence of a decrease in growth rate. It should be noticed that Cu additions to aluminum in solid solution decreased the stability of single site growth. However, it did not inhibit the nucleation of metastable sites resulting in multiple corrosion site attempts and multiple small sites. Once the θ phase formed in aged Al-Cu thin films, stability of sites was increased resulting in a single site continuing growth. The nucleation of metastable sites was

strongly suppressed by the combination of CCC with Deft primer and the samples finishing with polyurethane topcoat as single sites were observed under these 3 coating systems, which can be seen in Figure 1.4.10(c-e).

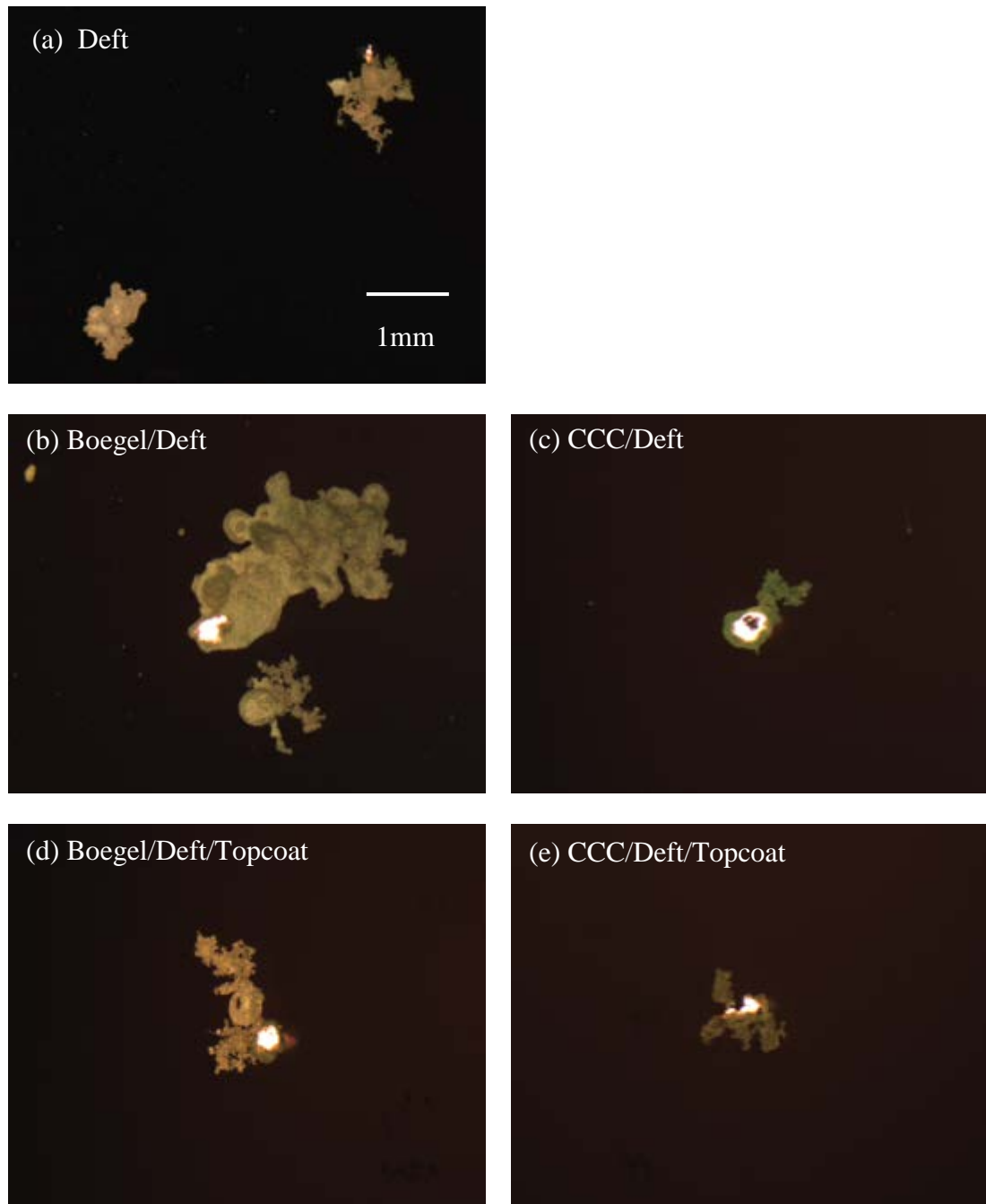


Figure 1.4.10 Images of corrosion sites in Al-Cu thin film at “As deposited” condition under different coating systems exposed to salt spray chamber for 32 days.

Corrosion growth kinetics were influenced by the metallurgical condition of the thin film substrates. The growth rate was much slower in the case of as-deposited thin films compared with the aged thin films under the same coating systems. This was evident in comparison of samples exposed for the same length of time. Slow growth of corrosion in the as-deposited samples is consistent with the inhibiting effect of Cu in Al-Cu solid solutions and the absence of θ phase particles that enhanced oxygen reduction and stimulate corrosion site growth [26].

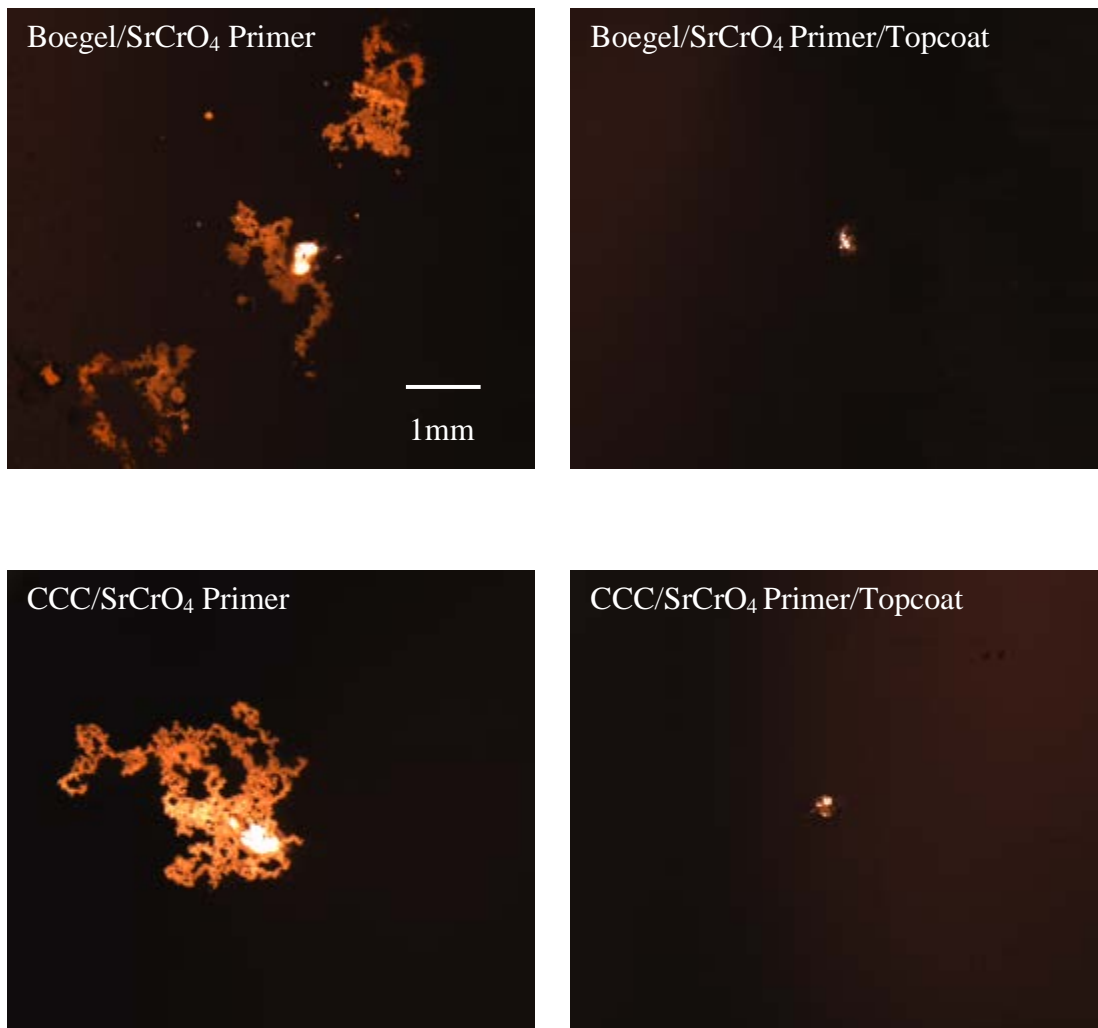


Figure 1.4.11 Images of single corrosion site in Al-Cu aged thin film under SrCrO_4 primer exposed to salt spray chamber for 231 days.

SrCrO₄-pigmented Primers Applied to Al-Cu Thin Film Metallizations A home-made primer comprising 5wt% SrCrO_4 pigment was applied to compare with the non-chromate coating systems. Experimental results showed that there was no indication of corrosion initiation or growth in as-deposited or aged Al-Cu thin films when SrCrO_4 pigmented epoxy primer and topcoat were used. Figure 1.4.11 shows images captured after the samples exposed to salt spray chamber for 231 days. It should be noted that for samples without the topcoat, corrosion sites propagated with a filamentary morphology across the defect. Corrosion

sites did not grow continuously. In some cases, corrosion sites remained passivated for a month or more. After 231 days, samples with a topcoat still did not show any signs of corrosion. Over time the samples were observed to fade indicating leaching of the SrCrO_4 pigment as it dissolved into salt spray environment. This released chromate inhibitor that reinforced the passivity of the Al-Cu thin films alloy substrates preventing corrosion.

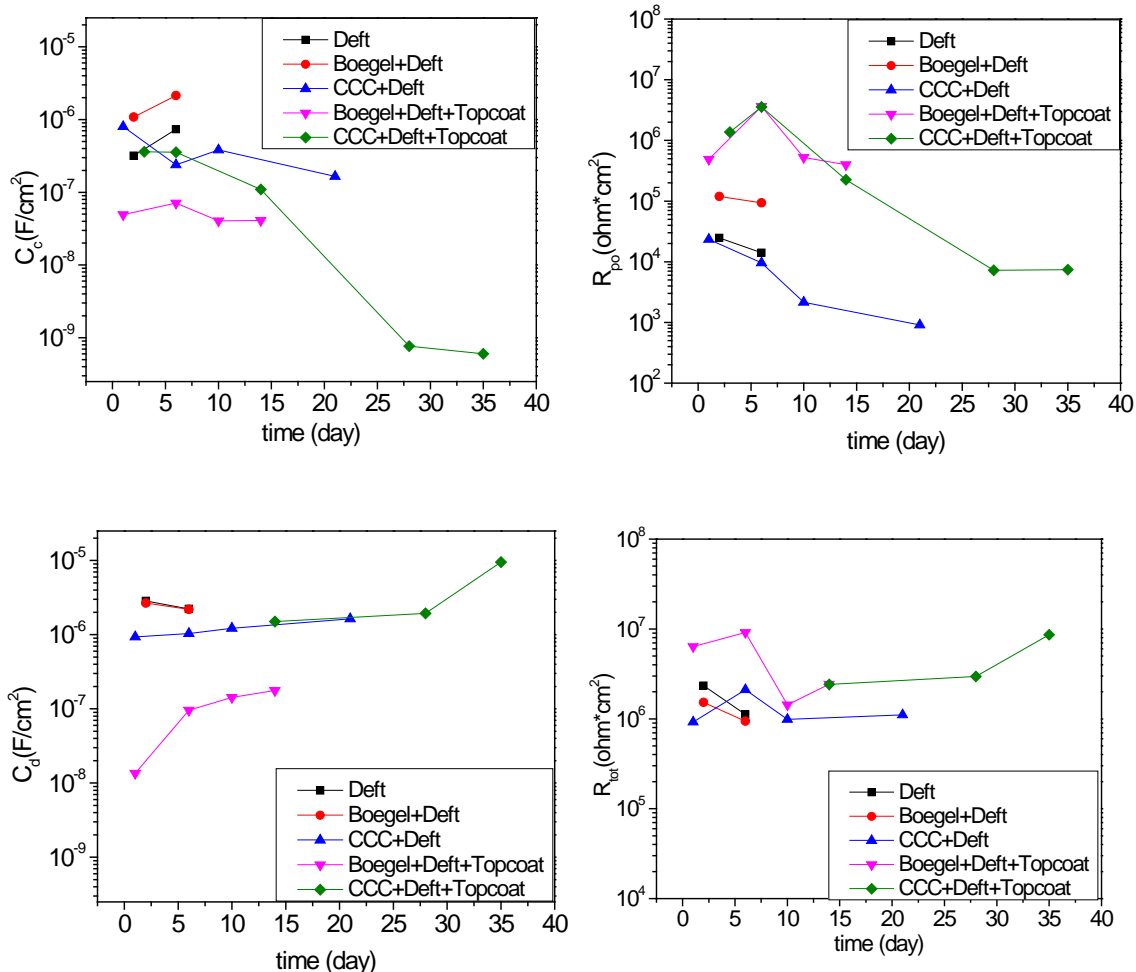


Figure 1.4.12 Coating and interface properties of Al-Cu aged thin films under different coating systems extracted from EIS spectra: Coating capacitance (C_c); Coating resistance (R_p); defect capacitance (C_d) and total resistance R_{tot} (resistance at 0.01Hz) as function of time.

EIS Results It has Electrochemical impedance spectroscopy (EIS) was carried out each time a sample was extracted from salt spray chamber. A droplet cell experiment set up was used to make the measurement. EIS spectra were analyzed and results were integrated with imaging experiments in order to study the nature of undercoating corrosion. Coating capacitance (C_c), pore resistance (R_p), defect capacitance (C_d) and total resistance R_{tot} (resistance at 0.01Hz) as function of time are shown in Figure 1.4.12. It was found that time dependent trends of these four characteristics were not obvious since most of curves exhibited irregular trends. Comparisons were made with the images captured with DOI method, which provided a direct observation of coating protection behavior and undercoating corrosion. However, the

discrimination among the different coating systems could be made by EIS. In general, samples coated with primer-only and Boegel conversion coating fell in the same range of values, which had the highest capacitance and lowest resistances, while for the topcoated samples, the highest resistances and lowest capacitance were observed. Therefore, EIS results correlated with interpretation derived from DOI.

ASTM G85-A5 Test It has been shown that cyclic corrosion test results correlate better with natural outdoor exposure results than do those from salt spray test exposure[13]. Therefore, ASTM G85 cyclic test protocols were developed as alternatives to salt spray exposure testing. One of the ASTM G85 protocol, known also as the Prohesion test, is commonly used for accelerated weathering testing.

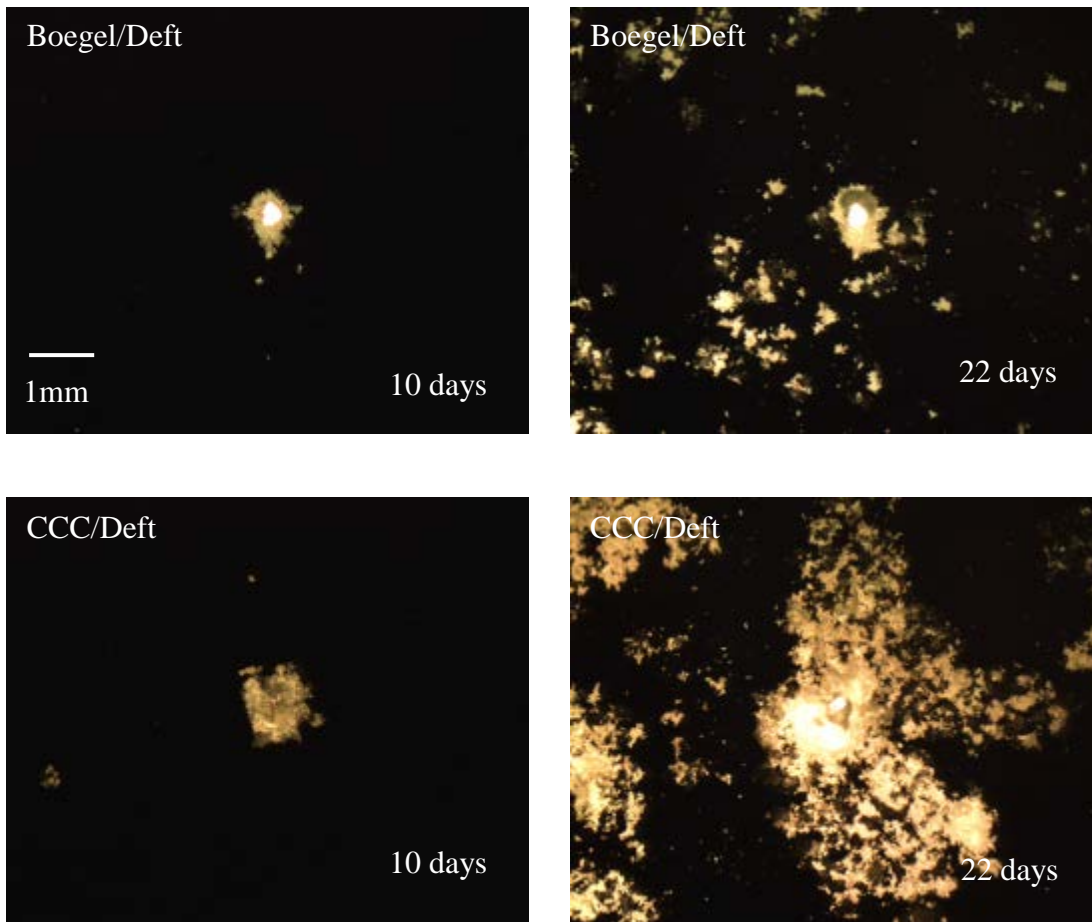


Figure 1.4.13 Images of corrosion sites in Al-Cu aged thin film under conversion coatings and primer exposed to ASTM G85 for different time.

Samples with the various coating combinations were exposed to ASTM G85 exposure conditions. Samples were removed from the chamber at regular intervals (usually one day) and corrosion morphologies were recorded using the DOI method. These experiments were terminated before the corrosion front undercut the edge of the exposure region.

Movie 1.4.6 shows corrosion damage accumulation on aged Al-Cu thin film samples coated with Deft primer (02GN084) only for 22 days. This movie shows a corrosion site growing

from an intentionally formed defect in the sample. The site that formed was round at first and gradually became irregularly shaped. Irregularly shaped sites also nucleated across the exposure area away from the intentionally introduced defect. These sites eventually grew bigger and connected with each other until the whole thin film was dissolved.

Figure 1.4.13 shows corrosion damage accumulated on Boegel/Deft and CCC/Deft samples. At exposure times less than 10 days, a single site was observed to have initiated from the defect. A site propagated to form an irregularly shape. At exposure times beyond 10 days, widespread corrosion site nucleation occurred as was observed in the case of thin films without conversion coatings.

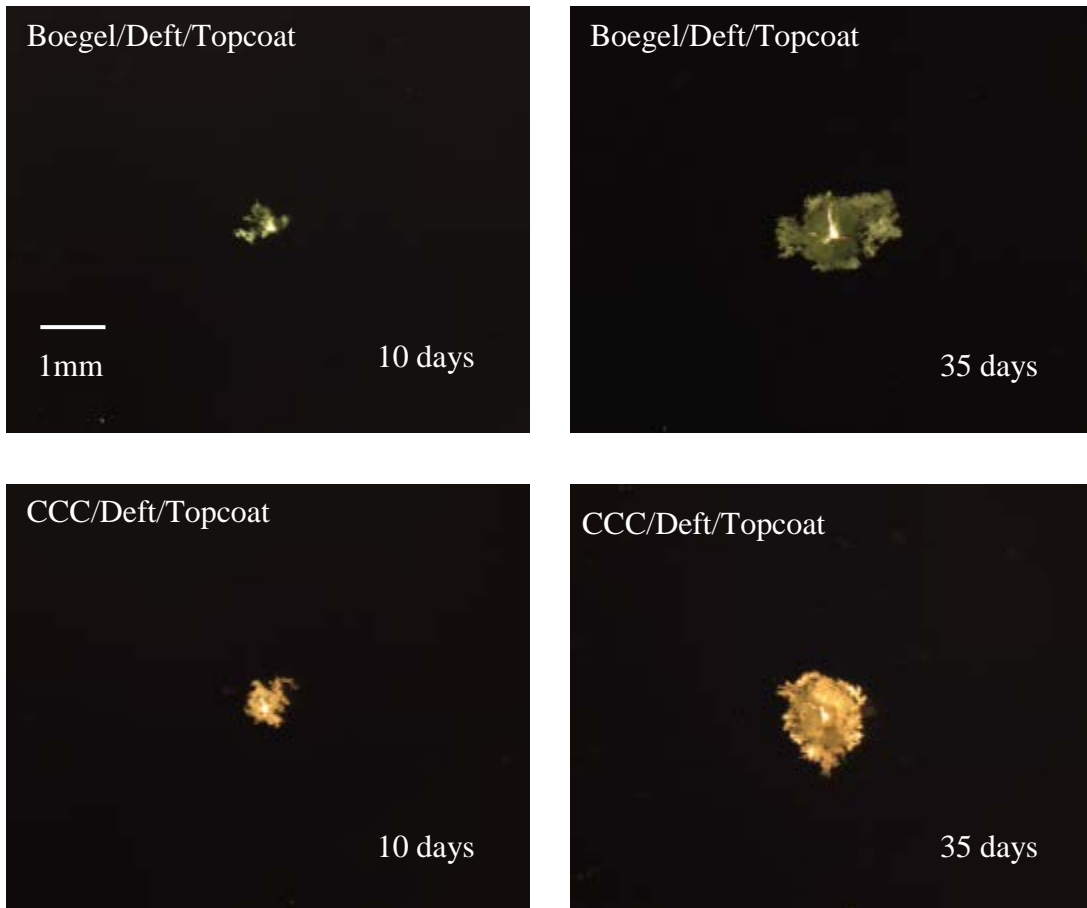


Figure 1.4.14 Images of Corrosion sites in Al-Cu aged thin film under conversion coatings, primer and topcoat exposed to ASTM G85 for different time.

Figure 1.4.14 illustrates the effect of a topcoat on corrosion damage accumulation. In these exposures, corrosion sites nucleated only at intentionally introduced defects and widespread corrosion site nucleation across the surface was suppressed. Corrosion morphologies were irregular as in other cases, and corrosion growth kinetics was obviously slowed compared to the other cases examined.

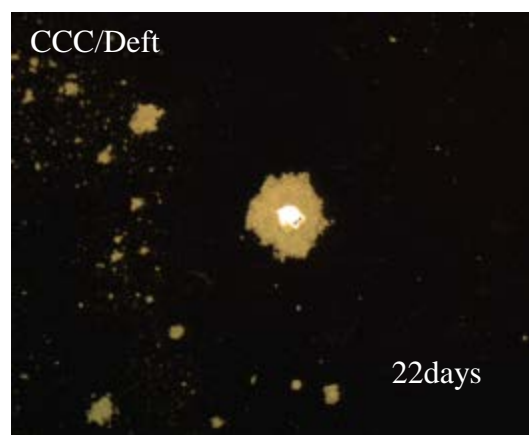
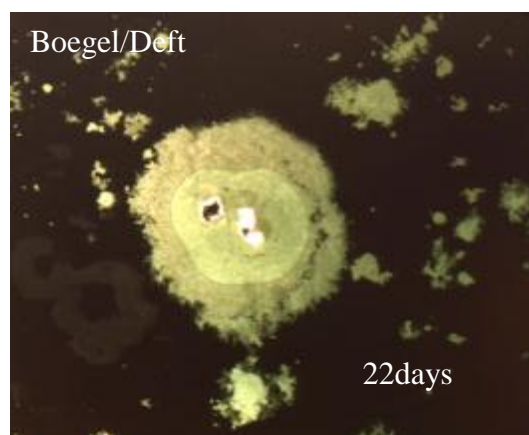
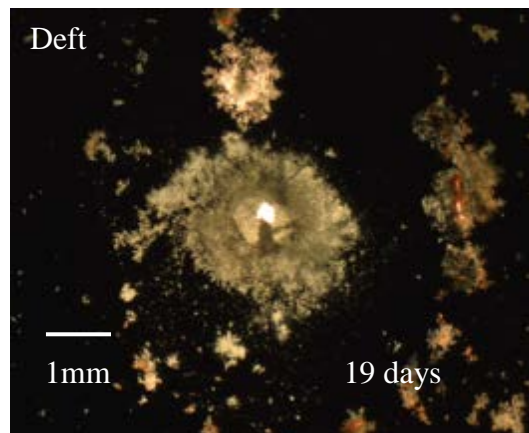


Figure 1.4.15 Images of corrosion sites in Al-Cu thin film at “As deposited” condition under different coating systems exposed to ASTM G85 for different exposure times.

As-deposited Al-Cu thin films subject to the same exposure conditions and coating configuration developed similar corrosion morphology as shown in Figure 1.4.15. The deterioration of corrosion under these conditions was less severe than aged thin film substrates

under the same coating systems and exposure period, which is consistent with the inhibiting effect of Cu in solid solution and the formation of θ phase in aged thin films that increased corrosion susceptibility.

Outdoor Exposure Samples were exposed, facing south, at a 45° of inclination at a site on The Ohio State University Campus, Columbus, Ohio. This is considered to be an urban environment. The period was from October of 2012 to May of 2013. During the exposure time, all meteorological data were recorded and saved (temperature ranged from 31.1° F to 54.1° F, humidity from 66.52% to 71.25%). However, no signs of corrosion were found on any sample. No coating degradation or blistering other than blanching of the coating in the exposure area was evident.

1.4.5 Discussion

The DOI method was used to investigate corrosion damage accumulation of Al-Cu thin films under various coating combinations exposed to accelerated weathering conditions such as ASTM B117, ASTM G-85-A5 and natural outdoor exposure. Due to the metallization thinness, the corrosion damage of thin films spread out laterally under the organic coatings forming a crevice between the glass substrate and the coating. In addition, thin film corrosion is clearly different than corrosion in bulk alloys, but useful comparisons between the two can be made. A key advantage of the thin film corrosion approach is that the anodic current density of the corrosion site can be determined optically, and no accounting of the cathodic reaction occurring on the electrode surface is needed, and thin film pit growth can be measured optically in a way that pit growth in bulk materials cannot.

The corrosion growth kinetics underneath of coating systems was characterized by estimating the current density using captured images of corrosion site size as a function of time. Compared with conventional electrochemical tests, which are not useful to separate the anodic and cathodic current densities, the anodic current density estimated from DOI method reflects the true metal dissolution at the corroded area.

In most experiments, single corrosion site was involved in the thin film corrosion underneath of the coating systems. These sites were irregularly shaped indicating that there were different local growth rates and different local current densities along the perimeter. In fact, observations showed that large segments of the site perimeter were passivated for extended periods of time. To assess the corrosion growth kinetics in view of average variations of current density along the corrosion site perimeter, Frankel's model of calculating pit current density was utilized to calculate an "average anodic current density" to characterize corrosion growth as a function of time[24].

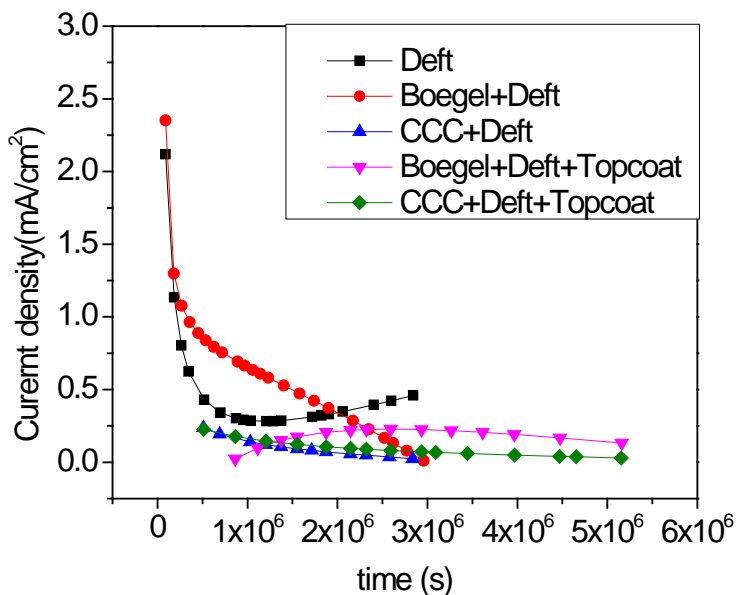
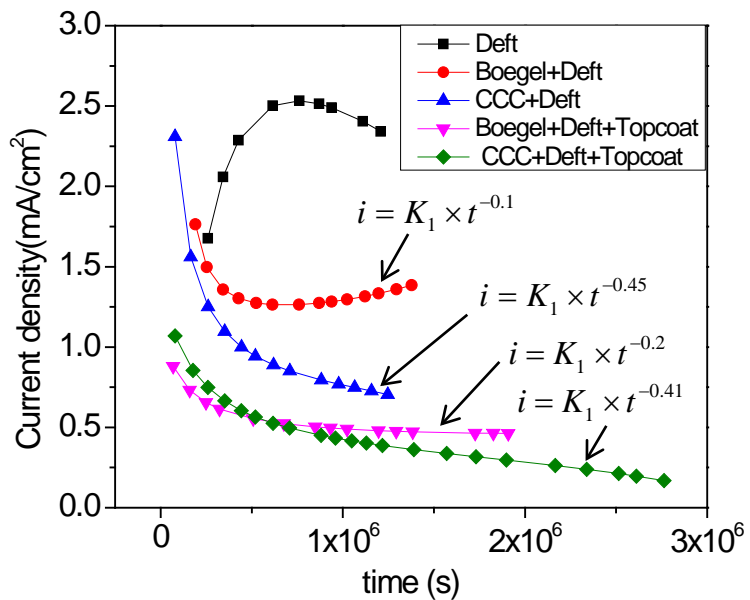


Figure 1.4.16 Average current densities of (a) Al-Cu-aged thin films;(b) Al-Cu as deposited thin films under variety coating systems exposed to salt spray tests.

Even though the morphology was irregular, the corrosion site perimeter P and bottom area A_b still could be collected and fitted as function of time in Equation 1.4.1 and 1.4.2. The average anodic current density was estimated using Equation 1.4.3.

$$P = a_1 t + a_2 t^2 \quad \text{Equation 1.4.1}$$

$$A_b = b_1 t^2 + b_2 t^3 \quad \text{Equation 1.4.2}$$

$$i_a(t) = \frac{\rho n F}{M} \frac{\partial A_p(t)}{\partial t} \frac{1}{P(t)} \quad \text{Equation 1.4.3}$$

Where a_1 , a_2 , b_1 and b_2 are constants, ρ is the density of Al (g/cm³), n is equivalents of change per mole of Al reacted (eq/mol), M is molar mass of Al (g/mol) and F is Faraday's constant (C(eq). Figure 1.4.16 shows the average anodic current densities for the different substrates and coating combinations. Figure 1.4.16(a) shows that Deft primer exhibited the highest anodic current density followed by the samples pretreated with conversion coatings. When a polyurethane topcoat was present, the anodic current densities decreased dramatically in the earliest stages of corrosion propagation and differences between the samples with different conversion coatings were no longer distinct.

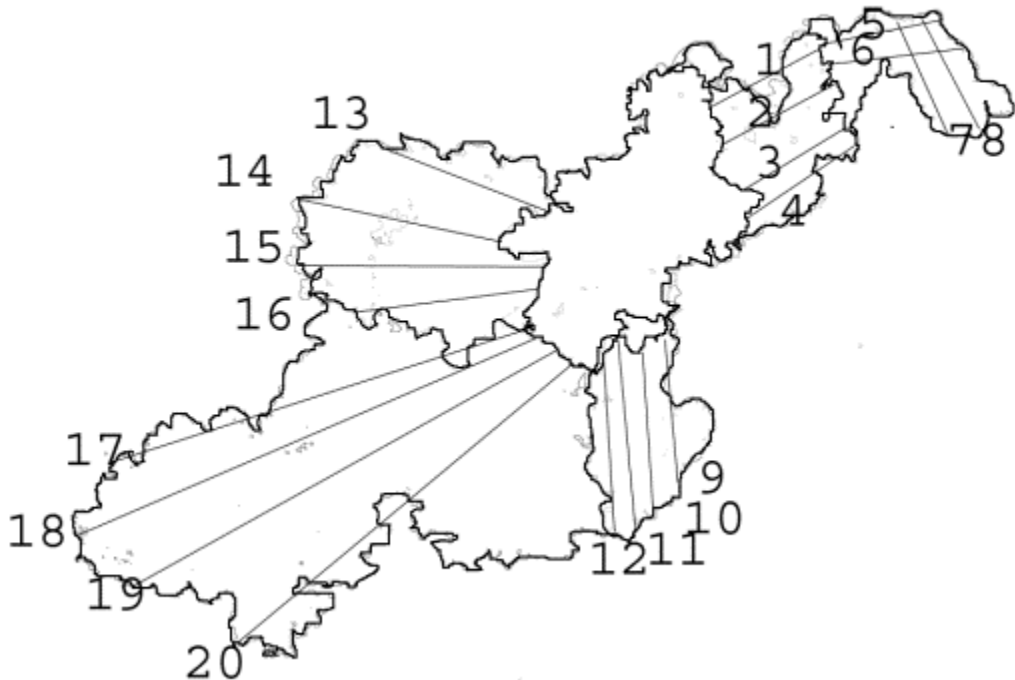


Figure 1.4.17 Outline of images for single corrosion site in Al-Cu aged thin film under Deft primer exposed to salt spray chamber at 19, 44, 94, 119, 160 hours. Lines with numbers showing the propagation directions along which corrosion rates were estimated.

The anodic current densities for all the coating combinations decayed with time except the sample with just the Deft primer, which first showed an increase in the average anodic current density. The average anodic current densities for the other coating combinations were fitted to a power law:

$$i = kt^b \quad \text{Equation 1.4.4}$$

The fitting results revealed that time exponent b varied between -0.1 to -0.45, which was similar to that observed for samples exposed under static immersion conditions (Section 1.3).

A comparison of average anodic growth kinetics between the two substrate metallurgical conditions in Figure 1.4.16 (a) and (b) shows that localized corrosion growth was slightly faster in aged material than as deposited material due to the corrosion inhibition effect of Cu in solid solution in as deposited thin films. Any difference in growth kinetics is diminished when the coating system is a good barrier as is the case when topcoats are present.

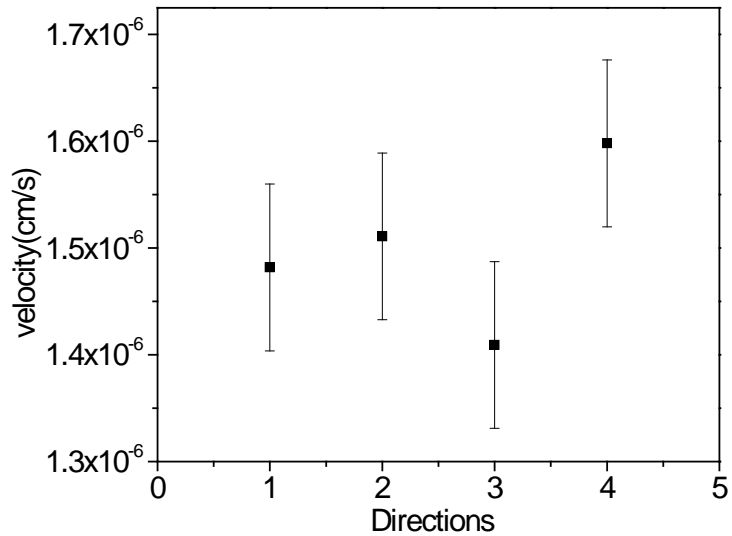


Figure 1.4.18 Corrosion site velocity as function of directions (as indicated in Figure 1.4.18, line 1-4) for the single corrosion site in Al-Cu aged thin film under Deft primer exposed to salt spray chamber.

The growth of corrosion sites occurred episodically and locally. In all but the smallest sites, large portions of the perimeter were passive at any given time during the exposure period. Therefore, it was of interest to estimate the current density at locally active regions using methods presented in Section 1.3. As an example, images captured at different times were overlapped, showing the evolution of corrosion morphology (Figure 1.4.17). The active corrosion site growth region was determined by superimposing collected before and after each exposure time step. The local average current density was estimated along various vectors following the methods presented in Section 1.3. The corrosion rate along a particular vector was calculated from the velocity of the corrosion front, $\Delta X / \Delta t$, the length of a corroding edge over a time of around 1 to 2 days. It was assumed that corrosion rate was constant within time intervals. The velocities were in the same range at different propagation directions within experimental uncertainty, as can be seen in Figure 1.4.18. Therefore, an average velocity was estimated from the velocities at different directions in order to present local velocity at a given time. In order to calculate the current density, Faraday's Law was applied:

$$i = \frac{\rho n F}{M} v \quad \text{Equation 1.4. 5}$$

where ρ is the density of Al (g/cm^3), n is equivalents of change per mole of Al reacted (eq/mol), M is molar mass of Al (g/mol), F is Faraday's constant (C/eq) and v is the velocity (cm/s). Using this method, the local current densities were determined as functions of time under various coating systems as shown in Figure 1.4.19. It should be noted that the local average current density values were more than 10 times higher than that of average current densities estimated by analyzing over the entire corrosion site perimeter. Local current densities did not have pronounced trends as function of time.

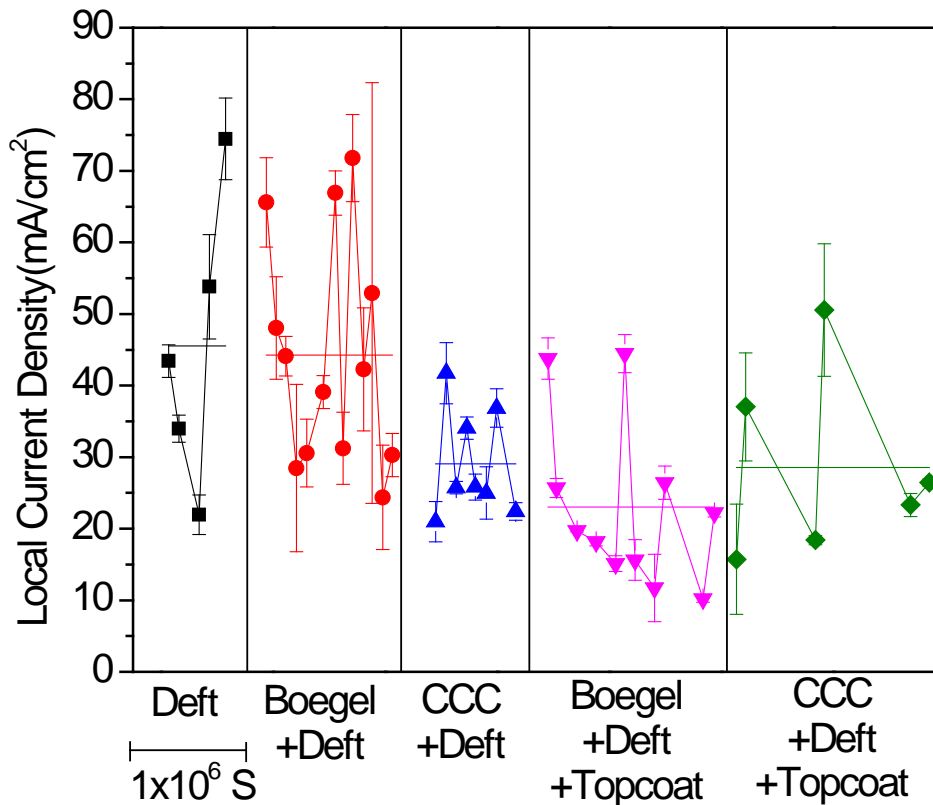


Figure 1.4.19 Local current densities as function of time for Al-Cu-aged thin films under variety coating systems exposed to salt spray tests.

In general, samples with just the Deft primer had the highest local average current densities. Boegel/Deft coating combinations did not slow the local corrosion growth as the CCC/Deft coating combinations did. As expected, application of a topcoat decreased the local growth rates.

Several significant and potentially important observations were made regarding corrosion morphologies and propagation rates that developed in the four different environments considered in this study. The comparisons of corrosion damage under these environments were made as follows:

1. Corrosion phenomenology:

The exposure of coated samples to static immersion as discussed in Section 1.3 resulted in a single and stable corrosion sites that propagated with a filamentary morphology independent of coating system. Irregularly shaped corrosion sites indicated that there were different local growth rates along the perimeter. In fact, observations showed that large segments of the corrosion site perimeter were passivated for extended periods of time.

Similar morphologies were found in the coated samples exposed to ASTM B117 salt spray. Higher corrosion rates were generally found in this case, which are discussed in the following section.

Corrosion morphologies were found to be different for the samples exposed to ASTM G85 compared to those in salt spray. In ASTM G85, the corrosion front moved at similar rates and resulted in a nearly round shaped corrosion site. It was observed that if some regions in periphery extended out locally, repassivation would occur in that region and the rest of the periphery would keep up with the corrosion front. Widespread corrosion site nucleation occurred across the exposed area. These sites eventually propagated and connected with each other until the whole thin film was consumed. Samples coated with conversion coatings, primer and topcoat strongly suppressed the nucleation and propagation of these small sites.

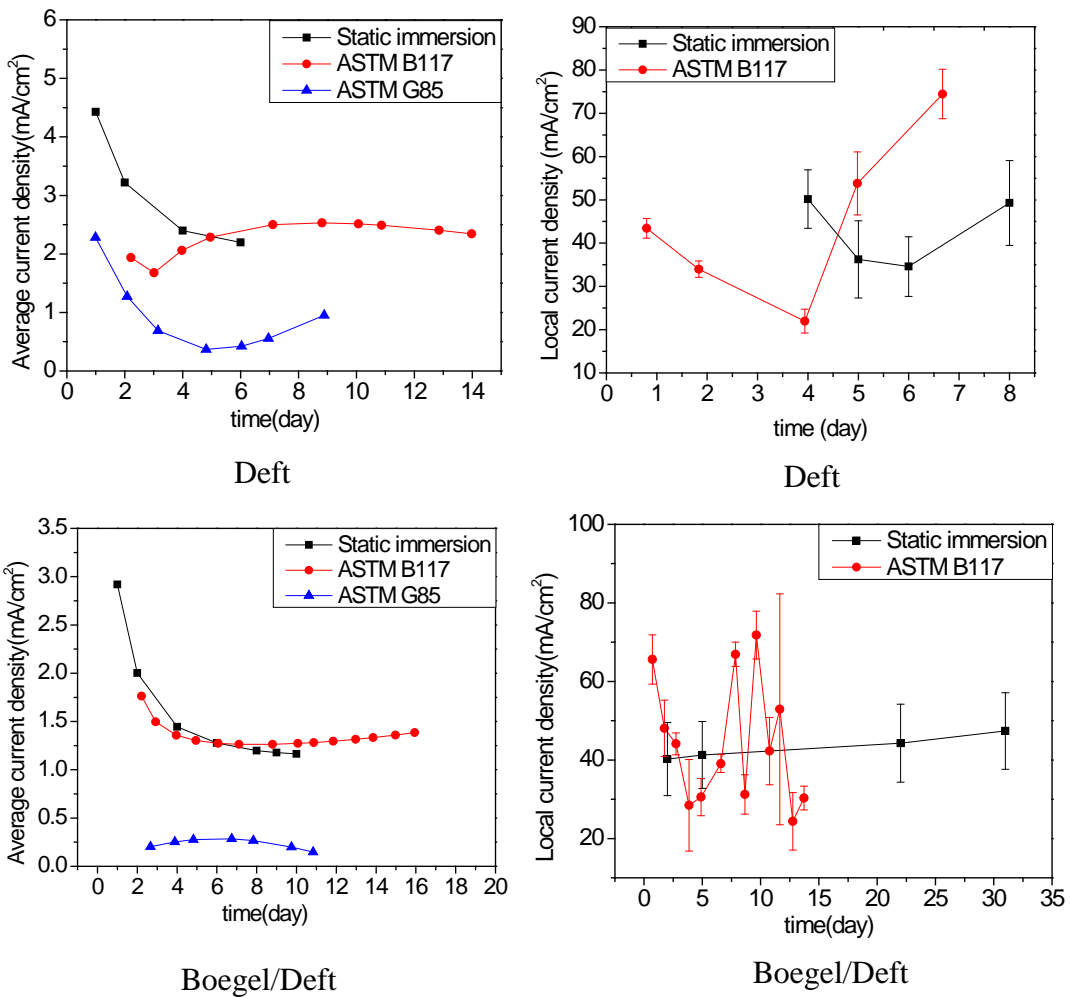
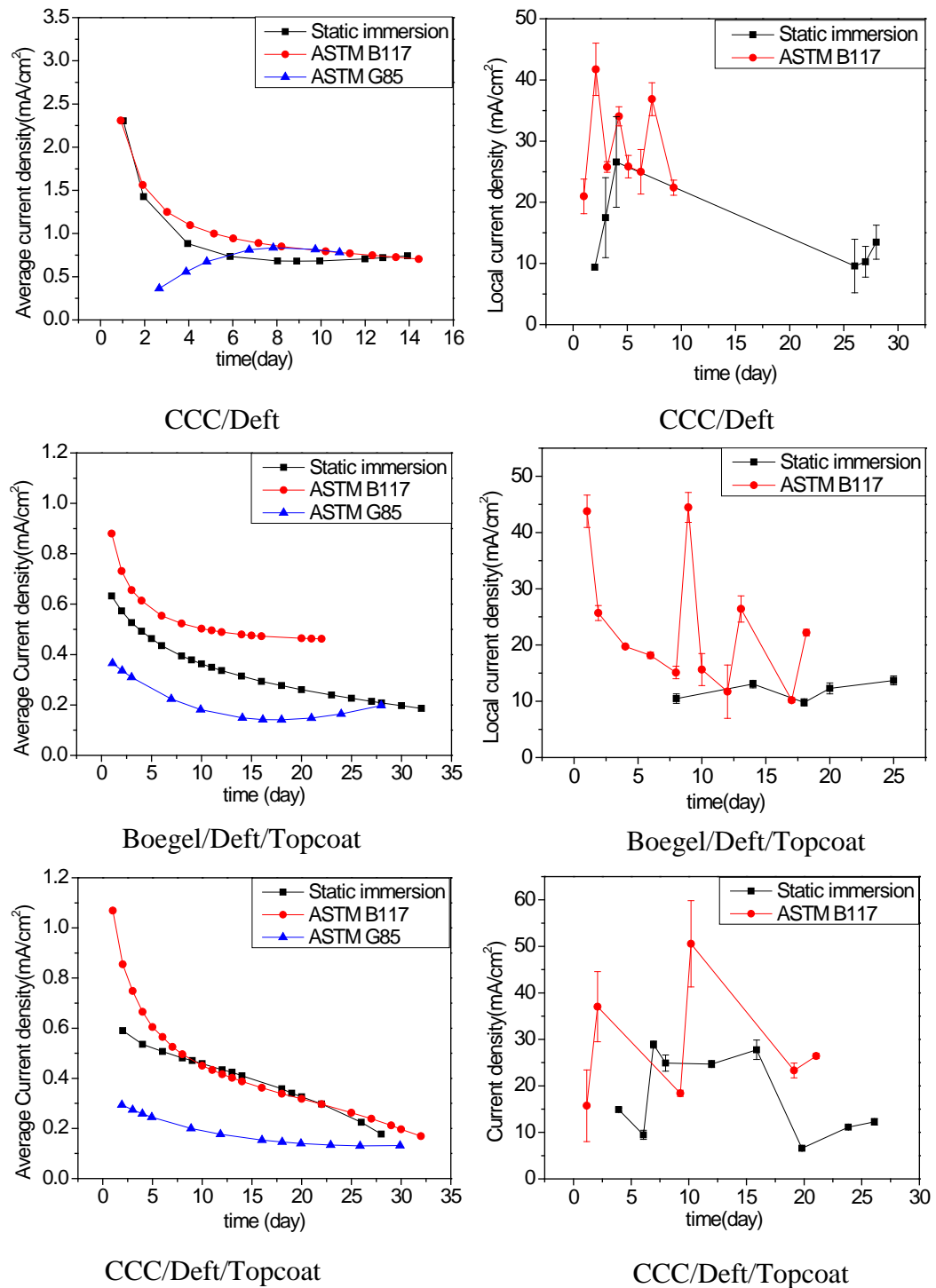


Figure 1.4.20 Comparison of average current densities (left) and local current densities (right) of Al-Cu aged samples under different coating systems exposed to 3 different environments. Continued.

Figure 1.4.20 Continued.



2. Current densities:

In general, coated samples exposed to ASTM B117 salt spray had higher corrosion propagation rates than those exposed under static immersion conditions. This was true of both average current density calculations and local current density calculations as shown in Figure 1.4.20. This was attributed to the fact that the salt spray chamber provides higher dose of NaCl (5 wt% NaCl solutions) and a higher temperature (35 °C) than static immersion (0.5 M NaCl solutions at room temperature around 25 °C), which facilitated the diffusion of oxygen and other electrolyte through the coatings that initiated corrosion on the substrates. Exceptions were found in the cases of samples coated with Deft primer-only and Boegel/Deft combinations. The average current density and local current density of these samples were found to fall in the same range in aqueous solutions and salt spray exposure conditions as can be seen in Figure 1.4.20. This was taken as an indication that the Deft primer and Boegel conversion coating could not block oxygen reduction. The lower concentration of oxygen in aqueous solutions was sufficient to support the corrosion process.

The presence of a CCC and topcoat strongly suppresses the cathodic reaction; oxygen reduction. The higher oxygen concentration in salt spray chamber resulted in average and local current densities that were higher than under constant immersion.

It has been calculated that the average current densities were the lowest for the samples exposed to ASTM G85 at early stage compared with other two environments as shown in Figure 1.4.20. It was known that the environment was changing during the ASTM G85 environment. It should be noted that the temperature of sample in ASTM G85 was generally higher than aqueous solutions (25°C). However, the low corrosion rates in ASTM G85 are attributed to the low humidity during dry cycle in ASTM G85, which significantly reduced the water content in the coatings. Therefore, the time of wetness was limited under ASTM G85 conditions.

Even though the average current densities were the lowest in the case of ASTM G85 environment, the widespread nucleation of corrosion significantly influenced undercoating damage, which indicates in the increasing aggressiveness of the environment. Topcoats act as a physical barrier. They retard the transport of electrolyte from environment to under layer primers in wet cycle. Thus, topcoat not only reduced the initiation of corrosion sites, but also slowed down the corrosion rates.

2. Total damage:

The total damage, which characterized the amount of corrosion (mass loss through Faraday's law) per unit area, was used to evaluate the aggressiveness of different environments. This was based on the calculation of charge density, computed as the integral of average current density over the exposure time. Results of samples coated with various coating systems in different exposure environments are shown in Table 1.4.1. It should be noted that charge density calculations provided direct comparisons of various coating system from different environments. In the case of sample coated with Deft primer-only and Boegel and primer combinations, the charge densities were observed to be higher when samples were subject to static immersion than in salt spray exposure, which was consistent with average current densities analysis. Samples coated with CCC and adding extra layer of topcoat on top of primer, exhibited higher corrosion rates in salt spray exposure than in static immersion. Overall, samples exposed to ASTM G85

showed slowest corrosion rates based on calculations of single corrosion site before widespread nucleation corrosion.

No signs of corrosion were indicated in the samples exposed to outdoor environment for all the coating systems. Therefore, corrosion morphology and corrosion kinetics could not be obtained and compared with the accelerated weathering tests.

Table 1.4.1 Charge density calculations of various coating systems exposure to different environments for a period of 5 days.

Coating Systems	Exposure Environment	Charge Density Charge/Area (Q/cm ²)
Deft	Static Immersion	1165
	ASTM B117	911
	ASTM G85	376
Boegel/Deft	Static Immersion	727
	ASTM B117	580
	ASTM G85	117
CCC/Deft	Static Immersion	483
	ASTM B117	578
	ASTM G85	299
Boegel/Deft/Topcoat	Static Immersion	230
	ASTM B117	289
	ASTM G85	162
CCC/Deft/Topcoat	Static Immersion	230
	ASTM B117	328
	ASTM G85	145

1.4.6 Conclusions

The effects of exposure environment on thin film corrosion underneath of organic coating systems was studied using two types of conversion coatings (Boegel and CCC), two primers (chromate-free primer and chromate pigmented primer) and with or without polyurethane topcoat on Al-4.9wt% Cu thin films at “as deposited” and “artificially aged” conditions. These environments include ASTM B117 salt spray, ASTM G85-A5 and outdoor exposure.

1. Corrosion site growth and morphology were recorded using the DOI method. Different corrosion morphologies were observed in each exposure environment. In salt spray exposure, single and multiple corrosion sites grew episodically with a filamentary morphology. In ASTM G85 corrosion sites first nucleated from the defect site followed by the widespread nucleation across the entire exposure area. No signs of corrosion were observed for samples in outdoor exposure.
2. Ex-situ experiments were also conducted on the corroded area under the coatings. Scanning electron microscopy (SEM) and energy dispersive spectroscopy (EDS) were performed after the coatings were removed at the end of each experiment. Results showed that Pr was released into corrosion sites in both cases of Deft primer-only and CCC/Deft samples. Cr was released from CCC in small amounts, but corrosion in samples where chromate was present in the coating system was minimal.
3. Methods for estimating localized corrosion kinetics were applied to samples exposed in the various environments. Average corrosion rates (current density in mA/cm²) were calculated using Faraday’s law by collecting corrosion site perimeter and bottom area. Results showed that the average current density was the highest in the case of samples exposed to salt spray chamber, followed by aqueous solutions and ASTM G85.
4. Local corrosion growth rates were derived from the corrosion growth velocity and were 10 times more than that of average current densities. The local current densities eliminated the contribution of passivated region of local corrosion sites, which occurred in most of the cases for thin films under coating systems. The local current density fell in the same range between salt spray chamber exposure and aqueous solutions, with slightly higher in salt spray chamber exposure.
5. Corrosion nucleation and growth is strongly suppressed under model chromate primers and less so under a Deft primer

1.4.7 References

1. Agarwala, V.S.a.A., S., *Corrosion Detection and Monitoring-a Review*. CORROSION 2000, March 26 - 31, 2000 , Orlando, Fl, 2000., 2000.
2. Grundmeier, G., W. Schmidt, and M. Stratmann, *Corrosion protection by organic coatings: electrochemical mechanism and novel methods of investigation*. Electrochimica Acta, 2000. **45**(15-16): p. 2515-2533.
3. Leidheiser, H., *Corrosion of Painted Metals - a Review*. Corrosion, 1982. **38**(7): p. 374-383.
4. Liao, C.M., et al., *In-situ monitoring of pitting corrosion in aluminum alloy 2024*. Corrosion, 1998. **54**(6): p. 451-458.

5. Otero, T.F., A. Porro, and A.S. Elola, *Prediction of Pitting Probability on 1050-Aluminum in Environmental-Conditions*. Corrosion, 1992. **48**(9): p. 785-791.
6. Fedrizzi, L., A. Bergo, and M. Fanicchia, *Evaluation of accelerated aging procedures of painted galvanised steels by EIS*. Electrochimica Acta, 2006. **51**(8-9): p. 1864-1872.
7. Gambina, F., *Corrosion resistance characterization of coating systems used to protect aluminum alloys using electrochemical impedance spectroscopy and artificial neural networks*, Ohio State University: Columbus, Ohio. p. xviii, 176 p.
8. ASTM, *ASTM B117-03 Standard Practice for Operating Salt Spray (Fog) Apparatus*. in Annual Book of ASTM Standards. ASTM: Philadelphia, PA, 2003.
9. Deflorian, F., S. Rossi, and M. Fedel, *Organic coatings degradation: Comparison between natural and artificial weathering*. Corrosion Science, 2008. **50**(8): p. 2360-2366.
10. Yang, X.F., et al., *Blistering and degradation of polyurethane coatings under different accelerated weathering tests*. Polymer Degradation and Stability, 2002. **77**(1): p. 103-109.
11. Bierwagen, G.P., et al., *Studies of a new accelerated evaluation method for coating corrosion resistance - thermal cycling testing*. Progress in Organic Coatings, 2000. **39**(1): p. 67-78.
12. ASTM, *ASTM G85-98 Standard Practice for Modified Salt Spray (Fog) Testing*. in Annual Book of ASTM Standards. ASTM: Philadelphia, PA, 1998.
13. Wang, D.H., et al., *In situ monitoring of a Mg-rich primer beneath a topcoat exposed to Prohesion conditions*. Corrosion Science, 2010. **52**(2): p. 441-448.
14. Allahar, K.N., et al., *Monitoring of a military vehicle coating under Prohesion exposure by embedded sensors*. Progress in Organic Coatings, 2009. **65**(1): p. 142-151.
15. Scully, J.R., *Electrochemical Impedance of Organic-Coated Steel - Correlation of Impedance Parameters with Long-Term Coating Deterioration*. Journal of the Electrochemical Society, 1989. **136**(4): p. 979-990.
16. Bierwagen, G., *The physical chemistry of organic coatings revisited - viewing coatings as a materials scientist*. Journal of Coatings Technology and Research, 2008. **5**(2): p. 133-155.
17. Amirudin, A. and D. Thierry, *Electrochemical Sensor for Monitoring Atmospheric Corrosion of Polymer-Coated Metal*. British Corrosion Journal, 1995. **30**(3): p. 214-220.
18. Armstrong, R.D. and J.D. Wright, *Impedance Studies of Poly Ethylmethacrylate Coatings Formed Upon Tin-Free Steel*. Corrosion Science, 1992. **33**(10): p. 1529-&.
19. Loveday, D., P. Peterson, and B. Rodgers, *Evaluation of organic coatings with electrochemical impedance spectroscopy - Part 2: Application of EIS to coatings*. Jct Coatingstech, 2004. **1**(10): p. 88-93.
20. Titz, J., et al., *Characterization of Organic Coatings on Metal Substrates by Electrochemical Impedance Spectroscopy*. Corrosion, 1990. **46**(3): p. 221-229.
21. Grandle, J.A. and S.R. Taylor, *Electrochemical Impedance Spectroscopy of Coated Aluminum Beverage Containers .1. Determination of an Optimal Parameter for Large-Sample Evaluation*. Corrosion, 1994. **50**(10): p. 792-803.
22. Stratmann, M., R. Feser, and A. Leng, *Corrosion Protection by Organic Films*. Electrochimica Acta, 1994. **39**(8-9): p. 1207-1214.
23. Grundmeier, G. and M. Stratmann, *Adhesion and De-adhesion mechanisms at polymer/metal interfaces: Mechanistic understanding based on in situ studies of buried interfaces*. Annual Review of Materials Research, 2005. **35**: p. 571-615.

24. Frankel, G.S., *The Growth of 2-D Pits in Thin-Film Aluminum*. Corrosion Science, 1990. **30**(12): p. 1203-1218.
25. Frankel, G.S., *MSE 735, Corrosion, Lecture notes*, . 2008. **Note 4**: p. 6.
26. Kim, Y. and R.G. Buchheit, *A characterization of the inhibiting effect of Cu on metastable pitting in dilute Al-Cu solid solution alloys*. *Electrochimica Acta*, 2007. **52**(7): p. 2437-2446.

1.5 Lessons Learned

DOI methods for studying undercoating corrosion have shown that results from corrosion testing using indirect electrochemical methods such as EIS must be interpreted with caution as artifacts may present as a high degree of corrosion resistance, when significant corrosion damage has occurred. The results of this study indicate how different standard exposure conditions act to develop corrosion damage on coated metals surfaces and may facilitate rational approaches to developing accelerated testing that mimic field exposure. These results also reinforce the idea that inhibiting oxygen reduction remains the foremost strategy for combating corrosion damage accumulation in high strength aluminum alloys.

1.6 Economic Summary

The method presented here represent a foundation for corrosion characterization work that can underpin and built confidence for commercialization of new coatings formulations and coating systems in shorter periods of time. The ability to reduce the development time for new coatings leads to an availability of a broader array of products and may reduce coating system life-cycle costs.

1.7 Implementation

A practical embodiment of a technique for direct optical interrogation of undercoating corrosion has been developed and described. This information is being made available publically and is presented in sufficient detail to allow unrestricted replication of the tools, techniques and analysis.

Task 2: Atmospheric Corrosion of Coated Steel; Relationship between Laboratory and Field Testing

2.1 Summary

This project established links between lab and field testing of coated steel samples with the goal of improving prediction of coating failure and painted component lifetime. Carbon steel samples were coated with different polymers, but most of the work was performed with PVB and Eponol coatings. Coating failure can result from changes in properties of the bulk coating polymer or of the coating/substrate interface. Bulk coating properties were assessed using infrared spectroscopy and interface properties with a Scanning Kelvin Probe (SKP). The SKP is a tool that measures the rate of cathodic delamination, and it has previously only been used on model systems. This is the first use of SKP as an assessment tool for the effects of prior degradation during exposure to corrosive conditions. The exposures included several outdoor sites in Hawaii and across the continental US, in ASTM standard cabinet tests, and in a specially constructed chamber that allowed control of certain atmospheric parameters. Both bulk polymer and interface degradation were observed. SKP was found to provide a sensitive assessment of the interface degradation, which allows for a shortening of the exposure time required for evaluation of a coating system. Field exposed samples exhibited both blisters and filiform corrosion (FFC). As a result, a more detailed analysis of FFC was performed, including experiments used to reproduce FFC in the lab. Raman spectroscopy was used to investigate the details of the iron oxide formed as a function of the form of corrosion and exposure conditions. It was possible to use the various measures to rank the corrosivity of the different field sites and to assess the important exposure parameters by investigating weather databases. The roles of exposure conditions, like UV and ozone, were investigated in the special chamber and in the standard cabinets. Finally, the degradation of some commercial coating systems was investigated.

2.2 List of Figures and Tables

Figure 2.1: Poly(vinyl butyral-co-vinyl alcohol-co-vinyl acetate) molecule (13)	107
Figure 2.2: Eponol TM 53 BH 35 molecule (12).....	107
Figure 2.3: Atmospheric chamber circuit controlling nitrogen/oxygen flows, humidity and ozone concentration.....	109
Figure 2.4: Spectra of the UVA (left) and UVB (right) lamps used in this work.....	111
Figure 2.5: Sample preparation for CD measurement.	113
Figure 2.6: CD measurement with the Scanning Kelvin Probe.	113
Figure 2.7: Potential scan examples to measured CD rate.....	114
Figure 2.8: Photographs of PVB coated steel after field exposures.	115
Figure 2.9: PVB coated 1018 CD-SKP after 2 weeks exposure in Daytona Beach, FL from Dec 2010.....	116

Figure 2.10: PVB coated 1018 CD-SKP after 2 months of exposure in Waipahu, HI from Jan 2012.....	117
Figure 2.11: PVB coated 1018 CD-SKP after 1 week of exposure in Lyon Arboretum, HI from Jan 2012.....	117
Figure 2.12: PVB coated 1018 CD-SKP after 2 months of exposure in Mauna Loa, HI from Oct 2012.....	118
Figure 2.13: PVB IR spectra after 2, 3, 4 months exposures in Lyon Arboretum from July 2011.	118
Figure 2.14: PVB IR spectra after 2 and 4 months exposures in Waipahu from July 2011.....	119
Figure 2.15: PVB IR spectra after 1 and 5 months exposures in Mauna Loa from Oct 2012 ...	119
Figure 2.16: PVB coated 1018 CD-SKP after 1, 3, 4, and 5 months of exposure in Thompson farm, NH from Jan 2012	120
Figure 2.17: PVB coated 1018 CD-SKP after 3 and 6 months of exposure in Thompson farm, NH from Oct 2010.	121
Figure 2.18: PVB coated 1018 CD-SKP after 1 week and 1 months of exposure in Columbus, OH from Aug 2011.	122
Figure 2.19: PVB coated 1018 CD-SKP after 2 weeks and 1 months of exposure in Columbus from May 2011.	122
Figure 2.20: PVB IR spectra after 2 months, 4 months and 1 year exposures in Columbus from Aug 2011.....	123
Figure 2.21: Eponol BLS coated 1018 CD-SKP after 1 year exposure in Columbus, OH from Aug 2011.....	123
Figure 2.22: Raman spectrum of uncorroded PVB coated steel.....	125
Figure 2.23: Raman spectrum of uncorroded Eponol coated steel	125
Figure 2.24: Raman spectrum of uncorroded Eponol BLS coated steel.....	126
Figure 2.25: Optical picture of bead-like corrosion formed under PVB during 2 months in Waipahu, HI.....	127
Figure 2.26: Optical picture of active filament growing under PVB after 2 weeks exposure in Kilauea Volcano, HI.	127
Figure 2.27: Sample photographs of PVB coated steel exposed in Campbell industrial park for 2 months (left) and Columbus for 1 year (right).....	128
Figure 2.28: From left to right, sample photographs of PVB coated steel exposed in Key West for 3 months, Lyon Arboretum for 1 and 3 months, Waipahu for 2 months and Ewa Nui for 2 months.....	128
Figure 2.29: Sample photographs of PVB coated steel exposed near Kilauea Volcano for 1 month.	128
Figure 2.30: Raman spectrum of akaganeite (β -FeOOH) formed in inactive filament heads... 129	129
Figure 2.31: Raman spectrum of green rust ($3\text{Fe}(\text{OH})_2\text{Fe}(\text{OH})_2\text{Cl}_n\text{H}_2\text{O}$) formed in active filament heads.	130
Figure 2.32: Raman spectrum of ferrihydrite ($5\text{Fe}_2\text{O}_3 \cdot 9\text{H}_2\text{O}$) formed in filament tail	130

Figure 2.33: Raman spectra of akaganeite intermediates formed in drying filament heads. a and b: Green rust, c and d: akaganeite intermediate	131
Figure 2.34: Raman spectra of akaganeite synthesized from FeCl_2 and NaOH . a: green rust, b: Intermediate and c: akaganeite.....	132
Figure 2.35: Raman spectrum of akaganeite ($\beta\text{-FeOOH}$) formed in bead-like corrosion in Waipahu, Campbell, Ewa Nui, Columbus and Key West.	133
Figure 2.36: Raman spectrum of goethite (a- FeOOH) formed in bead-like corrosion in Kilauea Volcano.	133
Figure 2.37: Raman spectrum of magnetite (Fe_3O_4) formed in bead-like corrosion in Lyon Arboretum.	134
Figure 2.38: Raman spectrum of amorphous formed in bead-like corrosion at all sites tested..	134
Figure 2.39: Raman spectrum of amorphous formed in bead-like corrosion at all sites tested..	135
Figure 2.40: Raman spectrum of lepidocrocite and goethite mixture formed in bead-like corrosion at all sites tested.	135
Figure 2.41: From left to right, sample photographs of Eponol coated steel exposed 2 months in Campbell Industrial Park, 1month in Lyon Arboretum, 2 months in Waipahu and 2 weeks Kilauea Volcano.....	136
Figure 2.42: From left to right, sample optical photographs of Eponol coated steel exposed 2 months in Campbell Industrial Park, 1month in Lyon Arboretum, 2 months in Waipahu and 2 weeks Kilauea Volcano.....	136
Figure 2.43: Eponol or Eponol BLS coated 1018 Raman spectra. Spectrum a: Akaganeite; spectrum b: Goethite; spectrum c: Lepidocrocite (Lyon Arboretum); spectrum d: Akaganeite intermediate (filament head).	137
Figure 2.44: PVB coated steel CD-SKP after 1 and 2 days of B117 exposure.	146
Figure 2.45: PVB coated steel CD-SKP after 2, 4 and 6 days of G154.....	147
Figure 2.46: PVB IR spectra after 2, 4 and 6 days of G154.	147
Figure 2.47: PVB coated steel CD-SKP after B117/G154 exposure.....	148
Figure 2.48: PVB coated steel CD-SKP after B117/G154 exposure.....	148
Figure 2.49: PVB coated steel CD-SKP after B117/G154 exposure.....	149
Figure 2.50: PVB coated steel CD-SKP after B117/G154 exposure.....	149
Figure 2.51: PVB coated steel CD-SKP after 4 days of UVA exposure in different environments.	150
Figure 2.52: PVB coated steel CD-SKP after 4 days of exposure at 100% RH in different environments.....	151
Figure 2.53: PVB coated steel CD-SKP after 2 days of UVA exposure at 100% RH in different environments.....	152
Figure 2.54: Eponol BLS coated steel CD-SKP after 4 days of UVA exposure with and without 100% RH.....	152
Figure 2.55: PVB coated steel CD-SKP after 4 days of UVA, $[\text{O}_3]$ 0.1 ppm exposure at 95% RH.	153

Figure 2.56: PVB coated steel CD-SKP after 4 days of UVB exposure at 95% RH with different $[O_3]$	154
Figure 2.57: PVB coated steel CD-SKP after 4 days of UVA, $[O_3]$ 0.1 ppm exposure with different RH	154
Figure 2.58: PVB coated steel CD-SKP after 4 days of UVB, $[O_3]$ 0.1 ppm exposure with different RH	155
Figure 2.59: PVB coated steel CD-SKP after 4 days of $[O_3]$ 0.1 ppm exposure at 95% RH with and without UV.....	155
Figure 2.60: Optical photographs of filifrom corrosion of Eponol coated 1018.	157
Figure 2.61: Optical photographs of FFC of PVB coated 1018. From left to right, the FFCs were initiated by 0.1 M NH_4Cl , 0.01 M $NaCl$ and 0.1 M $NaCl$	157
Figure 2.62: Potential map of PVB coated 1018 after 5 days of FFC test initiated with 0.01 M $NaHCO_3$ and 0.1 M $NaCl$. The values given on the map are local potentials in V/SHE.	158
Figure 2.63: Potential map of filament head of PVB coated 1018 after 5 days of filifrom corrosion test initiated with 0.01 M $NaHCO_3$ and 0.1 M $NaCl$	158
Figure 2.64: Potential profiles after FFC test of PVB coated 1018.....	159
Figure 2.65: Optical photographs of FFC under PVB (top) and Eponol (bottom) coated on steel initiated with 0.5 M HCl	160
Figure 2.66: Optical profilometry pictures of merging filaments under PVB.....	161
Figure 2.67: Optical picture before rust removal (left) and optical profilometry pictures after rust removal (right) of filaments under Eponol.	162
Figure 2.68: Filament depth and filament head diameter relationship under PVB.	163
Figure 2.69: Filament depth and filament head diameter relationship under Eponol.....	163
Figure 2.70: Iron dissolution flux as a function of filament head radius under PVB with surface and ohmic limited rate fits.	164
Figure 2.71: Iron dissolution flux as a function of filament head radius under Eponol with surface and ohmic limited rate fits.	165
Figure 2.72: CD-SKP of PVB coated 1018 with several TecTalis conversion coating treatment prepared by Henkel	167
Figure 2.73: 1 day CD-SKP of E-Coat coated 1018 prepared by Henkel after weathering exposures, start on coating edge	168
Figure 2.74: 2 days CD-SKP of 53030 phosphated 1018 prepared by NAVAIR after laboratory exposures, start 1000 μm away from coating edge.....	169
Figure 2.75: 3 days CD-SKP of 53030 grit blasted 1018 prepared by NAVAIR after laboratory exposures, start 1000 μm away from coating edge, start later.....	169
Figure 2.76: 4 days CD-SKP of 53022 phosphated 1018 prepared by NAVAIR after laboratory exposures, start 1000 μm away from coating edge.....	170
Figure 2.77: 4 days CD-SKP of 53022 grit blasted 1018 prepared by NAVAIR after laboratory exposures, start 1000 μm away from coating edge.....	171

Table 1: Field sites climate, location and elevation	108
Table 2: TOWs of the first month of exposure of PVB coated steel without artificial defect (40-43).	140
Table 3: TOWs of the first two months of exposure of PVB or Eponol coated steel with artificial defect (42, 43).	141
Table 4: Precipitation, atmospheric data of the first month of exposure of PVB coated steel without artificial defect (40, 41, 44, 45).	142
Table 5: Precipitation, atmospheric data of the first two months of exposure of PVB or Eponol coated steel without artificial defect (42, 44).....	143
Table 6: UV radiation of the first fourth month of exposure of PVB coated steel without artificial defect (45).	144
Table 7: Merging filament depths and diameters of Figure 2.66.....	161
Table 8: Surface and ohmic limited rate fitting equation with adjusted R^2 under PVB and Eponol.	165

2.3 Introduction and Background

Accelerated laboratory tests attempt to evaluate the anti-corrosion performance of coatings in a short time. Sometime, accelerated tests fail to mimic outdoor exposure because they alter the degradation mechanism (1). For this reason, field exposures are the most reliable tests to predict coating lifetime. However, field tests might require many years for coating degradation to initiate and they are often not reproducible. To reduce the time for initiation of degradation in the field, samples are exposed in harsh environments such as seaside Florida or Arizona. Additional sea water spray or sun irradiation enhancement is also possible to shorten field exposure duration. The degradation of a coated metal sample can be accelerated by creating an artificial defect in the coating (2).

The challenge of a reliable accelerated test is associated with the complexity of tropospheric chemistry. Only a few atmospheric and climatic parameters are included in accelerated tests. This simplification of outdoor exposure does not suit all coating or metal types. The most common laboratory accelerated test for atmospheric corrosion is ASTM B117, which involves a neutral salt spray. However, the results of B117 do not always correlate with atmospheric exposures. One recently-studied example of discrepancy between B117 and field exposure is the corrosion of silver as silver chloride does not form during exposure in a dark salt spray cabinet but was found to form in a chamber that included ozone and UV light (3). As a result of this work, various B117 chambers, including the one at the University of Virginia were modified to include UV light and ozone. Ozone is strong oxidant present in the troposphere which decomposes into stronger oxidants (atomic oxygen and hydroxyl radicals) under UV light (max decomposition at 254 nm) in a humid environment (4). The short lifetime of atomic oxygen and hydroxyl radical requires that they are formed in the accelerated test environment close to the

sample surface. Such a modified chamber, which couples a corrosive environment with UV and strong oxidants, can be useful to study the degradation of coated metal. ASTM G154 is another accelerated test that is used to study polymer degradation or weathering. The parameters used in the weathering chamber to accelerate polymer degradation are UV, temperature and moisture condensation, but corrosive salts are not included.

Coated metal degradation includes degradation of the bulk polymer and of the polymer/metal interface. Polymer/metal interface degradation may be influenced by bulk polymer degradation, but it is not a requirement. The physical and mechanical properties of the polymer are affected by polymer hydrolysis and photo-oxidation. These changes may facilitate oxygen, water and ion transport to the interface. The polymer/metal interface can degrade via blistering, cathodic delamination or filiform corrosion (FFC). Blisters usually initiate at impurities at the interface and then grow under osmosis pressure. Cathodic delamination can be part of the blister growth mechanism or it can initiate from a coating mechanical defect or edge. FFC is a directional defect that initiates only from a coating mechanical defect or edge. Studies showed that lateral oxygen, water or ion transport from uncoated area is faster than vertical transport through the coating film (5).

The progress of the delamination front during cathodic delamination is easily followed by the scanning Kelvin probe (SKP) (6). The cathodic delamination is caused by the intermediates and the hydroxide anion produced during oxygen reduction (7). The delamination rate is dependent on the chemical strength of the polymer/oxide adhesion, which is considered to occur by the adsorption of a polymer polar group on the metal surface hydroxide (8). The SKP has been widely used to study coating/oxide interface dipoles and coating performance (9, 10). The measurement of cathodic delamination by the SKP is abbreviated by CD-SKP in the rest of this report.

Many different types of polymer coatings exist. Poly(vinyl butyral) (PVB) is a transparent coating with good binding, flexibility and toughness properties. It is mainly used on laminated glass where it exhibits good adhesion with the glass material (11). PVB coatings have been used as a model coated metal system. Eponol 53 BH 35 is an ultra-high molecular epoxy resin diluted in methyl ethyl ketone and propylene glycol methyl ether (12). Eponol macromolecules are polymerized from bisphenol A diglycidyl ether (DGEBA) without curing agent. DGEBA is a common monomer for epoxy resin.

In this work, the degradation mechanisms of coated steel in the field were characterized. Coated steel without and with an artificial defect were exposed in diverse climates in the continental US and in the islands of Hawaii. The degradation of unscrubbed coated steel was analyzed with sensitive technique such as infra-red spectroscopy and CD-SKP. Sensitive techniques enable early degradation assessment before visual failure. The field exposure time can therefore be reduced. The corrosion products formed underneath coatings on steel during field exposure were identified by Raman spectroscopy. The condition of corrosion products formation is well-

documented in the literature. It is therefore possible to deduce the undercoating environment (oxygen, pH) and the eventual atmospheric compounds (chloride, sulfate) that played a role in the corrosion mechanism.

Field exposures are also useful to determine which degradation mechanisms should be reproduced and investigated in detail in the laboratory. Laboratory tests have the advantage of isolating and controlling the exposure conditions. ASTM accelerated tests were used to investigate the degradation mechanism and evaluate their discrepancies with the field exposures. Effects of ozone photolysis on coated steel were then investigated in an enclosed exposure cell. Laboratory experiments were also used to study cathodic delamination and FFC, which are two common coating delamination mechanisms present in the field.

2.4 Lessons Learned

One important lesson learned in this work is that it is possible to use research tools, i.e. SKP, to understand coating degradation and improve lifetime prediction assessments. It is a challenge to use SKP on real samples exposed to real environments, but the benefits are worth the effort.

2.5 Experimental

Several coatings on 1018 were tested. Two primer coatings were applied in the OSU laboratory. The details of their composition and preparation are described below. Other coatings were prepared by Henkel in Madison Heights, MI and NAVAIR in Patuxent River, MD.

Poly(vinyl butyral-co-vinyl alcohol-co-vinyl acetate) (PVB) composed of 80wt% of vinyl butyral, 20 wt% of vinyl alcohol and less than 1 wt% of vinyl acetate was purchased from Sigma-Aldrich. This primer molecule is represented in Figure 2.1. PVB granules were dissolved into 15 wt% in methyl alcohol.

EponolTM Resin 53-BH-35 was obtained from Momentive already dissolved to 35wt% in 2-butanone and propylene glycol methyl. EponolTM 53-BH-35 is an ultra-high molecular weight epoxy resin derived from bisphenol-A and epichlorohydrin with a repeating unit of 90 (see Figure 2.2). BLS® 1130 UV absorber from Mayzo was added to the resin to delay Eponol photo-oxidation during weathering exposure. This product is a hydroxyphenyl-benzotriazole derivative pre-dissolved in polyethylene glycol 300 to increase its solubility in the coating solvent. EponolTM 53-BH-35 without and with BLS® 1130 are referred to in this report as Eponol and Eponol BLS.

1018 sheets, cold rolled to 1/8" thick were purchased from McMaster-Carr. The substrates were cut into rectangular shapes of 6.35 cm by 1.9 cm. The surface was ground to 600 grit with CarbiMet™ 2 paper for all experiments. The surface was polished to 1200 grit with MicroCut™ S for optical profilometry imaging. Coatings were applied by a draw down bar on clean and freshly polished or ground steel surfaces. Alconox powdered precision cleaner was used to rinse the steel surfaces after polishing or grinding. The sample long edges were covered with electrical tape prior coating application. PVB coatings were air dried for 24 h after coating application. Eponol coatings were air dried for 7 days and then oven dried for 24 h at 75°C. Each set of samples prepared for weathering exposures included control samples. All samples were shipped for outdoor exposure in individual air-tight containers, which did not contain desiccant. The control samples were sent with the other samples, but were kept indoors in their air-tight containers. The control samples for the samples exposed in Columbus or in the laboratory were kept in a desiccator.

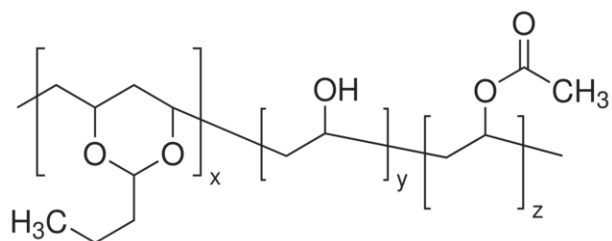


Figure 2.1: Poly(vinyl butyral-co-vinyl alcohol-co-vinyl acetate) molecule (13)

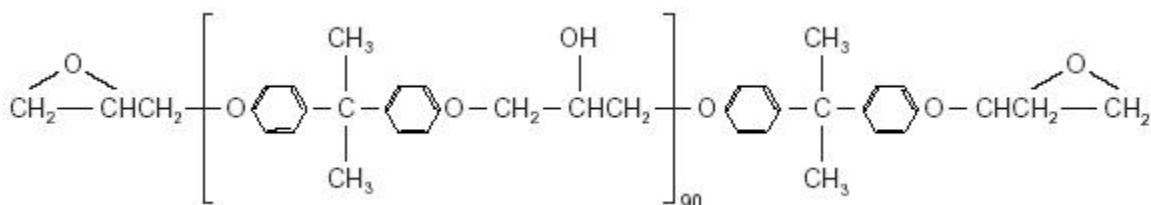


Figure 2.2: Eponol™ 53 BH 35 molecule (12)

2.5.1 Field exposure

Coated steel was exposed to different climates and air compositions in several US states: New Hampshire, Hawaii, Florida and Ohio. Some samples were exposed at Thompson Farm, NH which is a rural site located near Durham, NH. Atmospheric and weathering data were collected in this location and are available on the university web site. Florida is a popular marine exposure site to test coating lifetime. Samples were exposed at the Battelle Memorial Institute field site in

Daytona Beach and at the Naval Air station in Key West. The Hawaiian islands offer diverse micro-climates and air compositions. Researchers at the University of Hawaii maintain up to 10 field sites on Oahu Island and the big island of Hawaii. Atmospheric and weathering data were collected in each of these sites. Some samples were exposed at the campus of Ohio State University for convenience.

Weathering and the atmospheric were collected by the University of New Hampshire, the University of Hawaii, the National Climatic Data Center and the Environmental Protection Agency. Those data are presented in the result and discussion part. Table 1 shows the climate diversity of the field sites tested across the United States.

Table 1: Field sites climate, location and elevation

Sites	Climate	Location		Elevation
Thompson Farm, NH	Rural	43.1078	-70.9517	39.93
Daytona Beach, FL	Marine	29.04°N	80.94°W	Sea level
Key west, FL	Marine	24.55°N	81.78°W	Sea level
Lyon arboretum, HI	Humid	N21.33270	W157.802 92	152
Waipahu, HI	Dry, Corrosive	N21.37746	W158.017 76	Sea level
Ewa Nui, HI	Agriculture	21.37281	158.04541	61
Campbell industrial park, HI	Instructrial, Marine	N21.30141	W158.096 39	Sea level
Kilauea Volcano, HI	Volcanic, Marine	N19.31646 9	W155.152 686	567
Mauna Loa Observatory	Alpine	N19.53643 3	W155.576 862	3389

Columbus, OH	Suburban	40.002287	- 83.011850	244
--------------	----------	-----------	----------------	-----

2.5.2 Laboratory exposure

ASTM standards

Several ASTM standard environments were used. ASTM B117 is a continuous fog spray of 5 wt% NaCl at 35°C. ASTM G85 Annex 5 is a 1-h fog / 1-h dry-off cycle. During the fog period, no specific temperature is achieved and the fog composition is 0.35 wt% ammonium sulfate and 0.05 wt% sodium chloride. During the dry-off period, the chamber is purged with fresh air at 35°C. The ASTM G154 cycle 1 test is composed of 8-h UV at 60°C and 4-h condensation at 50°C. UVA lamps of 340 nm adjusted at 0.89 W/m²/nm irradiation were used for this exposure.

Atmospheric chamber apparatus

The atmospheric chamber represented in Figure 2.3 was used to control the oxygen and nitrogen flows, the humidity and the ozone concentration. This setup was strongly inspired by the apparatus developed by Liang et al. (3). The amount of water was regulated by a mixture of dry and humid nitrogen and the RH depended on the laboratory room temperature. Ozone concentration was adjusted by the nitrogen dilution and the oxygen flow. Ozone photolysis was stimulated in the chamber with a UV lamp placed on top of the cell.

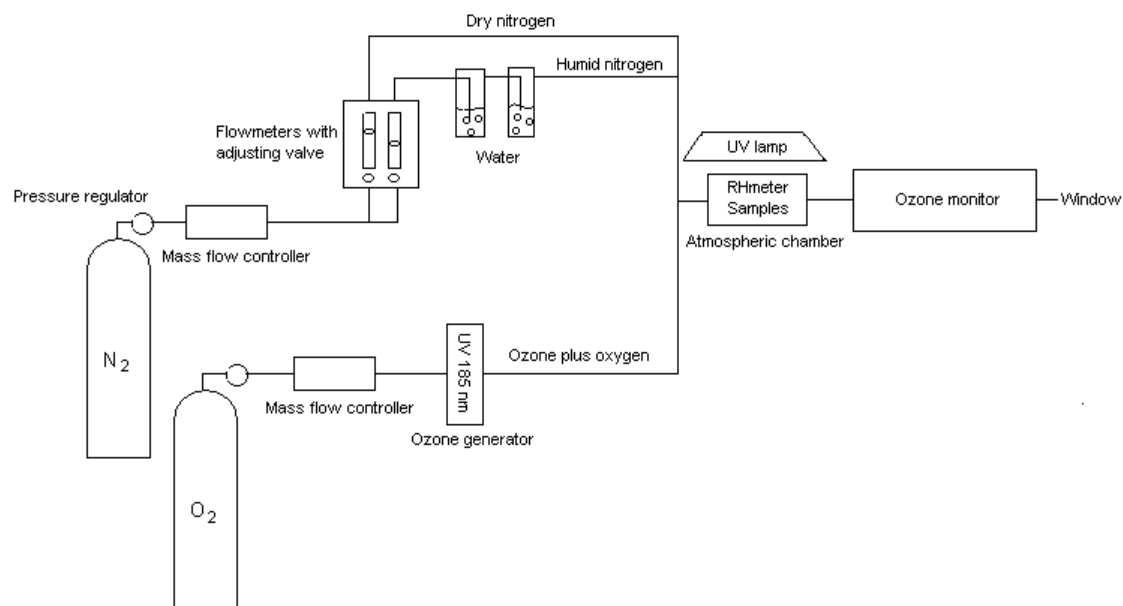


Figure 2.3: Atmospheric chamber circuit controlling nitrogen/oxygen flows, humidity and ozone concentration

- Gases:

Several gases were purchased for use in these experiments. Grade 4.8 nitrogen provided by Praxair had a purity of 99.998% and contained < 5 ppm of oxygen and < 3 ppm of water. Grade 4.3 oxygen provided by Praxair had a purity of 99.993% and contained < 3 ppm of water, < 10 ppm of nitrogen, < 1 ppm of total hydrocarbon content and < 40 ppm of argon.

- Flow controllers:

Two types of flow controllers were used in the circuit: mass flow controllers from Omega and molded polycarbonate flowmeters with valves from Key Instruments (KI). The mass flow controller ranged from 0 to 1000 mL/min for nitrogen and 0 to 10 mL/min for oxygen with a repeatability of $\pm 0.5\%$ and an accuracy of $\pm 1.5\%$. The oxygen mass flow controller cannot be used below 0.25 mL/min with the same accuracy. The KI flowmeters controlled the flow with an accuracy of $\pm 4\%$ and the flow was stable when the input flow was constant. These flow controllers ranged from 0.1-1 or 0.2-2.5 SCFH.

- Other instruments:

The ozone generator was a model 600 from Jelight. The ozone monitor was a 465L model from Teledyne. It measures the ozone concentration by UV absorption with an accuracy of 1% and repeatability of 0.5%. The zero calibration was performed every two years with ultra-high purity nitrogen (grade 5.0) to compensate for any drift. The ozone monitor was removed from the circuit during exposure because its pumping periodicity interfered with the continuous flow and lowered the flow controller accuracy. UVA or UVB mercury-vapor lamps were positioned above the atmospheric cell and their spectra are shown in Figure 2.4.

- Materials:

All tubes were PTFE with a $1/4$ "outer diameter and $1/8$ " inner diameter. Fittings were NPT adapter with leak-proof ferrule made from 316 SS or brass depending on the gas nature. The fitting of the glass threaded inlet and outlet of the atmospheric chamber and the water bottles were plastic with rubber O-ring to ensure airtightness. The atmospheric chamber was made from borosilicate glass and was closed with a quartz window that was squeezed against a rubber O-ring with a U-clamp on top of the chamber.

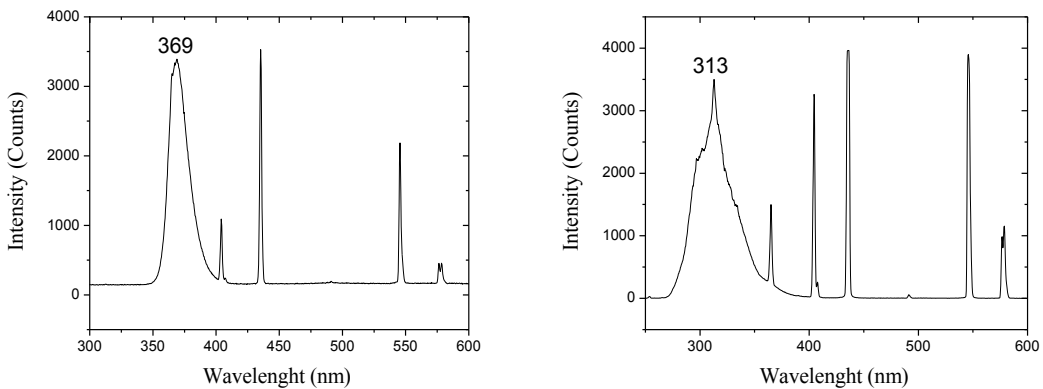


Figure 2.4: Spectra of the UVA (left) and UVB (right) lamps used in this work.

2.5.3 Instruments

- Raman spectroscopy

InViaTM Raman spectroscopy coupled with an optical microscope from Renishaw was used with a 663 nm HeNe laser. The spot size was about 1 μm and the maximum laser power was 6 mW. The laser power was adjusted from 100% to 10% according to the iron oxide heat stability. The exposure time was increased from 40 to 100 s to reduce the signal to noise ratio. The software WireTM 3.0 was used to operate the instrument. The Raman spectra were compared to reference spectra found in the literature of synthesized iron oxide. One synthesis was carried out to confirm the nature of an intermediate of akaganeite. Akaganeite was formed from FeCl_2 and NaOH where the concentration ratio $2[\text{FeCl}_2]/[\text{NaOH}]$ was larger than 8 (14). After precipitation, the solution was filtered without rinsing and analyzed immediately.

- Infra-red (IR) spectroscopy

Two Spectrum 100s FT-IR instruments from Perkin Elmer were used in reflection mode to analyze coated metals. One of the spectrometers was coupled to a Spectrum Spotlight 300 that had a microscope to direct the incident beam on the sample at 90°C. A mercury cadmium telluride (MCT) photon conductive detector cooled with liquid nitrogen was used in this case. The other spectrometer was used with a two-mirror infrared reflection-absorption spectroscopy (IRAS) set up. The incident beam and the reflected beam angles were adjusted to reach maximum energy. A triglycine sulfate (TGS) pyro electric detector was used in this case.

- Scanning Kelvin probe

A height-regulating scanning Kelvin probe (SKP) from K&M Soft Control was used to follow the progress of cathodic delamination (CD). The instrument was calibrated before each use with

the known and constant potential of Cu in saturated CuSO₄. The delta value that determines the probe/sample distance was fixed at 0.12. The scanning speed was set by the instrument at 0.4 $\mu\text{m/s}$. the probe diameter was 210 μm and the scanning step size was 100 μm .

- Optical profilometry

The sample topography was obtained with a Contour GT optical profiler from Veeco. The pictures were taken with the 5x objective in VSI mode. The entire sample picture was obtained with a stitching function. The iron dissolution volumes were calculated after tilt correction on 1x1 cm² picture portion with Vision64 software.

2.5.4 Cathodic delamination and FFC measurements

Cathodic delamination measurements

The sample preparation method for CD measurements with the SKP (CD-SKP) was borrowed from Leng et al. (6). A piece of electrical tape covered part of the top of the sample before coating application. The coating was then applied on top of the metal and the taped area. The sample was exposed to various environments with the tape in place. The tape was removed before CD-SKP when the sample was dried. Removing the tape left a clean coating edge that is represented in Figure 2.5. The uncoated area, which had the dimensions of the piece of tape width represented a defect in the coating. Epoxy glue was deposited along the sample edge to form a reservoir as shown in Figure 2.5. The 0.5 M NaCl electrolyte was contained between the epoxy glue wall and the coating edge. The SKP chamber was maintained at 100% relative humidity (RH) during CD measurement. Several samples were tested together in the SKP chamber to ensure identical exposure conditions and facilitate sample comparison (10). The defect was covered with electrolyte after the coating was saturated with water by exposure to humid air, which can take from 2 to 4 hours. The measurement was started immediately after covering the defect with electrolyte. CD-SKP is represented in Figure 2.6. The sample was naturally polarized when the electrolyte was deposited on the uncoated steel surface. The iron dissolution was located at the uncoated area in the defect and part of the cathodic reaction (oxygen reduction) occurred under the coating. Oxygen reduction product and intermediates are responsible for coating disbonding. The Kelvin probe placed above the coating measures primarily the local potential of the buried polymer/metal interface (15). The Kelvin probe was scanned above the coating repeatedly to locate the position of the delamination front with time. An example of potential scans is presented in Figure 2.7. On the left, the potential next to the defect is close to the corrosion potential of iron. On the right, the potential of the intact coating depends on the interaction nature of the coating/metal interface. The delamination front was located at the potential jump between the delaminated coating potential and the intact coating potential. The potential drop between the delamination front and the defect was characteristic of

the delaminated coating potential (6). The delamination front location was plotted as a function of time from the potential scans.

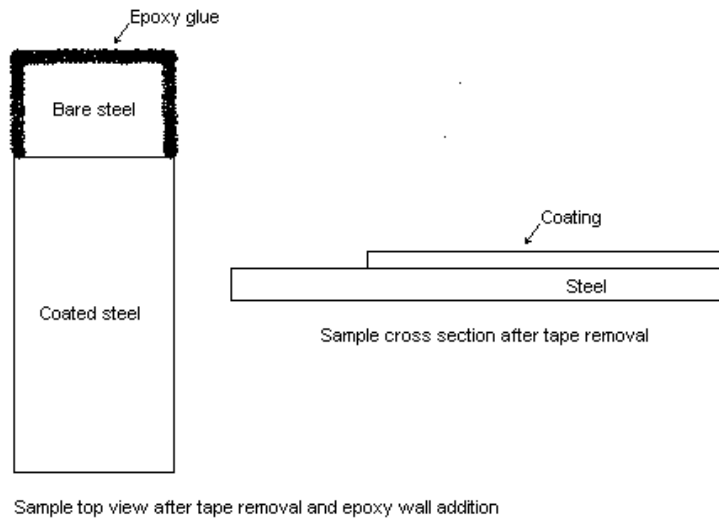


Figure 2.5: Sample preparation for CD measurement.

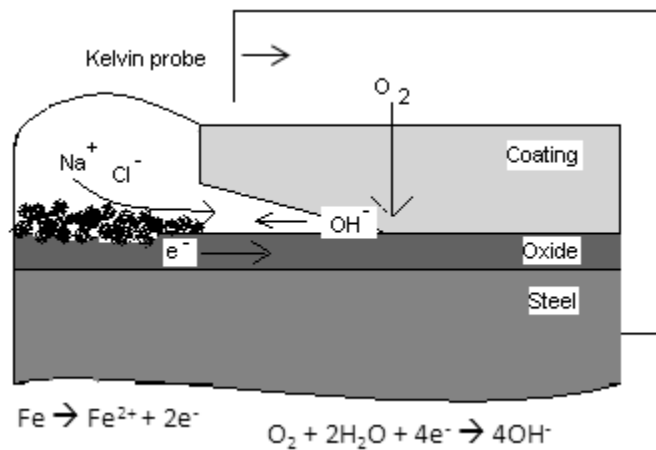


Figure 2.6: CD measurement with the Scanning Kelvin Probe.

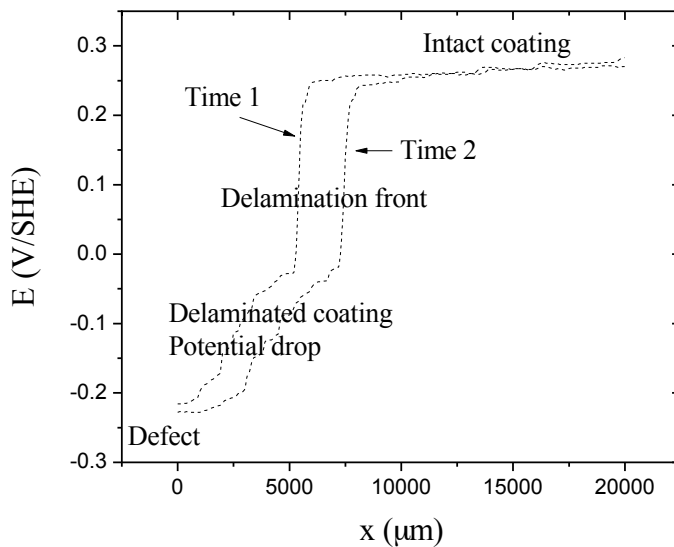


Figure 2.7: Potential scan examples to measured CD rate.

Filiform corrosion measurement

Two series of experiment employing different FFC tests were carried out. The first FFC test was inspired by ISO 4623. The scribed coated samples were immersed for 60 s in different electrolytes. The samples were then inserted in the oven at 40°C and 80% RH. The scratch contained electrolyte when inserted in the oven. The RH was kept constant in a sealed plastic container using beakers of saturated potassium chromate [OBrian 1947]. The electrolytes tested were 0.1 NaCl, 0.1 NaCl + 0.01M NaHCO₃, 0.1M NH₄Cl and 0.01M NaCl. SKP potential maps and potential lines were taken after a few days in the oven.

The second FFC test was similar to the one described by Williams and McMurray but the FFC measurement and the sample preparation were different from their approach (16). Tapes along the sample edge were removed after weathering exposure for the FFC test. 10 μ l of 0.5 M HCl was deposited along 1 cm of coating edge delimited with epoxy glue. FFC initiated from the coating edge. The electrolyte was air dried before insertion of the sample in an oven held at 40°C. The RH was maintained at 80% in a sealed plastic container with beakers of saturated ammonium sulfate solution (17). Optical photographs were taken at 3.5x magnification in black and white every day for several weeks. The corroded areas were calculated with ImageJ software from the images. The coating was dissolved in its initial solvent and rinsed with DI water. The corrosion products were dissolved in ultrasonic bath in 80°C, 0.5 M boric acid and 5.10⁻⁴ M glacial acetic acid solution. The sample topography was measured with optical profilometry. The filament grooves volumes were calculated with Vision64 software.

2.6 Results and discussion

2.6.1 Field exposures of coated steel without artificial defect

Cathodic delamination (CD) measurement with the scanning Kelvin probe (CD-SKP) should measure the kinetics of degradation and thus help in coating lifetime assessment. The CD rate is limited by the coating/oxide interface stability, which is affected by field exposure. The CD-SKP assessment of the coating/oxide interface degradation is complemented with IR spectroscopy analysis of the coating molecular degradation. PVB coated steel was tested in Daytona Beach, Waipahu, Lyon Arboretum, Thompson farm and Columbus. Eponol BLS coated steel was tested in Columbus.

Figure 2.8 shows images of samples after field exposures. The pictures were taken after removal of the tape along the coating edge. Corrosion initiated from the coating edge in corrosive sites. Daytona Beach, Lyon Arboretum and Waipahu are the most corrosive sites. No visual degradation was observed after 6 months of exposure at Thompson Farm. Some corrosion was observed on the sample exposed in Columbus but it grew slowly after it appeared. CD-SKP results for samples exposed at the different sites will presently be discussed in turn.

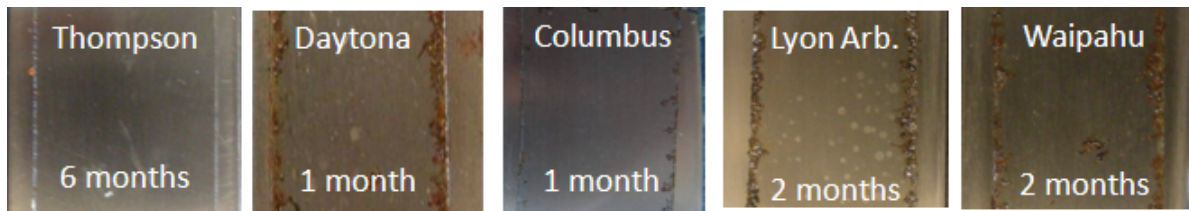


Figure 2.8: Photographs of PVB coated steel after field exposures.

Marine environment: Daytona Beach, FL

PVB coated steel samples were exposed at Daytona Beach for 2 weeks or 1 month. The samples faced the ocean on the beach. The coating failed dramatically after 1 month of exposure. After 2 weeks of exposure, the transparent coating was covered with small local white spots characteristic of polymer hydrolysis (18). The sample exposed at Daytona Beach for 2 weeks exhibited faster CD than the unexposed sample, as shown in Figure 2.9.

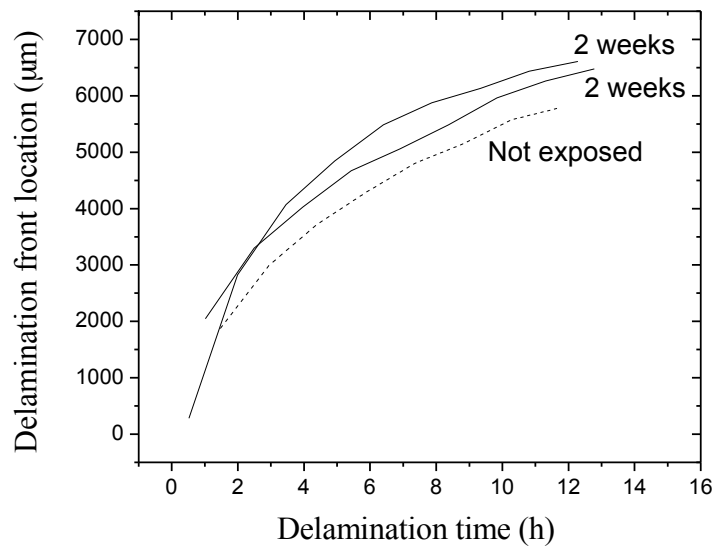


Figure 2.9: PVB coated 1018 CD-SKP after 2 weeks exposure in Daytona Beach, FL from Dec 2010.

Hawaii field exposures

PVB coated steels were exposed at Waipahu and Lyon Arboretum on the Island of Oahu and at Mauna Loa on the big Island. At all Hawaiian locations tested, the coating failed to protect the steel substrate within the first month. As shown in Figure 2.10, the CD started above 5000 μm after 2 months of exposure in Waipahu because coating delamination took place during the field exposure. As shown in Figure 2.12, the CD was accelerated after 2 months exposure in Mauna Loa. In contrast, the CD rate was slower after 1 week of exposure in Lyon Arboretum, Figure 2.11. IR spectroscopy results in Figure 2.13, Figure 2.14 and Figure 2.15 show an increase of carbonyl peak at 1725 cm^{-1} with field exposure time due to PVB photo-oxidation. The carbonyl group is the main product of the 1,3 dioxane ring opening that takes place during PVB photo-oxidation (19). PVB photo-oxidation occurred earlier and more rapidly in Waipahu than in Lyon Arboretum. PVB photo-oxidation started later in Mauna Loa than in Lyon Arboretum.

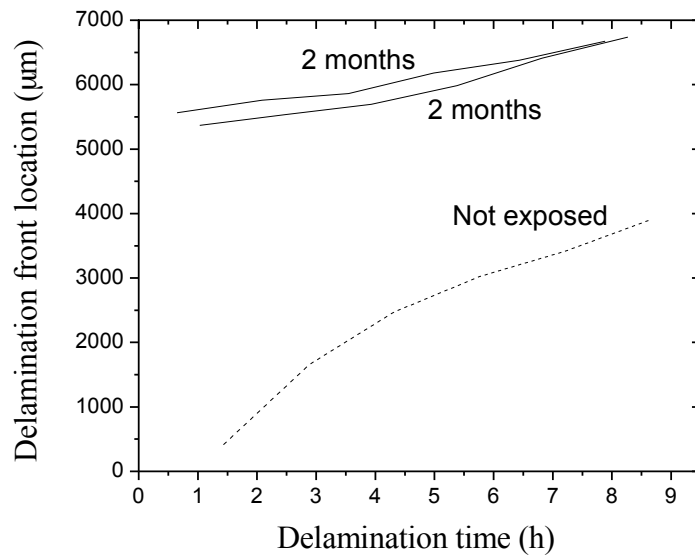


Figure 2.10: PVB coated 1018 CD-SKP after 2 months of exposure in Waipahu, HI from Jan 2012.

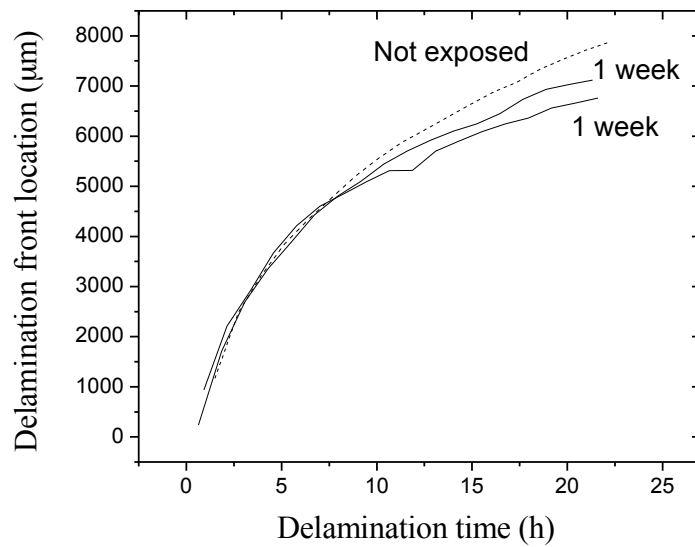


Figure 2.11: PVB coated 1018 CD-SKP after 1 week of exposure in Lyon Arboretum, HI from Jan 2012.

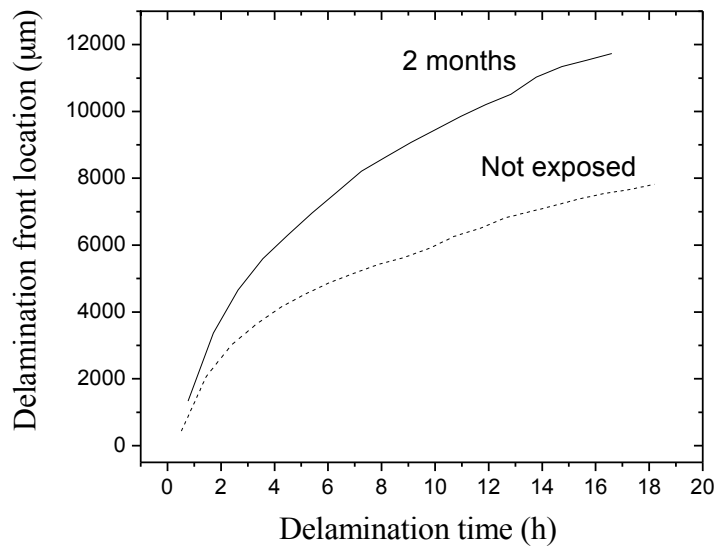


Figure 2.12: PVB coated 1018 CD-SKP after 2 months of exposure in Mauna Loa, HI from Oct 2012.

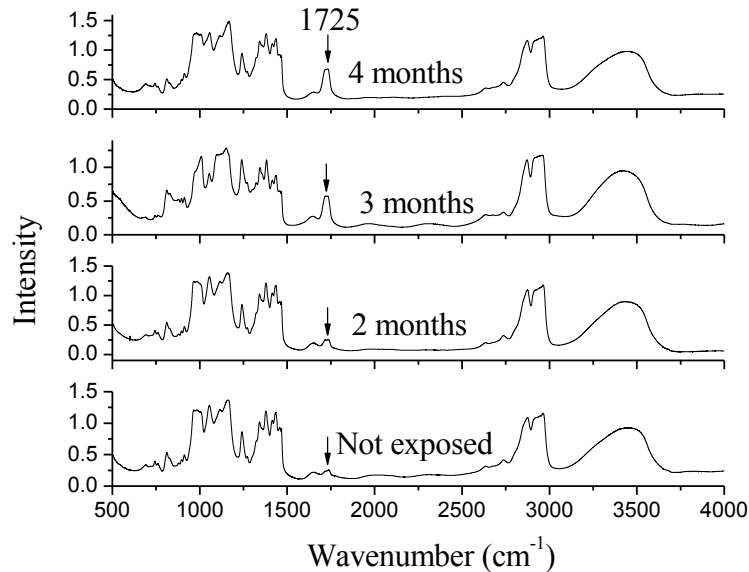


Figure 2.13: PVB IR spectra after 2, 3, 4 months exposures in Lyon Arboretum from July 2011.

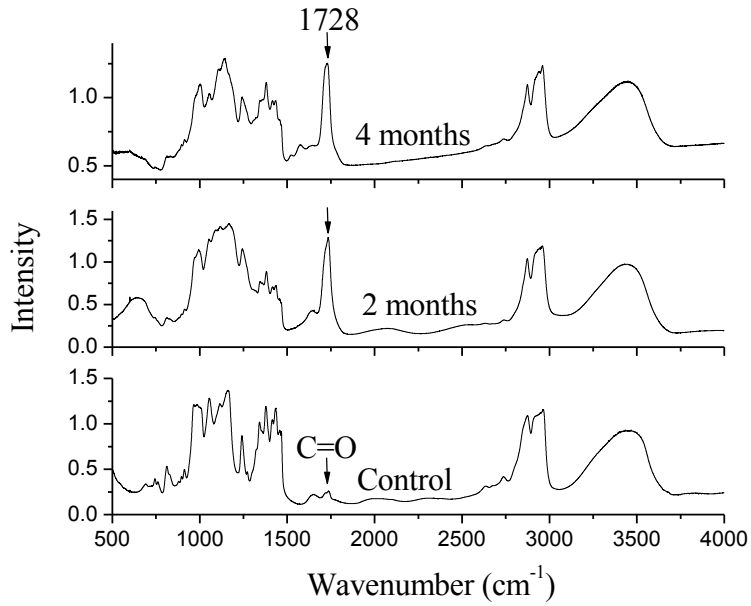


Figure 2.14: PVB IR spectra after 2 and 4 months exposures in Waipahu from July 2011.

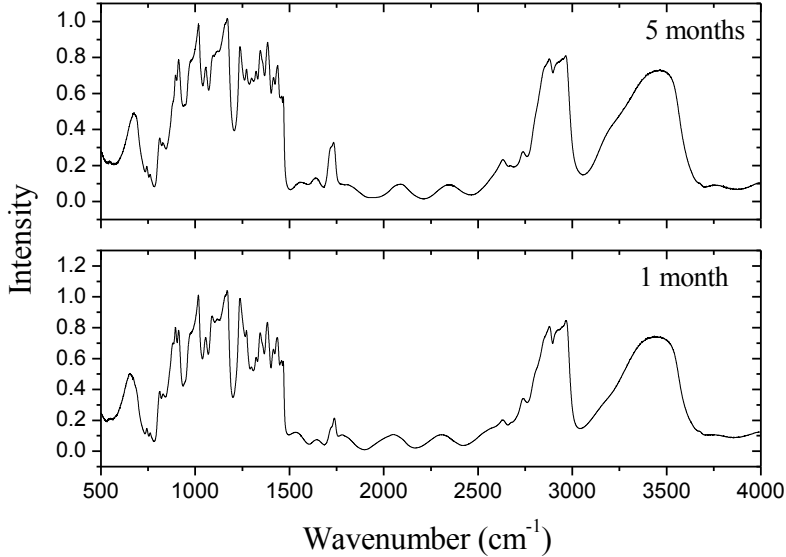


Figure 2.15: PVB IR spectra after 1 and 5 months exposures in Mauna Loa from Oct 2012.

Rural environment: Thompson Farm, NH

Two field exposure campaigns were conducted at Thompson Farm at different times and different exposure angles. The samples exposed from January 2012 were at 45° , while the samples exposed from Oct 2010 were vertical with and without a cover that provided shelter.

The samples looked visually intact after 6 months of exposure. The curves of CD rate after exposure are below the control curves in Figure 2.16 and Figure 2.17, indicating that the polymer/oxide interface stability was improved after short exposure time and this good stability was maintained throughout the 6 months of exposure. The CD rate shifted toward the control curve with exposure time. The polymer/oxide interface stability decayed progressively with exposure time but remained more stable than the polymer/oxide interface of the unexposed sample. IR spectroscopy did not reveal any sign of polymer photo-oxidation during the 6 months of exposure.

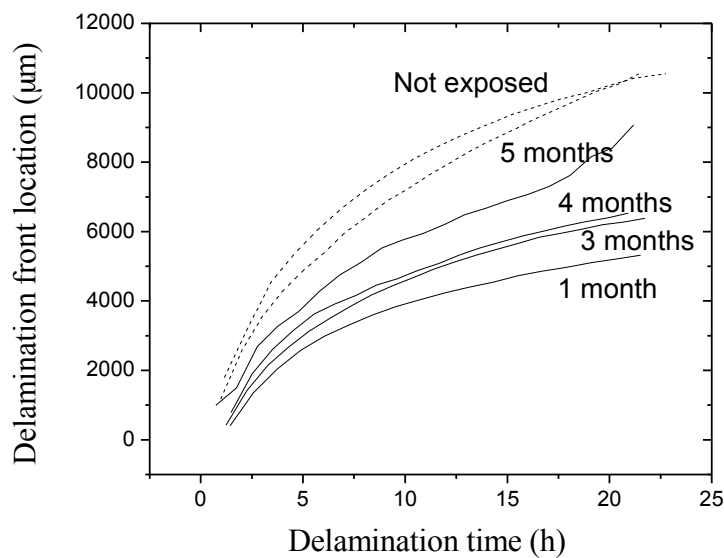


Figure 2.16: PVB coated 1018 CD-SKP after 1, 3, 4, and 5 months of exposure in Thompson farm, NH from Jan 2012.

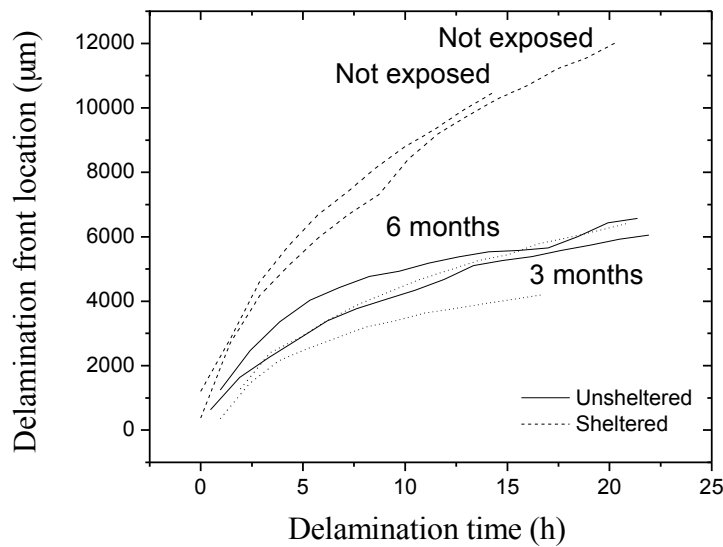


Figure 2.17: PVB coated 1018 CD-SKP after 3 and 6 months of exposure in Thompson farm, NH from Oct 2010.

Suburban environment: Columbus, OH

PVB coated steels and Eponol BLS coated steels were exposed in Columbus. The CD rate of PVB decreased after 1 week of exposure and increased after 2 weeks and 1 month of exposure, as shown in Figure 2.18 and Figure 2.19. The IR spectra of PVB after exposures in Columbus are shown in Figure 2.20. The coating/metal interface degradation occurred before PVB photo-oxidation, which was not detected within the first four months. Figure 2.21 shows that the CD of Eponol BLS was accelerated after exposure. The CD of Eponol BLS was slower than that of PVB by a factor of 170 before exposure and by a factor of 16 after exposure.

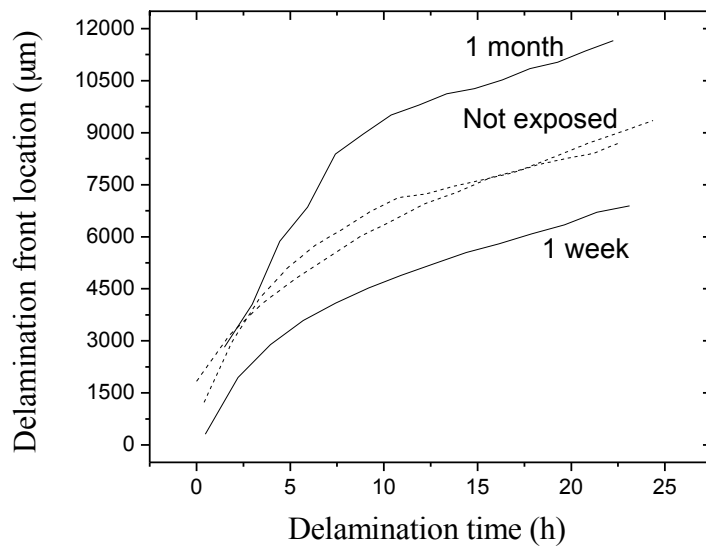


Figure 2.18: PVB coated 1018 CD-SKP after 1 week and 1 months of exposure in Columbus, OH from Aug 2011.

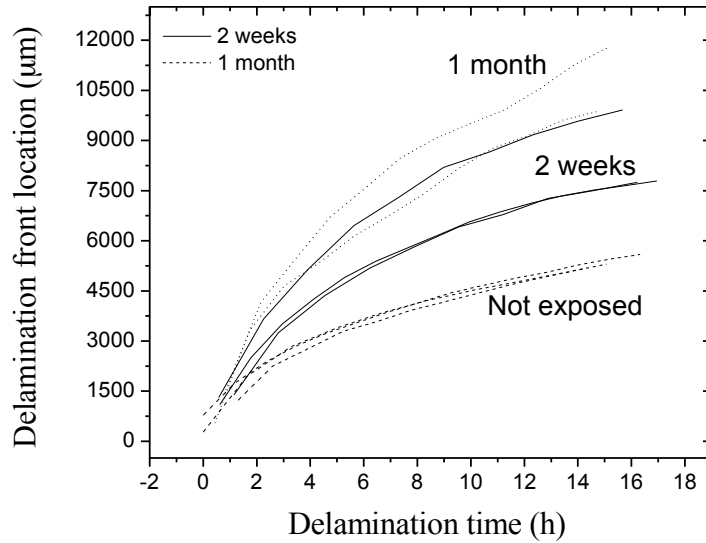


Figure 2.19: PVB coated 1018 CD-SKP after 2 weeks and 1 months of exposure in Columbus from May 2011.

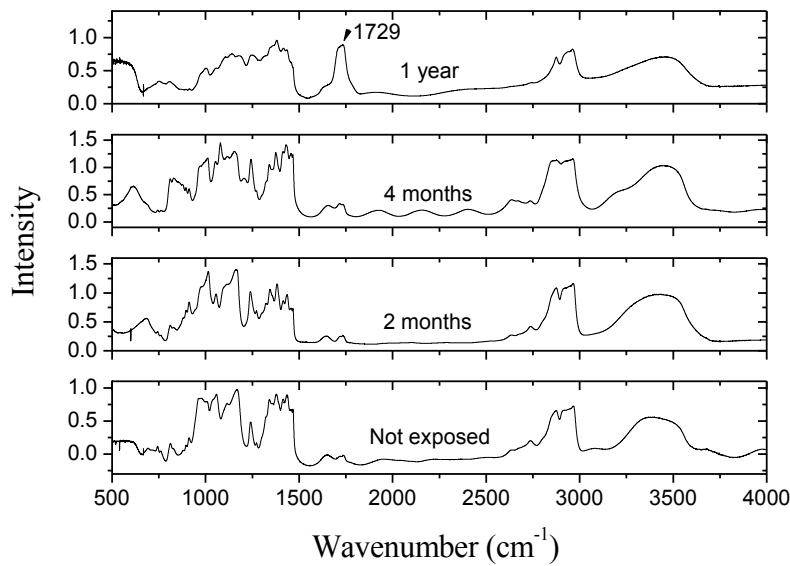


Figure 2.20: PVB IR spectra after 2 months, 4 months and 1 year exposures in Columbus from Aug 2011.

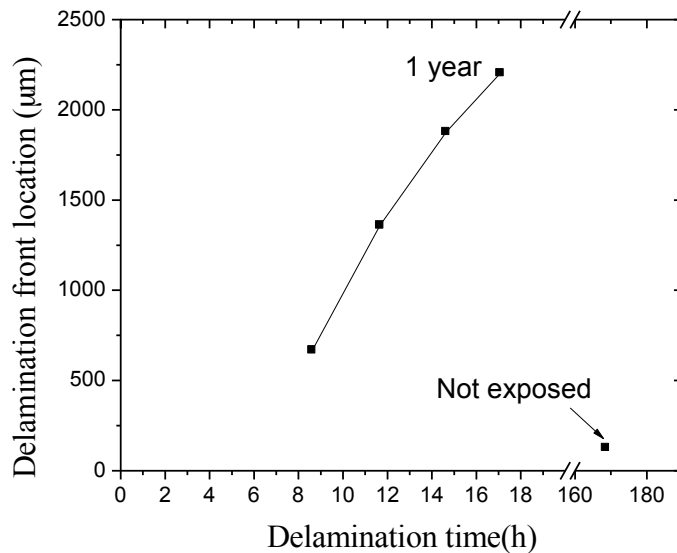


Figure 2.21: Eponol BLS coated 1018 CD-SKP after 1 year exposure in Columbus, OH from Aug 2011

The transparent nature of PVB and Eponol films allow visual assessment of the appearance of corrosion products. However, the CD-SKP method detects coating/metal interface degradation before corrosion products can be seen. The field sites ranked from the visual observations and the CD-SKP analysis are in good agreement. Daytona Beach, Waipahu and Lyon Arboretum are

aggressive environments in comparison with Thompson Farm, which is very mild. Therefore, CD-SKP is an easy and fast technique that can provide early assessment of PVB coating failure. The interface stability of PVB coated steel improved after short field exposure. IR detected carbonyl group increases that are the main product of PVB photo-oxidation. This peak is evident only when it exceeds the background associated with the polymer interference. For this reason, PVB photo-oxidation onset is not easily detected on the IR spectra. Carbonyl increase was observed after the onset of coating/metal interface degradation.

2.6.2 Field exposure of coated steel with artificial defect

It was shown above that the onset of coated steel degradation can be assessed by CD-SKP and IR spectroscopy before visual evidence of the degradation is revealed, which allows for shortening of field or laboratory exposures. In this section, an artificial defect was added to the system to shorten the time for degradation during field exposure. The corrosion mechanisms at the coating/metal interface are of interest. Iron oxides formed under the polymer coating were identified with Raman spectroscopy. The conditions (pH, oxygen and ions) under the coating prior to corrosion product formation were determined.

The Raman spectra of the polymer/metal interface include the peaks associated with both iron oxides and polymer, which overlap on corroded samples. Figure 2.22, Figure 2.23 and Figure 2.24 display the Raman spectra of steel coated with PVB, Eponol, and Eponol BLS, respectively, in the uncorroded condition. Because there was no corrosion, the peaks in these spectra all originated from the polymer coatings and were not considered during the analysis of corroded samples. An average of 20 spectra per sample were taken to characterize PVB coated steel. Fluorescence of Eponol during measurement complicated the analysis of some of the spectra obtained on Eponol and Eponol BLS coated samples and these spectra were therefore not considered further. Only representative spectra from specific areas are shown in this report.

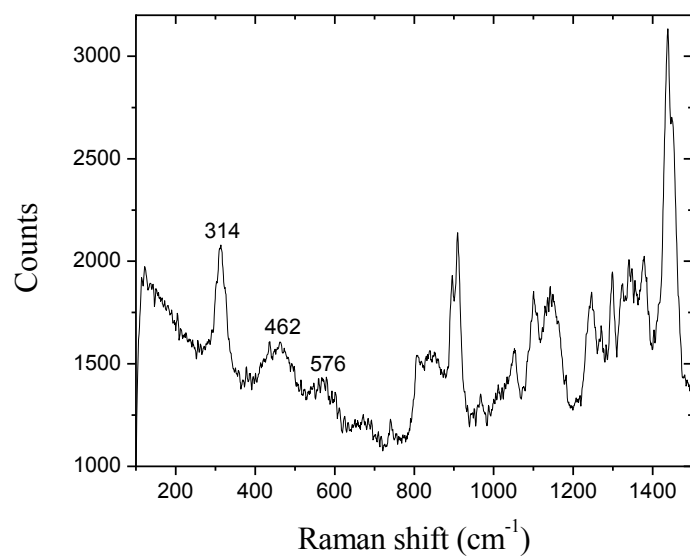


Figure 2.22: Raman spectrum of uncorroded PVB coated steel.

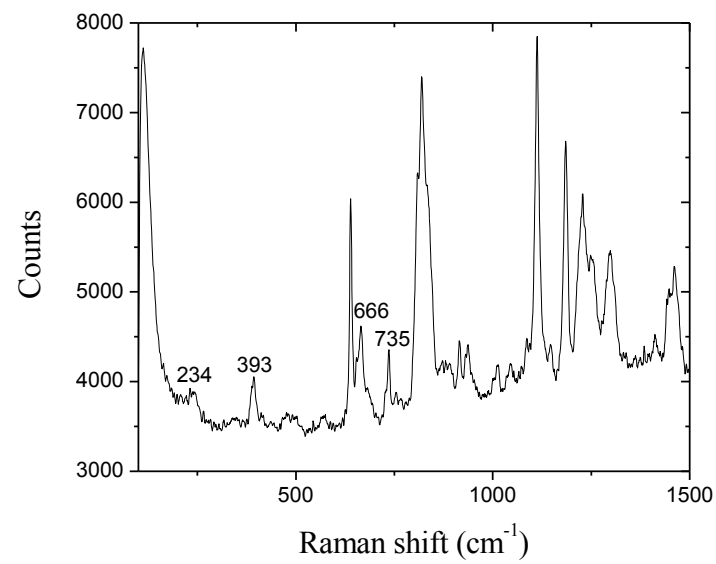


Figure 2.23: Raman spectrum of uncorroded Eponol coated steel.

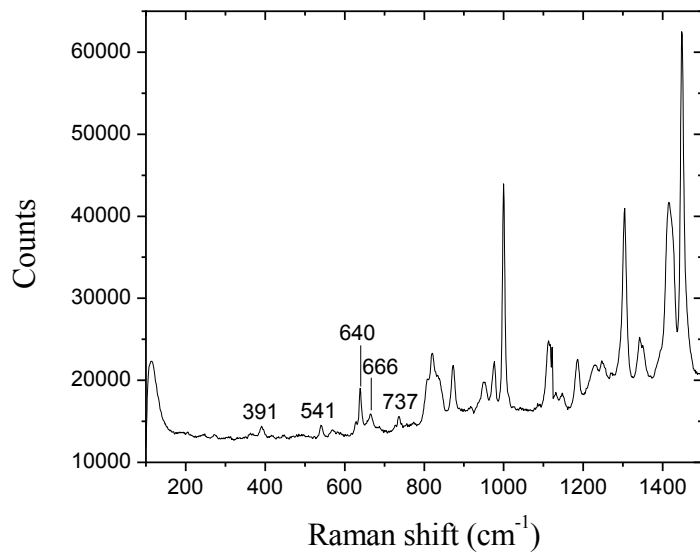


Figure 2.24: Raman spectrum of uncorroded Eponol BLS coated steel.

PVB

Two corrosion morphologies were observed under the optical microscope. The first one is referred to as bead-like corrosion in this report and was formed next to the coating defects (edges and scratches). The second one is referred to as filiform corrosion (FFC) and grew from the bead-like corrosion, not directly from the coating defect. Bead-like corrosion was composed of non-directional round-shaped precipitates with dark color surrounded by a thin uniform corrosion layer with lighter color, as shown in Figure 2.25. Close examination indicates that the FFC filament in Figure 2.26 has the characteristics of an active growing filament: V-shaped neck and head filled with electrolyte. Filaments stay active if the RH is above a critical value (20). If the RH is below this critical value, the salts in the electrolyte precipitate and the filament becomes inactive.

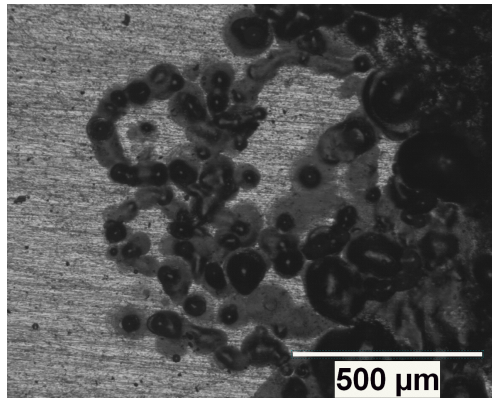


Figure 2.25: Optical picture of bead-like corrosion formed under PVB during 2 months in Waipahu, HI.



Figure 2.26: Optical picture of active filament growing under PVB after 2 weeks exposure in Kilauea Volcano, HI.

The field sites can be classified in three categories from mild to very corrosive, as shown in Figure 2.27, Figure 2.28 and Figure 2.29. Columbus and Campbell Industrial Park can be classified as mild. Most corrosion products on the samples exposed in Columbus for 1 year were formed during the first three months and they grew slowly throughout the rest of the year. The Campbell Industrial Park site is close to the shore and next to a coal power plant so it is unclear why the sample exposed in this site showed limited corrosion products. Key West, Lyon Arboretum, Waipahu and Ewa Nui can be classified as having intermediate corrosivity. The samples exposed in those sites exhibited similar amount of corrosion products, but considerably more than what was found at the mild sites. Kilauea Volcano has the highest chloride (33 mg/m²/day) and sulfate (29 mg/m²/day) deposition rates and the samples exposed in this site were heavily corroded in short periods of time. This site is classified as strongly corrosive.

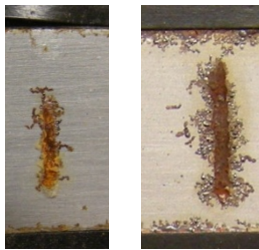


Figure 2.27: Sample photographs of PVB coated steel exposed in Campbell industrial park for 2 months (left) and Columbus for 1 year (right).

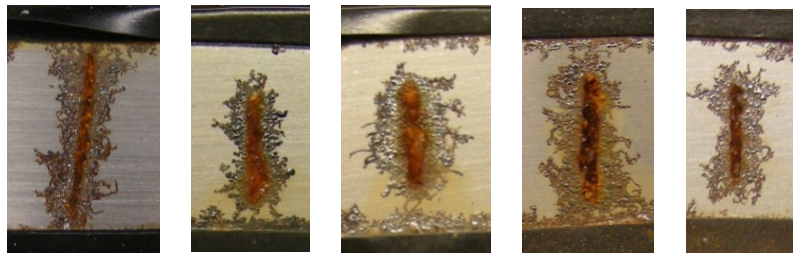


Figure 2.28: From left to right, sample photographs of PVB coated steel exposed in Key West for 3 months, Lyon Arboretum for 1 and 3 months, Waipahu for 2 months and Ewa Nui for 2 months.



Figure 2.29: Sample photographs of PVB coated steel exposed near Kilauea Volcano for 1 month.

PVB Filiform Corrosion

FFC was observed to propagate after removal from the field if the RH in the airtight container was sufficiently high. Corrosion products of the filament heads and the filament tail were measured with Raman spectroscopy. The oxides that constitute the filament were found to be independent of the field site. Akaganeite (β -FeOOH) was found in inactive filament heads, whereas green rust ($3\text{Fe(OH)}_2\text{Fe(OH)}_2\text{Cl}_n\text{H}_2\text{O}$) was found in active filament heads. Representative spectra of akaganeite and green rust with peaks at 431 and 506 cm^{-1} are shown in Figure 2.30 and Figure 2.31, respectively. These spectra agree with Raman spectra reported in the literature for these compounds (21, 22). Akaganeite forms in environments with high chloride concentration (23), and green rust is stable in low oxygen electrolyte above a certain $[\text{Cl}^-]/[\text{OH}^-]$ ratio (24). Several papers have described the blue-green color of the filament head

electrolyte (25). Akaganeite precipitates from chlorine-containing green rust, and the green rusts measured in the filament head are labeled GR1(Cl) (26). The tails of active filaments were composed of amorphous iron oxide, which seems to be ferrihydrite. A representative spectrum is shown in Figure 2.32. Ferrihydrite and feroxyhyte are two amorphous phases that have similar Raman spectra but the position of the peak at 700 cm^{-1} is shifted to high wavenumber for ferrihydrite and to lower wavenumber for feroxyhyte (21). Amorphous phase formation is possible when oxygen is abundant, thereby enabling fast oxidation (27). The conditions of formation of the iron oxides that constitute the filament support the mechanism of FFC. The filament head contains chloride anions where green rust is found and oxygen is present at the back of the filament head where amorphous phase precipitates (28).

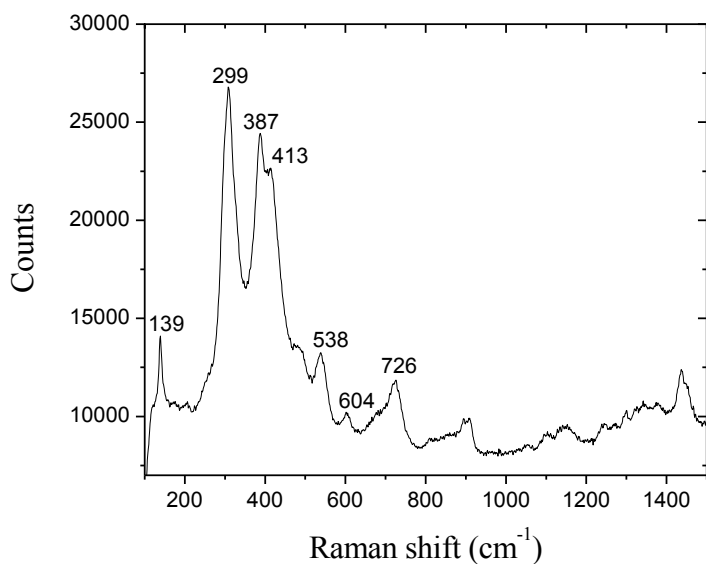


Figure 2.30: Raman spectrum of akaganeite (β -FeOOH) formed in inactive filament heads.

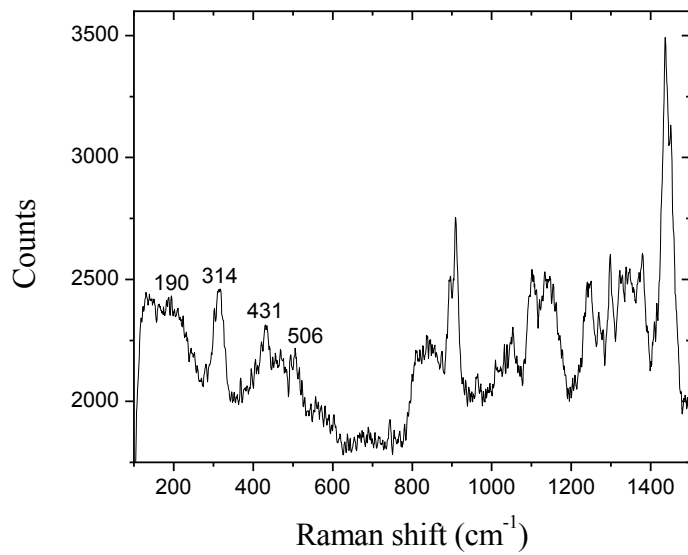


Figure 2.31: Raman spectrum of green rust ($3\text{Fe(OH)}_2\text{Fe(OH)}_2\text{Cl}_n\text{H}_2\text{O}$) formed in active filament heads.

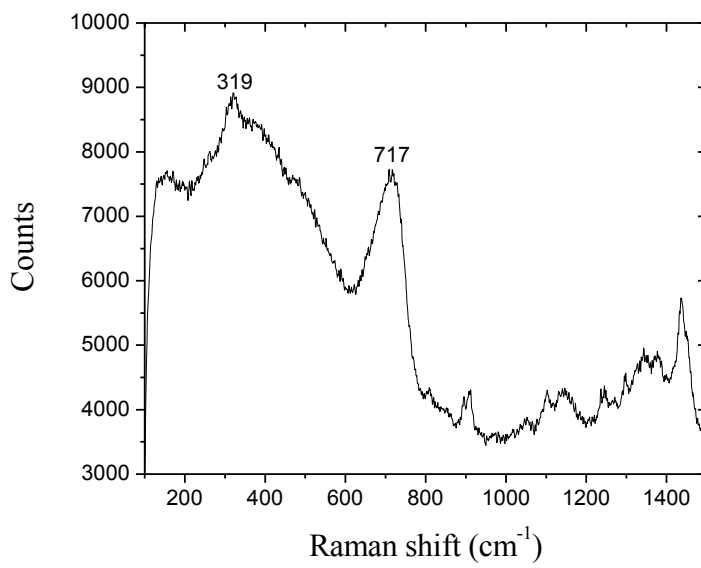


Figure 2.32: Raman spectrum of ferrihydrite ($5\text{Fe}_2\text{O}_3 \cdot 9\text{H}_2\text{O}$) formed in filament tail

Iron oxide formation in the confined electrolyte with limited oxygen access under organic coatings can be investigated using Raman spectroscopy. The crystallization steps from green rust to akaganeite can be isolated in this fashion. Filament head electrolytes at different levels of

precipitation were analyzed. The Raman spectra are ordered in Figure 2.33 to trace the crystallization steps from green rust to akaganeite. An intermediate was isolated with a sharp peak at 147 cm^{-1} in Figure 2.33c. This intermediate is not referenced in the literature because its characteristic peak is below 200 cm^{-1} and most detector filters in Raman spectrometers cut off at 200 cm^{-1} . The peak at 312 cm^{-1} belongs to the polymer. The peak at 189 cm^{-1} seems to belong to green rust because it is found with the two green rust peaks. The peak intensity at 147 cm^{-1} increased as the green rust peaks disappeared and was maximal before the appearance of akaganeite peaks. The peak intensity at 147 cm^{-1} decreased as the akaganeite peaks increased. The formation of this intermediate between green rust and akaganeite was confirmed in the laboratory where akaganeite was synthesized from FeCl_3 and NaOH . Figure 2.34 shows the Raman spectra of green rust, the akaganeite intermediate and akaganeite that were synthesized in the laboratory. The extra peaks of the spectrum b belong to the paper filter used to filter the solution.

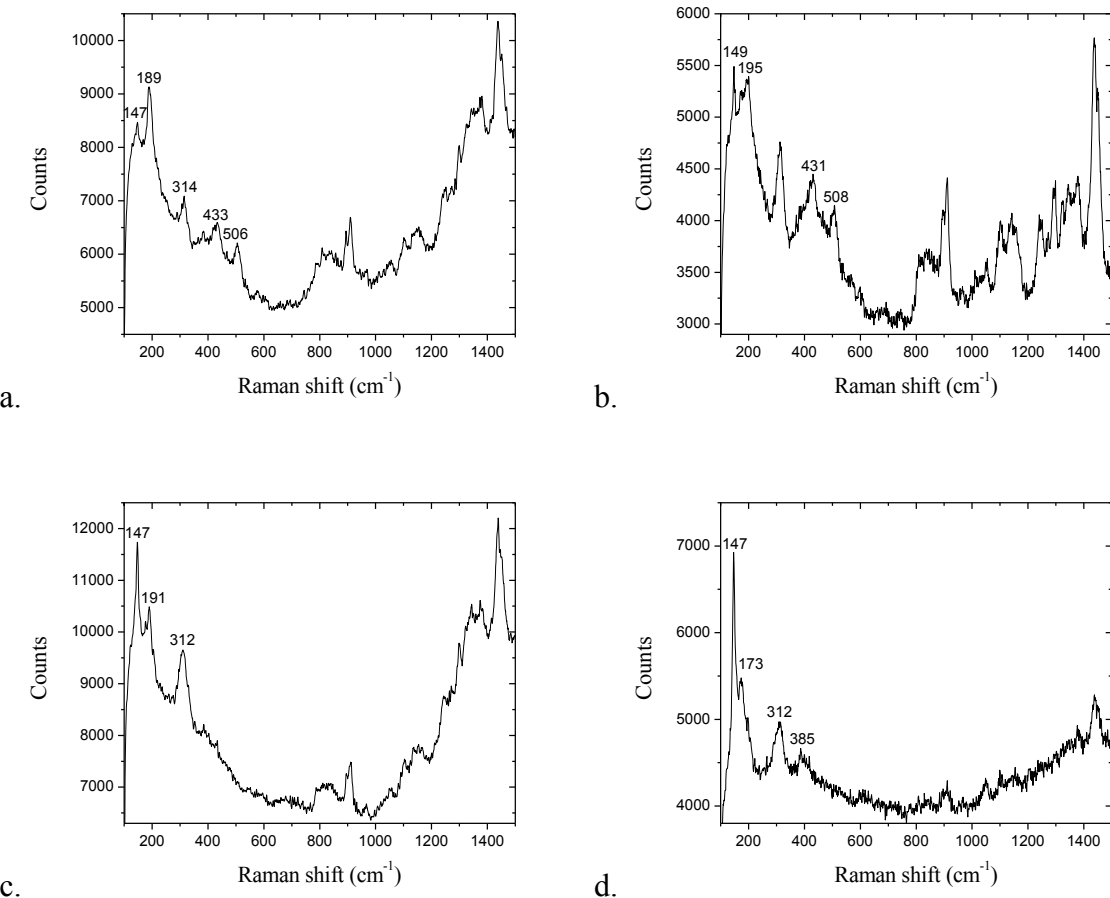


Figure 2.33: Raman spectra of akaganeite intermediates formed in drying filament heads. a and b: Green rust, c and d: akaganeite intermediate

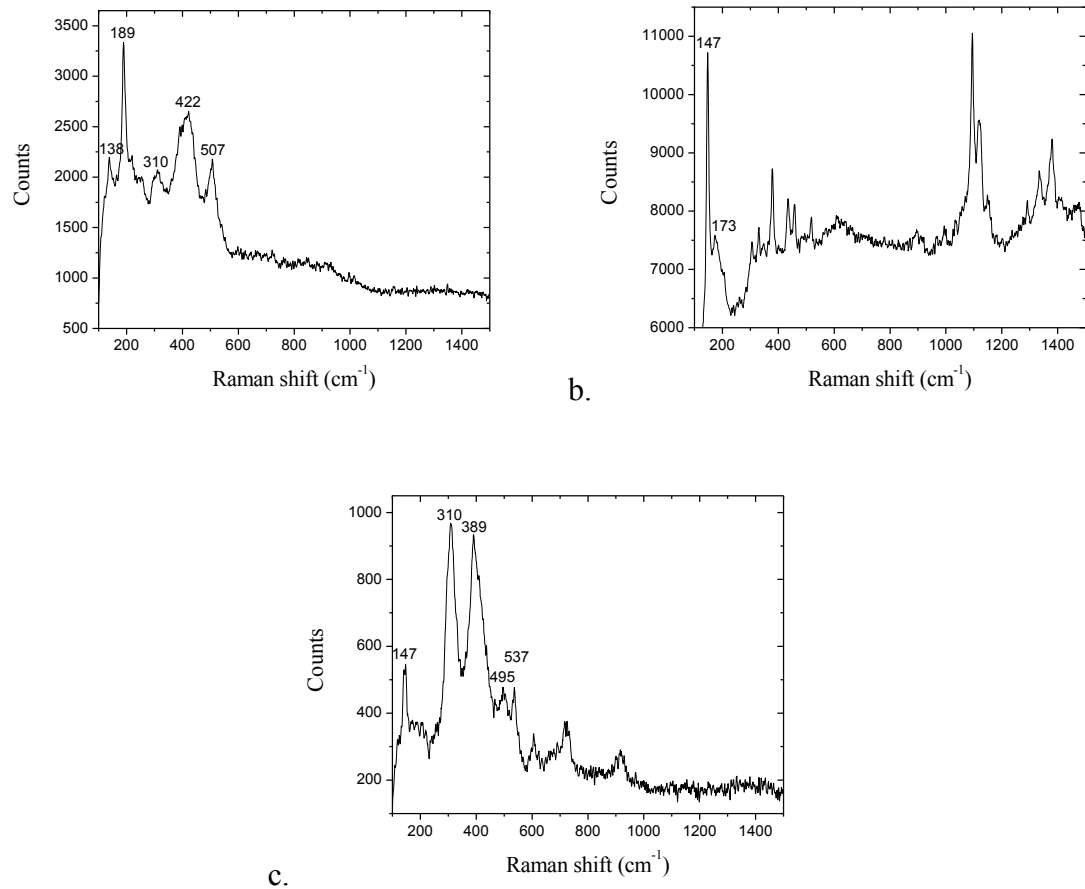


Figure 2.34: Raman spectra of akaganeite synthesized from FeCl_2 and NaOH . a: green rust, b: Intermediate and c: akaganeite

PVB Bead-like corrosion

Bead-like corrosion was composed of pure crystalline, crystalline mixture and amorphous phases. The pure crystalline phases were found in the bead centers or in local spots between two beads; their exact natures were field site specific. A mixture of amorphous and crystalline phases was found in the bead edge and in the uniform matrix surrounding the beads. Those phases were not field site specific and are shown in Figure 2.38, Figure 2.39 and Figure 2.40. Figure 2.39 and Figure 2.40 differentiate two types of amorphous iron oxides. Figure 2.38 shows the Raman spectrum of a mixture of goethite and lepidocrocite. The intense peak at 250 cm^{-1} is characteristic of lepidocrocite and the intense peak at 384 cm^{-1} is characteristic of goethite (29). Akaganeite is the most common pure crystalline phase found. Akaganeite shown in Figure 2.35 was found in Campbell Industrial Park, Key West, Waipahu, Columbus and Ewa Nui. Akaganeite was not found in the bead-like corrosion of the samples exposed in Lyon Arboretum and Kilauea Volcano. Magnetite and goethite were formed respectively in Lyon Arboretum and in Kilauea Volcano instead of akaganeite. A representative spectrum of magnetite formed in

Lyon Arboretum is shown in Figure 2.37 and a representative spectrum of goethite formed in Kilauea Volcano is shown in Figure 2.36.

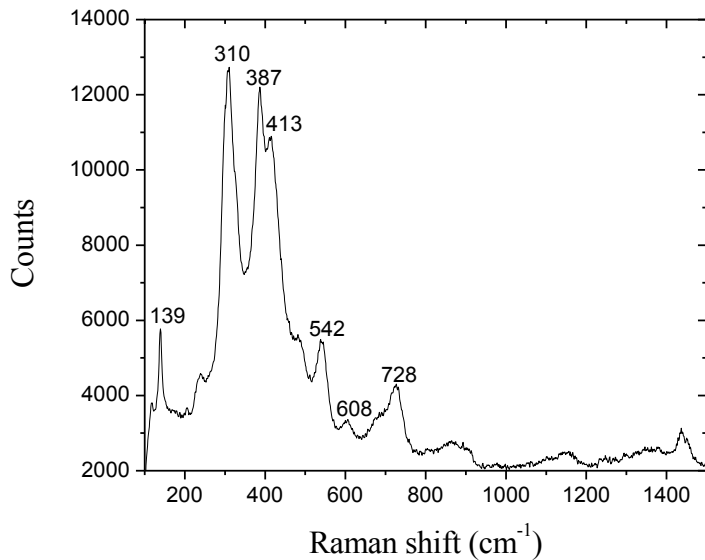


Figure 2.35: Raman spectrum of akaganeite (β -FeOOH) formed in bead-like corrosion in Waipahu, Campbell, Ewa Nui, Columbus and Key West.

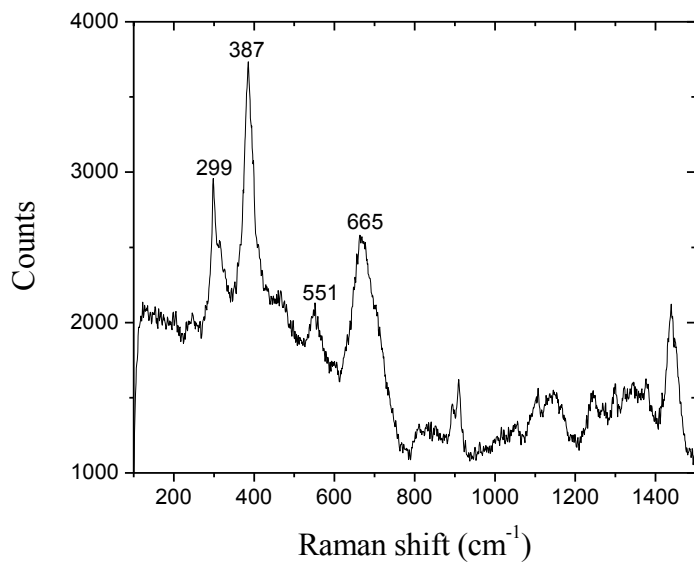


Figure 2.36: Raman spectrum of goethite (a-FeOOH) formed in bead-like corrosion in Kilauea Volcano.

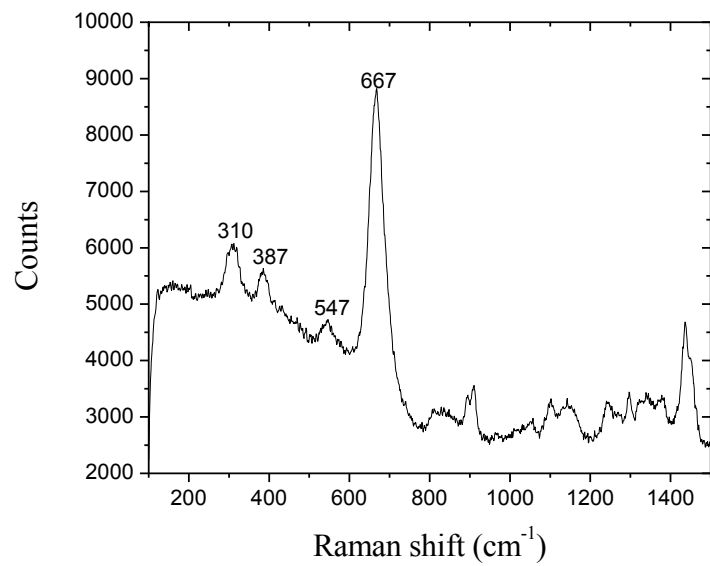


Figure 2.37: Raman spectrum of magnetite (Fe_3O_4) formed in bead-like corrosion in Lyon Arboretum.

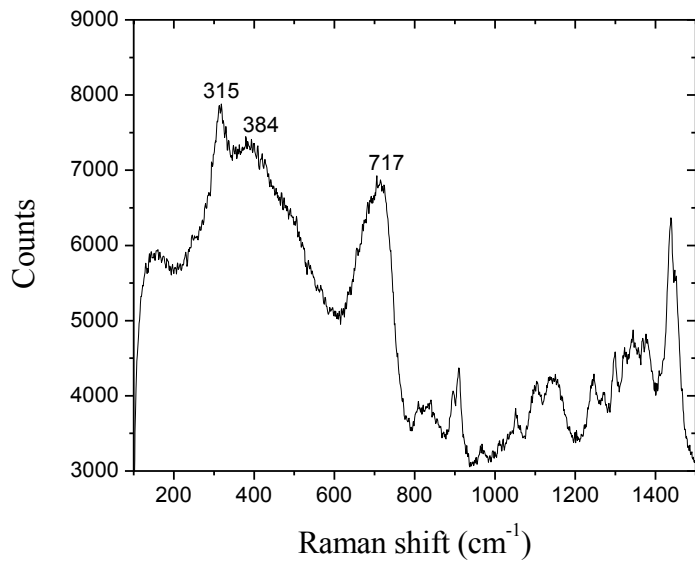


Figure 2.38: Raman spectrum of amorphous formed in bead-like corrosion at all sites tested.

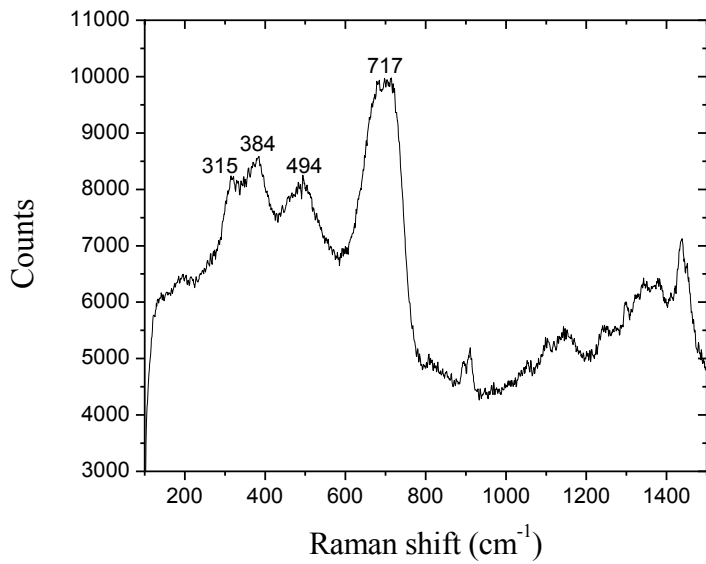


Figure 2.39: Raman spectrum of amorphous formed in bead-like corrosion at all sites tested.

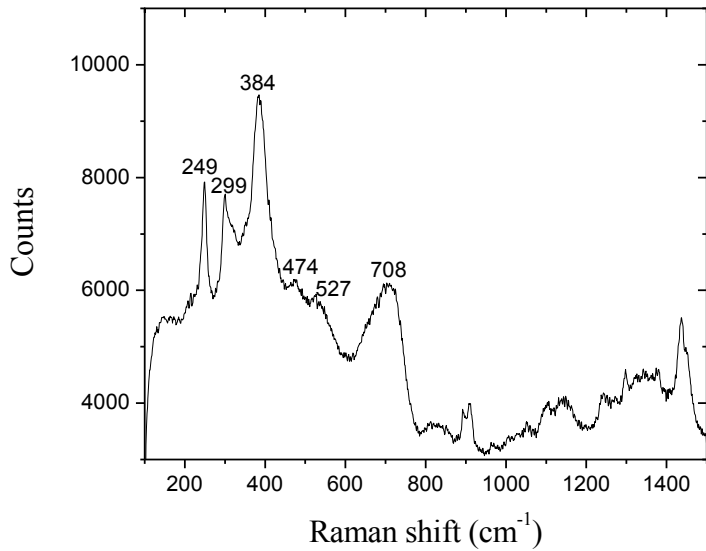


Figure 2.40: Raman spectrum of lepidocrocite and goethite mixture formed in bead-like corrosion at all sites tested.

Eponol

For Eponol-coated steel, corrosion formed next to the artificial defect and randomly under the coating. As above, the field sites were ranked qualitatively from mild to very corrosive and the ranking was the same as for PVB. As shown in Figure 2.41, Campbell Industrial Park was the

least corrosive site with no random corrosion and Kilauea Volcano was the most corrosive site. Figure 2.42 shows the corresponding higher magnification optical photographs. FFC under Eponol appeared different than under PVB. The filament widths were not uniform and the filaments were branched. The oxide film also appeared to be thinner. Raman spectra were collected for Eponol coated steel and representative spectra are gathered in Figure 2.43. The iron oxides formed under Eponol seem to be similar to those formed under PVB. Akaganeite was found in all sites at local spots and in filament heads. One akaganeite intermediate was found in a filament head. Goethite was found in most sites and lepidocrocite is only found in Lyon Arboretum.



Figure 2.41: From left to right, sample photographs of Eponol coated steel exposed 2 months in Campbell Industrial Park, 1 month in Lyon Arboretum, 2 months in Waipahu and 2 weeks Kilauea Volcano.

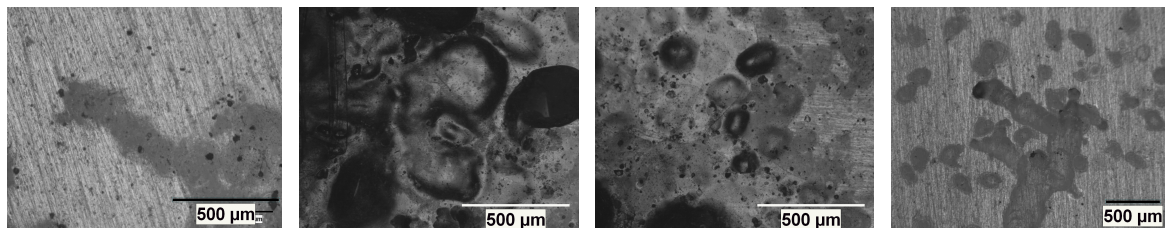
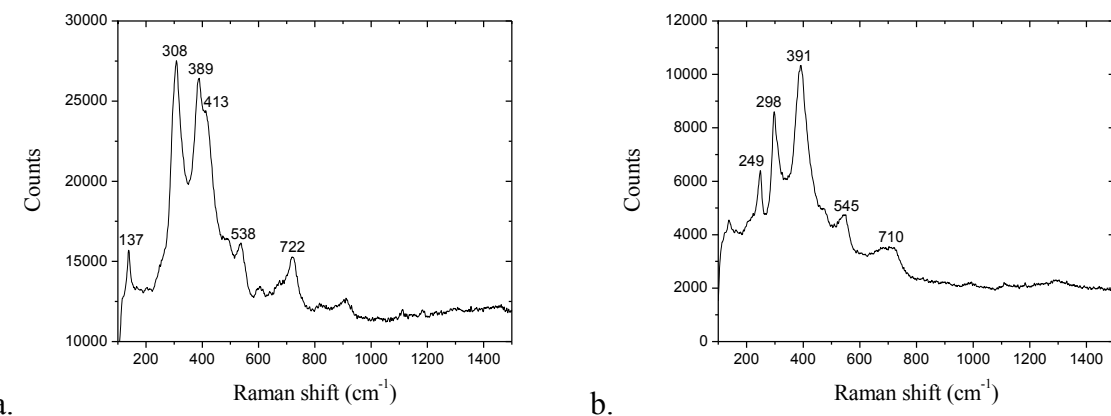


Figure 2.42: From left to right, sample optical photographs of Eponol coated steel exposed 2 months in Campbell Industrial Park, 1 month in Lyon Arboretum, 2 months in Waipahu and 2 weeks Kilauea Volcano.



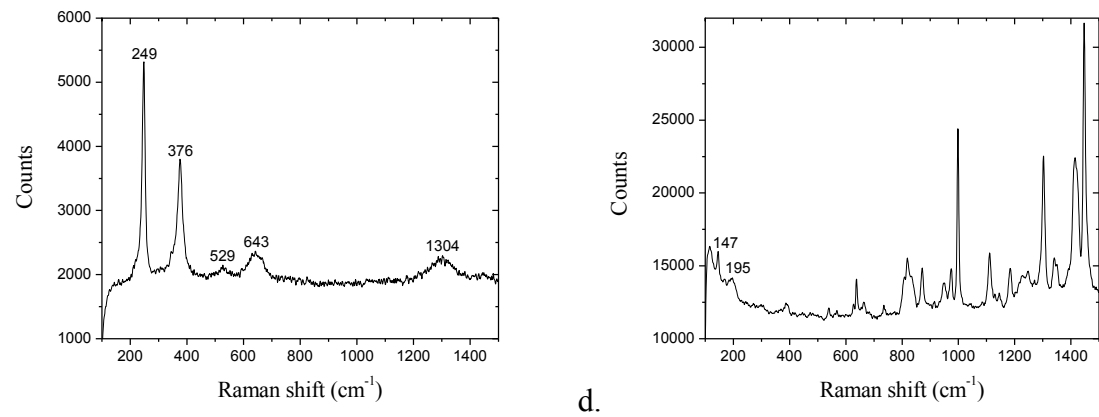


Figure 2.43: Eponol or Eponol BLS coated 1018 Raman spectra. Spectrum a: Akaganeite; spectrum b: Goethite; spectrum c: Lepidocrocite (Lyon Arboretum); spectrum d: Akaganeite intermediate (filament head).

2.6.3 Field exposures discussion

2.6.3.1 Field sites

Coated steels without and with an artificial defect were exposed in New Hampshire, Ohio, Florida and Hawaii. The coating transparency revealed the appearance of rust under the coating. In addition, the interface degradation was assessed with SKP-CD and the rust formation was investigated with Raman spectroscopy. The polymer bulk degradation was assessed with IR spectroscopy. The field sites were ranked above according to their corrosivity to the system. ISO 9223 classifies field sites corrosivity into categories that are calculated from the time of wetness (TOW), the sulfur dioxide and the airborne chloride deposition rate [x]. This standard defines the TOW as the number of hours where $\text{RH} \geq 80\%$ and $T > 0^\circ\text{C}$. It is assumed that those conditions enable the formation of thin electrolyte film on metallic surface that leads to corrosion. With the development of TOW sensors, it was demonstrated at multiple occasions that corrosion takes place below $\text{RH}: 80\%$ and $T < 0^\circ\text{C}$ (30). A certain number of meteorological and atmospheric data for the various field sites investigated were available and those data are discussed below in relation to the field site ranking shown above.

To line up with ISO 9223, the RH, the temperature, the sulfur dioxide and the airborne chloride are discussed below. The two latter parameters were not available for all field sites. The TOW values were calculated according to ISO 9223 from the RH and temperature data. Those data were available by the hour or minute. To complete the discussion on the TOW effect, some TOW measurements from galvanic sensors were added to the discussion. Ozone concentration data are also mentioned to study its potential effect on coated steel. Ozone is involved in several atmospheric oxidation reactions. For instance, it enhances the oxidation of sulfur by producing

radical OH (31). Therefore, ozone may have a direct or an indirect effect on coated steel. Airborne deposition transport to the sample is of two natures that are referred to as wet and dry deposition (32). In the case of wet deposition, the pollutants are dissolved in clouds, rain, fog or snow before reaching the samples. Further reactions take place after pollutant dissolution in droplets (32). Acid rains are a common example of wet deposition. Precipitation is a direct form of wetting. The wet deposition rate is often simplified by λC where C is the pollutant concentration and λ is the washout coefficient, which is proportional to the precipitation intensity (33). Dry deposition causes indirect metallic surface wetting by lowering the deliquescence point. Dry deposition flux is described as $V_g[S]_z$ where V_g is the deposition velocity and $[S]_z$ is the species concentration at a specific altitude z . Several deposition velocities specific of a species and a surface nature are reported in the literature (34). Meteorology and diurnal variation affect the deposition velocity measurement as well (35). Some forms of precipitation such as rain tend to wash out dry deposition (36). Precipitation and some sulfate and chloride deposition data were added to the discussion. UV radiation plays a role in the interface improvement mentioned above and also in coating degradation. Solar radiation intensities as a function of wavelength are discussed below.

The correlation of the meteorological and atmospheric data with the field site aggressiveness ranking is discussed in three types of tables. The first type of Table 2 and Table 3 include the temperature, the ISO 9223 TOW and the galvanic sensors TOW. The galvanic sensor measures a coupling voltage when the water film bridges the electrode gap. Dry deposition that causes deliquescence depends on surface nature. Therefore, the TOW depends on the sensor used. The hydrophobic nature of a coating in contrast with metal strongly affects the TOW. The species reactivity with the surface and the solubility lowers the surface resistance of the dry deposition velocity (37, 38). On the other hand, ISO 9323 TOW is not surface specific because it only depends on the RH and temperature. The second type of table (Table 4 and Table 5) includes precipitation intensities, the ozone and dioxide sulfate concentrations, sulfate and chloride airborne concentration and sulfate and chloride depositions. Precipitation is an important factor to consider with atmospheric data because it carries atmospheric pollutants and washes out dry depositions. The third type of table (Table 6) includes the temperature and the UV radiation. These parameters are relevant to coating aging (39). The tables divide the analysis of the coated steel without artificial defect from the coated steel with artificial defect. The routes of degradation are different in those two cases and the degradation assessment approach was also different. Each sample was exposed for different time periods, so to help the comparison, the first month, the first two months and the first four months of exposure are considered.

The field site ranking from least to most aggressive is summarized below. Recall that the interface degradation of coated steel without an artificial defect was determined from visual and CD-SKP assessments and the interface degradation of coated steel with an artificial defect was determined from visual assessment. The polymer degradation of the coated steel without artificial defect was investigated with IR spectroscopy.

Interface degradation of coated steel without defect:

- Thompson, NH << Columbus, OH < Mauna Loa, HI << Lyon Arboretum, HI < Waipahu, HI

Interface degradation ranking of coated steel with defect:

- Campbell, HI = Columbus, OH << Lyon, HI = Waipahu, HI = Key West, FL = Ewa Nui, HI << Kilauea, HI

Polymer degradation of coated steel without artificial defect:

- Thompson, NH < Columbus, OH << Lyon Arboretum, HI = Mauna Loa, HI < Waipahu, HI

TOW:

Table 2 and Table 3, the fourth column reports the TOW in hours per period according to the ISO 9223 definition ($RH \geq 80\%$, $T < 0^\circ C$). The conventional TOW unit reported in the ISO 9223 are hours per year. Only the first month of exposure was considered so the TOW is the number of hours where the condition ($RH \geq 80\%$, $T < 0^\circ C$) is met during the time period. The time period is mentioned in the second column of the table. This TOW is referred to as TOW(ISO) in the discussion. The last column report the average TOW in mV measured in the Hawaiian field sites. The sensor faced up maximum and minimum values of 25 mV and 0 mV, respectively. This TOW is referred to as TOW(Sensor) in the text.

As shown in Table 2, samples exposed in Thompson Farm and in Columbus did not show any sign of polymer degradation so their interface degradation can be compared. Both sites exhibited similar TOW(ISO). The samples were exposed in Columbus and in Thompson Farm at different seasons, which may partially explain the faster interface degradation in Columbus. Samples exposed in Mauna Loa, Lyon Arboretum and Waipahu exhibited polymer degradation as well as interface degradation. The lower temperature and TOW(ISO) in Mauna Loa during the first exposure month may explain the slower interface degradation. The climate in Lyon Arboretum is very humid in contrast with Waipahu, which has a dry climate. The month of January 2012 was an exceptionally humid month for Waipahu. The TOW(Sensor) recorded a higher value but a smaller value of TOW(ISO) for Waipahu in comparison with Lyon Arboretum. The sensor surface in Waipahu likely contained impurities that lowered the deliquescence point. Waipahu received more airborne chloride than Lyon Arboretum and less frequent rain that washed out dry deposition as shown in Table 4.

Table 2: TOWs of the first month of exposure of PVB coated steel without artificial defect (40-43).

Sites	Period (MM/YY)	Temp. (°C)	RH \geq 80%; T $<$ 0°C (h/period)	TOW (mV)
Thompson Farm, NH	10/10	10 \pm 5	274	
Thompson Farm, NH	03/12	6 \pm 8	171	
Columbus, OH	05/11	19	372	
Columbus, OH	08/11	25	222	
Mauna Loa observatory, Hi	10/12	9 \pm 3	116	
Lyon arboretum, HI	01/12	21 \pm 2	488	5.7
Waipahu, HI	01/12	23 \pm 3	159	11.4

Among the field sites of the Oahu Island in Hawaii, Campbell is the only one that shows practically no corrosion propagation under the coating from the artificial scratch after 2 months of exposure, Table 3. This site is situated in the plume of a coal power plant and approximately 1 km from the shore. The TOW(ISO) indicated that only 2 hours during 2 months of exposure exceeded 80% RH. In this case, this meteorological parameters explain the slow interface degradation. The samples exposed at Kilauea volcano exhibited excessive corrosion propagation compared to the other sites even though it was only exposed for 1 month. The TOW(ISO) or the TOW(Sensor) do not reflect this fast corrosion propagation. The ranking of the other field sites cannot be explained by TOW comparison as well. For instance, Lyon Arboretum and Waipahu exhibited a similar amount of corrosion even though the humidity was higher at Lyon Arboretum. Kilauea Volcano TOW(Sensor) was lower than Ewa Nui TOW(Sensor) even though the TOW(ISO) is higher. This means that the wettability or the deliquescence point was higher on the sensor exposed to Ewa Nui. The chloride deposition was higher at Kilauea than at Ewa Nui as shown in Table 5. Therefore, the chloride deposition cannot explain the lower wettability of the sensor surface exposed at Kilauea. The rain intensity was higher at Kilauea and the temperature was lower. These two meteorological parameters can explain the TOW(Sensor)

measured. The different pollutant composition at Ewa Nui and at Kilauea volcano influenced the wettability but the atmospheric data are not sufficient to make more conclusions on the details.

Table 3: TOWs of the first two months of exposure of PVB or Eponol coated steel with artificial defect (42, 43).

Sites	Period (MM/YY)	Temp. (°C)	RH \geq 80% (h/period)	TOW (mV)
Columbus, OH	07/12-08/12	26	271	
Key West, FL	05/12-06/12	28	358	
Lyon arboretum, HI	09/12-10/12	22±2	1139	15.3
Waipahu, HI	09/12-10/12	25±2	116	4.3
Ewa Nui, HI	09/12-10/12	25±2	125	9.4
Campbell industrial park, HI	07/12-08/12	26±2	2	2.0
Kilauea Volcano, HI	07/12	20±2	391	7.1

In Table 4 and Table 5, precipitation and atmospheric data are summarized. Ozone and sulfur dioxide are measured in ppm from UV photometric gas analyzers and pulsed fluorescence sulfur dioxide analyzers, respectively. Total daily sulfate and chloride ions from wet candles in mg/m² and from aerosol in ppt are reported in the table.

As shown in Table 4, the ozone concentration averages did not dramatically change from one place to another so this parameter cannot explain field site ranking. Only sulfur dioxide and sulfate ion are available at the Thompson Farm. The field site ranking in Hawaii can be explained through the daily chloride deposition measurement. Higher chloride deposition resulted in increased interface degradation. At Waipahu, the chloride deposition increased as the precipitation intensity decreased. Therefore, the pollutant deposition depends on the frequency and intensity of rain events.

Table 4: Precipitation, atmospheric data of the first month of exposure of PVB coated steel without artificial defect (40, 41, 44, 45).

Sites	Period (MM/YY)	Total monthly precip. (mm)	[O ₃] (ppb)	[SO ₂](ppb)	Total daily [SO ₄ ⁻] (mg/m ²)	Total daily [Cl ⁻] (mg/m ²)
Thompson Farm, NH	10/10	112.6	Max: 47.2 ⁽¹⁾ Mean: 23±8 ⁽¹⁾	Max: 5.7 ⁽¹⁾ Mean: 0.3±0.4 ⁽¹⁾	1999-2007 Aerosol 583 pptv ⁽⁴⁾	1999-2007 Aerosol 177 pptv ⁽⁴⁾
Thompson Farm, NH	03/12	62.5	Max: 64.9 ⁽¹⁾ Mean: 37±10 ⁽¹⁾	Max: 4.4 ⁽¹⁾ Mean: 0.4±0.5 ⁽¹⁾		
Columbus, OH	05/11	150	Max:61 ⁽²⁾⁽³⁾ Mean: 43±11 ⁽²⁾⁽³⁾			
Columbus, OH	08/11	63	Max:66 ⁽²⁾⁽³⁾ Mean: 49±10 ⁽²⁾⁽³⁾			
Columbus, OH	05/11	150	Max:61 ⁽²⁾⁽³⁾ Mean: 43±11 ⁽²⁾⁽³⁾			
Lyon arboretum, HI	07/11	199.6				1.9 ⁽⁵⁾
Lyon arboretum, HI	01/12	29.2				1.6
Waipahu, HI	07/11	14.2				7.0
Waipahu, HI	01/12	8.9				12.1
Mauna Loa observatory, HI	10/12	19	Max:60 ⁽¹⁾ Mean: 32±11			0.045

⁽¹⁾ Hourly average

⁽²⁾ Daily average (Max daily 8h)

⁽³⁾ 6 miles away from location

⁽⁴⁾ Daily average

⁽⁵⁾ Value not available so average of the 4 previous year of the same months

In Table 5, the chloride concentration is seen to increase with precipitation intensity when considering Lyon Arboretum, Waipahu, Ewa Nui and Campbell. The three latter locations are within a 5 miles radius of each other. The corrosion propagation under the coating after 2 months exposure were similar on the samples exposed to these locations except for Campbell.

Even though Campbell received the most chloride deposition, the corrosion did not progress under the coating because of the particular low TOW(ISO) and rain events within the 2 months of exposure. Kilauea Volcano received the highest depositions of sulfate and chloride and triggered the most corrosion underneath the coating. The deposition velocity on the wet candles can be calculated from the sulfur dioxide and the sulfate deposition flux.

Table 5: Precipitation, atmospheric data of the first two months of exposure of PVB or Eponol coated steel without artificial defect (42, 44).

Sites	Period (MM/YY)	Total monthly precip. (mm)	Average [O ₃] (ppb)	Average [SO ₂] (ppb)	Total daily [SO ₄ ²⁻] (mg/m ²)	Total daily [Cl ⁻] (mg/m ²)
Columbus, OH	07/12-08/12	55±13	Max: 85 ⁽¹⁾⁽²⁾ Mean: 58±14 ⁽¹⁾⁽²⁾			
Key West, FL	05/12-06/12	189±70				
Lyon arboretum, HI	09/12-10/12	193				1.2
Waipahu, HI	09/12-10/12	10				8.4
Ewa Nui, HI	09/12-10/12	8				10.6
Campbell industrial park, HI	07/12-08/12	5		Max: 2.8 ⁽³⁾⁽⁴⁾ Mean: 1.9±0.3 ⁽³⁾⁽⁴⁾	8.7	13.8
Kilauea Volcano, HI	07/12	15.2		Max: 1172 ⁽³⁾⁽⁵⁾ Mean: 55±215 ⁽³⁾⁽⁵⁾	37	24.4

⁽¹⁾Daily average (Max daily 8h)

⁽²⁾ 6 miles away from location

⁽³⁾ Daily average (Max daily 1h)

⁽⁴⁾ 2.8 miles away from location

⁽⁵⁾ 15 miles away in the Volcanic National Park

In Table 6, the total radiation in MJ/m² and the average radiation in Watt/m² are reported. The wavelength range depends on the sensitivity of the UV sensor. The polymer photo-oxidation was faster at Waipahu than at Lyon Arboretum because the solar intensities and temperature were

higher at Waipahu. The solar radiation, the temperature and the ozone concentration were higher at Columbus during the exposure time than at Mauna Loa. Therefore, the slower polymer photo-oxidation at Columbus cannot be explained with those parameters. The elevation at Columbus is 244 m above sea level while the elevation at Mauna Loa is 3389 m. Therefore, it can be assumed that the UV intensity is higher at Mauna Loa. The polymer photo-oxidation was slower at Thompson Farm for the exposure time period than at Columbus because the solar intensity and temperature were higher at Columbus. The elevation at Thompson Farm elevation was also slightly lower (40m) than at Columbus.

Table 6: UV radiation of the first fourth month of exposure of PVB coated steel without artificial defect (45).

Sites	Period (MM/YY)	Temp. (°C)	Total (0.400-1.100 μ m) (MJ/m ²)	(0.400-0.700 μ m) (W/m ²)	UV radiation (0.295-0.385 μ m) (W/m ²)
Thompson Farm, NH	10/10-01/11	2±8	594		
Columbus, OH	05/11-08/11	28	2790 ⁽¹⁾		
Lyon arboretum, HI	07/11-10/11	22±1		83.6	4.2
Waipahu, HI	07/11-10/11	25±2		219.6	14.7
Mauna Loa observatory, HI	10/12-01/13	7±7	2351		

⁽¹⁾ 70 miles away from location

2.6.3.2 Degradation mechanisms

Assessments were made of the interface and polymer degradation of field exposed coated steel with and without artificial defect. Interface and polymer degradation of coated steel without artificial defect were assessed with CD-SKP and reflective IR spectroscopy, respectively. Corrosion product and morphology formed at the polymer/metal were investigated with optical microscopy and Raman spectroscopy.

Coated steel exhibited interface improvement after few days in the field, which did not take place in the desiccator. The coating lifetime was elongated by this improvement so it should be taken into account in the coating failure prediction. UV and humidity, which were not present in the desiccator, may be responsible for this interface improvement. Short laboratory exposures with

UV and humidity were performed to understand their effects, and these results are presented in the next section.

Polymer/metal interface degraded with time before polymer photo-oxidation was detectable. The interface degraded during Thompson farm and Columbus exposures while no polymer photo-oxidation took place. The interface degraded during Mauna Loa exposure as the polymer underwent photo-oxidation. PVB photo-oxidation increases the content of carbonyl, which forms after ring opening of the 1,3 dioxane. The reflective IR spectroscopy probes the entire coating thickness. Therefore, it cannot be determined if the polymer photo-oxidation took place exclusively at the polymer surface or throughout the entire film. Polymer photo-oxidation affects the polymer properties such as wettability and water solubility (46, 47), which may influence the mechanism of interface degradation. In the absence of polymer photo-oxidation, the interface degradation may result from salt migration or water trapped at the interface. After several wet/dry cycles, it was observed that the potential of the buried interface was not reversible so the interface could not completely recover (9).

After field exposure, the corrosion morphology under PVB close to the scratch or the coating edge was described above as bead-like corrosion. FFC having heads with V-shaped boundaries grew from bead-like corrosion. FFC under Eponol looked different than under PVB. Under Eponol, the boundary separating the head from the tail was a straight line rather than V-shaped. Filament shapes were previously compared under 300 and 150 nm thick epoxy coating coated on 1045 steel (48). The authors reported that the filaments were shaped as a “string of beads” under the thinner coating (150 nm) and that the V-shaped neck was not observed. They also measured cathodic activity ahead of the filament head with SKPFM.

Iron oxides of FFC with V-shaped neck were identified using Raman spectroscopy as described above. The presence of green rust in active heads, akaganeite in inactive filament heads, and amorphous oxide in tails confirm the accepted mechanism of FFC described in the literature. Weathering and atmospheric parameters did not influence the FFC mechanism after initiation because the polymer acted as a barrier to the external environment. As described above, the bead-like corrosion centers were composed of akaganeite in most sites. Akaganeite is a crystalline oxyhydroxyde that forms in presence of high chloride concentration (14). Its tetragonal crystal structure relies on the insertion of chloride ions (49). If the chloride ions are drained out of akaganeite, the crystal structure rearranges into the orthorhombic goethite crystal structure. Concentrated chloride electrolytes are often encountered in atmospheric corrosion (50). Therefore it is suggested that the bead center was the main anode. The bead edge and the matrix surrounding were made of amorphous phase and a lepidocrocite / goethite mixture. Amorphous iron oxide precipitates when the reaction is accelerated by oxygen. Therefore, it is likely that the main anode reaction was supported by the oxygen reduction taking place around the bead center. The lepidocrocite / goethite mixture may be explained by the wet/dry atmospheric corrosion mechanism of iron proposed in the literature advanced by Evans and Taylor and experimentally proved by Stratmann (51, 52). Lepidocrocite is reduced instead of oxygen to support the anodic

reaction. During this process lepidocrocite is transformed into a reduced form of lepidocrocite that converts irreversibly into magnetite when the reaction is completed (52). Goethite does not reduce like lepidocrocite, so it accumulates in the rust when formed (53). Goethite is crystalline under many conditions where chloride ions are not necessary. The bead centers formed after exposure at Lyon Arboretum and at Kilauea Volcano were not composed of akaganeite: they were magnetite at Lyon arboretum and goethite at Kilauea Volcano. This is in contrast with FFC where the weathering and atmospheric parameters do not influence the mechanism of FFC after its initiation. FFC progresses away from the scratch, whereas bead-like corrosion takes place next to the scratch where it can be more easily influenced by atmospheric and weathering parameters.

2.6.4 Laboratory exposures without artificial defect

Laboratory exposures have the advantage of isolating weathering and atmospheric effects on coated steel degradation. ASTM laboratory tests and controlled atmospheric exposures were performed. Coated steel degradation was assessed with CD-SKP and IR spectroscopy. The effects of salt fog and weathering exposures on coated steel were studied using the ASTM B117 and G154 accelerated tests. Ozone photolysis was reproduced in a controlled environment and its effect on coated steel was studied.

ASTM standard exposures: B117 and G154

The continuous salt fog of B117 attacks the PVB/steel interface within few hours. The CD starts above 11000 μm in Figure 2.44 after 1 day of exposure due to pre-delamination in the B117 chamber.

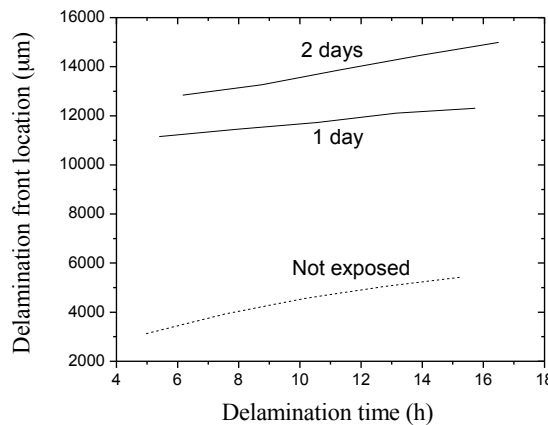


Figure 2.44: PVB coated steel CD-SKP after 1 and 2 days of B117 exposure.

The UV and condensation cycle of G154 at elevated temperature triggered PVB photo-oxidation after few days. G154 temperatures of 60°C and 50°C are below the PVB glass transition temperature, which is around 70°C. A sudden increase of the carbonyl peak at 1723 cm^{-1} in Figure 2.46 was noticeable after 6 days of exposure. The CD rate decreased after 2 days of G154 and then increased again after 6 days of G154, as shown in Figure 2.45. The polymer/oxide interface stability improved after short exposure time and decayed with longer exposure time. This PVB coated steel interface behavior was also observed in the field, as discussed above.

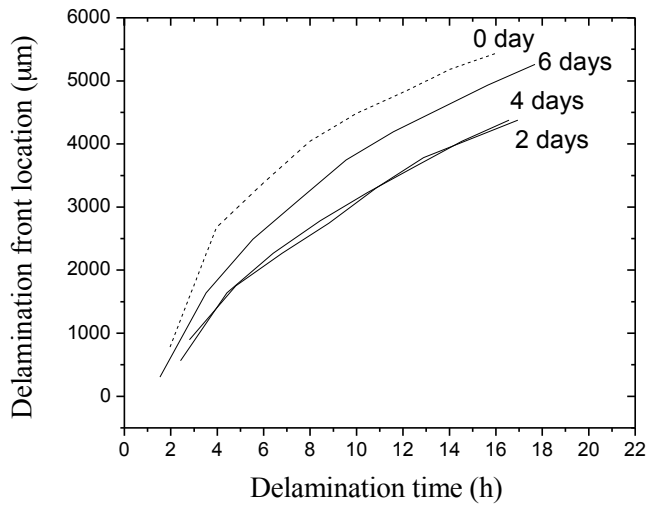


Figure 2.45: PVB coated steel CD-SKP after 2, 4 and 6 days of G154.

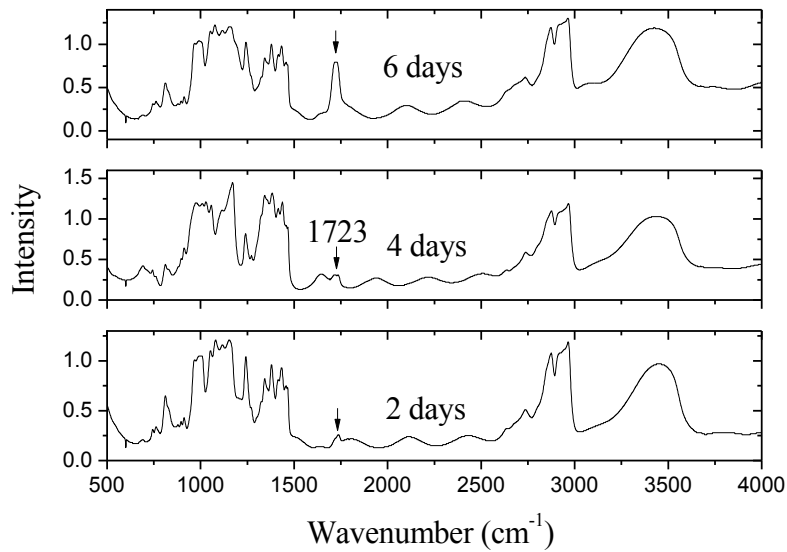


Figure 2.46: PVB IR spectra after 2, 4 and 6 days of G154.

Outdoor exposure combines corrosive and weathering environments so the effects of B117/G154 cycles on coated steel were investigated. The effect of B117 exposure before G154 exposure is shown in Figure 2.47 and Figure 2.48. The addition of 24 h of G154 after 6 h of B117 decreased the CD rate, as shown in Figure 2.47. Figure 2.48 shows that the CD increased again after longer G154 exposure. The polymer/oxide interface degradation after 6 h and 12 h of B117 was restored after short G154 exposure.

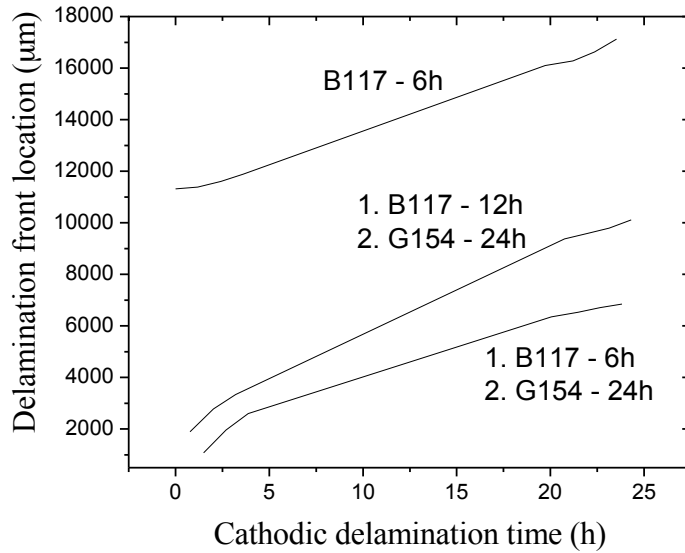


Figure 2.47: PVB coated steel CD-SKP after B117/G154 exposure.

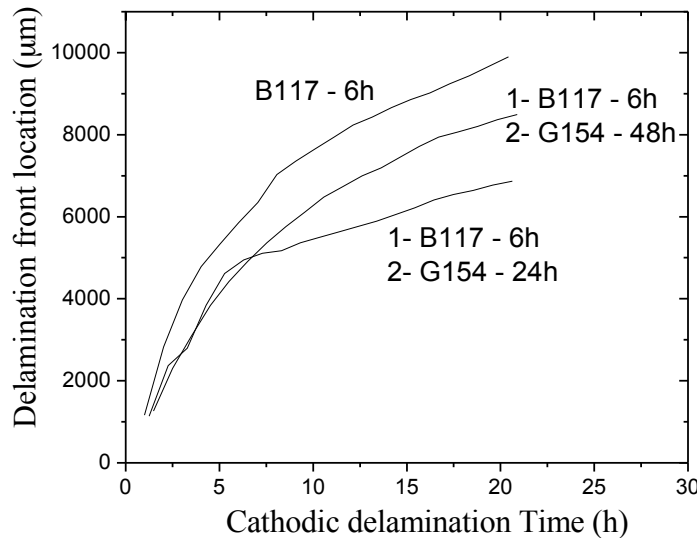


Figure 2.48: PVB coated steel CD-SKP after B117/G154 exposure.

The effect of G154 exposure before B117 exposure is shown in Figure 2.49 and Figure 2.50. After 48 h of G154 exposure, the CD rate decreased with the addition of 6h of B117. It is unclear why the CD rate decreased in this case. This experiment was reproduced and a smaller decrease was observed, Figure 2.50. Short pre-G154 exposure retarded the interface degradation during B117 exposure. The CD rate increased after 6 h of B117 when pre-exposed to G154 for 144 h as shown in Figure 2.49. PVB exhibited extensive photo-oxidation after 6 days (144 h) of G154 exposure. These results suggest that only short exposure to G154 exposure is beneficial for PVB/steel interface before PVB photo-oxidation takes place.

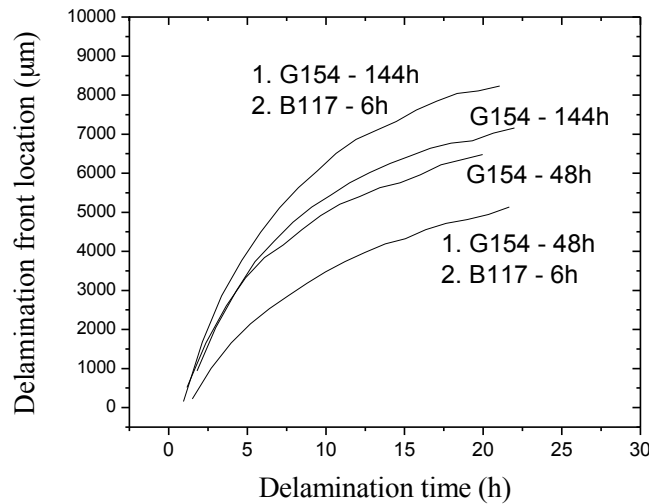


Figure 2.49: PVB coated steel CD-SKP after B117/G154 exposure.

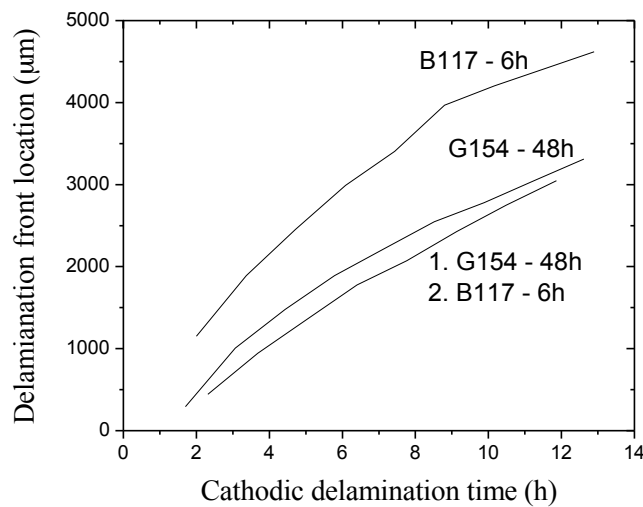


Figure 2.50: PVB coated steel CD-SKP after B117/G154 exposure.

Discussion

The effect of UV and humidity along with salt was investigated for PVB coated 1018 in a corrosive and a weathering chamber. The ASTM standard B117 and G154 were used in this study. The salt fog of B117 rapidly degraded the interface and induced delamination in few hours. The UV/condensation of G154 improved the interface stability after short exposure (1-4 days). It was also showed that short G154 exposure (1-2 days) after 6h of B117 recovered the degraded interface. Longer G154 exposure (6 days) accelerated interface degradation during B117. Those results show the importance of including B117 and G154 parameters into a reliable accelerated test to predict coating lifetime.

UV and water in laboratory air, clean air and nitrogen environments

The effects of weathering and atmospheric parameters were investigated in an enclosed atmospheric cell that was well controlled. UV, RH and ozone concentration were the three parameters of interest in this study. The first set of data addressed the effects of UV and humidity in different gaseous environments such as nitrogen, clean air or laboratory air. The second set of data focussed on the effects of ozone, UV and RH in a controlled nitrogen/oxygen environment. All of these exposures were short and no PVB molecular change was detected with IR spectroscopy. The coated steel interfaces after exposures were assessed with CD-SKP.

The PVB coated steel interface improved after short G154 exposure and field exposure. The important parameters to reproduce this interface improvement are UV and condensation. Figure 2.51 shows the effects of the gaseous atmosphere for exposures that included UV. The CD rate decreased significantly only after UV exposure in laboratory air. This indicates that the presence of humidity in the lab air is therefore necessary to improve the interface stability.

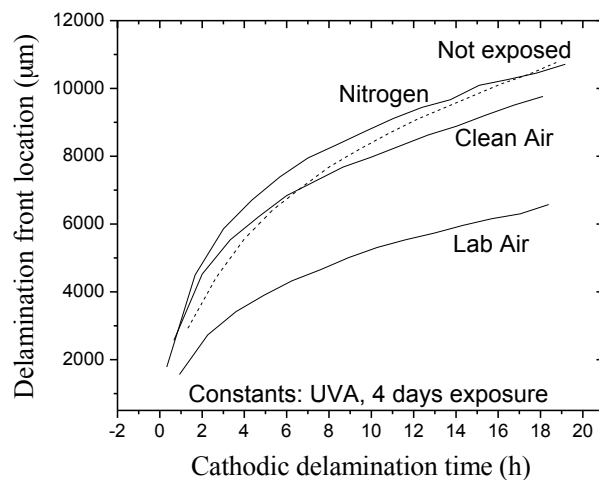


Figure 2.51: PVB coated steel CD-SKP after 4 days of UVA exposure in different environments.

Figure 2.52 shows the results of the same experiment, except without UV irradiation and with 100% RH instead of just with the natural lab RH, which was uncontrolled, but varied between 20-80%. In this case, the CD rate was reduced only after exposure in the nitrogen environment. In environments containing oxygen, UV was necessary for the interface improvement mechanism that involved UV and condensation. In the absence of oxygen, another mechanism involving only condensation improved the interface stability.

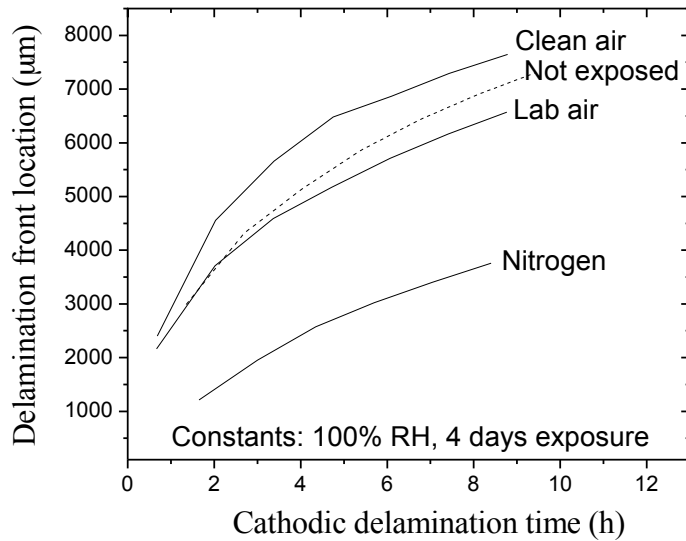


Figure 2.52: PVB coated steel CD-SKP after 4 days of exposure at 100% RH in different environments.

As shown Figure 2.53, the CD rate decreased after exposure in all environments with UV irradiation and 100% RH. The CD rate was similar after exposure in clean air and laboratory air. Therefore, the additional components in laboratory air, such as ozone and organics, did not influence the improvement in this exposure. However, the CD was slower after exposure in nitrogen than in lab or clean air.

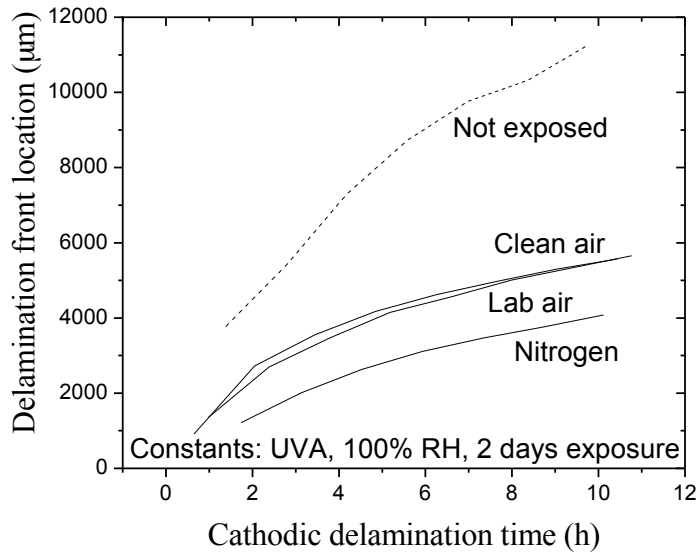


Figure 2.53: PVB coated steel CD-SKP after 2 days of UVA exposure at 100% RH in different environments.

Eponol BLS coated steel was exposed to UV and 100% RH in clean air. The CD was accelerated after both UV exposures in humid and dry environment, as shown in Figure 2.54.

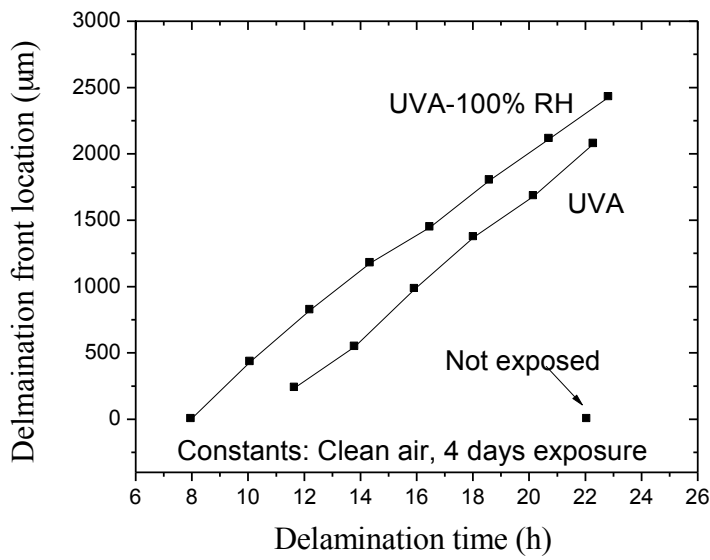


Figure 2.54: Eponol BLS coated steel CD-SKP after 4 days of UVA exposure with and without 100% RH

UV, ozone and RH exposures in controlled environments

UV and RH are the two important parameters to reproduce PVB/steel interface improvement observed in the field. UV is transmitted through the coating to the metallic surface if it is not first absorbed by the polymer. In a humid environment, water can be absorbed by the coating and diffuse to the metal surface where polymer-oxide bonds are replaced with water-oxide bonds (9). The access of oxygen and ozone to the metallic surface is less straightforward because oxygen and ozone can react with the polymer surface (46, 54). Figure 2.55 shows that CD was accelerated after exposure to an environment containing UV, ozone and RH in comparison to unexposed samples. In this grouping of experiments, the current set was the only one that included the CD of unexposed samples.

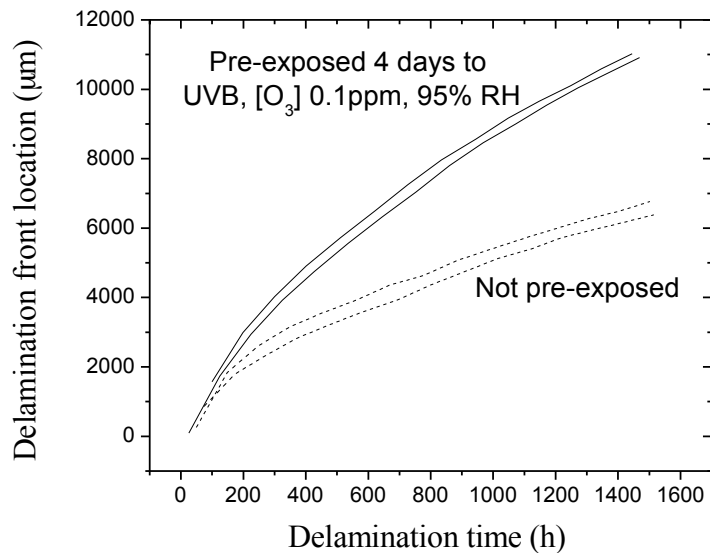


Figure 2.55: PVB coated steel CD-SKP after 4 days of UVA, $[O_3]$ 0.1 ppm exposure at 95% RH.

In Figure 2.56, the ozone concentration effect is investigated in the presence of UVB and 95% RH. The CD was strongly accelerated after exposure of 1 ppm of ozone. Lower ozone concentrations had little effect on the interface degradation.

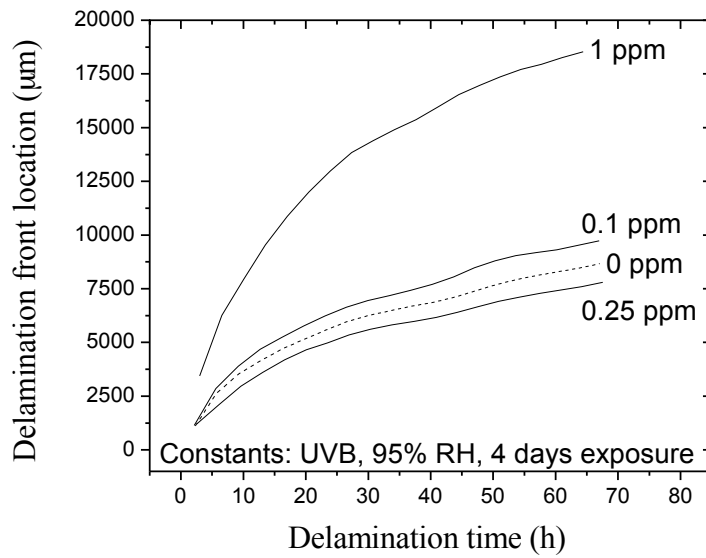


Figure 2.56: PVB coated steel CD-SKP after 4 days of UVB exposure at 95% RH with different $[O_3]$.

Figure 2.57 and Figure 2.58 show the effect of RH in the presence of UVA or UVB and 0.1 ppm of ozone. The CD rate decreased as the RH was increased. In Figure 2.58, the CD after dry exposure was slower than after humid exposure.

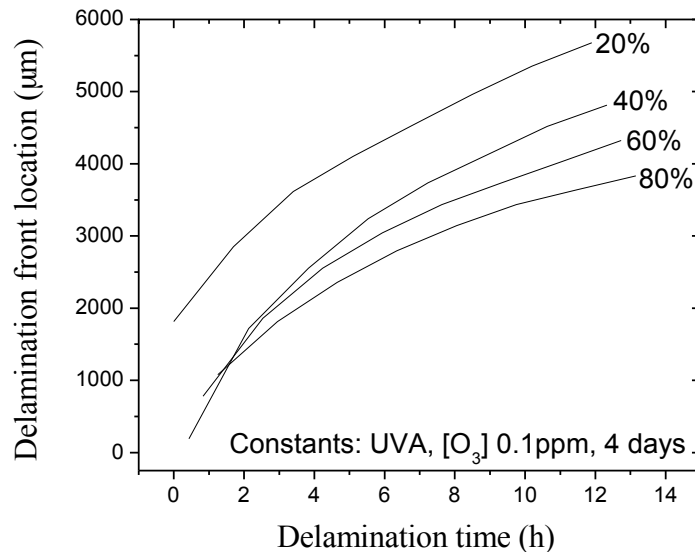


Figure 2.57: PVB coated steel CD-SKP after 4 days of UVA, $[O_3]$ 0.1 ppm exposure with different RH.

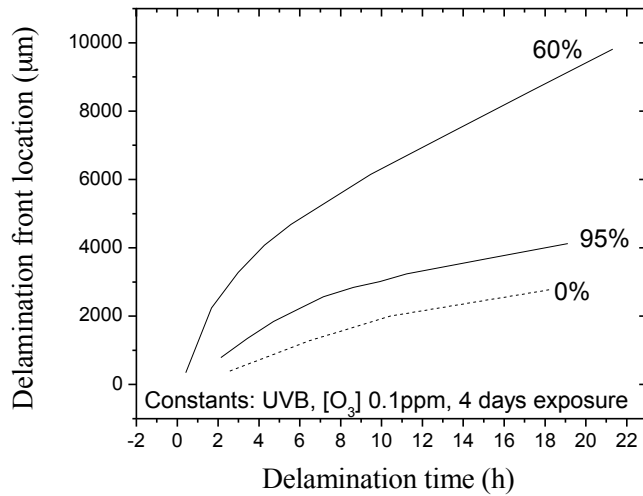


Figure 2.58: PVB coated steel CD-SKP after 4 days of UVB, $[O_3]$ 0.1 ppm exposure with different RH.

Figure 2.59 shows the effect of UV irradiation in presence of 0.1 ppm of ozone and 95% RH. The CD was faster after exposure without UV than with UV. The CD rate was similar after UVB and UVA exposure. The PVB molecule does not absorb radiation in the UV range so the shorter wavelengths emitted by the UVB lamp might not affect PVB (19). Also, the presence of ozone in the chamber can screen the shorter wavelength radiation. UVB caused more ozone photolysis product than UVA, but the results shown in Figure 2.56 indicate that a small ozone concentration (0.1 or 0.25 ppm) in the presence of UVB did not affect the PVB/steel interface.

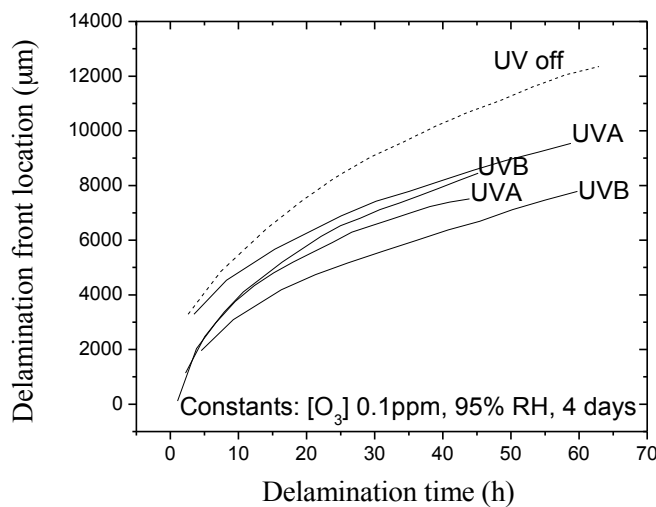


Figure 2.59: PVB coated steel CD-SKP after 4 days of $[O_3]$ 0.1 ppm exposure at 95% RH with and without UV.

Discussion

In a controlled atmospheric cell, the effects of ozone, humidity and UV can be decoupled. Ozone was investigated because it is a strong oxidant present in that troposphere that may accelerate the degradation. Ozone photolysis produces atomic oxygen $O(^1D)$ and ground state oxygen atom $O(^3P)$ (32). The production of $O(^1D)$ is maximal in the Hartley band (200-320 nm). However, its formation was observed up to 336 nm (55). UVA and UVB lamps, which have maximum output at 369 and 313 nm, respectively, were used in this work. Therefore, the production of $O(^1D)$ was limited. $O(^1D)$ decays to $O(^3P)$ or reacts with water to form radical OH. $O(^3P)$ is produced from ozone in the Huggins band (300-360 nm). $O(^1D)$ and $O(^3P)$ react differently with the polymer. $O(^1D)$ reacts through oxygen insertion while $O(^3P)$ and ozone react via hydrogen abstraction (56). The propagation mechanism of photo-oxidation breaks the polymer chain via tertiary hydrogen abstraction. It can be concluded that ozone can accelerate interface degradation when present above a threshold concentration. In contrast, UV and high RH can stabilize the PVB/steel interface.

2.6.5 Laboratory exposures of coated steel with artificial defect

FFC under PVB and Eponol was investigated in the laboratory because it was observed in the field. As described in the experimental section, two approaches were used to initiate FFC. The first approach used immersion in different solutions and the sample was not dried before placing it into the high temperature, high humidity environment to stimulate filiform growth. The presence of cations such as Na^+ in the solutions enabled CD from the scratch. In the second approach, the electrolyte was HCl and the electrolyte was dried before the high temperature exposure. CD did not occur because of the absence of Na^+ .

FFC test 1

FFC morphology was observed using the optical microscope to compare filament growth under Eponol and PVB. Figure 2.60 shows optical photographs of filaments that grew under Eponol. Along the edge of the main filament are smaller filaments growing at right angles. The line indicating the border between the filament head and tail is straight instead of V-shaped. This more open boundary may lead to chloride migration perpendicular to the growth direction, which allows for initiation of small filaments that grow sideways from the main filament.

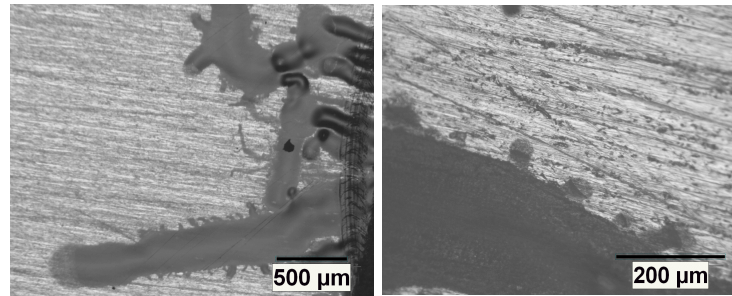


Figure 2.60: Optical photographs of filiform corrosion of Eponol coated 1018.

Figure 2.61 displays the optical photographs of FFC under PVB that was initiated with different electrolytes. Filaments under PVB can look linear with straight edges or like a “string of beads” with regular bulges (48). More and longer filaments grew when the electrolyte was 0.1M NH₄Cl than in 0.1 NaCl. The number of filaments and the filament growth kinetics increased with chloride concentration.

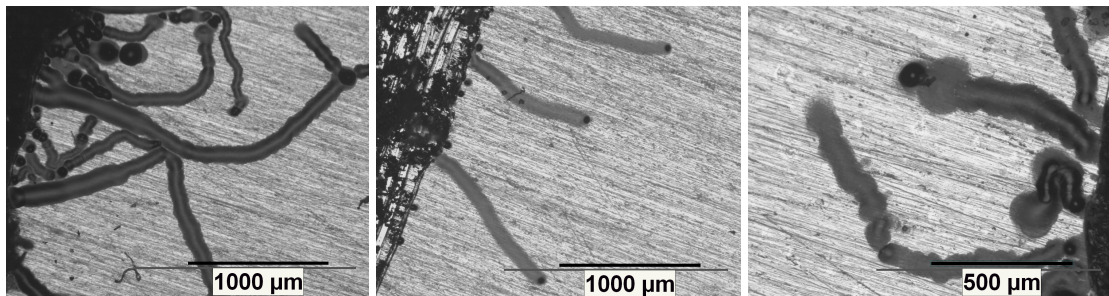


Figure 2.61: Optical photographs of FFC of PVB coated 1018. From left to right, the FFCs were initiated by 0.1 M NH₄Cl, 0.01 M NaCl and 0.1 M NaCl

The SKP potential map represented in Figure 2.62 is characteristic of all FFC tests containing 0.1 M sodium chloride. In this map the scratch is situated above the filament growth from top to bottom as shown by the black arrows. The corrugation of the potential map is considered to be a real effect (not an artifact) related to the polishing lines, which were periodic and perpendicular to the scratch. The polishing scratches affect the electrolyte transport under the polymer. The map is large enough to visualize the potential of the coating ahead of the filament. This coating potential is separated with a potential jump into two plateaus, one at 0.31 V/SHE and one at 0.23 V/SHE. This boundary suggests that CD had occurred in this region. The fact that the potential in the delaminated region is high indicates that this region had repassivated and CD had ceased at the time of the measurement. This was observed previously by Williams and McMurray who studied FFC of PVB coated iron foil (57). They found that cathodic delamination occurred before FFC initiation and proposed that cathodic delamination stops after exhaustion of cations.

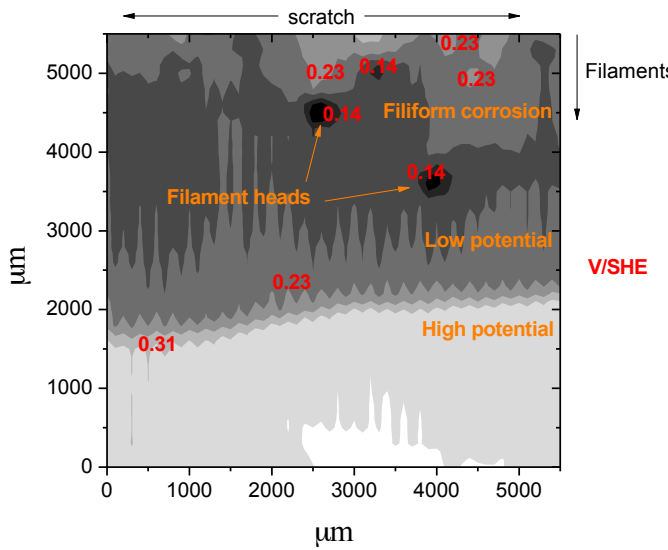


Figure 2.62: Potential map of PVB coated 1018 after 5 days of FFC test initiated with 0.01 M NaHCO_3 and 0.1 M NaCl . The values given on the map are local potentials in V/SHE.

Figure 2.63 shows a more detailed potential map of the region surrounding a filament head. This type of map was measured for several filament heads but not all of them. The filament growth direction is indicated by the orange arrow. The filament head, which was situated at the low potential spot (shown as black), was preceded by an elongated lower potential zone (dark grey). It is unclear why there was a lower potential zone but it seems that the filament direction was driven by this lower potential region.

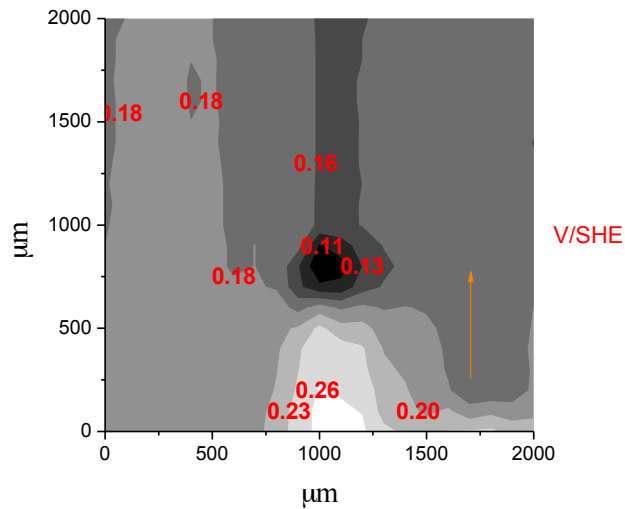


Figure 2.63: Potential map of filament head of PVB coated 1018 after 5 days of filiform corrosion test initiated with 0.01 M NaHCO_3 and 0.1 M NaCl .

Figure 2.64 shows the potential profiles after FFC tests initiated by different electrolytes. Those profiles are measured to highlight the pre cathodic delamination. No cathodic delamination occurred when Na^+ was replaced by NH_4^+ or when NaCl concentration was low (0.01 M vs. 0.1 M). Cathodic delamination is limited by the cation size and concentration as was previously shown by Leng et al. (58). This result is important in atmospheric corrosion where ammonium is more abundant than sodium (40).

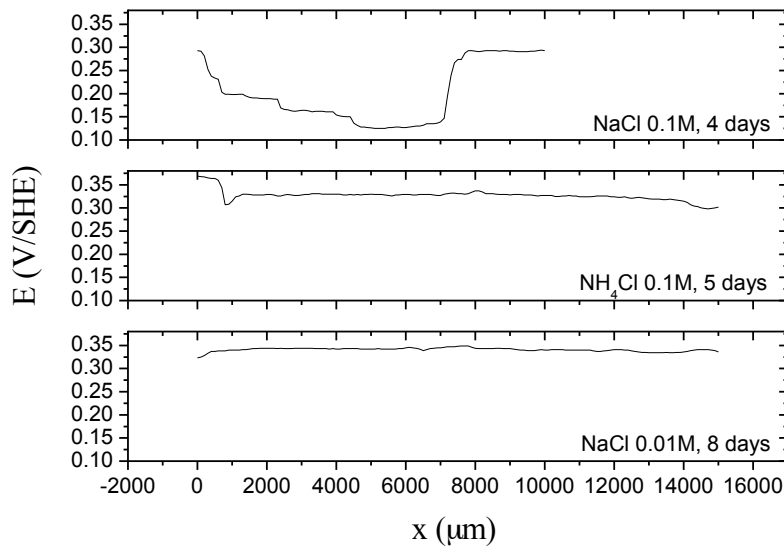


Figure 2.64: Potential profiles after FFC test of PVB coated 1018.

FFC test 2

The optical photographs in Figure 2.65 compare the FFC under PVB and Eponol coatings. No bead-shaped filaments formed under PVB in this FFC test. The electrolyte was dried before insertion of the sample in the oven. This difference in experimental procedure suppressed the formation of the bead-shaped attack. FFC started earlier under PVB than under Eponol and the filaments were generally thicker under Eponol than under PVB. The filament width was not uniform under Eponol and the filaments tended to branch by head splitting. The branched filaments are difficult to see in the picture due to their small sizes.

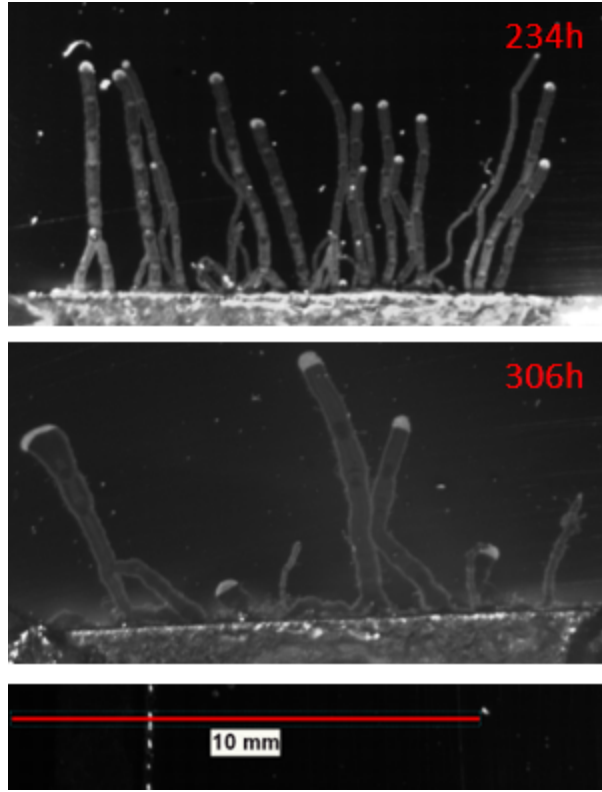


Figure 2.65: Optical photographs of FFC under PVB (top) and Eponol (bottom) coated on steel initiated with 0.5 M HCl.

Williams and McMurray proposed that the filament head volume (v) is proportional to the amount of chloride (16).

$$v = kN_{Cl^-} \quad (2.1)$$

They also described the filament head shape as an oblate hemispheroid (16) so the volume can be given as:

$$v = \frac{2}{3}\pi x r^2 \quad (2.2)$$

where x is filament height and r is filament radius. Assuming that the ratio (x/r) is constant, the filament head volume is proportional to the radius cubed (16):

$$v = k_1 r^3 \quad (2.3)$$

Setting Equation 2.1 and Equation 2.3, the amount of chloride is seen to be proportional to the radius cubed (16):

$$N_{Cl^-} = k_2 r^3 \quad (2.4)$$

Two filaments can merge when their heads reach the same point at the same time. This phenomenon was often seen under PVB and is shown in Figure 2.66 where filament 1 and 2 merged to form filament 3. The merged filament head contained the combined electrolyte of both filament heads. Therefore, the amount of chloride in filament 3 head was equal to the sum of the amount of chloride of the heads of filaments 1 and 2. Table 7 reports the filament width and the filament depth values measured from the optical profilometry pictures. The filament width was equal to the filament head diameter. The filament depth reported corresponds to the maximum depth of the filament channel. Equation 2.4 was verified for PVB coated steel as shown in Table 7. The sum of the radius cubes of filaments 1 and 2 was similar to the radius cubed of filament 3. The filament 3 depth was similar to the sum of the depths of filaments 1 and 2. Therefore, the amount of chloride and the filament head volume were proportional to the filament depth.

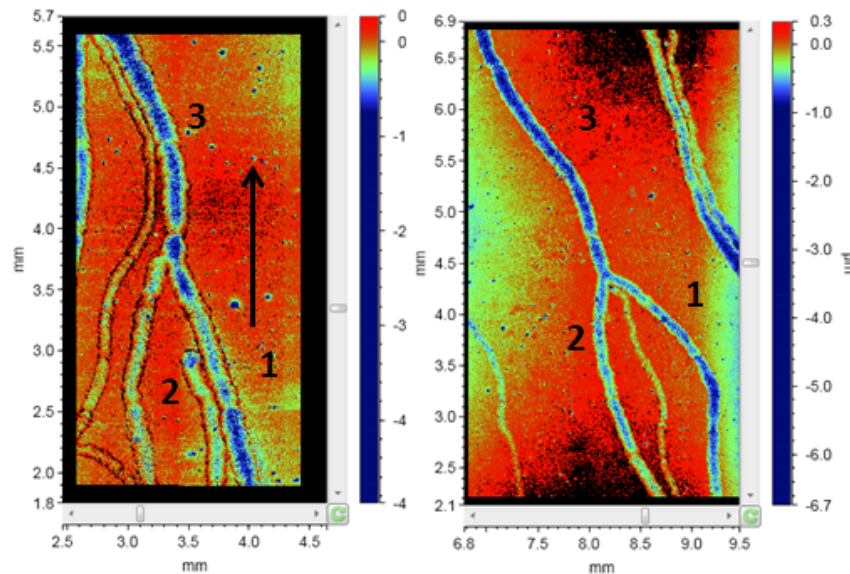


Figure 2.66: Optical profilometry pictures of merging filaments under PVB.

Table 7: Merging filament depths and diameters of Figure 2.66.

Filament number	1	2	3	1	2	3
Filament width (mm)	0.17	0.12	0.21	0.09	0.11	0.15
	0.18	0.13	0.19	0.1	0.12	0.13
$(r_1)^3 + (r_2)^3$ (mm ³)	0.00091			0.0003		
$(r_3)^3$ (mm ³)	0.001			0.00034		
Filament bottom depth (μm)	0.3	0.4	0.7	0.6	0.7	0.7
	0.3	0.4	0.9	0.5	0.6	1

Under Eponol, filaments often split as can be seen in the optical picture of Figure 2.67. After long exposure, thin filaments covering the main filament edge were visible. It is suspected that the thin filaments initiated from the main filament head but the filaments were not visible until they were some distance from the head when they had reached a detectable size. Another characteristic feature of FFC under Eponol is the change in filament width that can be seen in the optical pictures of Figure 2.67 and Figure 2.65. The amount of chloride in the main filament head was distributed among the split filaments. The filament maximum depths at different locations of the filament were measured and reported in the optical profilometry image of Figure 2.67. The filament depth was independent of the filament width and the amount of chloride. The average roughness next to this filament was 93.467 nm and the root mean square roughness was 0.192 μm . The filament might have been too shallow relative to the sample roughness to differentiate the filament depth.

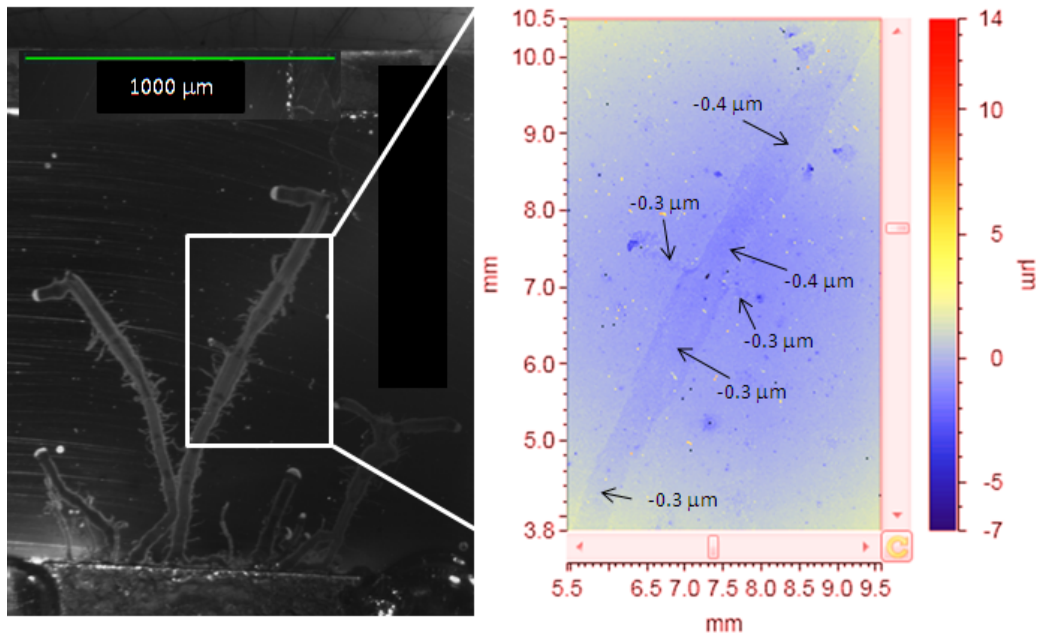


Figure 2.67: Optical picture before rust removal (left) and optical profilometry pictures after rust removal (right) of filaments under Eponol.

The average filament depth is plotted as a function of filament width in Figure 2.68 and Figure 2.69 for PVB and Eponol, respectively. The average depth was calculated from the filament groove volume divided by the filament contour area. The average depth was a small value close to the sample roughness. Despite the scattering of the average depth, a tendency between the filament depth and the filament width is apparent in both plots. The filament width is equal to the filament head diameter if the filament head is circular. The filament head shape and volume proposed by Williams and McMurray (16) and described by Equations 2.1-2.4 were therefore confirmed for PVB coated steel. For Eponol coated steel, the filament width was not constant and the filament head split. These observations indicate that the filament head shape varied

during the filament growth. Each point in Figure 2.68 and Figure 2.69 corresponds to one filament chosen on several samples. The filaments considered for Eponol coated steel corresponded to the filament portion that kept a constant width.

The filaments were thicker under Eponol and less deep than under PVB. As shown in Figure 2.68, the filament depth increased linearly with the filament width under PVB. Therefore, according to the oblate hemispheroid model, the filament depth increased with the filament head volume and the amount of chloride. In Figure 2.69, the filament depth increased with the filament width by one big step at values of about 0.55 mm under Eponol.

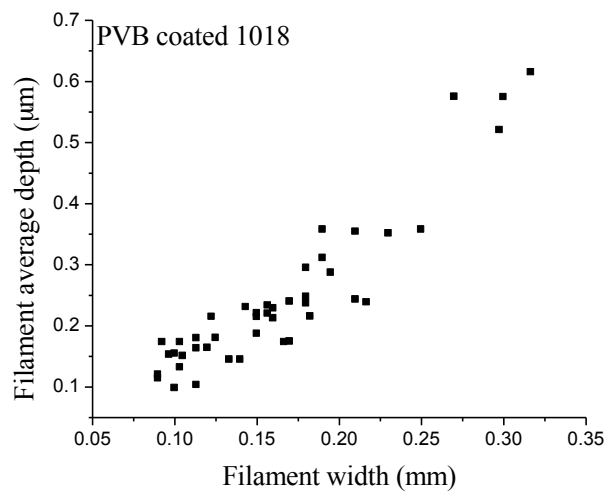


Figure 2.68: Filament depth and filament head diameter relationship under PVB.

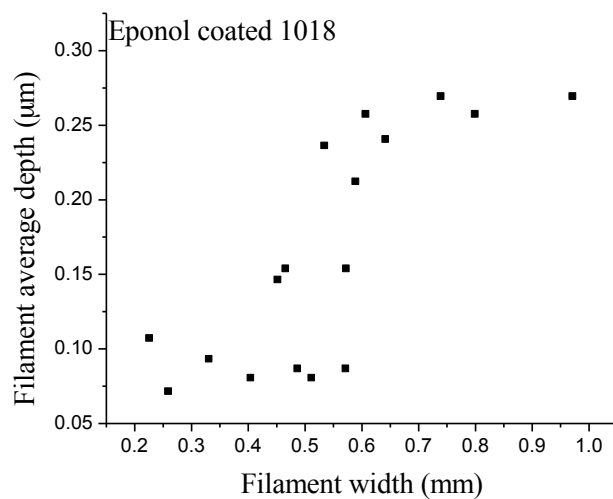


Figure 2.69: Filament depth and filament head diameter relationship under Eponol.

FFC rate is either controlled by electron transfer at the head surface or by ohmic/migration effects (16). Williams and McMurray developed a model to determine the rate-limiting step of FFC for PVB coated AA2024 (16). It was assumed that the filament head cell current was proportional to the delaminated area. This assumption might be valid for coated aluminum but the data for coated steel shown above contradict it. The Williams and McMurray model can be modified by setting the filament head current proportional to the iron dissolution flux that corresponds to Faraday's law. With this modification, the Williams and McMurray model states in both scenarios the following equations.

$$\text{Surface control: } \frac{dV}{dt} = kr^2 \quad (2.5)$$

$$\text{Ohmic control: } \frac{dV}{dt} = k' r \quad (2.6)$$

The iron dissolution fluxes are plotted as a function of head radius in Figure 2.70 and Figure 2.71. The head radius is the filament width divided by 2. The iron dissolution flux was taken as the delamination rate measured from the optical photographs multiplied by the average filament depth calculated and presented in Figure 2.68 and Figure 2.69. Each point corresponds to one filament. In the case of Eponol, only the filament portions with constant width and linear rate were considered. Equations 2.5 and 2.6 were fitted to the experimental data. Table 8 reports the equation constants and the quality of the fit given by R^2 . A constant was added to the equations to account for offset. The values of R^2 are above 0.9 for all of the fits. The R^2 value of the surface control fit was slightly higher than that for ohmic control for both coating systems. This suggests that surface control was more likely. However, both equations fit the data well so a definitive conclusion about the controlling mechanism cannot be drawn.

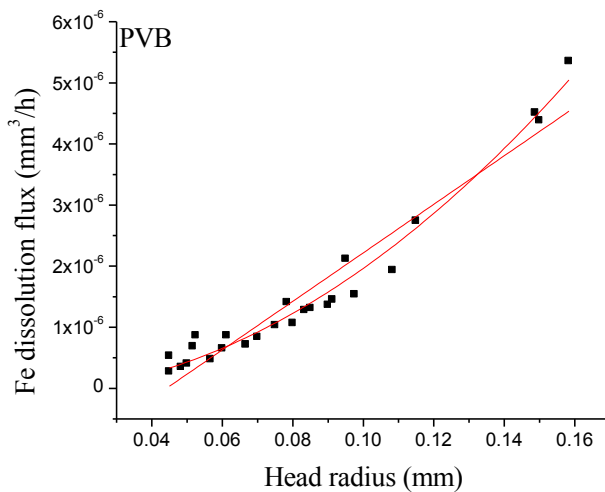


Figure 2.70: Iron dissolution flux as a function of filament head radius under PVB with surface and ohmic limited rate fits.

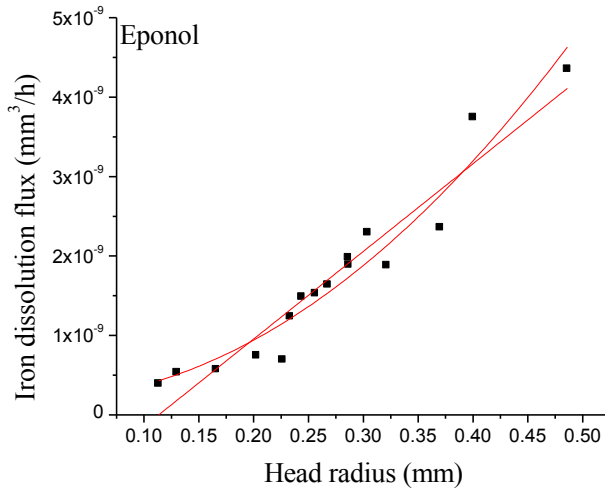


Figure 2.71: Iron dissolution flux as a function of filament head radius under Eponol with surface and ohmic limited rate fits.

Table 8: Surface and ohmic limited rate fitting equation with adjusted R^2 under PVB and Eponol.

	PVB		Eponol	
	Equation	R^2	Equation	R^2
Surface Control	$-8 \cdot 10^{-8} + 2.04 \cdot 10^{-4}r^2$	0.977	$2 \cdot 10^{-10} + 1.9 \cdot 10^{-8}r^2$	0.934
Ohmic Control	$-1.7 \cdot 10^{-6} + 4.0 \cdot 10^{-5}r$	0.924	$-1.2 \cdot 10^{-9} + 1.10 \cdot 10^{-8}r$	0.915

Filiform summary

The FFC morphologies of coated 1018 found in the field were reproduced in the laboratory. Filaments under Eponol in the lab grew side small filaments due to the straight boundary line between the filament head and tail. In contrast, under PVB the filament head/tail delimitation was V-shaped, which avoids filament head splitting. Another distinction of filament morphology is the change of width during growth under Eponol. This change in width can also be explained by the absence of V-shaped boundary, which prevents filament head dispersion. The constant FFC kinetics was affected by the change in shape of the filament head under Eponol. Two types of filaments were observed under PVB: bead-like and straight. The V-shaped boundary was not observed for the bead-like attack. Filament head characteristics seem to be the determining factor for the propagation mechanism and kinetics. Therefore, all observations of the head/tail

boundary are important to study FFC. The differences in filaments under Eponol and PVB can be explained by the coating mechanical properties and the coating adhesion nature. In comparison with PVB, Eponol is a stiffer polymer film that has a stronger adhesion with the metal. The filament head size is defined by the equilibrium the electrolyte pressure, the coating stiffness and the coating adhesion forces (59). Therefore, the filaments formed under Eponol are thicker than under PVB. Cathodic delamination before FFC initiation was measured in the laboratory with SKP. Cathodic delamination was not measured when ammonium cations were present instead of sodium cations. Furthermore cathodic delamination was not measured when the concentration of sodium chloride in the defect was low, but thin filaments were observed after 8 days. The cathodic delamination stopped before FFC progressed.

2.6.6 CD-SKP weathering exposure assessment applied to commercial coating system

CD-SKP is a promising technique to evaluate interface degradation after weathering exposures. Therefore, this technique was used to evaluate commercial coatings and conversion coatings prepared by Henkel and NAVAIR. CD was not always observed during the few days of exposure in the SKP due to the strong coating adhesion of commercial coating. However, SKP could detect changes in potential before and after weathering exposure. The Volta potential measured by the SKP reflects the potential of the buried interface (15). Any modifications of this interface in term of bonding or the presence of electrolyte are detected with the SKP. Wet/dry cycles were investigated previously with SKP (9). As shown below, short weathering exposures affected the potential measured.

Henkel prepared steel samples with several different types of TecTalis treatments, which are commercial Zr-based conversion coatings. The prepared samples were coated with PVB. As shown in Figure 2.72, CD-SKP detects the interface stability improvement brought by the conversion coating as indicated by slower CD rates. Longer TecTalis treatment time (120 s) increased the interface stability. The interface stability was slightly better with the TecTalis formula TT1820 compared to TT1800.

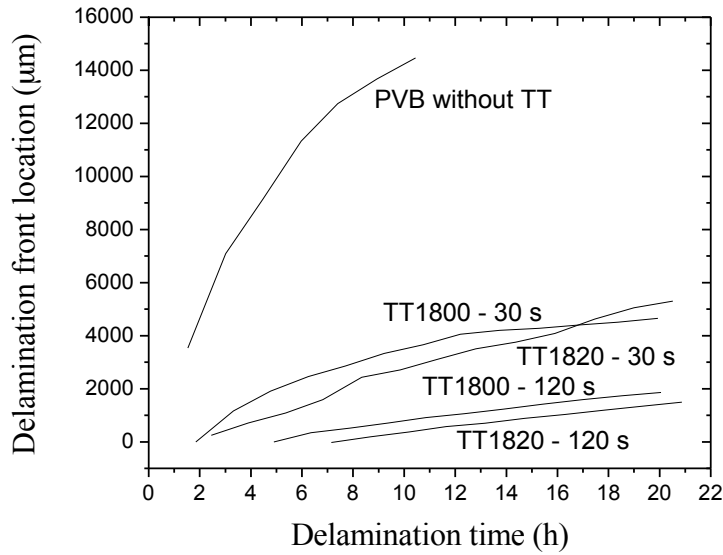


Figure 2.72: CD-SKP of PVB coated 1018 with several TecTalis conversion coating treatment prepared by Henkel.

E-Coat is an electrodeposited epoxy coating that was prepared by Henkel. Figure 2.73 shows potential scans taken by the SKP on e-coated samples during one day. The x-axis is the distance traveled by the Kelvin probe starting at the coating edge. The arrows show the direction of the curve shift with time. The bottom graph shows the potential curves of the unexposed samples, which exhibited no change even after 11 days of SKP exposure. In contrast, CD was observed for the sample that was previously exposed to ASTM G154. The progress of CD in the SKP chamber was noticeable within the first day of measurement after B117 exposure. Furthermore, coating delamination occurred during B117 exposure. The two upper graphs show the potential curves after exposures in G154 and outdoors in Columbus. The potential curves changed after a few hours in the SKP. There was no sharp jump in the potential curves to clearly indicate the location of the delamination front. Epoxy degrades readily as a result of the UV exposure outdoors in Columbus and in ASTM G154. This polymer degradation may be responsible for this change in the potential curve profile.

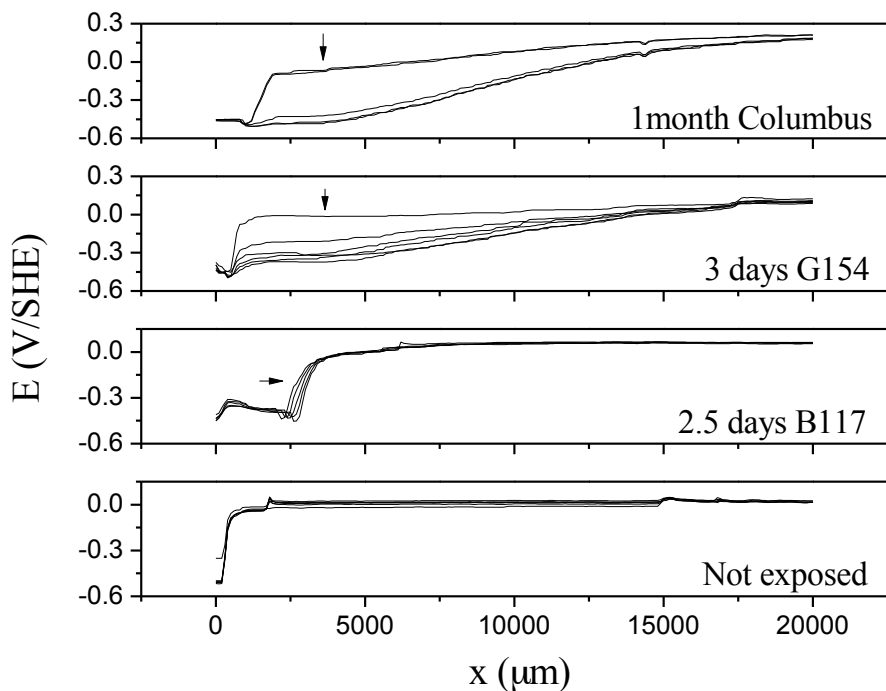


Figure 2.73: 1 day CD-SKP of E-Coat coated 1018 prepared by Henkel after weathering exposures, start on coating edge

Military ground vehicles are coated with 53022 and 53030 primers, which are solvent-based and water-reducible, respectively. The coating adhesion was improved with phosphated conversion coating or grit blast surface preparation. Figure 2.74 and Figure 2.74 display the potential profiles of primer 53030 with phosphated and grit blast surfaced preparations after 2 days in the SKP. As shown in Figure 2.74, no CD occurred after 2 days in the SKP. In Figure 2.74, cathodic delamination can be seen after 4 days of G154. For both surface preparations, the potential after B117 exposure was shifted to the corrosion potential of iron (-0.4 V/SHE). The potential profile of the unexposed sample was similar for both surface preparations. The potential next to the defect were shifted toward the iron dissolution potential.

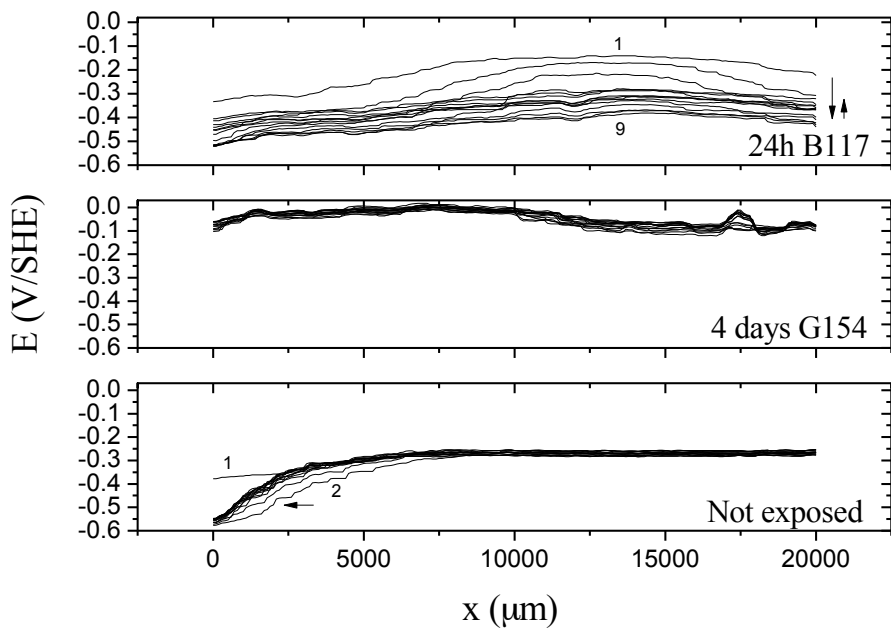


Figure 2.74: 2 days CD-SKP of 53030 phosphated 1018 prepared by NAVAIR after laboratory exposures, start 1000 μ m away from coating edge

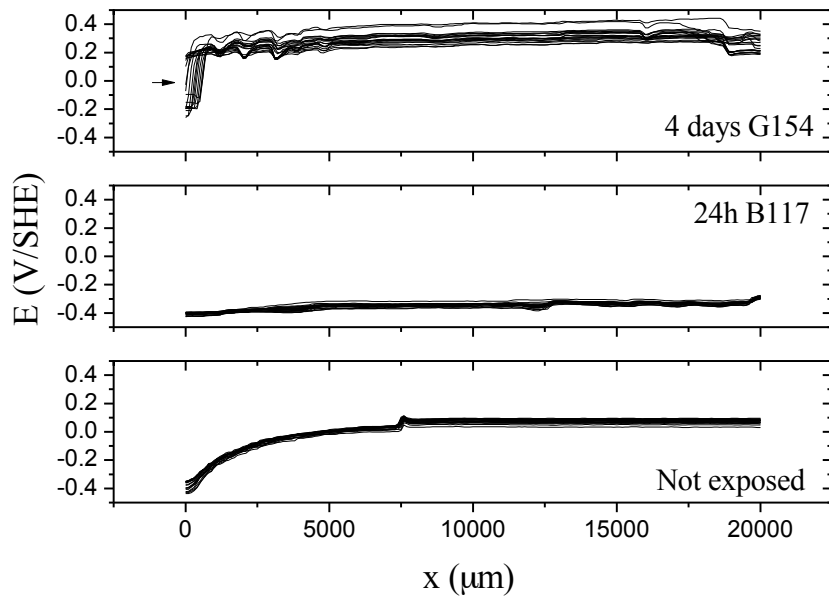


Figure 2.75: 3 days CD-SKP of 53030 grit blasted 1018 prepared by NAVAIR after laboratory exposures, start 1000 μ m away from coating edge, start later

Figure 2.77 and Figure 2.76 display the potential profiles of primer 53022 with phosphated and grit blast preparation after 4 days in the SKP. CD takes place after B117 exposure for both coating preparation. CD started later for the unexposed grit blast surface preparation. The potential after G154 increase indication a possible change of the coating/metal interface.

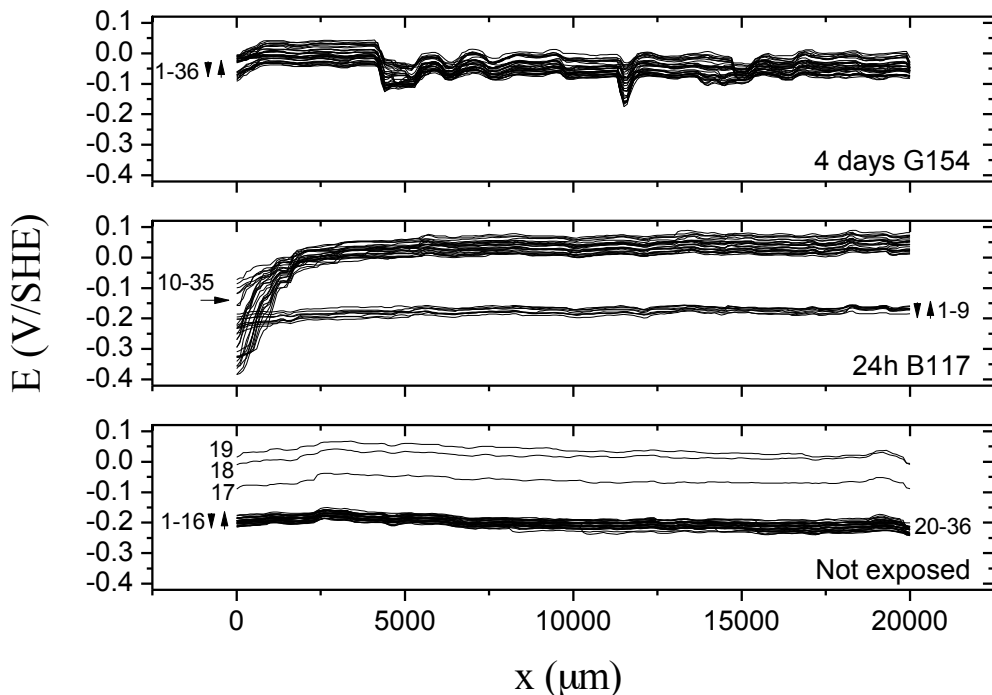


Figure 2.76: 4 days CD-SKP of 53022 phosphated 1018 prepared by NAVAIR after laboratory exposures, start 1000 μm away from coating edge

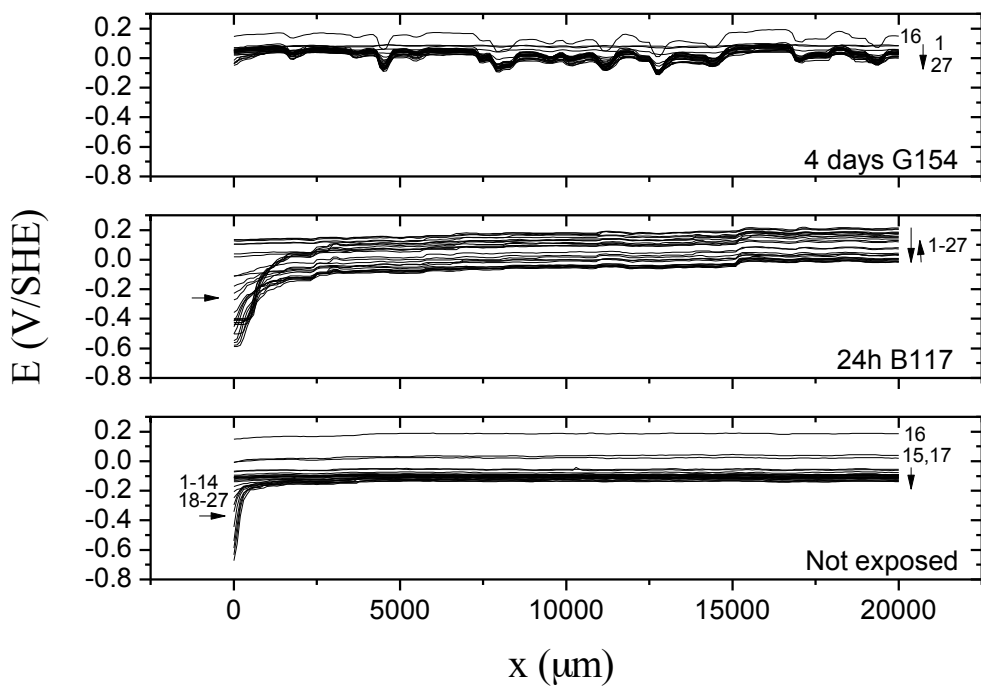


Figure 2.77: 4 days CD-SKP of 53022 grit blasted 1018 prepared by NAVAIR after laboratory exposures, start 1000 μm away from coating edge

Summary

CD rate under PVB was slowed down by the presence of a zirconium based conversion coating. The oxygen reduction taking place on the conversion coating may be reduced by the surface resistance. In addition, Zr conversion coating may improve PVB adhesion, which slows down CD. The effects of conversion bath formula and immersion time could be compared by CD-SKP.

Electrocoat epoxy coatings on 1018 were exposed to B117 and G154. After UV exposure, electrocoat epoxy coating underwent chain scission that changed the coating properties. During CD-SKP, an ohmic drop across more than 1 cm of the coated steel was established after a few hours. No potential jump shift associated with the progress of CD was observed. Instead, the coating potential close to the defect fell progressively toward the potential of the defect. This behavior suggested that CD might not be driven by cation transport from the defect. Vertical transport of cations through the coating layer was proposed to explain the potential progress observed. After B117 exposure, CD was measured in the SKP chamber.

Water-reducible and solvent-based military coatings coated on 1018 with phosphate conversion coating or grit blasted surface finish were exposed to B117 and G154. The phosphate conversion coating and the grit blasted surface finish provided similar interface stability to the coating

system. The CD-SKP of the water-reducible and solvent-based coating coated 1018 were presented separately.

The potential next to the defect of the unexposed water-reducible coating (53030) coated steel was deflected toward the defect potential but no CD progress was measured. This shows that oxygen reduction can take place under the coating next to the defect. However, this oxygen reduction is not sufficient to cause delamination. This deflection was not observed for the sample pre-exposed to G154. The potential of the water-reducible coating on steel exposed to B117 was lowered to the iron dissolution potential and no CD was measured due to the absence of polarization.

Solvent-based coating (53022) CD was measured after B117. This CD was faster than for the unexposed solvent base coating with grit blasted interface. The potential of the solvent based coating on steel exposed to G154 was higher than the unexposed sample and no CD was measured after 4 days in the SKP chamber. From those results, 4 days of G154 exposure might improve the coating/metal interface.

2.7 Economic Summary

This study is a step along the way of improving the capability to predict the failure of protective coatings. The economic impact of reduced corrosion of painted steel is considerable.

2.8 Implementation

The work performed in this study attempted to link lab and field exposures by exposing the same samples to different environments and using and the same advanced techniques to characterize them. SKP is still a lab-based technique not suitable for use by technicians, but it might someday be advanced to the state where it gains greater acceptance and use.

2.9 Conclusions

Coating lifetime prediction has been a challenge for many years. The development of new coating systems to improve protection or in response to new regulations has motivated efforts to find a reliable accelerated test. In this report, field and laboratory exposures were used to investigate the utility of accelerated laboratory tests for predicting outdoor exposure behavior. Degradation of the coating/metal interface after weathering exposure was the main focus of this work. The interface degradation was probed by CD-SKP and Raman spectroscopy Bulk polymer degradation was investigated by IR spectroscopy. PVB coated steel was the main system of investigation throughout the report. Eponol with BLS and commercial coatings on steel were investigated to a lesser extent.

PVB coated steel samples were exposed in several climates in the United States and tested with CD-SKP. CD-SKP was demonstrated to be a very sensitive technique for assessing changes in the interface after weathering exposure. Because of the sensitivity, interface degradation could be assessed using shorter periods of field exposure. The PVB/steel interface stability was improved after short exposure in the field. This improvement of the interface should improve coating lifetime and must be considered in accelerated test protocols. Interface degradation could be measured without PVB bulk degradation. When PVB bulk degradation took place at the same time as interface degradation, both degradation mechanisms could influence each other.

PVB coated steel samples with scribes were exposed at several locations and the iron oxides formed at the interface were identified with Raman spectroscopy. The corrosion mechanisms were discussed based on this iron oxide characterization. Bead-like corrosion formed next to the coating defect. FFC filaments with a V-shaped head propagated under the coating from the bead-like corrosion sites. The higher electrolyte and oxygen supply next to the scribe gave the bead-like corrosion its morphology. Oxygen surrounded the bead center where chloride was localized. The nature of the iron oxide in the bead center changed depending on the field site. In contrast, FFC was not influenced by the field site because it took place away from the coating defect. The iron oxide characterization of the filament head and tail confirmed the FFC mechanism most accepted in the literature.

The field site rankings deduced from the CD-SKP, IR spectroscopy and visual observations were discussed in accordance with the field site atmospheric and weathering data. The importance of chloride deposition and minimum relative humidity to enhance interface degradation were discussed. The importance of the UV portion of the solar radiation spectrum for accelerated polymer degradation was also demonstrated. The effect of sulfur could not be decoupled from the effect of chloride because both had the highest deposition rate in Kilauea Volcano. Kilauea Volcano was the most aggressive site tested. The average ozone concentration was slightly higher in urban areas than in rural areas or at high altitudes. The effects of ozone addition in laboratory tests were investigated.

CD-SKP was used to assess interface degradation after laboratory exposures. Exposures in ASTM B117 and G154 chambers were investigated separately and coupled. G154 exposure could restore interface degradation after B117 exposure and also could delay interface degradation in B117. Longer G154 exposure initiated polymer degradation that accelerated interface degradation in B117. Customized and more controlled laboratory exposures reproduced the PVB/metal interface improvement observed in the field. UV and humidity were the two parameters essential to improving the stability of this interface during short exposure. The effect of ozone photolysis by UV was investigated. High ozone concentration (1 ppm) accelerated interface degradation in 4 days. At lower concentration, the ozone may interact only with the polymer top layer leaving the interface unchanged. The interface degradation was stabilized as the relative humidity increased when PVB coated steel was exposed to low ozone concentration (0.1 ppm) and UV for 4 days.

FFC was reproduced in the laboratory under two experimental procedures. One was initiated with electrolyte that contained cations such as Na^+ and NH_4^+ and the electrolyte was not dried before FFC test. The other one was initiated with HCl that was dried before the FFC test. In the first FFC test bead-like filiform filaments were reproduced. Cathodic delamination prior to FFC was only measured with SKP when the test was initiated with 0.1 M NaCl. The differences between FFC growth and morphology under PVB and Eponol were also discussed. The dissolution depth of the filament trail under PVB increased linearly with chloride concentration. The dissolution depth of the filament trail under Eponol was shallower than under PVB. The main filaments under Eponol were bordered by small side filaments. The head/tail boundary under was observed to be straight and perpendicular to the filament growth instead of V-shaped, which allowed chloride migration to the side of the head and thus initiation of side filaments.

The interface degradation of commercial coatings such as electrocoat epoxy for automobile application and water-reducible and solvent-based coatings for military ground application was analyzed with CD-SKP after B117 and G154 exposures. Epoxy degradation triggered vertical transport to ensure coupling between uncoated and coated region instead of sideway transport from the defect. A phosphate conversion coating or a grit blasted surface finish under the military coatings gave similar interface improvement. B117 exposure had different impact on the water-reducible and the solvent-based coating interface. The interface of the water-reducible coating after B117 exposure could not be polarized because the potential across the interface surface was at the iron dissolution potential. The interface of the solvent base coating after B117 exposure was polarized and CD could occur.

In summary, the degradation mechanisms of coated steel without and with artificial defects were assessed with CD-SKP and Raman spectroscopy respectively. The mechanisms observed in the field were reproduced in the laboratory. CD-SKP was demonstrated to be a promising technique to probe interface degradation before visual coating failure occurred. This technique was successfully used to analyze interface degradation of commercial coating systems.

2.10 References

1. D. R. Bauer, M. C. P. Peck and R. O. Carter, *Journal of Coatings Technology*, **59**, 103 (1987).
2. *ISO 17872: Paints and varnishes - Guidelines for the introduction of scribe marks through coatings on metallic panels for corrosion testing* (2007).
3. Z. Y. Chen, D. Liang, G. Ma, G. S. Frankel, H. C. Allen and R. G. Kelly, *Corrosion Engineering Science and Technology*, **45**, 169 (2010).
4. W. B. DeMore, S. P. Sander, D. M. Golden, R. F. Hampson, M. J. Kurylo, C. J. Howard, A. R. Ravishankara, C. E. Kolb and M. J. Molina, *Chemical Kinetics and Photochemical Data for Use in Stratospheric Modeling*, in, JPL Editor, NASA (1997).
5. K. Wapner, M. Stratmann and G. Grundmeier, *Electrochimica Acta*, **51**, 3303 (2006).
6. A. Leng, H. Streckel and M. Stratmann, *Corrosion Science*, **41**, 547 (1999).
7. H. Leidheiser, W. Wang and L. Igetoft, *Progress in Organic Coatings*, **11**, 19 (1983).

8. C. Kemball, *Adhesion*, p. 19, Oxford University Press, London (1961).
9. A. Nazarov and D. Thierry, in *Localized in-Situ Methods for Investigating Electrochemical Interfaces*, p. 316 (2000).
10. R. Posner, K. Wapner, M. Stratmann and G. Grundmeier, *Electrochimica Acta*, **54**, 891 (2009).
11. N. M. S. Eldin and M. W. Sabaa, *Polymer Degradation and Stability*, **47**, 283 (1995).
12. Momentive, Technical Data Sheet: EPONOL™ Resin 53-BH-35, in (2007).
13. Sigma-Adrich, Poly(vinyl butyral-co-vinyl alcohol-co-vinyl acetate), in.
14. C. Remazeilles and P. Refait, *Corrosion Science*, **49**, 844 (2007).
15. M. Stratmann, R. Fesser and A. Leng, *Electrochimica Acta*, **39**, 1207 (1994).
16. G. Williams and H. N. McMurray, *Journal of the Electrochemical Society*, **150**, B380 (2003).
17. F. E. M. Obrien, *Journal of Scientific Instruments and of Physics in Industry*, **25**, 73 (1948).
18. T. Nguyen, J. Martin and E. Byrd, *Journal of Coatings Technology*, **75**, 37 (2003).
19. V. Reinohl, J. Sedlar and M. Navratil, *Polymer Photochemistry*, **1**, 165 (1981).
20. *ASTM D 2803-93: Standard Guide for Testing: FFC Resistance of Organic Coatings on Metal*, ASTM (withdrawn 2002).
21. D. Neff, L. Bellot-Gurlet, P. Dillmann, S. Reguer and L. Legrand, *Journal of Raman Spectroscopy*, **37**, 1228 (2006).
22. P. Refait, P. Girault, M. Jeannin and J. Rose, *Colloids and Surfaces a-Physicochemical and Engineering Aspects*, **332**, 26 (2009).
23. J. M. Genin, P. Bauer, A. A. Olowe and D. Rezel, *Hyperfine Interactions*, **29**, 1355 (1986).
24. P. Refait, D. D. Nguyen, M. Jeannin, S. Sable, M. Langumier and R. Sabot, *Electrochimica Acta*, **56**, 6481 (2011).
25. C. F. Sharman, *Nature*, **153**, 621 (1944).
26. P. Refait and J. M. R. Genin, *Corrosion Science*, **39**, 539 (1997).
27. P. Refait, O. Benali, M. Abdelmoula and J. M. R. Genin, *Corrosion Science*, **45**, 2435 (2003).
28. A. Bautista, *Progress in Organic Coatings*, **28**, 49 (1996).
29. S. J. Oh, D. C. Cook and H. E. Townsend, *Hyperfine Interactions*, **112**, 59 (1998).
30. W. H. J. Vermon, *Transactions of the Faraday Society*, **27**, 255 (1931).
31. R. Atkinson, D. L. Baulch, R. A. Cox, R. F. Hampson, J. A. Kerr, M. J. Rossi and J. Troe, *Journal of Physical and Chemical Reference Data*, **26**, 521 (1997).
32. B. J. Finlayson-Pitts and J. J. N. Pitts, *Chemistry of the Upper and Lower Atmosphere*, p. 969, Academic press (1999).
33. R. W. Shaw, *Atmosphere as Delivery Vehicle and Reaction Chamber for Acid Precipitation*, p. 243, Ann Arbor Science (1984).
34. G. M. Lovett, *Ecological Applications*, **4**, 629 (1994).
35. M. L. Wesely and B. B. Hicks, *Atmospheric Environment*, **34**, 2261 (2000).
36. I. S. Cole, W. D. Ganther and D. Lau, *Corrosion Engineering Science and Technology*, **41**, 310 (2006).
37. B. J. Huebert and C. H. Robert, *Journal of Geophysical Research-Atmospheres*, **90**, 2085 (1985).
38. W. L. Chameides, *Journal of Geophysical Research-Atmospheres*, **92**, 11895 (1987).

39. *ASTM G154: Standard Practice for Operating Fluorescent Ultraviolet (UV) Lamp Apparatus for Exposure of Nonmetallic Materials*, ASTM.

40. UNH's AIRMAP Observing Stations: University of New Hampshire atmospheric and weathering data, in (2001-2011).

41. NOAA Earth System Research Laboratory, in.

42. NOAA Global Hourly summary, in.

43. NOAA Climate data online, in.

44. United States EPA: Download Daily Data, in.

45. NOAA US Climate Reference Network, in.

46. M. J. Walzak, S. Flynn, R. Foerch, J. M. Hill, E. Karbaszewski, A. Lin and M. Strobel, *Journal of Adhesion Science and Technology*, **9**, 1229 (1995).

47. J. Zeno W. Wicks, Frank N. Jones, S. Peter Pappas, Douglas A. Wicks, *Organic Coatings: Science and Technology*, 3rd Edition, p. 746, Wiley.

48. P. P. Leblanc and G. S. Frankel, *Journal of the Electrochemical Society*, **151**, B105 (2004).

49. K. Stahl, K. Nielsen, J. Z. Jiang, B. Lebech, J. C. Hanson, P. Norby and J. van Lanschot, *Corrosion Science*, **45**, 2563 (2003).

50. C. Leygraf and T. Graedel, *Atmospheric Corrosion*, p. 368, Wiley interscience, New York (2000).

51. U. R. Evans and C. A. J. Taylor, *Corrosion Science*, **12**, 227 (1972).

52. M. Stratmann, K. Bohnenkamp and H. J. Engell, *Corrosion Science*, **23**, 969 (1983).

53. V. Lair, H. Antony, L. Legrand and A. Chausse, *Corrosion Science*, **48**, 2050 (2006).

54. N. Grassie and M. I. Guy, *Polymer Degradation and Stability*, **13**, 249 (1985).

55. W. Armerding, F. J. Comes and B. Schulke, *Journal of Physical Chemistry*, **99**, 3137 (1995).

56. J. F. Rabek, J. Lucki, B. Ranby, Y. Watanabe and B. J. Qu, *Acs Symposium Series*, **364**, 187 (1988).

57. G. Williams and H. N. McMurray, *Electrochemistry Communications*, **5**, 871 (2003).

58. A. Leng, H. Streckel and M. Stratmann, *Corrosion Science*, **41**, 579 (1999).

59. J. L. Delplancke, S. Berger, X. Lefebvre, D. Maetens, A. Pourbaix and N. Heymans, *Progress in Organic Coatings*, **43**, 64 (2001).

Task 3: Detection of Degradation at Polymer/Substrate Interfaces by Attenuated Total Reflection Fourier Transform Infrared Spectroscopy

3.1 Summary

Attenuated total reflection Fourier transform infrared (ATR-FTIR) spectroscopy has been used to detect changes at the interfaces between poly(vinyl butyral-*co*-vinyl alcohol-*co*-vinyl acetate) (PVB) and ZnSe upon exposure to ozone, humidity and UV-B light. Also, the response of PVB/Al interfaces to water has been studied and compared with the same for Eponol (epoxy resin, diglycidyl ether of bisphenol A)/Al interfaces. In the presence of ozone, humidity and UV-B radiation, an increase in carbonyl group intensity was observed at the PVB/ZnSe interface indicating structural degradation of the polymer near the interface. However, such changes were not observed when PVB-coated ZnSe samples were exposed to moisture and UV-B light in the absence of ozone showing that ozone is responsible for the observed structural deterioration.

Water uptake kinetics for the degraded PVB monitored using ATR-FTIR indicated a degradation of the physical structural organization of the polymer film. Exposure of PVB-coated Al thin film to deionized (DI) water showed water incorporation at the interface. There were evidences for polymer swelling, delamination, and corrosion of the Al film under the polymer layer. In contrast, delamination/swelling of the polymer was not observed at the Eponol/Al interface, although water was still found to be incorporated at the interface. Al-O species were also observed to form beneath the polymer layer. A decrease of the C-H intensities was detected at the PVB/Al interface during the water uptake of the polymer, whereas an increase of the C-H intensities was observed for the Eponol polymer under these conditions. This is assigned to rearrangement of the macromolecular polymer chains upon interaction with water.

2.2 List of Figures and Tables

Figure 3.1 Chemical structure of two coating polymers.

Figure 3.2 Schematic representation showing the total internal reflection of the IR beam and the generation of evanescent waves in the (a) PVB/ZnSe and (b) the PVB/Al sample configuration.

Figure 3.3 Schematic representation of the exposure setup.

Figure 3.4 (a) Sample in the cell being exposed to UV-B radiation, (b) Ozone and humid generation systems.

Figure 3.5 PVB film on a ZnSe IRE (a) *before* exposure to 0.1 ppm ozone, 90% RH and UV-B light and (b) *after* exposure to 0.1 ppm ozone, 90% RH (nitrogen) and UV-B light for 72 hrs.

Figure 3.6 ATR-FTIR spectra of PVB spin-coated on a ZnSe IRE.

Figure 3.7 ATR-FTIR spectra of PVB spin-coated on a ZnSe IRE before and after exposure to 0.1 ppm ozone, 90% RH and UV-B (310 nm) radiation for 72 hrs.

Figure 3.8 ATR-FTIR spectra of the degraded and non-degraded PVB samples in contact with DI water within 5 min of exposure, using pure ZnSe as background and averaged over 128 scans.

Figure 3.9 ATR-FTIR spectra of the degraded PVB sample showing abrupt water uptake upon exposure to DI water over a period of 2 hrs.

Figure 3.10 IR absorption intensities at 3450 cm^{-1} vs. exposure time for the degraded PVB film spin-coated on a ZnSe IRE in contact with DI water.

Figure 3.11 ATR-FTIR spectra of the non-degraded PVB sample showing gradual water uptake upon exposure to DI water over a period of 2 hrs.

Figure 3.12 IR absorption intensities at 3450 cm^{-1} vs. exposure time for the non-degraded PVB film spin-coated on a ZnSe IRE in contact with DI water.

Figure 3.13 ATR-FTIR spectra of PVB spin-coated on a ZnSe IRE before and after exposure to 90% RH and UV-B (310 nm) radiation for 72 hrs. The pure ZnSe IRE was used as the background for both spectra. Each spectrum is averaged over 400 scans. The inset shows the same spectrum zoomed in the region $1500\text{--}1800\text{ cm}^{-1}$ to show the intensity increase in the O-H deformation mode only.

Figure 3.14 ATR-FTIR spectra of a ZnSe IRE sputter-coated with a 50 nm Al film and a $10\text{ }\mu\text{m}$ PVB film in contact with DI water with the dry sample before exposure as background.

Figure 3.15 ATR-FTIR spectrum of a ZnSe IRE sputter-coated with a 50 nm Al film in contact with DI water for 5 hrs with the dry sample before exposure as background and averaged over 400 scans.

Figure 3.16 Peak fitting of the OH stretching region of pure DI water. The pure ZnSe was used as the background and averaged over 400 scans.

Figure 3.17 Peak fitting of the water OH stretching region from the 1 hr water exposed PVB/Al sample.

Figure 3.18 ATR-FTIR spectrum of a ZnSe IRE coated with 50 nm Al and PVB exposed to DI water for 3 hrs with the same sample exposed for 1 hr used as the background.

Figure 3.19 ATR-FTIR spectra of a ZnSe IRE spin-coated with a $10\text{ }\mu\text{m}$ PVB film in contact with DI water with the dry sample before exposure used as background.

Figure 3.20 ATR-FTIR spectra of both PVB and PVB/Al samples dried over 48 hrs after the water exposure experiments, using the respective dry samples (before exposure) as backgrounds.

Figure 3.21 Schematic of the possible interactions of water molecules with the Al oxide/hydroxide film at the PVB/Al interface.

Figure 3.22 ATR-FTIR spectra of a ZnSe IRE sputter-coated with a 50 nm Al film and a $10\text{ }\mu\text{m}$ Eponol film in contact with DI water with the dry sample before exposure used as background.

Figure 3.23 Peak fitting of the water OH stretching region from the 1 hr exposed Eponol/Al sample.

Figure 3.24 ATR-FTIR spectrum of a ZnSe IRE sputter-coated with a 50 nm Al film and a 10 μm Eponol film in contact with DI water for 15 hrs with the dry sample before exposure as background, zoomed in the region 2500–3700 cm^{-1} showing an increase in the C-H peak intensities and averaged over 400 scans.

Figure 3.25 ATR-FTIR spectrum of Eponol spin-coated on ZnSe and exposed to 90% RH for 20 hrs, using the dry sample before exposure as the background.

Table 3.1 Gaussian fit parameters for the pure water OH stretching region.

Table 3.2 Gaussian fit parameters for PVB confined water OH stretching region.

Table 3.3 Gaussian fitting parameters for Eponol confined water OH stretchin region.

3.3 Introduction and Background

In the past decades, both inorganic and organic polymeric coatings have been extensively applied on metal structures to prevent corrosion related failures.^{1–3} The anticorrosive properties of these coatings (individual components or as a whole) are assessed with the help of certain standard accelerated weathering tests. These studies evaluate the coating's response to UV radiation, humidity, thermal aging, mechanical deformation, electrolytes, and water permeation.^{4–5}

It is known that most polymers degrade irreversibly due to photolytic oxidation, leading to a concomitant deterioration in their aesthetic and performance parameters.⁶ Only wavelengths from approximately 290 to 3000 nm are able to reach the troposphere. Wavelengths below 290 nm are strongly absorbed by stratospheric ozone and other absorbing species in the upper atmosphere. Hence, tropospheric photochemistry is limited by this short wavelength cut off. The UV region is divided into three sub-regions, namely UVA (315–370 nm), UVB (290–315 nm) and the more harmful UVC (200–290 nm) which is filtered out by the ozone layer. The impact of high energy UV light is the most intense although the contributions from the visible and infrared wavelengths cannot be fully ignored.^{7,8}

The first and foremost criterion for photo-degradation to initiate is that the polymer should be able to absorb UV light. Hence, all aliphatic polymers without chromophores in their structures should ideally have a better photo stability in the terrestrial UV range 295–400 nm than aromatic or unsaturated polymers, but in reality the presence of extraneous substances (added during manufacture) and structural inhomogeneities make the polymer susceptible to attack.^{6,8} Exposure to UV radiation may either lead to changes in the chemical structure of the polymer due to formation of new functional moieties or fragmentation of the cross-linked macromolecules initiating at the weakest centers of the polymer. The number of degradation sites may increase due to transfer of excitation energy to the non-absorbing parts of the polymer chains via formation of transient species. Such changes ultimately affect the physical and mechanical properties of the coating negatively.⁸ There have been extensive studies on photo-degradation of some of the conventional organic coatings namely alkyd, epoxy, acrylate, polyurethane, and polyester employing electrochemical and spectroscopic (IR and UV-Vis) techniques.^{9–12} Also, physical/chemical models have been developed to link laboratory and outdoor exposure data.¹³ Polymer degradation is a complicated process and is contingent on a

combination of factors like irradiance, distribution of sunlight, ambient temperature, and dose-response characteristics of the polymer.¹⁴

In addition to sunlight, coatings are constantly exposed to different environments that range from immersion in water or burial in soil to heavily polluted industrial regions.² In urban areas with numerous pollution sources, ozone is a major pollutant in the atmosphere. Although stratospheric ozone protects all living organisms from the detrimental solar UV radiation, ozone in the troposphere may cause damage to living tissues and degrade numerous materials.¹⁵ Tropospheric ozone concentrations show heterogeneity since it is formed from a series of photochemical reactions involving volatile organic compounds and oxides of nitrogen whose emissions vary geographically, temporally and with altitude. Also, there is an influx of ozone from the stratosphere at times. Ozone concentrations in the range 30–40 ppb are essentially found worldwide. Industrial zones have been found to have ozone concentrations as high as 100–150 ppb. In conjunction with the appropriate UV wavelengths and moisture, ozone is known to undergo numerous photochemical reactions that result in the formation of highly reactive intermediates which, in turn, initiate polymer degradation.⁷ Hence, it is very important to have a thorough knowledge of the degradation pathways of polymers upon exposure to these agents to understand their performance abilities better.

Primer layers are very important functional components of coatings providing a corrosion-resistant barrier to the metal surface. They are typically 10–20 μm in thickness and promote adhesion between the topcoat and the surface to be painted. They are responsible for improving paint durability thereby providing extra protection to the material being painted.¹⁶ The performance of the primer is one of the determinants of the performance of the coating as a whole. Topcoats are chosen primarily based on their barrier properties since they serve as the first line of defense against corrosion. However, they also contain the pigments and additives necessary for aesthetic purposes.

Poly(vinyl butyral-*co*-vinyl alcohol-*co*-vinyl acetate) (PVB) is a non toxic polymeric resin known for its fine properties like transparency, insulation, impacting resistance and drawing performance (Figure 3.1a).¹⁷ It can be synthesized by a condensation reaction of butyraldehyde and poly(vinyl alcohol) using *N*-methyl-1-pyrrolidone as solvent.¹⁸ It exhibits special adhesiveness and transparency to both organic and inorganic glass, for which reason it is extensively used in laminated safety glass for automobile windshields.¹⁹ However, PVB is also applied as primers in multilayered coating systems for corrosion protection of metal structures.¹⁷ A great deal of research has been done on thermal and photochemical degradation of PVB using gravimetric and spectroscopic methods. According to studies by Nabil et al., thermal degradation in PVB initiates at the acetate group.²⁰ Liau et al. investigated the effect of 380 nm on the structure of PVB and found that under normal conditions, there is no photo-degradation of the polymer but addition of TiO₂-enhanced the photo-deterioration process.²¹ However, the most realistic approaches related to real-life scenarios would include exposure of PVB to different combinations of ozone, UV light, and humidity (resembles an industrial environment) rather than heat or light alone.

In addition to understanding what factors are responsible for polymer failure and the degradation mechanisms, it is important to know whether the exposure of PVB-coated substrates affects the polymer/substrate interface in a manner similar to the polymer bulk structure. Adhesively bonded structures seen everywhere today can be simply considered to be polymer-coated

substrates, whose longevity depends upon the stability of the polymer/substrate interfaces. Common substrates employed are metals and alloys due to their desirable properties like tensile strength and luster. Hydration and structural changes are known to be detrimental to such interfaces. This is also very likely because a polymer/substrate interface is often a fragile region with inferior properties compared to the material bulk.²² Metal-polymer interfaces are known to be fractal in nature and not smooth microscopically.²³ The structure of the metal oxide layer plays a crucial role in determining the initial integrity of the polymer/metal bonds and the bonding has been found to change with variations in temperature.^{23,24} One of the factors affecting the deterioration of such interfaces is the coating-to-metal adhesion. Several different theories of adhesion between polymers and substrates have been proposed, namely the physical adhesion theory, where Van der Waals/dispersion interactions are operative, the chemisorption theory which involves the formation of covalent, ionic or hydrogen bonds at the interface, the diffusion theory involving inter-diffusion of the polymer into the substrate bulk, the mechanical interlocking theory where the polymer chains anchor themselves into surface defects of the substrate and the weak boundary theory which states that absence of contaminants promote polymer-substrate adhesion.^{25,26} Another factor is the barrier properties of the polymer film to oxygen and water, which are also constituents of metal corrosion.²²

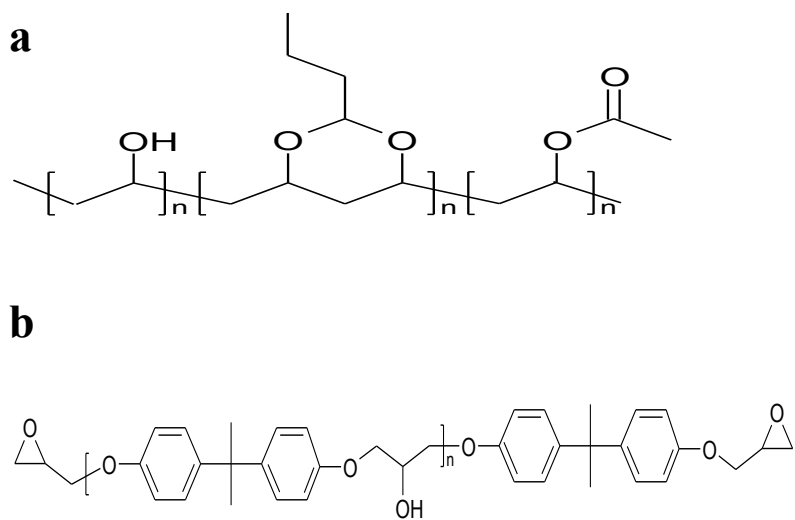


Figure 3.1. Chemical structure of two coating polymers. (a) Poly(vinyl butyral-*co*-vinyl alcohol-*co*-vinyl acetate) and (b) Eponol resin 53 BH 35.

If the activity of water is higher in the environment compared to the polymer-coated metal structure, it would spontaneously diffuse into the polymer network through pores or defects, and ultimately reach the polymer/metal interface, where it is known to cause adhesion loss between the polymer and the metal surface by displacing the weaker polymer/metal bonds by stronger water/metal oxide-hydroxide interactions.²⁷ It is possible that the hydrophilic metal

oxide/hydroxide surface may retain the water molecules at the buried polymer/metal interfaces over a period of time. In addition, the penetrating medium often results in an adjustment of the bulk structure of the polymer film, too. This includes reversible swelling, irreversible hydrolysis, cracking, and crazing.²² Severe changes in the physical properties of the resin are observed, such as tensile strength, net dielectric constant, and the glass transition temperature.²⁸ The ultimate impact can be delamination or stripping of the film from the metal surface. These complex processes are contingent on the structure and chemical properties of the polymer film (polarity, unsaturation, symmetry, chain orientation etc.), as well as size, shape and properties of the penetrant species.²⁹

Aluminum is a low density metal with good mechanical strength. As substrate, it is extensively used in outdoor applications that include siding, window trim, automotive elements and aircrafts. Also, the recent demand to reduce the use of fossil fuels has led to an increased interest in lightweight constructions like Al alloys.^{30,31} Hence, it is extremely crucial that adhesively bonded structures using aluminum last over extended period. In this context, a PVB-coated Al surface can be used as a model system to investigate how the corresponding polymer/metal interface responds to the ingress of water and how effective is a polymer like PVB in protecting the metal beneath it. Also, a comparison with an epoxy polymer/Al interface (epoxies are well known primer resins.²) is helpful. The epoxy resin used was the Eponol resin 53 BH 35 and is based on the diglycidyl ether of bisphenol A (DGEBA) (Figure 3.1b).

Probing changes at buried interfaces non-destructively has always been a challenging task. One of the potential limitations is that the technique should work at ambient pressure as applying a high vacuum might cause severe alterations of the surface. Moreover, real-time analysis and relevant climatic conditions are always desired. There have been numerous studies on water sorption by polymeric coatings using gravimetric procedures, which, however do not shed light on the polymer/metal interfacial region specifically.^{32,33} Commonly employed methods so far in determining changes at such interfaces are electrochemical techniques, for example, electrochemical impedance spectroscopy (EIS) and scanning Kelvin probe (SKP). While EIS is used to analyze the resistive and capacitive barrier properties of the polymer coating and the polymer/metal interface based on electric equivalent circuits, SKP functions by measuring local electrode potential changes beneath the polymer layer.^{31,34-36} Spectroscopic techniques have been employed to understand penetrant diffusion through coatings under a variety of conditions.^{37,38} However, there is still a lack of detailed knowledge about polymer/metal interfaces using this technique. For example, Ohman et al. have studied the transport of water and electrolyte species to Al/polymer interfaces and Nguyen et al. investigated the incorporation of water at Fe/polymer interfaces, additionally quantifying the amount of water trapped at such interfaces.^{22,27,31,39,40}

3.4 Lessons Learned

We have learned using ATR-FTIR spectroscopy that PVB films structurally degrade when exposed to 0.1 ppm ozone, 90% RH and UV-B light. Moreover, we have learned that exposed PVB showed a much greater water uptake. When exposed to humidity and UV-B alone, PVB exhibited no structural degradation, thus showing that ozone (or rather atomic oxygen formed from ozone) is required for structural deterioration of the polymer. With regard to the stability of the polymer/metal interface, we have learned that water is incorporated by PVB-coated films on

Al substrate, leading to swelling and delamination of the PVB films. Corrosion products (Al oxide/hydroxide) were also seen to form at the interfacial region, where a water layer is retained. Eponol-coated films on Al substrate are also capable of retaining water but we have learned that the interaction with water induces a macromolecular rearrangement within the polymeric chains. Corrosion products are formed rapidly upon exposure and remain constant afterwards. Although ATR-FTIR spectroscopy cannot discriminate between delamination and swelling processes, it has proven to be a useful technique in assessing the interfacial degradation as well as water intake by polymer films coated on metallic substrates.

3.5 Experimental

Materials

Poly(vinyl butyral-*co*-vinyl alcohol-*co*-vinyl acetate) resin (average M_w 70,000–100,000) was purchased from Sigma-Aldrich. The epoxy polymer, EponolTM resin 53-BH-35, was kindly provided by Hexion Specialty Chemicals (Columbus, OH).

Ion Sputter Deposition of Al films

For the ATR-FTIR measurements with the PVB/Al and Eponol/Al samples, an ATC ORION 5 UHV sputtering system (AJA International, Inc.) was used to deposit the Al thin films on ZnSe IREs, with a base working pressure of 5 mTorr. The base pressure was 10^{-7} Torr. A 20 sccm (standard cubic centimeter per minute) flow of Ar was used as the bombarding gas. A deposition rate of 0.8 Å/s was achieved by applying 250 W to the Al target (EJTALXX501A2, Kurt J. Lesker Co.; 99.999%, 1.00" diameter \times 0.125" thickness). The time required to deposit 50 nm films was initially calculated by depositing a film directly on to a quartz crystal microbalance located inside a vacuum chamber exactly at the same distance from the target as the ZnSe IRE. Keeping the same conditions, the sensor was then replaced by the ZnSe crystal and deposition was done for the same time.

Preparation of Spin-coated Polymeric Films

For PVB film preparation, 1.5 g of the polymer powder was dissolved in 18.5 g of 99% methanol (Fisher Scientific) and stirred overnight with a magnetic stirrer. Polymer films were then spin-coated from the solution onto the ZnSe IREs (with and without Al films) at 200 rpm for 5 min using a spin coater (TC100, MTI Corporation) (Figure 3.2). The film thickness was determined to be approximately 10 µm as found by a thickness gauge (Elcometer 456, Elcometer; standard used 49.8 µm). The samples were allowed to dry overnight in an evacuated desiccator to let the methanol evaporate. The PVB samples were then exposed in the setup to ozone, RH and UV-B whereas the PVB/Al samples were exposed to DI water followed by acquisition of ATR-FTIR spectra. Background spectra were obtained for both samples before film deposition and after film preparation before exposure. For the Eponol film preparation, the viscous resin was diluted with a 75/25 wt% solution of methyl ethyl ketone and propylene glycol methyl ether followed by overnight stirring. Thin films were then spin cast from the solution onto a ZnSe IRE (previously coated with a 50 nm Al film) using the above-mentioned spin coater at 120 rpm for 5 min, which generated a film thickness of 8-9 µm as measured by a surface profilometer (Dektak 3, Veeco). The samples were cured at 160°C for 12 hrs to ensure complete evaporation of the solvents and

were then exposed to DI water for acquiring ATR-FTIR spectra. Double distilled DI water was used for all experiments.

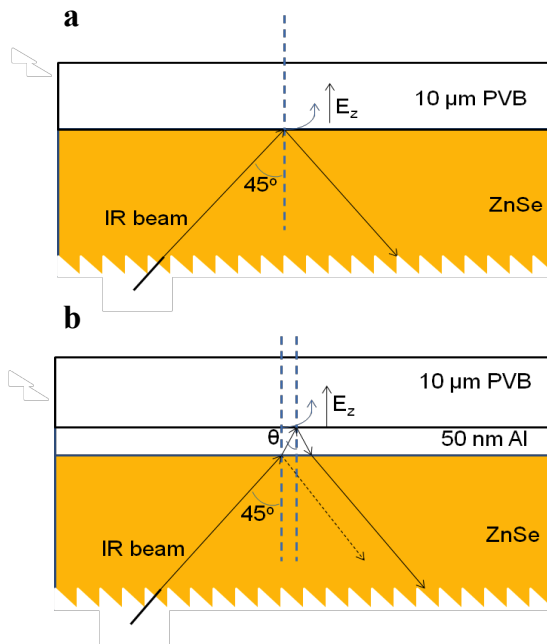


Figure 3.2. Schematic representation showing the total internal reflection of the IR beam and the generation of evanescent waves in the (a) PVB/ZnSe and (b) the PVB/Al sample configuration.

Exposure Setup

Exposure of the PVB samples were carried out in a custom-built setup, designed and constructed by Severine Cambier (Frankel Lab, Department of Materials Science and Engineering, OSU), that allowed the passage of optimum levels of ozone, moist air and UV-B radiation through a cell housing the sample. Figure 3.2 provides a schematic representation of the entire exposure setup. The setup consists of four major parts: the humid air generator, the ozone generator, the sample cell and the UV-B lamp. The humid air generation system uses a nitrogen cylinder to bubble nitrogen gas through two wash bottles filled with DI water. A by-pass around the wash bottles is used to mix dry nitrogen with the humid one in proportions required to maintain the desired humidity level, as given by a hygrometer (model 610, Testo) placed inside the cell. For the ozone generation system, dry oxygen gas from a cylinder is passed through an ozone generator (model 600, Jelight) and the emitted ozone concentration is determined with the help of an ozone monitor (model 465L, Teledyne Instruments,) placed at the end of the setup. The ozone level is controlled by changing the oxygen flow rate using a mass flow controller (Omega FMA5400/5500). The humid air and ozone flows are merged and directed into a leak proof glass cell with a quartz (UV transparent) cover housing the samples. The cell is placed directly under a UV-B Hg lamp (USHIO G15T8E) (Figure 3.3). The distance between the sample surface and the lamp was approximately 15 cm. For all the experiments, a 90% relative humidity (RH) was maintained by combining humid air at a flow rate of $\sim 3.7 \times 10^4 \text{ cm}^3/\text{hr}$ with dry air at a rate of $\sim 5.7 \times 10^3 \text{ cm}^3/\text{hr}$, whereas to obtain a 0.1 ppm (100 ppb) of ozone, the oxygen flow rate

employed was $\sim 1.1 \times 10^4 \text{ cm}^3/\text{hr}$. A total flow of $\sim 4.8 \times 10^4 \text{ cm}^3/\text{hr}$ was passed through the cell per hour.

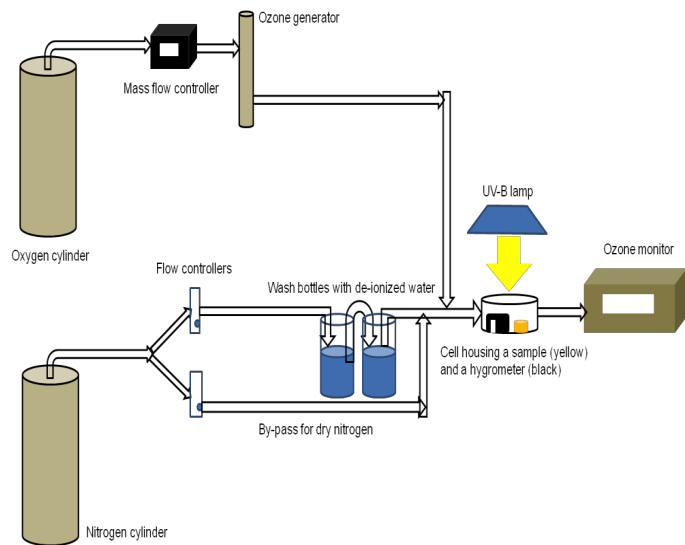


Figure 3.3. Schematic representation of the exposure setup (constructed by S. Cambier, Frankel Lab, Dept. of Material Sciences and Engineering, OSU).

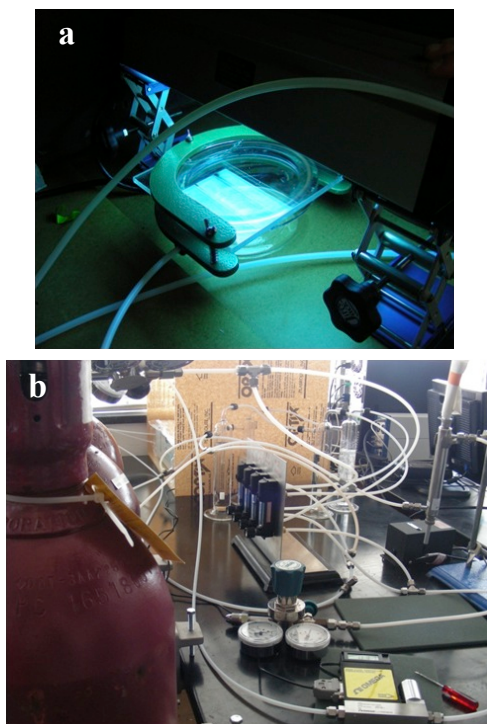


Figure 3.4. (a) Sample in the cell being exposed to UV-B radiation, (b) Ozone and humid generation systems (courtesy of S. Cambier, Frankel Lab, Dept. of Material Sciences and Engineering, OSU).

ATR-FTIR Spectroscopy

A Thermo Nicolet FTIR spectrometer (Avatar 370, Thermo Electron Corporation) that uses a DTGS detector was employed for the ATR-FTIR experiments. A 45° single bounce ZnSe internal reflection element (7002-402, Smiths Detection Ltd.; 20 mm diameter × 3 mm thickness) trough ATR accessory (Smart SpeculATR, Thermo Electron Corporation) was used to collect the spectra at a spectral resolution of 4 cm⁻¹. The spectra were averaged over 400 and 128 scans (as specified below respective spectra).

3.6 Results and Discussion

Degradation of Poly(vinyl butyral) upon Exposure to Ozone, UV Radiation, and Humidity

Exposure of PVB Films to Ozone, UV Radiation, and Moisture

With the aim of understanding the degradation pathways of PVB, the PVB-coated ZnSe crystals were exposed to 90% RH, 0.1 ppm ozone and UV-B radiation for 72 hrs. Figure 3.5 shows the physical appearance of the PVB film before and after exposure, respectively. It is clear that the exposed sample appears different from the unexposed one and shows numerous defects across the polymer surface.

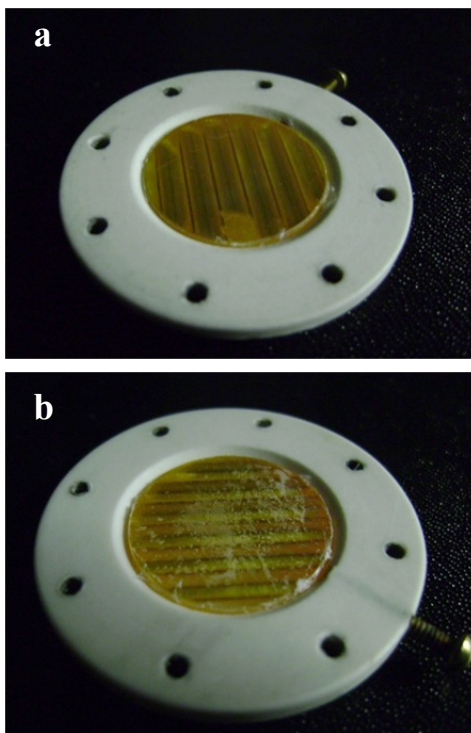


Figure 3.5. PVB film on a ZnSe IRE (a) *before* exposure to 0.1 ppm ozone, 90% RH and UV-B light and (b) *after* exposure to 0.1 ppm ozone, 90% RH (nitrogen) and UV-B light for 72 hrs.

Before beginning with the exposure experiments, an ATR-FTIR spectrum of PVB spin-coated on a ZnSe IRE was collected (Figure 3.6). The pure ZnSe crystal was used as the background. The absorption peak at 1000 cm^{-1} can be attributed to the C-OH stretching vibration of PVB. The peaks at 1140 cm^{-1} and lower frequencies primarily correspond to the C-O-C backbone, while those in the range $1250\text{--}1735\text{ cm}^{-1}$ are due to C=O vibrations and the alcoholic O-H deformation modes of the polymer. The bands in the range $2800\text{--}3000\text{ cm}^{-1}$ are assigned to symmetric and asymmetric C-H bond stretches. The O-H stretching modes of the OH moieties of the polymer can be seen at 3450 cm^{-1} .⁵¹ However, the broad band shape of the 3450 cm^{-1} peak indicates a certain degree of hydrogen bonding between the O-H moieties within the polymer chains. The broad shape is attributed to different hydrogen bonding environments, for example, a hydroxyl group bonded to two hydrogen bonds will vibrate at a higher frequency than that bonded to three hydrogen bonds. Because of these different environments, there is a distribution of intensities in the frequency range $3000\text{--}3700\text{ cm}^{-1}$. Free O-H groups resonate at the same frequency. Hence, the absence of hydrogen bonding is characterized by narrow/sharp peaks.⁵²

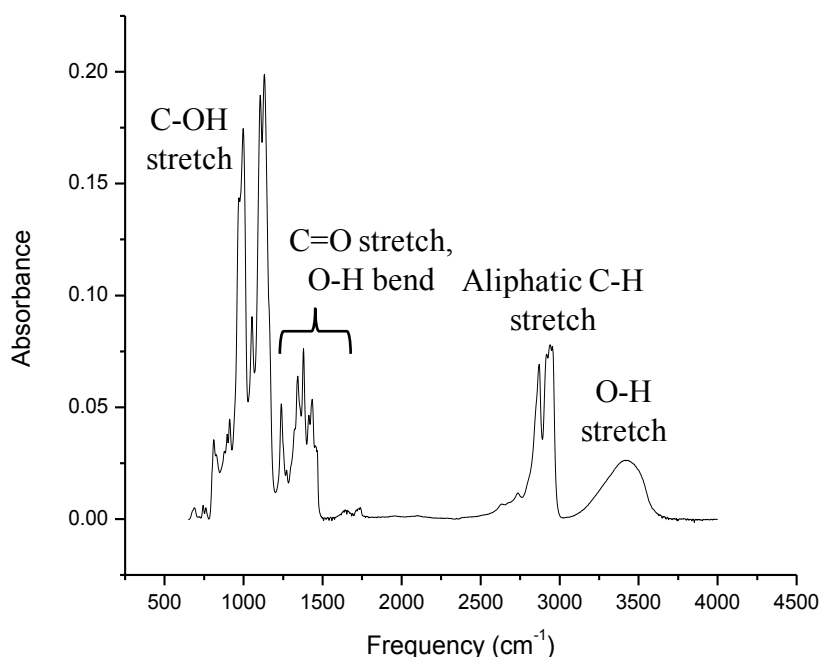


Figure 3.6. ATR-FTIR spectra of PVB spin-coated on a ZnSe IRE. The pure ZnSe IRE was used as the background. The spectrum is averaged over 400 scans.

Figure 3.7 shows the ATR-FTIR spectra of PVB before and after the above mentioned conditions. The pure ZnSe crystal was used as the background. As can be seen, there are four prominent changes in the spectrum before and after exposure. Firstly, the absorption peak at 3450 cm^{-1} was found to increase in intensity. This is due to the ingress of water into the polymer matrix.⁵³ However, there may be contribution from water formed within the polymer due to the

exposure since it is known to be a degradation product of PVB generated by dehydration of the vinyl alcoholic groups of the polymer.⁵⁴ Secondly, there is an increase in the 1640 cm^{-1} peak intensity. This is due to the O-H deformation mode of water. Again, there may be contribution from C=C vibrations because dehydration of the alcoholic groups leads to the formation of double bonds in the polymer chain. Butenal is also known to be a degradation product of PVB.⁵⁴ The OH bending modes of alcohols appear in the region 1420–1330 cm^{-1} .⁵⁵ This shows that exposure to 90% RH for 72 hrs leads to incorporation of water in the PVB film in close proximity to the PVB/substrate interface (since the evanescent field penetration depth is about 300 nm at 3450 cm^{-1} for the PVB/ZnSe interface) as well as generation of water as a degradation product. Thirdly, the inset of Figure 3.7 also shows the appearance of an absorption band at about 1580 cm^{-1} . This is likely due to all the carboxylate species that are generated in the polymer matrix after oxidation by ozone and requires further investigation.⁵⁵

Finally, there was an increase in intensity of the absorption peak at 1735 cm^{-1} , which is attributed to the C=O stretching mode.⁵⁶ Again, this change can be prominently seen in the inset figure, which zooms on the 1500–1800 cm^{-1} region. This hints to a structural change in the polymer film upon exposure to the combination of ozone, humidity, and UV-B radiation. Also, the fine structure superimposed on the absorption bands can be attributed to the rotational transitions of water molecules in the vapor phase. IR radiation has sufficient energy to excite rotational transitions whose energies are much smaller than that of vibrational transitions. As a matter of fact, rotational levels are significantly populated even at room temperature ($k_B T \approx 200 \text{ cm}^{-1} >$ rotational energy levels).

Water Uptake Kinetics in Degraded vs. Non-Degraded PVB Films

To understand if such an exposure had an effect on the physical structural organization of the polymer film, the degraded PVB sample was dried overnight to drive all of the excess water away and then exposed to DI water with the aim of monitoring the water uptake kinetics using ATR-FTIR spectroscopy. This was compared with the water uptake by an unexposed PVB sample, which was dried overnight as usual (to drive the excess methanol away). The aim was to see if the degraded polymer became less resistant to water compared to the intact polymer. Figure 3.8 shows the ATR-FTIR spectra of the degraded and non-degraded PVB samples in contact with DI water within 5 min of exposure. The pure ZnSe was taken as the background. As can be seen from the intensities (peak areas) of the 3450 and 1640 cm^{-1} absorption peaks, the degraded sample shows a significantly greater water uptake than the intact polymer. On the other hand, the absorption bands corresponding to C-H, C-OH, C-O-C stretch intensities were found to decrease for the degraded sample compared to the non-degraded one. The reason for this is probably swelling of the polymer film upon ingress of water. Due to structural degradation, the exposed sample now allows large amounts of water to enter the polymer matrix and reach the polymer/ZnSe interface. Hence, there is a significant decrease in the density of the macromolecular structure within the probing depth of the evanescent field. As this was not or hardly observed for the unexposed sample, the effect has to be attributed to structural changes of the polymer after exposure to ozone, humid air, and UV-B radiation.

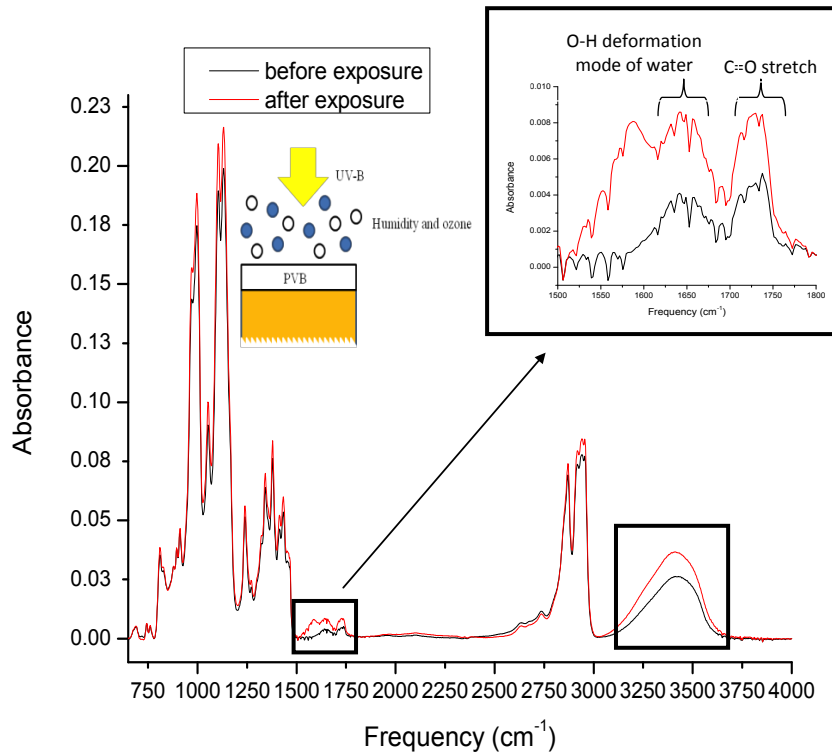


Figure 3.7. ATR-FTIR spectra of PVB spin-coated on a ZnSe IRE before and after exposure to 0.1 ppm ozone, 90% RH and UV-B (310 nm) radiation for 72 hrs. The pure ZnSe IRE was used as the background for both spectra. Each spectrum is averaged over 400 scans. The inset shows the same spectrum zoomed in the region $1500\text{--}1800\text{ cm}^{-1}$ to show the intensity increase in both C=O stretch and O-H deformation modes.

To understand the kinetics of water uptake through both the samples after the first spectrum was collected within 2 min of exposure, ATR-FTIR spectra were collected every 5 min for 2 hrs. Figure 3.9 shows the ATR-FTIR spectra of the degraded PVB sample upon exposure to DI water taken every 5 min over a period of 2 hrs. The ATR-FTIR spectrum of the PVB collected within 2 min of exposure to water was used as the background. Hence, the observed changes are only due to ingress of water in the film and there are no polymer bands visible. From the spectra, it can be seen that the degraded polymer gets saturated with water within the first 20 min of exposure. To understand better, the absorbance at 3450 cm^{-1} is plotted as a function of exposure time in Figure 3.10. As can be seen, the absorbance shows an abrupt increase from 0.1009 to 0.119 and remains almost constant (0.12) over the remaining exposure period. For the unexposed sample, the water uptake is much more gradual compared to the degraded PVB film (Figure 3.11). Here also, the ATR-FTIR spectrum of the intact polymer collected within 2 min of exposure to water was used as the background. The absorbance values were found to increase slowly but steadily from approximately 0.026 to 0.0641 over the span of 2 hrs as shown in Figure 3.12 but the polymer was not saturated in the investigated time period. This indicates that there has been deterioration in the water resistive properties of the film after exposure to ozone, humidity and UV-B radiation in a way that the PVB/ZnSe interface gets saturated within 20 min of exposure.

Also, the absorbance values are almost 4 times higher for the degraded sample, again due to a greater water uptake compared to the intact polymer. Exposure to ozone, humidity and UV-B radiation may have led to the formation of numerous cracks and pores in the polymer matrix leading to enhanced ingress of water through them to the PVB/ZnSe interface.

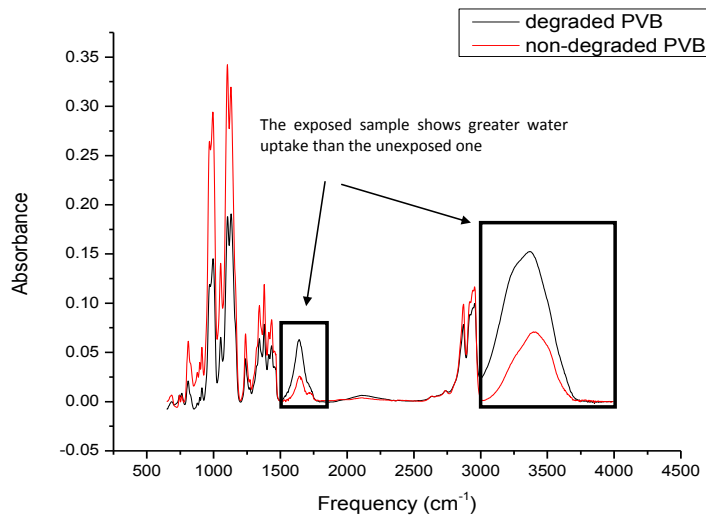


Figure 3.8. ATR-FTIR spectra of the degraded and non-degraded PVB samples in contact with DI water within 5 min of exposure, using pure ZnSe as background and averaged over 128 scans.

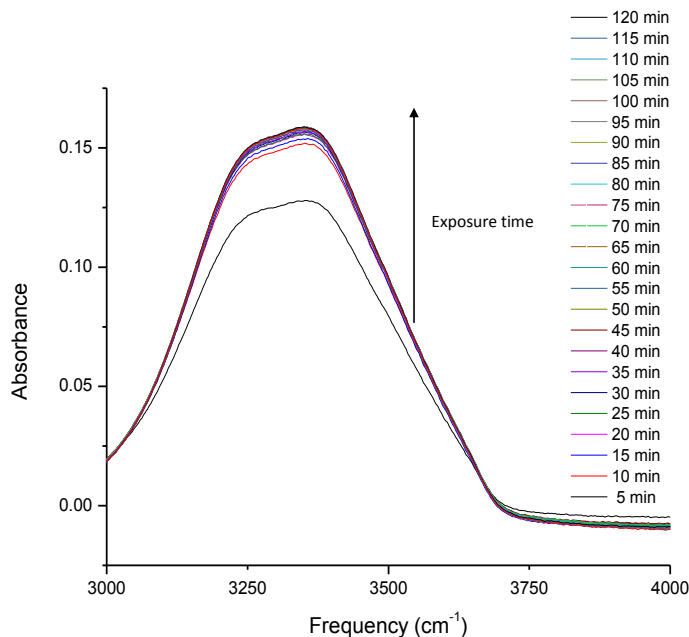


Figure 3.9. ATR-FTIR spectra of the degraded PVB sample showing abrupt water uptake upon exposure to DI water over a period of 2 hrs. The degraded polymer was used as the background after drying in a desiccator for 48 hrs. Each spectrum is averaged over 128 scans.

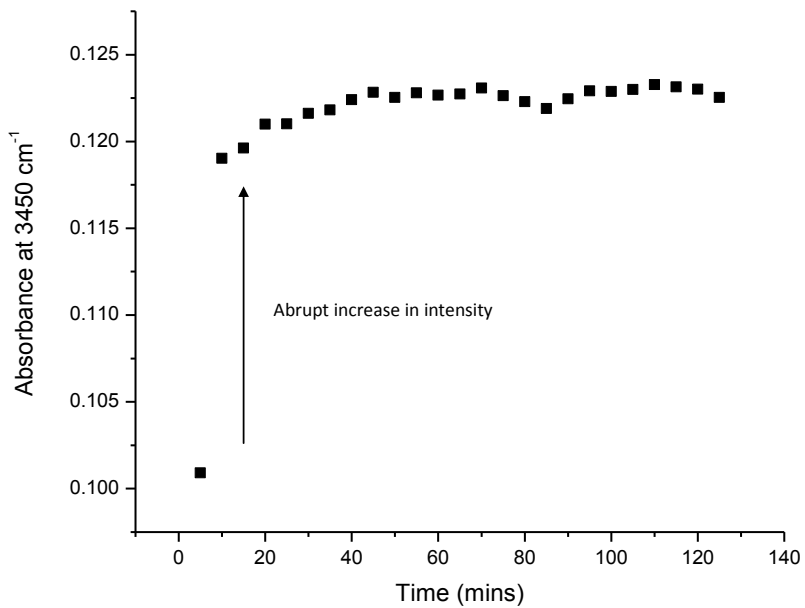


Figure 3.10. IR absorption intensities at 3450 cm^{-1} vs. exposure time for the degraded PVB film spin-coated on a ZnSe IRE in contact with DI water.

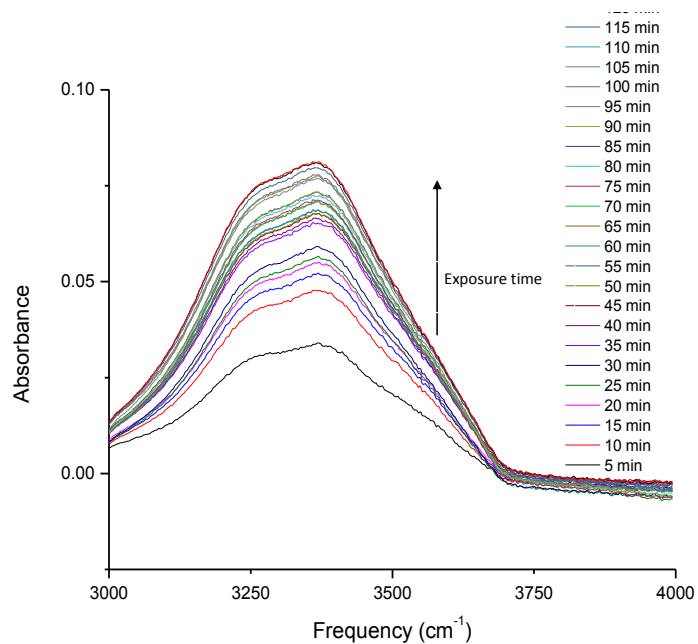


Figure 3.11. ATR-FTIR spectra of the non-degraded PVB sample showing gradual water uptake upon exposure to DI water over a period of 2 hrs. The dry polymer was used as the background. Each spectrum is averaged over 128 scans.

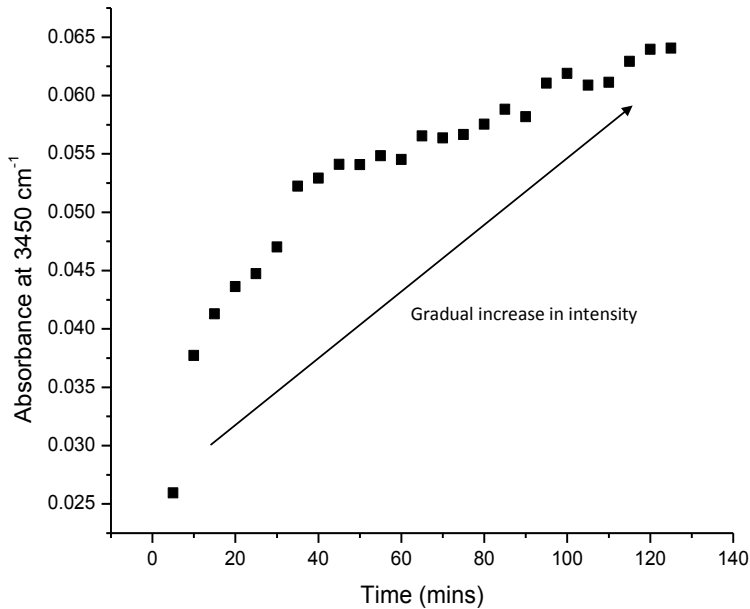


Figure 3.12. IR absorption intensities at 3450 cm^{-1} vs. exposure time for the non-degraded PVB film spin-coated on a ZnSe IRE in contact with DI water.

Exposure to UV and Moisture

To verify if ozone is responsible for the structural changes in the PVB film, a PVB film spin-coated on ZnSe was then exposed to 90% RH and UV-B only. Figure 3.13 shows the corresponding ATR-FTIR spectra before and after exposure. The pure ZnSe crystal was used as the background for both spectra. First, only a slight increase in O-H stretch intensity is observed which is due to water transport to the PVB/ZnSe interface. The presence of water is also evident from an increase in the 1645 cm^{-1} peak intensity, which is attributed to the water O-H deformation mode. To understand this better, the spectra have been zoomed in the $1500\text{--}1800\text{ cm}^{-1}$ region as shown in the inset of Figure 3.13. It is interesting to note that the increase in the O-H stretch band is almost negligible and much smaller than that observed when PVB was exposed to ozone, humidity and UV-B radiation. This indicates that for the sample exposed to all the three agents, the increase in the O-H stretch peak was not contributed by the external water alone. In that case, the sample exposed to moisture and UV-B should have shown a similar change in the O-H stretch intensity. This however supports the fact that water is indeed generated as a degradation product when the sample is exposed to all the three agents and hence, accounts for the observed difference in the intensities of the OH band for the samples exposed to different sets of parameters.

Second, there was no change in the $\text{C}=\text{O}$ stretch intensity at 1735 cm^{-1} as seen from the inset of Figure 3.13. Again, the observed fine structure is due to the rotational transitions of the gaseous water molecules excited by the IR energy. It is important to recall that nitrogen gas is used to generate the humid air and there was no source of oxygen (atomic or molecular) for this exposure. So, this proves that an oxygen (atomic or molecular) source is required to bring about structural degradation of PVB.

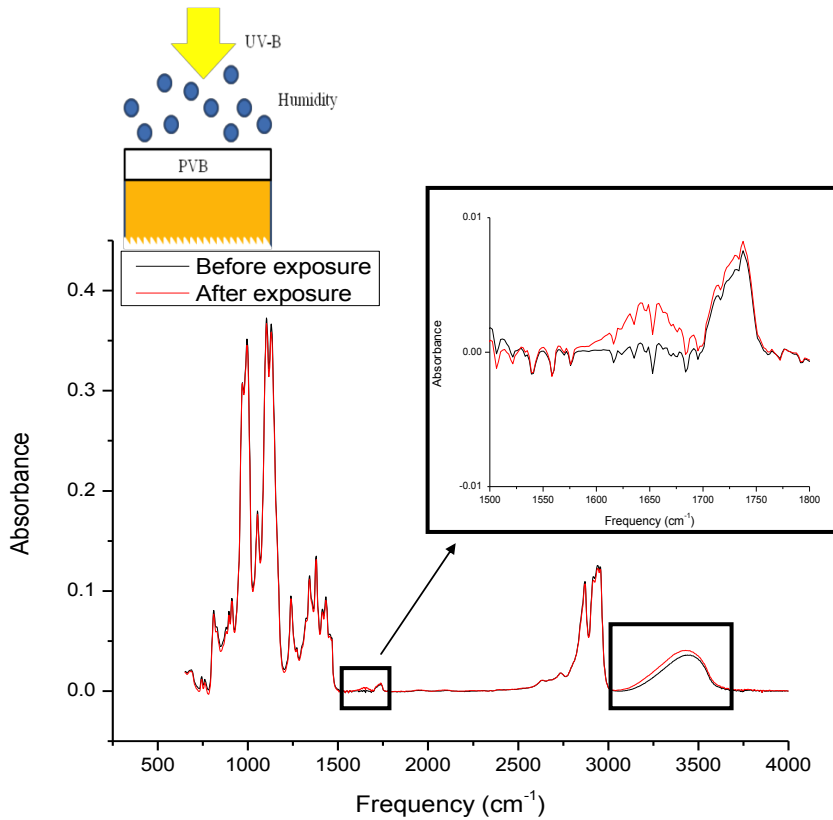


Figure 3.13. ATR-FTIR spectra of PVB spin-coated on a ZnSe IRE before and after exposure to 90% RH and UV-B (310 nm) radiation for 72 hrs. The pure ZnSe IRE was used as the background for both spectra. Each spectrum is averaged over 400 scans. The inset shows the same spectrum zoomed in the region 1500–1800 cm⁻¹ to show the intensity increase in the O-H deformation mode only.

Water Uptake by Polymer-coated Aluminum: Stability of Al/Polymer Interfaces

Water Uptake by PVB-Coated Aluminum

To investigate the response of the PVB/Al interfacial zone to water, samples described above were exposed to DI water. Figure 3.14 shows the corresponding ATR-FTIR spectra at different exposure times. The background spectrum was collected from the dry sample before exposing it to water and is represented by the horizontal line at zero absorbance. Hence the spectral features indicate only the changes occurring at the PVB/Al interface upon exposure to water. As can be seen from the spectra, a broad and strong band appeared between 3000 and 3700 cm⁻¹, with a maximum at around 3450 cm⁻¹ and continued to grow as a function of exposure time. This peak is attributed primarily to both symmetric and asymmetric OH stretching vibrations of water molecules although there may be minimal contributions from OH stretching due to aluminum hydroxide formation at the interface.^{22,31} The increase in peak area indicates that the evanescent field generated at the PVB/Al interface encounters more and more water molecules within its reach with increase in exposure time and also possibly formation of Al hydroxides at the probed interface. It is known that water is capable of displacing the weaker polymer-metal interactions

with stronger water-metal oxide/hydroxide bonds (40-65 kJ/mol) at the interface, the process being thermodynamically favored.⁴⁰ The band at 1650 cm^{-1} can be assigned to the deformation mode of water molecules while those at and below 1100 cm^{-1} are attributed to contributions from other water modes and Al corrosion products. It is known that various Al-O and Al-OH modes appear in the region $850\text{--}1100\text{ cm}^{-1}$.⁶⁰ These can be a mixture of OH bending vibrations and twisting of AlOOH and also, Al-O vibrations of Al_2O_3 .³¹ With increase in exposure times, a small but sharp peak appeared at about $980\text{--}1000\text{ cm}^{-1}$. The inset in Figure 3.14 shows that this peak actually grows with time and is assigned to the longitudinal stretching vibrations of Al-O²² indicating that ingress of water at the PVB/Al interface corrodes the Al thin film beneath the PVB layer. This peak is also observed when a 50 nm Al film (without PVB) is exposed to DI water for 5 hrs (Figure 3.15). The Al film before exposure was used as the background. Other Al-O/Al-OH modes are also visible in the $850\text{--}1200\text{ cm}^{-1}$ region in addition to the obvious water peaks at 3400 and 1640 cm^{-1} . The negative peak at around 2350 cm^{-1} is due to a decrease in CO_2 within the probing depth of the evanescent field upon exposure to water.

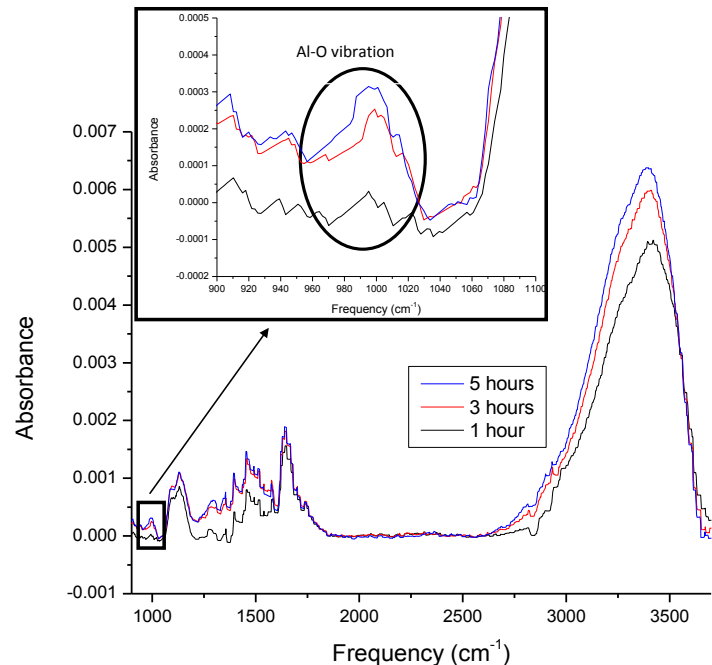


Figure 3.14. ATR-FTIR spectra of a ZnSe IRE sputter-coated with a 50 nm Al film and a $10\text{ }\mu\text{m}$ PVB film in contact with DI water with the dry sample before exposure as background. The exposure times were 1, 3 and 5 hrs respectively. Each spectrum is averaged over 400 scans.

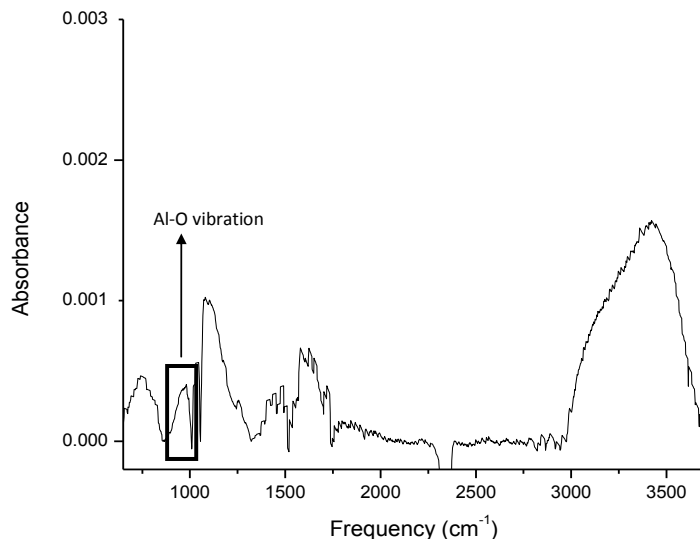


Figure 3.15. ATR-FTIR spectrum of a ZnSe IRE sputter-coated with a 50 nm Al film in contact with DI water for 5 hrs with the dry sample before exposure as background and averaged over 400 scans.

The OH stretch band ($3000\text{--}3700\text{ cm}^{-1}$) shape is highly indicative of the physical state of water incorporated at the PVB/Al interface. It is well known that water confined in a hydrophilic polymer behaves differently than water in bulk liquid phase due to interactions of water molecules with the polar groups of the polymer leading to their restricted motion, either directly or through other water molecules.⁶¹ Water has been found to exist in the form of clusters, chains and dimers etc. in hydrophilic polymers.⁵³ Water might also be incorporated in the porous oxide/hydroxide film at the interface. To understand how this compares with the pure water structure, the ATR-FTIR spectrum of DI water (OH stretching region) along with its calculated fit including the component peaks is depicted in Figure 3.16. The overall spectrum could be fitted using three Gaussian peaks. In accordance with the generally accepted assignments,⁶² the component peak at about 3200 cm^{-1} can be attributed to the strong intermolecular coupling of water molecule symmetric stretch modes within a symmetric hydrogen bonding environment. The peak at about 3400 cm^{-1} is due to the weaker interactions of water stretching vibrations associated with a more distorted hydrogen bonding network. The peak at about 3510 cm^{-1} is assigned to the coupling of the asymmetric stretching vibrations of the water molecules. The fitting result for water incorporated at the PVB/Al interface is shown in Figure 3.17. Similar to pure water, water trapped at the PVB/Al interface can also be fitted using the three Gaussian peaks described above. Tables 2.1 and 2.2 give the fitting parameters for pure water and water in the PVB film, respectively. As can be seen from the difference in band shape of the two spectra, there is an increased contribution from the weakly hydrogen-bonded water molecules (peak at 3400 cm^{-1}) relative to the strongly bonded ones (3200 cm^{-1}) in the polymer than in pure water. Such an observation can be attributed to the breaking of the water network upon entering the polymer matrix and the weaker hydrogen bonding of water molecules to the polymer functional groups (polar sites), although the details of the electronic perturbation of the water molecules due to PVB is difficult to infer with this information.

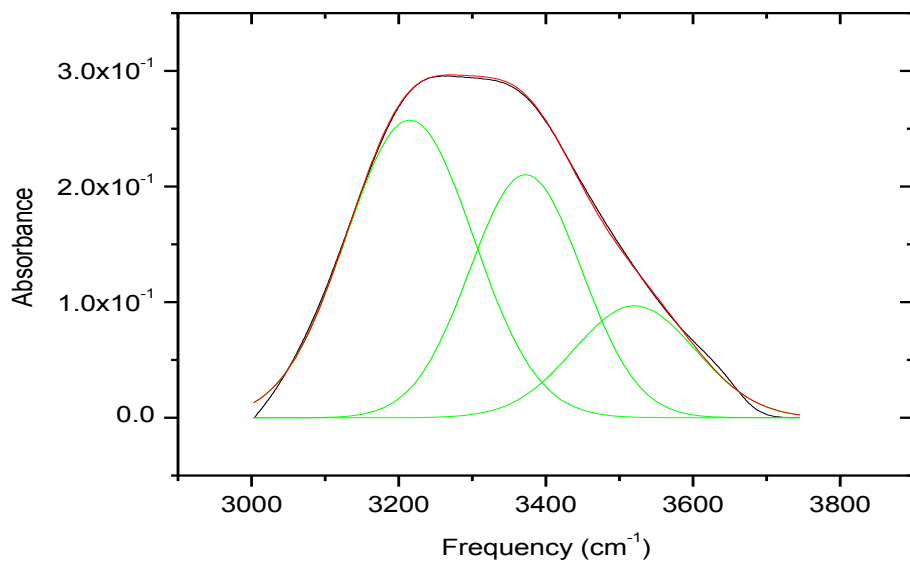


Figure 3.16. Peak fitting of the OH stretching region of pure DI water. The pure ZnSe was used as the background and averaged over 400 scans.

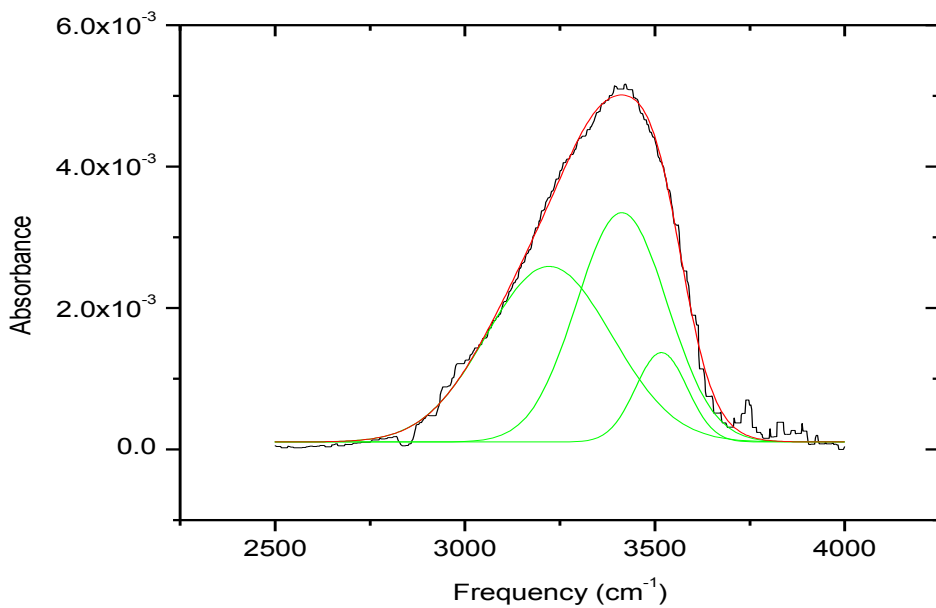


Figure 3.17. Peak fitting of the water OH stretching region from the 1 hr water exposed PVB/Al sample.

Table 3.1 Gaussian fit parameters for the pure water OH stretching region.

Peak	Peak Area	Peak Center (cm ⁻¹)	Peak Height	FWHM (cm ⁻¹)
1	55.5743	3214.9	0.25735	204.36
2	40.1993	3372.5	0.21012	179.73
3	20.0390	3520.5	0.09677	195.18

Table 3.2 Gaussian fit parameters for PVB confined water OH stretching region.

Peak	Peak Area	Peak Center (cm ⁻¹)	Peak Height	FWHM (cm ⁻¹)
1	1.03023	3221.4	0.00248	389.78
2	0.97111	3413.1	0.00324	281.29
3	0.21646	3517.2	0.00126	160.79

To understand the changes in the C-H stretching region (2800–3000 cm⁻¹) in more detail, the 5 hrs exposed sample was plotted using the one hour exposed sample as the background as shown in Figure 3.18. Negative peaks in the region 2850–2960 cm⁻¹ indicate that there is a decrease in C-H intensities with longer exposure to water. There can be two plausible explanations for such an observation. First, water incorporation in the polymer matrix may lead to swelling of the resin with the effect that the macromolecular structure of the polymer would be less dense within the probing depth of the evanescent wave. Second, the water reaching the interface will result in hydrolysis in wet de-adhesion processes. The polymer will partly de-adhere from the substrate and in that case, the absorption bands would be negative with respect to the intact interface.^{22,27,40} However, it is not possible to distinguish between swelling and delamination using ATR-FTIR data. Delamination and swelling effects are even more prominent when a ZnSe IRE spin-coated with a 10 μm PVB film only is exposed to DI water (Figure 3.19). The C-H region has been zoomed in the inset of that figure.

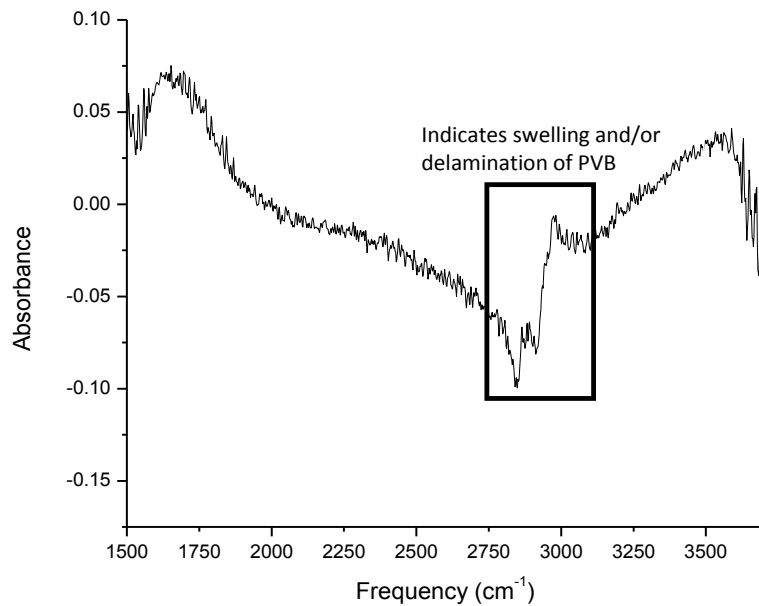


Figure 3.18. ATR-FTIR spectrum of a ZnSe IRE coated with 50 nm Al and PVB exposed to DI water for 3 hrs with the same sample exposed for 1 hr used as the background. The spectrum is averaged over 400 scans.

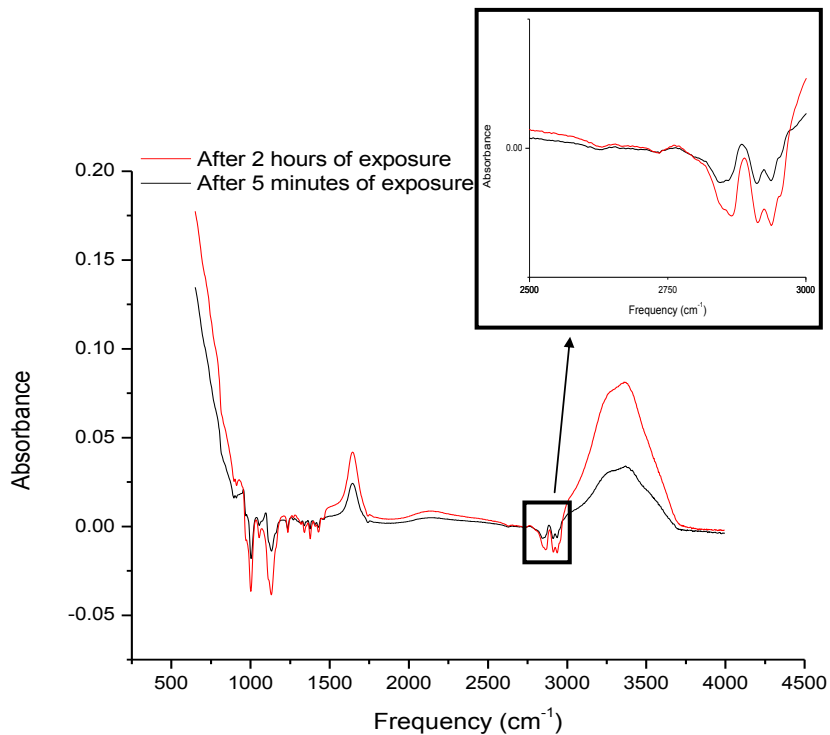


Figure 3.19. ATR-FTIR spectra of a ZnSe IRE spin-coated with a 10 μm PVB film in contact with DI water with the dry sample before exposure used as background. The exposure times shown are 5 min and 2 hrs. Each spectrum is averaged over 400 scans.

Water Retention at the PVB/Al Interface

After the water exposure experiments were concluded, both the PVB and PVB/Al samples were stored in an evacuated desiccator for over 48 hrs until they appeared visually dry. Then, ATR-FTIR spectra were collected using these dried samples to see if water could still be detected at the corresponding interfaces (Figure 3.20). The respective dry sample data before exposure were used as the background. While the PVB sample showed no trace of water, an appreciable OH stretch band was still observed for the PVB/Al sample. This means that although PVB lost most of the water absorbed during exposure reversibly, a significant amount of water was trapped at the PVB/Al interface. It indicates that the now hydrophilic Al surface seems to be responsible for such water retention. Extensive research on aluminum surfaces has revealed the complex nature of such surfaces.⁶⁴⁻⁶⁶ On an Al surface, a thin layer of oxide is always spontaneously formed in contact with air.³⁰ It is known that native surface layers on Al are made up of an anhydrous inner layer of amorphous Al₂O₃ covered by a hydrated outer layer, the latter being extremely important for the adhesion properties of the metal.⁶⁷ α -Al₂O₃ (corundum) and γ -Al₂O₃ are known to be the common Al oxides. The oxy-hydroxides include α -AlO(OH) (diaspore) and γ -AlO(OH) (boehmite), while bayerite, gibbsite and nordstrandite are the three forms of hydroxides formed. In contact with water, hydroxyl functionalities are incorporated into either octahedral or tetrahedral sites on the crystal structure of alumina.^{30,64} The oxide layers are generally considered to be non-crystalline and porous. Investigation on the nature of the oxide film on Al has revealed that the composition of the oxide ranges from anhydrous to trihydroxide, depending on the temperature and pressure at which it was formed. It is known that films grown in the range 20–90°C exhibit a duplex structure consisting of an inner layer of a porous structure of pseudoboehmite (or poorly crystalline boehmite) and an outer layer of large bayerite crystals.⁶⁷ This is the temperature range relevant for the present study. It is known that boehmite is composed of layers of edge shared AlO₆ octahedra with terminal hydroxyl groups.⁶⁸ This oxide/hydroxide layer might differ morphologically when under a polymer layer but is still responsible for making the metal surface hydrophilic. Also, it is known that on a metal oxide/hydroxide surface, a water monolayer would spontaneously bond with the surface hydroxyl groups by replacing the weaker polymer-oxide/hydroxide linkages. Probably, such a surface structure is responsible for retaining water molecules at the interface by formation of hydrogen bonding as envisioned in Figure 3.21.

Water Uptake by Eponol-coated/Al Interface

It is interesting to compare the stability of the PVB/Al interface to water with that of a second polymer. Epoxy polymers are known to exhibit high adhesion and a good resistance to heat and chemicals. Hence, an epoxy polymer based on diglycidyl ether of bisphenol A (DGEBA) was chosen for the purpose. It can be synthesized by reaction of bisphenol A and epichlorohydrin.⁶⁹ Different components in the structure are known to perform specific functions to improve the resin's performance, for example, the polar –OH groups enhance adhesion with the substrate, while the chain length determines the flexibility of the polymer.⁶⁹ Commercially, the resin comes in a blend of solvents, methyl ethyl ketone and propylene glycol methyl ether (75:25 wt.%) and has the name Eponol resin 53 BH 35.

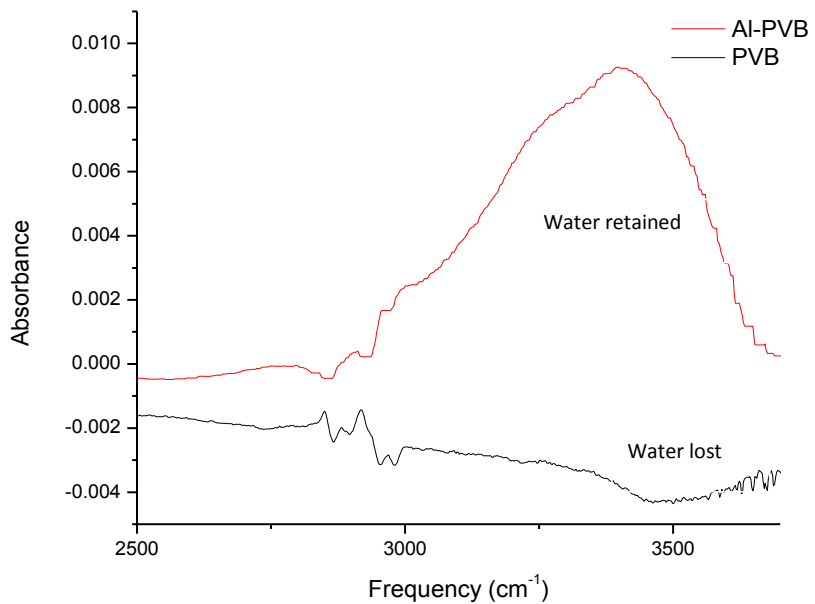


Figure 3.20. ATR-FTIR spectra of both PVB and PVB/Al samples dried over 48 hrs after the water exposure experiments, using the respective dry samples (before exposure) as backgrounds. Each spectrum is averaged over 400 scans.

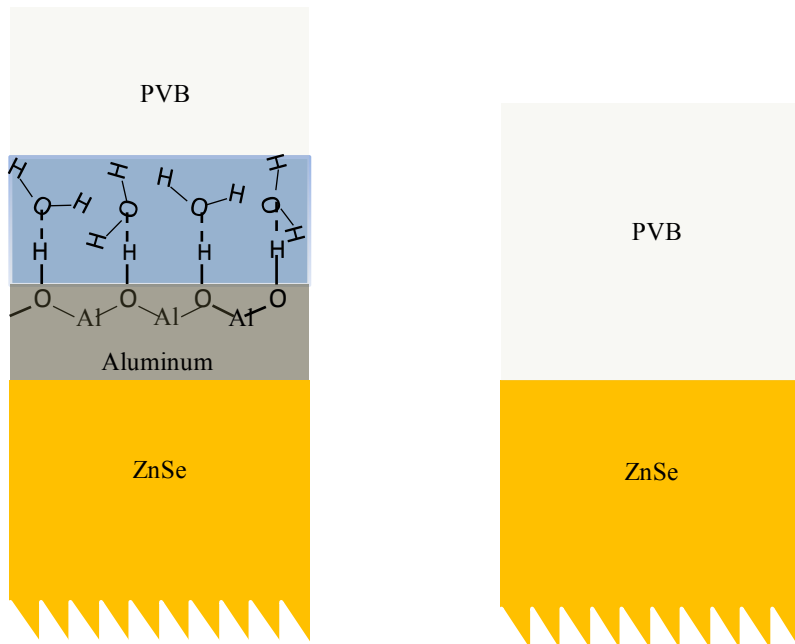


Figure 3.21. Schematic of the possible interactions of water molecules with the Al oxide/hydroxide film at the PVB/Al interface. PVB (right) loses water completely after drying.

Similar to the PVB/Al samples, an Eponol-coated Al/ZnSe sample was exposed to DI water. The resulting changes of the Eponol/Al interface structure were monitored with time. The corresponding ATR-FTIR spectra are shown in Figure 3.22. The dry sample before exposure was used as the background. The increase in intensity of the OH peak in the region 3000–3700 cm^{-1} indicates that more water was present at and near the Eponol/Al interface because the penetration depth of the evanescent wave at the Eponol/Al interface is smaller than that at the PVB/Al interface (Figures 2.2a and b). This is further corroborated by an increase in the water OH deformation mode intensity at 1640 cm^{-1} . The peak at around 980–1010 cm^{-1} , attributed to the longitudinal Al-O modes was observed within the first hour of exposure but was found to remain almost constant over the remaining exposure period, in contrast to the PVB/Al system, where the peak was found to increase with time. The horizontal line at zero absorbance indicates the background i.e. the polymer-coated Al before exposure to DI water.

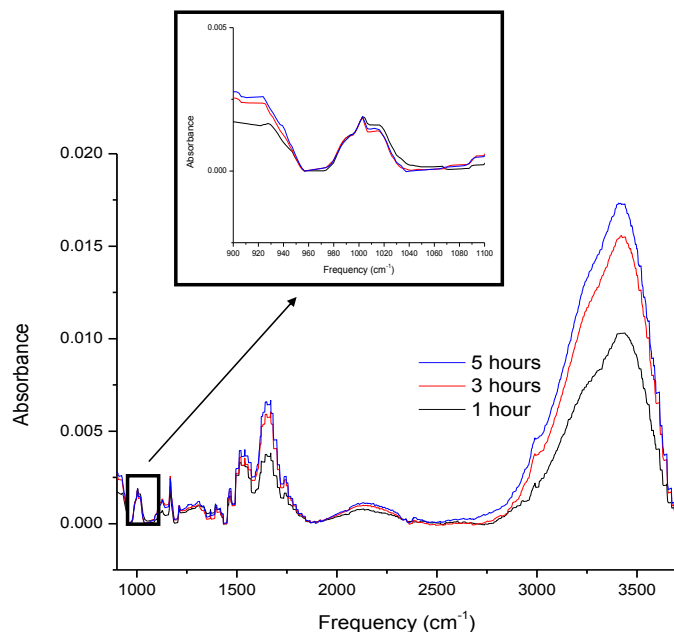


Figure 3.22. ATR-FTIR spectra of a ZnSe IRE sputter-coated with a 50 nm Al film and a 10 μm Eponol film in contact with DI water with the dry sample before exposure used as background. The exposure times were 1, 3 and 5 hrs respectively. Each spectrum is averaged over 400 scans.

Similar to the PVB/Al system, fitting results of the water OH stretching region reveal that there is an increase in water molecules residing in a weakly hydrogen bonded environment relative to that seen in pure bulk water, where the dominant contribution comes from associated (strongly hydrogen-bonded) chains of water molecules (Figure 3.23). The spectral fit parameters are given in Table 3.3.

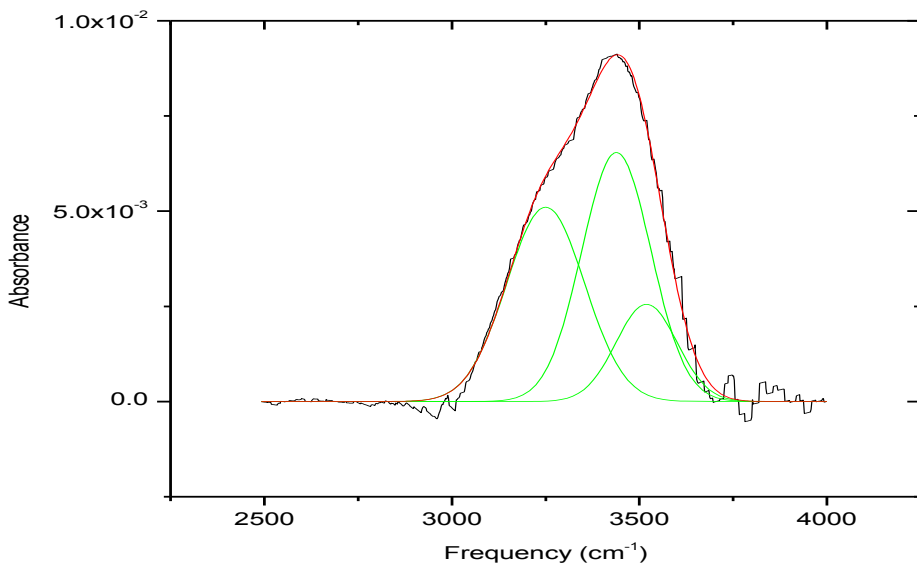


Figure 3.23. Peak fitting of the water OH stretching region from the 1 hr exposed Eponol/Al sample.

Table 3.3 Gaussian fitting parameters for Eponol confined water OH stretching region.

Peak	Peak Area	Peak Center (cm ⁻¹)	Peak Height	FWHM (cm ⁻¹)
1	1.33398	3250.1	0.0052	245.62
2	1.51372	3438.7	0.0065	217.46
3	0.52275	3519.1	0.0026	192.42

Interestingly, both aliphatic and aromatic C-H peaks were found to increase in intensity relative to the dry sample with exposure time, again, in a striking contrast to what was observed at the PVB/Al interface when exposed to water. This increase is especially prominent after the sample was exposed to water for 15 hrs. Figure 3.24 shows the corresponding ATR-FTIR spectrum. The dry sample before exposure was used as the background. Such an increase in C-H intensity was also observed when an Eponol-coated ZnSe sample (no Al) was exposed to 90% RH for 20 hrs. Figure 3.25 shows the corresponding ATR-FTIR spectrum. The dry polymer before exposure was used as the background. The reason for this observation is not fully understood but is probably related to a rearrangement of the macromolecular polymer chains within the matrix upon interaction with water molecules. It is clear that Al does not play a role in this C-H intensity increase. Although there is not sufficient data to understand the processes going on when water interacts with Eponol, it is clear that there are no swelling/delamination effects. On the basis of these observations, it can be inferred that Eponol protects the aluminum film beneath itself better compared to PVB.

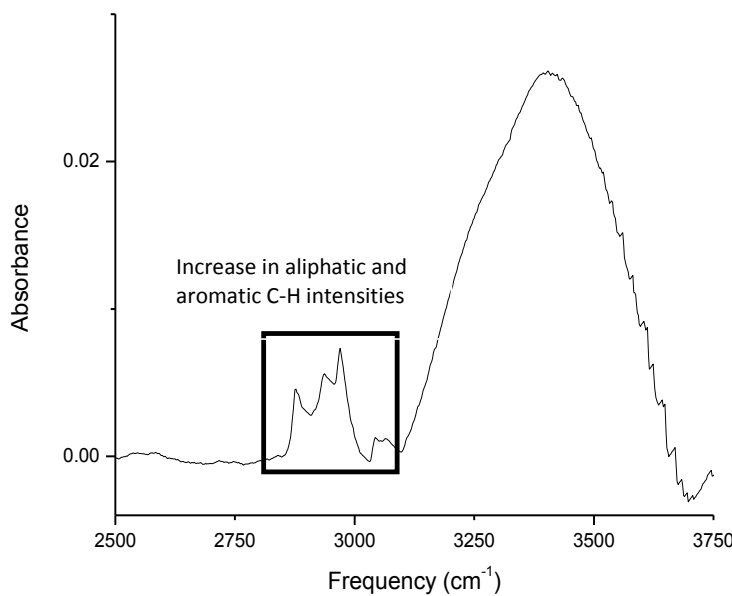


Figure 3.24. ATR-FTIR spectrum of a ZnSe IRE sputter-coated with a 50 nm Al film and a 10 μm Eponol film in contact with DI water for 15 hrs with the dry sample before exposure as background, zoomed in the region 2500–3700 cm^{-1} showing an increase in the C-H peak intensities and averaged over 400 scans.

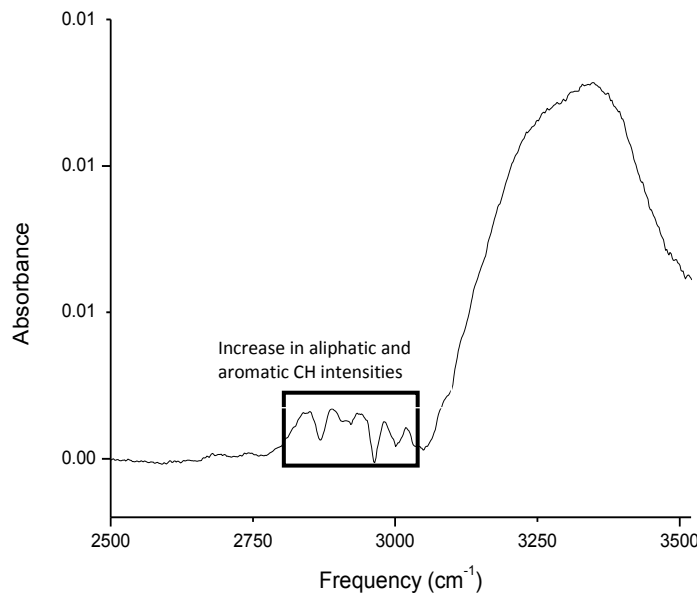


Figure 3.25. ATR-FTIR spectrum of Eponol spin-coated on ZnSe and exposed to 90% RH for 20 hrs, using the dry sample before exposure as the background. The spectrum is averaged over 400 scans.

3.7 Economic Summary

This project was started before there was an emphasis placed on economic justification of the work, so no summary is presented.

3.8 Implementation

Any implementation of ATR-FTIR spectroscopy to the investigation of buried polymer/metal interfaces will need to make use of this work to understand the link between spectroscopic changes and specific structural events in the polymer and at the interface.

3.9 Conclusions

In the first part of this study, PVB was used as the test polymer, whose degradation upon exposure to ozone, humidity and UV-B radiation was assessed employing ATR-FTIR spectroscopy. The polymer was found to structurally degrade when exposed to 0.1 ppm ozone, 90% RH and UV-B light as evident from the formation of carbonyl products, which proceeds via ring opening and chain scission. Also, the exposed PVB showed a much greater water uptake with it getting saturated within a very short time compared to its unexposed counterpart. Interestingly, there was no sign of structural degradation when the polymer was exposed to humidity and UV-B alone, without the ozone. This proves that ozone (or rather atomic oxygen formed from ozone) is required for structural deterioration of the polymer. These changes were detected at a few nanometers from the PVB/ZnSe interface within a 10 μ m PVB film.

In the second part, the response of a PVB/Al interface to water was studied *in situ* over time using ATR-FTIR spectroscopy. The interface was formed between a 10 μ m PVB film spin-coated on a 50 nm Al film. From the relevant ATR-FTIR spectra, water was found to be incorporated at the interface leading to swelling and delamination of the polymer from the Al surface. Corrosion products (Al oxide/hydroxide) were also seen to form at the interfacial region. The PVB/Al interface was also found to retain water at the interface, long after the water on the sample dried. A comparison with an epoxy resin, diglycidyl ether of bisphenol-A also forming an interface with Al gave some contrasting results. Although water was still detected at the interface, the C-H intensities were seen to increase. This is probably due to a rearrangement of the macromolecular polymer chains upon interaction with water. Corrosion products were seen to form within the first hour of exposure and remained constant throughout the remaining time.

This study is an attempt to get a better understanding of polymer degradation and the stability of polymer/metal interfaces, representing a key to improve the durability of adhesively bonded structures. However, extensive research is required to gain a thorough insight into the physical and chemical mechanisms responsible for the failure of coatings. Quantification of such degradation employing appropriate mathematical models would be equally helpful. For example, a useful study can be the quantification of the absorption band at 1585 cm^{-1} observed when a PVB film is exposed to ozone, humidity and UV-B radiation that would give us the total amount of carboxylate moieties (oxidized carbon) generated due to the degradation. Again, it would be interesting to understand the extent of damage in the bulk of the polymer using transmission

FTIR spectroscopy, in tandem with the interfaces. A comparison between the two would help understand the extent of impact at different depths of the polymer film which may shed light on the mechanistic aspects of such degradation. Moreover, the approach should be extended to multilayer structures of polymers and other aggressive media like SO_2 , NO_x and temperature cycling. Finally, these laboratory exposed samples should be compared to field samples for lifetime predictions of coating formulation.

3.10 References

1. Sorensen, P.A.; Kiil, S.; Dam-Johansen, K.; Weinell, C.E. Anticorrosive Coatings: A Review. *J. Coat. Technol. Res.* **6**, 135–176 (2009).
2. Fragata, F.; Salai, R.P.; Amorim, C.; Almeida, E. Compatibility and Incompatibility in Anticorrosive Painting The Particular Case of Maintenance Painting. *Prog. Org. Coatings* **56**, 257–268 (2006).
3. Deflorian, F.; Rossi, S.; Fedel, M. Organic Coatings Degradation: Comparison between Natural and Artificial Weathering. *Corrosion Sci.* **50**, 2360–2366 (2008).
4. Fedrizzi, L., Bergo, A., Fanicchia, M. Evaluation of Accelerated Aging Procedures of Painted Galvanised Steels by EIS. *Electrochim. Acta* **51**, 1864–1872 (2006).
5. Hare, C.H. Mechanisms of Photolytically Induced Degradation. *J. Protective Coatings Linings* **17**, 1–10 (2000).
6. Finlayson-Pitts, B.J.; Pitts, Jr., J.N. *Chemistry of the Upper and Lower Atmosphere Theory, Experiments and Applications*. Academic Press, San Diego, CA, USA, 2000.
7. Pospisil, J.; Nespurek, S. Photostabilization of Coatings. Mechanisms and Performance. *Prog. Polym. Sci.* **25**, 1261–1335 (2000).
8. Perrin, F.X.; Irigoyen, M.; Aragon, E.; Vernet, J.L. Artificial Aging of Acrylurethane and Alkyd Paints: A Micro-ATR Spectroscopic Study. *Polym. Degrad. Stabil.* **70**, 469–475 (2000).
9. Allen, N.S.; Parker, M.J.; Regan, C.J. The Durability of Water-borne Acrylic Coatings. *Polym. Degrad. Stabil.* **47** 117–127 (1995).
10. Lin, S.C.; Bulkin, B.J.; Pearce, E.M. Epoxy Resins. III. Application of Fourier Transform IR to Degradation Studies of Epoxy Systems. *J. Polym. Sci.: Polym. Chem. Ed.* **17**, 3121–3148 (1979).
11. Malanowski, P.; Huijser, S.; van Benthem, R.A.T.M.; van der Ven, L.G.J.; Laven, J.; de With, G. Photodegradation of Poly(neopentyl isophthalate) Part I: Laboratory and Outdoor Conditions. *Polym. Degrad. Stabil.* **94**, 2086–2094 (2009).
12. Martin, J.W.; Nguyen, T.; Byrd, E.; Dickens, B.; Embree, N. Relating Laboratory and Outdoor Exposures of Acrylic Melamine Coatings I. Cumulative Damage Model and Laboratory Exposure Apparatus. *Polym. Degrad. Stabil.* **75**, 193–210 (2002).
13. Andrade, A.L.; Hamid, S.H.; Hu, X.; Torikai, A. Effects of Increased Solar Ultraviolet Radiation on Materials. *J. Photochem. Photobiol. B* **46**, 96–103 (1998).
14. http://www.ucar.edu/learn/1_7_1.htm (last accessed on 11-4-2010)
15. <http://web.archive.org/web/20080311005238/http://homeimprovement.superpages.com/painting/do-i-need-to-use-paint-primer.html> (last accessed on 11-4-2010)

16. http://www.motochem.com/cp_06/PVB_Polyvinyl_Butyral.htm (last accessed on 11-4-2010)
17. Fernandes M.D.; Fernandes, M.J.; Hoces, P. Synthesis of Poly(Vinyl Butyral)s in Homogenous Phase and Their Thermal Properties. *J. Appl. Polym. Sci.* **102**, 5007–5017 (2006).
18. http://en.wikipedia.org/wiki/Polyvinyl_butyral (last accessed on 11-4-2010)
19. Safy El-Din, N.M.; Sabaa, M.W. Thermal Degradation of Poly(vinyl butyral) Laminated safety glass. *Polym. Degrad. Stabil.* **47**, 283–288 (1995).
20. Liau, L.C.K.; Tung, M. Kinetic Investigation of Photocatalytic Effects on Poly(vinyl butyral) Photodegradation. *Ind. Eng. Chem. Res.* **45**, 2199–2205 (2006).
21. Ohman, M.; Persson, D.; Leygraf, C. In Situ ATR-FTIR Studies of the Aluminium/Polymer Interface upon Exposure to Water and Electrolyte. *Prog. Org. Coatings* **57**, 78–88 (2006).
22. Lee, L.H. Molecular Bonding and Adhesion at Polymer-Metal Interphases. *J. Adhesion* **46**, 15–38 (1994).
23. Venables, J.D. Review Adhesion and Durability of Metal-Polymer Bonds. *J. Mater. Sci.* **19**, 2431–2453 (1984).
24. http://www.roymech.co.uk/Useful_Tables/Adhesives/Adhesive_Bond.html (last accessed on 11-4-2010)
25. <http://www.rsc.org/ebooks/archive/free/BK9780854045433/BK9780854045433-00001.pdf>, Chapter 1 Introduction to Adhesion and Adhesives (last accessed on 11-4-2010)
26. Nguyen, T.; Byrd, E.; Lin, C. A Spectroscopic Technique for In Situ Measurement of Water at the Coating/Metal Interface. *J. Adhesion Sci. Technol.* **5**, 697–709 (1991).
27. Berger, C.M.; Henderson, C.L. The Effect of Humidity on Water Sorption in Photoresist Polymer Thin Films. *Polymer* **44**, 2101–2108 (2003).
28. Sangaj, N.S., Malshe, V.C. Review Permeability of Polymers in Protective Organic Coatings. *Prog. Org. Coatings* **50**, 28–39 (2004).
29. Leygraf, C.; Graedel, T.E. *Atmospheric Corrosion*. John Wiley and Sons, New York, NY, USA, 2000.
30. Ohman, M.; Persson, D. An Integrated In Situ ATR-FTIR and EIS Set-up to Study Buried Metal-Polymer Interfaces Exposed to an Electrolyte Solution. *Electrochim. Acta* **52**, 5159–5171 (2007).
31. Thijs, H.M.L.; Remzi Becer, C.; Guerrero-Sanchez, C.; Fournier, D.; Hoogenboom, R.; Schubert, U.S. Water Uptake of Hydrophilic Polymers Determined by a Thermal Gravimetric Analyzer with a Controlled Humidity Chamber. *J. Mater. Chem.* **17**, 4864–4871 (2007).
32. Hu, D.S.G., Chou, K.J.N. Kinetics of Water Swelling and Development of Porous Structure in Ionic Poly(acrylonitrile-acrylamide-acrylic acid) Hydrogels. *Polymer* **37**, 1019–1025 (1996).
33. McIntyre, J.M.; Pham, H.Q. Electrochemical Impedance Spectroscopy; A Tool for Organic Coatings Optimizations. *Prog. Org. Coatings* **27**, 201–207 (1996).
34. Posner, R.; Giza, G.; Vlasak, R.; Grundmeier, G. In Situ Electrochemical Scanning Kelvin Probe Blister-Test Studies of the De-adhesion Kinetics at Polymer/Zinc Oxide/Zinc Interfaces. *Electrochim. Acta* **54**, 4837–4843 (2009).
35. Nazarov, A.P.; Thierry, D. Scanning Kelvin Probe Studies of Metal/Polymer Interfaces. *Electrochim. Acta* **49**, 2955–2964 (2004).

36. Hajatdoost, S.; Sammon, C.; Yarwood, J. FTIR-ATR Studies of Diffusion and Perturbation of Water in Polyelectrolyte Thin Films. Part 4. Diffusion, Perturbation and Swelling Processes for Ionic Solutions in SPEES/PES Membranes. *Polymer* **43**, 1821–1827 (2002).

37. Mura, C.; Yarwood, J.; Swart, R.; Hodge, D. Infrared-ATR Studies of the Hydration and Dehydration of Formulated PVC Films. *Polymer* **42**, 4141–4152 (2001).

38. Ohman, M.; Persson, D.; Leygraf, C. A Spectroelectrochemical Study of Metal/Polymer Interfaces by Simultaneous In Situ ATR-FTIR and EIS. *Electrochem. Solid-State Lett.* **10**, C27–C30 (2007).

39. Nguyen, T.; Byrd, E.; Bentz, D.; Lin, C. In Situ Measurement of Water at the Organic Coating/Substrate Interface. *Prog. Org. Coatings* **27**, 181–193 (1996).

40. Mirabella, F.M. *Modern Techniques in Applied Molecular Spectroscopy*. John Wiley & Sons, New York, NY, USA, 1998.

41. http://las.perkinelmer.com/content/technicalinfo/tch_ftiratr.pdf (last accessed on 11-4-2010)

42. http://www.piketech.com/technical/application-pdfs/ATR_Theory_andApplication.pdf#zoom=100% (last accessed on 11-4-2010)

43. Philippe, L.; Sammon, C.; Lyon, S.B.; Yarwood, J. An FTIR/ATR In Situ Study of Sorption and Transport in Corrosion Protective Organic Coatings I. Water Sorption and the Role of Inhibitor Ions. *Prog. Org. Coatings* **49**, 302–314 (2004).

44. Fieldson, G.T.; Barbari, T.A. The use of FTi.r.-a.t.r Spectroscopy to Characterize Penetrant Diffusion in Polymers. *Polymer* **34**, 1146–1153 (1993).

45. www.refractiveindex.info (last accessed on 11-4-2010)

46. http://www.texloc.com/closet/cl_refractiveindex.html (last accessed on 11-4-2010)

47. http://www.chemicalbook.com/ChemicalProductProperty_EN_CB3749115.htm (last accessed on 11-4-2010)

48. Mattox, D.M. *Handbook of Physical Vapor Deposition (PVD) Processing. Film Formation, Adhesion, Surface Preparation and Contamination Control*. 2nd ed., William Andrew, New York, NY, 2010.

49. Zhigal'skii, G.P.; Jones, P.K. *The Physical Properties of Thin Metal Films*. Taylor & Francis, New York, NY, USA, 2003.

50. Zhang, Y.; Ding, Y.; Li, Y.; Gao, J.; Yang, J. Synthesis and Characterization of Polyvinyl butyral – Al(NO₃)₃ Composite Sol Used for Alumina Based Fibers. *J. Sol-Gel Sci. Technol.* **49**, 385–390 (2009).

51. Scatena, L.F.; Brown, M.G.; Richmond, G.L. Water at Hydrophobic Surfaces: Weak Hydrogen Bonding and Strong Orientation Effects. *Science* **292**, 908–912 (2001).

52. Vlasak, R.; Klueppel, I.; Grundmeier, G. Combined EIS and FTIR-ATR Study of Water Uptake and Diffusion in Polymer Films on Semiconducting Electrodes. *Electrochim. Acta* **52**, 8075–8080 (2007).

53. Liau, L.C.K.; Yang, T.C.K.; Viswanath, D.S. Mechanism of Degradation of Poly(vinyl butyral) Using Thermogravimetry/Fourier Transform Infrared Spectroscopy. *Polym. Eng. Sci.* **36**, 2589–2600 (1996).

54. Silverstein, R.M.; Webster, F.X.; Kiemble, D.J. *Spectrometric Identification of Organic Compounds*, 7th ed., John Wiley & Sons, New York, NY, USA, 2005.

55. Gu, X.; Stanley, D.; Byrd, W.E.; Dickens, B.; Vaca-Trigo, I.; Meeker, W.Q.; Nguyen, T.; Chin, J.W.; Martin, J.W. Chapter 1 – *Linking Accelerated Laboratory Test with Outdoor Performance Results for a Model Epoxy Coating System*. In: *Service Life Predictions of*

Polymeric Materials (J.W. Martin, R.A. Ryntz, J. Chin, R.A. Dickie, eds.), Springer, Heidelberg, Germany, pp. 3–28, 2009.

56. Reinohl, V.; Sedlart, J.; Navratil, M. Photo-oxidation of Poly(vinyl butyral). *Polym. Photochem.* **1**, 165–175 (1981).
57. Liu, R.; He, B.; Chen, X. Degradation of Poly(vinyl butyral) and its Stabilization by Bases. *Polym. Degrad. Stabil.* **93**, 846–853 (2008).
58. Liau, L.C.K.; Yang, T.C.K.; Viswanath, D.S. Reaction Pathways and Kinetic Analysis of PVB Thermal Degradation Using TG/FT-IR. *Appl. Spectrosc.* **50**, 1058–1065 (1996).
59. Phambu, N. Characterization of Aluminum Hydroxide Thin Film on Metallic Aluminum Powder. *Mater. Lett.* **57**, 2907–2913 (2003).
60. Ping, Z.H.; Nguyen, Q.T.; Chen, S.M.; Zhou, J.Q.; Ding, Y.D. States of Water in Different Hydrophilic Polymers – DSC and FTIR studies. *Polymer* **42**, 8461–8467 (2001).
61. Liu, D.; Ma, G.; Levering, L.M.; Allen, H.C. Vibrational Spectroscopy of Aqueous Sodium Halide Solutions and Air-Liquid Interfaces. Observation of Interfacial Liquid Depth. *J. Phys. Chem. B* **108**, 2252–2260 (2004).
62. Sammon, C.; Mura, C.; Yarwood, J.; Everall, N.; Swart, R.; Hodge, D. FTIR-ATR Studies of the Structure and Dynamics of Water Molecules in Polymeric Matrices. A Comparison of PET and PVC. *J. Phys. Chem. B* **102**, 3402–3411 (1998).
63. Alexander, M.R., Thompson, G.E., Beamson, G., Characterization of the Oxide/Hydroxide Surface of Aluminum Using X-ray Photoelectron Spectroscopy: A Procedure for Curve Fitting the O 1s Core Level. *Surf. Interface Anal.* **29**, 468–477 (2000).
64. Jeurgens, L.P.H.; Sloof, W.G.; Tichelaar, F.D.; Borsboom, C.G.; Mittemeijer, E.J. Determination of Thickness and Composition of Aluminum-Oxide Overlayers on Aluminum Substrates. *Appl. Surf. Sci.* **144-145**, 11–15 (1999).
65. Stralin, A.; Hjertberg, T. Influence of Surface Composition on Initial Hydration of Aluminum in Boiling Water. *Appl. Surf. Sci.* **74**, 263–275 (1994).
66. Van Gils, S., Melendres, C.A., Terryn, H., Quantitative Chemical Composition of Thin Films with Infrared Spectroscopic Ellipsometry: Applications to Hydrated Oxide Films on Aluminum. *Surf. Interface Anal.* **35**, 387–394 (2003).
67. Dickie, S.A.; Mcquillan, A.J. In-Situ Infrared Spectroscopic Studies of Adsorption Processes on Boehmite Particle Films: Exchange of Surface Hydroxyl Groups Observed upon Chelation with Acetylacetone. *Langmuir* **20**, 11360–11636 (2004).
68. Wicks Jr., Z.W.; Jones, F.N.; Pappas, S.P.; Wicks, D.A. *Organic Coatings Science and Technology*, 3rd ed., John Wiley & Sons, New York, NY, USA, 2007.
69. Khanna, A.S. *High-Performance Organic Coatings*. CRC Press, Boca Raton, FL, USA 2008.

Task 4: Assessment of Coating Adhesion Degradation by AFM Scratching

4.1 Summary

The effects of environmental exposure on polymer coating degradation were studied by atomic force microscopy (AFM) scratching. Adhesion was assessed by the coating removal rate during controlled-force contact mode scratching in the AFM. Low carbon steel coupons were coated by an ultra high molecular weight epoxy resin and exposed to environments with high relative humidity and exposure to ultraviolet light. AFM scratching was performed both in air and in water to assess the effect of water on adhesion degradation. The average coating removal rate increased when samples were first degraded by environmental exposure and by scratching in water. AFM scratching is shown to be a quantitative method for the assessment of adhesion and adhesion degradation for coatings less than about 4 μm in thickness.

5.2 List of Figures and Tables

Figure 4.1. Calibration plot of normal force as a function of set-point for Si AFM probe coated with Au on the cantilever and doped diamond on the tip ($k = 42\text{N/m}$) with air probe holder and solution probe holder.

Figure 4.2. (a) AFM height images and threshold images during AFM scratching. Scan area 100 $\mu\text{m} \times 100 \mu\text{m}$, Z range of height images 4500 nm (b) 3D topography images of 1st and 7th scans.

Figure 4.3. Raman spectra for scratched and epoxy resin coated areas.

Figure 4.4. Average coating removal rate for different samples. The various bars for a given condition indicate the results for replicate experiments. The numbers and error bars represent the average and standard error, respectively, for the different scans on each sample. The number of scans for each of the samples is as follows. Non-exposed: 10 times; UVB, high RH, in air: 5-7 times; non-exposed, in situ: 7-10 times; UVB, high RH, in situ: 3 times.

Figure 4.5. FT-IR spectra for coated samples exposed with and without exposure to UVB in humid air and non-exposed coated sample.

Table 4.1. Average distance removed during each scan of the sample shown in Figure 4.2.

4.3 Introduction and Background

Understanding the adhesion of protective polymer coatings to substrates is critical for the prediction of coating performance. Different methods to measure the adhesion of thin coatings exist but experimental measurements of polymer adhesion are qualitative or problematic [1,2]. For instance, ASTM D3359 describes procedures for scribing a cross hatch pattern in the coating

and then applying and removing tape [3]. The response is classified according to the amount of coating area detached. Pull-off tests described in ASTM D4541 provide a quantitative assessment of adhesion, but they are often not reproducible, the glue used to attach the dolly can affect the coating, and failure often does not occur at the coating/substrate interface [4]. Additionally, testing wet adhesion, i.e. adhesion of films immersed in aqueous solutions, by standardized tests such as the pull-off test is difficult because of problems like attaching the dolly to a wet coating. A standardized scratch test has been developed for testing adhesion of hard coatings such as alumina, TiN, and diamond-like carbon by dragging a stylus along the coating surface with increasing normal force and measuring the load at which the coating fails in a brittle fashion [5,6]. Atomic Force Microscopy (AFM) has been used to test adhesion of ultrathin coatings (< 2 nm) by measuring the friction signal [7]. However, scratch testing approaches have not been used for testing the adhesion of polymer coatings.

AFM scratching has recently been introduced as an approach for quantitative measurement of polymer coating adhesion [8]. A controlled force was applied between the AFM cantilever tip and the sample surface, and the tip was rastered across the edge of an applied thin polymer coating. The tip moved from an uncoated region across the edge of the coating with the cantilever aligned in the direction of scratching. Coating adhesion was determined by the number of raster scans required to remove the coating at different forces [8].

In this work, the AFM scratching approach is extended to assess coating adhesion degradation by prior exposure to aggressive conditions and by scratching in water. AFM scratching can be used to provide a quantitative measurement of wet adhesion, which is not possible by other methods. The coating adhesion is assessed in this work by the coating removal rate during each raster scan, as described below.

4.4 Lessons Learned

After doing this work, it was realized that the AFM scratching technique for the assessment of coating adhesion has severe limitations. The first is that determination of the stress applied to the coating by the tip during scratching is very difficult. The normal stress is easy to assess, but the force was dependent on bending of the AFM cantilever in complex modes. Furthermore, wear of the tip, even diamond coated tips, during AFM scratching changed the contact area and thus the stress. Finally, the polymer removal by the AFM tip involved polymer wear as much as de-adhesion, so it depended on bulk polymer properties as well as interfacial properties.

4.5 Experimental

Carbon steel 1018 coupons were abraded to 800 grit, cleaned with detergent, DI water, and ethanol, and then kept in a desiccator for 24 h. A thin coating of an ultra high molecular weight epoxy resin (eponol 53-BH-35, Momentive) was applied so that it partially covered the

sample surface. A mixture of 30% resin dissolved in a 75:25 wt% mixture of 2-butanone:1-methoxy-2-propanol was applied using a draw down bar leaving an edge of the coating on the surface. The polymer thicknesses varied between 2-4 μm . It should be noted that the technique is limited to thin polymer coatings owing to z-direction limitations in topography variations in the AFM scanner, which is about 4.5 μm for the instrument used in this work. Some samples were exposed for two days in a chamber with 90% relative humidity (RH) and incident ultraviolet B (UVB) light with intensity of approximately 0.83 mW/cm^2 . A temperature increase of several degrees C was noted in the exposure chamber.

AFM scratching was performed using a Veeco Dimension 3000 AFM in contact mode at a set-point of 8 V, which is a measure of the applied force as described below. In situ AFM scratching was performed in a deionized (DI) water droplet that was placed on edge of coating for 1 h prior to testing. A silicon AFM probe coated with gold on the cantilever surface and with doped diamond on the tip (DDESP-10, Bruker, $k = 42\text{N/m}$) was used for scratching in both air and water. The rastered area, 100 $\mu\text{m} \times 100 \mu\text{m}$ was covered by 512 parallel scan lines.

Two different probe holders were used, for measurements in air and in water, respectively. The calibration curves for set-point vs. force are different for the two different probe holders, Figure 4.1. The set-point voltage is the signal from the AFM photodiode measuring laser beam reflected off of the bent cantilever [9]. At a given set-point, the air probe holder exhibited a higher force than the solution probe holder. Specifically, at the set-point of 8 V used in this work, the force was found to be 28 μN and 20 μN , in air and in solution, respectively.

A Nanoscope 7.3 controller was used to apply the controlled force and obtain data. ImageJ software was used to measure amount of coating removed during each raster scan. Raman spectroscopy was performed with a Renishaw inVia Raman microscope to evaluate the effectiveness of AFM scratching and infrared spectroscopy was performed with a Perkin-Elmer Spectrum 100 MIR-TGS detector to study structural changes in the polymer.

4.6 Results and Discussion

Figure 4.2a shows AFM height images after different scans for a sample with a coating that is about 4.1 μm in thickness that had been previously exposed to UVB and high RH, with AFM scratching performed in air. These are typical images obtained in this work during AFM scratching. The coating is on the left side of these images and uncoated steel is on the right. AFM scratching by the tip was from right to left and the cantilever was aligned in the scratching direction. 3-D renderings of the first and last images are given in Figure 4.2b.

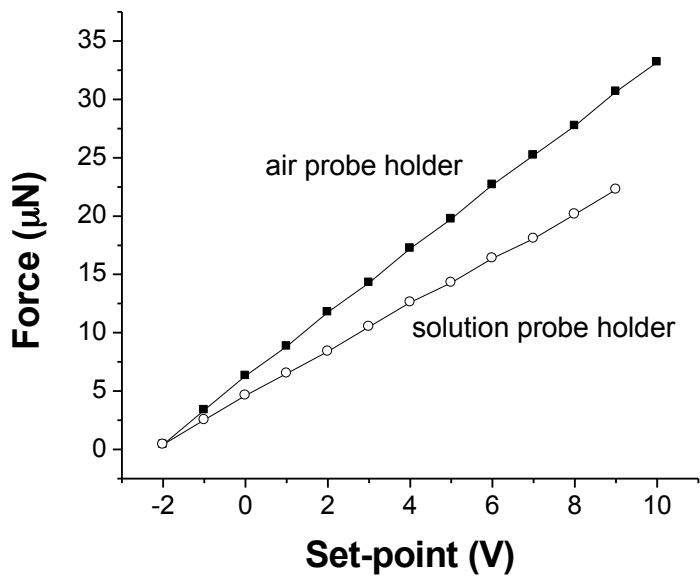
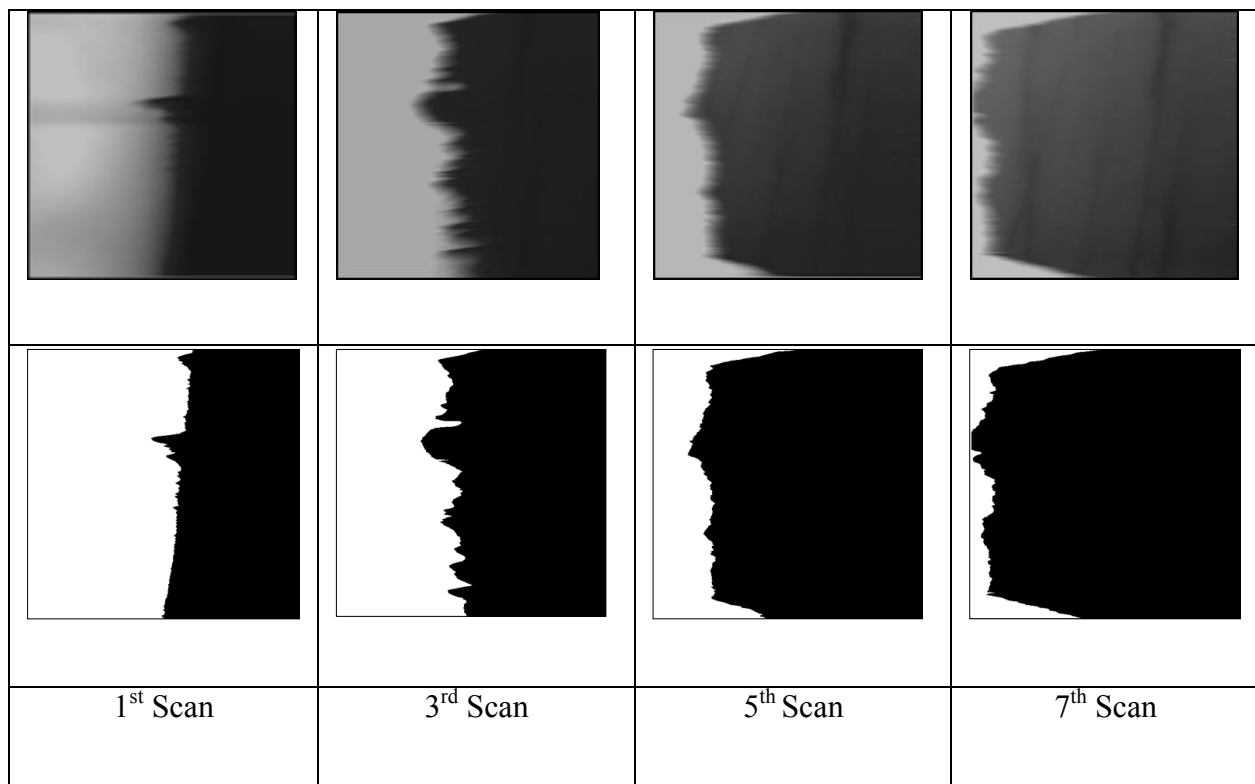
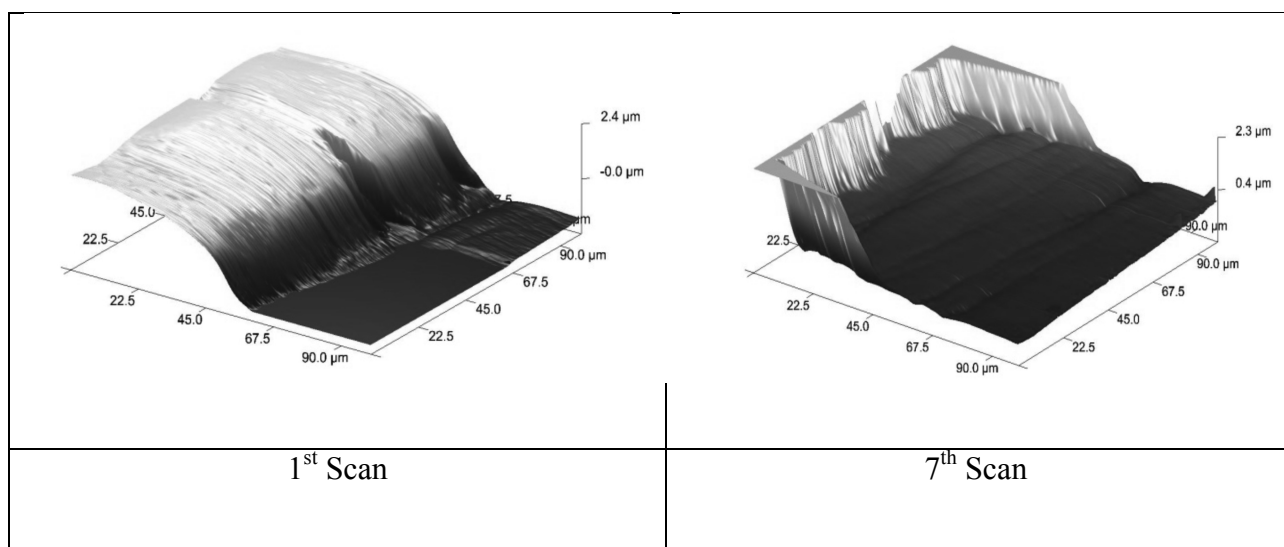


Figure 4.1. Calibration plot of normal force as a function of set-point for Si AFM probe coated with Au on the cantilever and doped diamond on the tip ($k = 42\text{N/m}$) with air probe holder and solution probe holder.

Grayscale thresholding by the image analysis software was used to determine the coating edge for each image as shown in the bottom of Figure 4.2a. These images show that the edge of the coating moved from right to left with each scan as the coating was removed from the substrate surface by AFM scratching. The Raman spectra in Figure 4.3 provide evidence for total removal of the coating in this region. The peaks from the polymer coating, for instance the peak around 2950 cm^{-1} associated with the C-H bond, are absent after scratching. Close examination of the topographic image of the lower scratched region of the 7th scan in Figure 4.2b shows some features. However, these features are associated with scratches in the steel substrate generated during sample preparation. The evidence indicates that the coating is completely removed from the surface in increments during AFM scratching so that the removal rate can be used as a measure of the coating adhesion strength.



(a)



(b)

Figure 4.2. (a) AFM height images and threshold images during AFM scratching. Scan area 100 μm x 100 μm , Z range of height images 4500 nm (b) 3D topography images of 1st and 7th scans.

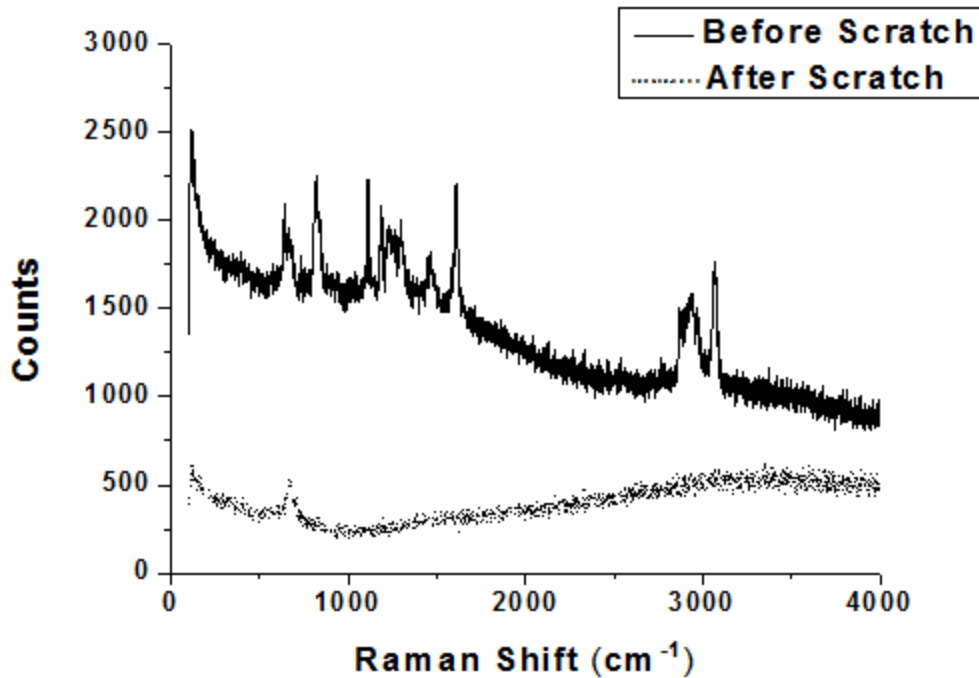


Figure 4.3. Raman spectra for scratched and epoxy resin coated areas.

The average coating removal distance for each scan was calculated by dividing the area of the coating removed by the length of the coating edge that was scratched. There was some variation of this distance for sequential scans of the same sample, as shown in Table 4.1. The average value of the amount of coating removed per scan was used as a measure of the adhesion strength of the polymer coating. By comparing this value for different exposed samples, it is possible to determine the effects of exposure on polymer adhesion degradation.

Table 4.1. Average distance removed during each scan of the sample shown in Figure 4.2.

Scan number	Average distance removed (μm)
2	6.46
3	10.1
4	7.88
5	5.58
6	6.85
7	5.15

Average values of coating removal per scan for different samples are shown in Figure 4.4. Non-exposed samples remained unchanged after 10 scans in air at a set-point of 8 V. In contrast, a removal rate of 7.7 $\mu\text{m}/\text{scan}$ was observed for samples that had been previously

exposed to high RH and UVB and then tested in air. The coating removal rate was about 6.6 $\mu\text{m}/\text{scan}$ for a sample that had no prior exposure but was tested in situ under DI water. Even though the force applied at the 8 V set-point was lower for in situ scratching than air scratching, the coating removal rate was greatly increased as a result of polymer adhesion degradation in the DI water environment. The highest coating removal rate, 25.5 $\mu\text{m}/\text{scan}$, and thus the greatest degradation of adhesion, was observed on samples previously exposed to high RH and UVB and tested by AFM scratching in DI water. The data show that the prior exposure and in situ testing separately and together synergistically degrade polymer adhesion.

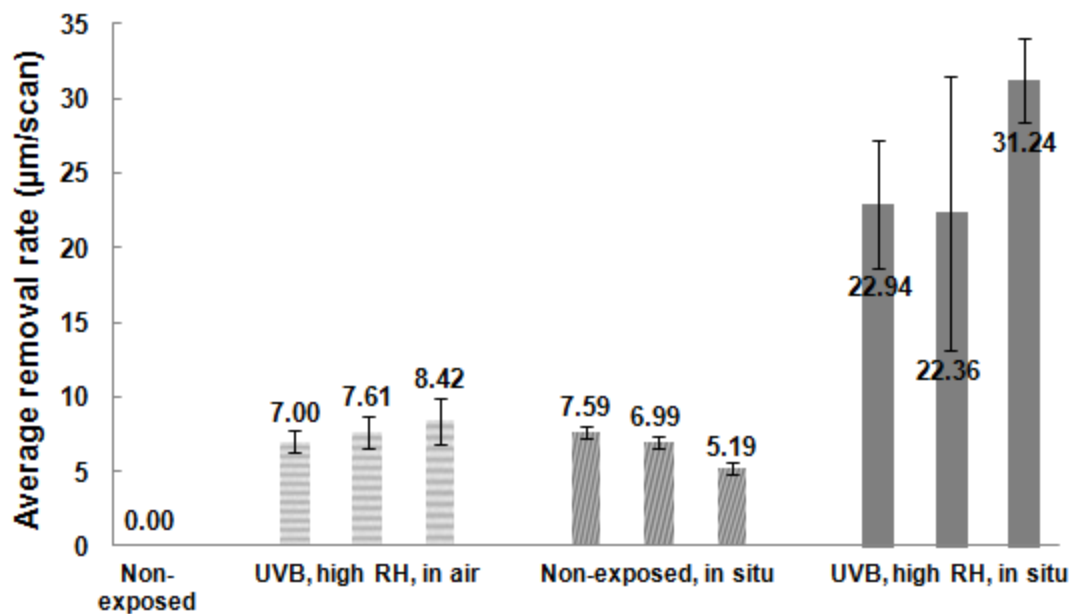


Figure 4.4. Average coating removal rate for different samples. The various bars for a given condition indicate the results for replicate experiments. The numbers and error bars represent the average and standard error, respectively, for the different scans on each sample. The number of scans for each of the samples is as follows. Non-exposed: 10 times; UVB, high RH, in air: 5-7 times; non-exposed, in situ: 7-10 times; UVB, high RH, in situ: 3 times.

FT-IR spectra of the unexposed epoxy resin and the resin after exposure in high RH with or without incident UVB are shown in Fig. 5. Exposure to UVB resulted in a new peak at 1739 cm^{-1} associated with the $\text{C}=\text{O}$ bond that is not present in the unexposed sample or in the sample exposed to RH without UVB. This product was the result of photo-oxidation, which caused scission of the main chain ($\text{C}-\text{O}-\text{C}$) at 1265 cm^{-1} [10]. It is possible that this polymer degradation resulting in more channels allowing a higher rate of water penetration, which degraded the interface and decreased adhesion.

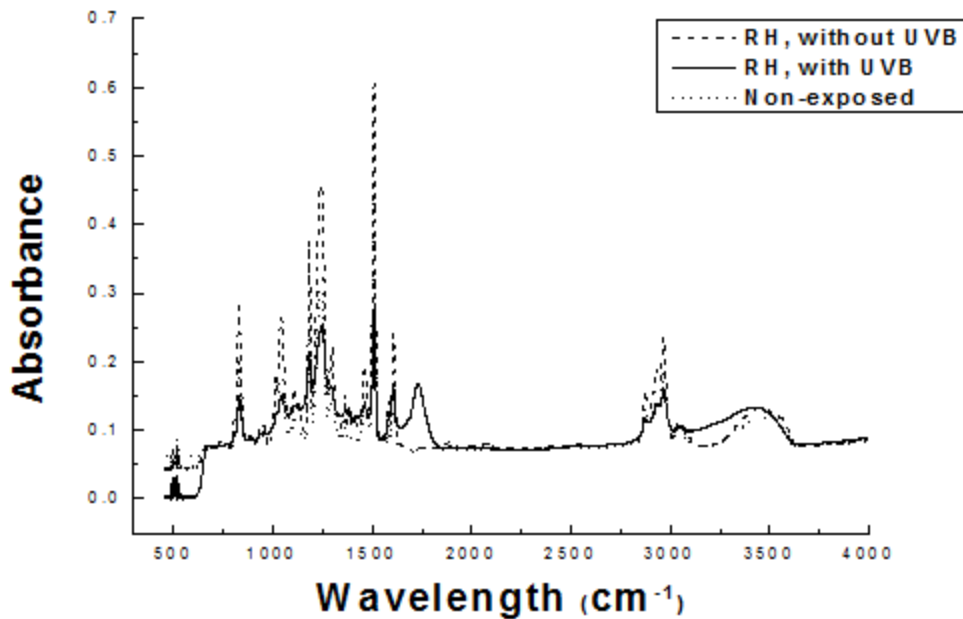


Figure 4.5. FT-IR spectra for coated samples exposed with and without exposure to UVB in humid air and non-exposed coated sample.

The mechanics involved with dragging the AFM tip across the edge of a polymer coating are complicated and beyond the scope of this communication. Nonetheless, the process results in removal of coating from the substrate. Furthermore, conditions expected to degrade coating adhesion have clear effects on the removal process. Therefore, it is reasonable to assume that the rate of coating removal at a fixed tip force can be used as a quantitative measure of the coating adhesion strength. Even though the technique is limited to thin polymer coatings, adhesion is controlled by the interface characteristics, which could be the same for thin and thick coatings.

4.7 Economic Summary

There is no economic impact of this work as of now.

4.8 Implementation

There is no plan to implement this work as of now. However, it has been published and so is available in the literature for others to take up and use.

4.9 Conclusions

AFM scratching at a fixed force was performed across the edge of a thin coating of ultra high molecular weight epoxy resin on steel substrates shown to be an effective approach for quantitative assessment of polymer coating adhesion degradation. Coating adhesion was degraded by scratching in a DI water environment or by prior exposure to UVB and high relative humidity.

4.10 References

- [1] R. Jacobsson, Thin Solid Films 34 (1976) 191-199.
- [2] S.D. Brown, J. Adhesion Sci. Tech. 8 (1994) 687-711.
- [3] ASTM D3359, "Standard Test Methods for Measuring Adhesion by Tape Test," Annual Book of ASTM Standards, ASTM International, West Conshohocken, PA, 2005.
- [4] ASTM D4541, "Standard Test Method for Pull-Off Strength of Coatings Using Portable Adhesion Testers," Annual Book of ASTM Standards, ASTM International, West Conshohocken, PA, 2005.
- [5] V. Bellido-Gonzalez, N. Stefanopoulos, F. Degulhen, Surf. and Coating Tech. 74-75 (1995) 884-889
- [6] ASTM, Standard C1624-05, "Standard Test Method for Adhesion Strength and Mechanical Failure Modes of Ceramic Coatings by Quantitative Single Point Scratch Testing," Annual Book of ASTM Standards, ASTM International, West Conshohocken, PA, 2005.
- [7] S. Sundararajan and B. Bhushan, J. Mater. Res. 16 (2001) 437-445.
- [8] S. Adhikari, G.S. Frankel, B.D. Bammel and J. Zimmerman, accepted for publication in J. Adhesion Sci. Tech. 8/11.
- [9] B. Cappella and G. Dietler, Surf. Sci. Reports 34 (1999) 1-104.
- [10] M.-S. Lin, M.-W. Wang, C.-T. Lee, S.-Y. Shao, Polymer Degrad. Stab 60 (1998) 505-510.

Task 5: Atmospheric corrosion of Cu

5.1 Summary

The effects of UV, ozone and NaCl on the atmospheric corrosion of Cu have been studied by two types of laboratory exposures of Cu. The first type was exposure of Cu with NaCl deposited before exposure. Initial stage of Cu corrosion was studied via this type of laboratory exposure. The other was exposure of Cu with constant deposition of NaCl during exposure. Kinetics of Cu corrosion under constant deposition of NaCl was studied via the second type of lab exposure.

The corrosion products were analyzed by x-ray diffraction and quantified by coulometric reduction. Surface morphology after exposure was studied by scanning electron microscopy. The protection effect of naturally-formed copper oxide was shown by comparing the corrosion behaviors of Cu and Ag with UV and ozone but in the absence of NaCl. UV illumination had a significant accelerating effect on Cu corrosion regardless of presence of ozone. With ozone and NaCl, the accelerating effect of UV was more evident at low RH (60%) than at high RH (90%). Loading of NaCl is critical for formation of $\text{Cu}_2(\text{OH})_3\text{Cl}$, a common corrosion product of Cu in marine environment. Oxidation of Cu_2O to $\text{Cu}_2(\text{OH})_3\text{Cl}$ in the presence of NaCl by oxygen and ozone is a possible pathway for formation of $\text{Cu}_2(\text{OH})_3\text{Cl}$.

A laboratory environment chamber with a constant deposition rate of NaCl was built. With this chamber, the corrosion behavior of Cu during constant NaCl deposition was investigated with different CO_2 concentrations and ultraviolet (UV) illumination. An Na_2CO_3 solution was found to be more suitable than KCl solutions for quantification of Cu corrosion products. Cuprite was always the dominant corrosion product during exposure of Cu in various environments. UV illumination accelerated formation of cuprite significantly but had very little effect on formation of cupric corrosion product. CO_2 in the environment was important in determination of cupric corrosion products. With 350 ppm CO_2 , paratacamite was the dominant product, while tenorite was dominant with <1 ppm CO_2 . This explains why tenorite is not a common cupric corrosion product in the field. Pitting corrosion was always the dominant form of corrosion at the beginning of the exposure period but uniform corrosion dominated at later times. The new environment chamber enables the determination of Cu corrosion kinetics in the lab, especially the formation of paratacamite, which provides insight into Cu atmospheric corrosion in the field.

5.2 List of Figures and Tables

Figure 5.1. Schematic drawing of home-built environment chamber with constant deposition of NaCl.

Figure 5.2. Potentiometric measurement of NaCl concentration in wet candle.

Figure 5.3. Reduction charge of bare Ag and Cu in nitrogen environment with different concentration of ozone. All samples were exposed for 22 h with UV illumination at 90% RH. Ag reduction charges were taken from literature (1) and are shown here for comparison.

Figure 5.4. Reduction curves of as polished Cu, Ag and Cu exposed to 1.5 ppm ozone, 90% RH air, UV for 22h without NaCl.

Figure 5.5. Reduction curve of Cu exposed to 900 ppb ozone, 90% RH air, UV for 6 h with 9 $\mu\text{g}/\text{cm}^2$ NaCl.

Figure 5.6. GIXRD spectra of Cu exposed to UV, 250 ppb ozone, 90% RH air, 4 $\mu\text{g}/\text{cm}^2$ NaCl for 22.5 h. A: exposed to UV, incident angle 0.5°; B: exposed to dark, incident angle 0.5°; C: exposed to UV, incident angle 3°; D: exposed to dark, incident angle 3°; E: as polished Cu, incident angle 3°.

Figure 5.7. GIXRD spectra of Cu exposed to 250 ppb ozone, 90% RH air for 22.5 h. Incident angle is 0.5°. A: 32 $\mu\text{g}/\text{cm}^2$ NaCl with UV; B: 32 $\mu\text{g}/\text{cm}^2$ NaCl in dark; C: 16 $\mu\text{g}/\text{cm}^2$ NaCl with UV.

Figure 5.8. SEM and EDX mapping of Cu exposed with 16 $\mu\text{g}/\text{cm}^2$ NaCl, 250ppb ozone in 90% RH air for 22.5 h.

Figure 5.9. Reduction charge of Cu and Ag exposed with different loading of NaCl. a: Cu was exposed to 90% RH air and 250 ppb ozone, with or without UV illumination for 22.5 h. b: Cu was exposed to 90% RH air and 250 ppb ozone, with or without UV for 10 h. Exposure results of Ag are from (1) where Ag was exposed to 90% RH, UV and 630 ppb ozone for 22h.

Figure 5.10. SEM image of Cu exposed with 16 $\mu\text{g}/\text{cm}^2$ NaCl in 90%RH air with 250 ppb ozone and UV for 22.5 h. a: lightly corroded area; b: heavily corroded area. The leaf-shape feature in the image Figure 5.10a is remaining NaCl.

Figure 5.11. Reduction charge of Cu exposed to 16 $\mu\text{g}/\text{cm}^2$ NaCl, 250 ppb ozone, 90% RH air and UV for different times.

Figure 5.12. Reduction charge of samples exposed to 250 ppb ozone and NaCl in air, with UV radiation or in dark. Loading of NaCl was 4 $\mu\text{g}/\text{cm}^2$. The dashed lines are extrapolations of the lines from lower RH to facilitate the comparison with the increased charge at high RH.

Figure 5.13. SEM image pictures of Cu exposed to 250 ppb ozone, 90%RH air, 16 $\mu\text{g}/\text{cm}^2$ NaCl and UV for 22.5 h. a: as exposed; b and c: rinsed with before SEM.

Figure 5.14. Accumulated deposition of NaCl vs deposition period for saturated and 5 wt% NaCl solutions in the bubbler beaker.

Figure 5.15. Analysis of Cu exposed to humid air, 0.1 $\text{mg}/\text{cm}^2\text{h}$ NaCl. a)reduction curve in 0.1 M Na_2CO_3 for sample exposed with UV b)reduction curve in 0.1 M Na_2CO_3 for

sample exposed in dark): XRD spectra of sample from b) before reduction and after reduction through the first two plateaus only.

Figure 5.16. Reduction curve of two samples exposed to 100% RH humid air, $0.1 \text{ mg/cm}^2 \text{h}$ NaCl for 23 h. A: reduced in 0.1 M KCl with -0.05 mA/cm^2 ; B: reduced in 0.1 M Na_2CO_3 with -0.05 mA/cm^2 .

Figure 5.17. Cu exposed to humid air with $0.1 \text{ mg/cm}^2 \text{h}$ NaCl for 3 h. Solid line: Reduction curve. Dashed line: Derivative of the reduction curve. Note that cupric here represents cupric compounds such as paratacamite or atacamite.

Figure 5.18. a) Weight loss and loss in thickness of Cu exposed to humid air and $0.1 \text{ mg/cm}^2 \text{h}$ NaCl, with UV (solid lines) or in dark (dashed lines). b) formation rate of cuprite and paratacamite and corrosion rate of Cu, derivative of data showed in Figure 5.18a.

Figure 5.19. Schematic illustration of the interaction between photons and n-type cuprite. CB: conduction band; VB: valence band, modeled after (2-3).

Figure 5.20. SEM images of Cu exposed to low and high CO_2 . a)and b)Cu exposed to humid air with less than 1 ppm CO_2 and $0.1 \text{ mg/cm}^2 \text{h}$ NaCl for 58.5 h. Broken film in figure 5.20b is remaining NaCl as confirmed by EDS. c)and d)Cu exposed to humid air with 350 ppm CO_2 and $0.1 \text{ mg/cm}^2 \text{h}$ NaCl for 60.5 h. Flakes in d) are paratacamiteas confirmed by EDS.

Figure 5.21. Reduction curve of Cu exposed to humid air with less than 1 ppm CO_2 and $0.1 \text{ mg/cm}^2 \text{h}$ NaCl for 23.5 h. Cu was reduced in 0.1 M Na_2CO_3 .

Figure 5.22. Effect of CO_2 concentration on Cu corrosion. a) equivalent weight loss of Cu exposed to humid air with 350 ppm or $< 1 \text{ ppm CO}_2$. NaCl deposition rate is $0.1 \text{ mg/cm}^2 \text{h}$. Subscript L and solid lines are Cu exposed to $< 1 \text{ ppm CO}_2$. Subscript H and dashed lines are Cu exposed to 350 ppm CO_2 . For Cu exposed to $< 1 \text{ ppm CO}_2$, W_p is weight loss due to formation of tenorite instead of paratacamite. b) formation rate of cuprite and paratacamite and corrosion rate of Cu, derivative of data showed in a).

Figure 5.23. Images of Cu exposed to humid air(350 ppm CO_2) and $0.1 \text{ mg/cm}^2 \text{h}$ in dark. a), b) and c) are samples after exposure. d), e) and f) are exposed samples after soaked in 6.5 M HCl for 5 min and 1 min in 1 M H_2SO_4 to remove corrosion products. a)and d) are samples exposed for 4h; b) and e) are 12 h; c) and f) are samples exposed for 23.5 h.

Figure 5.24. a)profiles of Cu with one droplet of saturated NaCl in 98% RH for 1 h, 23 h and 69 h respectively. Dashed line: geometrical profile of the droplet. Solid line: Volta potential. b)morphology of the same Cu sample after 72 h exposure and remove corrosion product by strong acid.

Figure 5.25. Maximum pit depth and equivalent weight loss of Cu exposed in various environments.

Table 5.1. Corrosion rate of Cu exposed to different environments, $\mu\text{m/d}$.

Table 5.2. Corrosion products of Cu exposed to $0.1 \text{ mg/cm}^2\text{h}$ NaCl and humid air.

5.3 Introduction and Background

Cu has been widely used for electronic and heat exchange applications due to its high electrical and thermal conductivity. It also has fairly good atmospheric corrosion resistance so it has been frequently used for art works and building construction such as roofs and gutters (4). Cu is also suggested by the International Standards Organization for use as an atmospheric corrosivity monitor (5). Due to its wide application in atmospheric environments, atmospheric corrosion of Cu has been studied using both field and lab exposures.

Cuprite (Cu_2O) is one of the most common Cu corrosion products formed on field-exposed Cu (6). During outdoor exposure cuprite is also the initial corrosion product on top of which other complex Cu compounds can form. In industrial environments, posnjakite ($\text{Cu}_4(\text{OH})_6\text{SO}_4\cdot\text{H}_2\text{O}$), brochantite ($\text{Cu}_4(\text{OH})_6\text{SO}_4$) and antlerite ($\text{Cu}_3(\text{OH})_4\text{SO}_4\cdot\text{H}_2\text{O}$) (6-8) are the most common compounds found on Cu. Greenish atacamite ($\text{Cu}_2(\text{OH})_3\text{Cl}$) and its polymorph paratacamite ($\text{Cu}_2(\text{OH})_3\text{Cl}$) (6, 8-12) usually appear after several months of marine exposure. The mechanism of formation of $\text{Cu}_2(\text{OH})_3\text{Cl}$ is still not well understood. $\text{Cu}_2(\text{OH})_3\text{Cl}$ deposits are usually porous (12), so its formation should be avoided if Cu is used as structural material. However, for decorative applications, formation of $\text{Cu}_2(\text{OH})_3\text{Cl}$ might be desirable because of its attractive greenish color.

Ozone, O_3 , a common pollutant and strong oxidant present in atmosphere, strongly accelerates Cu corrosion during lab exposure (13). It is well known that ozone is very sensitive to UV, which accelerates photolysis of ozone to create molecular dioxygen and atomic oxygen (14-15). A combination of UV and ozone can dramatically increase corrosivity and result in fast corrosion (1, 16). Furthermore, it has been reported that copper oxide is very sensitive to UV alone (17). Interaction between photons and naturally-formed copper oxide usually improves the passivity of Cu (2, 18). Therefore, it is of interest to study atmospheric corrosion behavior of Cu in the presence of ozone and UV. This paper reports the effects of ozone, UV and NaCl on Cu corrosion and formation of $\text{Cu}_2(\text{OH})_3\text{Cl}$.

NaCl has a strong accelerating influence on Cu corrosion in the field, especially in marine environments (8, 12). The effects of NaCl have also been investigated in laboratory-based atmospheric corrosion studies (19-24). NaCl has been shown to accelerate the breakdown of the naturally formed and protective copper oxide by the formation of copper chloride complexes (23), especially at high relative humidity (RH). When the RH is higher than the critical relative humidity of NaCl, 75% (25), deposition of $4 \mu\text{g}/\text{cm}^2$ of NaCl before exposure increases the Cu corrosion rate of Cu by about one order of magnitude during 10 days exposure (20).

NaCl has also been shown to be critical for formation of $\text{Cu}_2(\text{OH})_3\text{Cl}$ (7). In the presence of NaCl, cuprite (Cu_2O) can be readily oxidized to atacamite or paratacamite, which are isomers of $\text{Cu}_2(\text{OH})_3\text{Cl}$ (24). However, because of difficulties generating a constant deposition rate of NaCl during lab exposure, there is a lack of information on the kinetics of $\text{Cu}_2(\text{OH})_3\text{Cl}$ formation and how $\text{Cu}_2(\text{OH})_3\text{Cl}$ affects the Cu corrosion rate.

Methods used to introduce NaCl onto a surface for laboratory study of atmospheric corrosion of Cu and other metals include deposition of NaCl particles before exposure by fast evaporation of ethanolic NaCl solution (20, 23), thermophoretic deposition (26-27) or printing (28). A disadvantage of prior deposition for the study of Cu corrosion kinetics is that the available NaCl in the environment decreases with time due to formation of $\text{Cu}_2(\text{OH})_3\text{Cl}$ or CuCl during exposure. Furthermore, deposited NaCl particles can alter the form of corrosion because localized attack can initiate at the edge of a particle or under a particle where deliquescence of NaCl occurs first (20).

The CO_2 concentration has been shown to have a critical influence on the initial Cu corrosion reaction in the presence of NaCl particles (21, 29). With lower CO_2 , secondary spreading of NaCl is much more significant (29) and formation of CuCl is impeded (21). Therefore, depending on loading of NaCl, the effects of CO_2 concentration on Cu corrosion can be different.

This report describes a new chamber to provide constant deposition of NaCl during atmospheric exposure of Cu as well as normal laboratory exposure of Cu with NaCl pre-deposited. In this report, the combined effects of UV illumination and CO_2 on Cu atmospheric corrosion kinetics during constant NaCl deposition are studied. An appropriate coulometric reduction technique to easily quantify the amounts of Cu_2O and $\text{Cu}_2(\text{OH})_3\text{Cl}$ is also described.

5.4 Lessons Learned

This work has shown that the understanding gained from previous studies on the atmospheric corrosion of metals can only partially be applied to different metals, even when testing under the same conditions. Unfortunately, this means that considerable work is required to understand and predict the effects of various accelerating factors on the atmospheric corrosion of metals. There are no “short cuts” to achieving that knowledge.

5.5 Experimental

Environment chamber design

Two types of environment chambers were built for laboratory exposure of Cu. The key difference between them was the way how NaCl was deposited. For the first type, NaCl was loaded on the Cu samples before exposure by fast evaporation of NaCl ethanol solution according to procedures described elsewhere (30). Loading of NaCl ranged from 4 to 32 $\mu\text{g}/\text{cm}^2$.

For the second one, a continuous NaCl was provided by bubbling of NaCl solution inside of the chamber. Therefore NaCl continuously deposited onto Cu surface during exposure.

Detail of the first type of chamber was described elsewhere (1). Ozone concentration, UV intensity and relative humidity can be accurately controlled in this chamber. The UV light was generated by a mercury UV lamp with primary energy at 254 nm. The UV intensity was 3.6 mW/cm² for all exposures performed under UV illumination. Lab air or nitrogen was used as the carrier gas for ozone and the total flow rate was 830 cc/min.

Figure 5.1 is a schematic representation of the second type of home-built environment chamber that can provide a continuous and constant rate of NaCl deposition from an aerosol. A 200-ml beaker of saturated NaCl solution inside the chamber was bubbled with air through a glass frit tip, labeled inlet flow A. The beaker of saturated NaCl solution (6.2 M) contained enough undissolved NaCl particles to maintain saturation during the entire exposure time. Inlet flow A needed to be pre-humidified to avoid blocking of the frit by precipitation of NaCl associated with concentration buildup adjacent to the frit (31). The exposure location of the Cu samples was maintained at a position 53 mm away from the frit bubbler.

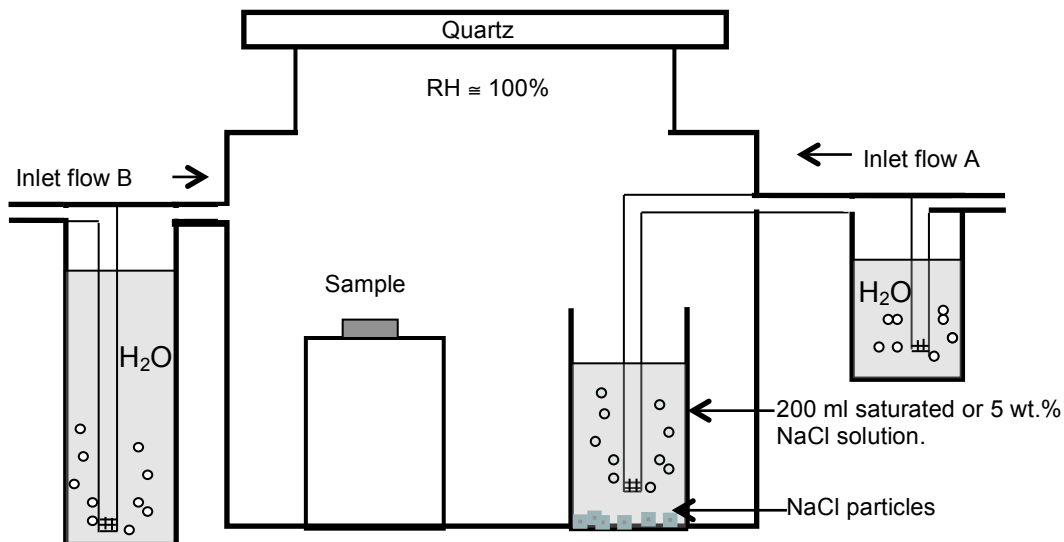


Figure 5.1. Schematic drawing of home-built environment chamber with constant deposition of NaCl.

During exposure, the area of the Cu samples covered by NaCl droplets increased gradually. After approximately 12 h exposure, samples were completely covered by a thin layer of aqueous NaCl solution.

Another flow of air, inlet flow B, was used to maintain the RH around 100% when the saturated solution was used for flow A. Unless otherwise specified, the air used in this work contained 350 ppm CO₂ and the RH during exposure was always close to 100%. Ultra-purified air with less than 1 ppm CO₂ was also used to study the effect of CO₂. The flow rates of inlet flows A and B were 15 cc/min and 436 cc/min, respectively. Mass flow controllers were used to control the flows accurately. Flow A and flow B were started at least three days before exposure of the Cu to reach steady state conditions in the bubblers and in the chamber. Once exposure of the Cu started, the flows were maintained, even during the periods of sample changes.

The top cover of this chamber was a 4 mm thick quartz glass window, which allowed UV light (254 nm) to penetrate through into the chamber. The UV intensity was 3.2 mW/cm² at the top side of the quartz window. The Cu samples were exposed in the dark unless it is specified that they were exposed under UV illumination.

In some cases, the beaker in the chamber contained 5 wt. % NaCl. Under these conditions, inlet flow A was 830 cc/min and inlet flow B was not used. This is similar to the salt bubble chamber described previously for the study of Ag atmospheric corrosion (32).

Measurement of NaCl deposition rate

NaCl aerosols were generated in the chamber by flow A. The deposition rate of NaCl was measured by pseudo-wet-candle collection followed by potentiometric titration. NaCl aerosols were collected with a cylindrical thin-wall beaker without a spout (1 mm in thickness and 2.2 cm inside diameter). The beaker was placed in the chamber at a location where its mouth was at the same distance from the frit and the same height as where the samples were exposed. It had 5 ml of deionized (DI) water inside before collection. After exposure, all NaCl droplets on the top and inside of the wall as well as the inside solution were carefully transferred into a large beaker by rinsing with DI water at least three times. The total volume of the final NaCl solution, including all rinsing water, was controlled to 100 - 120 ml to reduce errors.

This NaCl solution was potentiometrically titrated with AgNO₃. Three concentrations of AgNO₃, 0.1 M, 0.04 M and 0.004 M, were used depending on the amount of NaCl. The working electrode was an Ag wire and the reference electrode was a saturated mercurous sulfate electrode (MSE). A 0.1 ml aliquot of the AgNO₃ solution was added repeatedly and the solution was stirred with a glass rod for about 5 s after each addition. A steady potential was noted after waiting at least 100 s. The equivalence point was determined by the maximum of the derivative curve of potential vs AgNO₃ volume, as shown in Figure 5.2. The deposition rate of NaCl, D, in mg/cm²h was determined from equation 5.1.

$$D = \frac{58.5 \times V \times M}{t \times A} \quad [5.1]$$

where V is the volume of AgNO₃ at the equivalence point in ml, M is concentration of AgNO₃ in mol/L, t is deposition time in h, and A is area in cm².

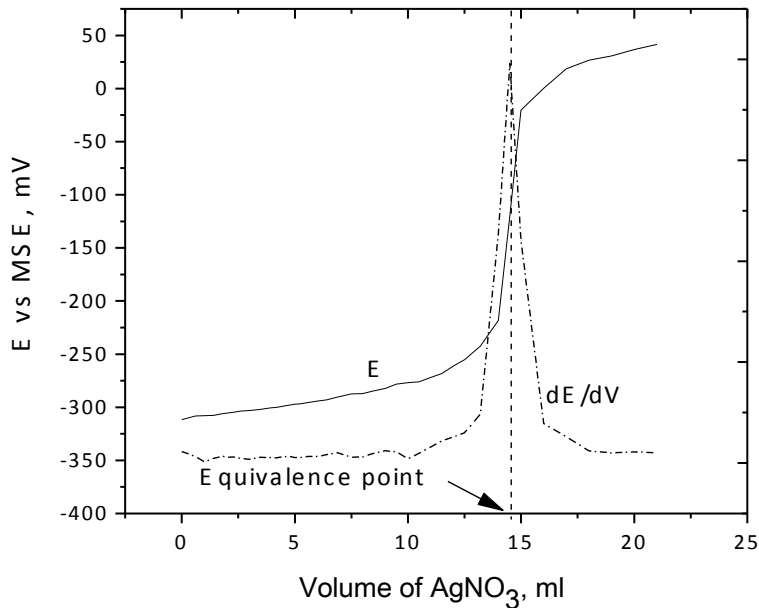


Figure 5.2. Potentiometric measurement of NaCl concentration in wet candle.

Sample preparation

All Cu coupons were 99.99 % pure and 17 mm x 17 mm x 1.6 mm in size. For samples exposed in the first kind of environment chamber, they were ground 400 and 600 grit papers. For samples exposed in the second kind of environment chamber, they were sequentially grounded down to 1200 grit, followed by 6 μm and then 1 μm diamond polishing. After grounding and polishing, all samples were ultrasonically cleaned in 99.5 wt% ethanol, and dried with a fan immediately and then they were stored in a desiccator for 24 h before exposure.

Identification and quantification of corrosion products

After exposure, the morphology of corroded Cu was observed using scanning electron microscopy (SEM) and energy dispersive spectroscopy (EDS). Corrosion products were identified by X-ray diffraction (XRD) or Grazing Incidence XRD (GIXRD).

The amount of corrosion product was then quantified by coulometric reduction technique using 0.1 M KCl (33) or 0.1 M Na_2CO_3 (34) as the supporting electrolyte. For samples exposed in the first kind of chamber, they were reduced in the 0.1 M KCl, as suggested by the ASTM B825 standard (33). The reduction current density was 0.1 mA/cm^2 and a saturated calomel electrode (SCE) was used as reference electrode. The Cu corrosion rate was calculated by equation 5.2, by assuming cuprous ions are the dominant corrosion product.

$$C = \frac{10 \times M \times R}{n \times F \times D \times t} \quad [5.2]$$

where C is corrosion rate in $\mu\text{m}/\text{d}$, M is atomic weight of Cu, 64 g/mol, R is total reduction charge in mC/cm^2 , n=1 is the number of electrons transferred, F is the Faraday constant, 96500 C/mol, D is density of Cu, 8.96 g/cm², and t is exposure duration in d. The accelerating effect of UV was quantified by the acceleration factor (AF), which is defined by equation 5.3:

$$AF = \frac{Q_{uv}}{Q_d} \quad [5.3]$$

where Q_{uv} is reduction charge of Cu exposed with UV illumination and Q_d is the reduction charge of Cu exposed to the same environment but in the dark.

For Cu exposed in the second kind of environment chamber, they were reduced in 0.1 M Na_2CO_3 . Because cupric corrosion products were significant present and reduction of cuprous ions and cupric ions can be clearly differentiated with 0.1M Na_2CO_3 . This will be discussed later.

A constant reduction current density of 0.05 mA/cm² was used when samples were reduced in 0.1 M Na_2CO_3 . A conventional three electrode flat cell was used to carry out the reduction testing. Saturated calomel electrode (SCE) was used as a reference electrode and a platinum mesh was used as an auxiliary electrode. All potentials mentioned in this paper are respect to SCE unless specified otherwise.

Pit depth measurement

To determine pit depth, unreduced samples were pickled in 6.5 M HCl for 5 min followed by soaking in 1 M H_2SO_4 for 1 min. They were then rinsed with DI water for less than 30 s, sprayed with ethanol and immediately air dried. Pit depth was measured by optical profilometry. At least 6 spots close to center of samples with area 0.26 to 1.73 mm² were scanned. No pits were generated during acid pickling and drying of a control sample that was not first exposed in the chamber.

Scanning Kelvin Probe (SKP) measurement

A 2 μL droplet of saturated NaCl solution was transferred onto as-polished Cu and the Cu sample was immediately placed in the airtight SKP chamber. The relative humidity in the chamber was kept at 98% by wet air flow (containing ambient CO_2) before loading of the sample. After loading of the sample, the relative humidity increased back to 98% within 10 min. As a result, the droplet did not dry out before or during SKP measurement. A line scan across the droplet was carried out at a scan rate of 0.8 $\mu\text{m}/\text{s}$ and with 4 μm step size. Details of the SKP measurements are described elsewhere (35).

5.6 Results and Discussion

Exposure of Cu without NaCl

Bare Cu (no NaCl) was exposed in dry (RH ~ 0) or humid (RH 90%) lab air or pure nitrogen with different concentrations of ozone for 22 h. Bare Cu stayed shiny after exposure and seemed not to corrode at all. The reduction charges of bare Cu were much less than reduction charges of

bare Ag even with higher ozone concentration, as Figure 5.3 shows. It is surprising that corrosion rate of Cu was much slower than Ag, because Ag is a more noble metal than Cu.

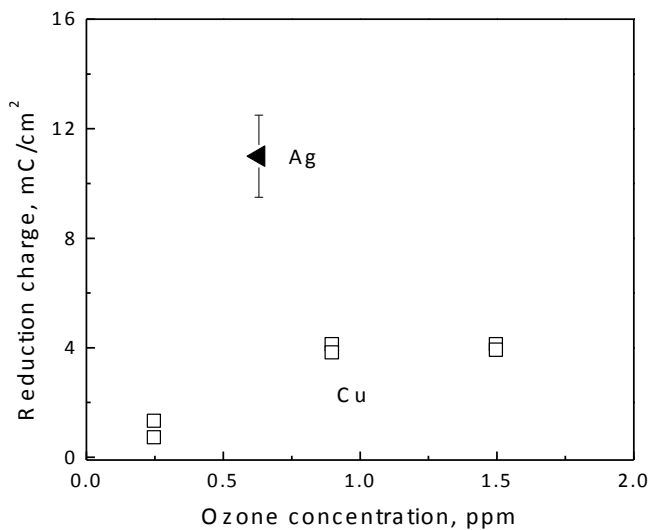


Figure 5.3. Reduction charge of bare Ag and Cu in nitrogen environment with different concentration of ozone. All samples were exposed for 22 h with UV illumination at 90% RH. Ag reduction charges were taken from literature (1) and are shown here for comparison.

Figure 5.4 shows reduction curves of as-polished Cu and Ag stored in a dessicator for 24 h after polishing. As-polished Cu has a distinct reduction plateau at -0.65 V before hydrogen evolution started. This potential corresponds to reduction of naturally-formed copper oxide, which is mainly Cu_2O (36). The thickness of the naturally-formed copper oxide is about 2.5 nm by estimation from reduction charge. This is consistent with previous reduction analysis and measurement by XPS depth profile analysis (36-38). Generally, it is believed that this naturally-formed oxide has a bilayer structure (38). The inner layer is dense Cu_2O , which has fairly good protection and a very thin outer layer is porous CuO or $\text{Cu}(\text{OH})_2$ (36, 38). The naturally-formed Cu_2O layer is likely nonstoichiometric or amorphous with a mixture of $\text{Cu}(0)$ and $\text{Cu}(\text{I})$ and is reduced at a higher potential than crystalline Cu_2O (39-40). It is difficult to differentiate reduction of this naturally-formed Cu_2O with CuO , because CuO is also reduced at around -0.65 V (41-42). Crystalline Cu_2O is usually induced by corrosion and is reduced at lower potentials ranging from -0.75 to -0.9 V (39, 43-45).

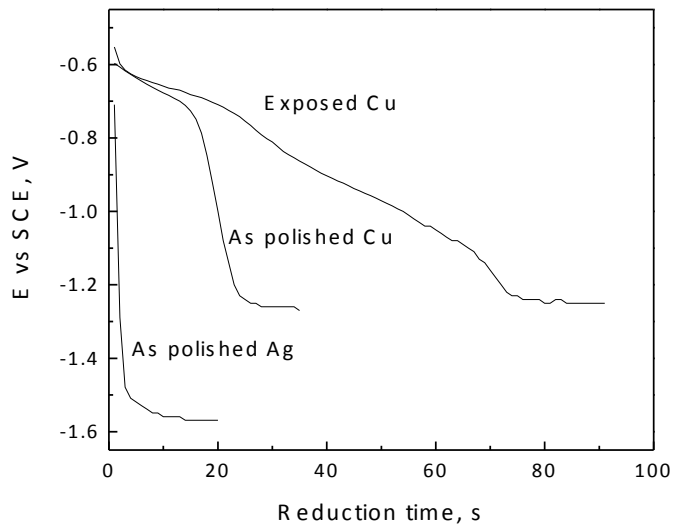


Figure 5.4. Reduction curves of as polished Cu, Ag and Cu exposed to 1.5 ppm ozone, 90% RH air, UV for 22h without NaCl.

The Ag reduction curve does not have a reduction plateau before hydrogen evolution. This means that the naturally-formed oxide layer is very thin or does not exist on Ag. This suggests that bare Cu corroded slower than Ag because it was protected by its naturally-formed oxide, even though Ag is more noble than Cu.

Figure 5.4 also shows a typical reduction curve of bare Cu exposed. It roughly has two reduction plateaus. The first one is around -0.65 V and the second one is very broad, ranging from -0.8 to -1.1 V. The oxide film formed in the presence of ozone during exposure might be very similar to that formed on Cu exposed in humid air at 60 °C, which results in formation of a duplex oxide layer (42). The outside layer is CuO and the inner one is Cu₂O. So the first plateau at -0.65 V might be a combination of one-step reduction of newly formed CuO (41-42) and reduction of naturally-formed oxide. The second plateau is probably due to newly formed Cu₂O during exposure. The oxide layer formed during exposure of Cu was only about 3 nm from the reduction charge, which is slightly thicker than the as polished Cu.

Identification of corrosion products of Cu exposed with NaCl

Cu corrosion became much more severe when the surface was contaminated with NaCl. Significant brownish patinas appeared after 5 hour exposure with only 4 $\mu\text{g}/\text{cm}^2$ NaCl. As loading of NaCl increased up to 16 $\mu\text{g}/\text{cm}^2$ NaCl, small green spots scattered on sample surface and become prevalent after exposure.

Figure 5.5 shows a typical reduction curve of Cu with NaCl exposed to a humid environment. It only has one big plateau around -0.75 to -0.85 V. Normal XRD analysis indicates that only Cu₂O forms during exposure and usually it coexists with remaining NaCl. Therefore, the big plateau corresponds to reduction of Cu₂O. This is also consistent with previous research (39, 43-45). As

shown in Figure 5.5 the reduction potential of the products on corroded Cu usually starts higher than this big plateau and then decreases to a lower value within a few tens of seconds and then increases back to the big plateau. The reduction prior to the big plateau is probably due to reduction of Cu corrosion products with higher oxidation state. This is supported by GIXRD in Figure 5.6. As the incident angle decreases from 3° to 0.5° , broad peaks near CuO character peaks appear. This indicates the presence of a thin CuO layer at the outermost surface.

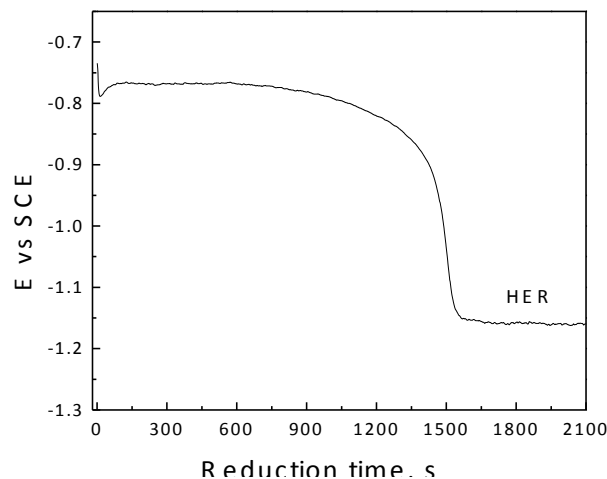


Figure 5.5. Reduction curve of Cu exposed to 900 ppb ozone, 90% RH air, UV for 6 h with 9 $\mu\text{g}/\text{cm}^2$ NaCl.

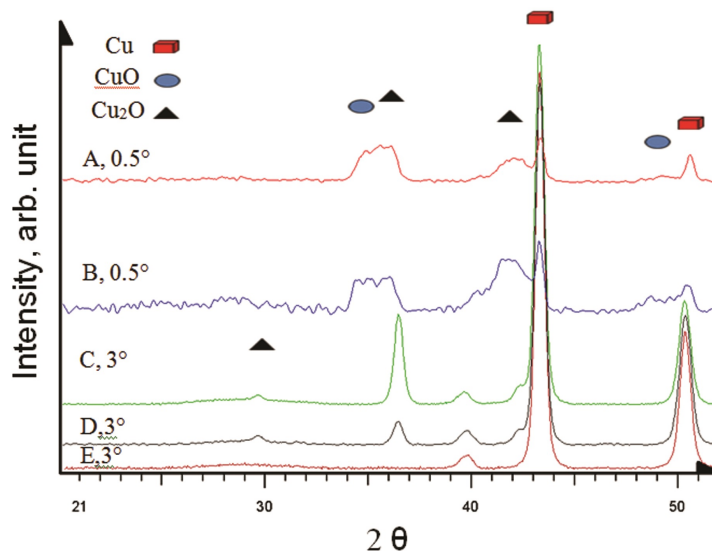


Figure 5.6. GIXRD spectra of Cu exposed to UV, 250 ppb ozone, 90% RH air, 4 $\mu\text{g}/\text{cm}^2$ NaCl for 22.5 h. A: exposed to UV, incident angle 0.5° ; B: exposed to dark, incident angle 0.5° ; C: exposed to UV, incident angle 3° ; D: exposed to dark, incident angle 3° ; E: as polished Cu, incident angle 3°

With an NaCl loading of $16 \mu\text{g}/\text{cm}^2$, 250 ppb ozone in 90% RH air for only 22.5 h, the formation of paratacamite ($\text{Cu}_2(\text{OH})_3\text{Cl}$) as well as cuprite were confirmed by GIXRD analysis, Figure 5.7. Paratacamite is a common greenish corrosion product formed during field exposure in marine environments (9-10, 12). SEM and EDS mapping observation also indicate the presence of scattered regions enriched in O and Cl but depleted in Cu on samples exposed with $16 \mu\text{g}/\text{cm}^2$ or more NaCl, as Figure 5.8 shows. This confirms the presence of $\text{Cu}_2(\text{OH})_3\text{Cl}$ and also proves that no continuous $\text{Cu}_2(\text{OH})_3\text{Cl}$ film formed during exposure.

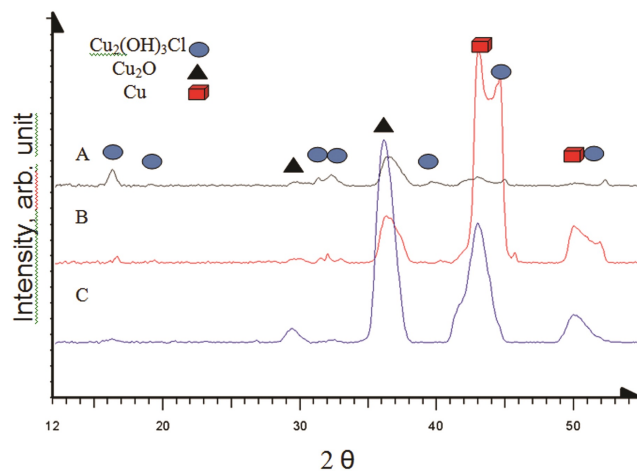


Figure 5.7. GIXRD spectra of Cu exposed to 250 ppb ozone, 90% RH air for 22.5 h. Incident angle is 0.5° . A: $32 \mu\text{g}/\text{cm}^2$ NaCl with UV; B: $32 \mu\text{g}/\text{cm}^2$ NaCl in dark; C: $16 \mu\text{g}/\text{cm}^2$ NaCl with UV.

Effect of NaCl on Cu corrosion

Figures 5.9a and 5.9b show the reduction charge for Cu exposed with different NaCl loadings in different environments for 22.5 h or 10 h. With NaCl on the Cu surface, even at the low loading of $4 \mu\text{g}/\text{cm}^2$, the reduction charge increases dramatically from almost zero to more than $100 \text{ mC}/\text{cm}^2$ after exposure to 90% air and 250 ppb ozone for 22.5 h. The effect of NaCl on the reduction charge of products formed on Ag, which was reported previously (1), is much less significant than Cu corrosion. The reduction charge of Ag even slightly decreases after addition of $8 \mu\text{g}/\text{cm}^2$ NaCl.

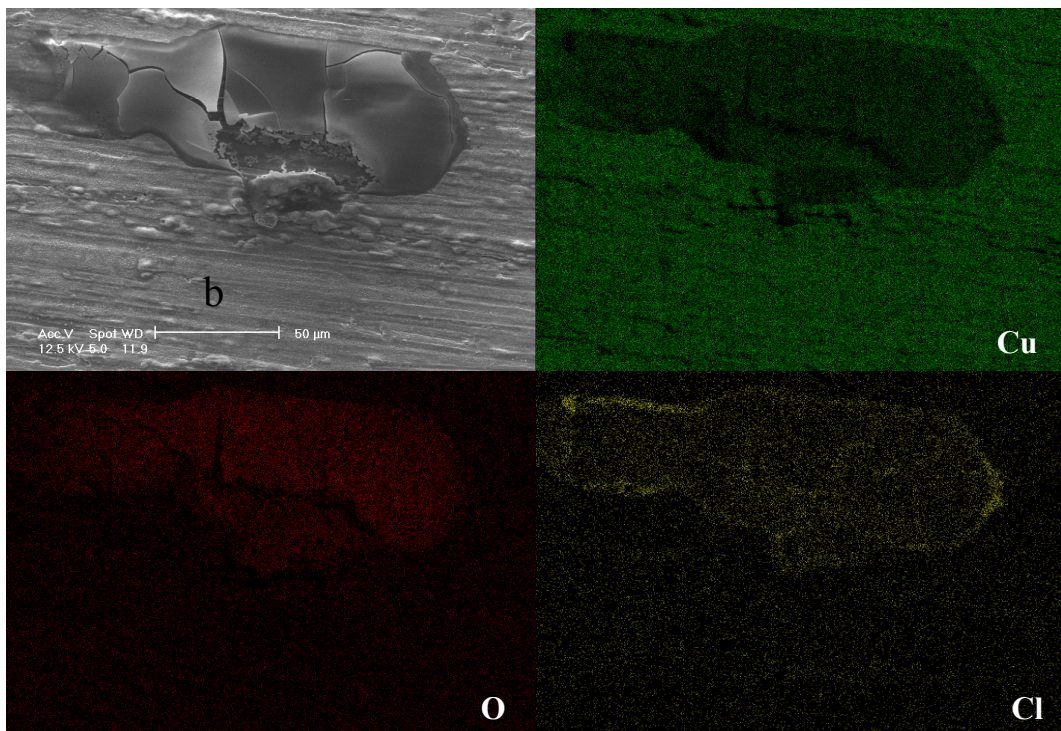


Figure 5.8. SEM and EDX mapping of Cu exposed with $16 \mu\text{g}/\text{cm}^2$ NaCl, 250 ppb ozone in 90% RH air for 22.5 h.

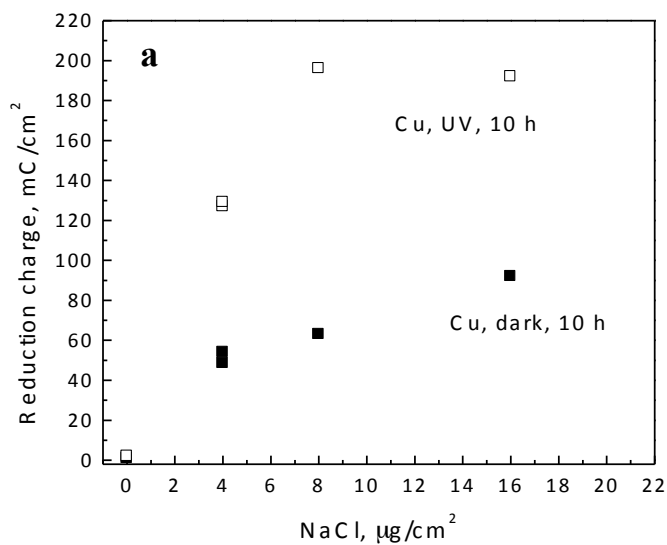
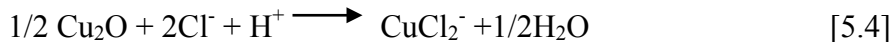


Figure 5.9. Reduction charge of Cu and Ag exposed with different loading of NaCl. a: Cu was exposed to 90% RH air and 250 ppb ozone, with or without UV illumination for 22.5 h. b: Cu was exposed to 90% RH air and 250 ppb ozone, with or without UV for 10 h. Exposure results of Ag are from (1) where Ag was exposed to 90% RH, UV and 630 ppb ozone for 22h.

It is been reported that presence of chloride can result in breakdown of the naturally-formed copper oxide layer by formation of CuCl_2^- (23, 38, 46), according to:



After breakdown of the naturally-formed oxide, normal atmospheric corrosion of Cu starts. Reduction of oxygen and ozone are the dominant cathodic reactions accompanying the anodic oxidation of copper to cuprous ions. The reduction charge of Cu exposed to $32 \mu\text{g/cm}^2$ NaCl and 250 ppb ozone for 22.5 h is as high as 198 mC/cm^2 , which is equal to a corrosion rate of $0.28 \mu\text{m/d}$ according to equation 1. This is much higher than the normal Cu corrosion rate in the field, which ranges from 0.5 to 3 $\mu\text{m/year}$ (7), because the NaCl loading and ozone concentration are much higher than what is typically found in real environments.

The accelerating effect of NaCl on the initial Cu corrosion during 22.5h exposure period decreases when NaCl increases from 4 to $32 \mu\text{g/cm}^2$, as shown in Figure 5.9. When NaCl increases from 16 to $32 \mu\text{g/cm}^2$, in both dark and UV-illuminated environments, the corrosion rate does not increase significantly. This result is different than previous research, which indicates that the Cu corrosion rate increases linearly as NaCl loading increases from 2 to $33.5 \mu\text{g/cm}^2$ for Cu exposed longer than 10 days (20, 23). During initial Cu corrosion, corrosion resistance is mainly due to the protective naturally-formed copper oxide. It is probably because the loading of NaCl is not critical for breakdown of the naturally-formed oxide as long as it reaches some threshold value. Thus the acceleration effect of loading of NaCl on the initial corrosion decreases as the loading increases. However, NaCl depletion by consumption to form corrosion product is more important during long term exposure. Therefore loading of NaCl is much more critical for long term exposure and the linear relationship between corrosion rate of long-term exposed Cu and the loading of NaCl was found before (20, 23).

The corrosion morphology is not uniform. The SEM image in Figure 5.10a of a sample exposed with NaCl, O_3 , RH, and UV shows shallow pits at a lightly corroded area of the sample. However, at a more heavily corroded area, pits are rarely observed in a top-down view, because the pits as well as the adjacent area are completely covered by corrosion product, as Figure 5.10b shows. Owing to the role of H^+ , the conversion from naturally-formed copper oxide to CuCl_2^- (equation 5.4) is promoted in acidic solutions. It is likely that, at the beginning, a localized acidic environment forms due to pitting initiation. The increase of acidity in pits results in further breakdown of the naturally-formed oxide layer and then uniform corrosion takes over. Corrosion products, mainly Cu_2O , cover Cu surface. That is why pits are rarely observed at heavily corroded area, as shown in Figure 5.10b.

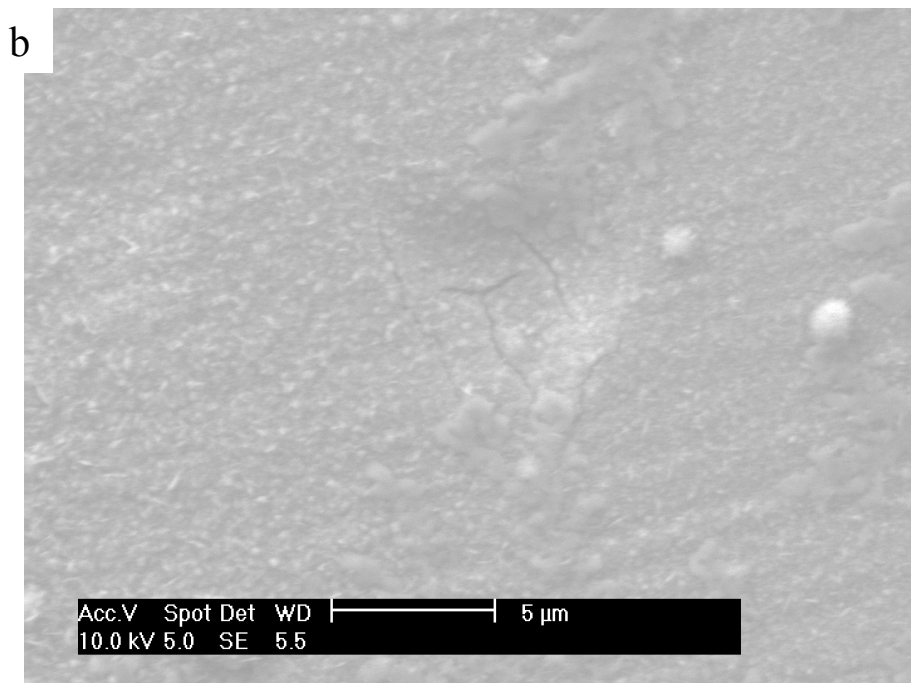
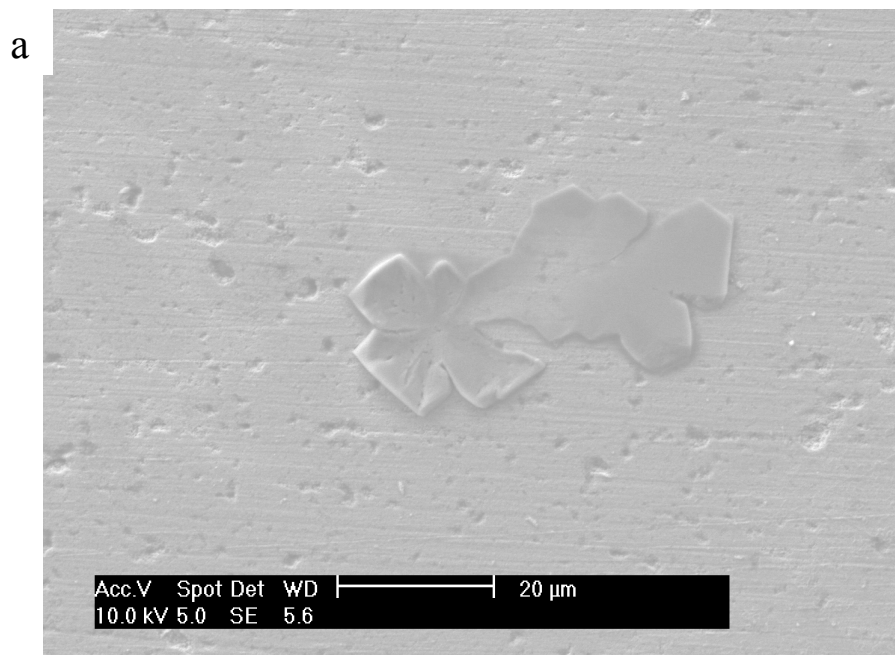


Figure 5.10. SEM image of Cu exposed with $16 \mu\text{g}/\text{cm}^2$ NaCl in 90%RH air with 250 ppb ozone and UV for 22.5 h. a: lightly corroded area; b: heavily corroded area. The leaf-shape feature in the image Figure 5.10a is remaining NaCl.

Figure 5.11 shows that the kinetics of Cu corrosion with 16 $\mu\text{g}/\text{cm}^2$ NaCl are close to linear within 45 h. This is different than the parabolic kinetics found for Cu via oxidation by oxygen without NaCl (41) and supports the breakdown of naturally-formed oxide due to the presence of NaCl. However, the reported corrosion rate of Cu exposed to 500 ppb ozone and 22 to 33 $\mu\text{g}/\text{cm}^2$ NaCl for 4 weeks (23) is much less than the short term exposure corrosion rate of Cu reported in this paper. This is probably caused by a decrease of Cu corrosion rate from reaction and depletion of NaCl after long exposures.

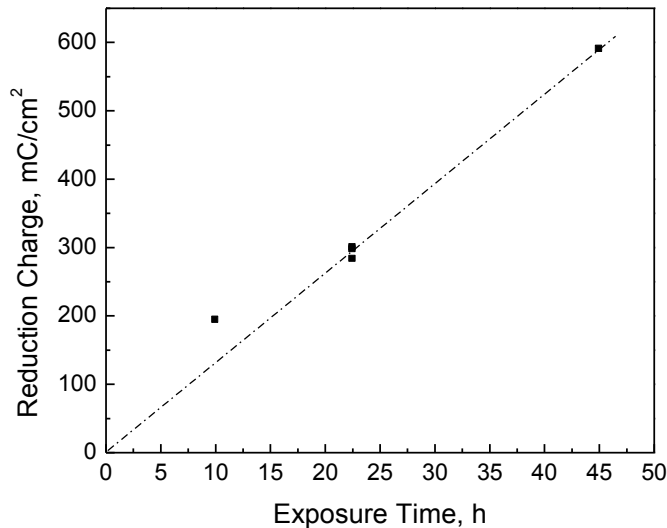
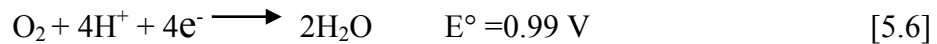
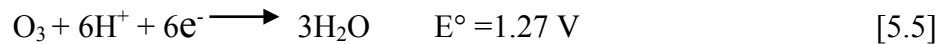


Figure 5.11. Reduction charge of Cu exposed to 16 $\mu\text{g}/\text{cm}^2$ NaCl, 250 ppb ozone, 90% RH air and UV for different times.

Effect of Ozone and UV

Table 5.1 lists corrosion rates of Cu exposed in nitrogen/ozone or air/ozone environments. The corrosion rates of Cu exposed to 900 ppb ozone in nitrogen and Cu exposed to pure air are on the same order, even though the NaCl loading of Cu exposed in nitrogen was smaller. This means the corrosivity of 900 ppb ozone in nitrogen is at least similar to that of air for Cu. It is because ozone is a much stronger oxidant than oxygen. In a dark environment, the main cathodic reactions are the reduction of ozone and oxygen (reactions 5.5 and 5.6).



The standard reduction potential of ozone is 280 mV more positive than oxygen (47). In a neutral solution, the reversible potential of ozone reduction with 900 ppb ozone is 0.8 V, which is about 230 mV more positive than reversible potential of oxygen reduction in ambient air environment (0.57 V), assuming partial pressures of ozone and oxygen are 9×10^{-7} and 0.21 atm, respectively. With addition of 250 ppb ozone, corrosion rate of Cu exposed in air with $16 \mu\text{g}/\text{cm}^2$ NaCl increased evidently as Table 5.1 shows. This proves the corrosivity of ozone on Cu corrosion again.

Table 5.1. Corrosion rate of Cu exposed to different environments, $\mu\text{m}/\text{d}$.

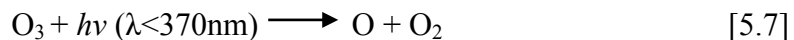
	9 $\mu\text{g}/\text{cm}^2$ NaCl, 6 h, 90% RH	16 $\mu\text{g}/\text{cm}^2$ NaCl, 22.5h, 90% RH	
	Nitrogen, 900 ppb ozone	Air, no ozone	Air, 250 ppb ozone*
Dark	0.09	0.11	0.14
UV	0.17	0.22	0.25
AF	1.9	2	1.8

* Average of three samples.

It has been proven that a strong interaction between photons and cuprous oxide has significant effect on Cu aqueous corrosion (2, 18, 48-50). Since the naturally-formed cuprous oxide is a p-type semiconductor with a band gap of 2.4 eV (51), UV illumination results in a cathodic photocurrent that improves passivity (2, 48). But the newly formed cuprous oxide in sodium chloride or sodium borate solution is n-type semiconductor with similar band gap (18, 49-50). So under illumination of UV, extra anodic photocurrent can be generated, which increases corrosion rate, although it is still not clear why newly formed Cu_2O is n-type.

Table 5.1 also indicates acceleration effect of UV on Cu corrosion. The AF on Cu corrosion is about 2 when Cu is exposed to air without ozone at 90% RH. This is similar to the acceleration effect of UV on Cu in the absence of ozone (6, 52). It suggests that newly formed Cu_2O during atmospheric corrosion of Cu is also an n-type semiconductor. Interaction between photons and newly formed Cu_2O generates extra anodic photocurrent and doubles the corrosion rate (52).

In the presence of ozone and UV radiation, atomic oxygen is generated by photolysis of ozone (reaction 5.7).



Atomic oxygen is extremely aggressive and previous research has shown that atomic oxygen could result in faster corrosion of Ag than ozone (1, 16, 53), especially at low RH. Therefore the presence of the atomic oxygen could increase the acceleration effect of UV. However, this effect is limited at high RH in the presence of NaCl contamination, because of the protection provided by liquid NaCl solution formed due to deliquescence of NaCl (1). Such a liquid layer blocks access of the atomic oxygen to the sample surface and reduces the acceleration effect of the

atomic oxygen (1). This explains why AF on Cu exposed to ozone/nitrogen at 90% RH is almost the same as Cu exposed to pure air.

Effect of RH

Figure 5.12 presents reduction charge of Cu exposed at different RH with $4\mu\text{g}/\text{cm}^2$ NaCl and 250 ppb ozone. The corrosion rate of Cu increases as RH increases with or without UV illumination. In a dry environment with RH close to zero, little moisture is present on the Cu surface. The main corrosion mechanism is oxidation of Cu directly by ozone and oxygen. Since the naturally-formed oxide layer is still protective, the corrosion behavior of Cu with NaCl at dry environment is very similar to bare Cu. Therefore reduction charge of Cu in dry environment even with NaCl was close to zero as was the case for bare Cu.

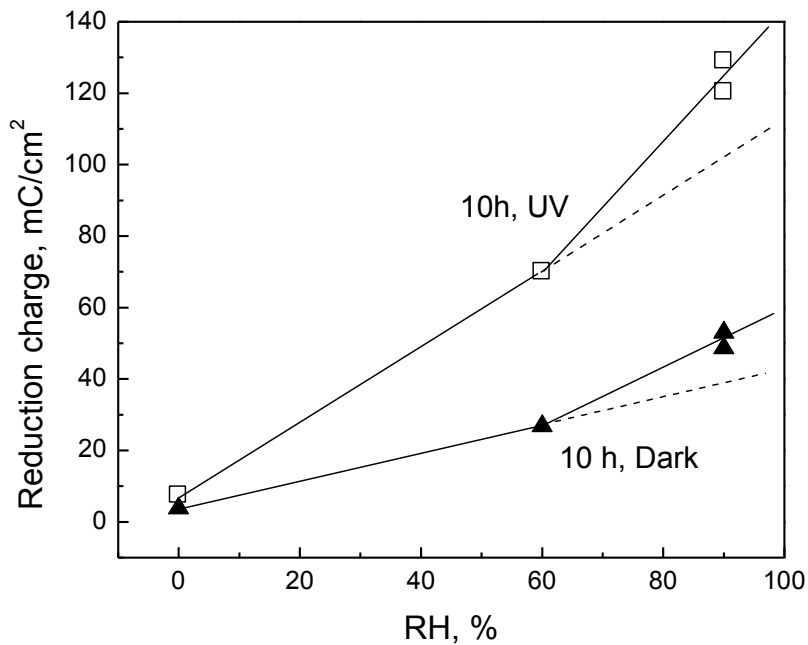


Figure 5.12. Reduction charge of samples exposed to 250 ppb ozone and NaCl in air, with UV radiation or in dark. Loading of NaCl was $4\mu\text{g}/\text{cm}^2$. The dashed lines are extrapolations of the lines from lower RH to facilitate the comparison with the increased charge at high RH.

As RH increases, the moisture layer thickness on Cu increases. At 60% RH, adsorption of water can reach to about 5 monolayers, with properties similar to bulk water (54). Strandberg and Johansson (23) suggested that part of the NaCl dissolves into the moisture layer so the air formed oxide layer can be attacked by Cl^- , which results in fast corrosion at 60% RH.

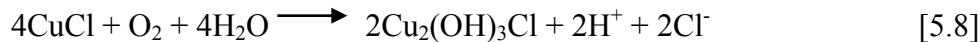
Although water vapor pressure increases linearly as RH increases, the Cu corrosion rate increases nonlinearly as Figure 5.12 shows. At high relative humidity environment, higher than the critical relative humidity (CRH) for deliquescence of NaCl, 75%, NaCl starts to deliquesce and eventually a bulk layer of sodium chloride solution is formed (55). At 90% RH, the equilibrium NaCl concentration is about 2.7 M (25). Environmental SEM proves that all NaCl particles are completely dissolved within a few minutes at this RH (1). The aqueous NaCl layer also increases the area for cathodic reactions dramatically. Therefore at 90% RH, the dramatic increase of surface Cl^- and more catalytic surface for reduction of oxygen and ozone resulted in the nonlinear acceleration effect of RH from 60% to 90% RH shown in Figure 5.12.

Figure 5.12 also indicates that RH influences the effect of UV. At 60% RH, AF is 2.6, and it decreases to 2.4 as RH increases to 90%. This is because the accelerating effect of UV on Cu corrosion includes two mechanisms. The first one is the abovementioned anodic photocurrent due to interaction between photon and cuprous oxide. The second one is generation of atomic oxygen from photolysis of ozone. This effect will be largely limited at high RH as explained before. Therefore the acceleration effect of UV decreases as RH increases.

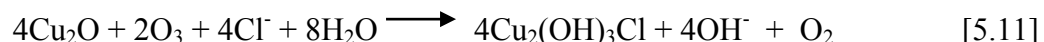
The AF of UV on Cu exposed to $4 \text{ }\mu\text{g}/\text{cm}^2$ NaCl in Figure 5.12 is slightly higher than Cu exposed to more NaCl listed in Table 5.1. It is very likely that surface coverage of NaCl is less than 1 with only $4 \text{ }\mu\text{g}/\text{cm}^2$ NaCl. So atomic oxygen can still attack sample surface to accelerate Cu corrosion, which enhances the acceleration effect of UV.

Formation mechanism of $\text{Cu}_2(\text{OH})_3\text{Cl}$

Oxidation of CuCl (reaction 5.8) is considered as an important pathway to form $\text{Cu}_2(\text{OH})_3\text{Cl}$ (54, 56). Similarly, oxidation of CuCl_2^- was also suggested (23) as shown in reaction 5.9.

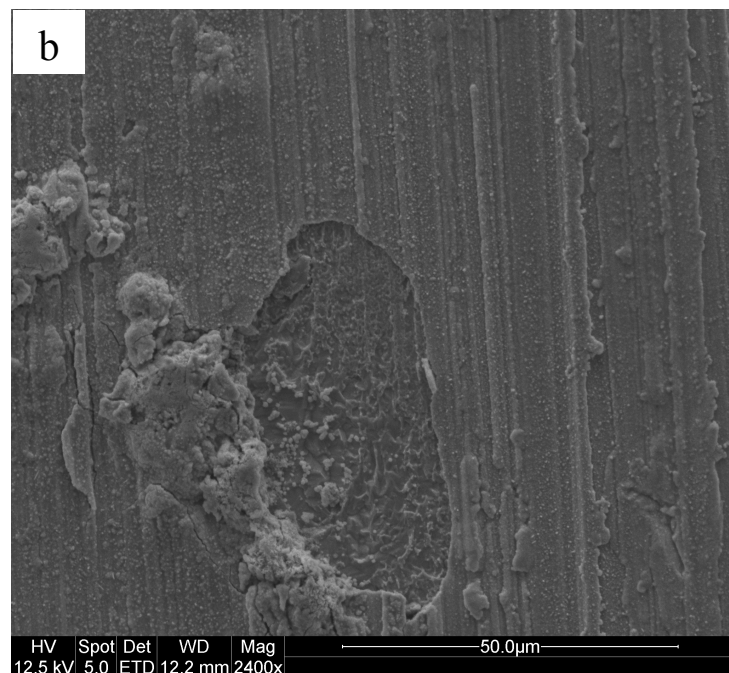
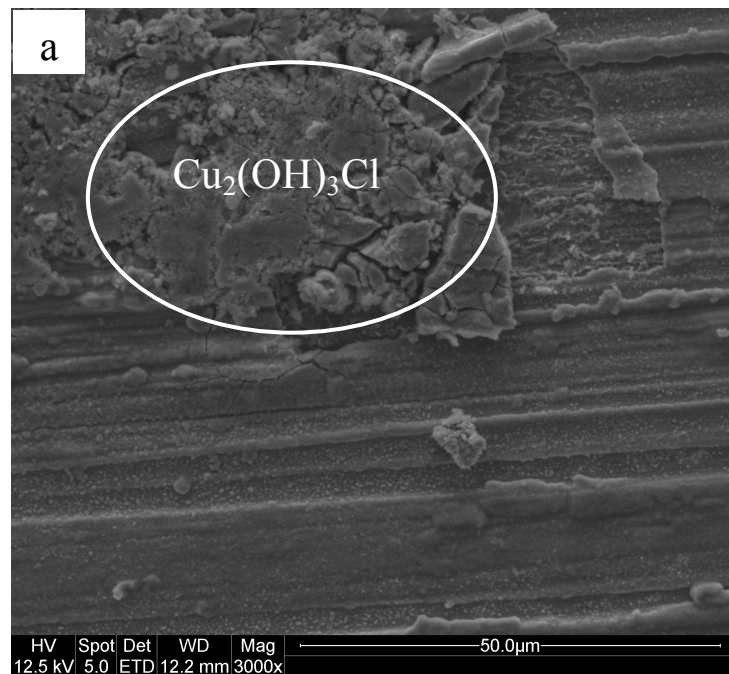


CuCl is not always reported as the Cu corrosion product even for Cu exposed in a marine environment. CuCl is often absent after lab exposure with NaCl too, especially when ozone is involved during exposure (20, 22-23). This suggests another pathway for formation of $\text{Cu}_2(\text{OH})_3\text{Cl}$ without formation of CuCl . Previous research indicates phase transformation of cuprite powders into atacamite (an isomer of $\text{Cu}_2(\text{OH})_3\text{Cl}$) in the presence of NaCl in humid air (24), as equation 5.10 depicts. Therefore direct oxidation of Cu_2O by either oxygen or ozone (equation 5.11) could be a possible alternative for formation of paratacamite during Cu corrosion.



Free energies of formation of $\text{Cu}_2(\text{OH})_3\text{Cl}$ (paratacamite), Cu_2O , Cl^- , H_2O , O_3 and OH^- are -319.8 , -34.98 , -31.4 , -56.7 , 34 and -37.6 kcal/mol respectively (56-57). So the Gibbs free energy changes of reactions 9 and 10 are -355 and -778 kcal respectively. Therefore, these reactions are both thermodynamically possible. This mechanism also results in a dramatic increase in volume because the density of $\text{Cu}_2(\text{OH})_3\text{Cl}$ is only 60% of the density of Cu_2O , while its molecular

weight is also larger, which results in a loose attachment of $\text{Cu}_2(\text{OH})_3\text{Cl}$ on Cu_2O . It is very easy to strip off the greenish species from the sample surface. Microscopically, it is often to find that formation of $\text{Cu}_2(\text{OH})_3\text{Cl}$ is associated with film rupture of Cu_2O , and the surface under $\text{Cu}_2(\text{OH})_3\text{Cl}$ usually looks like fresh Cu surface as Figure 5.13 shows. This also supports a transformation from Cu_2O to $\text{Cu}_2(\text{OH})_3\text{Cl}$.



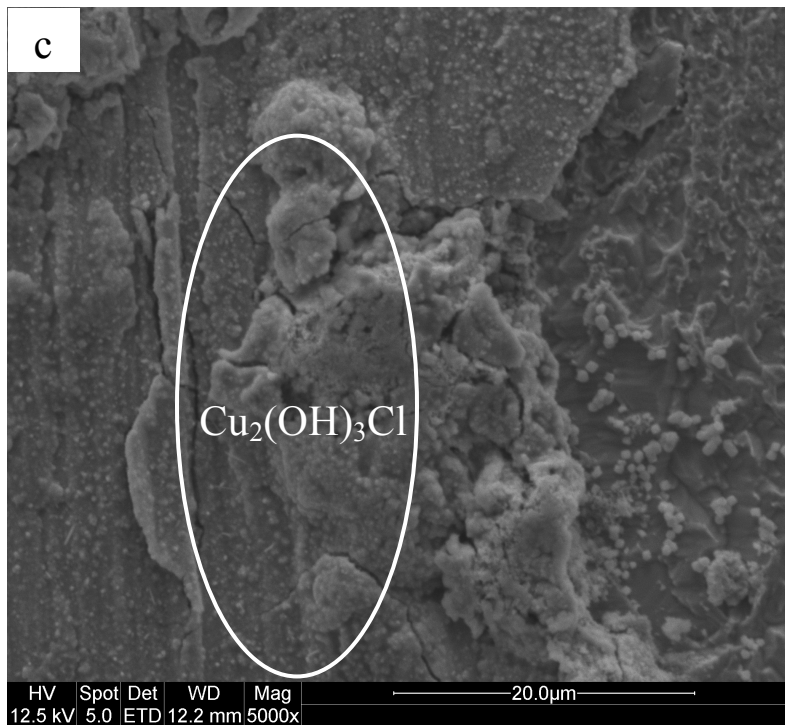


Figure 5.13. SEM image pictures of Cu exposed to 250 ppb ozone, 90%RH air, 16 $\mu\text{g}/\text{cm}^2$ NaCl and UV for 22.5 h. a: as exposed; b and c: rinsed with before SEM.

According to reactions 5.10 and 5.11, not only ozone can increase formation rate of Cu₂(OH)₃Cl but also chloride. Even with ozone, no Cu₂(OH)₃Cl formed during exposure with 8 $\mu\text{g}/\text{cm}^2$ or less NaCl. Thus, it is likely that the kinetics of reactions 5.10 and 5.11 increase dramatically when Cl⁻ concentration reaches some critical value. Although the nominal chloride concentration depends on RH and not on NaCl loading, local concentration is possibly much higher than the nominal value, e.g. at local anodes. So the formation of Cu₂(OH)₃Cl only occurs at some locations, which results in the scattered greenish spots over the sample surface.

Deposition rate of NaCl in the environment chamber

The accumulated amount of deposited NaCl per unit area in mg/cm^2 is plotted in Figure 5.14. When the bubbler beaker contained 5 wt% NaCl, the rate of NaCl accumulation, given by the slope of the curve in Figure 5.14, decreased with time even though a continuous NaCl aerosol was generated. Continuous bubbling in the solution for 96 h at 830 cc/min resulted in a decrease in the volume of the solution by about 40 ml. This change in the conditions in the beaker resulted in a decrease in NaCl deposition rate from 0.026 $\text{mg}/\text{cm}^2\text{h}$ at the beginning to 0.01 $\text{mg}/\text{cm}^2\text{h}$ after about 100 h.

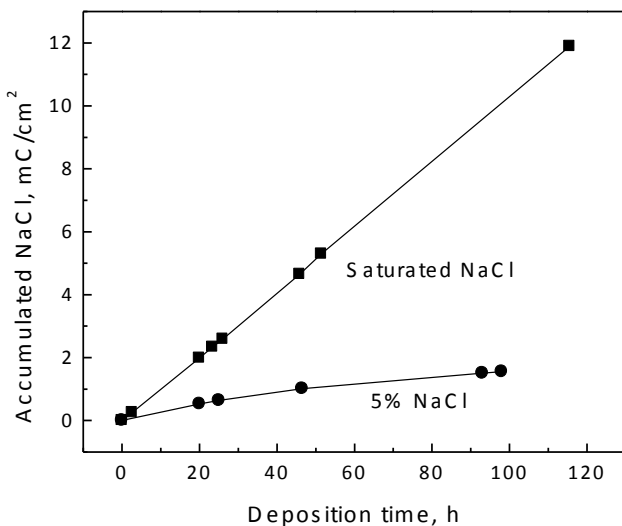


Figure 5.14. Accumulated deposition of NaCl vs deposition period for saturated and 5 wt% NaCl solutions in the bubbler beaker.

When the bubbled beaker in the chamber contained saturated NaCl solution instead of 5 wt.% NaCl, a lower rate of input flow A was needed to get a particular NaCl deposition rate. As a result, the rate of decrease of solution volume in the beaker was lower. For a 15 cc/min flow, the loss of the solution over the first 24 h was about 1 ml. Even though this change is very small, the deposition rate still decreased during bubbling unless input flow B was added. With the addition of the water-saturated air in flow B, the RH in the chamber was maintained at very close to 100%. This value is much higher than the equilibrium RH of saturated NaCl (75%), so the saturated solution in the beaker absorbed water during bubbling. Because the saturated solution contained excess NaCl, the solution remained at the saturation concentration during bubbling. As long as enough water was absorbed to compensate for the loss due to bubbling, the volume of the solution in the beaker stayed constant during bubbling. The decrease of volume in the saturated solution was less than 0.4 ml after bubbling the saturated NaCl solution for 120 h, with flows A and B of 15 and 436 cc/min, respectively. Figure 5.14 shows that the NaCl deposition rate under these conditions was absolutely constant at 0.1 mg/cm²h. All the exposures of Cu mentioned in this paper, except the SKP measurement, were performed with an NaCl deposition rate of 0.1 mg/cm²h. The deposition rate of NaCl associated with the most severe marine environment (e.g. ISO9223, S₃ category) is usually less than 0.00625 mg/cm²h (5). Therefore the NaCl deposition rate in the lab chamber is more than an order of magnitude higher than the deposition rate in severe field environments.

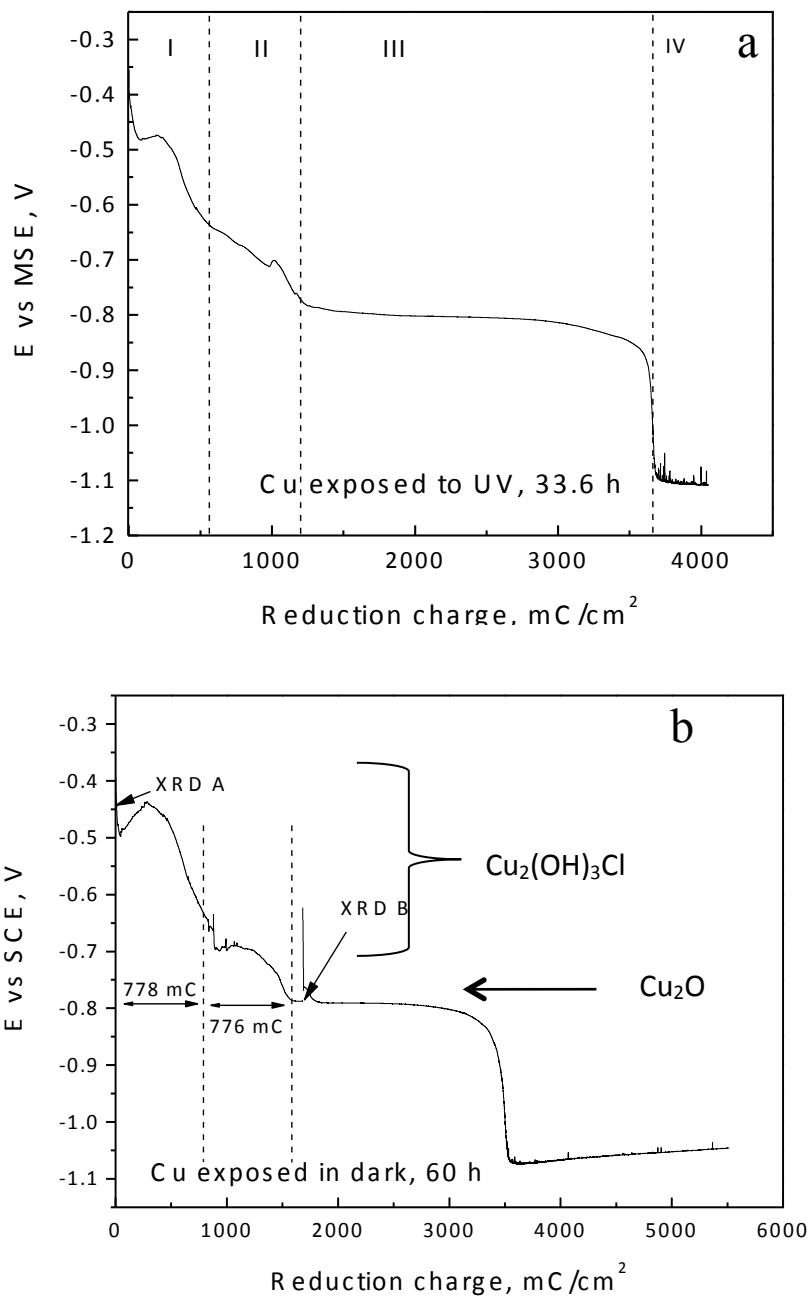
The deposition rate of NaCl can be changed by adjusting flow A or using a dispersion frit with different efficiency. However, it would be necessary to adjust flow B as well to maintain a constant deposition rate.

The RH in this chamber has to be maintained higher than 75% so that the saturated NaCl solution in the beaker continues to absorb water from the ambient atmosphere. It should be possible to achieve an RH between 75% and 100% while maintaining a constant NaCl deposition rate using an additional inlet of dry air, but this was not tried. Another limitation is that the NaCl deposition rate depends on the distance from the frit bubbler. Therefore, for accurate comparison of results, all samples must be exposed at the same location and they cannot be too big or else non-uniform corrosion could occur.

Calibration of coulometric reduction technique

XRD analysis indicated that paratacamite and cuprite formed on Cu exposed with 350 ppm CO₂ for longer than 15 h. Quantitative determination of the amounts of each was performed using coulometric reduction. Figure 5.15a shows a typical reduction curve of Cu with paratacamite and cuprite. Four regions can be discerned: -0.35 to -0.65 V, -0.65 to -0.8 V, a big plateau at -0.8 V and then hydrogen evolution at around -1.1 to -1.2 V. The first two regions do not have very well defined plateaus but have very similar amounts of reduction charge. Before reduction, the samples had greenish product interspersed on a reddish-brown corroded surface. The greenish species disappeared at the end of the first two regions.

To identify the species corresponding to each reduction region, another sample exposed for 60 h in the dark with similar amount of corrosion products was reduced in two steps, as shown in Figure 5.15b. XRD analysis confirmed the presence of paratacamite and cuprite on the exposed sample before reduction, as shown in Figure 5.15c. Reduction of this sample was interrupted after about 1600 s when the potential dropped to -0.8 V SCE. The partially reduced area (within the o-ring) was still reddish-brown but was covered by some loose black powder instead of the greenish species. The black powder was likely Cu from the reduction of corrosion products and it was easily rinsed off with DI water after the sample was taken out of the cell. The unreduced area (outside of the o-ring) was hand-polished with SiC paper carefully to remove the corrosion products. XRD was then performed on the partially reduced product, and only cuprite was identified on the sample (Figure 5.15c). This sample was then reassembled into the cell and reduction was continued. Only one plateau at -0.8 V was observed, as shown in Figure 5.15b. This experiment shows that the plateau at around -0.8 VSCE corresponds to reduction of cuprite and the first two regions or plateaus are likely due to reduction of paratacamite.



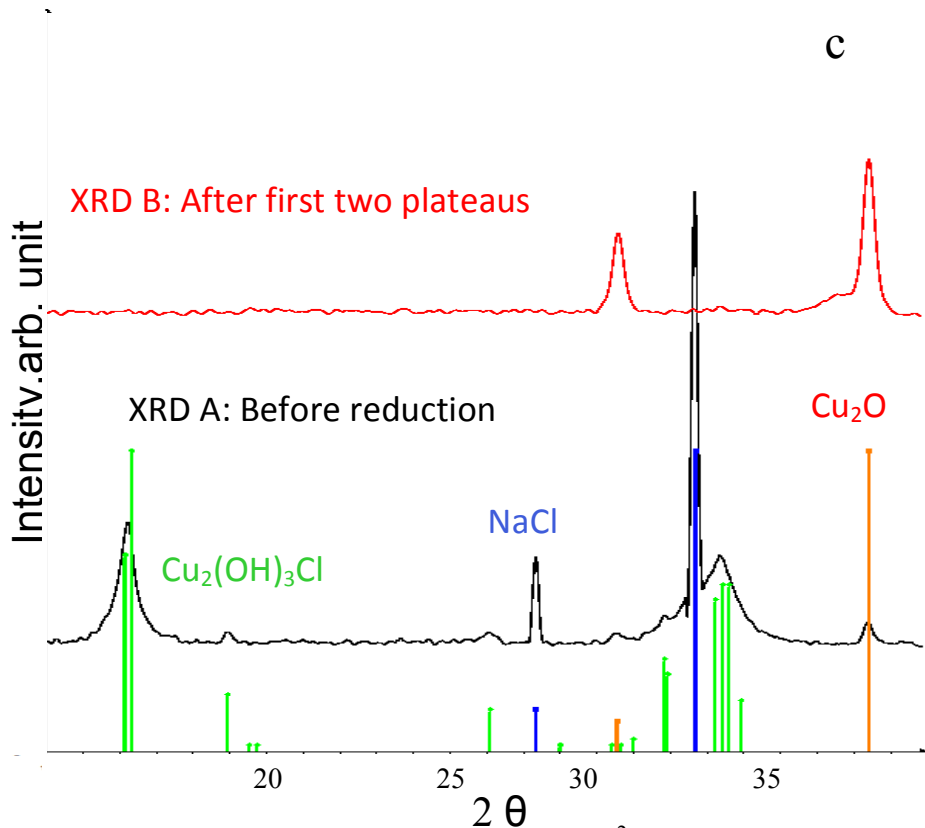


Figure 5.15. Analysis of Cu exposed to humid air, $0.1 \text{ mg/cm}^2\text{h}$ NaCl. a) reduction curve in $0.1 \text{ M Na}_2\text{CO}_3$ for sample exposed with UV b) reduction curve in $0.1 \text{ M Na}_2\text{CO}_3$ for sample exposed in dark c) XRD spectra of sample from b) before reduction and after reduction through the first two plateaus only.

The reduction potential of Cu_2O , -0.8 V SCE , is consistent with previously reported values of -0.75 to -0.9 V SCE in KCl (45, 58), KOH (45) or $\text{Na}_2\text{B}_4\text{O}_7$ (59). There are few reports on the coulometric reduction of $\text{Cu}_2(\text{OH})_3\text{Cl}$. Malvaut et al. reported a peak reduction potential of paratacamite by linear sweep voltammetry in $0.1 \text{ M Na}_2\text{B}_4\text{O}_7$ of -0.61 V SCE (59), which is in the range of the first two plateaus in Figure 5.15a. Interestingly, the first two plateaus have almost the same amount of reduction charge. This suggests that reduction of paratacamite in Na_2CO_3 is a two-step process.

The distinction between the first two regions becomes less apparent as the amount of corrosion products decreases. Reduction curve B in Figure 5.16 shows reduction of Cu exposed in the same environment as the one in Figure 5.15b but for a short time, 23 h, and then reduced in Na_2CO_3 . XRD analysis indicates the presence of cuprite and paratacamite after exposure as well. This reduction curve can be divided into two regions with a flat plateau for reduction of Cu_2O in region II. Here, region I corresponds to the reduction of paratacamite. Although there is no clear distinction of two reduction plateaus in region I, its shape is similar to the overall shape of the first two plateaus in Figures 5.15a and 5.15b.

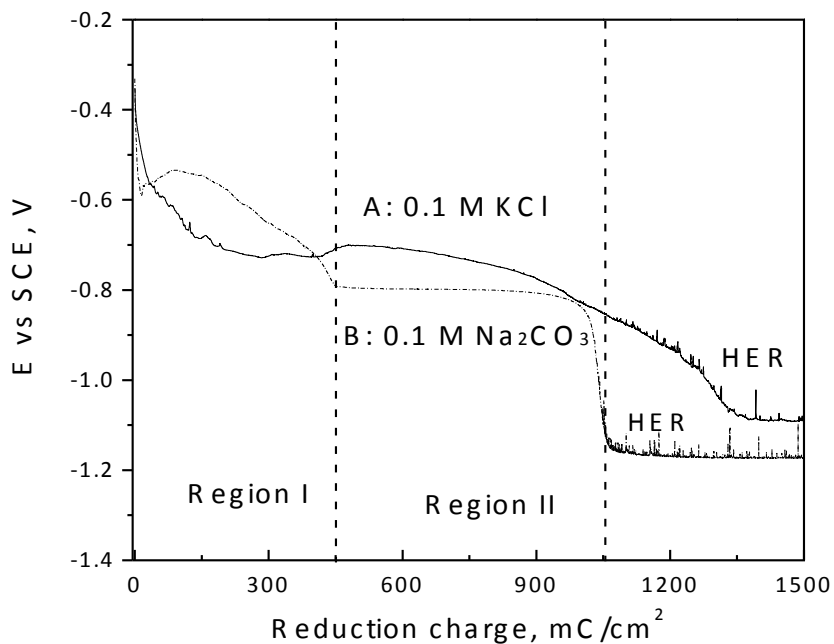


Figure 5.16. Reduction curve of two samples exposed to 100% RH humid air, $0.1 \text{ mg/cm}^2 \text{h}$ NaCl for 23 h. A: reduced in 0.1 M KCl with -0.05 mA/cm^2 ; B: reduced in 0.1 M Na_2CO_3 with -0.05 mA/cm^2 .

Curve A in Figure 5.16 is for another sample that was exposed to the same environment but reduced in 0.1 M KCl as suggested by ASTM B825 (33). It is quite different, with only one broad plateau ranging from -0.6 to -0.8 V so that the reduction of paratacamite and cuprite cannot be clearly differentiated. This is the same as reduction of tenorite and cuprite, which cannot be differentiated in neutral KCl but can be in alkaline solution, e.g. 1 M KOH (41, 45). Copper hydroxyl oxides ($\text{Cu}_2(\text{OH})_3\text{Cl}$ and $\text{Cu}(\text{OH})\text{Cl}$) are only stable at around pH 3.5 to 5.5 (7, 60), while Cu_2O is more stable in neutral to alkaline environments. 0.1 M Na_2CO_3 is basic with a pH of 11.5, which resulted in different reduction potentials for paratacamite and cuprite. A clearer distinction between the hydrogen evolution reaction (HER) and reduction of corrosion products was also found in Na_2CO_3 than in KCl. This increases the accuracy of quantification of corrosion products with the coulometric reduction technique. Therefore reduction of Cu corrosion products in Na_2CO_3 solution rather than KCl is recommended.

Identification and quantification of corrosion products

Table 5.2 lists corrosion products of Cu exposed to humid air with an NaCl deposition rate of $0.1 \text{ mg/cm}^2 \text{h}$ as determined by XRD. Similar to field-exposed Cu, the initial corrosion product identified by XRD was cuprite and then paratacamite formed later. For Cu exposed less than 4 h, there was insufficient corrosion product to be detected by XRD, but the reduction curve confirms the presence of cuprite after exposure as Figure 5.17 indicates. Besides reduction of cuprite, it also shows a reduction plateau around -0.6 to -0.7 V. This is probably due to reduction of trace

cupric compounds, although XRD could not identify the presence of a cupric compound after exposure.

Table 5.2. Corrosion products of Cu exposed to 0.1 mg/cm²h NaCl and humid air

Exposure duration, h	Corrosion products identified by XRD
1 to 4	N/A
8 to 15	Cu ₂ O
> 15	Cu ₂ O and Cu ₂ (OH) ₃ Cl

As the NaCl deposition rate increases in a marine environment, e.g. by wave splashing, paratacamite formation becomes much faster. Detection of Cu₂(OH)₃Cl by XRD was reported after one month exposure (10), while it usually could take several months up to years before Cu₂(OH)₃Cl is detected by XRD under normal NaCl deposition conditions(6). A typical deposition rate of NaCl in a marine environment without splash or spray is less than 0.00625 mg/cm²h (5), which is much less than the deposition rate during most lab exposures. In this work, detection of paratacamite by XRD on Cu exposed for only 15 h with an NaCl deposition of 0.1 mg/cm²h clearly indicates that formation of paratacamite can be dramatically accelerated by increasing the NaCl deposition rate.

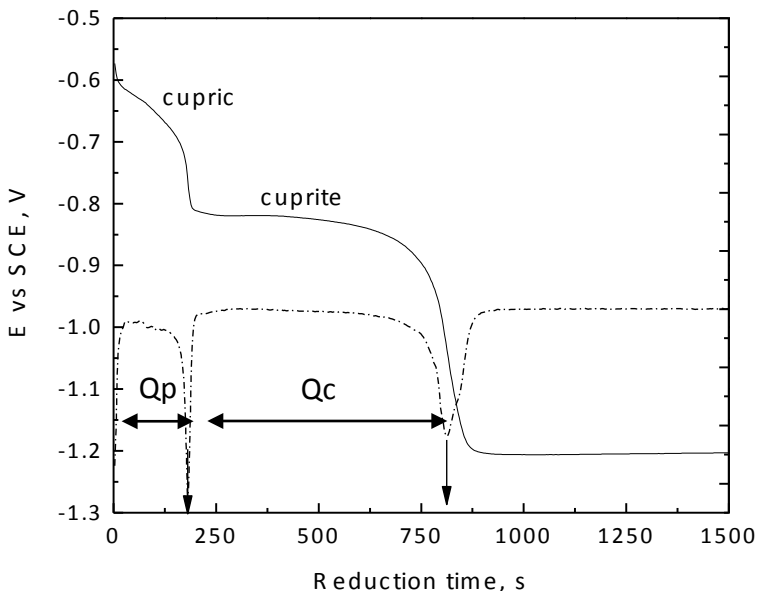


Figure 5.17. Cu exposed to humid air with $0.1 \text{ mg/cm}^2\text{h}$ NaCl for 3 h. Solid line: Reduction curve. Dashed line: Derivative of the reduction curve. Note that cupric here represents cupric compounds such as paratacamite or atacamite.

An equivalent weight loss of Cu can be calculated from reduction curves by the following equation:

$$W = \frac{10000 \times (Q_c + 0.5 \times Q_p) \times M}{F} \quad [5.12]$$

where W is total weight loss in g/m^2 , Q_c is reduction charge corresponding to reduction of cuprite in C/cm^2 , Q_p is reduction charge corresponding to reduction of paratacamite in C/cm^2 , M is molecular weight of Cu, 64 g/mol , and F is the Faraday constant, 96500 C/mol .

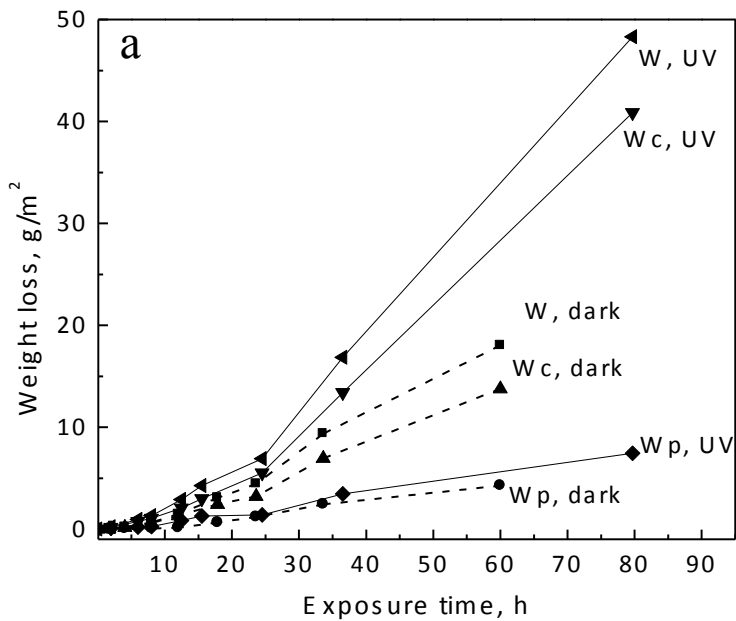
The approach used for determination of Q_c and Q_p is described in Figure 5.17. The length of each plateau is determined by local minima of the derivative of the reduction curve (58). Although no paratacamite was detected by XRD for samples exposed less than 15 h, the reduction charge above the cuprite reduction plateau can still be assigned to Q_p , since it was due to reduction of Cu^{2+} ions. Besides the calculation of total Cu weight loss, the weight loss due to formation of cuprite or paratacamite can be calculated separately with equations 5.13 and 5.14, respectively:

$$W_c = \frac{10000 \times Q_c \times M}{F} \quad [5.13]$$

$$W_p = \frac{10000 \times Q_p \times M}{2 \times F} \quad [5.14]$$

where W_c is weight loss due to formation of cuprite and W_p is weight loss due to formation of paratacamite in g/m^2 .

Figure 5.18a summarizes weight loss data of Cu exposed to humid air with $0.1 \text{ mg}/\text{cm}^2\text{h}$ NaCl deposition rate up to 80 h with UV or in a dark environment. Figure 5.18b presents the derivative of each curve in Figure 5.18a, showing the formation rates of cuprite and paratacamite and the total corrosion rate of Cu. Generally, the formation of cuprite was much faster than paratacamite and it has the most dominant influence on the Cu corrosion rate. At the beginning, only part of the Cu surface was covered with NaCl droplets. The covered area kept increasing during exposure until the whole sample surface was fully covered with NaCl solution after about 12 h. During this period, the formation rate of cuprite and total corrosion rate were relatively low but kept increasing, while the formation rate of paratacamite stayed close to zero. After the surface was completely covered with NaCl solution, the cuprite and paratacamite formation rates, and thus the Cu corrosion rate, all increased significantly, which was likely due to continuous increase of NaCl loading. Eventually, the rates all became relatively stable. A constant Cu corrosion rate has been found previously for lab exposure of Cu in mixed flowing gas and field exposure of Cu for three years (11, 61). The corrosion rate of Cu and formation of Cu_2O are both constant when the corrosion product layer is not thick enough. After exposure of Cu in the field for a few tens of years, when the corrosion product layer is thicker than $10 \mu\text{m}$, the corrosion products become protective and corrosion rate decreases (7). Therefore, a decrease of the Cu corrosion rate is very likely if the Cu is exposed in the lab chamber for a longer period.



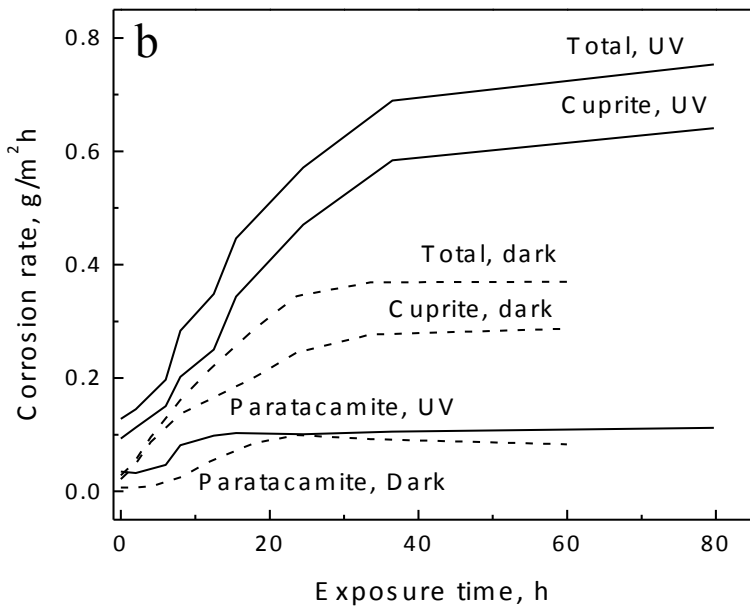


Figure 5.18. a)Weight loss and loss in thickness of Cu exposed to humid air and $0.1 \text{ mg/cm}^2 \text{ h}$ NaCl, with UV (solid lines) or in dark (dashed lines). b)formation rate of cuprite and paratacamite and corrosion rate of Cu, derivative of data showed in Figure 5.18a.

It is very clear that addition of UV illumination accelerates Cu corrosion significantly, which is mainly because the formation rate of cuprite is accelerated by UV illumination by about a factor of 2 during the whole exposure from 4 to 60 h. The formation rate of paratacamite is just slightly higher than in the dark. The acceleration effect of UV reported in Figure 5.18 is very similar to the previously reported effect of $\text{H}_2\text{S}/\text{UV}$ on Cu corrosion(17).

Naturally formed cuprous oxide is a p-type semiconductor with a band gap of 2.4 eV(51). UV photons ($\lambda < 370 \text{ nm}$, $E > 3.4 \text{ eV}$) have enough energy to generate electron-hole pairs. This only leads to cathodic photocurrent, which reduces the passive current and increases the corrosion resistance (2). N-type cuprite with a similar band gap of 2 eV usually forms in slightly acidic to alkaline solution during corrosion, which can lead to anodic photocurrent and increase the corrosion rate (18, 62-63). Therefore, because Figure 5.18 clearly shows the acceleration effect of UV, it is likely that n-type cuprite formed during exposure of Cu in humid air and was more dominant than p-type cuprite.

With the presence of n-type cuprite on the anodic area of Cu, an ohmic junction and Schottky barrier format local anodes, as shown schematically in Figure 5.19, which is similar to the model suggested by Gerischer (3) and Burleigh (2, 64) on metals with n-type oxide under anodic polarization. Once a photon with energy larger than band gap hits cuprite, especially on the local anode area, a hole-electron pair forms (equation 5.15). Electrons can drift back to the Cu

substrate, assuming the ohmic resistance is negligible, and migrate to cathodic areas to support reduction of oxygen (equation 5.16), while holes move towards the surface.

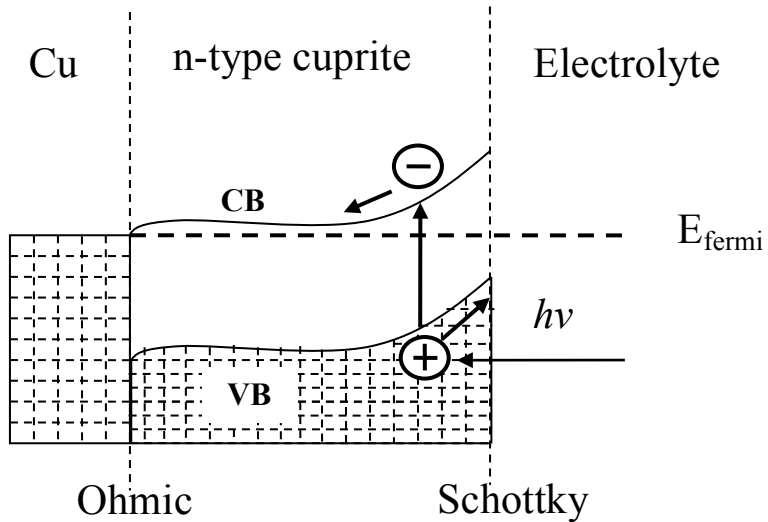
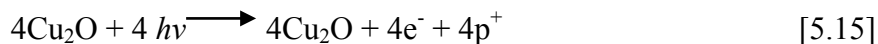


Figure 5.19. Schematic illustration of the interaction between photons and n-type cuprite. CB: conduction band; VB: valence band, modeled after (2-3).

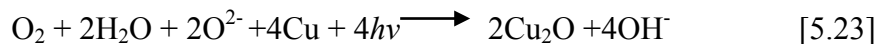
Three possible pathways are proposed. First, Cu^+ is oxidized to Cu^{2+} (equation 5.17). Then a reverse disproportionation reaction of cupric and metallic Cu to generate cuprous ions occurs as equation 5.18 suggests. This is similar to reverse disproportionation of $\text{Cu}_4(\text{SO}_4)(\text{OH})_6$ and metallic Cu proposed previously for formation of cuprite in the presence of ammonium sulfate (65). Equation 5.19 is the overall reaction of the first pathway. $\text{Cu}(\text{OH})$ as an intermediate decomposes to form cuprite rapidly according to equation 5.20 (18).



The other two possible routes are formation of oxygen atoms instead of cupric ions by holes with O^{2-} in Cu_2O (equation 5.21) or by holes with OH^- (equation 5.22):



Gerischer suggests formation of O_2 by a series of reactions between O^{2-} and photons resulting in dissolution of Zn into ambient solution under UV illumination(3). Since the formation rate of Cu_2O increases under UV illumination, it is more likely that atomic O (from equation 5.21 or 5.22) diffuses through oxygen vacancies towards the Cu/oxide interface and then react with Cu to form oxide. In this situation, the overall reactions are equations 5.23 and 5.24, corresponding to 5.21 and 5.22 respectively.



Reaction 5.23 can generate oxygen vacancies, which is consistent with characterization of n-type semiconductors.

The proposed reaction paths all indicate that photons have very little effect on the formation of cupric ions, although the first pathway might generate some less dominant cupric ions because reaction 5.18 is very likely a slow step. This is supported by the small increase of W_p with UV illumination compared to Cu exposed in dark, as Figure 5.18 shows. This increase is probably because of unreacted cupric ions converting to $Cu(OH)_2$, CuO or some precursor of paratacamite. Actually, a greenish species started to appear after Cu was exposed to UV for 6 h in the environment chamber with constant deposition of NaCl, about two hours earlier than Cu exposed in dark. The greenish species is likely paratacamite, although XRD could not identify it.

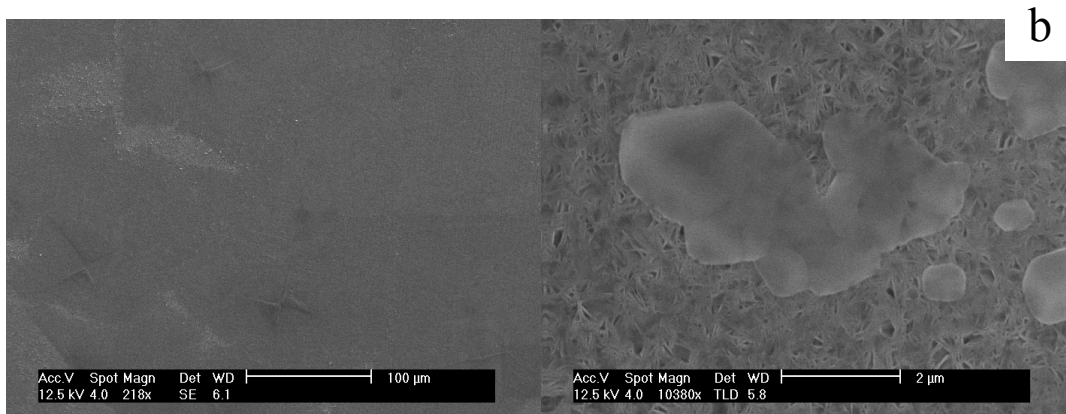
Effect of CO_2 on Cu corrosion with NaCl

The corrosion behavior of Cu exposed with low CO_2 (< 1ppm) is different than that of Cu exposed with 350 ppm, which is close to the ambient concentration of CO_2 in the air. Cu exposed to a low CO_2 atmosphere exhibited a black surface covered with white salt. In contrast, Cu exposed to high CO_2 had a reddish-brown surface with greenish paratacamite interspersed, which is similar to what forms on Cu exposed in the field (6). The black color is due to the presence of black compound tenorite (CuO), which became detectable by XRD on Cu exposed longer than 20 h with low CO_2 . However no paratacamite or other cupric compound was identified by XRD. SEM images of these two samples are also quite different as Figure 5.20 indicates. The corrosion product on Cu exposed with low CO_2 was more compact than that formed on Cu exposed with high CO_2 , although it still had some fine porosity, Figures 5.20a and 5.20b. Cu exposed with

high CO₂ had a much less dense product layer covered with paratacamite flakes as Figures 5.20c and 5.20d indicate.

Figure 5.21 is a typical reduction curve of Cu exposed with low CO₂. In contrast to the curve for Cu exposed to high CO₂ in Figure 5.16, the reduction plateau of cuprite at -0.8 V SCE was relatively small. A broad plateau from -0.7 to -0.76 V is due to reduction of tenorite, as it has been shown that reduction of tenorite occurs at a more positive potential than reduction of cuprite in alkaline solution (45). The part of the curve above the tenorite reduction plateau was always very small and might due to reduction of some other trace cupric compounds. The amounts of Cu₂O and CuO formed during exposure with low CO₂ can still be quantified with equations 5.13 and 5.14 separately by their reduction charges.

The equivalent weight loss and corrosion rate of Cu exposed to high and low CO₂ is compared in Figure 5.22. Generally, the corrosion rate of Cu exposed to low CO₂ (<1 ppm) was relatively constant with time in contrast to the behavior of Cu exposed to high CO₂ (350 ppm). It is interesting to notice that during the first 5 h, Cu exposed to low CO₂ corroded faster than Cu exposed to high CO₂. This is similar to exposure of Cu with NaCl particles. With low NaCl loading, Cu corroded faster with low CO₂ (< 5 ppm), while at high NaCl loading, Cu corroded faster with high CO₂ (350 ppm) (21, 29). This was attributed to the fact that NaCl droplets are more spread out with low CO₂ (21, 29). So during the first 5 h, before the Cu surface is completely covered with NaCl droplets, samples exposed to low CO₂ had higher surface coverage of NaCl solution for the same loading of NaCl. This explains why Cu corroded faster with low CO₂ during the first 5 h. For Cu exposed longer than 5 h, the corrosion rate of Cu exposed to low CO₂ became slower than for Cu exposed to high CO₂.



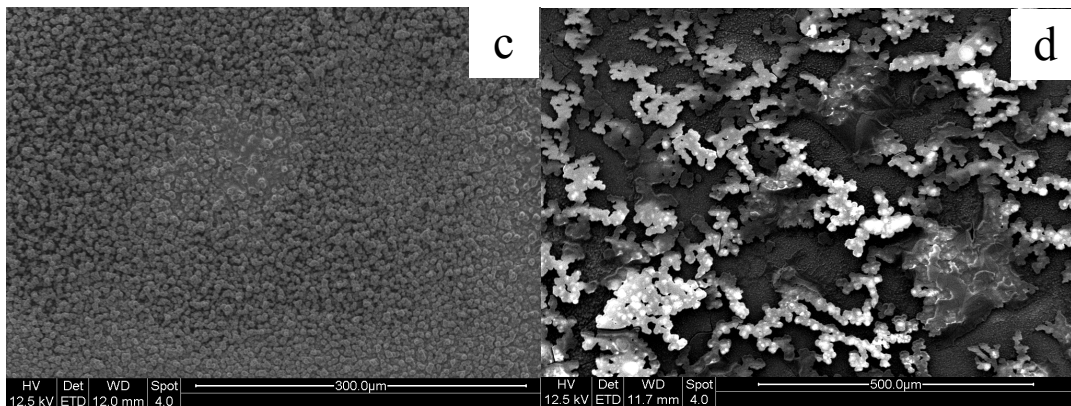


Figure 5.20. SEM images of Cu exposed to low and high CO_2 . a)and b)Cu exposed to humid air with less than 1 ppm CO_2 and $0.1 \text{ mg}/\text{cm}^2\text{h}$ NaCl for 58.5 h. Broken film in figure 5.20b is remaining NaCl as confirmed by EDS. c)and d)Cu exposed to humid air with 350 ppm CO_2 and $0.1 \text{ mg}/\text{cm}^2\text{h}$ NaCl for 60.5 h. Flakes in d) are paratacamite as confirmed by EDS.

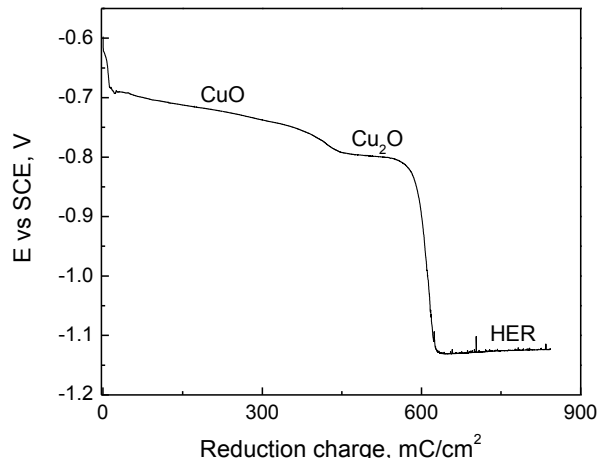


Figure 5.21. Reduction curve of Cu exposed to humid air with less than 1 ppm CO_2 and $0.1 \text{ mg}/\text{cm}^2\text{h}$ NaCl for 23.5 h. Cu was reduced in 0.1 M Na_2CO_3 .

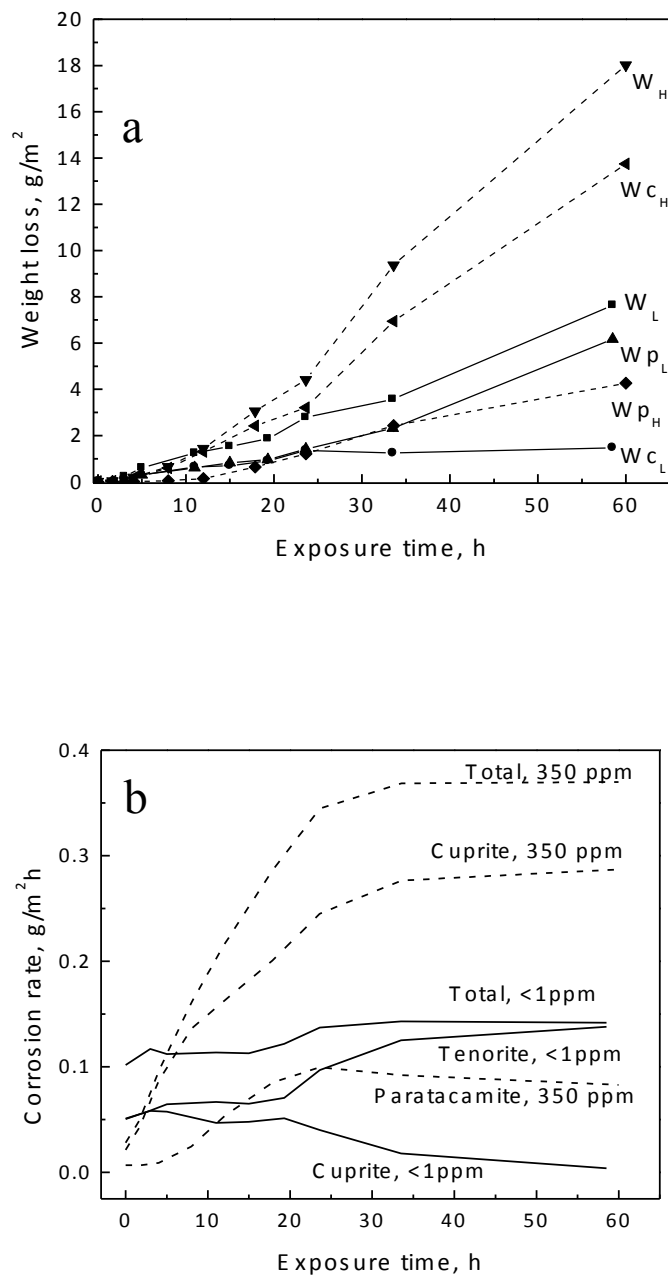


Figure 5.22. Effect of CO_2 concentration on Cu corrosion. a) equivalent weight loss of Cu exposed to humid air with 350 ppm or < 1 ppm CO_2 . NaCl deposition rate is $0.1 \text{ mg}/\text{cm}^2\text{h}$. Subscript L and solid lines are Cu exposed to < 1 ppm CO_2 . Subscript H and dashed lines are Cu exposed to 350 ppm CO_2 . For Cu exposed to < 1 ppm CO_2 , W_p is weight loss due to formation of tenorite instead of paratacamite. b) formation rate of cuprite and paratacamite and corrosion rate of Cu, derivative of data showed in a).

Since no $\text{Cu}_2(\text{OH})_3\text{Cl}$ formed during exposure of Cu to low CO_2 , the actual loading of NaCl on Cu was actually more than for Cu exposed to low CO_2 than to high CO_2 . This is supported by the observation that samples exposed to low CO_2 had much more white NaCl remaining on the surface than samples exposed to high CO_2 after they were taken out of the chamber and dried. However, even with more NaCl, the corrosion rate of Cu exposed to low CO_2 was still much less than for the Cu exposed to high CO_2 . This is mainly due to the presence of CuO , which can provide a high degree of corrosion protection. It has been shown that the initially formed Cu_2O has a porous structure (66). CuO forms in the Cu_2O pores to block them and increase corrosion resistance (66-68). Figures 5.20a and b confirm the relatively compact surface morphology of Cu exposed with low CO_2 . With high CO_2 , paratacamite was the main cupric compound instead of tenorite. Most of the paratacamite was just flakes loosely attached to sample surface as Figure 5.20d shows. These flakes were not as protective as the compact oxide layer formed in low CO_2 environment. On the other hand, after 10 h exposure, almost the whole sample surface was covered with NaCl droplets, so there was no surface coverage difference between Cu exposed to low CO_2 and high CO_2 . Therefore after 5 h exposure, before the whole surface was covered with NaCl solution, the corrosion rate of Cu in low CO_2 was slower than Cu exposed to high CO_2 .

pH has a strong influence on the formation or stability of Cu_2O , CuO and $\text{Cu}_2(\text{OH})_3\text{Cl}$. Cu_2O forms at $\text{pH} > 4$, while formation of CuO occurs at $\text{pH} > 6.7$ (68). $\text{Cu}_2(\text{OH})_3\text{Cl}$ is stable between pH 3.8 to 5.5 (7, 60). Using software from OLI Systems Inc., the equilibrium pH of water with 350 ppm CO_2 was calculated to be about 5.7 but as the CO_2 concentration drops to less than 1 ppm, the pH increases above 6.8. So with low CO_2 , CuO is the dominant cupric corrosion product. This also explains why CuO is not the dominant cupric compound in the field because the CO_2 concentration in the ambient atmosphere is about 300 to 600 ppm (69). With high CO_2 , the formation of $\text{Cu}_2(\text{OH})_3\text{Cl}$ is likely to occur at local anode areas where local pH is lower than the bulk aqueous layer. That is probably why dispersed $\text{Cu}_2(\text{OH})_3\text{Cl}$ appeared after relative short term exposure.

Morphology and localized corrosion of exposed Cu

The surfaces of samples exposed to 350 ppm CO_2 for less than 12 h had significant circular features with a diameter of a few hundred micrometers as Figures 5.23a and b show, which suggests a strong effect of the initial droplets formed by the deposited NaCl solution aerosol. For samples exposed longer, the circular features become less evident and the sample surface was much more uniform. However, after corrosion products were dissolved in strong acid, circular features were the dominant feature on the metallic substrate. As shown in Figures 5.23 d-f, attack was localized in the form of small pits at the periphery of circles with similar size as the circular features that appeared after exposure. This morphology was even observed for samples exposed for relatively long times and did not have circular features in the corrosion product layer.

Although some pits were occasionally present at the center of a circle, these peripheral pits suggest that oxidation of Cu primarily occurred around the edge of the initially-formed droplets. The mechanism of formation of these pits is not known. However, it is completely different than the classical Evans droplet model on steel, where oxidation of iron occurs under the center of a droplet of 0.1 M NaCl as an anode and reduction of oxygen occurs under the edge as a cathode because oxygen is more available at the edge of droplet (70). For Cu exposed to less than 1 ppm CO_2 , the circular features were less significant. More pits were found close to centers of droplets.

This suggests that a stronger secondary spreading of droplets with low CO₂ (21, 29) can impede formation of the circular features.

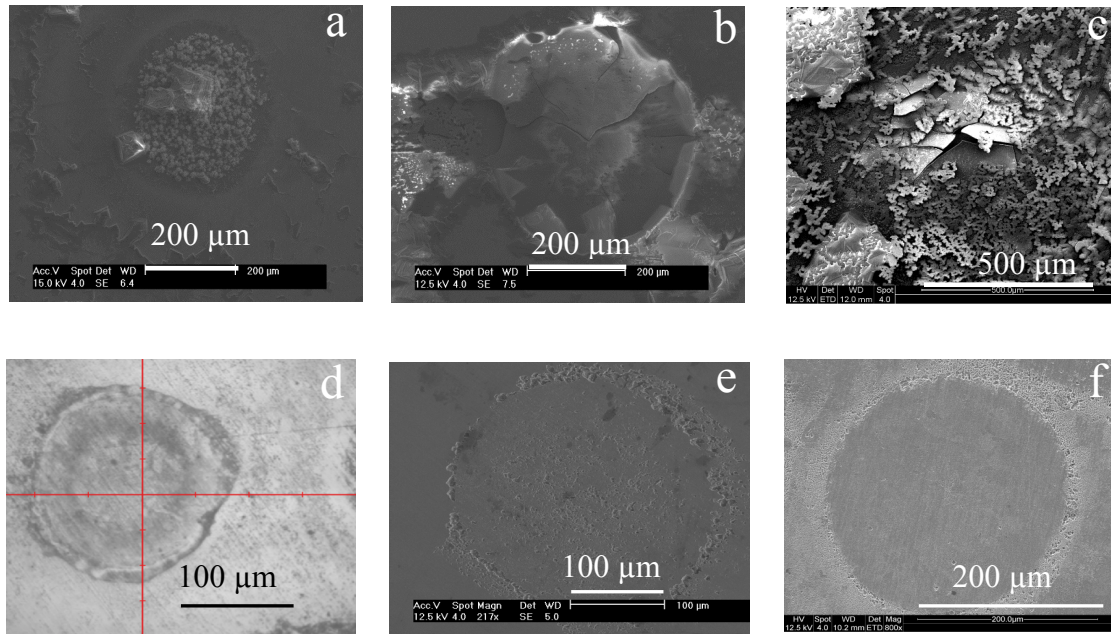


Figure 5.23. Images of Cu exposed to humid air (350 ppm CO₂) and 0.1 mg/cm²h in dark. a), b) and c) are samples after exposure. d), e) and f) are exposed samples after soaked in 6.5 M HCl for 5 min and 1 min in 1 M H₂SO₄ to remove corrosion products. a) and d) are samples exposed for 4h; b) and e) are 12 h; c) and f) are samples exposed for 23.5 h.

Figure 5.24a presents Volta potential profiles from SKP measured across the surface of Cu exposed with a single saturated NaCl droplet in 98% RH, which simulates the exposure conditions in the home-built chamber. At the beginning, the potential under the droplet was much lower than the surrounding area and a dramatic potential change occurred right outside of the edge of the droplet. This is the same as previous results on Cu with single NaCl droplet in 85% RH (29), which suggests a thin electrolyte layer surrounding the droplet. Reduction of oxygen is likely to occur within this thin electrolyte area. Probably because of the formation of insoluble cuprite and the thin electrolyte layer, a large ohmic potential drop is generated between the anode and cathode. Therefore, oxidation of Cu takes place very close to the cathode, at the outer periphery of the droplet. This may explain why small pits formed around the periphery of the droplet.

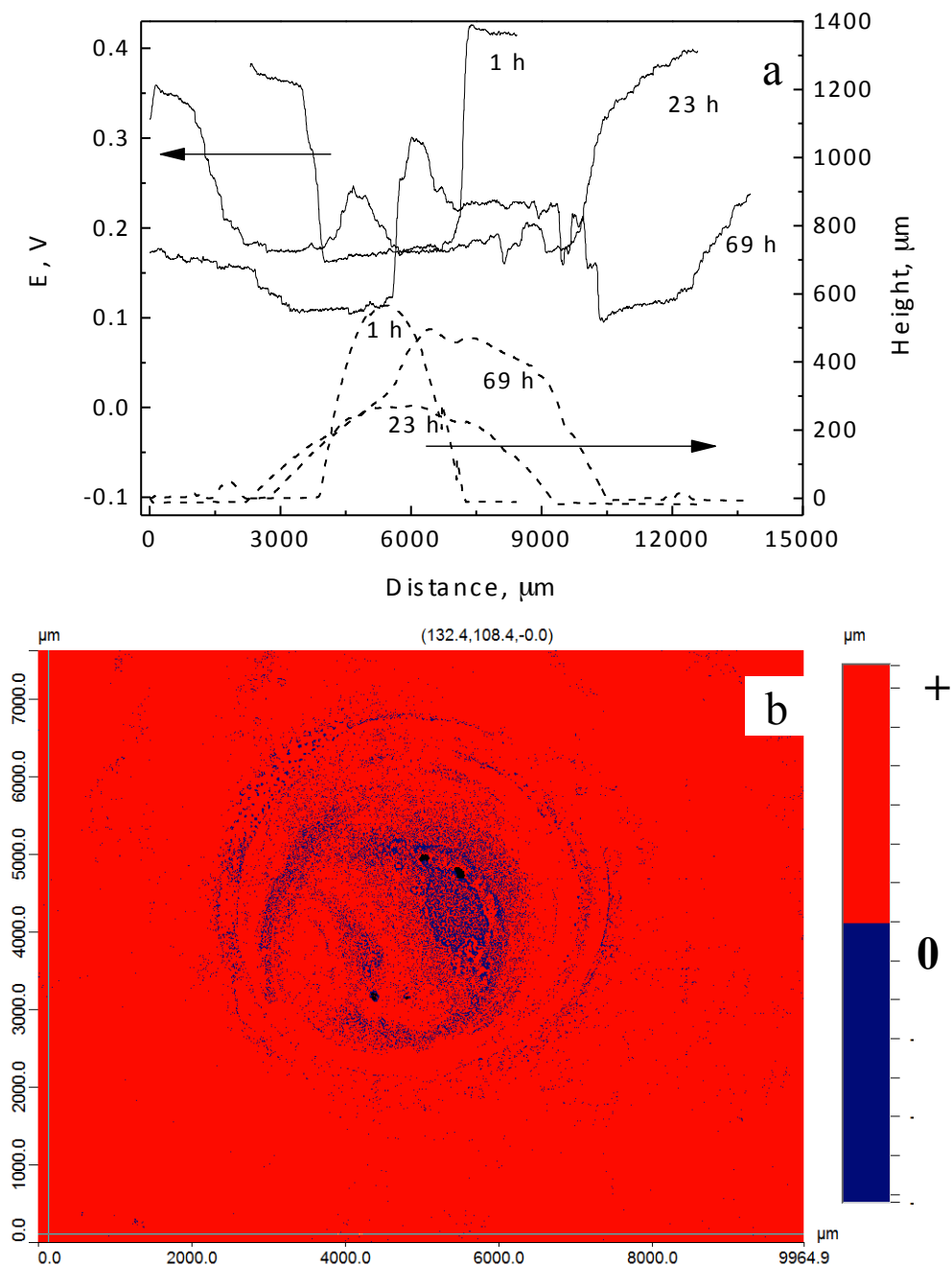


Figure 5.24. a) profiles of Cu with one droplet of saturated NaCl in 98% RH for 1 h, 23 h and 69 h respectively. Dashed line: geometrical profile of the droplet. Solid line: Volta potential. b) morphology of the same Cu sample after 72 h exposure and remove corrosion product by strong acid.

In the 98% RH SKP chamber, the NaCl-saturated droplet kept absorbing water and growing during the measurement. However, the low potential region was always observed around the edge of the droplet. The topography of the sample after exposure for 72 h and removal of the

corrosion product shows a sequence of circular rings of pits that probably formed as the droplet grew, Figure 5.24b. The eventual increase of potential under the droplet is probably due to formation of paratacamite and depletion of NaCl, which results in an inactive region.

The maximum pit depth from optical profilometry and equivalent weight loss calculated from reduction charge of Cu exposed to different environments are presented in Figure 5.25. Generally, at the beginning, the pit depth increased much faster than weight loss, and then it slowed down. This suggests that corrosion of Cu with constant deposition was more localized at the beginning and then became more uniform.

The maximum pit depth of Cu exposed to UV is about three times that of Cu exposed in dark environment as Figure 5.25 shows. This is consistent with the explanation given above, that extra anodic photocurrent is generated due to interaction between UV photons and local anodes. For Cu exposed with low CO₂, localized corrosion is more severe than Cu exposed with high CO₂, although its total corrosion rate is lower. This again supports that the notion that corrosion products formed in low CO₂ environment are more protective.

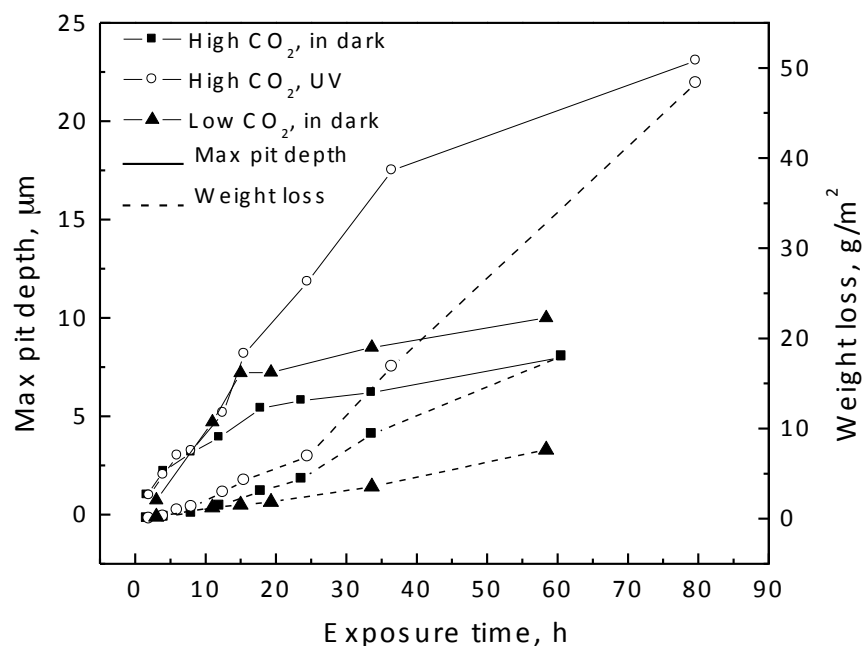


Figure 5.25. Maximum pit depth and equivalent weight loss of Cu exposed in various environments.

5.7 Economic Summary

Cu is used widely in industrial and consumer products. All of these applications find use in the DoD. This project was initiated before a focus on economic considerations was made in the

TCC. However, it is expected that a reduction in the extent of Cu corrosion that would be possible through an improved understanding of the Cu atmospheric corrosion mechanisms would be considerable.

5.8 Implementation

There are no plans to implement any of the findings in a product or standard. However, the developed constant rate chloride deposition scheme will certainly find use in accelerated test programs.

5.9 Conclusions

A new environment chamber with constant deposition of NaCl was designed and used for laboratory exposure of Cu. The initial stage of atmospheric corrosion behavior of Cu exposed to ozone, UV and NaCl and corrosion behavior of Cu with UV and CO₂ under constant deposition of NaCl were studied. The following can be concluded:

- Due to protection of naturally-formed copper oxide, bare Cu corrodes extremely slowly with high ozone and UV illumination, even slower than Ag.
- With the addition of a trace amount of NaCl, corrosion of Cu becomes much more severe because of breakdown of the naturally-formed oxide by chloride.
- UV has significant acceleration effect on Cu corrosion. The anodic current generated by interaction between photons and n-type Cu₂O is the dominant mechanism regardless of RH. When NaCl on Cu surface does not deliquesce, atomic oxygen generated by photolysis of ozone also accelerates corrosion. Therefore the acceleration effect of UV is more significant at low RH.
- With enough loading of NaCl (>16 μ g/cm²) and 250 ppb ozone, formation of Cu₂(OH)₃Cl can occur within a short exposure time, i.e. 22.5 h. Oxidation of Cu₂O to form Cu₂(OH)₃Cl by oxygen and ozone is a possible reaction pathway, which is thermodynamically possible. SEM images also indicate a conversion from Cu₂O to Cu₂(OH)₃Cl.
- The features in Cu coulometric reduction curves were associated with different corrosion products, allowing the coulometric reduction method to be used for quantification of the different products.
- With 350 ppm CO₂, paratacamite and cuprite are the dominant corrosion products like Cu exposed in the field. When CO₂ drops to less than 1 ppm, which increases pH of aqueous layer on Cu, tenorite and cuprite are dominant. Corrosion products formed in low CO₂ are much more dense and protective than corrosion products formed in high CO₂. Therefore, CO₂ is very aggressive for Cu corrosion.
- UV has a strong acceleration effect on formation of cuprite due to interactions between UV photons and cuprite but UV has little effect on the formation of paratacamite.
- In various environments with UV illumination or different concentration of CO₂, during the beginning of exposure, localized corrosion is always dominant, but uniform corrosion

becomes dominant after exposure of approximately 20 to 30 h. Therefore, localized corrosion is not a severe concern for long term exposure of Cu in these environments.

5.10 References

1. D. Liang, H. C. Allen, and G. S. Frankel, *Journal of the Electrochemical Society*, 2010. **157**(4): p. C146-C156.
2. T. D. Burleigh and R. M. Latanision, *Journal of the Electrochemical Society*, 1987. **134**(1): p. 135-138.
3. H. Gerischer, *Journal of the Electrochemical Society*, 1966. **113**(11): p. 1174-&.
4. D. De la Fuente, J. Simancas, and M. Morcillo, *Corrosion Science*, 2008. **50**(1): p. 268-285.
5. ISO, *Corrosion of Metals and Alloys - Corrosivity of Atmospheres - Classification*. 9223:1992.
6. T. E. Graedel, K. Nassau, and J. P. Franey, *Corrosion Science*, 1987. **27**(7): p. 639.
7. T. E. Graedel, *Corrosion Science*, 1987. **27**(7): p. 741-769.
8. M. Watanabe, M. Tomita, and T. Ichino, *Journal of the Electrochemical Society*, 2001. **148**(12): p. B522-B528.
9. L. Veleva, S. A. Tomas, and E. Marin, *Corrosion Science*, 1997. **39**(9): p. 1641-1655.
10. L. Veleva, P. Quintana, and R. Ramanauskas, *Electrochimica Acta*, 1996. **41**(10): p. 1641-1645.
11. S. Syed, *Corrosion Engineering Science and Technology*, 2008. **43**(3): p. 267-272.
12. L. Nunez, E. Reguera, and F. Corvo, *Corrosion Science*, 2005. **47**(2): p. 461-484.
13. S. Zakipour, J. Tidblad, and C. Leygraf, *Journal of the Electrochemical Society*, 1995. **142**(3): p. 757-760.
14. B. Finlayson-Pitts and J. Pitts, *Chemistry of the Upper and Lower Atmosphere*. 2000, San Diego: Academic Press.
15. E. Knipping, M. Lakin, K. Foster, P. Jungwirth, D. Tobias, R. Gerber, D. Dabdub, and B. Finlayson-Pitts, *Science*, 2000. **288**(5464): p. 301-306.
16. Z. Y. Chen, D. Liang, and G. Ma, *Corrosion Engineering Science and Technology*, 2010. **45**(2): p. 169-180.
17. T. E. Graedel, J. P. Franey, and G. W. Kammlott, *Science*, 1984. **224**(4649): p. 599-601.
18. B. Millet, C. Fiaud, and C. Hinnen, *Corrosion Science*, 1995. **37**(12): p. 1903-1918.
19. Z. Y. Chen, D. Persson, and C. Leygraf, *Journal of the Electrochemical Society*, 2005. **152**(12): p. B526-B533.
20. Z. Y. Chen, S. Zakipour, and C. Leygraf, *Corrosion*, 2004. **60**(5): p. 479-491.
21. Z. Y. Chen, D. Persson, F. Samie, S. Zakipour, and C. Leygraf, *Journal of the Electrochemical Society*, 2005. **152**(12): p. B502-B511.
22. Z. Y. Chen, S. Zakipour, and C. Leygraf, *Corrosion*, 2005. **61**(11): p. 1022-1034.
23. H. Strandberg and L. G. Johansson, *Journal of the Electrochemical Society*, 1998. **145**(4): p. 1093-1100.
24. H. Strandberg, *Atmospheric Environment*, 1998. **32**(20): p. 3521-3526.
25. S. L. Clegg, P. Brimblecombe, and Z. Liang, *Aerosol Science and Technology*, 1997. **27**(3): p. 345-366.

26. R. P. Frankenthal, R. Lobnig, D. J. Siconolfi, and J. D. Sinclair, *Journal of Vacuum Science & Technology a-Vacuum Surfaces and Films*, 1993. **11**(4): p. 2274-2279.

27. D. Liang, H. C. Allen, G. S. Frankel, Z. Y. Chen, R. G. Kelly, Y. Wu, and B.E. Wyslouzil, *Journal of the Electrochemical Society*, 2010. **157**(4): p. C146-C156.

28. E. Schindelholz and R. G. Kelly, *Electrochemical and Solid State Letters*, 2010. **13**(10): p. C29-C31.

29. Z. Y. Chen, D. Persson, A. Nazarov, S. Zakiour, D. Thierry, and C. Leygraf, *Journal of the Electrochemical Society*, 2005. **152**(9): p. B342-B351.

30. H. Lin and G. S. Frankel, *Corrosion, Corrosion*, 2013, accepted for publication, available at <http://dx.doi.org/10.5006/0926>.

31. T. M. Whitworth, U. W. Siagian, and R. Lee, *Separation Science and Technology*, 2003. **38**(16): p. 4009-4025.

32. E.B. Neiser, *Atmospheric Corrosion of Silver and Its Relation to Accelerated Corrosion Testing*, in *Materials Science and Engineering* 2010, University of Virginia

33. ASTM, *B825-02, Standard Test Method for Coulometric Reduction of Surface Films on Metallic Test Samples*. 2008.

34. M. Watanabe, M. Tomita, and T. Ichino, *Journal of the Electrochemical Society*, 2002. **149**(3): p. B97-B102.

35. B. Maier and G. S. Frankel, *Corrosion*, 2011. **67**(5): p. 15.

36. T. L. Barr, *Journal of Vacuum Science & Technology*, 1977. **14**(1): p. 660-665.

37. J. A. Allen, *Transactions of the Faraday Society*, 1952. **48**: p. 273-279.

38. S. K. Chawla, B. I. Rickett, N. Sankararaman, and J. H. Payer, *Corrosion Science*, 1992. **33**(10): p. 1617-1631.

39. M. Lenglet, K. Kartouni, and D. Delahaye, *Journal of Applied Electrochemistry*, 1991. **21**(8): p. 697-702.

40. H. Gil and C. Leygraf, *Journal of the Electrochemical Society*, 2007. **154**(11): p. C611-C617.

41. S. Nakayama, A. Kimura, M. Shibata, S. Kuwabata, and T. Osakai, *Journal of the Electrochemical Society*, 2001. **148**(11): p. B467-B472.

42. M. Seo, Y. Ishikawa, M. Kodaira, A. Sugimoto, S. Nakayama, M. Watanabe, S. Furuya, R. Minamitani, Y. Miyata, A. Nishikata, and T. Notoya, *Corrosion Science*, 2005. **47**(8): p. 2079-2090.

43. Y. Y. Su, S. Nakayama, and T. Osakai, *Corrosion Reviews*, 2011. **29**(1-2): p. 51-71.

44. Y. Y. Su and M. Marek, *Journal of the Electrochemical Society*, 1994. **141**(4): p. 940-942.

45. S. Nakayama, T. Kaji, and M. Shibata, *Journal of the Electrochemical Society*, 2007. **154**(1): p. C1-C6.

46. M. Drogowska, L. Brossard, and H. Menard, *Corrosion*, 1987. **43**(9): p. 549-552.

47. J. G. Ibanez, R. Mayen-Mondragon, M. T. Moran-Moran, A. Alatorre-Ordaz, B. Mattson, and S. Eskerstrand, *Journal of Chemical Education*, 2005. **82**(10): p. 1546-1548.

48. C. B. Breslin and D. D. Macdonald, *Electrochimica Acta*, 1998. **44**(4): p. 643-651.

49. E. M. M. Sutter, B. Millet, C. Fiaud, and D. Lincot, *Journal of Electroanalytical Chemistry*, 1995. **386**(1-2): p. 101-109.

50. W. Siripala and K. P. Kumara, *Semiconductor Science and Technology*, 1989. **4**(6): p. 465-468.

51. W.H. Strehlow and E.L. Cook, *Journal of Physical and Chemical Reference Data*, 1973. **2**(1): p. 163.
52. H. Lin and G. S. Frankel, *Journal of the Electrochemical Society*, 2013. **160**(8): p. C336-C344.
53. Y. Wan, E. N. Macha, and R. G. Kelly, *Corrosion*, 2012. **68**(3): p. 1-10.
54. Thomas E. Graedel Christofer Leygraf, *Atmospheric Corrosion*. 1 ed. The Electrochemistry Society. 2000: John Wiley & Sons Inc. 354.
55. G. Biskos, A. Malinowski, and L. M. Russell, *Aerosol Science and Technology*, 2006. **40**(2): p. 97-106.
56. D A Scott, *Journal of the American Institute for Conservation*, 1990. **29**(2): p. 193.
57. *Crc Handbook of Chemistry and Physics* 61 ed. 1980, CRC Press.
58. S.J. Krumbein, Newell B. , Pascucci V. , *Journal of Testing and Evaluations*, 1989. **17**(6): p. 357-367.
59. J. Y. Malvault, J. Lopitaux, D. Delahaye, and M. Lenglet, *Journal of Applied Electrochemistry*, 1995. **25**(9): p. 841-845.
60. M. Pourbaix, *Journal of the Electrochemical Society*, 1976. **123**(2): p. C25-C36.
61. K. Demirkan, G. E. Derkits, D. A. Fleming, J. P. Franey, K. Hannigan, R. L. Opila, J. Punch, W. D. Reents, M. Reid, B. Wright, and C. Xu, *Journal of the Electrochemical Society*, 2010. **157**(1): p. C30-C35.
62. F. Di Quarto, S. Piazza, and C. Sunseri, *Electrochimica Acta*, 1985. **30**(3): p. 315-324.
63. U. Bertocci, *Journal of the Electrochemical Society*, 1978. **125**(10): p. 1598-1602.
64. T. D. Burleigh, C. Ruhe, and J. Forsyth, *Corrosion*, 2003. **59**(9): p. 774-779.
65. R. Lobnig, J. D. Sinclair, and M. Stratmann, *Journal of the Electrochemical Society*, 2003. **150**(6): p. A835-A849.
66. D. W. Shoesmith, T. E. Rummery, D. Owen, and W. Lee, *Journal of the Electrochemical Society*, 1976. **123**(6): p. 790-799.
67. S.B. Adelaju and Y.Y. Duan, *British Corrosion Journal*, 1994. **29**: p. 309-314.
68. S. B. Adelaju and H. C. Hughes, *Corrosion Science*, 1986. **26**(10): p. 851-870.
69. J. E. McRae and T. E. Graedel, *Journal of Geophysical Research-Oceans and Atmospheres*, 1979. **84**(NC8): p. 5011-5017.
70. U.R. Evans, *The Corrosion and Oxidation of Metals; Scientific Principles and Practical Applications*. 1960: London, E. Arnold.

Task 6: A Simultaneous In Situ Kelvin Probe and Raman Spectroscopy Analysis of Electrode Potentials and Molecular Structures at Polymer Covered Salt Layers on Steel

6.1 Summary

A probe head for Raman spectroscopy was installed in the sample chamber of a height-regulated Kelvin Probe (KP) in order to focus a laser beam on polymer coated steel samples directly beneath the KP needle and to detect light scattered at the sample surface. This allowed a simultaneous analysis of the polymer/metal interface structure based on Raman spectra and on Volta potential studies performed by the Kelvin Probe during sample exposure in humid and dry air. The interface sensitivity of the assembled setup was demonstrated with the detected sulfate signatures in Raman spectra recorded from Na_2SO_4 particles precipitated at the buried polymer/steel interface. The observed spectral changes were compared to KP data of potential shifts induced by structural rearrangement processes during drying and humidification of the interfacial region. To track the lifting and descent of the polymer layer, the distance between Kelvin Probe needle and polymer surface was monitored in parallel to the KP potential. These data reveal that spectral alterations, potential shifts and distance changes occurred with varying sequence, but were clearly interrelated. The combined KP-Raman spectroscopy approach consequently provides spectroelectrochemical information that is not available from each technique separately and that will be helpful for more detailed interface studies in the future.

6.2 List of Figures and Tables

Figure 6.1 Schematic illustration of sample composition and geometric arrangement of laser beam and Kelvin Probe needle for the combined KP-Raman spectroscopy approach.³⁰

Figure 6.2 Raman spectra of the O-H- and C-H_x-stretching regions recorded on a sodium sulfate covered and subsequently PVB-coated steel sheet.

Figure 6.3 Water uptake study performed on a Na_2SO_4 covered and subsequently PVB-coated steel sheet.

Figure 6.4 Na_2SO_4 Raman spectrum recorded during the first 200 s of the experiment presented in Fig. 6.3.

Figure 6.5 Na_2SO_4 Raman spectra recorded during the experiment presented in Fig. 6.3.

Figure 6.6 Na_2SO_4 Raman spectra recorded during the experiment presented in Fig. 6.3.

Figure 6.7 Water uptake study performed on a Na_2SO_4 covered and subsequently PVB-coated steel sheet.

Figure 6.8 Na_2SO_4 Raman spectra recorded during the experiment presented in Fig. 6.7.

Figure 6.9 Drying study performed on a Na_2SO_4 covered and subsequently PVB-coated steel sheet.

Figure 6.10 Na_2SO_4 Raman spectra recorded during the experiment presented in Fig. 6.9.

Figure 6.11 Na_2SO_4 Raman spectra recorded during the experiment presented in Fig. 6.9.

Figure 6.12 Na_2SO_4 Raman spectra recorded during the experiment presented in Fig. 6.9.

Figure 6.13 Drying study performed on a Na_2SO_4 covered and subsequently PVB-coated steel sheet.

Figure 6.14 Na_2SO_4 Raman spectra recorded during the experiment presented in Fig. 6.13.

6.3 Introduction and Background

The stability of polymer/oxide/metal interfaces is often determined by their resistance to interfacial incorporation of water and hydrated ions. Water diffusion and ion transport via free volume or directly through the polymer matrix is dependent on the macromolecular network structure as well as on the presence of pores and defects in the organic film. Water uptake results in a change of the viscoelastic properties of the polymer, in its plasticization and the substitution of electrostatic forces between the coating and the substrate surface by adsorbed water molecules.^{1–5} De-adhesion processes are strongly enhanced if salt particles are present at the polymer/oxide/metal interface. Ions such as chloride will promote the dissolution of the substrate material including iron. Even if these species do not directly take part in degradation processes, their hygroscopic properties will support the formation of electrolyte droplets at the interface, which often results in osmotic blistering of the organic coating.^{6–10}

De la Fuente et al. investigated such processes electrochemically with the Kelvin Probe (KP).⁶ The authors analyzed polymer/steel interfaces that were contaminated with sub-microscopic salt particles utilizing the KP as a non-destructive method for the analysis of Volta potentials on conductive samples and at buried interfaces.^{11–16} The KP metallic needle, the sample surface directly beneath and the air between both needle and substrate form a parallel-plate capacitor. Structural rearrangement processes at the sample cause an adjustment of the capacitance, which can be translated into changes of the Volta potential and subsequently referenced to the standard hydrogen electrode after calibration. If equipped with a height-regulation circuit, Kelvin Probes can constantly monitor the distance between the KP needle and substrate surface in parallel to the Volta potential measurement.^{17–24}

Kelvin probes have previously been successfully coupled with other methods for sophisticated surface and interface analysis. For example, combinations of the KP with infrared spectroscopy,^{25,26} scanning electrochemical microscopy²⁸ and the blister test^{24,28,29} have been reported. Recently, a combined Kelvin Probe-Raman spectroscopy approach was introduced allowing simultaneous detection of electrode potentials and Raman spectra for a localized in-situ investigation of the properties of oxide covered metal substrates exposed to different atmospheres.³⁰ In this approach a 532 nm laser beam was focused beneath the KP needle by a two-channel excitation and detection probe head for Raman spectroscopy. Light scattered at the sample surface was detected and sent to an external detector system via fiber optics for analysis. It was shown that both methods can be operated independently of each other if it is ensured that the laser does not hit the KP needle.³⁰ Generally, experimental setups for localized spectro-electrochemical in-situ analysis of processes that occur at buried polymer/oxide/metal interfaces

are rare. The present publication consequently focuses on the introduction of such an experimental approach.

Polymer-coated steel was selected to check the interface sensitivity of the combined KP-Raman spectroscopy assembly and sulfate species at the buried interface were investigated based on vibrational spectra recorded during sample exposure in humid and dry air. Spectral alterations, potential shifts and changes of the topography of the polymer surface were continuously monitored. The experiments show that both KP potential transients and Raman spectra recorded on these substrates provide valuable complementary data that enable sophisticated investigation of polymer/metal interfaces.

6.4 Lessons Learned

We have learned that a combined Kelvin probe-Raman spectroscopy approach of buried PVB/ Na_2SO_4 /steel interfaces can provide complementary information about changes in the polymeric layer as well as from the salt solvation. For instance, we have learned that an increase in atmospheric humidity results in a decrease of the Volta potential and attenuation of Raman peak intensities induced by gradual changes in thickness of the PVB layer and solvation of sulfate salt particles, respectively, which confirmed a reduction of interface stability. Conversely, an increase of the Volta potential following drying indicated a stabilization of the interface, which, however, was not observed until de-solvation of sodium sulfate initiated. Overall, we have learned that, in addition to established surface analysis methods, an in-situ simultaneous KP-Raman approach can help in further understanding the complexity of structural rearrangements processes at buried polymer/metal interfaces.

6.5 Experimental

Sample preparation

As-received 1018 steel sheets (1388K15, McMaster-Carr) ASTM A36 specifications were cleaned by ultrasonication in acetone. Na_2SO_4 crystals were precipitated on the steel surface from saturated aqueous sodium sulfate solution. The samples were subsequently bar-coated with a 15 % solution of poly(vinyl butyral-*co*-vinyl alcohol-*co*-vinyl acetate) (PVB, Sigma Aldrich) in methanol. PVB had an average molecular mass of 70,000–100,000 g/mol, a glass transition temperature of 72–78 °C and was composed of 0–1.5 wt. % acetate, 18–20 wt. % hydroxyl and 80 wt. % vinyl butyral. The samples were dried overnight at 40 °C in flowing dry nitrogen. This resulted in a 70–90 μm thick polymer layer which was investigated by an Elcometer 456 (Elcometer, USA) thickness measurement device. All used chemicals were of analytical grade. The PVB-coated substrates were subsequently exposed to dry (< 5 % RH) or humid air (> 85 % RH) inside the KP sample chamber.

Raman/Kelvin Probe Setup

Kelvin probe measurements were performed with a passively height-regulated, custom-made KP apparatus. Details about the hardware and the circuitry of the electronic devices are presented elsewhere.²⁴ The distance between the 500 μm diameter KP needle and the sample surface was continuously monitored and the height of the KP needle was adjustable by a manually operated micrometer screw. All KP experiments were point measurements and performed at ambient temperature. Volta potential changes detected by the KP were converted to the standard

hydrogen electrode (SHE) scale after calibration against Cu/CuSO₄.^{22–24,31} The KP sample chamber was continuously purged with air of different relative humidity (RH).

For the Raman spectroscopy measurements, a 532 nm continuous-wave, diode-pumped laser (Millenium II, Spectra-Physics, USA) was operated with an output energy of 200 mW. The laser light was sent to the KP chamber via fiber optics and focused on the sample by a RamanProbe™ (RPS532-12-15, InPhotonics, USA). The probe head was mounted to a *xyz* translation stage (Thorlabs, USA) that was manually adjusted. Details of the combined KP-Raman spectroscopy setup are given in Fig. 6.1 and further described elsewhere.³⁰ Laser light with a power of 100 mW was incident on the sample at an angle of ~ 50° from surface normal, with a focal length of 7.5 mm, and a beam diameter of 150 μ m at the focal spot. Light scattered from the substrate surface was collected by the Raman probe head, sent via a fiber optic to a monochromator (SpectraPro 500i, Princeton Instruments, USA) equipped with a 1200 groove/mm grating, and detected by a back-illuminated liquid nitrogen cooled deep depletion CCD (1340/400-EB, Roper Scientific, USA). The detector was calibrated versus the 436.833 nm emission line from a fluorescent lamp and fine calibration was completed using the Raman spectrum of solid crystalline powder naphthalene (purity: > 99 %, Sigma Aldrich, USA). Data were processed with SpectraSense software (version 4.33, Princeton Instruments). The monochromator entrance slit width was 100 μ m, the spectral resolution was approximately 4 cm^{-1} , and data were continuously acquired during a series of sequentially recorded spectra; the data acquisition time for all spectra was either 200 or 240 s. Visual inspection of the sample surface revealed that no laser-induced macroscopic degradation artifacts such as burn spots formed during experiments.

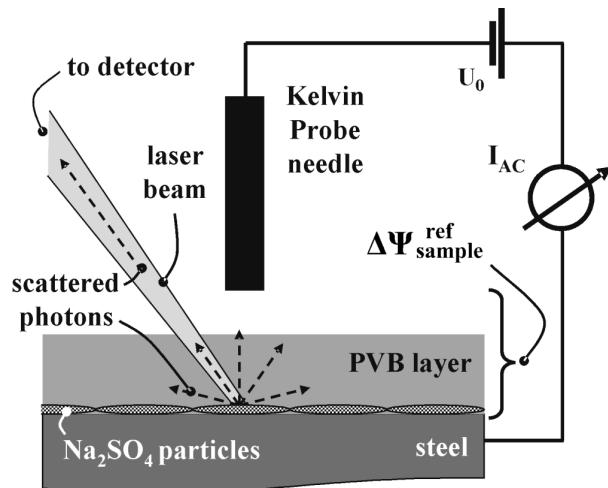


Figure 6.1. Schematic illustration of sample composition and geometric arrangement of laser beam and Kelvin probe needle for the combined KP-Raman spectroscopy approach.³⁰ $\Delta\Psi_{sample}^{ref}$ refers to the Volta potential difference between sample and needle ('reference') that is detected by the Kelvin probe.

6.6 Results and Discussion

Evaluation of the Interface Sensitivity of the Kelvin Probe-Raman Spectroscopy Approach

Initial experiments were performed to gauge whether a combined Kelvin probe-Raman spectroscopy analysis is suitable for investigations of structural and electrochemical rearrangement processes at buried interfaces. Therefore, Na_2SO_4 salt crystals were precipitated on a steel sheet and subsequently covered by a layer of PVB. The Raman laser was focused on the sample surface beneath the KP needle (Fig. 6.1).³⁰ Previously it was demonstrated that hematite signatures of iron oxide structures on steel were easily identifiable applying this geometric arrangement.³¹ To evaluate whether it is also appropriate for analysis of polymer layers in the presence of the KP probe head and Kelvin Probe needle, Raman spectra in the C-H_x stretching and water O-H stretching region were recorded. Fig. 6.2a shows a typical spectrum collected after a PVB-coated steel sample was exposed to dry air for several hours. Two characteristic symmetric stretching vibrational peaks of the PVB hydrocarbon backbone are clearly visible at 2870 and 2915 cm^{-1} , respectively, and there is no evidence of spectral distortions typically detected when the incoming Raman excitation beam hit the KP needle.³⁰ Fig. 6.2a indicates only slight retention of methanol molecules from the solvent liquid in the polymer after curing and only marginal incorporation of water into the macromolecular polymer structure in dry air, because the intensity of the O-H vibration peaks above 3100 cm^{-1} is low.³² Therefore, additional swelling of the polymer layer should occur in at high RH. Fig. 6.2b shows that the PVB coating soaks up water in humid air even when it is simultaneously exposed to the Raman laser. Water uptake is confirmed by the broad O-H vibrational band present between 3100 cm^{-1} and 3630 cm^{-1} typical of liquid water.³³⁻³⁶ The peak at approximately 3260 cm^{-1} is generally attributed to O-H stretching from strongly hydrogen bound four-coordinated water molecules, whereas the peak centered at 3440 cm^{-1} is usually assigned to weaker O-H stretches.³³⁻³⁶ However, water signatures do not allow unambiguous differentiation between structural rearrangements that occur within the polymer bulk and at the PVB/ Na_2SO_4 /steel-interface. In order to sufficiently probe structural changes at the interface of interest, the characteristic S-O vibrations of sulfate were examined as these modes have been shown to be highly sensitive to local molecular environment.³⁸

Fig. 6.3 reflects a combined spectroelectrochemical study performed during an exposure of the sample to humid air. The interface potential (black line) as well as topography changes of the polymer surface (grey line) were monitored simultaneously. The diagram shows that the PVB surface was slowly, but continuously elevated by almost 50 μm within the first 225 min of the experiment while the RH inside the KP chamber increased above 85 % RH. This implies lifting and swelling of the organic layer. To investigate if this observation is connected to changes in polymer/sulfate/steel-interface structures the vibrational modes of the Na_2SO_4 precipitate were monitored with Raman spectroscopy. Fig. 6.4 presents a Raman spectrum of the wavenumber range between 350 cm^{-1} and 1400 cm^{-1} that was recorded during the initial 200 s of the experiment. Peaks observed for solid sulfate salts typically occur near 453 and 470 cm^{-1} (ν_2 symmetric S-O bending vibrations), 622 cm^{-1} , 634 cm^{-1} and 650 cm^{-1} (ν_4 asymmetric S-O bending vibrations), 993 cm^{-1} (ν_1 symmetric S-O stretching vibration) and between 1085 and 1185 cm^{-1} (ν_3 asymmetric S-O stretching vibrations).³⁷⁻⁴² The spectrum presented in Fig. 6.4 is characteristic of anhydrous Na_2SO_4 crystal structures excepting the weak peaks observed between 800-900 cm^{-1} and above 1200 cm^{-1} which are attributed to polymer finger-print

modes.^{37,38} This confirms that the assembled KP-Raman spectroscopy instrument is generally able to detect salt particles with molecular cations and/or anions at buried polymer/metal interfaces.

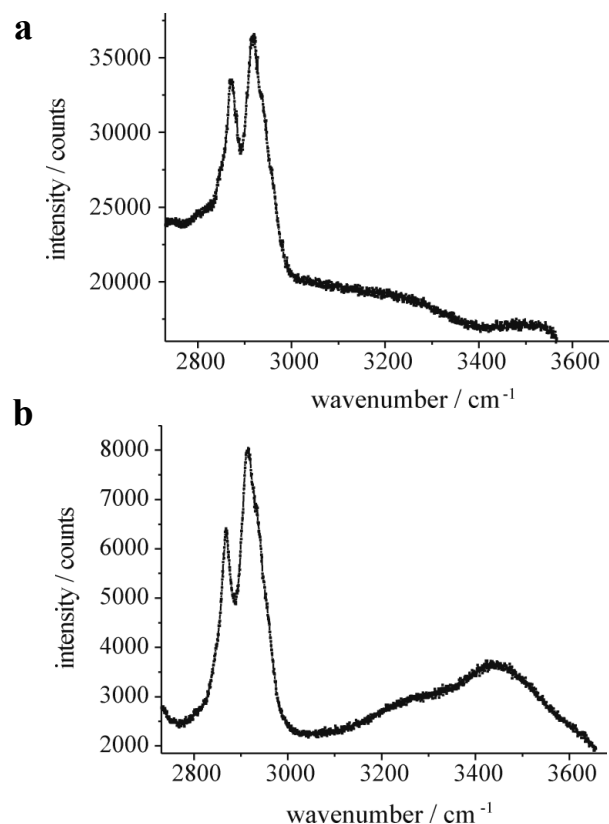


Figure 6.2. Raman spectra of the O-H- and C-H_x-stretching regions recorded on a Na₂SO₄ covered and subsequently PVB-coated steel sheet. (a) Measurement performed after sample exposure to dry air for several hours. Acquisition time: 20 min. (b) Spectrum recorded after sample exposure to 532 nm laser light for several hours in humid air. Acquisition time: 4 min.

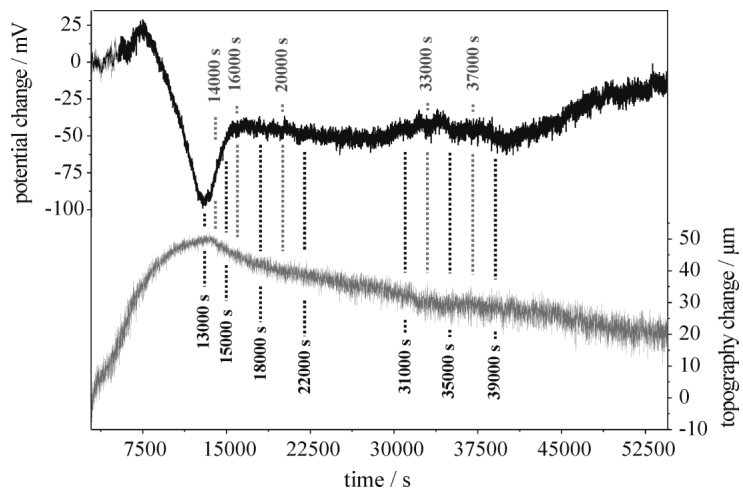


Figure 6.3. Water uptake study performed on a Na_2SO_4 covered and subsequently PVB-coated steel sheet. Purging of the KP sample chamber with humid air was initiated several minutes before the measurement started. Black curve: Volta potential changes detected by the KP on the sample. Grey curve: Topography changes of the sample surface, detected by the KP. Positive distance values refer to lifting of the PVB layer surface, negative to subsidence processes. Times indicated correspond to Raman spectra presented in Figs. 6.5 and 6.6.

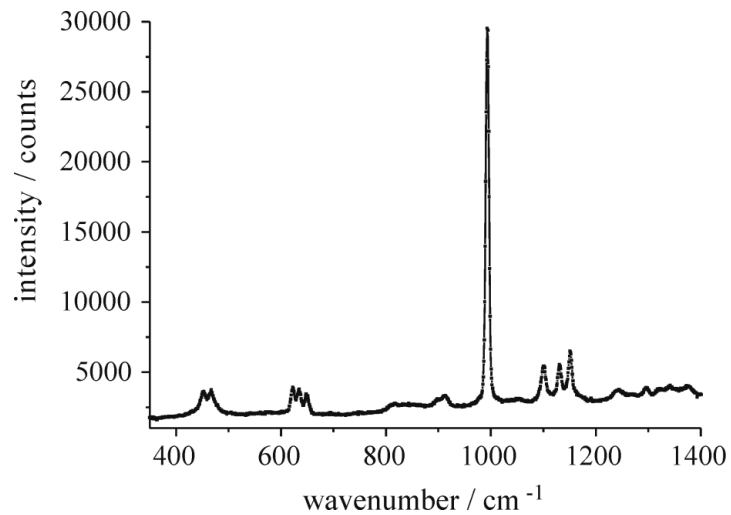


Figure 6.4. Na_2SO_4 Raman spectrum recorded during the first 200 s of the experiment presented in Fig. 6.3.

Fig. 6.5a shows that lifting of the PVB layer surface during the first four hours of the experiment did not result in the evolution or disappearance of the sulfate peaks. However, the baseline shifted to higher counts and peak intensities in the Raman spectra started to attenuate just before lifting of the polymer reached a maximum at around 13500 s. These spectral changes are assigned to an increase of the photonic background scatter level resulting from focus point changes of the laser beam at the polymer/sulfate interphase zone with polymer swelling. Within the following hour, a distinct descent of the coating surface is indicated by Fig. 6.3. The rate of decrease slowed at 16000 s. After this time, no further peak intensity decrease was observed in Fig. 6.5a and the interface potential achieved a constant level in Fig. 6.3. During the following hours, the Raman spectra baseline decreased (see Fig. 6.5b). Notable spectral changes are evident between 31000 and 39000 s. Fig. 6.6 shows that a peak appeared during this period on the red side of the anhydrous sulfate symmetric stretching peak at 983 cm^{-1} . This new peak is assigned to the solvated sulfate symmetric S-O stretching mode and reflects the partial hydration of the Na_2SO_4 particles.³⁸⁻⁴² The unaltered v_3 asymmetric S-O stretching vibration peak triplet between 1090 and 1170 cm^{-1} indicates that the sodium sulfate crystals did not completely dissolve.^{38,42} Fig. 6.3 indicates that the PVB layer descent slowed during sulfate solvation. Moreover, the interface potential started to continuously increase after 39000 s when the major growth of the 983 cm^{-1} peak ceased.

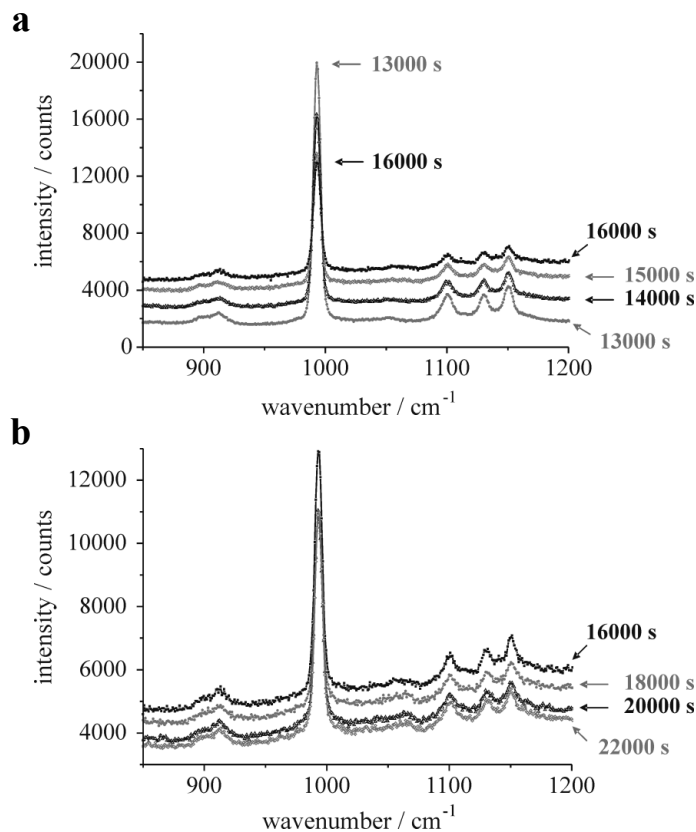


Figure 6.5. Na_2SO_4 Raman spectra recorded during the experiment presented in Fig. 6.3. Acquisition time: 200 s. (a) Measurements performed between $t = 13000$ and 16000 s. (b) Measurements performed between $t = 16000$ and 22000 s.

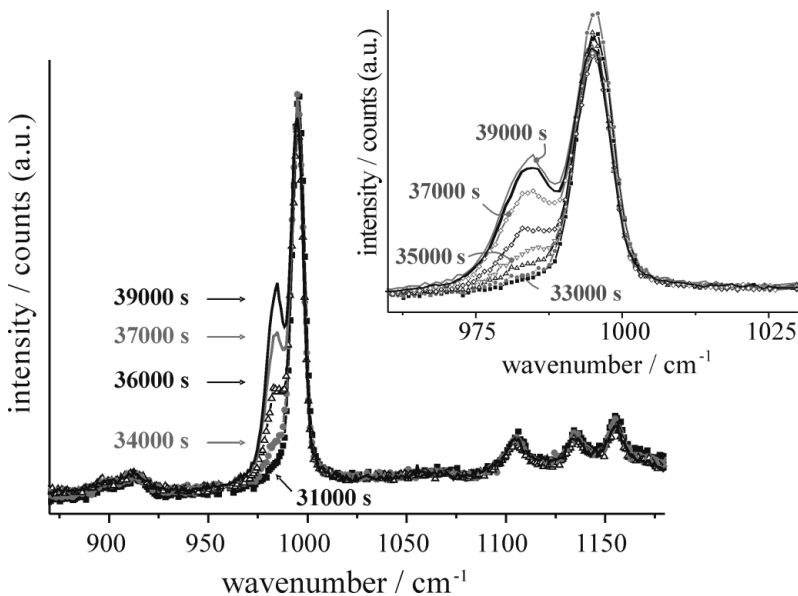


Figure 6.6. Na_2SO_4 Raman spectra recorded during the experiment presented in Fig. 6.3. Acquisition time: 200 s. Measurements performed between $t = 31000$ and 39000 s. Details of the ν_1 symmetric S-O stretching vibration peaks are displayed in the upper right corner.

The observed potential changes, spectral alterations, and variations of the sample topography presented in Figs. 6.3, 6.5 and 6.6 are clearly interrelated. They occurred either coincidently or successively and confirm adequate overlap of the KP and Raman laser probed sample areas.³⁰ The interface potential detected by the Kelvin probe varied by less than 125 mV in total. This implies that no major degradation was induced at the steel substrate for the selected experimental conditions, as processes such as cathodic delamination at polymer/metal interfaces are usually connected with distinctly larger potential shifts of several hundred millivolts.^{13-15,43} The observed variations of the Volta potential are consequently assigned to slight changes of the capacitive properties during lifting and descent of the PVB layer. Correlated minor adjustments of interface dipole moments of the investigated sample are a possible explanation.^{43,44} Monitoring topography changes at the PVB surface reveals that the initial bulging of the coating layer by 50 μm in the first four hours is too large to be solely attributable to swelling of the macromolecular network during water uptake. Therefore, lifting has to be supported by de-adhesion processes at the PVB/ Na_2SO_4 /steel interface. Raman analysis additionally shows that blister formation can occur without changes to the hydration state of the sodium sulfate particles although the water amount within the sample has to increase during exposure to humid air (see Fig. 6.2b). This indicates that plastic deformation of the macromolecular structure occurs while free volumes and pores within the polymer bulk fill up with H_2O . Sodium sulfate is hygroscopic, but the critical threshold quantity of water at the polymer/ Na_2SO_4 /steel interface that allows for the detection of water uptake by the salt crystals is not exceeded before 31000 s. Additionally, the observed hydration of sulfate does not induce sufficient volume increase at the buried interface to affect the PVB surface topography (see Fig. 6.3) and the humidity increase does not result in an evolution of iron oxide peaks in the Raman spectra, which would indicate oxidation

processes at the steel surface. This means that, while active dissolution of steel may occur, it does not result in major growth of voluminous corrosion products into the Na_2SO_4 layer. In summary, the simultaneous KP-Raman approach offers insight into interfacial degradation processes that cannot be achieved by applying each technique separately.

Incremental and Continuous Polymer De-adhesion during Humidification

Simultaneous KP-Raman measurements are also suited for monitor swelling and de-adhesion kinetics at PVB/sulfate/steel compounds starting from extremely dry interfaces. Fig. 6.7 presents measurements made after overnight exposure of the sample to air of $< 5\% \text{ RH}$. The sudden jump in the topography indicates almost instantaneous initiation of polymer swelling and de-adhesion when purging of the KP chamber with humid air started at 1680 s. Within the following 6 min, the PVB surface was lifted by 38 μm . During the subsequent 110 min no further topographic change of the sample surface was detected. The interface potential exhibited a peak between 1680 and 2500 s and then a slow decay. These potential shifts result from the release of charge that formed on top of the PVB layer during exposure to dry atmosphere and not from notable changes of the sample structure. A stable potential level was achieved at around 5400 s. It is approximately 80 mV lower than it was previously in dry air and indicates minor structural adaptations of the polymer/substrate interphase zone rather than major degradation processes.

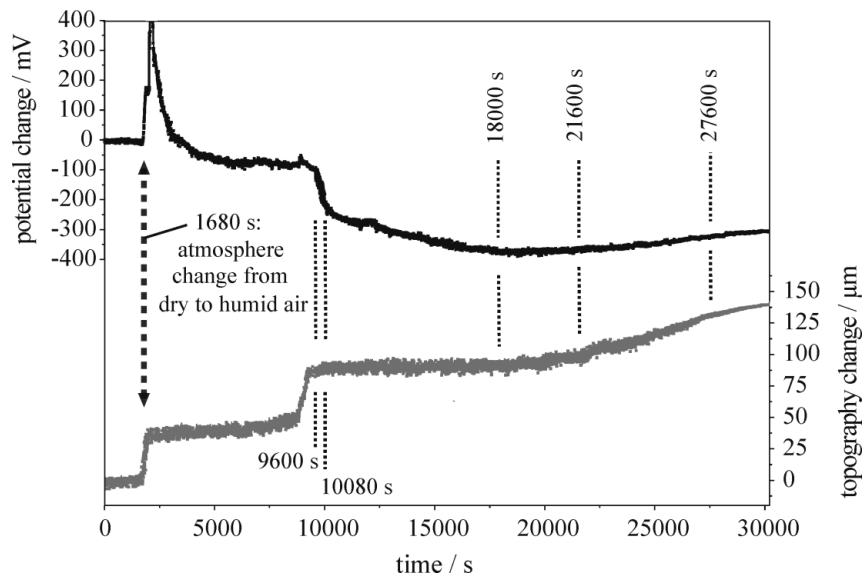


Figure 6.7. Water uptake study performed on a Na_2SO_4 covered and subsequently PVB-coated steel sheet. The sample was exposed to dry air for several hours prior to the experiment. Purging of the KP sample chamber with humid air was initiated at $t = 1680 \text{ s}$. Black curve: Volta potential changes detected by the KP on the sample. Grey curve: Topography changes at the sample surface, detected by the KP. Positive distance values refer to lifting of the PVB layer surface, negative to subsidence processes. Times indicated correspond to Raman spectra presented in Fig. 6.8.

At approximately 8800 s another sudden bulging of the sample surface was detected along with a concomitant decrease of the interface potential by about 200 mV. An almost constant potential level was achieved only a few minutes after this incident. During the subsequent stages of the experiment the kinetics of the surface topography adjustments changed from sudden, incremental bulging to more uniform lifting processes. Fig. 6.6 shows that the polymer surface was continuously elevated by 50 μm between 18000 and 30000 s, which was not accompanied by major changes of the Volta potential. The Raman spectra collected within this time range allow for a more detailed investigation of these phenomena. Fig. 6.8a presents how the Raman spectra changed during the first two PVB de-adhesion incidents on the solvation state of Na_2SO_4 beneath the polymer layer. No changes to the sulfate peaks were observed during the first two hours of the experiment, which includes the sudden lifting of the PVB layer at 1680 s. In contrast, the second de-adhesion incident at 8800 s was associated with partial solvation of Na_2SO_4 crystals as revealed by the small shoulder that developed at 982 cm^{-1} . The shoulder intensity then remained nearly constant with only slight increases observed during the third bulging incident in the final stage of the experiment (see Fig. 6.8b). Negligible changes to the S-O bending modes at lower wavenumbers nor to the ν_3 asymmetric S-O stretching modes at higher wavenumbers were observed during the course of the experiment.

Grayscale thresholding by the image analysis software was used to determine the coating edge for each image as shown in the bottom of Figure 4.2a. These images show that the edge of the coating moved from right to left with each scan as the coating was removed from the substrate surface by AFM scratching. The Raman spectra in Figure 4.3 provide evidence for total removal of the coating in this region. The peaks from the polymer coating, for instance the peak around 2950 cm^{-1} associated with the C-H bond, are absent after scratching. Close examination of the topographic image of the lower scratched region of the 7th scan in Figure 4.2b shows some features. However, these features are associated with scratches in the steel substrate generated during sample preparation. The evidence indicates that the coating is completely removed from the surface in increments during AFM scratching so that the removal rate can be used as a measure of the coating adhesion strength.

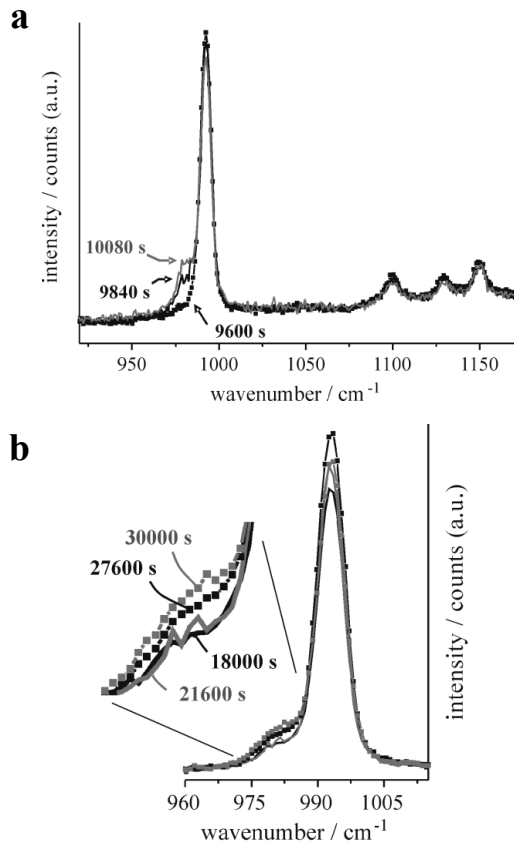


Figure 6.8. Na_2SO_4 Raman spectra recorded during the experiment presented in Fig. 6.7. Acquisition time: 240 s. (a) Measurements performed between $t = 9600$ and 10080 s. b) Measurements performed between $t = 18000$ and 30000 s. Details of the ν_1 symmetric S-O stretching vibration peak region are shown.

The data presented in Figs. 6.7 and 6.8 reflect the diversity and complexity of possible processes at salt contaminated polymer/oxide/metal interfaces. Mechanical tension within the PVB structure can be instantaneously released by de-adhesion of the organic layer (see Fig. 6.7, $t = 1680$ s). Even the uptake of small amounts of water from the atmosphere appears to be sufficient for initiation of unbonding. The solvation state for the majority of the hygroscopic Na_2SO_4 particles did not change (within our detection limits), but the H_2O quantity nevertheless seemed to be large enough to induce interfacial wet de-adhesion processes. This is indicated by a correlated decline of the interface potential, which usually refers to a reduction of the organic/substrate interface stability.¹³⁻¹⁵ In this context, the second de-adhesion incident at 8800 s was more destructive than the first one, because the topography change was larger, the potential shift was more pronounced and partial solvation of sulfate occurred. This indicates a relatively abrupt incorporation of additional water into the polymer/sulfate salt/steel interphase zone and a distinct increase of the interfacial water amount. Compared to nitrate or chloride, which can specifically catalyze active dissolution of steel substrates, SO_4^{2-} species often indirectly support

degradation processes. For example, their presence at the sample surface will result in a compaction of the electric double layer and thereby potentially accelerate any electrochemical processes, especially as steel surfaces are not passivated by Na_2SO_4 solutions. Therefore, even if partial solvation of Na_2SO_4 is not automatically connected to subsequent interface degradation (see Section 3.1), it nevertheless surely promotes further swelling/de-adhesion of the polymer layer as is indicated by Fig. 6.7 for the final stage of the experiment.

Structural Adjustments of the PVB/Sodium Sulfate/Steel Interface during Drying

Valuable information about structural adjustments at buried polymer/metal interfaces can be also obtained by the initiation of drying processes. Fig. 6.9 shows a measurement that was performed after overnight exposure to air of > 90 % RH of a steel sample with deposited Na_2SO_4 and a PVB coating. Volta potentials and Raman spectra were recorded in humid atmosphere before purging of the KP chamber with dry air started at 1340 s. This resulted in an instantaneous decline of the polymer surface by more than 175 μm in height. De-swelling proceeded extremely fast and the topography change was distinctly larger than related processes described in previous sections. Consequently, such observations cannot be solely explained by simple compaction of the macromolecular PVB structure due to water loss. Indeed these results imply that the polymer layer descends as a whole because of changes beneath it. Supporting this assumption are the results presented by Fig. 6.10, which shows Raman spectra recorded during the first 7200 s of the experiment. The spectral signatures in Fig. 6.10 reflect almost fully solvated sulfate species with the ν_1 symmetric S-O stretching vibration centered at $\sim 980 \text{ cm}^{-1}$ and the ν_3 asymmetric S-O stretching vibration peaks between 1075 cm^{-1} and 1175 cm^{-1} converged onto one degenerate, broad peak indicating T_d symmetry for the sulfate compounds.^{38,39,45} From 1340 s on, the intensity of the ν_1 signal starts to decrease, but neither a correlated shift of peak positions nor an evolution of additional peaks is detected. The Fig. 6.10 inset shows this peak in more detail and confirms that no change of the SO_4^{2-} solvation state occurs during the first 7200 s of the experiment. These results again indicate that the focal spot of the Raman laser at the PVB/sodium sulfate interphase region changed (see also Section 3.1). Synergistic processes that comprise a decrease of the PVB layer thickness, a reduction of free or liquid filled volumes at the PVB/ Na_2SO_4 /steel interface zone as well as a correlated shrinking of blisters on the polymer coated metal substrate in dry air are considered to be likely sources contributing to focal spot changes.

Fig. 6.11 shows Raman spectra that feature the largest degree of change observed during the entire experiment. These spectra reflect distinct adjustments of the spectral sulfate signature upon dehydration between about 14000 and 16000 s during which no pronounced variations of the Volta potential and very unspecific slight lifting of the PVB surface were monitored (see Fig. 6.9). First, the intensity of the ν_1 symmetric S-O stretching vibration peak at 983 cm^{-1} decreased until the signal was greatly diminished. Secondly, the peak corresponding to the anhydrous sulfate ν_1 symmetric S-O stretching vibration grew at 993 cm^{-1} and quickly became the most intense signal of the spectrum. Finally, the broad band between 1075 cm^{-1} and 1175 cm^{-1} resolved again to a ν_3 asymmetric S-O stretching vibration peak triplet. These spectral features clearly reflect the quick and thorough dehydration of the sodium sulfate crystals. Furthermore, the spectrum acquired at 16080 s strongly resembles spectra from dry Na_2SO_4 crystals³⁸ (see also Fig. 6.4).

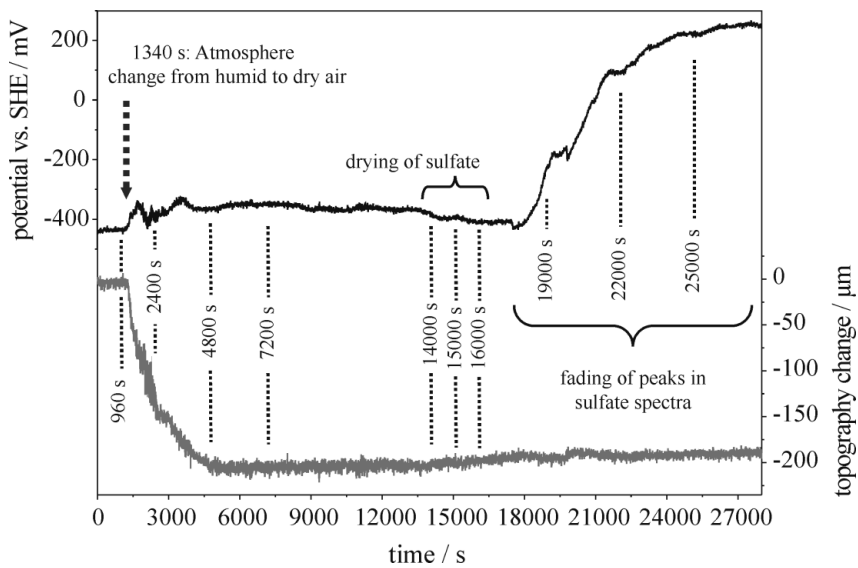


Figure 6.9. Drying study performed on a Na_2SO_4 covered and subsequently PVB-coated steel sheet. The sample was exposed to humid air for several hours prior to the experiment. Purging of the KP sample chamber with dry air was initiated at $t = 1340$ s. Black curve: Volta potential changes detected by the KP on the sample. Grey curve: Topography changes at the sample surface, detected by the KP. Positive distance values refer to lifting of the PVB layer surface, negative to subsidence processes. Times indicated correspond to Raman spectra presented in Figs. 6.10, 6.11 and 6.12.

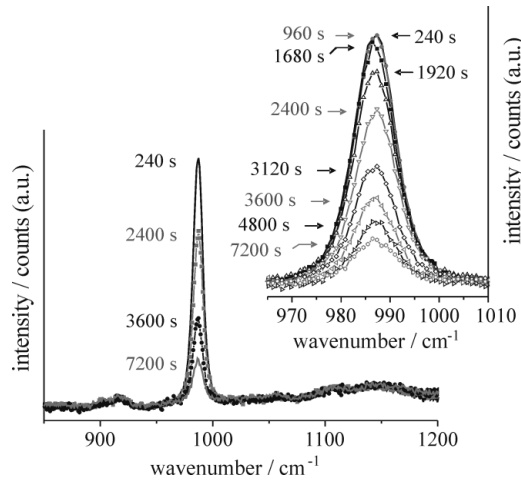


Figure 6.10. Na_2SO_4 Raman spectra recorded during the experiment presented in Fig. 6.9. Acquisition time: 240 s. Measurements performed between $t = 240$ and 7200 s. Details of the ν_1 symmetric S-O stretching vibration peak are displayed in the upper right corner.

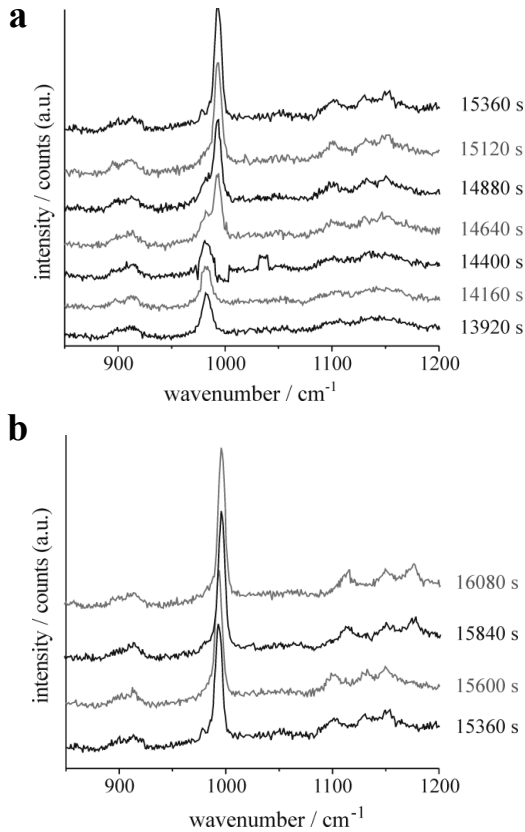


Figure 6.11. Na_2SO_4 Raman spectra recorded during the experiment presented in Fig. 6.9. Acquisition time: 240 s. (a) Measurements performed between $t = 13920$ and 15360 s. (b) Measurements performed between $t = 15360$ and 16080 s.

Fig. 6.12a shows that the dominant peak at 993 cm^{-1} decreased again during the following 8600 s. This was accompanied by a loss of spectral resolution, as from $t = 24720$ s on identification of the ν_3 asymmetric S-O stretching vibration peak triplet became difficult. A tremendous increase of the baseline counts and the correlated baseline shift resulted in spectral distortions rendering further interpretation impossible (see Fig. 6.12b). The CCD detector saturated at around 27840 s.

The spectra seem to reflect similar behavior to that observed in Figs. 6.10 and Fig. 6.5a, which was attributed to off-focus effects. However, two specific differences only observed in Fig. 6.12 needs to be addressed. First of all, the spectra all feature an intense broad background that increases in intensity with time and was not detected before. This is attributed to a large increase of the scatter for the green laser light inside the KP chamber and not to fluorescence of the sample. This situation seems to resemble KP-Raman observations made on hematite samples when the laser beam was incident on the KP needle.³⁰ Secondly, a simultaneous Volta potential

increase of more than 600 mV was observed between 18000 and 28000 s (see Fig. 6.9). This is usually connected with a stabilization of the interface and partial or complete de-activation of local galvanic cells that are responsible for corrosion of the base material.^{14,15}

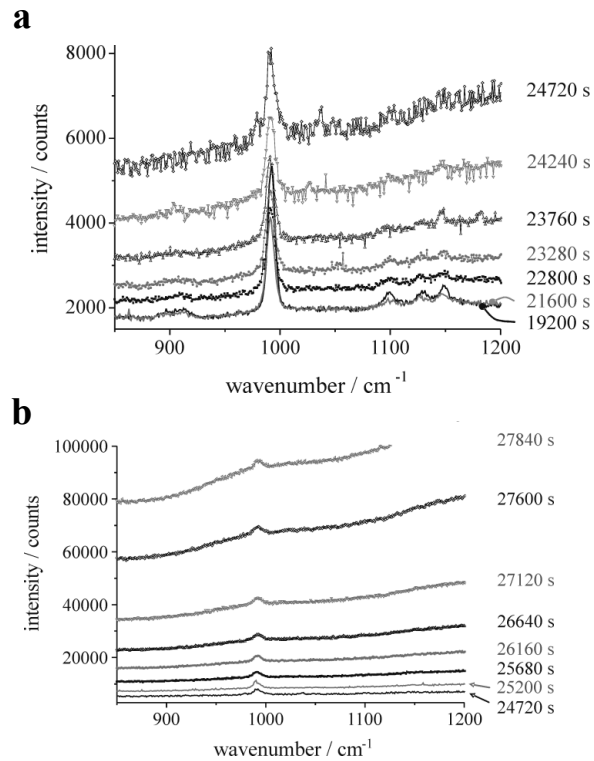


Figure 6.12. Na_2SO_4 Raman spectra recorded during the experiment presented in Fig. 6.9. Acquisition time: 240 s. (a) Measurements performed between $t = 19200$ and 24720 s. (b) Measurements performed between $t = 24720$ and 27840 s.

Charging of the PVB surface in dry air may amplify the potential increase, but this should be minor as large charging effects would prevent high-quality measurements with the KP instrument employed in the present study. Sample charging is almost ruled out because a good signal to noise ratio for the Volta potential was maintained and the distance between KP needle and PVB surface remained nearly constant between 18000 and 28000 s (see Fig. 6.9). The constancy for the distance measurements also indicates that the large background observed for spectra in Fig. 6.12 did not result from a topography change of the polymer surface. The laser beam itself was not responsible for the observed Volta potential change, because that should have caused a decrease in potential rather than the observed increase.³⁰ In the case where the laser beam directly hits the KP needle, deviated distance signals would be additionally detected.³⁰ Such processes, however, are not observed in Fig. 6.9. Although a definitive explanation for the Raman baseline shifts observed for Fig. 6.12 spectra cannot be given, it is

reasonable to assume that effects such as clouding of the PVB layer may play a significant role because occasionally the PVB-coated samples partially lost transparency during cyclic exposure to humid and dry air.

To demonstrate that drying processes at PVB/Na₂SO₄/steel interfaces are not generally connected to distortions of simultaneously recorded Raman spectra, Fig. 6.13 presents an experiment that started from partially solvated sulfate species during sample exposure to humid air. Fig. 6.14 indicates incomplete SO₄²⁻ solvation by the observed doublet of the ν_1 S-O stretching vibration signals recorded at 960 s (for peak assignment see above). At 1460 s purging of the KP sample chamber with dry air started. A simultaneous increase of the interface potential and descent of the polymer layer surface were detected instantaneously. In parallel, the intensity of the S-O peak at 982 cm⁻¹ decreased due to drying of the interface zone. Fig. 6.14 shows that sulfate dehydration was still ongoing at 7200 s, but completed within the next 240 s, because the ν_3 asymmetric S-O stretching vibration peak triplet quickly formed between 1075 and 1175 cm⁻¹ while the signal at 982 cm⁻¹ almost disappeared. These results confirm that water evaporation at the polymer/Na₂SO₄ interface as well as within the PVB layer initiates almost immediately by a rapid reduction of the atmospheric RH level. However, water activity in the surrounding polymer phase must decrease below a certain threshold level for dehydration of sodium sulfate to proceed and this may be delayed if the initial water content of the sample is large (see Fig. 6.9).

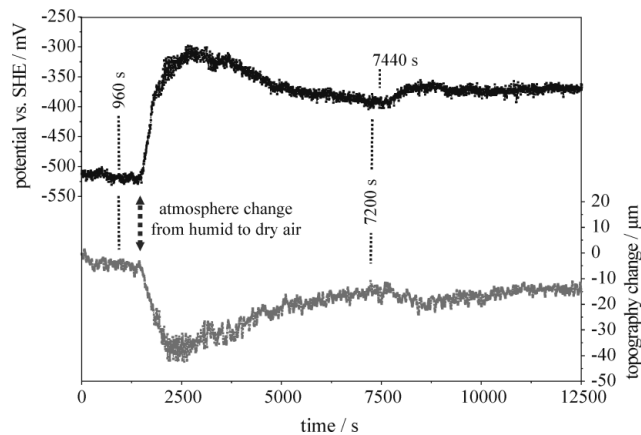


Figure 6.13. Drying study performed on a Na₂SO₄ covered and subsequently PVB-coated steel sheet. The sample was exposed to humid air for several hours prior to the experiment. Purging of the KP sample chamber with dry air was initiated at $t = 1250$ s. Black curve: Volta potential changes detected by the KP on the sample. Grey curve: Topography changes at the sample surface, detected by the KP. Positive distance values refer to lifting of the PVB layer surface, negative to subsidence processes. Times indicated correspond to Raman spectra presented in Fig. 6.14.

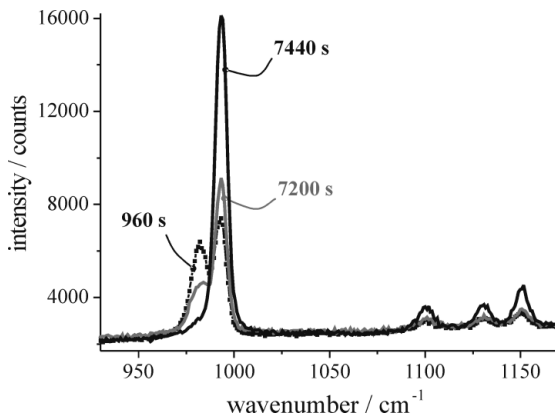


Figure 6.14. Na_2SO_4 Raman spectra recorded during the experiment presented in Fig. 6.13. Acquisition time: 240 s. Measurements performed at $t = 960$, 7200, and 7440 s.

Both Fig. 6.10 and 6.14 demonstrate that the introduction of less than $0.006 \text{ mW}/\mu\text{m}^2$ of laser energy into the sample did not induce detectable drying of the PVB/sodium sulfate interface during initial stages of the experiment at high RH. No topography, potential or spectral changes were observed before the atmospheric humidity was reduced. However, it is unlikely that the input laser energy had no impact on RH dependent processes at all. Fig. 6.6, for example, shows that complete sulfate solvation, as is reflected by Fig. 6.10, cannot be achieved within 10 hrs of sample exposure to humid air while the laser is in operation. Consequently, for polymer/substrate interface structures that are known to be especially sensitive to laser irradiation, periodic recording of single Raman spectra during the course of the experiment is suggested instead of continuous analysis. Reduction of the spectral acquisition time and application of minimal laser power are general considerations for Raman spectroscopy to avoid laser-induced processes on the investigated sample and these also apply to the combined KP-Raman spectroscopy approach.³⁰ In this context, the measurements discussed in the present study altogether confirm that sophisticated spectroelectrochemical in-situ analysis is necessary for a detailed understanding of bonding, adhesion and degradation mechanisms as well as for structural determination at buried polymer/metal interfaces.

6.7 Economic Summary

This project was started before there was an emphasis placed on economic justification of the work, so no summary is presented.

6.8 Implementation

Any implementation of the combined Kelvin probe/Raman spectroscopy method to the surface analysis of buried polymer/metal interfaces will need to make use of this work in order to be able

to properly correlate potential and spectroscopic observations to specific structural events at the interface.

6.9 Conclusions

A combined Kelvin probe-Raman spectroscopy approach was introduced for the in-situ analysis of buried PVB/ Na_2SO_4 /steel interfaces. Simultaneous recording of Volta potentials and sulfate spectra showed that the assembled instrument is capable of interface sensitive measurements. The interrelation of spectral alterations, potential changes and variations of the KP needle/substrate distance confirmed an adequate overlap of Raman and KP probed areas on the sample. Laser induced drying processes at the PVB/ Na_2SO_4 interface were not detected, but may have decelerated the solvation of Na_2SO_4 crystals. An increase of the atmospheric humidity instantaneously resulted in bulging of the PVB layer and was partially connected to an attenuation of peak intensities in the Raman spectra. Subsequent solvation of some portion of the sulfate particles manifested in the evolution of the symmetric S-O stretching vibration peak at $\sim 980 \text{ cm}^{-1}$ attributed to solution phase SO_4^{2-} , but did not induce any volume increase at the polymer/sulfate interface that was detectable at the sample surface. Sudden, incremental polymer lifting during humidification was connected with a decrease of the Volta potential, which confirmed a reduction of the interface stability. Drying studies at water saturated PVB/ Na_2SO_4 interfaces revealed a quick and pronounced depression of the polymer surface of up to $200 \mu\text{m}$, which was connected to an attenuation of the spectral Raman intensity. Increase of the Volta potential indicated a stabilization of the interface, which, however, was not observed until desolvation of sodium sulfate initiated. The presented data reflect the diversity and complexity of structural adjustment processes at buried interfaces and show that the simultaneous KP-Raman approach complements established methods for analysis.

6.10 References

1. Chiang, M. Y. M.; Fernandez-Garcia, M. Relation of Swelling and T_g Depression to the Apparent Free Volume of a Particle-Filled, Epoxy-Based Adhesive. *J. Polym. Sci.* **87**, 1436–1444 (2003).
2. Feng, J.; Berger, K. R.; Douglas, E. P. Water Vapor Transport in Liquid Crystalline and Non-Liquid Crystalline Epoxies. *J. Mater. Sci.* **39**, 3413–3423 (2004).
3. Soles, C. L.; Yee, A. F. A Discussion of the Molecular Mechanisms of Moisture Transport in Epoxy Resins. *J. Polym. Sci., Part. B: Polym. Phys.* **38**, 792–802 (2000).
4. Linossier, I.; Gaillard, M.; Romand, M. A Spectroscopic Technique for Studies of Water Transport Along the Interface and Hydrolytic Stability of Polymer/Substrate Systems. *J. Adhesion* **70**, 221–239 (1999).
5. Posner, R.; Sundell, P. E.; Bergman, T.; Roose, P.; Heylen, M.; Grundmeier, G.; Keil, P. UV-Curable Polyester Acrylate Coatings: Barrier Properties and Ion Transport Kinetics Along Polymer/Metal Interfaces Corrosion, Passivation, and Anodic Films. *J. Electrochem. Soc.* **158**, C185–C193 (2011).

6. de la Fuente, D.; Rohwerder, M. Fundamental Investigation on the Stability of the Steel/Coating Interfaces Contaminated by Submicroscopic Salt Particles. *Prog. Org. Coat.* **61**, 233–239 (2008).
7. Morcillo, M. Soluble Salts: Their Effect on Premature Degradation of Anticorrosive Paints *Prog. Org. Coat.* **36**, 137–147 (1999).
8. Alblas, B. P.; van London, A. M. The Effect of Chloride Contamination of the Corrosion of Steel Surfaces: A Literature Review. *Protect. Coat. Eur.* 18, 16–25 (Febr. 1997).
9. de la Fuente, D.; Bohm, M.; Houyoux, C.; Rohwerder, M.; Morcillo, M. The Settling of Critical Levels of Soluble Salts for Painting. *Prog. Org. Coat.* **58**, 23–32 (2007).
10. M. Gomez, P. Perez, A. Collazo, M. Izquierdo, A. Sanchez, *Surf. Coat. Int.* **77**, 20– (1994).
11. Kelvin, L. V. Contact Electricity of Metals. *Philos. Mag.* **46**, 82–120 (1898).
12. Williams, G.; McMurray, H. N. Polyaniline Inhibition of Filiform Corrosion on Organic Coated AA2024-T3. *Electrochim. Acta* **54**, 4245– (2009).
13. Nazarov, A.; Prosek, T.; Thierry, D. Application of EIS and SKP Methods for the Study of the Zinc/Polymer Interface. *Electrochim. Acta* **53**, 7531–7538 (2008).
14. Posner, R.; Santa, M.; Grundmeier, G. Wet- and Corrosive De-Adhesion Processes of Water-Borne Epoxy Film Coated Steel: I. Interface Potentials and Characteristics of Ion Transport Processes Corrosion, Passivation, and Anodic Films. *J. Electrochem. Soc.* **158**, C29–C35 (2011).
15. Santa, M.; Posner, R.; Grundmeier, G. Wet- and Corrosive De-Adhesion Processes of Water-Borne Epoxy Film Coated Steel: II. The Influence of γ -Glycidoxypolytrimethoxysilane as an Adhesion Promoting Additive Corrosion, Passivation, and Anodic Films. *J. Electrochem. Soc.* **158**, C36–C41 (2011).
16. Santa, M.; Posner, R.; Grundmeier, G. In Situ Study of the Deterioration of Thiazole/Gold and Thiazole/Silver Interfaces during Interfacial Ion Transport Processes. *J. Electroanal. Chem.* **643**, 94–101 (2010).
17. Johnson, K. B.; Hansen, W. N. An Acoustically Driven Kelvin Probe for Work-Function Measurements in Gas Ambient. *Rev. Sci. Instrum.* **66**, 2967–2976 (1995).
18. Zisman, W. A New Method of Measuring Contact Potential Differences in Metals. *Rev. Sci. Instrum.* **3**, 367–370 (1932).
19. Stratmann, M.; Streckel, H. On the Atmospheric Corrosion of Metals which are Covered with Thin Electrolyte Layers—I. Verification of the Experimental Technique. *Corr. Sci.* **30** (1990), 681–696.
20. Rohwerder, M.; Leblanc, P.; Frankel, G. S.; Stratmann, M. In: *Analytical Methods for Corrosion Science and Engineering* (P. Marcus, F. Mansfeld, eds.), Marcel Dekker, New York, 2005, p. 605.
21. Trasatti, S. Structure of the Metal/Electrolyte Solution Interface: New Data for Theory. *Electrochim. Acta* **36**, 1659–1667 (1991).
22. Turcu, F.; Rohwerder, M. High-Resolution Kelvin Probe Microscopy in Corrosion Science: Scanning Kelvin Probe Force Microscopy (SKPFM) versus Classical Scanning Kelvin Probe (SKP). *Electrochim. Acta* **53**, 290–299 (2007).
23. Leng, A.; Streckel, H.; Stratmann, M. The Delamination of Polymeric Coatings from Steel. Part 1: Calibration of the Kelvin Probe and Basic Delamination Mechanism. *Corros. Sci.* **41**, 547–578 (1999).

24. Wapner, K.; Schönberger, B.; Stratmann, M.; Grundmeier, G. Height-Regulating Scanning Kelvin Probe for Simultaneous Measurement of Surface Topology and Electrode Potentials at Buried Polymer/Metal Interfaces. *J. Electrochem. Soc.* **152**, E114–E122 (2005).

25. Persson, D.; Axelsen, S.; Zou, F.; Thierry, D. *Electrochem. Solid State Lett.* **4**, B7– (2001).

26. Raake, J.; Giza, M.; Grundmeier, G. Combination of FTIR Reflection Absorption Spectroscopy and Work Function Measurement for In-Situ Studies of Plasma Modification of Polymer and Metal Surfaces. *Surf. Coat. Technol.* **200**, 280–283 (2005).

27. Maljusch, A.; Schönberger, B.; Lindner, A.; Stratmann, M.; Rohwerder, M.; Schuhmann, W. Integrated Scanning Kelvin Probe-Scanning Electrochemical Microscope System: Development and First Applications. *Anal. Chem.* **83**, 6114–6120 (2011).

28. Posner, R.; Giza, G.; Vlasak, R.; Grundmeier, G. In Situ Electrochemical Scanning Kelvin Probe Blister-Test studies of the De-adhesion Kinetics at Polymer/Zinc Oxide/Zinc Interfaces. *Electrochim. Acta* **54**, 4837–4843 (2009).

29. Posner, R.; Giza, G.; Marazita, M.; Grundmeier, G. Ion Transport Processes at Polymer/Oxide/Metal Interfaces under Varying Corrosive Conditions. *Corros. Sci.* **52**, 1838–1846 (2010).

30. Posner, R.; Jubb, A. M.; Frankel, G. S.; Stratmann, M.; Allen, H. C. A Simultaneous Kelvin Probe and Raman Spectroscopy Approach for In Situ Surface and Interface Analysis. *Electrochim. Acta* **76**, 34–42 (2012).

31. Posner, R.; Marazita, M.; Amthor, S.; Roschmann, K. J. Influence of Interface Chemistry and Network Density on Interfacial Ion Transport Kinetics for Styrene/Acrylate Copolymer Coated Zinc and Iron Substrates. *Corros. Sci.* **52**, 754–760 (2010).

32. Mamnone, J. F.; Sharma, S. K.; Nicol, M. Raman Spectra of Methanol and Ethanol at Pressures up to 100 kbar. *J. Phys. Chem.* **84**, 3130–3134 (1980).

33. Tian, C.S.; Shen, Y. R. Sum-Frequency Vibrational Spectroscopic Studies of Water/Vapor Interfaces. *Chem. Phys. Lett.* **470**, 1–6 (2009).

34. Sovago, M.; Campen, R. K.; Bakker, H. J.; Bonn, M. Hydrogen Bonding Strength of Interfacial Water Determined with Surface Sum-Frequency Generation. *Chem. Phys. Lett.* **470**, 7–12 (2009).

35. Auer, B. M.; Skinner, J. L. Water: Hydrogen Bonding and Vibrational Spectroscopy, in the Bulk Liquid and at the Liquid/Vapor Interface. *Chem. Phys. Lett.* **470**, 13–20 (2009).

36. Nickolov, Z. S.; Earnshaw, J. C.; McGarvey, J. J. Water Structure at Interfaces Studied by Total Internal Reflection Raman Spectroscopy. *Colloids Surf., A* **76**, 41–49 (1993).

37. Berenblut, B. J.; Dawson, P.; Wilkinson, G. R. A Comparison of the Raman Spectra of Anhydrite (CaSO_4) and Gypsum ($\text{CaSO}_4 \cdot 2\text{H}_2\text{O}$). *Spectrochim. Acta, Part A* **29**, 29–36 (1973).

38. Jubb, A. M.; Allen, H. C. Sulfate Adsorption at the Buried Fluorite–Solution Interface Revealed by Vibrational Sum Frequency Generation Spectroscopy. *J. Phys. Chem. C* **116**, 9085–9091 (2012).

39. Hug, S. J. *In Situ* Fourier Transform Infrared Measurements of Sulfate Adsorption on Hematite in Aqueous Solutions. *J. Colloid Interface Sci.* **188**, 415–422 (1997).

40. Pye, C. C.; Rudolph, W. W. An ab Initio and Raman Investigation of Sulfate Ion Hydration. *J. Phys. Chem. A* **105**, 905–912 (2001).

41. Rudolph, W. W.; Irmer, G.; Hefter, G. T. Raman Spectroscopic Investigation of Speciation in $\text{MgSO}_4(\text{aq})$. *Phys. Chem. Chem. Phys.* **5**, 5253–5261 (2003).

42. Lefèvre, G. In Situ Fourier-Transform Infrared Spectroscopy Studies of Inorganic Ions Adsorption on Metal Oxides and Hydroxides. *Adv. Colloid Interface Sci.* **107**, 109–123 (2004).
43. Nazarov, A.; Thierry, D. Studies in the Electrical Double Layer at Metal/Polymer Interfaces by Scanning Capacitive Probe. *Protection Metals.* **39**, 55–62 (2003).
44. Wielant, J.; Posner, R.; Grundmeier, G.; Terryn, H. Interface Dipoles Observed after Adsorption of Model Compounds on Iron Oxide Films: Effect of Organic Functionality and Oxide Surface Chemistry. *J. Phys. Chem. C* **112**, 12951–12957 (2008).
45. Lambert, A. G.; Davies, P. B.; Neivandt, D. Implementing the Theory of Sum Frequency Generation Vibrational Spectroscopy: A Tutorial Review. *Appl. Spectrosc. Rev.* **40**, 103–145 (2005).

Task 7: Laser Effects on Volta Potential Transients Recorded by a Kelvin Probe

7.1 Summary

A laser beam focused beneath a Kelvin probe needle allows for evaluation of laser-induced Volta potential shifts that can be used to identify (ir)reversible structural rearrangements at the sample surface. This work investigates the impact of laser irradiation on different substrate materials and the influence of laser power and wavelength to explore possible additional areas of analytical applications. Complete and instantaneous potential recovery was achieved with a 785 nm beam, whereas inverse and less meaningful potential shifts result for highly reflective Si-wafers. Moreover, similarities to photovoltage transients recorded on solar cell devices are discussed.

7.2 List of Figures and Tables

Figure 7.1 Potential and distance transients recorded on bare steel irradiated with a 785 nm laser beam (output energy: 100 mW) focused beneath the KP needle.

Figure 7.2 Potential and distance transients recorded on hematite-covered steel irradiated with a 785 nm laser beam focused beneath the KP needle and operated at output energies between 10 mW and 200 mW.

Figure 7.3 Potential and distance transients recorded on a ZnO covered zinc foil irradiated with a 785 nm laser beam (output energy: 100 mW) focused beneath the KP needle.

Figure 7.4 Potential and distance transients recorded on a Si wafer irradiated with a 785 nm laser beam (output energy: 100 mW) focused beneath the KP needle.

7.3 Introduction and Background

A combined Kelvin probe (KP) and Raman spectroscopy approach was previously introduced for spectroelectrochemical surface analysis.^{1,2} A 532 nm laser beam with probing area partly placed beneath the KP needle allows the collection of Raman spectra. Photons scattered at the sample surface influence the electrical properties of the KP plate capacitor formed by the needle tip, the sample surface, and the air gap in between. Convoluted laser-induced processes at the needle and/or sample surface possibly involve drying, adsorption/desorption of organic contaminants, photoelectric effects, and structural rearrangement of crystalline phases.^{1,2} The decrease in Volta potentials observed for laser-exposed bare steel never fully relaxed back to the initial state, while those for hematite (α -Fe₂O₃)-covered steel immediately recovered after laser exposure.¹ Recovery kinetics were strongly dependent on relative humidity but also reminiscent of photovoltage transients observed with ZnO or TiO₂ films deposited on Si wafers and solar cell devices.^{1,3-5}

To explore contributions from photovoltage and to check whether reversible and minimized laser-induced Volta potential changes can be detected with the KP, in this work transients resulting from sample exposure to 785 nm laser beams of varying power are compared to those previously observed with a 532 nm laser. Steel, macroscopic hematite layers on steel as well as ZnO and Si substrates are investigated to further assess the applicability of a KP for sophisticated spectroelectrochemical *in situ* approaches.

7.4 Lessons Learned

We have learned that the use of a Raman laser at 785 nm in the investigation of electrode substrates (alloys like steel and metal oxides like ZnO-covered Zn) with a combined Kelvin probe induces reversible reduction and instantaneous adjustment of Volta potentials, in contrast to results obtained at smaller wavelengths (532 nm). In addition, we have learned that photovoltage effects are unlikely to be responsible for these observations. Also, photo-induced potential shifts do not linearly increase with increasing laser power. More importantly, we have learned that for a highly specular substrate (Si wafer), the scattered Raman light raises the surface potential. This suggests that in order to minimize irreversible laser-induced potential shifts, Kelvin probe and Raman spectroscopy measurements should not be simultaneously performed on specular surfaces.

7.5 Experimental

Materials

As-received 1018 steel sheets (1388K15, McMaster-Carr) were ultrasonicated in acetone prior to laser exposure. Macroscopic hematite layers were prepared by annealing clean steel coupons in a muffle furnace (550-14 Isotemp, Fisher Scientific) for 5 h at 600°C in air.^{1,6} Zinc foil was purchased from Goodfellow (ZN00301; 99.95+ %, 0.2 mm thick) and annealed for 4 h at 300°C in air to form a covering ZnO film. Pieces of Si(100) wafers from Si-Tech, Inc. (62729961; 50-65 Ω) were used following successive ultrasonication in acetone and methanol.

Raman/Kelvin Probe Setup

A Raman laser probe was built in the sample chamber of a custom-made KP from the Max-Planck-Institute for Iron Research (Düsseldorf, Germany) (Fig. 7.1).^{1,2} The distance between the 500 μm diameter KP needle and the sample surface was continuously monitored. Volta potential measurements were performed in humid air (RH ≥ 80%) at ambient temperature. A continuous wave (CW) 785 nm multimode laser source (PI-ECL-785-300-SH, Process Instruments) was coupled to a fiber optic probe (RP785/12-5, InPhotonics; 7.5 mm focal length, 135 μm beam diameter at the focal spot) that focused a beam on a probing area partly beneath the KP needle at an angle of ~ 50°.

7.6 Results and Discussion

Volta Potential Transient on Bare Steel

Fig. 7.1 presents a Volta potential transient recorded on bare steel. After 5 min, a 785 nm laser beam was switched on and focused beneath the KP needle so that partial overlap between the area probed by the KP and that irradiated by the laser was achieved.¹ Similar to previous observations made with a CW 532 nm beam, an instantaneous reduction of the potential of ~40–50 mV resulted, whereas the signal describing the separation distance between the sample and KP tip remained unchanged.¹ The distance monitoring for the employed KP is based on a sensitive potential measurement by an electric circuit and it was shown that this constant distance signal indicates that the KP needle was not placed directly in the laser beam path although photons reflected at the sample surface may hit the needle.¹ At $t = 15$ min, the laser was turned off and the potential immediately recovered. This was not observed when a CW 532 nm beam was used, for which irreversible potential changes were correlated to the formation of hematite on the substrate surface.¹ A CW 632.8 nm laser also did not induce such crystalline rearrangement¹ and Fig. 7.1 now confirms that potential shifts are fully reversible even after several light on-off cycles if the laser wavelength is long enough.

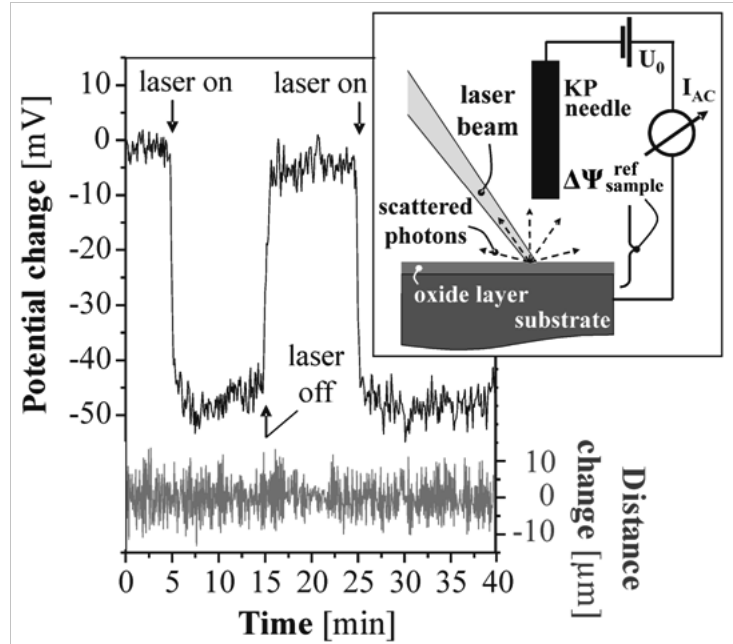


Figure 7.1. Potential and distance transients recorded on bare steel irradiated with a 785 nm laser beam (output energy: 100 mW) focused beneath the KP needle. Upper right corner: Schematic illustration of the experimental setup.^{1,2}

Volta Potential Transient on Hematite-Covered Bare Steel

Fig. 7.2 shows equivalent potential transients recorded on steel covered with a macroscopic layer of hematite. Complete and instantaneous potential recovery is observed independent of the energy output of the 785 nm laser. Very small potential changes are detectable at 10 mW (< 5

mV), whereas increasingly larger changes are observed at higher laser power outputs (~15, 25 and 30 mV at 50, 150 and 200 mW, respectively). The absolute values should not be directly compared to those detected on bare steel due to possibly varying overlaps between laser irradiated and KP probed substrate areas. However, the observed trends are reproducible and meaningful because Fig. 7.2 clearly shows a non-linear dependence between laser power output and KP potential shifts. This means that light-induced deviations of Volta potentials detected, e.g. while Raman spectra are recorded, can be effectively minimized with reduced laser power. Moreover, if higher energy output is required, the absolute value of inevitable potential shifts that have to be taken into account seems to be limited.

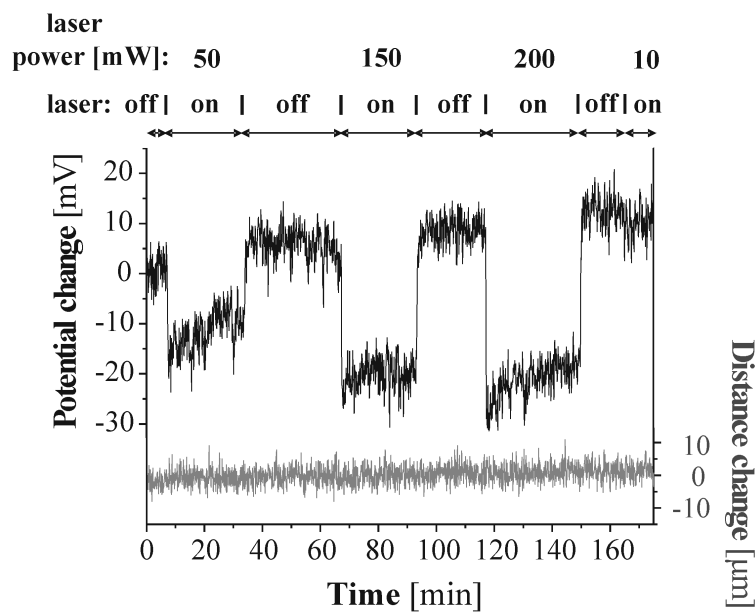


Figure 7.2. Potential and distance transients recorded on hematite-covered steel irradiated with a 785 nm laser beam focused beneath the KP needle and operated at output energies between 10 mW and 200 mW.

In contrast to experiments performed with a 532 nm laser on $\alpha\text{-Fe}_2\text{O}_3$, irradiation with 785 nm (i.e., ~ 1.6 eV) laser light should not exceed the band gap of hematite (typically, $E_g \approx 2.2$ eV⁷). It suggests that the instantaneous recovery of laser-induced KP potential shifts presented in Fig. 7.2 is not related to photovoltage effects. This conclusion is not limited to iron oxides, since in Fig. 7.3 a similar effect is observed with a Zn foil covered by a macroscopic ZnO layer. Again, immediate and completely reversible laser-induced potential changes are detected and the energy level of the large ZnO band gap ($E_g > 3$ eV) is not exceeded by the 785 nm laser.⁸

Volta Potential Transient on Highly Reflective Si Wafer

A contrasting case is shown in Fig. 7.4 for a highly reflective Si substrate. When a 785 nm beam of 100 mW is focused on a Si wafer below a KP needle, an instantaneous, large potential increase is observed, which slowly relaxes towards the initial value after the laser is turned off. The polarity of potential change is opposite, but the general shape is similar to the transients shown in Figs. 7.1 to 7.3, and to those that resulted when focusing a CW 532 nm beam on hematite at high RH¹. However, in this case, the signal corresponding to the substrate/tip separation distance changes when the light is turned on and off, as shown in Fig. 7.4. It indicates that the laser beam reflected off of the mirror-like wafer surface and irradiated the KP needle, which changed the electrical and capacitive properties of the KP needle. Under these conditions, meaningful Volta potential measurements are not possible. The transients shown in Fig. 7.4 are influenced by parasitic signals in the electrical circuit of the KP and therefore hardly reflect sample properties. In particular, the polarity of the potential change and the slow relaxation of the potential upon turning off the laser probably result from artifacts associated with the circuitry rather than physical properties of the sample. Very reflective surfaces should be consequently analyzed by separate spectroscopic and electrochemical measurements at the same sample spot rather than by a simultaneous KP-Raman spectroscopy experiment. The data presented in Fig. 7.4 also imply that artifacts from reflected laser light might influence the characteristics of photovoltage transients recorded with a KP on inorganic thin layers like ZnO deposited on carriers such as Si wafers or solar cell devices³⁻⁵

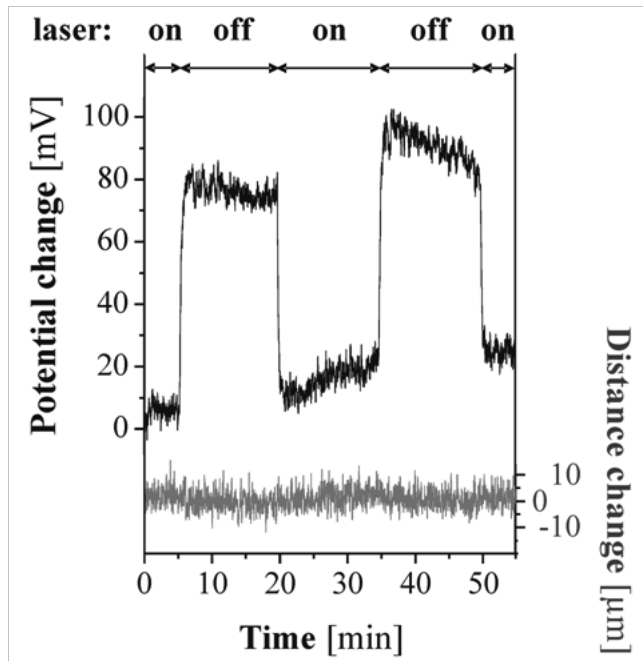


Figure 7.3. Potential and distance transients recorded on a ZnO covered zinc foil irradiated with a 785 nm laser beam (output energy: 100 mW) focused beneath the KP needle.

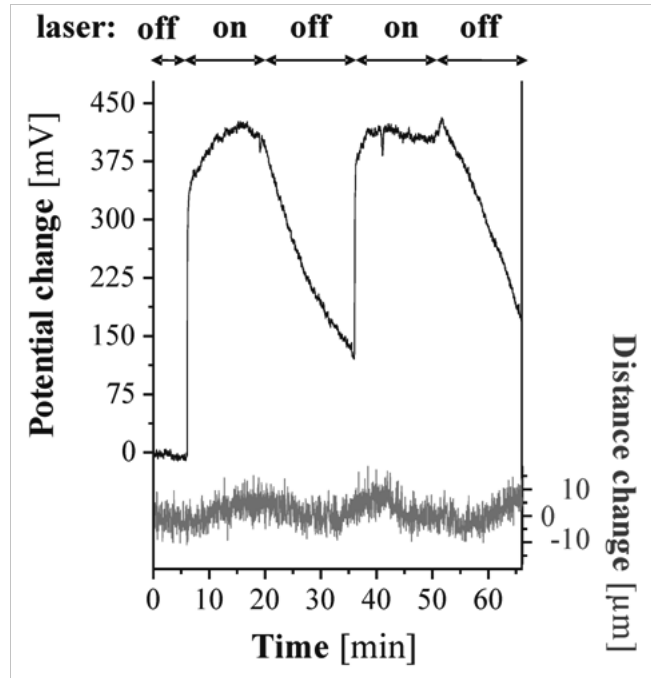


Figure 7.4. Potential and distance transients recorded on a Si wafer irradiated with a 785 nm laser beam (output energy: 100 mW) focused beneath the KP needle.

7.7 Economic Summary

This project was started before there was an emphasis placed on economic justification of the work, so no summary is presented.

7.8 Implementation

Any implementation of the combined Kelvin probe/Raman spectroscopy method for electro-optical analysis will need to make use of this work to ensure that low energetic (longer wavelength) lasers and minimized output power output are used, especially when it comes to matte finished sample surfaces. This is the first work reporting this effect.

7.9 Conclusions

In contrast to potential transients obtained with a 532 nm laser, measurements performed at a longer wavelength (785 nm) induce reversible reduction and instantaneous adjustment of Volta potentials on steel, hematite-covered steel and ZnO-covered Zn. Complete and instantaneous recovery of the Volta potential was observed under all conditions for these electrodes when 785 nm light was used. Photovoltage effects are unlikely to contribute to the results. Light-induced potential shifts do not linearly increase with increasing laser power. In contrast,

reflections of the laser beam off of reflective Si wafers raise the potential, suggesting that KP and Raman spectroscopy measurements should not be simultaneously performed on mirror-like surfaces. Undesired irreversible laser-induced potential shifts can be consequently avoided employing low energetic lasers and minimized power output on matte finished sample surfaces, which confirms a general applicability of KPs for electro-optical analysis.

7.10 References

1. Posner, R.; Jubb, A.M.; Frankel, G.S.; Stratmann, M.; Allen, H.C. A Simultaneous Kelvin Probe and Raman Spectroscopy Approach for In-Situ Surface and Interface Analysis. *Electrochim. Acta* **76**, 34–42 (2012).
2. Posner, R.; Jubb, A.M.; Frankel, G. S.; Stratmann, M.; Allen, H.C. A Simultaneous In Situ Kelvin Probe and Raman Spectroscopy Analysis of Electrode Potentials and Molecular Structures at Polymer Covered Salt Layers on Steel. *Electrochim. Acta* **83**, 327–334 (2012).
3. Li, W.; Wu, C.W.; Qin, W.G.; Wang, G.C.; Lu, S. Q.; Dong, X.J.; Dong, H. B.; Sun, Q. L. Characterization of Photovoltage Evolution of ZnO Films Using a Scanning Kelvin Probe System. *Physica B: Cond. Matter* **404**, 2197–2201 (2009).
4. Rühle, S.; Cahen, D. Observation of Transition Metals at Shunt Locations in Multicrystalline Silicon Solar Cells. *J. Appl. Phys.* **95**, 1556–1561 (2004).
5. I. D. Baikie, Surface Potential and Surface Photovoltage of Oxide and Nitride coated Multicrystalline Silicon Solar Cells Using a Scanning Kelvin Probe. *Material Research Society Symposium Proceedings* **808**, A9.12 (2004).
6. A. M. Jubb and H. C. Allen, Vibrational Spectroscopic Characterization of Hematite, Maghemite, and Magnetite Thin Films Produced by Vapor Deposition. *ACS Appl. Mater. Interfaces* **2**, 2804–2812 (2010).
7. Cornell, R. M.; Schwertmann, U. *The Iron Oxides: Structure, Properties, Reactions, Occurrences and Uses*, 2nd ed., Wiley-VCH, Weinheim, Germany, 2003.
8. Srikant, V.; Clarke, D. R. On the Optical Band Gap of Zinc Oxide. *J. Appl. Phys.* **83**, 5447–5451 (1998).